CERN 84 -09
8 August 1984

ORGANISATION EUROPÉENNE POUR LA RECHERCHE NUCLÉAIRE
CERN EUROPEAN ORGANIZATION FOR NUCLEAR RESEARCH

FOURTH TOPICAL WORKSHOP ON PROTON-ANTIPROTON COLLIDER PHYSICS

Berne, 5-8 March 1984

PROCEEDINGS

Editors: H. Hänni
J. Schacher

GENEVA
1984

© Copyright CERN, Genève, 1984

Propriété littéraire et scientifique réservée pour tous les pays du monde. Ce document ne peut être reproduit ou traduit en tout ou en partie sans l'autorisation écrite du Directeur général du CERN, titulaire du droit d'auteur. Dans les cas appropriés, et s'il s'agit d'utiliser le document à des fins non commerciales, cette autorisation sera volontiers accordée.
Le CERN ne revendique pas la propriété des inventions brevetables et dessins ou modèles susceptibles de dépôt qui pourraient être décrits dans le présent document; ceux-ci peuvent être librement utilisés par les instituts de recherche, les industriels et autres intéressés. Cependant, le CERN se réserve le droit de s'opposer à toute revendication qu'un usager pourrait faire de la propriété scientifique ou industrielle de toute invention et tout dessin ou modèle décrits dans le présent document.

Literary and scientific copyrights reserved in all countries of the world. This report, or any part of it, may not be reprinted or translated without written permission of the copyright holder, the Director-General of CERN. However, permission will be freely granted for appropriate non-commercial use.
If any patentable invention or registrable design is described in the report, CERN makes no claim to property rights in it but offers it for the free use of research institutions, manufacturers and others. CERN, however, may oppose any attempt by a user to claim any proprietary or patent rights in such inventions or designs as may be described in the present document.

CERN 84 -09
8 August 1984

ORGANISATION EUROPÉENNE POUR LA RECHERCHE NUCLÉAIRE
CERN EUROPEAN ORGANIZATION FOR NUCLEAR RESEARCH

FOURTH TOPICAL WORKSHOP ON PROTON-ANTIPROTON COLLIDER PHYSICS

Berne, 5-8 March 1984

PROCEEDINGS

Editors: H. Hänni
J. Schacher

GENEVA
1984

Universität Bern
Physikalisches Institut
Laboratorium für
Hochenergiephysik

4th TOPICAL WORKSHOP ON PROTON ANTIPROTON COLLIDER PHYSICS

Previous workshops:
Collège de France 1979, University of Wisconsin 1981, Rome University 1983

BERN, MARCH 5-8, 1984

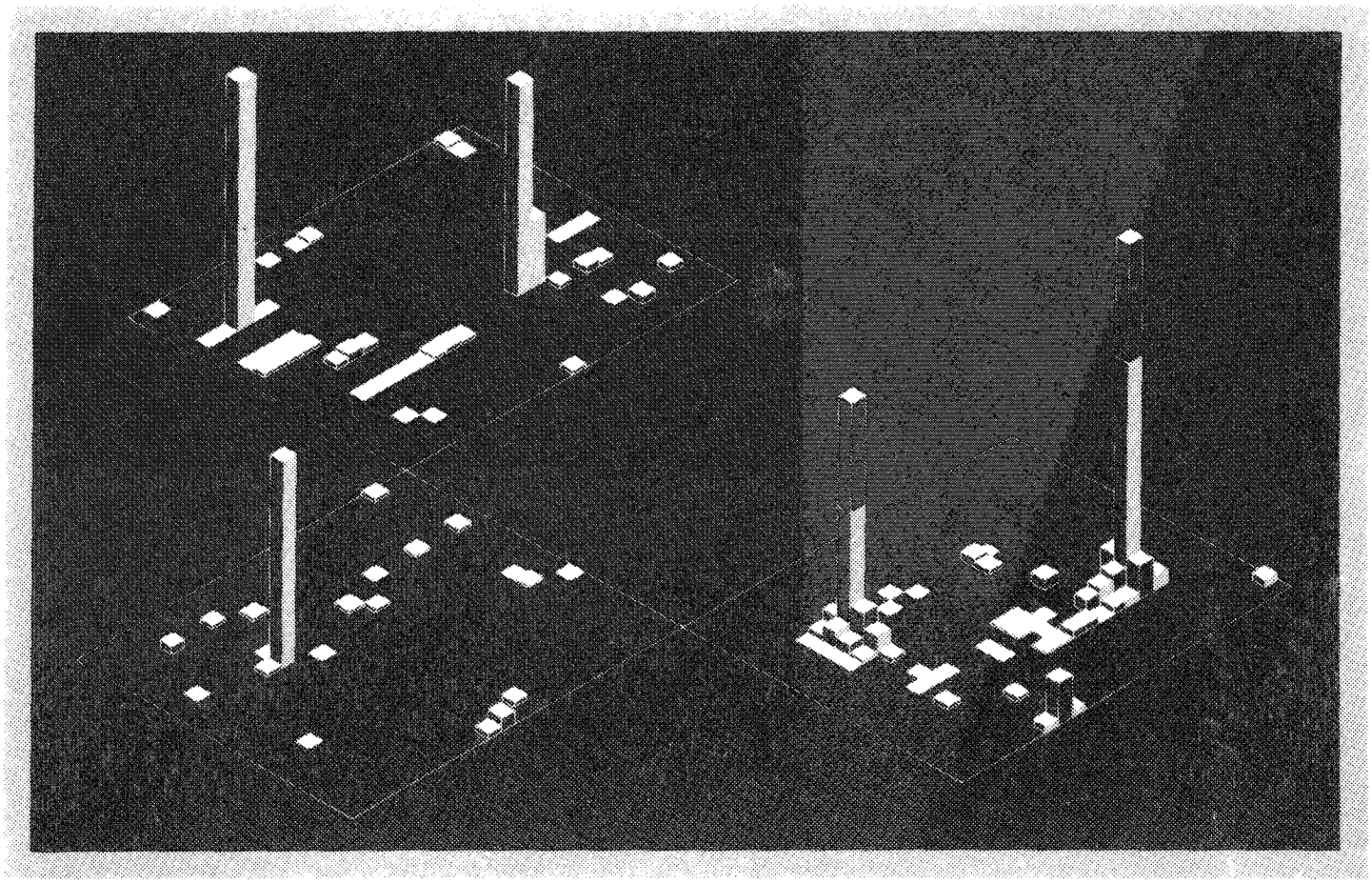

TOPICS:
- $W^{\pm}$ and Z^{0} physics
- Jets and QCD
- Heavy flavours, Higgs, ...
- Supersymmetry and substructure
- Present and future $p\bar{p}$ and pp-colliders
- Future $p\bar{p}$-physics

ADVISORY COMMITTEE

G. Brianti
P. Darriulat
B. Hahn
P. Minkowski
J. Mulvey
D. Nanopoulos
C. Rubbia
G. Salvini
A. Tollestrup

LOCAL ORGANIZING COMMITTEE

K. Borer
J. Gasser
H.Hänni
B. Hahn (Chairman)
P. Mani
J. Schacher
F. Stocker
W. Zeller

ADDRESS

Mrs. I. Mani
Laboratorium für
Hochenergiephysik
Sidlerstrasse 5
CH-3012 Bern
Switzerland

ABSTRACT

The most exciting topic at this Workshop was clearly the experimental hint for new unexpected phenomena, reported by the UA1 and UA2 Collaborations: At the CERN SPS Collider ($\sqrt{s}$ = 540 GeV), a few events were observed with high missing transverse energy in association with an isolated electromagnetic cluster or one or more hard jets (UA1) or an isolated electron and one or two hard jets (UA2).
Due to the enhanced data sample, the discovery of the intermediate vector bosons W and Z in 1983 was undoubtedly confirmed, and the nice agreement of their properties with the predictions of the electroweak theory was shown. In addition, many new results on experimental and theoretical jet physics were presented.
The Tevatron Collider project and its planned experiments at Fermilab were discussed, and there were contributions about the possible future developments in theory (compositeness, supersymmetry) as well as in experimental high energy physics (Supercollider, Juratron).

FOREWORD

It was with great pleasure that we, the members of the High Energy Physics Lab of the University of Berne (Switzerland), have organized the 4th Topical Workshop on Proton-Antiproton Collider Physics, which was held in the aula of the Berne University on March 5-8 1984. We would like to thank everybody who has contributed to it in one way or another to make it successful.
Our special thanks go to the speakers whose talks formed the flesh of the conference and who have been so kind as to send us their written versions within a reasonable time (with a few exceptions, of course).

The highlight of the previous Workshop held in Rome in January 1983 was clearly the presentation of the first candidates for the leptonic decay of the charged intermediate vector boson W with exactly the features expected from the Glashow-Salam-Weinberg model of the electroweak interaction. In this respect, the Berne Workshop has brought not only the confirmation of the existence of the W boson and of its neutral partner, the Z boson, but impressive verification of the electroweak theory as a whole: The properties of the intermediate vector bosons measured by UA1 and UA2 at the CERN $p\bar{p}$ collider are in excellent agreement with the predictions of the standard model.
However, while the so called "conventional" physics seemed to be safer than ever, the attention of the participants was driven to a few unexpected events which may well lead high energy physics beyond the minimal model of the weak interaction: UA1 has reported on events with high missing transverse energy containing an isolated electromagnetic cluster or one or more hard jets. UA2 in its turn has found a few events with high missing transverse energy, an isolated electron and one or two hard jets. None of these events are likely to come from ordinary W or Z production and decay, or from other known processes. The UA2 events, of which one is compatible with W-pair production, suggest an unknown massive state well above the W and Z mass. A hint of such a new massive object is also seen in the two-jet mass distribution of UA2.
Whether all these new phenomena will stay and be confirmed at the 5th $p\bar{p}$ Workshop, which will be held at Saint-Vincent in the Aosta valley from February 25th to March 2nd 1985, we do not know. But surely with the next CERN $p\bar{p}$ run at $\sqrt{s}$=630 GeV starting in September of this year there is an exciting time to come for the high energy physics community. In this sense the Berne Workshop has just signaled the start of a race into an "exotic" land of new physics.

The exciting adventure of exploring this new land will be shared soon by our colleagues working at Fermilab, as we learned from various interesting talks about the Tevatron $p\bar{p}$ collider project and its experiments CDF and D0.

Finally we hope that those who attended this conference enjoyed their time in Berne. Our University is proud of having been given the opportunity to host this Workshop, following its tradition as a place where revolutionary physics has evolved.

We would like to thank A. Günther from CERN as well as the CERN Authorities for their permission and support in bringing these Proceedings out as a CERN yellow report.

Hans Hänni, Univ. of Berne
Jürg Schacher, Univ. of Berne

ACKNOWLEDGEMENTS

We would like to thank Prof. Fritz Gygi for the hospitality he offered in the new aula of the University of Berne, as well as for his nice opening speech of the conference.
We are also grateful to the Vice President of the Government of the Canton of Berne, Dr. Hans Krähenbühl, who not only provided a cocktail party at the Berne Rathaus, but also delivered a welcome speech which was highly appreciated.
Special thanks go to Mrs. Ida Mani and to Mrs. Vera Dvorak for their excellent secretarial work. They have been kindly assisted during the conference by Mrs. Mirella Keller of CERN.
We gratefully acknowledge the financial support of the Scientific Institutions and other Authorities that made this Workshop possible:

- CRISMATEC, Grenoble, France

- Schweizerischer Nationalfonds zur Förderung der wissenschaftlichen Forschung

- Schweizerische Naturforschende Gesellschaft

- Bernische Kraftwerke AG

- Gfeller Telecommunications, Bern

- Phil. nat. Fakultät der Universität Bern

The Organizing Committee

CONTENTS

	Page No.
Foreword	vii
B. Hahn Introduction	1
Jet Physics	5
W. Scott (UA1 Collaboration) Jets in the UA1 experiment	6
J.R. Hansen (UA2 Collaboration) High p_T jets from $p\bar{p}$ collisions at $\sqrt{s}$ = 540 GeV in UA2	20
R.D. Field Jet topologies in hadron-hadron collisions	46
G. Schierholz Comparison of quark and gluon jets	84
Z. Kunszt Triple and quadruple jets	102
B. Humpert Jets: what we can still learn ...	108
W.M. Geist Recent results from high transverse momentum processes at the ISR	114
R.K. Ellis Transverse momentum distributions of jets and weak bosons	132
W,Z Physics and Standard Model	141
J. Schacher (UA2 Collaboration) Production of high mass $e\nu$ and e^+e^- pairs in the UA2 experiment at the CERN $p\bar{p}$ collider	142
W.J. Marciano Electroweak interaction parameters	165
P. Minkowski ($W^{\pm}$,Z): Production from $p\bar{p}$ and decay	181
M. Greco QCD p_T effects in W/Z and jet production	202
F. Herzog Testing the WWγ coupling of the Glashow-Salam-Weinberg model at $p\bar{p}$ colliders	209

The New Events 217

C. Rubbia (UA1 Collaboration)
Experimental observation of events with large missing transverse energy accompanied by a jet or a photon(s) in $p\bar{p}$ collisions at $\sqrt{s}$ = 540 GeV 218

A. Roussarie (UA2 Collaboration)
Observation of electrons produced in association with hard jets and large missing transverse momentum in $p\bar{p}$ collisions at $\sqrt{s}$ = 540 GeV 219

Heavy Flavours and Related Topics 231

R. Frey (UA1 Collaboration)
$D^{*\pm}$ production at the CERN SPS collider 232

C. Jarlskog
Weak mixing angles and heavy flavours 237

F. Halzen and A.D. Martin
The search for new flavours 260

W.J. Stirling
The minimum mass technique for detecting new heavy states in high energy hadron collisions 276

UA5 Results 285

P. Carlson (UA5 Collaboration)
New results from UA5: strange particle (K^0, Λ, Ξ^-) production and large fluctuation in multiplicities 286

$p\bar{p}$ and pp Elastic Scattering 307

A. Martin
Elastic scattering 308

R. Henzi
New shape-effects in proton-antiproton elastic scattering 314

F. Cervelli
New measurement of elastic scattering and total cross-section at the CERN $p\bar{p}$ collider 322

LEAR Physics 323

K. Kilian
Physics with antiprotons at LEAR 324

Upgrading of CERN $p\bar{p}$ Collider and Experiments 343

B. de Raad
The SPS $p\bar{p}$ collider. Present performance and future prospects 344

R. Billinge
$p\bar{p}$-source at CERN 357

H. Hoffmann
UA1 improvement programme 365

P. Jenni (UA2 Collaboration)
UA2 future 366

Fermilab $p\bar{p}$ Collider and Experiments 367

M. Harrison
The Fermilab $p\bar{p}$ collider 368

D. Theriot
The collider detector (CDF) at Fermilab - An overview 379

M.D. Marx
The DØ project at Fermilab 396

J. Freeman
Transverse energy physics with the CDF calorimeter 416

G.E. Theodosiou
DØ: Missing-p_T physics and detector design considerations 425

K. Kondo
CDF electromagnetic shower counters 432

Supercolliders 441

I. Hinchliffe
Supercollider physics 442

G. Brianti
Large hadron collider in the LEP tunnel 456

Beyond the Standard Model 473

D. Wyler
Higgs scalars and alternatives 474

R.D. Peccei
Compositeness and the Fermi scale 483

G. Pancheri
Excited fermions 502

A. Masiero
Gluino mass and CP violation in supersymmetric models 519

C. Kounnas
Low energy particle spectrum from supergravity 526

D. Nanopoulos
Supersymmetry 533

Summary and Conclusions 535

J. Ellis
New collider physics 536

List of participants 575

LIST OF CHAIRMEN

G. Brianti (CERN)
I. Butterworth (CERN)
P. Darriulat (CERN)
L. Di Lella (CERN)
G. Ekspong (Univ. of Stockholm)
R. Gatto (Univ. of Geneva)
M. Jacob (CERN)
H. Leutwyler (Univ. of Berne)
D. Nanopoulos (CERN)
G. Salvini (Univ. of Rome)
W. Selove (Univ. of Pennsylvania)
A. Tollestrup (Fermilab)

Introduction

Hopefully more interesting things are to appear during this conference than I will be able to say in this introduction. Therefore I limit myself to a few remarks which have to do with the efforts done exactly 20 years ago, when we were searching for the W at Brookhaven and at CERN with ν-beams. At that time it was suggested by Lee, Yang and Yamaguchi, that we should look for the W in the interaction $\nu_\mu A \to W^+ \mu^- X$ with $W^+ \to e^+ \nu_e$ or $\mu^+ \nu_\mu$

with the nice signatures of a μ-pair or a μ-e pair. In the spark chamber group at CERN we were just 13 physicists, mostly Professors, and we had a lot of fun since several μ-μ and μ-e pair candidates showed up. At the Siena Conference in 1963 Louis Alvarez asked the authoritarian question: "When I go home to Berkeley can I say to my colleagues you have found the W, yes or no ?". There was a loud silence, from which he concluded that the answer was no and he was right. A careful analysis showed that the interesting candidates must have been due to non interacting charged pions or to electron showers coming from neutral pions, the decay γ's converting very close to the vertex. For general amusement, I should mention that in the 1964 publication it read at one place immediate boson instead of intermediate boson and indeed the W disappeared immediately. Only a lower limit for the W-mass of approximately 2 GeV could be quoted in the paper of the spark chamber experiment. The personal merit for the limit was 150 MeV per physicist.

Subsequently the limit was pushed up by Brookhaven to 8 GeV. Then a long time span elapsed until the Rome and Berne meeting with new discoveries inbetween, in particular that of the weak neutral currents. The efforts increased with respect to machines, detectors, number of physicists, but not much on the financial side. Five years ago the experimentalists and the machine physicists and engineers got a difficult home work assignment given by a number of theoreticians. As you know, this task was not easy and I

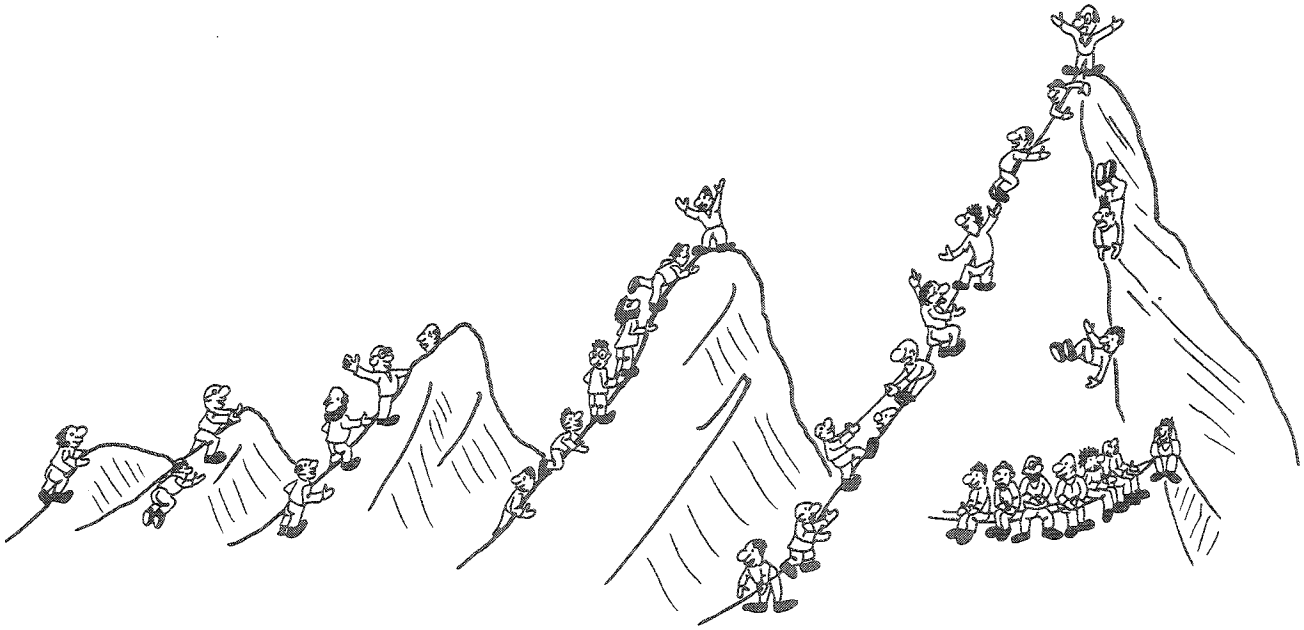

consider the technical and experimental achievements a minor miracle, since they were accomplished in a style, which I call the pseudodemocratic collective style which is strongly contradictory to what we would expect of scientists, who are by definition intro or extraverted individuals. But obviously it depends on the goal.

The situation is illustrated in the following picture, which represents the climbing by more and more competitors of a mountain chain which becomes higher and higher. Some climbers must be pushed by their colleagues, some return and give up, some fall down and a few succeed to be among the first group. I am further tempted to compare the situation to a sport race, the difference being that in sport, you can be first and get a medal but in physics you can be first and have a discovery and a medal. The personal merit per physicist in this marathon is the discovery of 500 MeV each of the W and Z°, which have been found in this picture on the last mountain, the one which looks like the Matterhorn.

Where are we now at this workshop ? We are sitting in a comfortable bivouac at some altitude and are thinking. There is no big or bigger unclimbed mountain in sight. Instead there is a predesert in view and there is already one man rushing away, whose name I prefer not to mention. This time the machine people and the experimentalists are taking the lead. There is only very vague guidance by the theoreticians as to where to go, and in fact they take from the hands of the experimentalists each crazy event and rush to interpret it prematurely. I leave to John Ellis, who was so kind as to accept the job of drawing the conclusions at the end of the workshop, the task of forecasting the future.

To close my introduction I would like to say a word on the Bernese. They are internationally known to be very slow but good natured and agreeable. I am from Basle. Anyhow, we have nice weather here in Berne, and I recommend that you partake of this conference for your pleasure. I wish you a nice stay in Berne and maybe also some surprises in Physics.

Beat Hahn

Jet Physics

JETS IN THE UA1 EXPERIMENT

W.G. Scott (UA1 Collaboration)
Rutherford Appleton Laboratory, UK
and CERN, Geneva, Switzerland

1. TWO-JET CROSS-SECTION

1.1 Introduction

The UA1 two-jet cross-section based on the 1982 data has been published already[1]. We review that data briefly here and make a few additional comments.

1.2 Theory

A point we emphasize particularly is the theoretical simplicity of the two-jet cross-section in QCD. In a very good approximation the entire two-jet cross-section may be described in terms of a $(1 - \cos\theta)^{-2}$ dependence on c.m.s. scattering angle θ which is completely analogous to the Rutherford scattering formula, and a single pure flavour singlet structure function:

$$F(x) = G(x) + 4/9\ [Q(x)+\bar{Q}(x)]\ . \qquad (1)$$

This approximate description becomes exact in the limit $\cos\theta \to 1$, i.e. for small c.m.s. scattering angles.

1.3 Angular distributions

The angular distributions for various $x_1 x_2$ intervals are shown in Fig. 1. The combined angular distribution obtained on the assumption that the angular dependence is independent of x_1 and x_2 is shown in Fig. 2. The combined angular distribution (Fig. 2) uses all the available statistics but has the disadvantage that x_1 and x_2 (and hence, for example, the relative contributions of the various subprocesses) are varying across the plot. In general we prefer the angular distributions separated in x_1 and x_2.

In Fig. 2 the axes have been chosen to display a power law dependence $(1 - \cos\theta)^n$ for $\cos\theta \to 1$. The data have a tendency to rise above the leading order predictions ($n = 2$) for large $\cos\theta$ and this is reflected in the fitted value of n ($n = 2.38 \pm 0.10$ for $\cos\theta > 0.4$).

A similar effect has been observed previously in an ISR experiment[2] and was satisfactorily accounted for largely in terms of the variation of α_s with Q^2.

Figure 3 shows the combined angular distribution plotted versus the variable $\chi = (1 + \cos\theta)/(1 - \cos\theta)[\cot^2 \theta/2]$, defined by Combridge and Maxwell[3]. If the angular dependence follows the Rutherford law precisely then the χ distribution will be flat. In Fig. 3 the solid curves represent the χ dependence predicted by leading order QCD and the broken curves indicate the expected modification due to the Q^2 dependence of α_s. We conclude that it will be necessary to account properly for the Q^2 dependence of α_s before any attempt is made to distinguish the various subprocesses on the basis of the angular distribution.

1.4 Factorization test

Figure 4 shows the test of factorization in x_1 and x_2. We remark that the factorization test is independent of the assumed value of K and largely independent of energy scale uncertainties and smearing corrections.

1.5 Structure functions

Figure 5 shows the structure function F(x) computed from the two-jet data assuming factorization in x_1 and x_2 and K = 2. Note that the variation of α_s with Q^2 has been taken into account in the determination of the structure function. The systematic error (due to the uncertainty in the jet energy scale) is estimated to be $\simeq \pm 30\%$.

Over most of the available range in x the data show a largely exponential x dependence suggestive of a statistical sharing of momentum between the partons[4]. The data are in fair agreement with measurements of F(x) extrapolated in Q^2 from fixed target (neutrino) experiments[5,6] where the gluon contribution has been inferred from measurements of the scaling violations.

As a final step we subtract from the two-jet data the quark and antiquark contributions (as extrapolated from the fixed target experiments) in

order to obtain the gluon structure function directly. The gluon structure function is shown in Fig. 6 where the plotted errors include the estimated systematic errors on the two-jet data. Two fits have been made to the data:

$$G(x) = (12.0 \pm 3.2)(1 - x)^{16.0\pm2.6} \qquad x = 0.05\text{–}0.8$$
$$= (7.9 \pm 1.8)(1 - x)^{11.6\pm1.9} \qquad x = 0.1\text{–}0.80 \ . \tag{2}$$

We conclude that for these values of Q^2 the gluon distribution is a very rapidly falling function of x and in particular for $x \geq 0.3$ the contribution of the gluons is unmeasurably small.

1.6 Jet charge asymmetry

Figure 7 shows some preliminary data on the mean charge of the leading track/jet as a function of the pseudo-rapidity of the jet. The data are based (in part) on 1983 jet data analysed with a high E_T threshold ($E_T > 40$ GeV). There is a marked preference for jets with positive leading tracks in the proton arm and jets with negative leading tracks in the antiproton arm, demonstrating clearly that not all the jets detected result from gluon-gluon scattering. It is possible that such an effect could serve as a basis for isolating a valence quark structure function in $p\bar{p}$ experiments.

2. JETS IN W/Z EVENTS

2.1 Introduction

In this section we report on a preliminary study of jets in events, with an identified $W^{\pm}$ or Z^{o} (W/Z) events), for example:

$$p\bar{p} \rightarrow (W + \text{jet})x \ . \qquad \hookrightarrow e\nu \tag{3}$$

2.2 Data sample

The data is based on a sample of 75 W/Z events[7,8]. Jets have been defined using the UA1 jet algorithm. Table 1 lists the number of events with 0, 1, 2, etc. jets for the various W/Z channels.

In Fig. 8 the histogram represents the E_T spectrum of all jets in the W/Z sample. The spectrum extends to $E_T \simeq 25$ GeV. The effective threshold for jets defined by the jet algorithm is $E_T \simeq 5$ GeV.

2.3 The W/Z jet correlation

Figure 9 shows the transverse momentum of the W/Z plotted versus the E_T of the highest E_T jet for events with ≥ 1 jet. For W events the transverse momentum of the W(p_T^W) is measured by the vector sum of the transverse momentum in all the calorimeter cells. Clearly the transverse momentum of the W/Z and the E_T of highest E_T jet are strongly correlated.

In Fig. 10a the histrogram shows the difference in the azimuthal angle ϕ measured around the beams between the transverse momentum vector of the W/Z and the highest E_T jet. Figure 10b shows the same histogram for additional jets apart from the highest E_T jet. Clearly the highest E_T jet is predominantly back to back in ϕ with the W/Z while additional jets apart from the highest E_T jet are essentially uncorrelated with the W/Z.

We can conclude that for W/Z events with jets, the transverse momentum of the W/Z is locally compensated by the highest E_T jet.

2.4 W/Z jet c.m.s. angular distribution

Jet production in W/Z events is expected in QCD mainly as a result of initial state gluon bremsstrahlung by the annihilating quark or antiquark. Very naively we expect:

$$\frac{d\sigma}{d\cos\theta^*} \approx \frac{GM_W^2\alpha_s}{\hat{s}} \frac{1}{(1-\cos\theta^*)} \qquad (4)$$

where $\hat{s}$ is the W/Z jet c.m.s. energy (M_{WJ}) squared and θ^* is the angle of the W/Z (or jet) momentum measured with respect to the beam in the W/Z jet c.m.s. system. The angular dependence $(1-\cos\theta^*)^{-1}$ appearing in Eq. (4) is characteristic of bremsstrahlung and corresponds roughly (exactly in the limit $\cos\theta^* \to 1$) to a flat pseudo-rapidity distribution. We can test the bremsstrahlung interpretation by plotting the data versus $\cos\theta^*$ and M_{WJ} and comparing with detailed theoretical predictions.

In this report we focus attention on the distribution in cos θ^*. Since the acceptance for low E_T jets is necessarily somewhat uncertain we compare the W/Z jet data with a selected sample of multijet events. The multijet sample is selected such that M_{JJ} = 70-90 GeV ($\simeq M_{W/Z}$) and the c.m.s. scattering angle θ (defined by the two highest E_T jets) satisfies cos θ < 0.2. The additional jets in the multijet events (apart from the two highest E_T jets) are believed to be predominantly due to initial state bremsstrahlung processes. In Fig. 8 and Fig. 10 the data points with error bars represent the multijet data.

In Fig. 11a the histogram represents the distribution in cos θ^* for the highest E_T jet in the rest frame of the W/Z and the highest E_T jet. Figure 11b shows the same distribution for additional jets (apart from the highest E_T jet). For the additional jets cos θ^* has been computed in the rest frame of the W/Z and the highest E_T jet. In each case the data points with error bars represent the corresponding distributions defined from the multijet data. Both histograms show a pronounced peaking at cos $\theta^* \simeq \pm 1$ in fair agreement with the multijet data. In Fig. 12 we compare the overall yield of jets/event in W/Z events with the yield of additional jets/event in the multijet events as a function of cos θ^*. The solid curve shows a $(1 - \cos\theta)^{-1}$ dependence normalized to the W/Z data in the region cos $\theta^* < 0.9$. We conclude that the yield of jets in W/Z events and the yield of jets in multijet events are comparable and show a similar cos θ^* dependence consistent with $(1 - \cos\theta^*)^{-1}$.

2.5 Conclusion

Further studies should include an analysis of the W/Z jet mass plot. Provisionally we conclude that the majority of jets in W/Z events are probably due to initial state bremsstrahlung processes.

REFERENCES

1) G. Arnison et al., UA1 Collaboration, Phys. Lett. 136B (1984) 294.

2) A.L.S. Angelis et al., CCOR Collaboration, Nucl. Phys. B 209 (1982) 284.

3) B. Combridge and C. Maxwell, Nucl. Phys. B238 (1984).

4) C. Angelini and R. Pazzi, Phys. Lett. 113B (1982) 343.

5) H. Abramowicz et al., CDHS Collaboration, Z. Phys. C 12 (1982) 282.
F. Eisele, private communication.

6) F. Bergsma et al., Phys. Lett. 123B (1983) 269.
K. Winter, private communication.

7) G. Arnison et al., UA1 Collaboration, Phys. Lett. 129B (1983) 213.

8) G. Arnison et al., UA1 Collaboration, Phys. Lett. 126B (1983) 398.

Table 1

Number of events/jets for various W/Z channels

Channel	Total	≥ 1 jet	1 jet	2 jets	3 jets	Total no. of jets
$W \to e\nu$	52	14	10	2	2	20
$W \to \mu\nu$	14	4	4	–	–	4
$Z \to e\bar{e}$	4	3	–	2	1	7
$Z \to \mu\bar{\mu}$	5	3	1	–	2	7
TOTAL	75	24	15	4	5	38

Figure captions

Fig. 1 : Angular distributions for various $x_1 x_2$ intervals.

Fig. 2 : The combined angular distribution computed assuming the angular dependence is independent of x_1 and x_2.

Fig. 3 : The combined angular distribution plotted versus $\chi = \cot^2 \theta/2$.

Fig. 4 : Tests of factorization in x_1 and x_2.

Fig. 5 : The UA1 structure function. The curves are based on measurements of structure functions in fixed target (neutrino) experiments extrapolated to $Q^2 = 2000\ GeV^2$.

Fig. 6 : The gluon structure function G(x) obtained for the two-jet data by subtracting the quark and antiquark contribution measured (and extrapolated) from neutrino experiments.

Fig. 7 : The mean charge of the leading track/jet plotted versus the pseudo-rapidity of the jet.

Fig. 8 : The E_T spectrum of jets in W/Z events (histogram) compared to multijet data (data points).

Fig. 9 : Scatter plot of the E_T of the highest E_T jet versus the transverse momentum of the W/Z. The Z^0 events are represented by the open circles.

Fig. 10 : a) The azimuthal angle ϕ between the transverse momentum vector of the W/Z and the highest E_T jet (histogram). The data points represent the multijet data.
b) The same as for a) but for additional jets apart from the highest E_T jet.
In a) and b) the shaded area represents the contribution of the jets in Z^0 events alone.

Fig. 11 : a) The distribution in $\cos \theta^*$ for the highest E_T jet in W/Z events.
b) For additional jets apart from the highest E_T jet (histograms). The data points represent the corresponding plots for the multi-jet data.

Fig. 12 : The overall yield of jets/event in W/Z events (closed circles) and in multijet events (open circles) as a function of $\cos \theta^*$. The curve shows a $(1 - \cos \theta^*)^{-1}$ dependence normalized to the data with $|\cos \theta^*| < 0.9$.

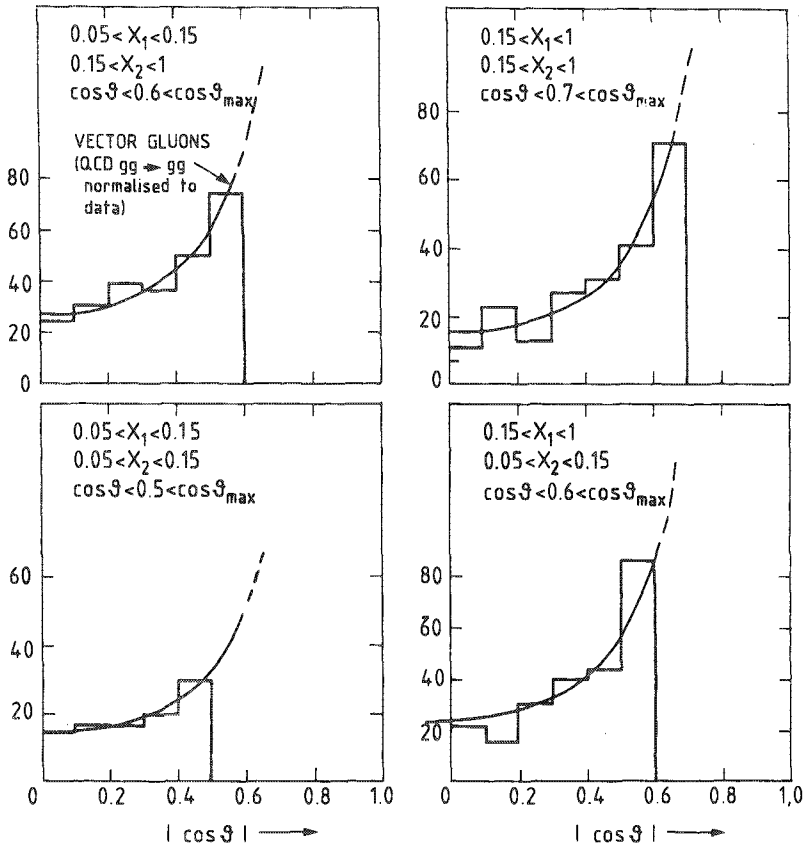
0.05<X1<0.15
0.15<X2<1
cosϑ<0.6<cosϑmax
VECTOR GLUONS
(QCD gg → gg
normalised to
data)
0.15<X1<1
0.15<X2<1
cosϑ<0.7<cosϑmax
0.05<X1<0.15
0.05<X2<0.15
cosϑ<0.5<cosϑmax
0.15<X1<1
0.05<X2<0.15
cosϑ<0.6<cosϑmax
| cosϑ | ⟶
| cosϑ | ⟶

Fig. 1

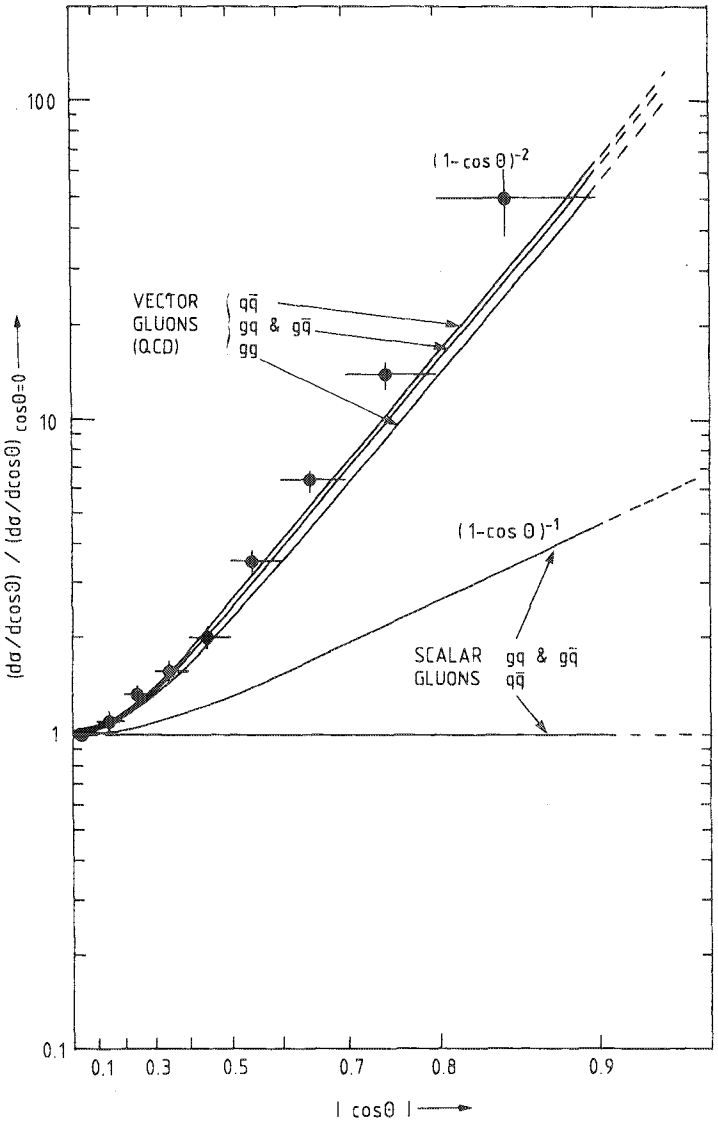
(dσ/dcosϑ) / (dσ/dcosΘ) cosΘ=0 ⟶
| cosΘ | ⟶
(1-cos Θ)⁻²
VECTOR
GLUONS
(QCD)
qq̄
gq & gq̄
gg
(1-cos Θ)⁻¹
SCALAR
GLUONS
gq & gq̄
qq̄

Fig. 2

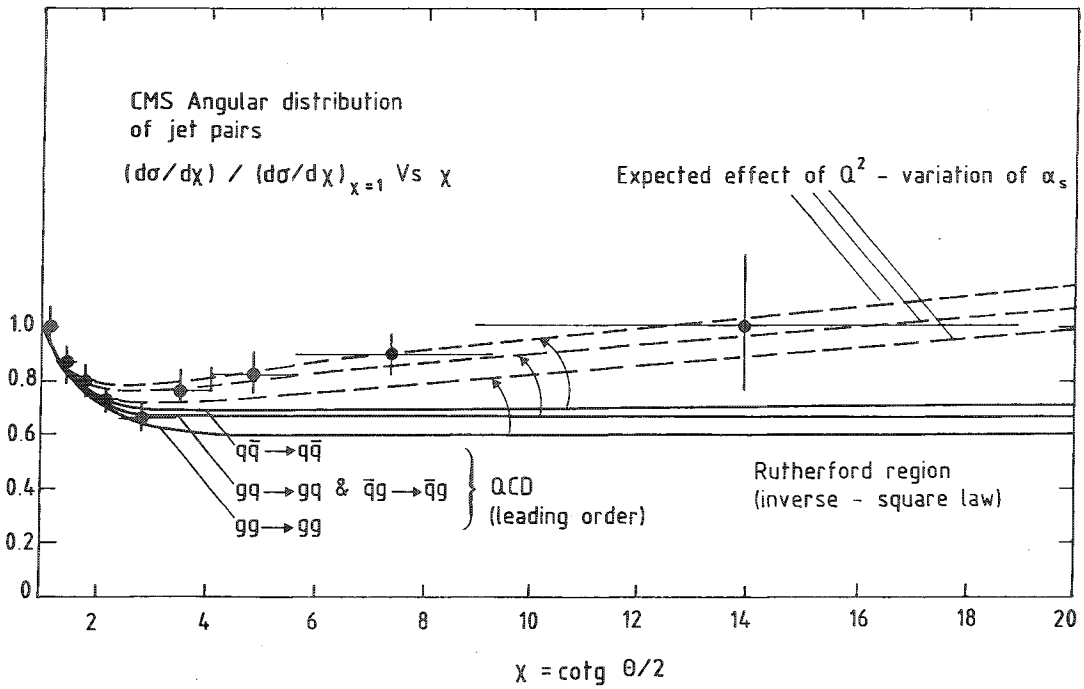
CMS Angular distribution
of jet pairs
$(d\sigma/d\chi) / (d\sigma/d\chi)_{\chi=1}$ Vs χ
Expected effect of Q^2 - variation of α_s
$q\bar{q} \rightarrow q\bar{q}$
$gq \rightarrow gq$ & $\bar{q}g \rightarrow \bar{q}g$
$gg \rightarrow gg$
QCD
(leading order)
Rutherford region
(inverse - square law)
1.0
0.8
0.6
0.4
0.2
0
2
4
6
8
10
12
14
16
18
20
$\chi = \cot g\ \theta/2$

Fig. 3

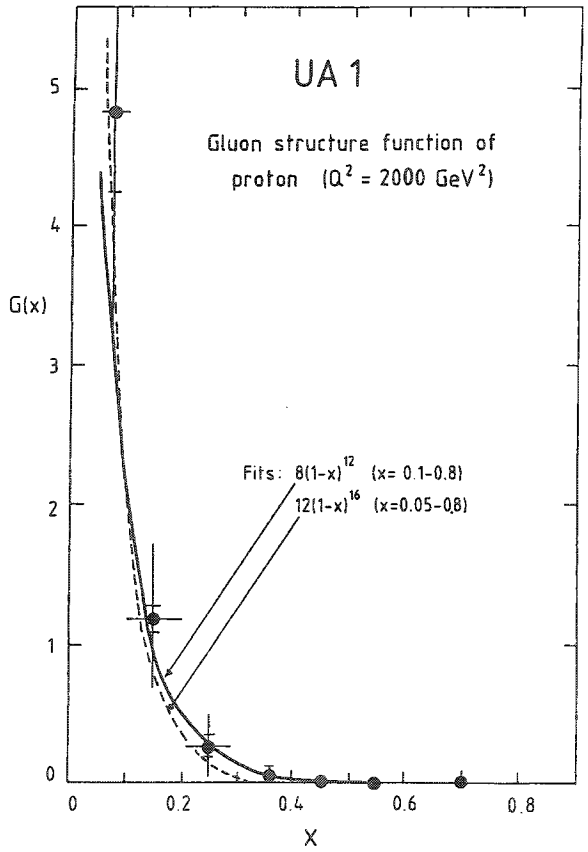
UA 1
Gluon structure function of
proton (Q^2 = 2000 GeV^2)
Fits: $8(1-x)^{12}$ (x= 0.1-0.8)
$12(1-x)^{16}$ (x=0.05-0.8)
G(x)
5
4
3
2
1
0
0
0.2
0.4
0.6
0.8
X

Fig. 4

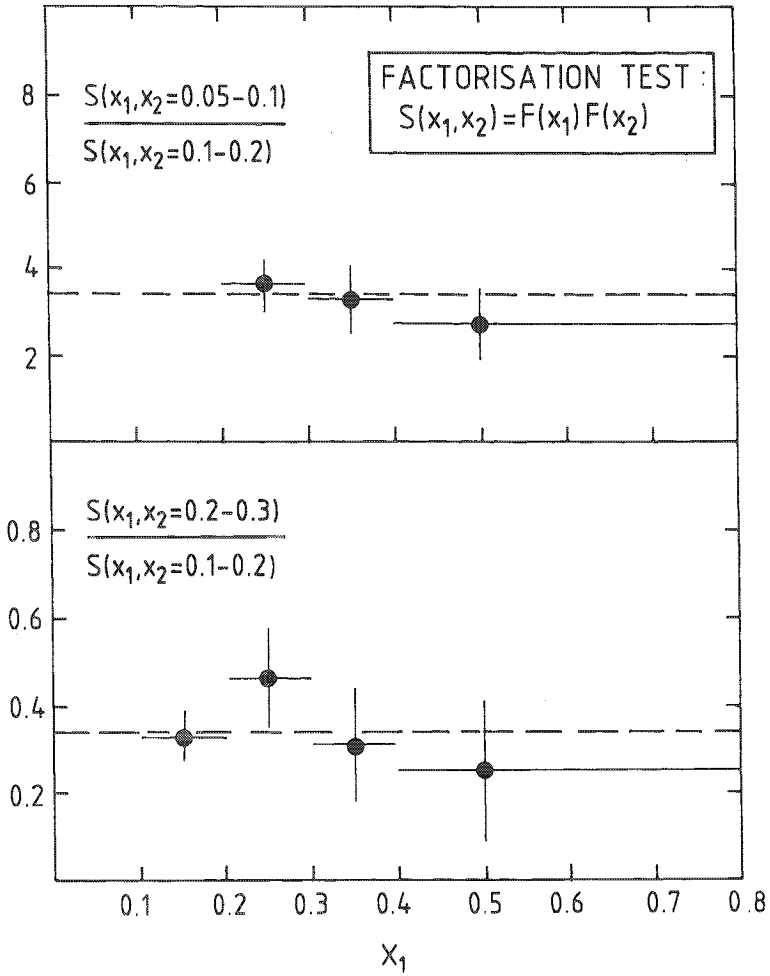
FACTORISATION TEST :
$S(x_1,x_2)=F(x_1)F(x_2)$
$\frac{S(x_1,x_2=0.05-0.1)}{S(x_1,x_2=0.1-0.2)}$
$\frac{S(x_1,x_2=0.2-0.3)}{S(x_1,x_2=0.1-0.2)}$
8
6
4
2
0.8
0.6
0.4
0.2
0.1
0.2
0.3
0.4
0.5
0.6
0.7
0.8
X_1

Fig. 5

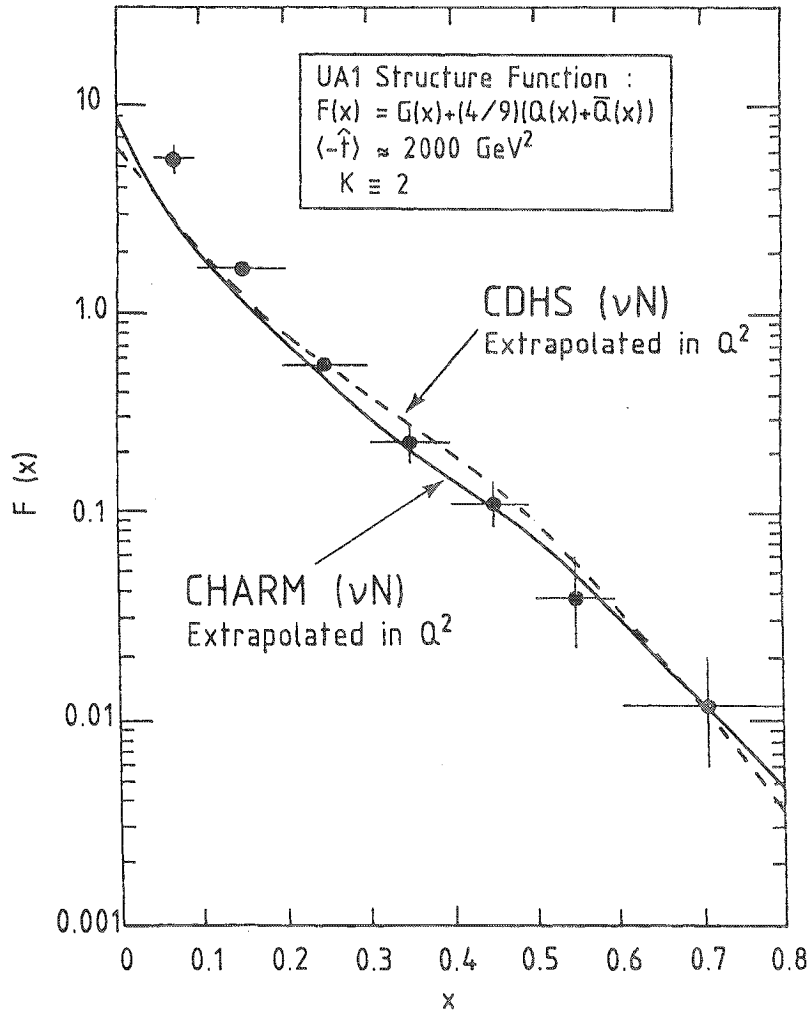
UA1 Structure Function :
$F(x) = G(x)+(4/9)(Q(x)+\bar{Q}(x))$
$(-\hat{t}) \approx 2000\ GeV^2$
$K \equiv 2$
CDHS (νN)
Extrapolated in Q^2
CHARM (νN)
Extrapolated in Q^2
F (x)
10
1.0
0.1
0.01
0.001
0
0.1
0.2
0.3
0.4
0.5
0.6
0.7
0.8
x

Fig. 6

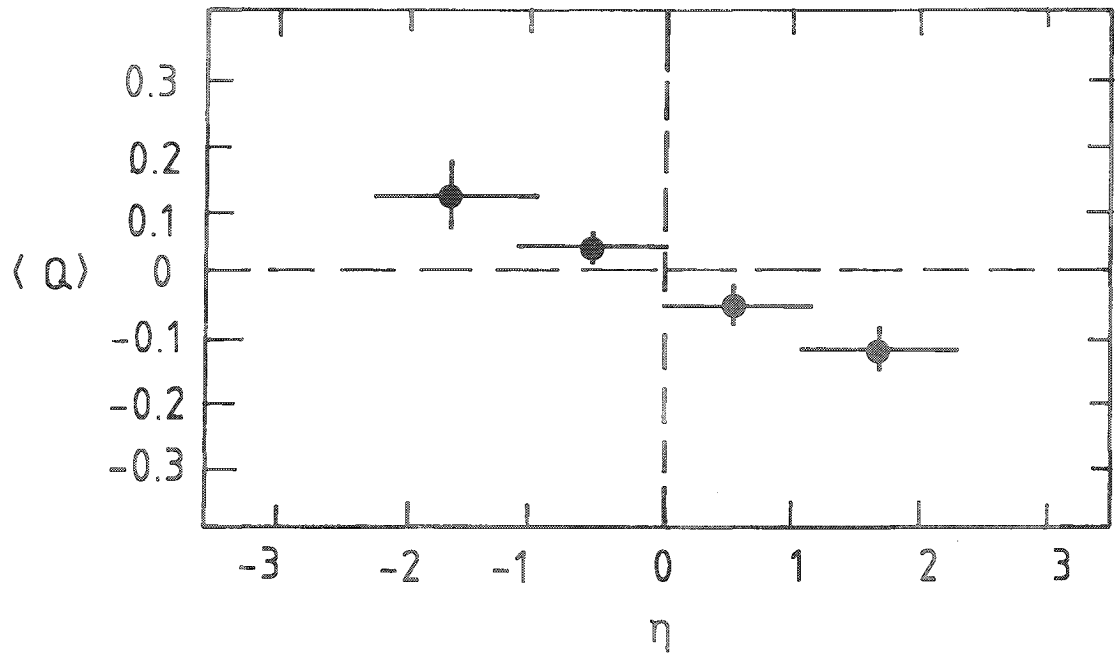
0.3
0.2
0.1
⟨ Q ⟩ 0
-0.1
-0.2
-0.3
-3
-2
-1
0
1
2
3
η

Fig. 7

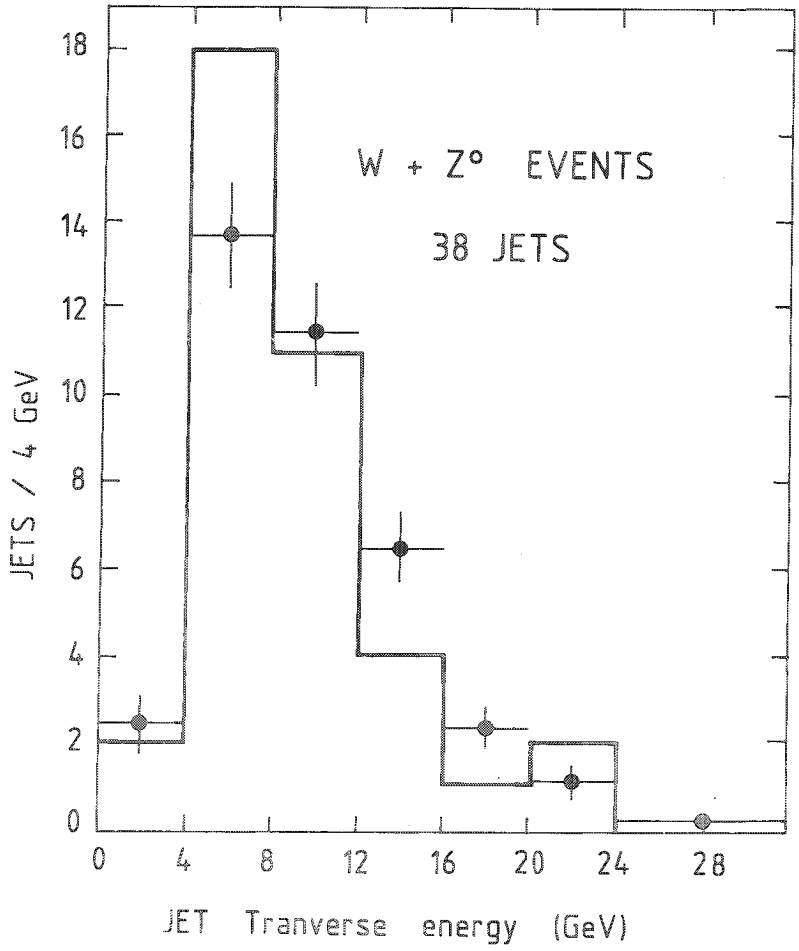
W + Z° EVENTS
38 JETS
JETS / 4 GeV
0
2
4
6
8
10
12
14
16
18
0
4
8
12
16
20
24
28
JET Tranverse energy (GeV)

Fig. 8

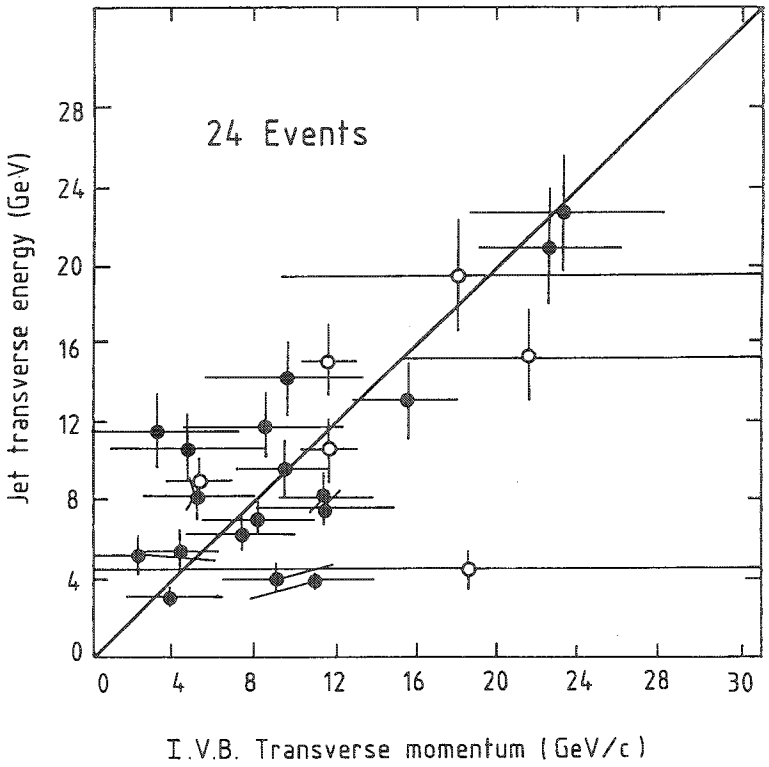
24 Events
Jet transverse energy (GeV)
I.V.B. Transverse momentum (GeV/c)
0
4
8
12
16
20
24
28
30

Fig. 9

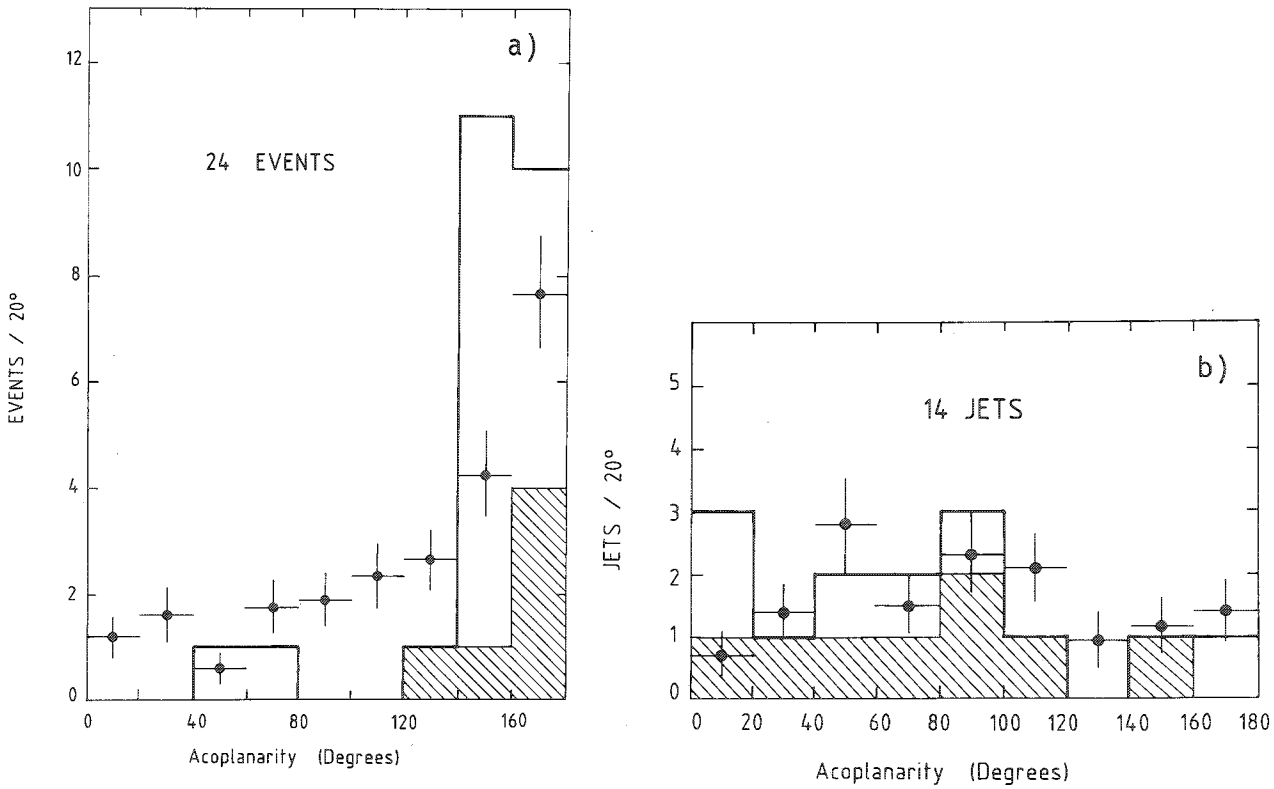
a)
24 EVENTS
EVENTS / 20°
Acoplanarity (Degrees)
b)
14 JETS
JETS / 20°
Acoplanarity (Degrees)

Fig. 10

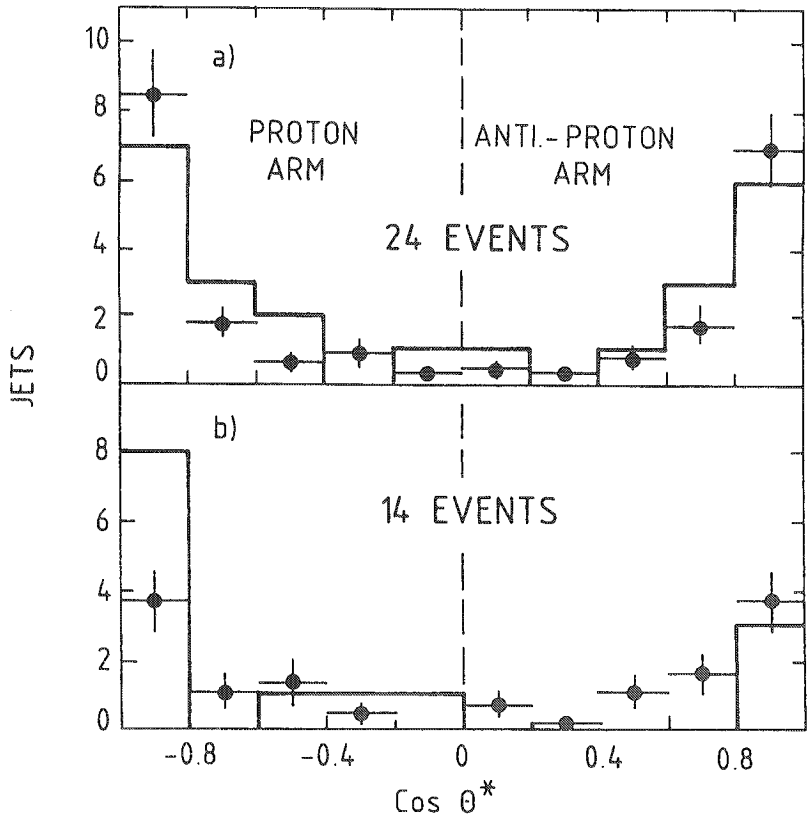
a)
PROTON ARM
ANTI.-PROTON ARM
24 EVENTS
b)
14 EVENTS
JETS
Cos θ*

Fig. 11

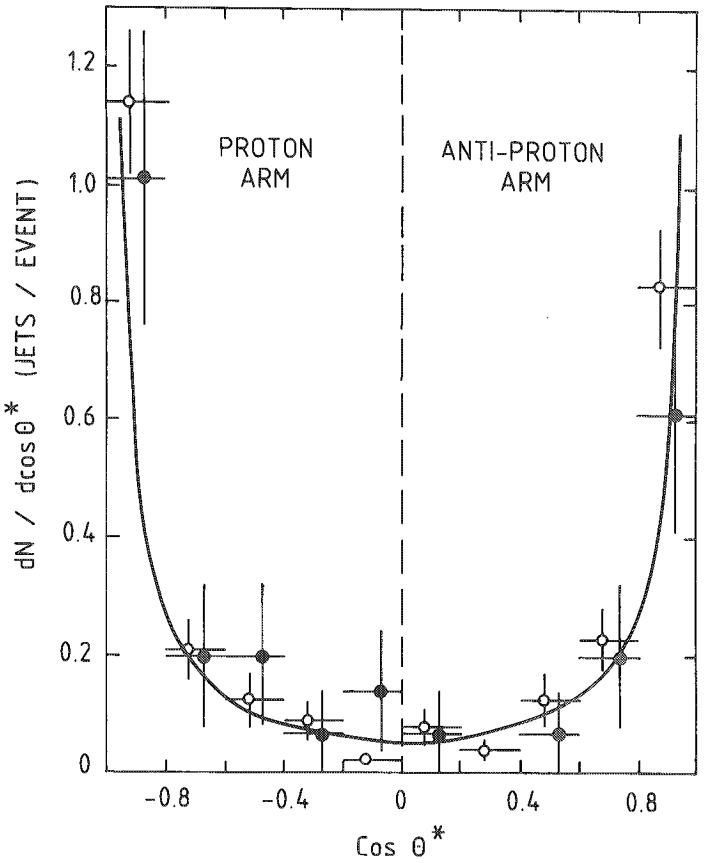
PROTON ARM
ANTI-PROTON ARM
dN / dcosθ* (JETS / EVENT)
Cos θ*

Fig. 12

HIGH P_T JETS FROM $p\bar{p}$ COLLISIONS AT $\sqrt{s}$ = 540 GEV IN UA2

The UA2 Collaboration

Bern - CERN - Copenhagen (NBI) - Orsay (LAL) -
Pavia - Saclay (CEN)

Presented by John Renner Hansen

ABSTRACT

The production and properties of very large transverse momentum hadron jets has been measured in the UA2 experiment at the CERN $\bar{p}p$ Collider for $\sqrt{s}$ = 540 GeV using a highly segmented calorimeter. Events with very large transverse energy depositions (ΣE_T up to 250 GeV in the pseudo-rapidity interval $-1 < \eta < 1$) are observed to be strongly dominated by a two-jet structure. Some of the characteristics of parton scattering and fragmentation are discussed and cross-sections for inclusive jet production is presented for p_T up to 150 GeV. The two-jet invariant mass distribution up to m_{jj} = 280 GeV is shown and the results are compared with the predictions of QCD models. A search for bumps in the m_{jj} distribution is reported.

1. INTRODUCTION

The recent unambiguous identification of jets in hadronic collisions [1-4] at the CERN $\bar{p}p$ Collider and at the ISR has revived the interest in this field after the first observation of large transverse momentum (p_T) processes in early ISR experiments [5]. The prediction that the hard scattering of hadron constituents should result in the production of two hadronic jets having the same large transverse momenta as the scattered partons [6,7] has been verified in a direct way at the CERN $\bar{p}p$ Collider with the observation of a dominant two-jet structure in events depositing very large transverse energy into the central calorimeters of the UA1 [3] or UA2 [1] experiments. In fact one of the most outstanding benefits of the very successful operation of the CERN $\bar{p}p$ Collider [8] at a centre of mass energy $\sqrt{s}$ = 540 GeV is the possibility for detailed measurements of hadronic jet production and their fragmentation properties [9-11] in an energy domain where hard processes can be separated clearly from the soft hadronic interactions [12].

2. APPARATUS

The UA2 detector, Fig. 1, has been described in detail elsewhere [13,14]. At the centre of the UA2 apparatus a vertex detector consisting of cylindrical proportional and drift chambers measures particle trajectories in a region without magnetic field. The vertex detector is surrounded by a highly segmented electromagnetic and hadronic calorimeter (the central calorimeter) which covers polar angles $40^\circ < \theta < 140^\circ$ ($-1 < \eta < 1$). The forward regions ($20^\circ < \theta < 37.5^\circ$ and $142.5^\circ < \theta < 160^\circ$) are each instrumented with twelve toroidal magnet sectors followed by drift chambers, multitube proportional chambers and electromagnetic calorimeters.

The present results have been obtained mainly with the central calorimeter. It is segmented into 240 cells, each covering 15° in ϕ and 10° in θ and built in a tower structure pointing to the centre of the interaction region. The cells are segmented longitudinally into a 17 radiation length thick electromagnetic compartment (lead-scintillator)

followed by two hadronic compartments (iron-scintillator) of two absorption lengths each. Following an initial energy calibration of all cells in a 10 GeV electron, muon and pion beam from the CERN PS the calorimeter response has been tracked with a light flasher system, measurements of the direct-current induced by a Co^{60} radioactive source and by measuring the average energy flow into each cell for unbiased $\bar{p}p$ collisions. The systematic uncertainty in the energy calibration for the data discussed here is less than ±1.5% for the electromagnetic calorimeter and less than ±3.5% for the hadronic one.

The response of the calorimeter to electrons, single hadrons and multi-hadrons (produced in a target in front of the calorimeter) has been measured at the CERN PS and SPS machines using beams from 1 to 70 GeV. The energy resolution for electrons is measured to be $\sigma_E/E = 0.14/\sqrt{E}$ (E in GeV) whereas for hadrons it varies from 32% at 1 GeV to 11% at 70 GeV , approximately proportionally to $E^{-1/4}$.

Details of the construction, calibration and performance of the calorimeter are reported in Ref. [14].

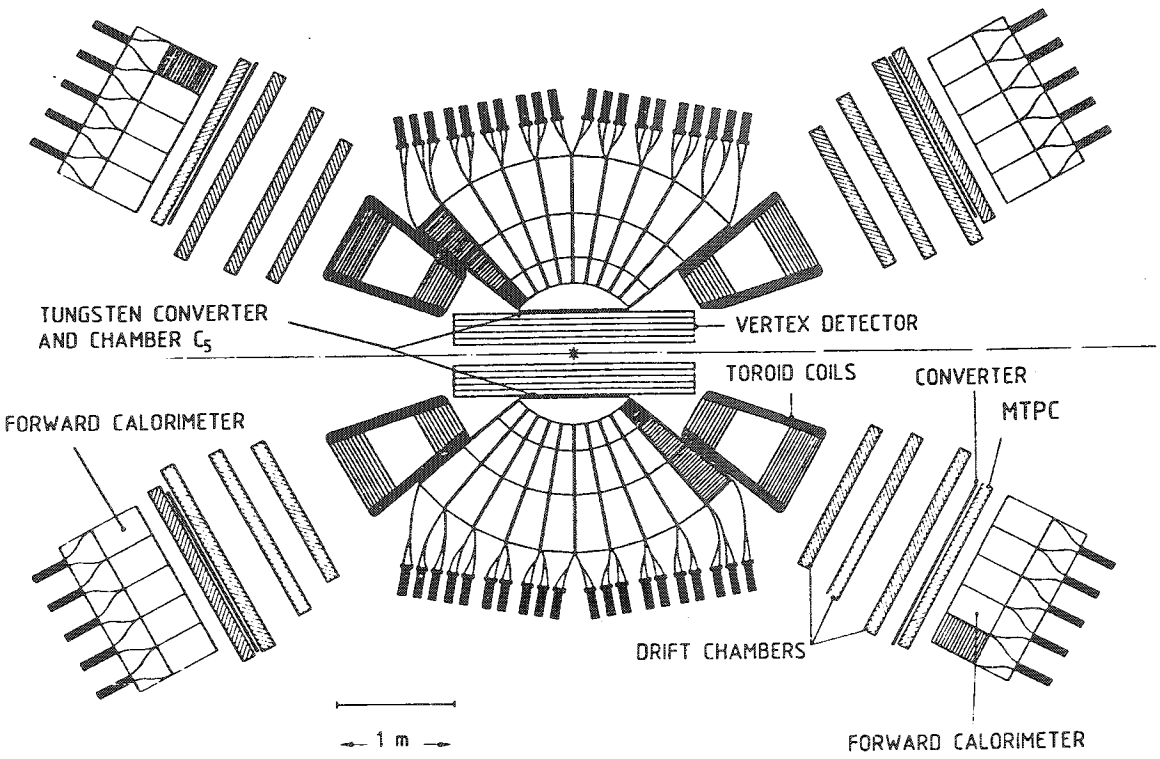

Fig. 1. Schematic detector assembly, showing UA2 in a longitudimal cut parallel to the beams.

3. DATA TAKING AND REDUCTION

The data presented in this paper were recorded during the 1983 CERN $\bar{p}p$ Collider run with a trigger selecting $\bar{p}p$ collisions which deposited a large total transverse energy (ΣE_T) into the central calorimeter. The gains of the photomultipliers were adjusted such that their response is proportional to transverse energy, and their signals were linearly added. The sum was required to exceed a threshold, normally at about 40 GeV except for special low threshold data runs.

Background from sources other than $\bar{p}p$ collisions was suppressed at the trigger level by requiring a coincidence of the ΣE_T condition with two signals ("minimum bias" trigger) obtained from scintillator arrays covering an angular range $0.44^\circ < \theta < 2.84^\circ$ on both sides of the collision region [15]. The loss of genuine large ΣE_T $\bar{p}p$ events due to this requirement was measured in special runs where this condition was removed. For $\Sigma E_T > 40$ GeV the loss is consistent with zero and < 5% at 90% confidence level, independent of ΣE_T. Background from cosmic rays was found to be negligible.

A sample of "minimum bias" events was recorded simultaneously with the ΣE_T data to provide a measurement of the luminosity. Data with $\Sigma E_T > 40$ GeV were recorded for a total integrated luminosity $\int \mathcal{L} dt = 112$ nb^{-1}. An uncertainty of ±20% was estimated for $\int \mathcal{L} dt$ from the observed fluctuations during different running conditions and from the overall uncertainty in the cross-section accepted by the "minimum bias" trigger [15].

The full data sample was used in the following analysis for $\Sigma E_T > 60$ GeV; smaller samples and special runs were used for lower thresholds [16].

The events collected with the ΣE_T trigger include a small (< 10%) background contamination. Beam halo particles can either satisfy the triggering condition directly or appear as an accidental overlap with a "minimum bias" $\bar{p}p$ interaction. The background events exhibit a characteristic pattern in the detector different from that of large ΣE_T $\bar{p}p$ events. They are rejected from the data sample if any of the following conditions is satisfied :

i) if they are associated with an early signal in the small angle scintillator arrays ;

ii) if they have an abnormally large total transverse energy fraction in the hadronic compartments (more than 60% in the second one or more than 95% in both together) ;

iii) if they contain only one cluster (as defined below) with more than 90% of its energy in the hadronic compartments.

These requirements reduce the background contamination in the data sample to < 5% independent of ΣE_T. The loss of good events introduced by the cuts is negligible. This has been verified by applying the time-of-flight requirement on minimum bias events and by using test beam data for the energy deposition criteria.

4. TRANSVERSE ENERGY DISTRIBUTION

The response of the electromagnetic calorimeter compartments to energy deposited by photons (or electrons) differs from that of hadrons by typically 20%, depending on energy. We have adopted a constant set of weighting factors (1.18, 1.00, 1.06) for the three compartment energies (electromagnetic, first and second hadronic) that optimizes the resolution and linearity of the calorimeter response to high energy hadrons, as described in detail in Ref. [14].

The total hadronic energy in a cell of the calorimeter is measured as the weighted sum of the energies in the three compartments where each compartment contributing to the sum must exceed 150 MeV, which is well above pedestal fluctuations.

The observed ΣE_T distribution, normalized using the integrated luminosity, is presented in Fig. 2 for two pseudo-rapidity intervals ($-1 < \eta < 1$ and $-0.54 < \eta < 0.54$). The transverse energies are summed over all cells in the full azimuthal acceptance $\Delta\phi = 360°$ under the approximation that the event vertex is located at the centre of the detector. The event vertex has been reconstructed for a sample of the

events used for the cross-section measurement. Its distribution along the $\bar{p}p$ beam axis is well centered in the detector and has a r.m.s. spread of 10 cm. No acceptance correction has been applied to the data shown in Fig. 2. We estimate that the uncertainty in the energy scale of ΣE_T due to systematic effects (150 MeV minimum compartment energy requirement, calibration errors, neglecting event vertex position, etc.) is less than ±10%.

The ΣE_T distributions of Fig. 2 show a clear departure from exponential when ΣE_T exceeds ~60 GeV. This corresponds to the transverse energy where the two-jet production cross-section begins to dominate over soft hadronic interactions, as explained below.

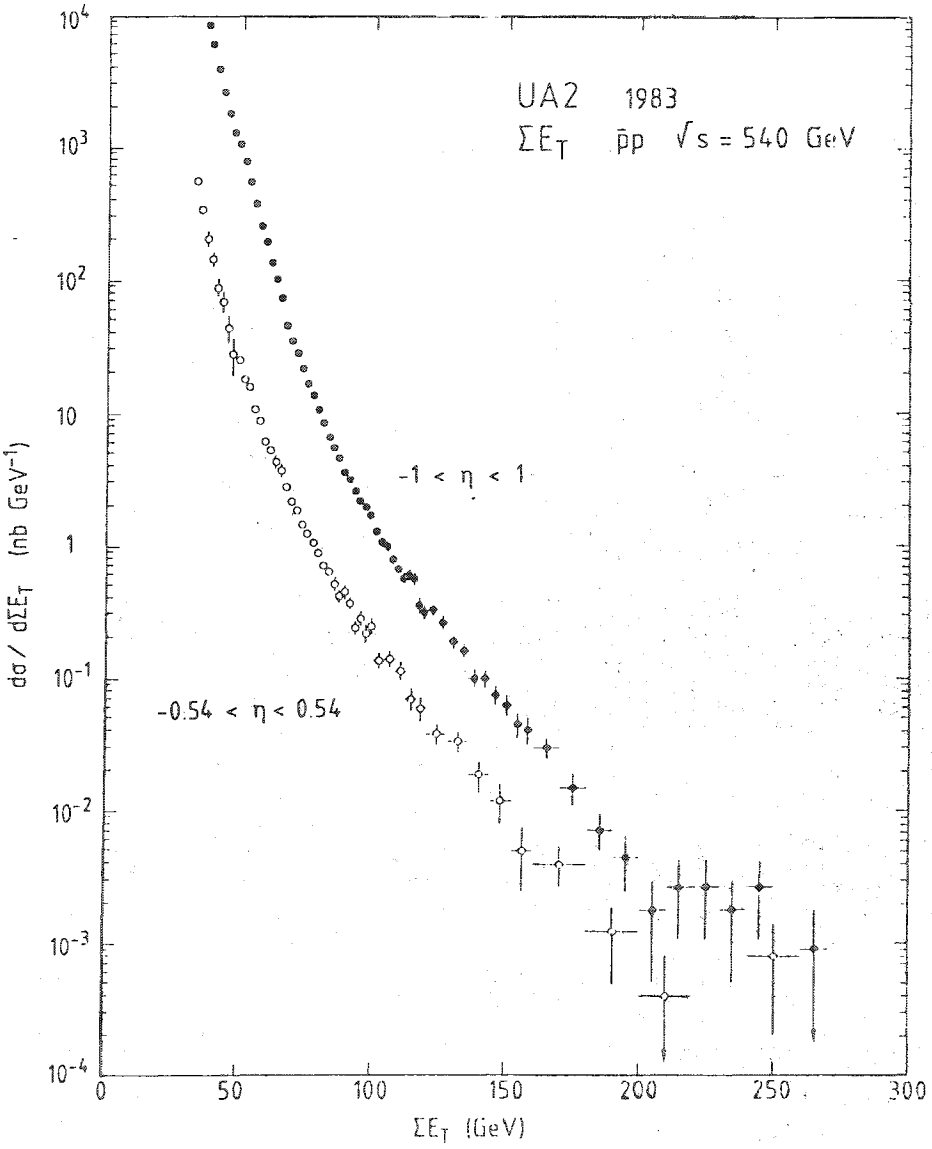

Fig. 2. Observed total transverse energy ΣE_T distributions for two pseudo-rapidity (η) intervals.

5. TWO-JET DOMINANCE

In order to investigate the pattern of energy distribution in the events a straightforward clustering algorithm has been adopted which takes advantage of the fine granularity of the calorimeter segmentation. All cells which share a common side and have a cell energy $E_{cell} > 400$ MeV are joined into a cluster. Clusters having two or more local maxima separated by a valley deeper than 5 GeV are split. In each event the clusters are ranked in order of decreasing transverse energies denoted by $E_T^1 > E_T^2 > E_T^3 \ldots$. The clusters contain typically 3 cells for $E_T = 2$ GeV and 10 cells for $E_T = 40$ GeV.

The fractions $h_1 = E_T^1/\Sigma E_T$ and $h_2 = (E_T^1 + E_T^2)/\Sigma E_T$ describe the transverse energy accounted for in each event by the cluster (respectively the two clusters) with the largest transverse energy. An event containing only two jets of equal transverse energy would have $h_1 = 0.5$ and $h_2 = 1$ in an ideal detector. The mean values of h_1 and h_2 are shown in Fig. 3a as a function of ΣE_T. Their behaviour illustrates the emergence of a dominant two-jet structure at large ΣE_T, as previously reported [1,9]. The effect becomes even more pronounced at the largest values of ΣE_T reached in this experiment. The dependence on ΣE_T of the mean values of the ratio $r_{21} = E_T^2/E_T^1$ and $r_{32} = E_T^3/E_T^2$ are displayed in Fig. 3b. They show the same effect : as ΣE_T increases, r_{21} approaches about 0.9 whereas r_{32} decreases below 0.1. A very large fraction of the total transverse energy of large ΣE_T events is shared on average by two clusters only.

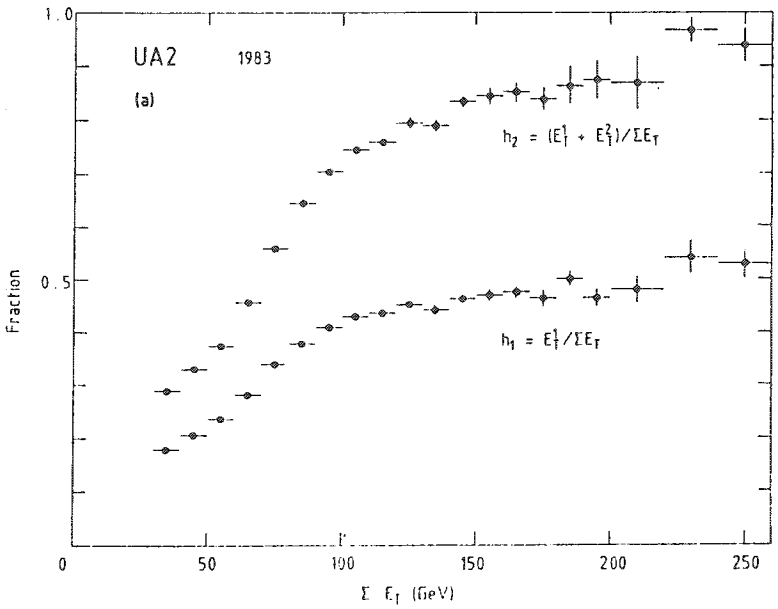

Fig. 3. a) The fractions h_1 and h_2 of the total transverse energy ΣE_T contained in the cluster, and the two clusters respectively, having the largest ΣE_T are displayed versus ΣE_T.

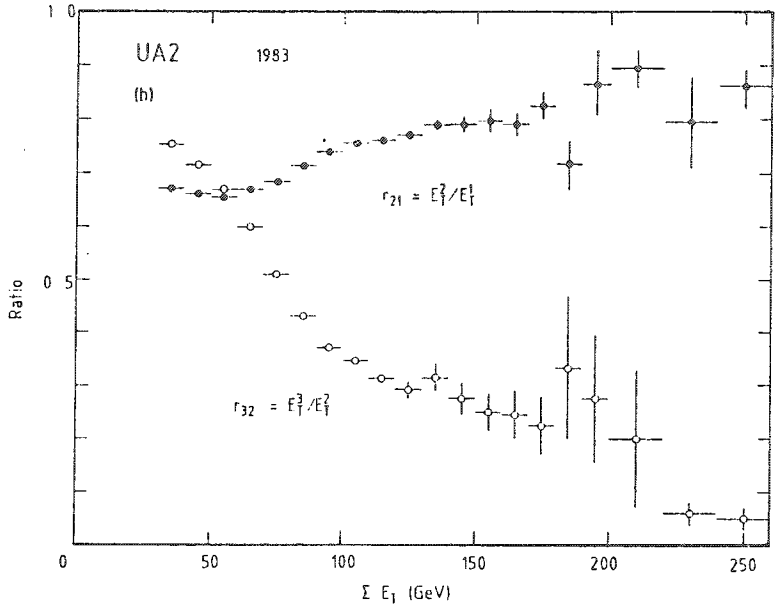

b) Dependence on ΣE_T of the ratios $r_{21} = E_T^2/E_T^1$ and $r_{32} = E_T^3/E_T^2$ (see text).

In order to give a qualitative feeling of the behaviour of a third jet in high ΣE_T events, we define the variables $\varepsilon_i = E_i^{cm}/m_{jjj}$ (i=1,2,3). E_i^{cm} is the cm-energy of jet 'i' where $E_1^{cm} > E_2^{cm} > E_3^{cm}$, m_{jjj} is the 3-jet invariant mass. To define a 3-jet event we require $E_T^3 > 3$ GeV. No fiducial cut is applied. The two independent variables ε_3 and $Q=(\varepsilon_1-\varepsilon_2)/\sqrt{3}$ measure the fraction of available energy carried away by the third jet and the energy sharing between the two most energetic jets. The accepted region of the (ε_3,Q) plane is restricted by kinematics to a triangle with its corners at A = (0,0) , B=(.25,1/$\sqrt{48}$) and C=(1/3,0).

The distribution of events in this kind of Dalitz plot , Fig. 4, has the following features:

i) the events near A are characterised by a soft third jet and equal energy sharing between the two dominating jets. These events are typically associated with soft gluon bremsstrahlung from the jets or with the underlying event.

ii) events near B are of the collinear type, where two jets of equal size balance the major jet in the event.

iii) the region near C contains events wih 3 equally strong jets.

Fig. 4 gives a good feeling of the relative population of the three regions, for events with $m_{jjj} > 50$ GeV/c². As expected from Fig. 3b, three-jet events are dominated by the soft gluon configurations. The region of the diagram for which ε_3 is greater than .15 contains of the order of 20% of the events.

A study of the Dalitz plot in smaller mass bins does not show any resonant structure.

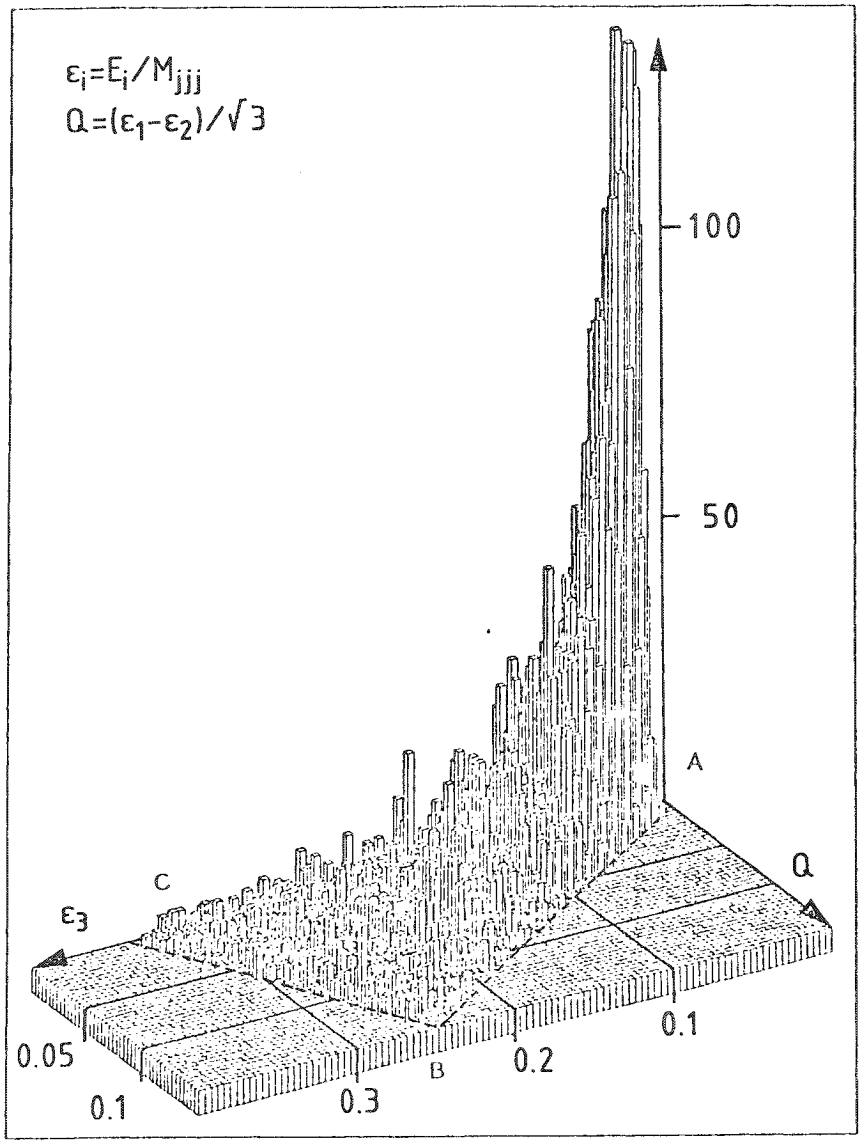

Fig. 4. Three-jet Dalitz diagram.

6. CHARGE PARTICLE MULTIPLICITY IN JETS

The charged particle multiplicity is measured by the vertex detector, Fig. 1, whose angular coverage is much larger than that of the central calorimeter: it extends down to $\Theta=20^0$ and over the full azimuthal range. As a result the charged particle multiplicity measurement is almost free of acceptance corrections. The main uncertainties in this measurement arise from two sources:

i) the efficiency of the vertex detector and of the associated pattern recognition algorithm especially in regions of high particle density,

ii) the procedure that defines which of the observed tracks are to be associated with the jet and which are not.

In order to address these problems, our analysis is restricted to the transverse plane, where the track reconstruction efficiency is highest, and where particles not associated with the jets are expected to contribute a uniform azimuthal distribution.

Events are considered in which two clusters, having an invariant mass in excess of 40 GeV/c^2 and a azimuthal separation greater than 150°, are observed with $|\eta|<.7$. $\rho(\Delta\phi)$, the distribution of the azimuthal separation $\Delta\phi$ between each track in the vertex detector and the centroid of the highest transverse energy cluster are shown in Fig. 5 for two intervals of m_{jj}, the invariant mass associated with the two highest energy clusters. Clear peaks are seen at $\Delta\phi=0$ and $\Delta\phi=\pi$, as expected for two jet events. The distribution is more peaked for the larger m_{jj} slice, showing that higher energy jets are more collimated. The distribution in $\Delta\phi$ is not symmetric about $\Delta\phi=\pi/2$. This is partly explained by the fact that the two jets are not exactly back-to-back in the transverse plane and partly by the fact that a broad high multiplicity jet will tend to deposit less energy in a leading calorimeter cluster than a more collimated lower multiplicity jet. Therefore in selecting the higher transverse energy cluster there is a bias favouring the selection of the narrower, lower multiplicity jet.

The transverse track finding efficiency of the vertex detector was measured in the angular range covered by the toroid spectrometer, by comparing the two detectors for field off data. The efficiency was found

to be 94.8 % ± .8% and the fraction of spurious tracks was 21 %. The loss of tracks from the finite two-track resolution was estimated from the distribution of the azimuthal separation between pairs of neighbour tracks, and evaluated to be in the range from 16 % to 31 % depending on local multiplicity. The data was also corrected for γ conversions and π^0 Dalitz decays. As a check on this procedure the mean charge multiplicity was measured for minimum bias events and compared with results obtained by the UA5 collaboration [17] in the same pseudo -rapidity range ($|\eta| < 2$). The result 13.4 ± .3 , is in good agreement with the UA5 measurement, 13.45 ± .15.

As illustrated in Fig. 5 the track density is approximately constant over a large $\Delta\phi$ range around $\Delta\phi=\pi/2$, where it takes a value ρ_0. On the average ρ_0 is measured to be twice as large as in minimum bias events.

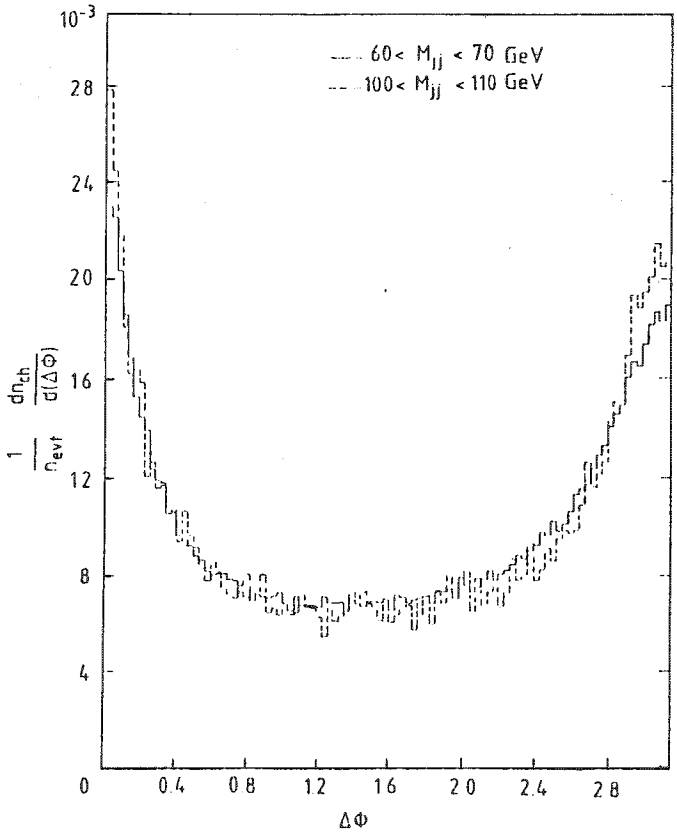

Fig. 5. Azimuthal separation $\Delta\phi$ between the centroid of E_T and all charged transverse vertex tracks.

Particles not associated with the jets are assumed to make a uniform contribution, $\lambda\rho_0$, to $\rho(\Delta\phi)$. This assumption was checked by measuring the track density in the forward spectrometers for events containing a jet near $\Theta=90^0$. The distribution of $\Delta\phi$, the azimuthal separation between the forward track and the highest transverse energy cluster is flat.

A priori λ may take any value between 0 and 1; lacking knowledge of λ, we evaluate a lower bound of the mean track multiplicity in jets, $\langle n_{ch}\rangle$, by setting $\lambda=1$. The values obtained, as a function of m_{jj} , are displayed in Fig. 6. To avoid the bias caused by the asymmetric $\Delta\phi$ distribution discussed above we define the jet multiplicity as the avaraged multiplicity of the two jets. The results are compared with e^+e^- data [18] which we treat the same way as the collider data to find ρ_0, using the fact that $\lambda=0$ in e^+e^- two-jet final state.

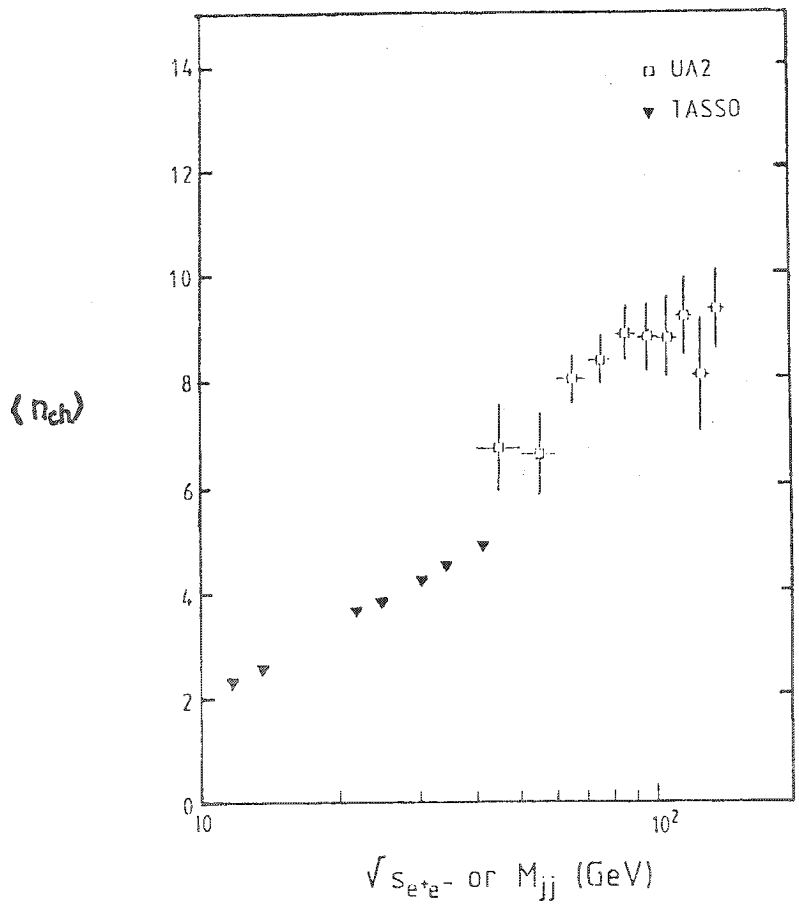

Fig. 6. Lower bound on mean charged particle multiplicities in jets $\langle n_{ch}\rangle$ as a function of $\sqrt{s}_{e^+e^-}$ and of the invariant two-jet mass m_{jj} for $p\bar{p}$. The two UA2 points corresponding to low masses, come from low threshold data and have for that reason big error bars.

Fig. 6 indicates a larger charged particle multiplicity in jet events from the collider than in similar events observed in e^+e^- collisions at lower energies. Even if λ were equal to 1, which would imply that jet fragments do not populate the region $\Delta\phi=\pi/2$, the charged particle multiplicity of jets observed in our data would be at least as large than that of the extrapolated e^+e^- data. These results are consistent with expectations based on QCD calculations, which predict that at relatively low $x_T=2E_T/\sqrt{s}$ gluon jets having higher multiplicity than quark jets [19,20] tend to dominate [21] in $\bar{p}p$ collisions.

7. TWO JET CMS SCATTERING ANGLE, Θ^*

The fundamental parton-parton scattering process has been studied through the resulting angular distribution of jet.

Events were selected by requiring two clusters with $E_T^1+E_T^2 > 46$ GeV. The p_T of the two-jet system is chosen to be smaller than 20 GeV/c and $\Delta\phi_{jj}$ (the angle between the two cluster centroids) to be greater than 160^0. The two latter conditions force the two jets to be back to back, not letting a third jet disturb the angular measurement.

The scattering angle Θ^* is measured from the external bisector of the p and $\bar{p}$ momenta in the two-jet cm-system (Collins-Soper frame). The measurement was done in a way free of acceptance corrections, by choosing increasing intervals of $|x_F|$, each time ensuring that the maximum $|x_F|$ and Θ^* correspond to fully contained jets. The data from each interval are normalized and added, with the errors adjusted accordingly. Fig. 7 shows the final result. The main QCD subprocesses result in $\cos\Theta^*$ distributions inside the shaded region of Fig. 7 , leaving no chance, with the present data sample, to disentangle the individual contributions.

It is anyhow clear that scalar gluons would not be able to describe the observed $\cos\Theta^*$ distribution on their own, since all associated curves are below the data points (not shown in Fig. 7).

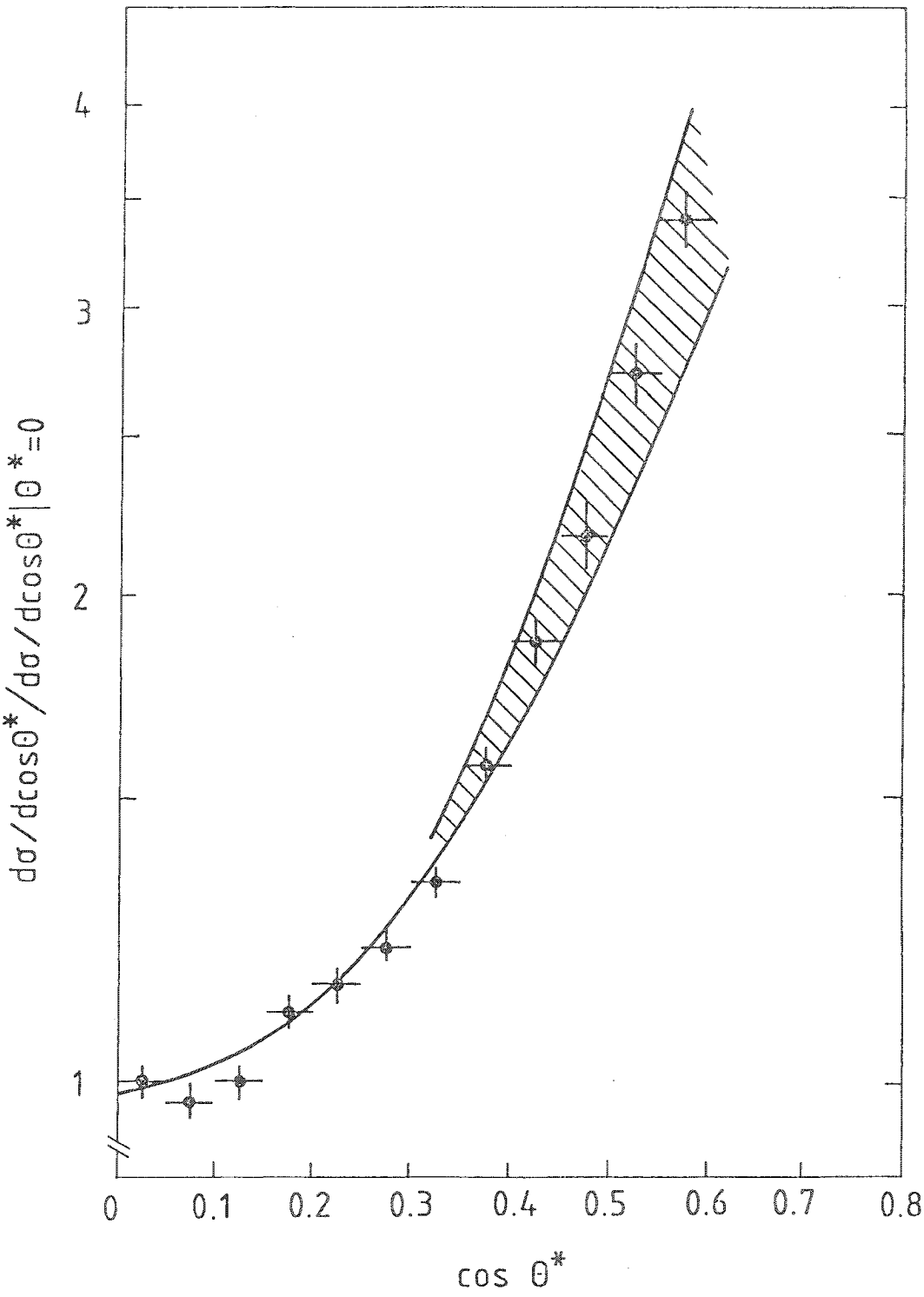

Fig. 7. CMS scattering angle distribution, $\cos\Theta^*$. The shaded region indicates where the contribution from most of the 8 QCD subprocceses will fall.

8. INCLUSIVE JET PRODUCTION CROSS-SECTIONS

For a measurement of the inclusive jet production cross-sections

$$\bar{p}p \rightarrow \text{jet} + \text{anything} \quad (1)$$
$$\bar{p}p \rightarrow \text{jet}_1 + \text{jet}_2 + \text{anything} \quad (2)$$

events are selected containing at least one cluster with E_T exceeding the ΣE_T threshold for reaction (1) and with $E_T^1 + E_T^2$ larger than the ΣE_T threshold (and E_T^1, $E_T^2 > 10$ GeV) for reaction (2), after inclusion of nearby clusters as explained below. The jet direction and transverse energy are measured from the centroid and energy of the associated clusters with respect to the event vertex.

The individual clusters are taken to be massless [7] in the following procedure, equating therefore p_T and E_T. Actually, by attributing a zero-mass momentum vector ($|\bar{p}|=E$) to each cell which participates to a cluster one observes a mean invariant "cluster mass" of 9 GeV for clusters having $E_T > 30$ GeV. This value results from the combined effects of shower and cell sizes and of actual jet masses, and is in agreement with a Monte Carlo simulation [22] described below. For jets having $p_T > 30$ GeV this calculation predicts a mean ratio $|\bar{p}_T|/E_T = 0.86$, where $|\bar{p}_T|$ and E_T are summed over all generated final state particles.

In order to partly account for final state gluon radiation effects, as reported and discussed in Ref. [9], the jet momenta are defined by adding to the measured momentum vector of the selected cluster those of all clusters having $E_T > 3$ GeV and separated by an angle ω from the selected cluster momentum vector such that $\cos\omega > 0.2$. About 20% of the jets with $p_T > 30$ GeV include at least one such nearby cluster with $E_T > 3$ GeV. Note that in this case the jet acquires a mass and p_T differs from E_T. The inclusion of these nearby clusters increases the observed transverse momentum distribution (p_T) for jets by about 15%, roughly independent of p_T.

The evaluation of the cross-sections for reactions (1) and (2) from these events requires the measurement of the integrated luminosity for the normalization and the determination of the detector acceptance

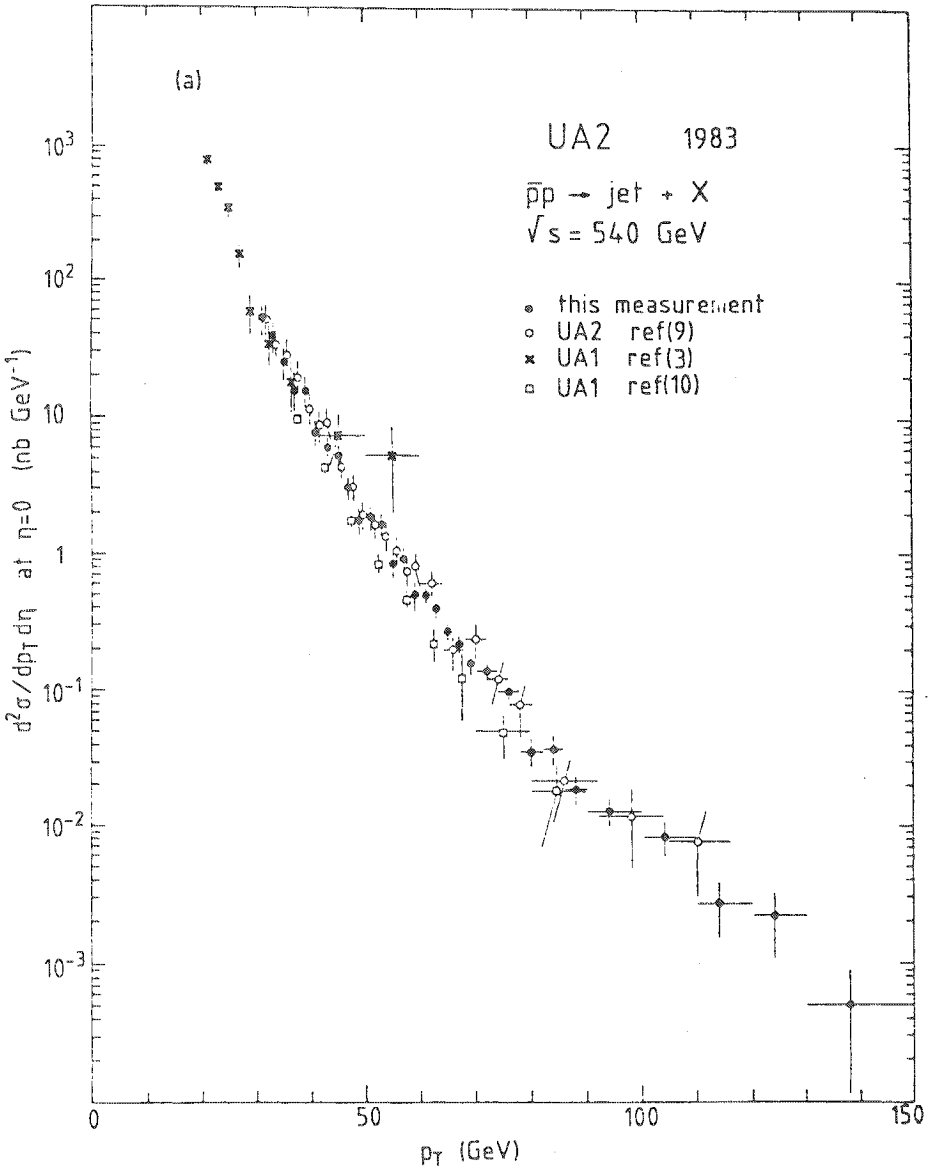

Fig. 8. a) Inclusive jet production cross-section. The additional systematic uncertainty is ±45%. Previous measurements are from Refs. [3,9,10].

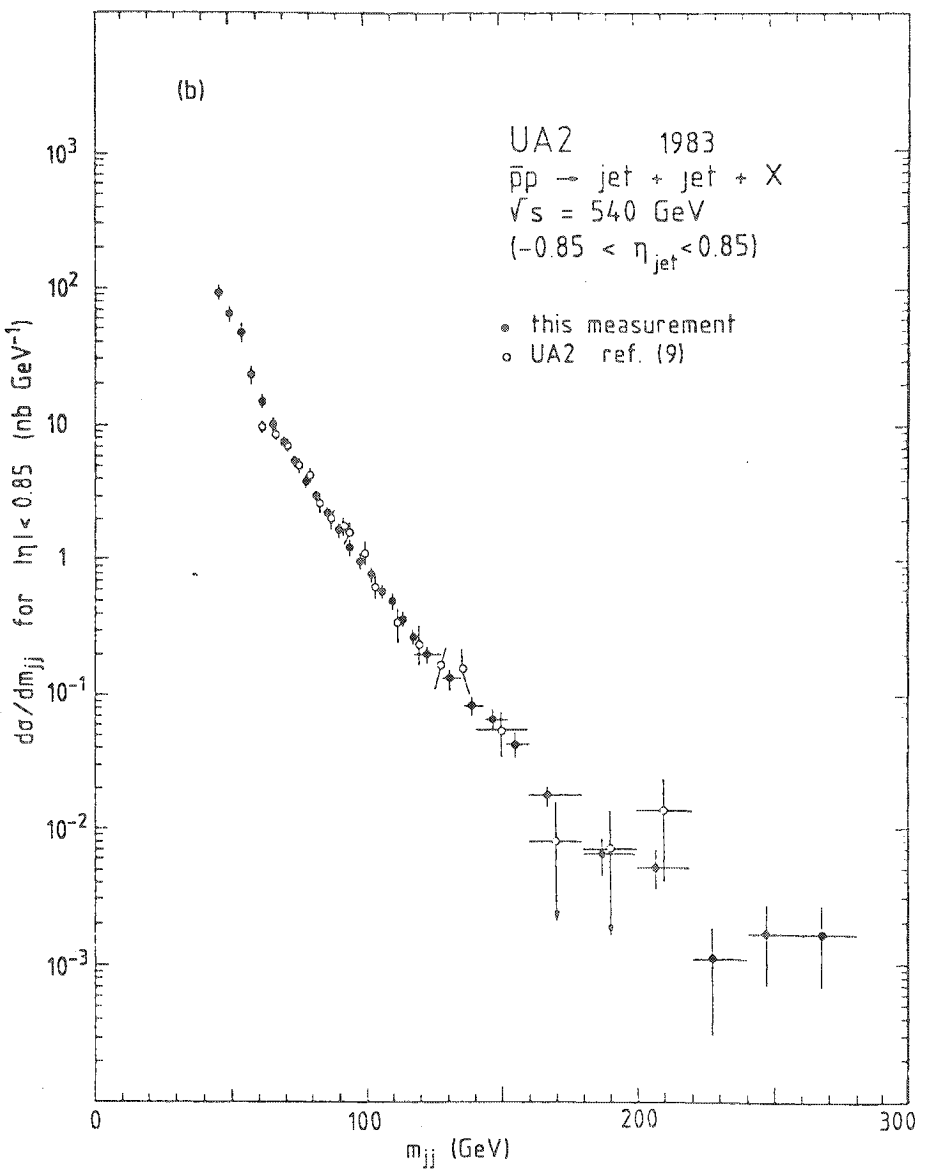

b) Two-jet production cross-section with both jets in the pseudo-rapidity range $-0.85 < \eta < 0.85$. The additional systematic uncertainty is ±45%. The previous measurement is from Ref. [9].

including the effects of the energy smearing on the steeply falling p_T spectra. A Monte Carlo simulation of the detector is used to calculate the acceptance. The Monte Carlo events are processed through the same analysis chain as the data. The simulation reproduces the details of the event configuration and of the detector response, using the same weighting factors for the three calorimeter compartment energies as for the data. In particular, the distribution of cluster size and both hadronic fragmentation and shower development are adequately described [9]. The comparison of the transverse momentum (p_T) and the two-jet invariant mass (m_{jj}) distributions of the reconstructed Monte Carlo events with those of the initial partons used as input provides the acceptance functions $\varepsilon(p_T)$ and $\varepsilon(m_{jj})$ by which the observed cross-sections must be divided to obtain the corrected jet and two-jet cross-sections. The function $\varepsilon(p_T)$ varies from about 0.8 to 1.0 over the range $30 < p_T < 150$ GeV and $\varepsilon(m_{jj})$ from about 0.5 to 0.8 over the range $50 < m_{jj} < 250$ GeV. The uncertainty due to the model dependence of the acceptance calculation has been studied by using different independent models [9,22], by changing the details of the jet fragmentation and by varying relevant analysis parameters, such as the accepted rapidity range, the parameters of the clustering algorithm, weighting factors for the calorimeter compartment energies etc... The systematic uncertainty on ε is estimated to be ±35%.

The cross-section for inclusive jet production $d^2\sigma/dp_T d\eta$ at $\eta = 0$ is shown in Fig. 8a and the cross-section for two-jet production $d\sigma/dm_{jj}$ with both jets in the interval $-0.85 < \eta < 0.85$, is displayed in Fig. 8b. The quoted errors include the statistical errors and an energy-dependent systematic uncertainty on the acceptance functions. Further uncertainties have to be considered in addition to the systematic error on the acceptance (±35%). The normalization is affected by the ±20% systematic uncertainty in the knowledge of the integrated luminosity, and the systematic error on the calorimeter energy calibration is contributing another ±20%. The overall systematic uncertainty on the cross-sections for the reactions (1) and (2) is estimated to be ±45% after adding the three contributions in quadrature.

Also shown in Figs. 8a and 8b are the cross-sections obtained previously by the same experiment [9] with a much smaller data sample (from the 1982 running period). For these data an additional systematic

error of ±40% has been quoted. The two measurements are in very good agreement. One should note though that the systematic uncertainties of the two results have largely common origins and the two evaluations are not independent. The inclusive jet production cross-section reported by the UA1 experiment [3,10] is also shown in Fig. 8a. The systematic uncertainty for this measurement is given in [10] as a factor 1.65. Even though the UA1 data points are about a factor 1.5 to 2 below the present measurement, both experiments are consistent in the region of overlap within systematic errors.

It is natural at this stage to look for bumps in the jet mass spectrum, having in mind the standard-model predictions for heavy intermediate vector boson decay into $q\bar{q}$.

For an event to enter the masss distribution, it is required to have at least two clusters, each with transverse energy in excess of 10 GeV. The centroid of the biggest cluster must have $|\eta| < .7$ and all other clusters considered in the mass determination must fulfil $|\eta| < .85$. Other clusters are merged with one of the two highest E_T clusters when they satisfy the criteria described earlier (E_T>3 GeV, cosω>.2), thus reducing the event to two main jets, with total transverse energy ΣE_T^{cl}, and a remaining event having transverse energy $\widetilde{\Sigma E}_T = \Sigma E_T - \Sigma E_T^{cl}$. Events having $\widetilde{\Sigma E}_T > 15$ GeV, for which the definition of two jet system may be ambiguous, are rejected. We also reject events having more than 6 GeV transverse energy measured in the F/B calorimeters (where the acceptance is reduced).

In each retained event we increase the transverse momentum vector of the weakest of the two jets to balance that of the strongest. Monte Carlo calculations show that this procedure partially compensates for losses (heavy flavor decays into undetected leptons, soft gluons at large angles to the jets), and for measurement errors, and results in an improved resolution and a more accurate mass determination. In the W region the mass resolution is of the order of 10 GeV/c^2.

The QCD background, assumed to have a form exp(bm+cm^2), was fitted in the mass region 40 GeV to 68 GeV (low threshold), 56 GeV to 68 GeV and 108 GeV to 148 GeV (high threshold) (excluding the region 72 GeV to 104 GeV), resulting in a χ^2=17.5/19 dof.

Although the spectrum is well reproduced by the exponential QCD background distribution, we tried to superimpose two gaussian

distributions with a fixed width of 10 GeV/c^2, describing the contribution from W and Z decays into qq. The two gaussians are linked together, through the standard model, by requiring the number of Z's relative to the number of W's (n_Z/n_W) to be .41, and $m_Z = 1.15\ m_W$

The new fit gives χ^2=22/32 dof. and m_W=79 ± 8 GeV/c^2. From the value and error obtained in the fit for the W contribution we deduce, after acceptance corrections, an upper limit on the $W^{\pm}$ production cross section: $\sigma_{W^+} + \sigma_{W^-} < 9$ nb (95 % cl).

A further search for mass bumps in the region above 100 GeV/c^2 using the same method, but this time with only one gaussian and with the mass and width as free parameters, results in an excess of 50 ± 16 events above background, at m = 147 GeV/c^2 and σ = 13 GeV/c^2. Fig. 9 shows the mass spectrum above 100 GeV/c^2. ——— indicates the pure background fit, ····· the background contribution to the combined fit and – – – the final fit leading to a χ^2=11.7/20 dof.

A study of these high mass events in terms of their configurations is under way and more work is needed to assess the significance of this enhancement.

9. COMPARISON WITH QCD CALCULATIONS

The measurements of the inclusive jet production cross-sections, reactions (1) and (2), can be compared directly with QCD predictions. In principle such comparisons do not require any assumption on the fragmentation mechanism: to the extent that jets are correctly identified they correspond directly to the hard scattered partons [7]. The observations [1,3,9,10] of the predicted increase of the yield of jets having $p_T > 20$ GeV at the CERN $\bar{p}p$ Collider with respect to top ISR energy (by about four orders of magnitude [21]) is a remarkable success of the QCD parton picture.

Several QCD calculations have since been reported. In the following the data are compared with those of Refs. [23-25]. Two major uncertainties affect the theoretical predictions [26] : scale ambiguities (choice of Q^2) in the leading logarithm calculations and, related to it, the choice of the Λ parameter in the strong coupling constant $\alpha_s(Q^2)$,

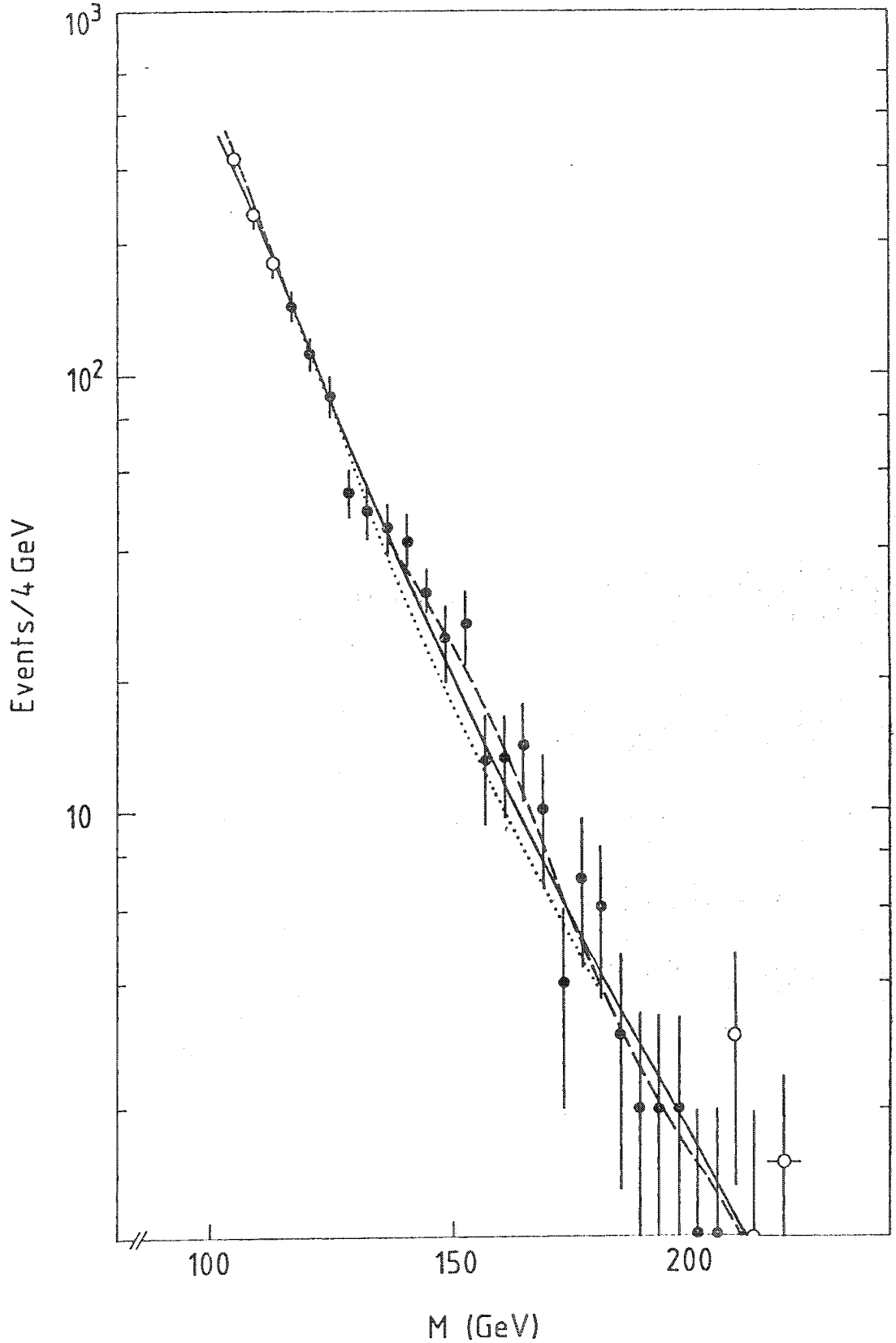

Fig. 9. Multi-jet mass spectrum above 100 GeV/c^2. —— indicates the pure background fit, ····· the background contribution to the combined fit and – – – the final fit leading to a χ^2=11.7/20 dof.

and the parametrization used for the parton densities (structure functions) in the incoming p and $\bar{p}$. Furthermore higher order (in α_s) contributions to the jet production cross-sections are not fully included. The influence of these theoretical ambiguities has been studied, for example, in Refs. [23-25]. The calculations ignore fragmentation effects and assume massless partons.

A comparison between data and a range of these predictions is indicated in Figs. 10a and 10b as a shaded band [27]. The solid curve in Fig. 10a corresponds to the prediction of Ref. [21] and almost coincides with the results of Refs. [23,24], not separately shown, for the theoretical assumptions listed in [28]. The latter results are also displayed in Fig. 10b as a solid curve. The data are at a level comparable to the QCD predictions.

It has been suggested that a possible substructure of quarks and leptons would manifest itself as a new contact interaction visible at large momentum transfers [29]. The cross-sections for reactions (1) and (2) are expected to deviate at large p_T or m_{jj} from the QCD behaviour depending on the energy scale ξ which characterizes the strength of this new interaction (and the physical size of the composite states). For example, for ξ = 200 GeV, the cross-section of reaction (1) is expected to be one order of magnitude larger than the QCD prediction ($\xi = \infty$) at $p_T > 100$ GeV (Fig. 10a). A determination of ξ from the data is in principle possible but the uncertainties attached to the QCD calculations limit its accuracy. By comparing the measured cross-section for reaction (1) to the QCD calculations of Ref. [23,28] we find a fair agreement ($\chi^2 = 45$ for 29 degrees of freedom) if we multiply the QCD cross-sections by a p_T independent scale factor of 1.9. The remaining deviation can be expressed in terms of a lower limit on ξ by using the calculation of Ref. [30]. This method, which is model dependent, gives $\xi > 275$ GeV (95% CL).

In conclusion it has been further demonstrated that two-jet production is the dominant hadronic process at large transverse energies at the CERN $\bar{p}p$ Collider. The jet production cross-sections are adequately described by QCD models.

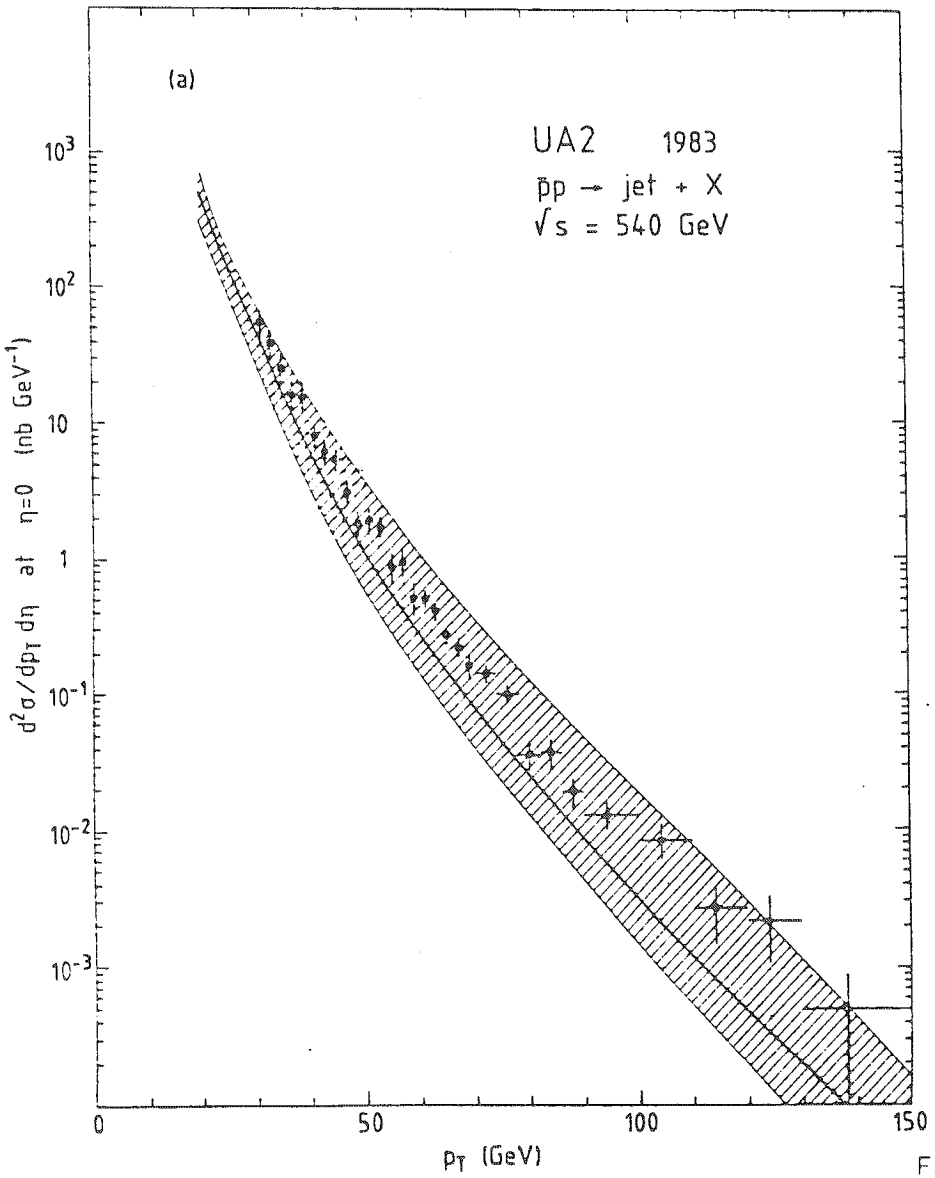

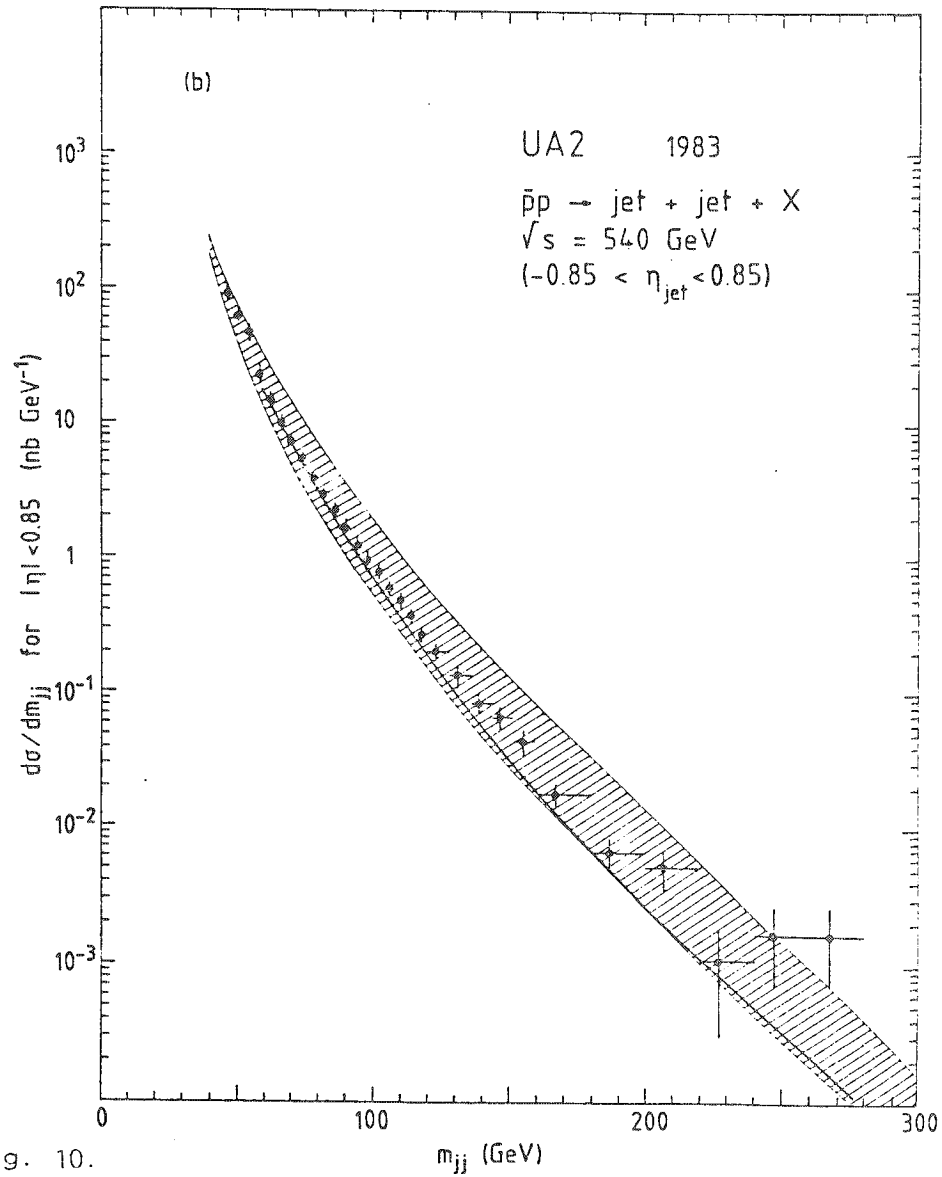

Fig. 10.

a) Comparison of the inclusive jet production cross-section with QCD calculations (see text).

b) Comparison of the two-jet production cross-section with both jets in the pseudo-rapidity range $-0.85 < \eta < 0.85$ with QCD calculations (see text).

REFERENCES AND FOOTNOTES

1. UA2 Collaboration, M. Banner et al., Phys. Lett. 118B (1982) 203.
UA2 Collaboration, P. Bagnaia et al., Phys. Lett. 138B (1984) 430.

2. Axial Field Spectrometer Collaboration, T. Åkesson et al., Phys. Lett. 118B (1982) 185 and 193.

3. UA1 Collaboration, G. Arnison et al., Phys. Lett. 123B (1983) 115.

4. COR Collaboration, A.L.S. Angelis et al., Phys. Lett. 126B (1983) 132.

5. For reviews see for example :
Jets in High Energy Collisions, Physica Scripta 19 (1979), edited by K. Hansen and P. Hoyer;
P. Darriulat, Ann. Rev. Nucl. Part. Sci. 30 (1980) 159.

6. R.P. Feynman, Photon Hadron Interactions, Benjamin, New York, 1972;
S.M. Berman and M. Jacob, Phys. Rev. Lett. 25 (1970) 1683
S.M. Berman, J.D. Bjorken and J.B. Kogut, Phys. Rev. 4D (1971) 3388.

7. J.D. Bjorken, Phys. Rev. D8 (1973) 4098.

8. The Staff of the CERN $\bar{p}p$ Project, Phys. Lett. 107B (1981) 231.

9. UA2 Collaboration, P. Bagnaia et al., Z. Phys. C 20 (1983) 117.

10. UA1 Collaboration, G. Arnison et al., Phys. Lett. 132B (1983) 214.

11. UA1 Collaboration, G. Arnison et al., Phys. Lett. 132B (1983) 223, and CERN-EP/83-198.

12. T. Åkesson and H. Bengtsson, Phys. Lett. 120B (1983) 133.

13. B. Mansoulié, The UA2 apparatus at the CERN $\bar{p}p$ Collider, proceedings 3rd Moriond workshop on $\bar{p}p$ physics, editions Frontières, 1983, p. 609;
M. Dialinas et al., The vertex detector of the UA2 experiment, LAL-RT/83-14, ORSAY, 1983;
C. Conta et al., The system of forward-backward drift chambers in the UA2 detector, CERN-EP/83-176, submitted to Nucl. Instrum. Methods;
K. Borer et al., Multitube proportional chambers for the localization of electromagnetic showers in the UA2 detector, CERN-EP/83-177, submitted to Nucl. Instrum. Methods.

14. A. Beer et al., The central calorimeter of th UA2 experiment at the CERN $\bar{p}p$ Collider, CERN-EP/83-175, submitted to Nucl. Instrum. Methods.

15. The cross-section seen by the "minimum bias" trigger counters is 43.9 ± 3.5 mb as measured by:
UA4 Collaboration, R. Battiston et al., Phys. Lett. 117B (1982) 126 and G. Sanguinetti, proceedings 3rd Moriond workshop on $\bar{p}p$ physics, editions Frontières, 1983, p.25.

16. The integrated luminosities for the data used at low thresholds are $\int \mathcal{L} dt$ = 0.56 nb^{-1} for ΣE_T from 30 to 40 GeV, 5.8 nb^{-1} from 40 to 50 GeV and 12.3 nb^{-1} from 50 to 60 GeV.

17. UA5 Collaboration, K. Alpgard et al., Phys. Lett. 115B (1982) 71.

18. TASSO collaboration, M. Althoff et al., DESY 83-010.

19. B.R. Webber, Contribution to the XVIII Rencontre de Moriond on Proton-Antiproton collider physics, La Plagne, March 19-25, 1083 and CERN TH-3569 (1083)

20. G. Sterman and S. Weinberg, Phys. Rev. Lett. 39 (1977) 1436.
K. Shizuya and S-H. H. Tye, Phys. Rev. Lett. 41 (1978) 787.
M.B. Einhorn and B.G. Weeks, Nucl. Phys. B146 (1978) 445.

21. R. Horgan and M. Jacob, Nucl. Phys. B179 (1981) 441.

22. ISAJET programme, written by F. Paige and S. Protopopescu, BNL report 31987 (1981).

23. B. Humpert, Two-jet production in $\bar{p}p$ collisions, to be published, and private communication.

24. N.G. Antoniou et al., Hadron and jet production at Collider and ISR, Mc Gill Univ. preprint (1983), and Phys. Lett. 128B (1983) 257.

25. Z. Kunszt and E. Pietarinen, Phys. Lett. 132B (1983) 453.

26. G. Altarelli, QCD at the Collider, Ref. Th. 3733-CERN, to be published in the proceedings of the International School of Subnuclear Physics, Erice, Italy, 3-14 Aug. 1983.

27. The upper bounds in Figs.10a and 10b correspond to a calculation of Ref. [23] using $\Lambda = 0.5$ GeV, $Q^2 = 2\,s\,t\,\hat{u} / (s^2 + t^2 + \hat{u}^2)$ and the structure functions (SF) of R. Baier et al., Z. Phys. C 2 (1979) 265. The lower bound in Fig. 10a is from Ref. [25] with $\Lambda = 0.5$ GeV, $Q^2 = 4p_T^2$ and SF from J.F. Owens and E. Reya, Phys. Rev. D17 (1978) 3003. The lower bound in Fig. 10b uses the same SF and is from Ref. [23].

28. The calculations of Ref. [21] uses $Q^2 = p_T^2$, $\Lambda = 0.5$ GeV and SF of the type J.F. Owens et al., Phys. Rev. D18 (1978) 1501. The curve shown from Ref. [23] uses the SF of H. Abramowicz et al., Z. Phys. C13 (1982) 199, $\Lambda = 0.5$ GeV and Q^2 as given in [27]. The curve from Ref. [24] is obtained with $\Lambda = 0.2$ GeV, $Q^2 = 2\,p_T^2$ and SF from M. Glück et al., Z. Phys. C13 (1982) 119.

29. E. Eichten et al., Phys. Rev. Lett. 50 (1983) 811 ;
M. Abolins et al., proceedings of the DPF summer study on elementary particle physics, Snowmass, Colorado 1982, p.274.

30. B. Humpert, Jet-jet production in the multi-TeV range, Ref. TH.3817-CERN (Feb. 1984).

JET TOPOLOGIES IN HADRON-HADRON COLLISIONS †

R. D. Field
Particle Theory Group
Department of Physics
University of Florida
Gainesville, Florida 32611

Abstract

Event topologies in pp collisions at W=60 GeV and in $\bar{p}p$ collisions at W=540 GeV resulting from a QCD Monte-Carlo model are examined. The model includes gluon radiation both in the initial and final states and the outgoing hadrons are labeled according to whether they arise before or after the hard parton-parton collision. Transverse energy flows and transverse energy grids are studied with emphasis, not on "jet finding", but on the patterns of energy deposition. These patterns are quantified by examining the multiplicity of transverse energy clusters each of which has energy greater than some fixed amount. At high transverse energy the model produces events that are slightly less "two-jet" like than the UA2 data. However, the predicted frequency of occurrence of three cluster events is in good agreement.

†Work supported in part by the U. S. Department of Energy under contract No. DE-AS-05-81-ER40008.

I. Introduction

In leading order QCD, mesons are produced at large transverse momentum in hadron-hadron collisions as the result of a hard parton-parton collision; one parton from the beam and one from the target hadron. The resulting elastic parton-parton scattering produces two outgoing partons which subsequently "fragment" into jets of hadrons producing the familiar four jet event topology shown in Fig. 1 (two large p_T jets, a beam jet, and a target jet).

The effects of soft and collinear gluon emissions off the incoming partons are treated by assigning a Q dependence to the parton structure functions. Similarly, the soft and collinear gluon emissions off the outgoing partons results in a Q dependence of the parton fragmentation functions. The Q dependences are prescribed by perturbation theory (e.g. the Altarelli-Parisi equations [1]). However, since to leading order, one only need consider the case where the gluon radiation is either soft or collinear, one is still left with an effective two-to-two subprocess.

The first attempts to include noncollinear gluon emission in hadron-hadron collisions were made by Fox and Kelly [2] and by Field, Fox and Kelly [3] and by Odorico [4]. Here one approximates the effects of $2 \to N$ subprocesses by including the noncollinear emission of gluons off both the initial and final state partons in the "leading pole" approximation [5-7]. Final state partons have timelike invariant masses with the radiated partons being kinematically constrained to have invariant masses less than their parents with the difference being converted into the transverse momentum of the emitted partons. The radiated partons themselves radiate more partons until all invariant masses have been degraded to some cut-off mass, μ_A, thus producing a "parton shower". Initial partons also form a shower, but in this case the partons have spacelike invariant mass. The initial partons are

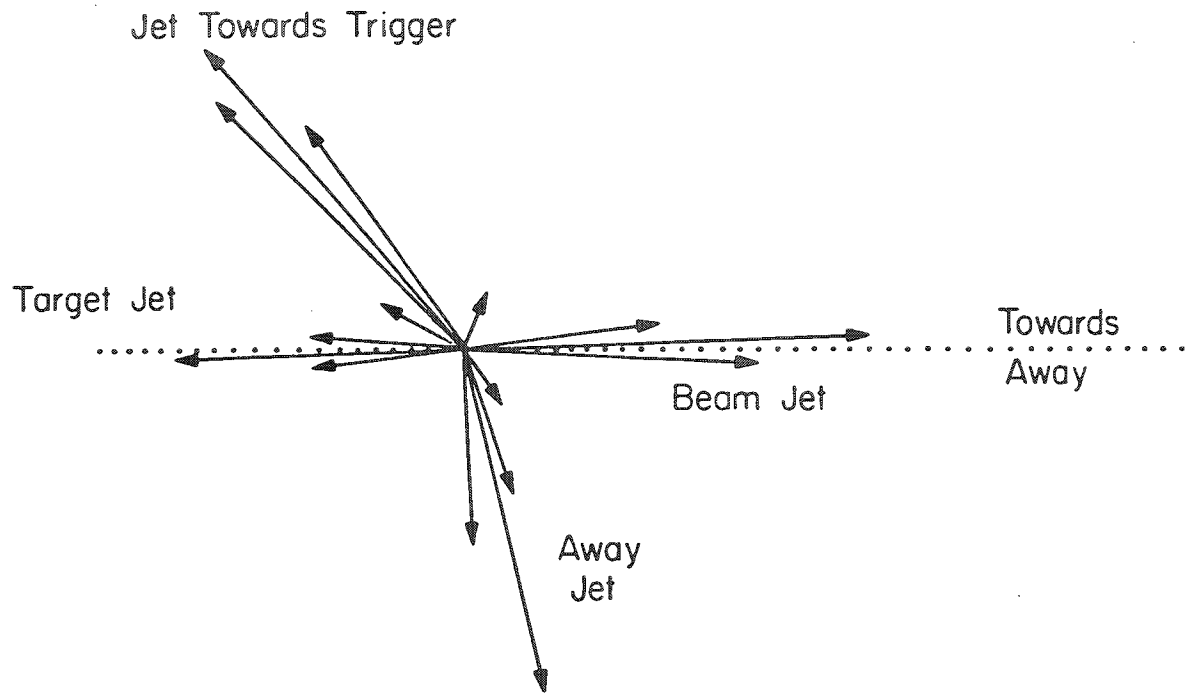

Fig. 1. Illustration of the four jet event structure resulting from a beam hadron (entering from the left along the dotted line) colliding with a target hadron (entering from the right along the dotted line) in the CM frame: two jets (collections of particles moving in roughly the same direction) with large transverse momentum, p_T, and two with small p_T that result from the break up of the beam and target hadrons.

evolved from an initial invariant mass of $-(\mu_B)^2$ to a maximum (negative) invariant mass of $Q^2 = -4\hat{p}_T^2$, where $\hat{p}_T$ is the transverse momentum of the hard parton-parton subprocess [8].

In order to compare with experiment one must have a model for the way the outgoing partons turn into hadrons. The approach adapted by Wolfram and myself [9] involves keeping track of the color strings (or clusters). All gluons are forceably split into $q\bar{q}$ pairs and color singlet clusters are formed with a distribution of invariant mass. For e+e- annihilations we choose a small cut-off invariant mass, μ_A, and allowed all clusters to "decay" isotropically in their rest frame according to a simple phase-space prescription. To get a completely color neutral system in hadron-hadron collisions it is necessary to include the clusters containing the color "hole" that remains after a parton is removed from the beam and target hadron ("holes" are assigned the full remaining momentum after the parton is removed). In our contribution to the Erice workshop [10] Fox and I used the phase-space method for clusters of mass less than 3 GeV. Larger mass clusters were parameterized by back-to-back Field-Feynman [11] jets in the color string CM frame.

In the analysis presented here I do not keep track of color strings and fragment each parton (and "hole") independently in the hadron-hadron CM frame according to the Field-Feynman prescription. In addition, I take the invariant mass cut-offs $\mu_A=\mu_B=2$ GeV and the QCD perturbative parameter $\Lambda=0.4$ GeV. I do not believe that this is the most sensible hadronization procedure [10]. However, with this fragmentation scheme I can keep track of where the outgoing hadrons came from. This is illustrated in Fig. 2. Type 1 hadrons are those arising from the initial partons A_1, A_2, ... etc. plus the hadrons coming from the fragmentation of the "hole" h_a. Similarly, type 2 hadrons arise from initial partons B_1, B_2, ... etc. plus "hole" h_b. Outgoing

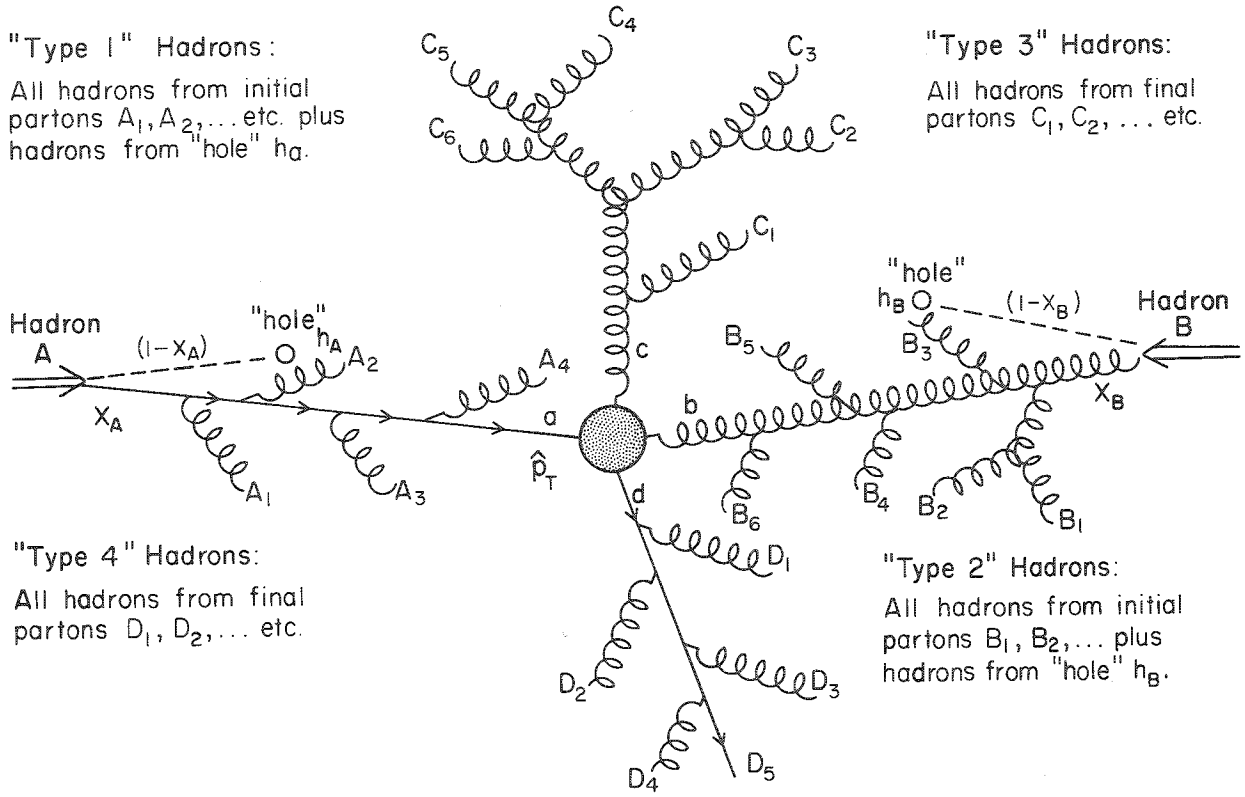

Fig. 2. Illustration of a hard scattering QCD parton-shower Monte-Carlo event in which the hadrons are labeled according to where they originate. Type 1 hadrons arise from the fragmentation of initial partons A_1, A_2, ... etc. plus the fragmentation of the "hole" h_a (which is assigned fractional momentum $1-x_a$). Similarly, type 2 hadrons arise from the fragmentation of initial partons B_1, B_2, ... etc. plus "hole" h_b. Type 3 and type 4 hadrons arise from the fragmentation of outgoing partons C_i and D_i, respectively, with $\hat{p}_T$ being the transverse momentum of the hard constituent scattering, ab → cd.

partons C_i and D_i fragment into hadrons of type 3 and type 4, respectively. I have been careful not to call, for example, type 3 hadrons a "jet". Type 3 hadrons may form several jets or no jets or type 3 and type 1 hadrons may conspire to form one jet. The definition of a "jet" is at the discretion of the experimenter. The motivation here is to see in the Monte-Carlo for various triggers and energies not only the event topology but where the hadrons originated. I am not interested in fitting the data perfectly but instead in learning more about the underlying QCD dynamics.

In the naive four jet language of Fig. 1, type 1 and type 2 hadrons represent the beam and target jets, respectively, while type 3 and type 4 hadrons constitute the two large p_T jets. QCD as we shall see is not so simple. Sometimes type 1 or type 2 hadrons will form a large p_T jet. Sometimes type 3 hadrons will split and form two or three jets, etc.

II. Proton-Proton Collisions at W=60 GeV

Fig. 3 shows the cross sections for various transverse energy triggers at W=60 GeV resulting from the Monte-Carlo with $\hat{p}_T > 2$ GeV. The total cross section for this $\hat{p}_T$ range is 2.1 mb at this CM energy. At low values of the total transverse energy, E_T, the cross section depends simply on the solid angle subtended and the back-to-back $\Delta\phi=45^0$, the side-to-side $\Delta\phi=45^0$, and the single $\Delta\phi=90^0$ triggers all result in roughly the same cross section. As E_T increases the back-to-back trigger dominates over the other two indicating a two jet (really a two blob) topology. The large aperture $\Delta\phi=360^0$ cross section results are in rough agreement with the preliminary AFS data [12].

The AFS large aperture $\Delta\phi=360^0$ data at W=60 GeV indicate a rapid change in the event structure at E_T values of about 30 GeV. Below this value of E_T events are more spherical, whereas above this value events are more "two jet

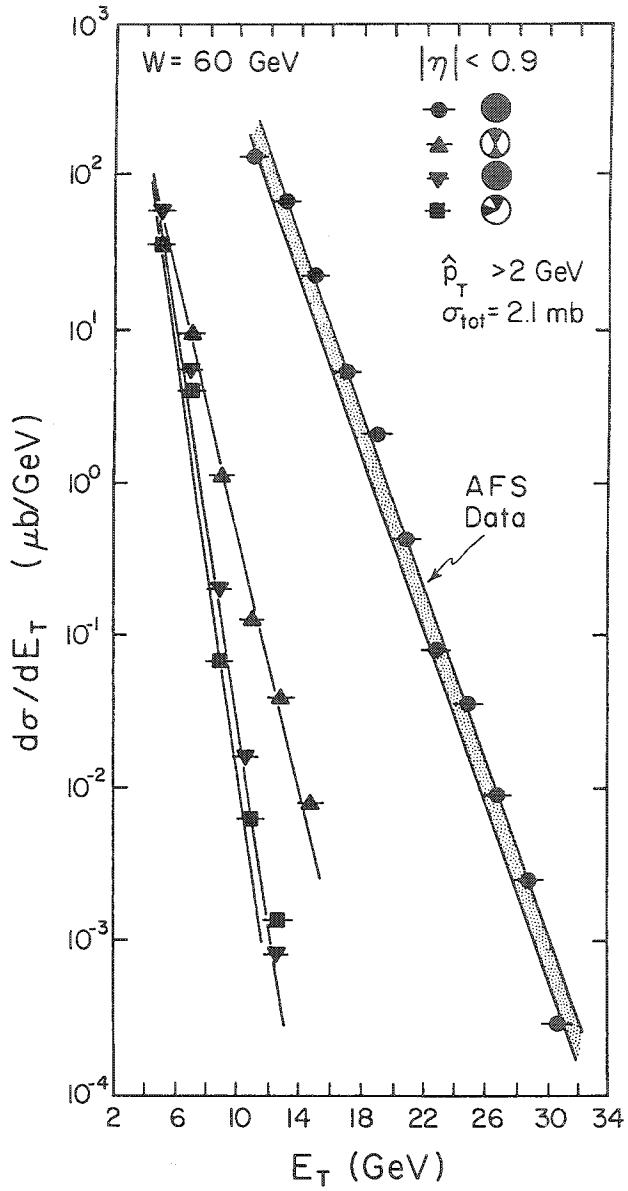

Fig. 3. Total transverse energy, E_T, cross section for pp collisions at W=60 GeV and pseudorapidity range $-0.9 < \eta < 0.9$ resulting from the QCD Monte-Carlo model integrated over the hard scattering region $\hat{p}_T > 2$ GeV which yields a contribution to the total cross section of 2.1 mb. The solid dots are for a large aperture $\Delta\phi=360^0$ trigger while the up and down pointing triangles are for a $\Delta\phi=90^0$ and a back-to-back $\Delta\phi=45^0$ trigger, respectively. The squares are for a side-to-side $\Delta\phi=45^0$ trigger. Preliminary AFS data [12] are indicated by the shaded region.

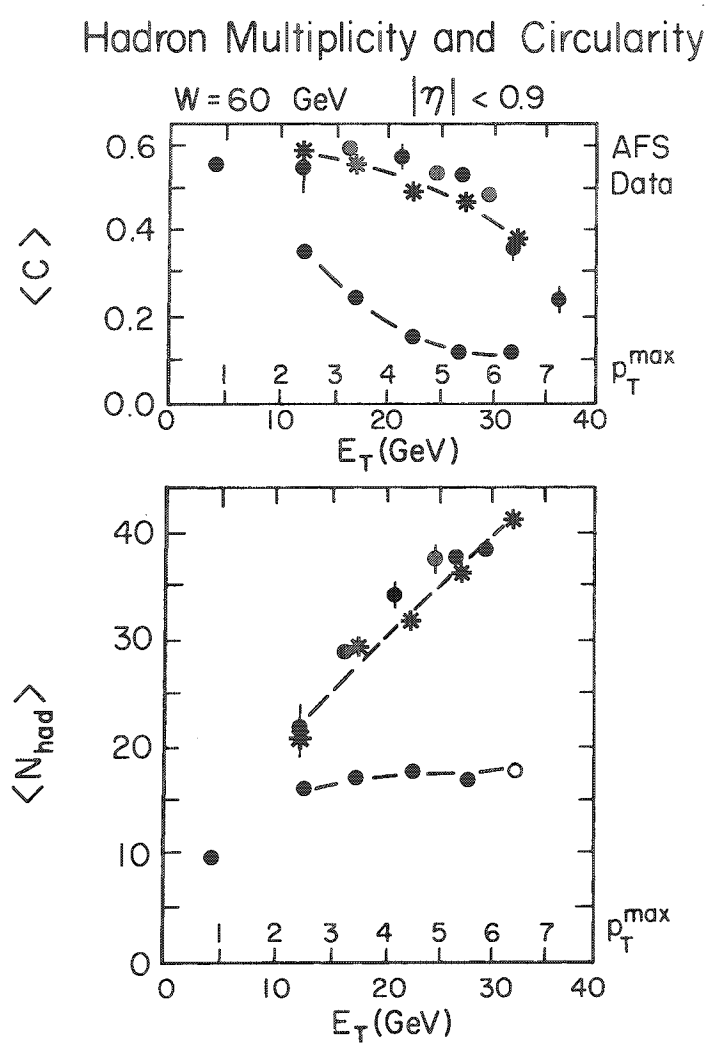

Fig. 4. Comparison of AFS data [12] (solid dots) and the QCD Monte-Carlo model (asterisk and dashed lines) on the average circularity (upper graph) and average hadron multiplicity (lower graph) for a large aperture $\Delta\phi=360^0$ calorimeter trigger versus the total transverse energy, E_T, in pp collisions at W=60 GeV. Also shown are the results of the QCD Monte-Carlo for the average circularity and hadron multiplicity (open circles) plotted versus the maximum transverse momentum in the event, p_T^{max}.

like" in nature. This is indicated by the rapid change in the average value of the circularity shown in Fig. 4 [13]. Different triggers preferentially select different parton substructures. Large aperture calorimeter triggers are biased in favor of parton subprocesses involving large amounts of gluon Bremsstrahlung [3,10]. Higher and higher E_T values are produced by a larger and larger multiplicity of hadrons each having only a slightly increasing mean p_T. As seen in Fig. 4, as the E_T increases so does the total multiplicity of hadrons.

Fig. 5 and Fig. 6 show the average transverse energy flow about the circularity axis for large aperture $\Delta\phi=360^0$ triggers in the range $10 < E_T < 15$ GeV and $25 < E_T < 30$ GeV, respectively. The average circularity has decreased from 0.57 to 0.46. Nevertheless, the transverse energy contribution from hadrons of type 1 and 2 has increased (shaded region). The central core of the energy flow pattern expands both in the direction of the circularity axis (y-axis) and in the perpendicular direction (x-axis) as the total E_T increases indicating large gluon Bremsstrahlung contributions. In spite of this, the average circularity resulting from the Monte-Carlo does begin to decrease at around E_T=30 GeV (Fig. 4). It is not clear whether this change is as rapid as seen in the data since at present I do not have sufficient statistics to produce a point at 40 GeV.

Single particle triggers, on the other hand, bias on against large amounts of gluon radiation. Nature cannot afford to waste the energy. This can be seen in Fig. 4 where the average circularity and hadron multiplicity is also ploted versus the maximum p_T in the event, p_T^{max}. Fig. 7 shows that the energy flow perpendicular to the direction of the maximum p_T hadron (x-axis) actually decreases slightly as p_T^{max} increases which is in contrast to the expanding central core for the large aperture calorimeter trigger (Fig. 5 and Fig. 6).

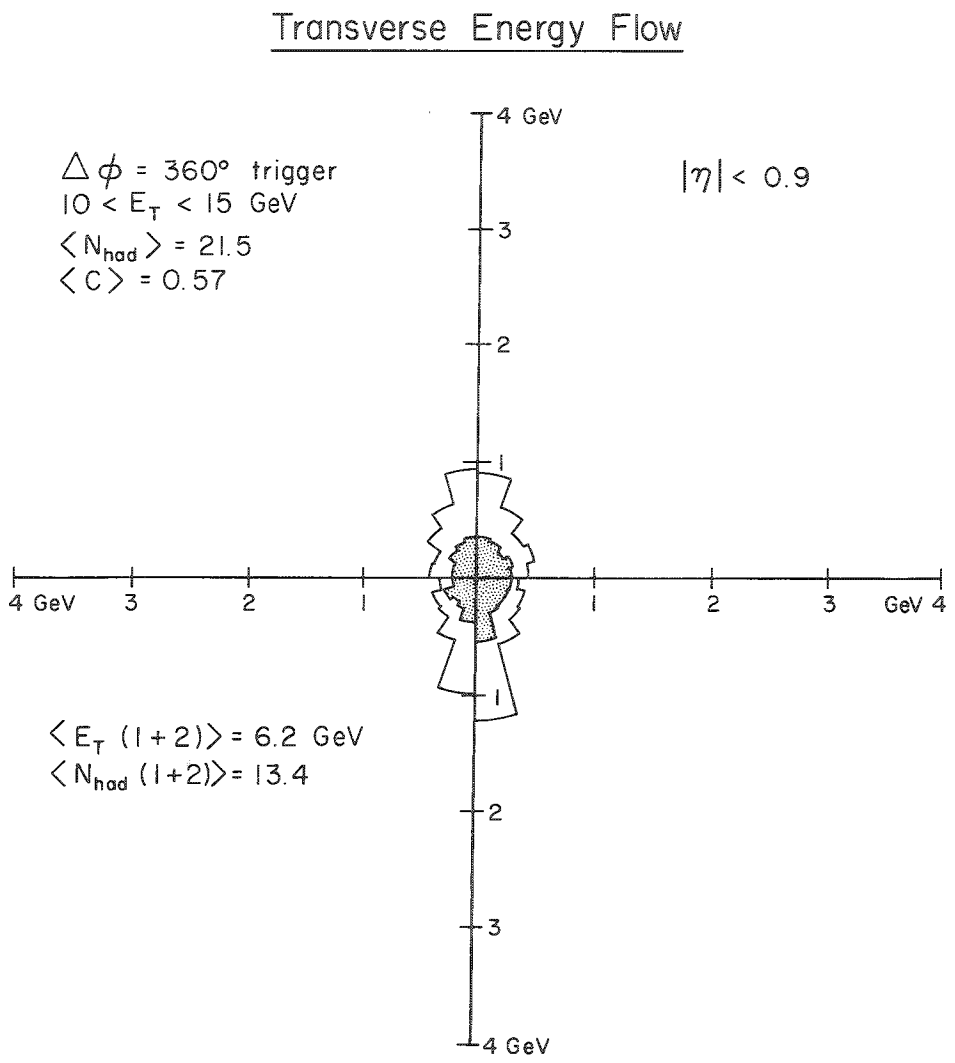

Fig. 5. Average transverse energy flow with respect to the circularity axis (y-axis) resulting from the Monte-Carlo model with a large aperture $\Delta\phi=360^0$ calorimeter trigger for pp collisions at W=60 GeV for the total transverse energy range $10 < E_T < 15$ GeV. Each bin represents the total amount of transverse energy in the range $\Delta\phi=18^0$ and $|\eta| < 0.9$ with ϕ measured with respect to the circularity axis on an event-by-event basis. The shaded region is the amount of energy arising from hadrons of type 1 and type 2 (see Fig.2).

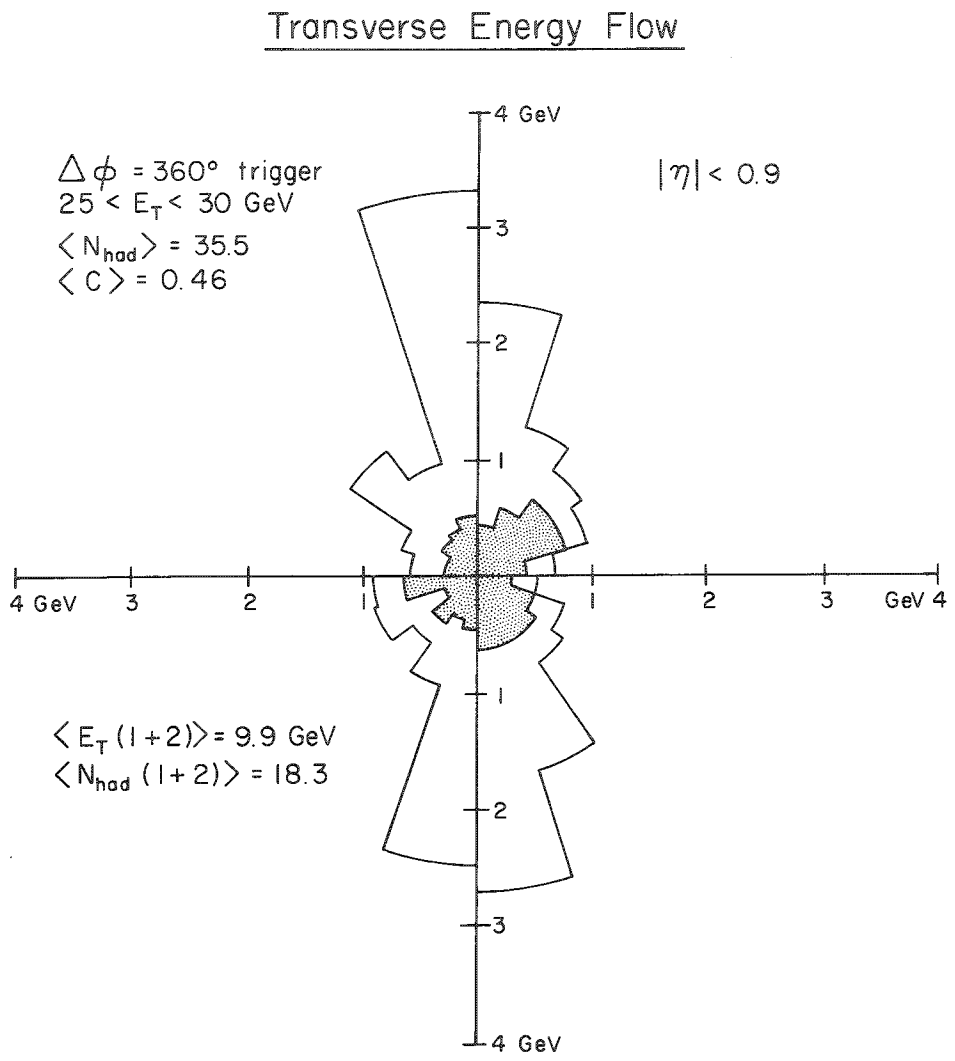

Fig. 6. Same as Fig. 5 but for the total transverse energy range $25 < E_T < 30$ GeV.

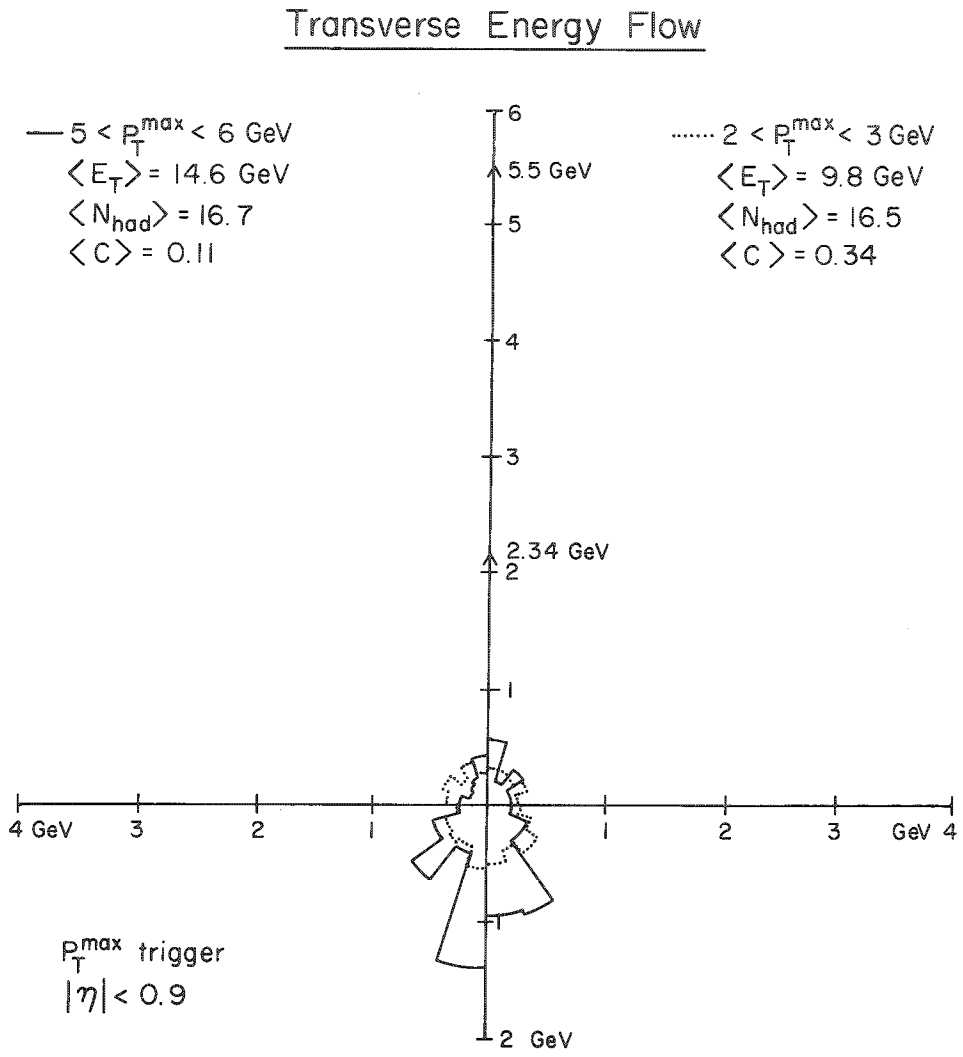

Fig. 7. Same as Fig. 5 but for two different ranges for the maximum transverse momentum particle in the event, p_T^{max}, and where the y-axis is now the direction of that particle.

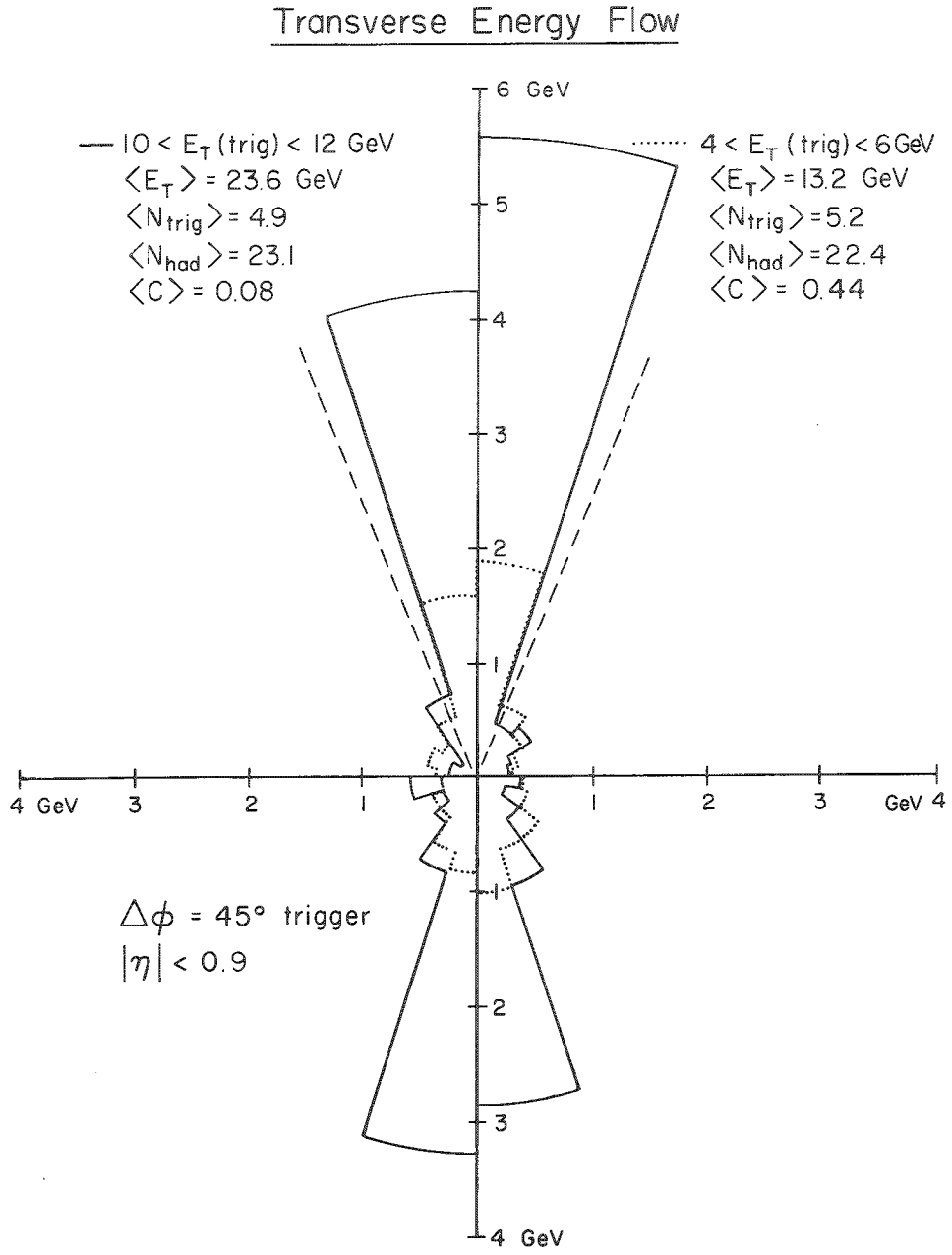

Fig. 8. Same as Fig. 5 but for two different ranges of a small aperture $\Delta\phi=45^0$ trigger and where the positive y-axis is now the center of the trigger.

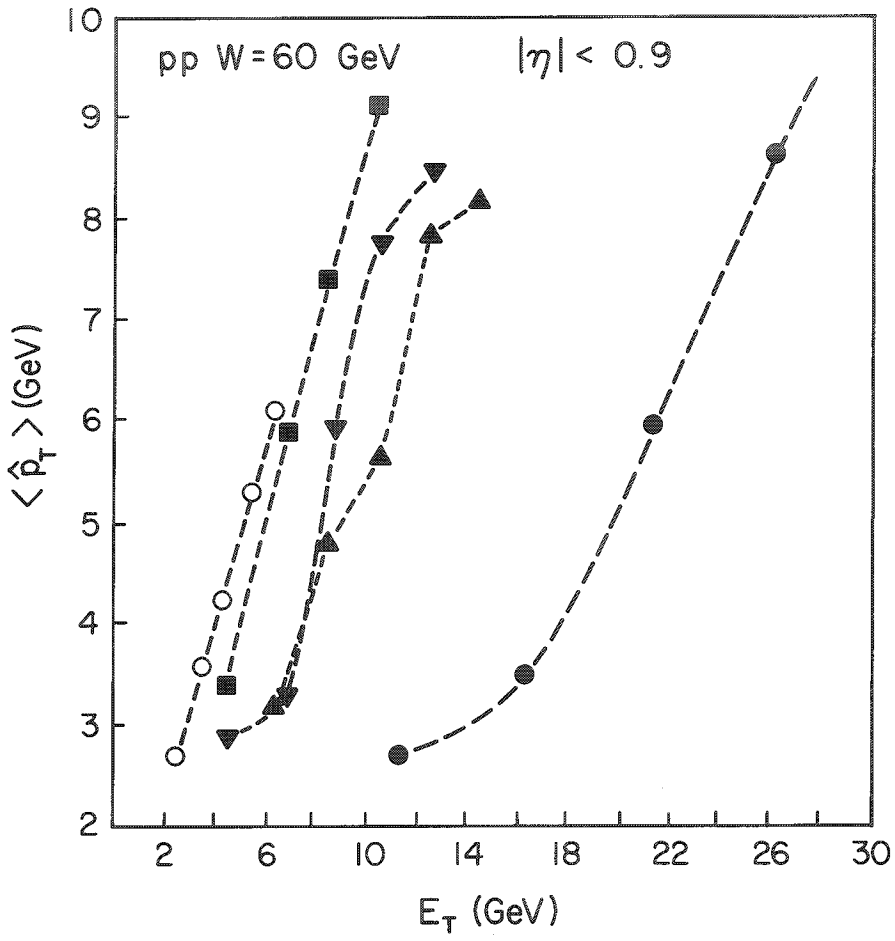

Fig. 9. Average value of the transverse momentum of the hard scattering parton-parton elastic subprocess, $\hat{p}_T$, resulting for the QCD Monte-Carlo in pp collisions at W=60 GeV versus the total trigger transverse energy, E_T. The solid dots correspond to a large aperture $\Delta\phi=360^0$ trigger. The solid squares and the down pointing triangles correspond to a $\Delta\phi=45^0$ and a $\Delta\phi=90^0$ trigger while the up pointing triangles refer to a back-to-back $\Delta\phi=45^0$ trigger. The open circles correspond to events in which the maximum single particle p_T is labeled on the x-axis (not E_T). In all cases the pseudorapidity range is $|\eta| < 0.9$. The hard scattering transverse momentum is, of course, not an observable that is directly accessible experimentally.

Small aperture calorimeter triggers fall in between the extremes of a large aperture trigger and a single particle trigger. As seen in Fig. 8, demanding large transverse energies into a single $\Delta\phi=45^0$ trigger (positive y-axis) results in event topologies that are considerably more two-jet like in nature than the large aperture $\Delta\phi=360^0$ results. Here the central core changes very slightly as the trigger energy increases.

Clearly each energy and each trigger favors a different underlying parton substructure. In QCD the parton substructure is more complicated (and more fluctuating) than in the naive parton model. By comparing event topologies for various triggers one can reveal the QCD substructure. Fig. 9 shows that the hard scattering regime can be reached by any of the various triggers. However, the energy of the trigger and the event shape may be quite different. For example, if one would like to explore hard scatterings at $\hat{p}_T$=6 GeV, one can take single p_T events at p_T=6 GeV, small aperture $\Delta\phi=45^0$ triggers at E_T=7 GeV, or large aperture $\Delta\phi=360^0$ triggers at E_T=22 GeV. All should be explained equally well by a correct model of QCD. The amusing thing is that each have about the same cross section. As is now well known, the idea that one can examine the hard scattering perturbative regime with a large cross section by going to large aperture calorimeter triggers is not correct.

III. Antiproton-Proton Collisions at W=540 GeV

Fig. 10 compares data on the large aperture $\Delta\phi=360^0$ total E_T cross section for $p\bar{p}$ collisions at W=540 GeV with the QCD Monte-Carlo integrated over the hard scatter range $10 < \hat{p}_T < 38$ GeV. The dashed curve represents 42,000 events, but unfortunately can only be compared with data over the limited region $50 < E_T < 100$ GeV. To compare at higher E_T values would

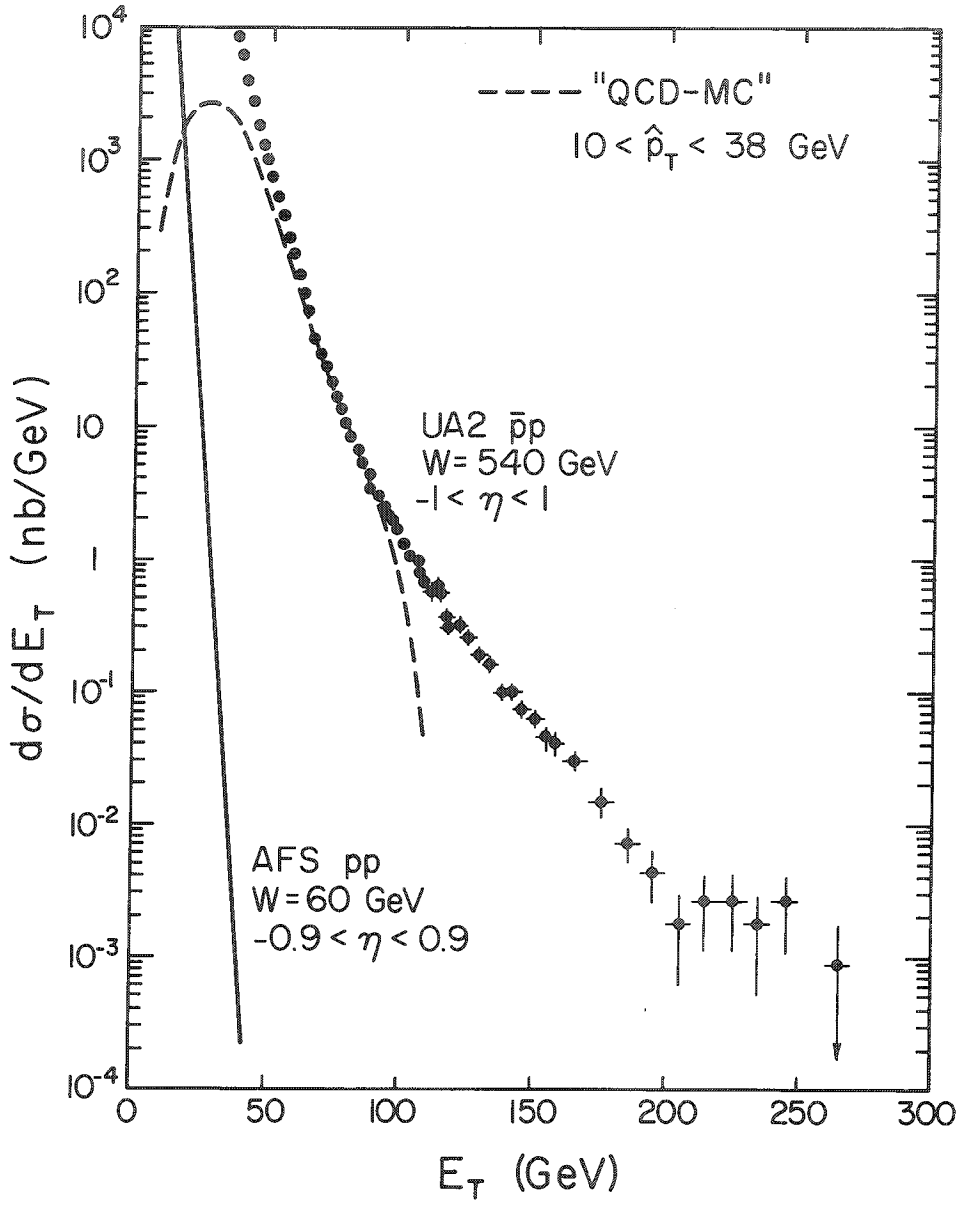

Fig. 10. Comparison of UA2 data [17] on the total transverse energy, E_T, cross section for a large aperture $\Delta\phi=360^0$ calorimeter trigger in $\bar{p}p$ collisions at W=540 GeV and for a pseudorapidity range $|\eta| < 1$ (solid dots) with the QCD Monte-Carlo model integrated over the hard scattering range $10 < \hat{p}_T < 38$ GeV (dashed curve). Also shown are the AFS data of Fig. 3.

require generating more events at large $\hat{p}_T$ values. Below E_T=50 GeV the cross section receives significant contributions from the region $\hat{p}_T$ < 10 GeV. Over the range 50 < E_T < 100 GeV the QCD Monte-Carlo agrees roughly with the data. Also shown in Fig. 10 is the AFS E_T cross section of Fig. 3 which also roughly agrees with the Monte-Carlo at W=60 GeV. This indicates that the energy dependence of the large aperture $\Delta\phi=360^0$ E_T cross section is correctly described by the model. It has previously been reported that QCD can reproduce the observed energy dependence of the single jet cross section which is extracted from the data by "jet finding" algorithms [14,15]. This analysis shows that the large aperture $\Delta\phi=360^0$ total E_T cross section is also in agreement with expectations from QCD.

Complicated "jet finding" algorithms are useful if one wants to compare the naive four jets structure of leading order QCD (Fig. 1) with data. As I mentioned above algorithms have been used to extract single jet cross sections that agree roughly with leading order QCD. On the other hand, the topological structure of QCD seems to be quite rich and what we are really interested in is how transverse energy is deposited. Here the idea is not to identify "jets" as such, but to identify patterns of energy deposition. The problem becomes one of pattern recognition and in finding observables that reflect the patterns. One way to accomplish this is to form a transverse energy grid ("lego plot") as is shown in Fig. 11 [16]. Following the analysis of UA2 [17], I divide the solid angle into bins of $\Delta\phi=10^0$ and $\Delta\phi=15^0$ and sum all the transverse energy into each bin. A 4π detector would contain 432 cells, but with the UA2 pseudorapidity cut $|\eta|<1.0$ (i.e. $40° < \theta < 140°$) one is left with 240 cells. Cells with energy less than some minimum, E_T^{min}, are ignored and clusters of cells are formed by including in a cluster all cells with a common side. Clusters are then ordered according to the total E_T of all the cells in

the cluster with cluster #1 having the highest E_T. I do not split clusters with a "valley" of E_T greater than 5 GeV into two smaller clusters as does UA2 [17]. I am not interested in finding jets (after all a jet depends on ones definition anyway), but in the patterns of energy deposition.

Figs. 11, 12, and 13 and Table 1 give the properties of the three larges E_T events resulting from the QCD Monte-Carlo with $10 < \hat{p}_T < 38$ GeV. Event 1 in Fig. 11 might be labeled a "two cluster event", since the first two clusters have E_T values of 55.8 and 28.2 GeV, respectively, while the remaining clusters are all less than 10 GeV. However, as seen in Table 1 even in the pseudorapidity region $|\eta|<1$ the event contains 57 type 2 hadrons yielding 67 GeV of transverse energy. Only 27% of the transverse energy of cluster #1 arises from hadrons of type 3 and 4. Actually cluster #2 and 3 are really the "naive two-jets" of Fig. 1. (Type 3 and 4 hadrons make up 100% and 92% of the transverse energy of cluster 2 and 3, respectively.) Event 2 in Fig. 12 has three clusters with energies greater than 20 GeV, with cluster #1 coming entirely from type 1 hadrons. Event #3 in Fig. 13 also has three clusters with transverse energies greater than 20 GeV. Cluster #3 consists of one cell of energy 25.7 GeV which arose from an outgoing quark that radiated no gluons and hence produced a narrow jet. Outgoing gluons tend to radiate lots of additional gluons sometimes depositing their transverse energy in several clusters. For example, cluster #3 and #4 in event #2 (Fig. 12) both consist primarily of hadrons of type 4 (Table 1) which arose from an initial gluon that split into many gluons.

Clearly anything can happen in a single event and these three events are probably not typical. However, they do illustrate the rich structure of the QCD Monte-Carlo. In particular, they demonstrate the importance of including both initial and final state Bremsstrahlung. Table 2 and Figs. 14-20 represent an attempt to quantify these findings.

TABLE 1

Some properties of three large E_T events in $\bar{p}p$ collisions at W=540 GeV resulting from the QCD Monte-Carlo with $\Delta\phi=360^0$ and the pseudorapidity, η, range as marked.

	Event #1		Event #2		Event #3	
	All η	$\|\eta\|<1$	All η	$\|\eta\|<1$	All η	$\|\eta\|<1$
Type 1 hadrons:						
N_{had}	24	5	81	45	8	1
E_T(GeV)	8.3	2.0	71.5	49.8	4.4	0.9
Type 2 hadrons:						
N_{had}	100	57	39	7	116	66
E_T(GeV)	95.0	67.0	14.6	2.6	84.9	64.6
Type 3 hadrons:						
N_{had}	39	35	49	35	30	27
E_T(GeV)	53.9	52.9	36.2	32.0	50.8	49.2
Type 4 hadrons:						
N_{had}	50	36	42	36	9	7
E_T(GeV)	37.2	31.2	60.5	57.4	27.3	26.8
All hadrons:						
N_{had}	213	133	211	123	163	101
E_T(GeV)	194.4	153.1	182.8	141.8	167.4	141.5

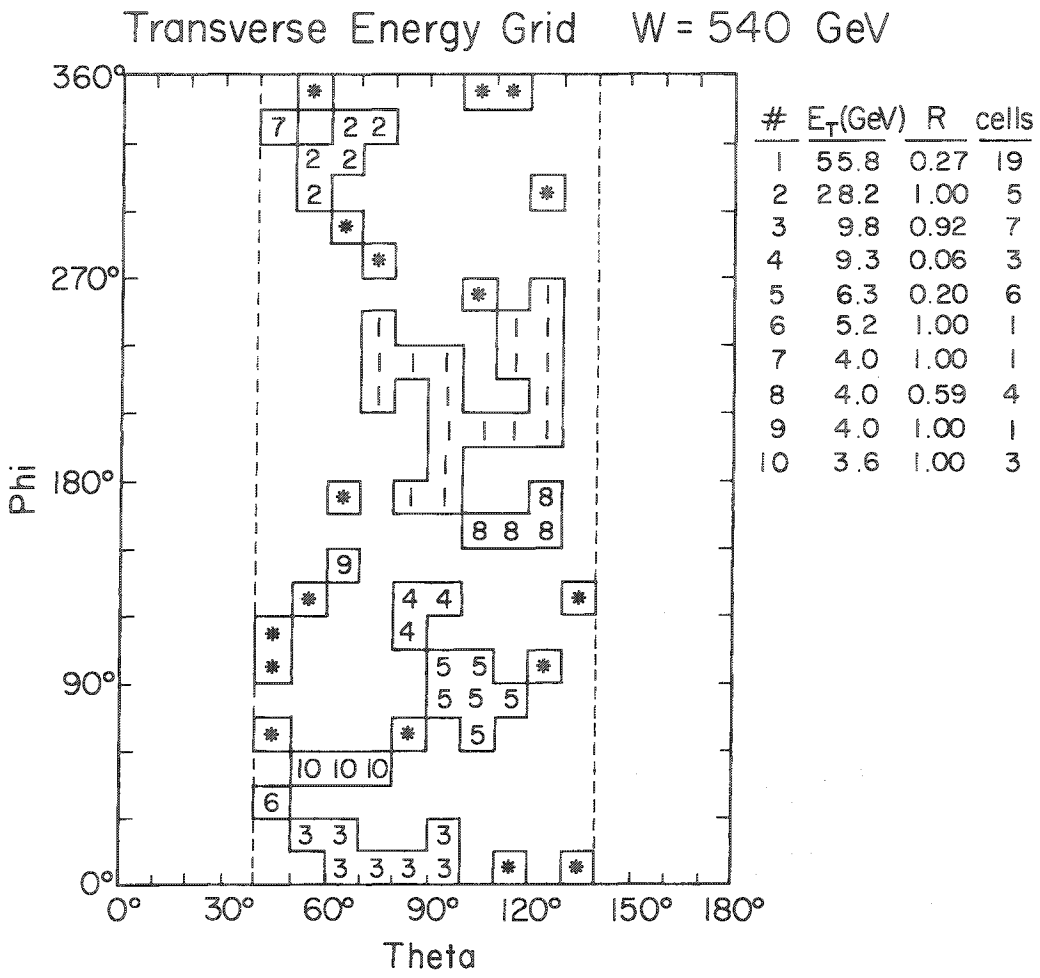

Fig. 11. Transverse energy grid for event #1 of Table 1. The solid angle $40° < \theta < 140°$ and $0° < \phi < 360°$ is divided into cells of $\Delta\theta = 10^0$ and $\Delta\phi = 15^0$ and cells with total transverse energy less than $E_T^{min} = 0.4$ GeV are omitted. Clusters are formed by including in a cluster all cells with a common side and are ordered according to their total transverse energy. The top 10 clusters are shown in the figure with the asterick referring to cells which belong to lower ranked clusters. The quantity R refers to the fraction of the total energy of a given cluster that is due to hadrons of type 3 and 4 (see Fig. 2).

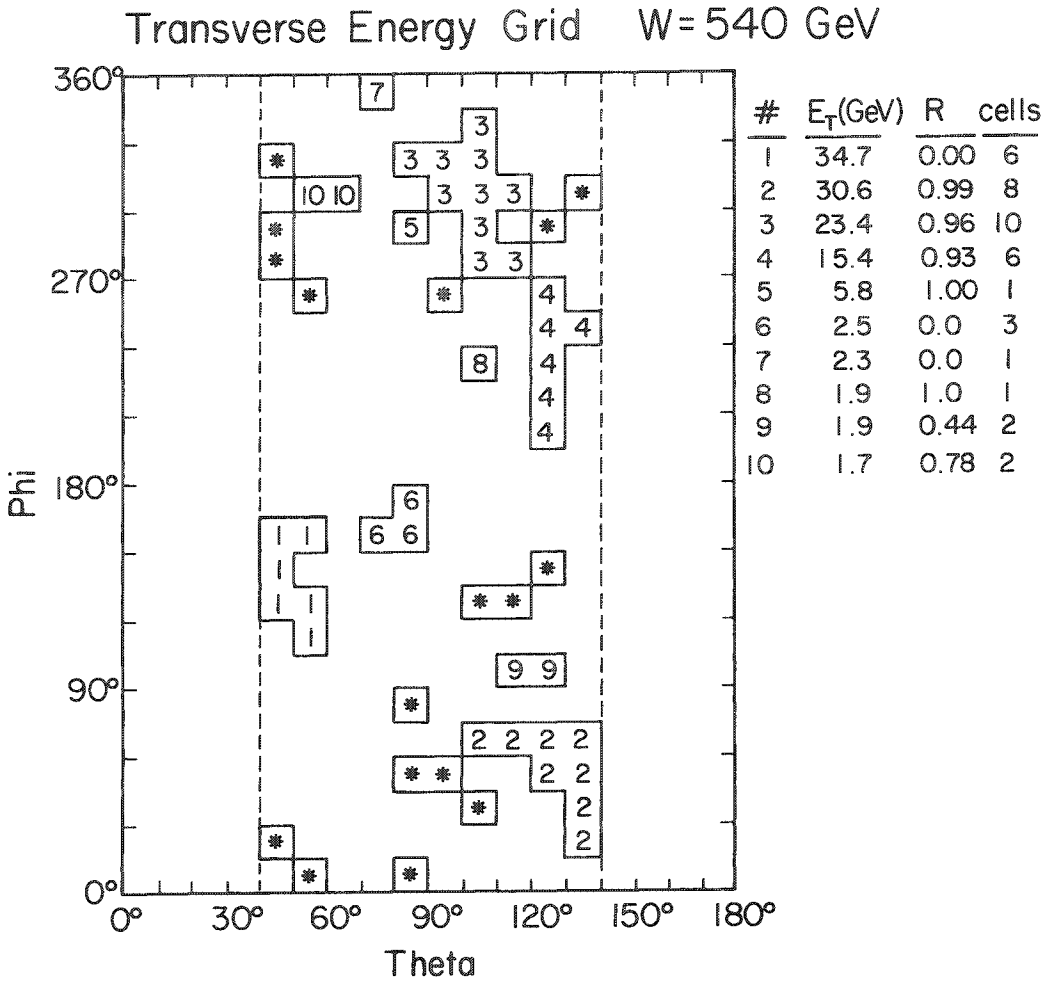

Fig. 12. Same as Fig. 11 but for event #2 in Table 1.

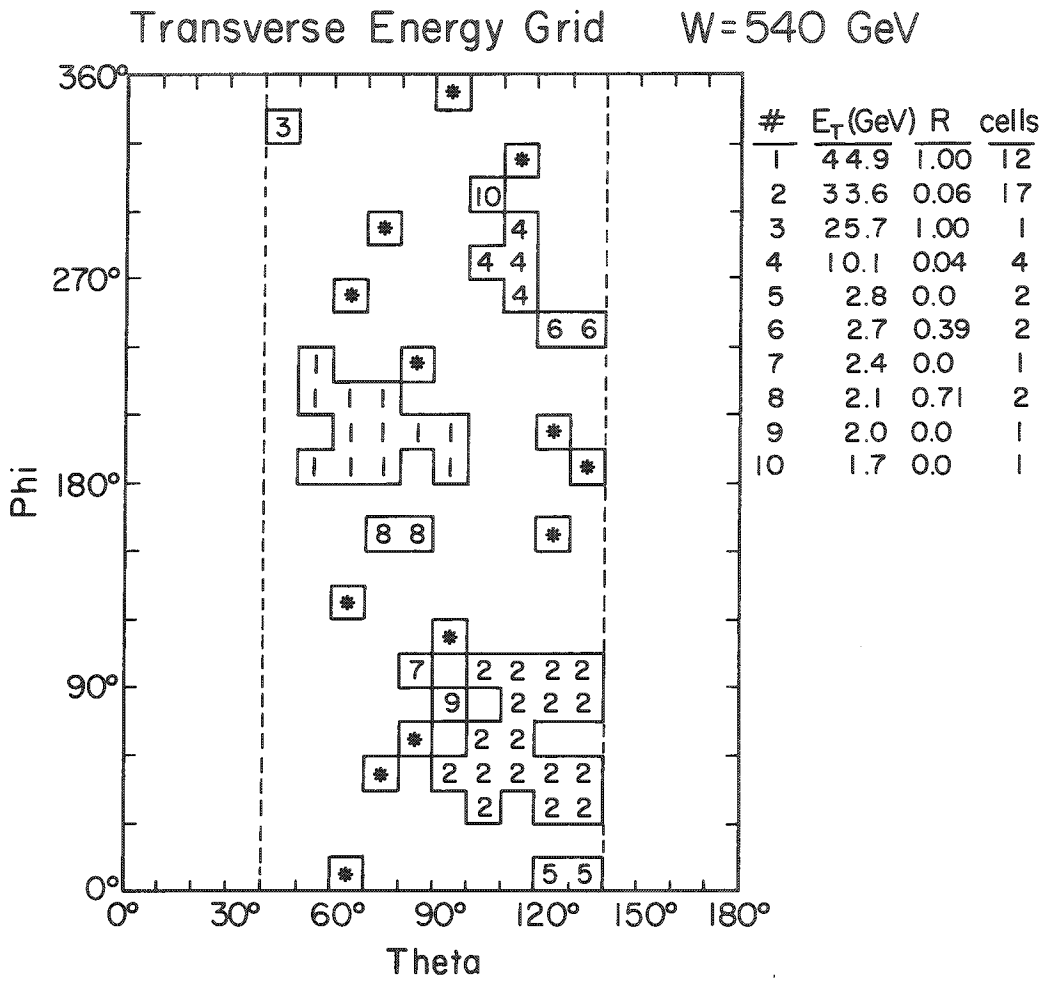

Fig. 13. Same as Fig. 11 but for event #3 in Table 1.

In the E_T range 50 - 100 GeV an average event contains mostly empty cells. Table 2 shows that in the range $80 < E_T < 90$ GeV on the average 70 cells contain energy with 47 remaining with $E_T^{min} < 0.4$ GeV (out of a possible 240 cells). On the average only 20% of the cells contain transverse energy greater than 0.4 GeV. The average cell multiplicity is compared with data from UA2 [17] in Fig. 14. At E_T=100 GeV the Monte-Carlo has a slightly higher cell multiplicity (about 6 cells out of 240), but I do not feel that this difference is significant. In the Monte-Carlo the 47 cells then combine to form 24 clusters on the average, which is a clear indication of "clustering". At these values of E_T cluster #1, #2, and #3 contain on the average 8, 5, and 4 cells, respectively, with 90% of the transverse energy of cluster #1, 88% of cluster #2, and 52% of cluster #3 arising from hadrons of type 3 and 4.

Fig. 15 shows the first real discrepancy between the QCD Monte-Carlo and the UA2 data. The average values of $h_1=E_T$ (cluster #1)/E_T (total) and $h_{12}=E_T$ (cluster #1 + #2)/E_T (total) resulting from the Monte-Carlo are larger than the data at E_T=50 GeV and smaller than the data at 100 GeV. The difference at the lower E_T values might be due partially because I do not "split" large clusters into smaller ones as does UA2. However, the discrepancy at the large E_T values is genuine. Unfortunately, I do not have results from the Monte-Carlo at higher E_T, say 200 GeV, where the differences may be even greater. Clearly at $E_T > 75$ GeV the data contain more energy on the average in the first cluster and the first two clusters than the results from the Monte-Carlo while the average values of $r_{21}=E_T$(cluster #2)/E_T(cluster #1) and $r_{32}=E_T$(cluster #3)/E_T(cluster #2) roughly agree.

One might be tempted to say that the data is more "two-jet" like at high E_T than the QCD Monte-Carlo. I believe, however, that this interpretation is

TABLE 2

Average event properties for a large aperature $\Delta\phi=360^0$, $|\eta|<1$ calorimeter trigger at W=540 GeV resulting from the QCD Monte-Carlo where the maximum number of cells $N_{max}=240$ and where $E_T(3+4)$ refers to the total transverse energy resulting from hadrons of type 3 and type 4 contributing to a particular cluster, cℓ,

	$50<E_T<60$ GeV	$80<E_T<90$ GeV
$\langle N_{had}\rangle$	73	90
$\langle N_{cell}(E_T^{min}=0)\rangle$	61	70
$\langle N_{cell}(E_T^{min}=0.4$ GeV$)\rangle$	37	47
$\langle N(cluster)\rangle$	23	24
$\langle E_T(cluster\ \#1)\rangle$	14 GeV	27 GeV
$\langle E_T(3+4)/E_T(tot)\rangle$ cℓ#1	0.83	0.90
$\langle E_T(3+4)/E_T(tot)\rangle$ cℓ#2	0.67	0.88
$\langle E_T(3+4)/E_T(tot)\rangle$ cℓ#3	0.52	0.52
$\langle N_{cell}\rangle$ cℓ#1	5	8
$\langle N_{cell}\rangle$ cℓ#2	6	5
$\langle N_{cell}\rangle$ cℓ#3	3	4
$\langle N_{cell}(E_T^{min}=0)/N_{max}\rangle$	0.25	0.29
$\langle N_{cell}(E_T^{min}=0.4$ GeV$)/N_{max}\rangle$	0.15	0.20

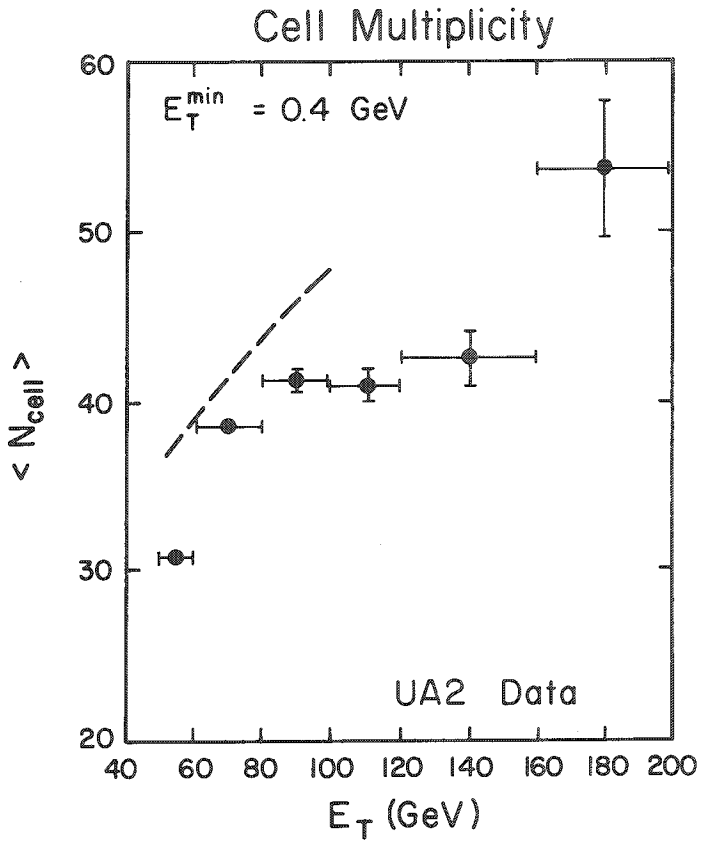

Fig. 14. Comparison of UA2 data [17] on the average cell multiplicity (see Fig. 11) with E_T^{min}=0.4 GeV in $\bar{p}p$ collisions at W=540 GeV versus the total transverse energy for a large aperture $\Delta\phi=360^0$ calorimeter trigger with the results of the QCD Monte-Carlo model. The pseudorapidity range is as in Fig. 11 ($|\eta| < 1.0$).

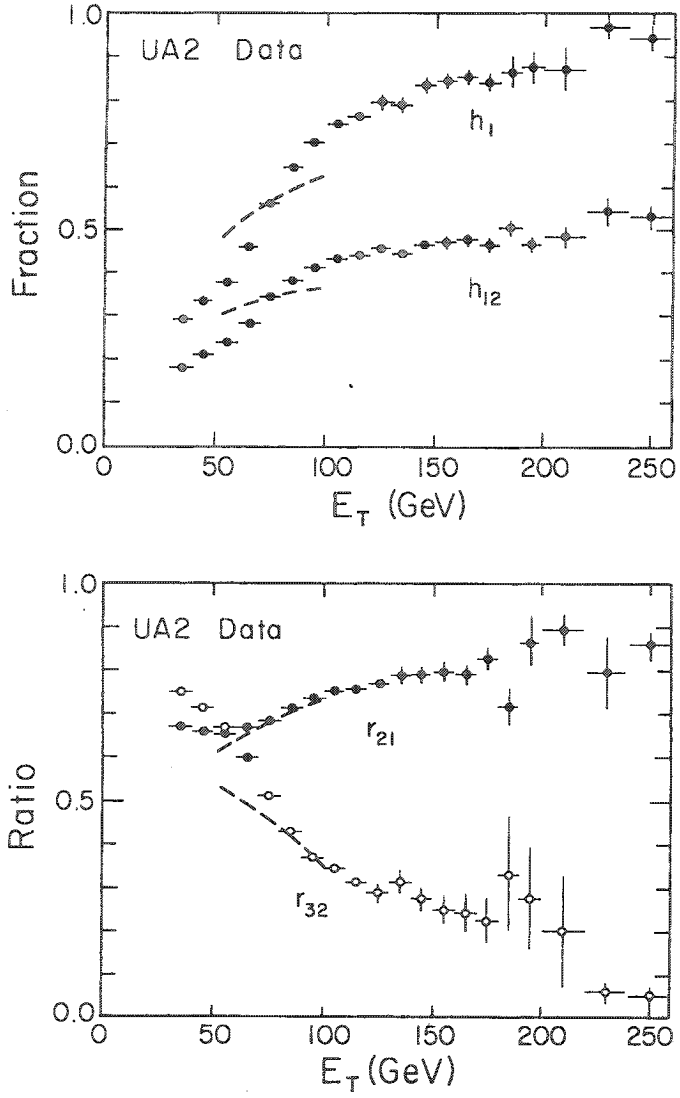

Fig. 15. (upper) Comparison of UA2 data [17] (solid dots) on the average fraction of the total transverse energy, E_T, carried by cluster #1, $h_1=E_T(cl\#1)/E_T(tot)$, and the average fraction carried by the top two clusters, $h_{12}=E_T(cl\#1+cl\#2)/E_T(tot)$ in $\bar{p}p$ collisions at W=540 GeV with the QCD Monte-Carlo model (dashed curves). (lower) Comparison of UA2 data (solid and open dots) on the ratio of the transverse energy of cluster #2 to that of cluster #1, $r_{21}=E_T(cl\#2)/E_T(cl\#1)$ and the ratio of cluster #3 to cluster #2, $r_{32}=E_T(cl\#3)/E_T(cl\#2)$ with the results of the QCD Monte-Carlo model (dashed curves). The pseudorapidity range is as in Fig. 11 ($|\eta| < 1.0$).

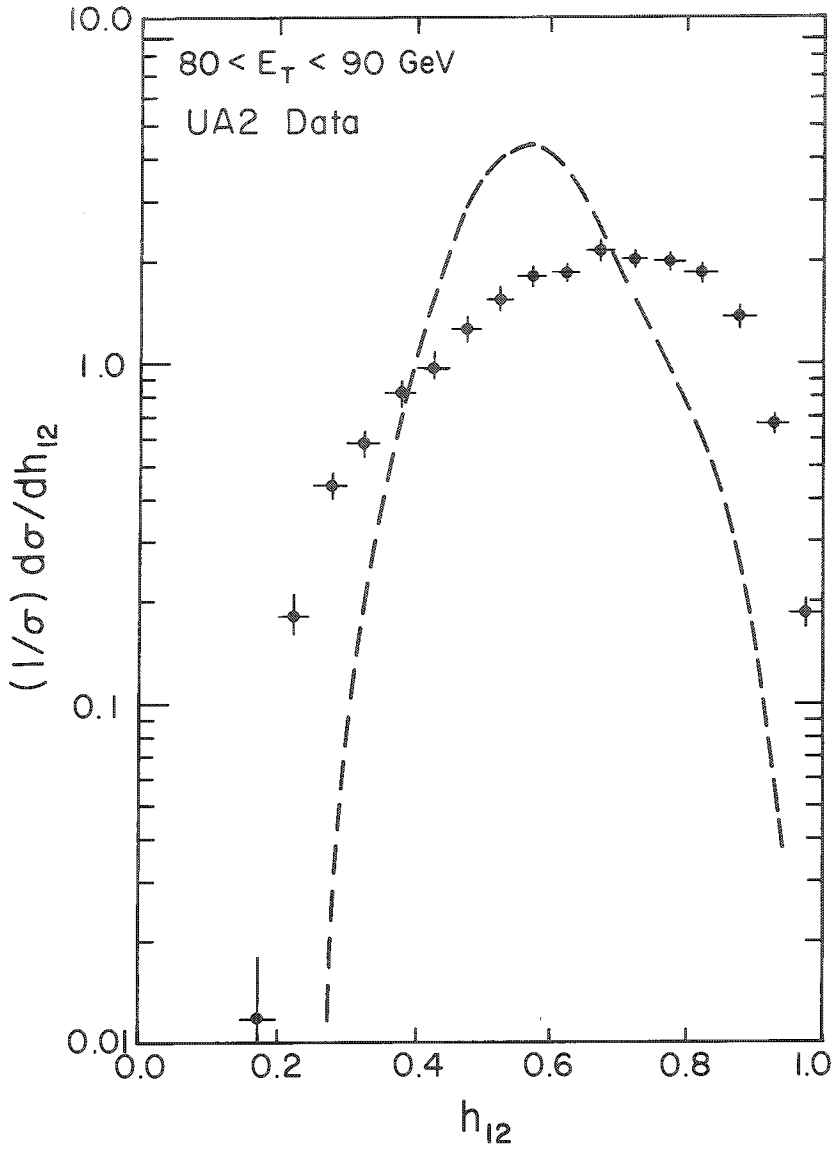

Fig. 16. Comparison of UA2 data [17] (solid dots) on the distribution of the fraction of total transverse energy, E_T, carried by the top two clusters, $h_{12}=E_T(cl\#1+cl\#2)/E_T(tot)$ for the range $80 < E_T < 90$ GeV in $\bar{p}p$ collisions at W=540 GeV with the QCD Monte-Carlo model (dashed curve). The pseudorapidity range is as in Fig. 11 ($|\eta| < 1.0$).

slightly misleading. Fig. 16 compares the distribution of h_{12} from the Monte-Carlo with the UA2 data in the range $80 < E_T < 90$ GeV. Although the data have a slightly higher average h_{12} than the Monte-Carlo, the UA2 values of h_{12} are distributed over a broad range with 22% of the events, at this energy, having $h_{12} < 0.5$. (The experimental distribution of h_{12} is broader than that produced by the Monte-Carlo.) So although the Monte-Carlo contains a little less transverse energy in the first two clusters, as is indicated by the model, there is a lot more structure in the data at this energy than just two clusters!

It is very important to look for and to quantify the multicluster topologies for they result from the rich substructure of QCD. In addition, the QCD Monte-Carlo model indicates that these topologies are much more prevalent than in e+e- annihilations at existing energies where two clusters (i.e. two jets) truly dominate. One way to quantify cluster patterns is to observe the multiplicity of clusters each of which has transverse energy greater than some value, E_T^{each}. Fig. 17 shows the average cluster multiplicities versus total E_T for E_T^{each}=0 (curve d), 1 GeV (curve e), 5 GeV (curve f), 10 GeV (curve g), and 20 GeV (curve h). Fig. 18 gives the probability of finding an event with $N_{c\ell}$ clusters each of which has energy greater than 5, 10, and 20 GeV for two different total E_T bins resulting from the QCD Monte-Carlo. Clearly the maximum number of clusters with E_T^{each} greater than, say, 20 GeV is limited by energy conservation with the average number increasing rapidly near the kinematic threshold. In QCD, however, these mean values become greater than 2 as the total transverse energy is increased. (Curve h in Fig. 17 for $E_T^{each} > 20$ GeV eventually crosses 2.0 at higher total E_T values.) In the naive parton model of Fig. 1 it would be very unlikely to find more than two clusters with E_T greater than, say, 10 GeV,

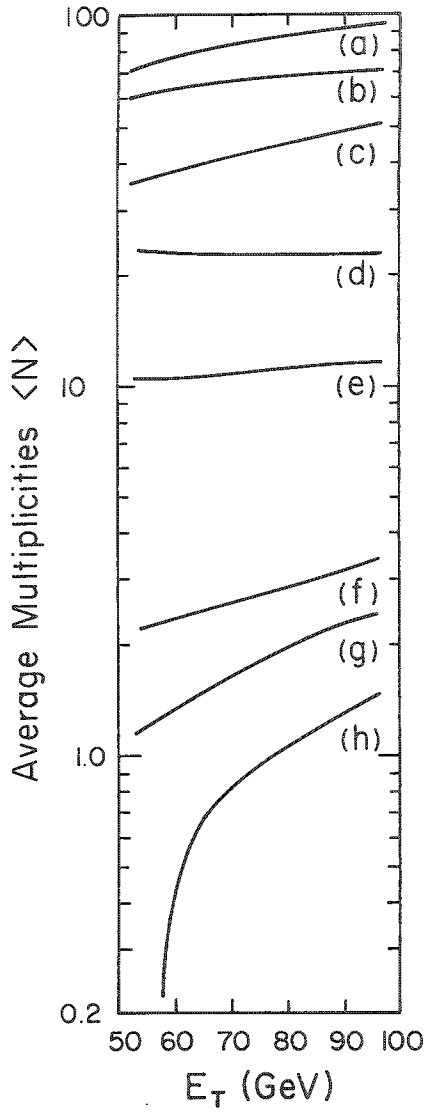

Fig. 17. Average multiplicities resulting from the QCD Monte-Carlo model for $\bar{p}p$ collisions at W=540 GeV for a large aperture $\Delta\phi=360^0$ trigger versus the total transverse energy, E_T: (a) hadron multiplicity; (b) cell multiplicity with E_T^{min}=0.0; (c) cell multiplicity with E_T^{min}=0.4 GeV; (d) cluster multiplicity with E_T^{min}=0.4 GeV; (e) cluster multiplicity with E_T^{min}=0.4 GeV and where each cluster has E_T^{each} > 1.0 GeV; (f) same as (e) but with E_T^{each} > 5.0 GeV; (g) same as (e) but with E_T^{each} > 10.0 GeV; (h) same as (e) but with E_T^{each} > 20.0 GeV. Clusters and cells are defined in Fig. 11 and the pseudorapidity range is as in Fig. 11 ($|\eta| < 1.0$).

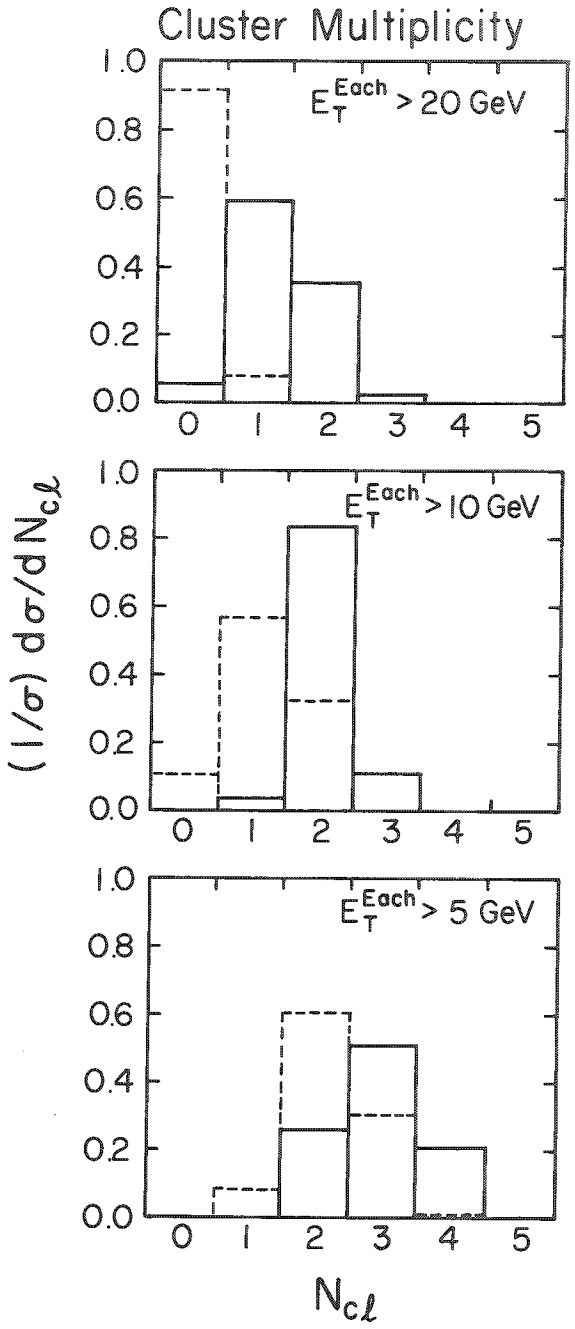

Fig. 18. Prediction of the QCD Monte-Carlo model in $\bar{p}p$ collisions at W=540 GeV for the probability of finding in a given event with total E_T in the range $50 < E_T < 60$ GeV (dashed lines) and $80 < E_T < 90$ GeV (solid lines) $N_{c\ell}$ clusters, each of which has transverse energy greater than 20 GeV (top), 10 GeV (middle), and 5 GeV (lower). Clusters are defined in Fig. 11 and the pseudorapidity range is as in Fig. 11 ($|\eta| < 1.0$).

whereas the QCD Monte-Carlo gives a 10% probability of finding 3 clusters with $E_T^{each} > 10$ GeV for the total transverse energy in the range $80 < E_T < 90$ GeV (Fig. 18).

The average multiplicity of clusters with $E_T^{each} > 10$ GeV is compared with UA2 data in Fig. 19. At lower total E_T values the Monte-Carlo produces fewer clusters with energy greater than 10 GeV than seen by UA2. However, above E_T=75 GeV the agreement is good. This is seen more clearly in Fig. 20 where the distribution of clusters with $E_T^{each} > 10$ GeV is displayed for the total E_T range $50 < E_T < 60$ GeV and $80 < E_T < 100$ GeV. The agreement in the higher E_T range is quite spectacular with both data and the Monte-Carlo yielding three clusters with $E_T^{each} > 10$ GeV in about 20% of the events. The agreement may be fortuitous, however, since as seen in Fig. 18 this might be the precise point where the model predictions cross the data. I must run off more events at larger E_T before any definite conclusions can be made.

IV. Summary and Conclusions

Hadrons of type 1 and type 2 are quite often referred to in a derogatory manner as "background" to the high p_T event. However, as we have seen these hadrons play an integral role in the overall high p_T event topology. There is an event-by-event dynamical correlation between these hadrons and the hadrons of type 3 and type 4. It is incorrect to consider large p_T events as an incoherent superposition of two large p_T jets plus a "minimum bias" background. The great majority of minimum bias events contain no hard scattering, whereas essentially all large E_T event occur as the result of a hard parton-parton collision. Given that a hard scattering has occurred, one should be able to approximate the complete event structure from QCD perturbation theory including the "background" hadrons (i.e. type 1 and type

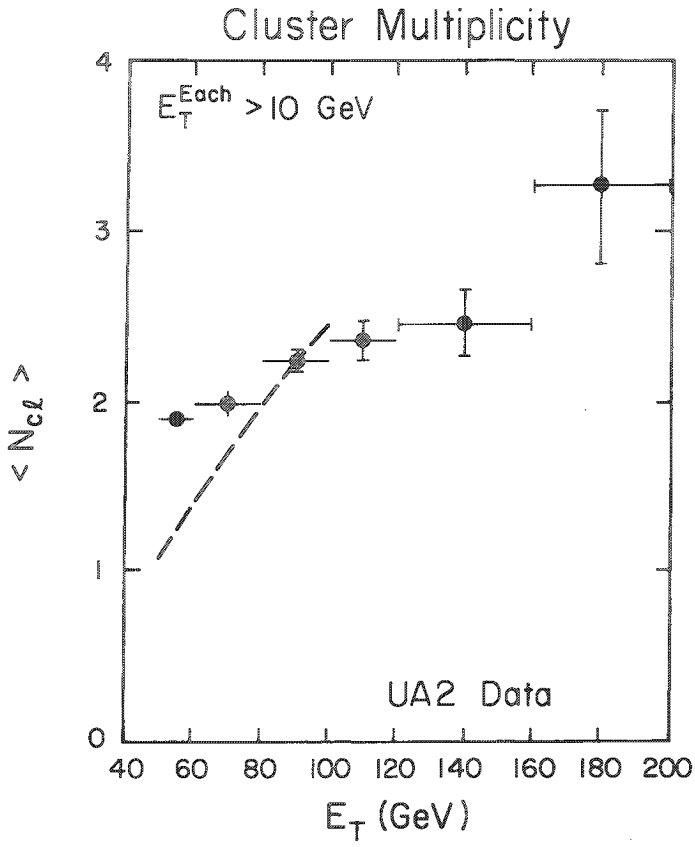

Fig. 19. Comparison of UA2 data [17] (solid dots) on the average multiplicity of clusters each of which has transverse energy greater than 10 GeV versus the total transverse energy, E_T, for $\bar{p}p$ collisions at W=540 GeV with the QCD Monte-Carlo model (dashed curve). The pseudorapidity range is as in Fig. 11 ($|\eta| < 1.0$).

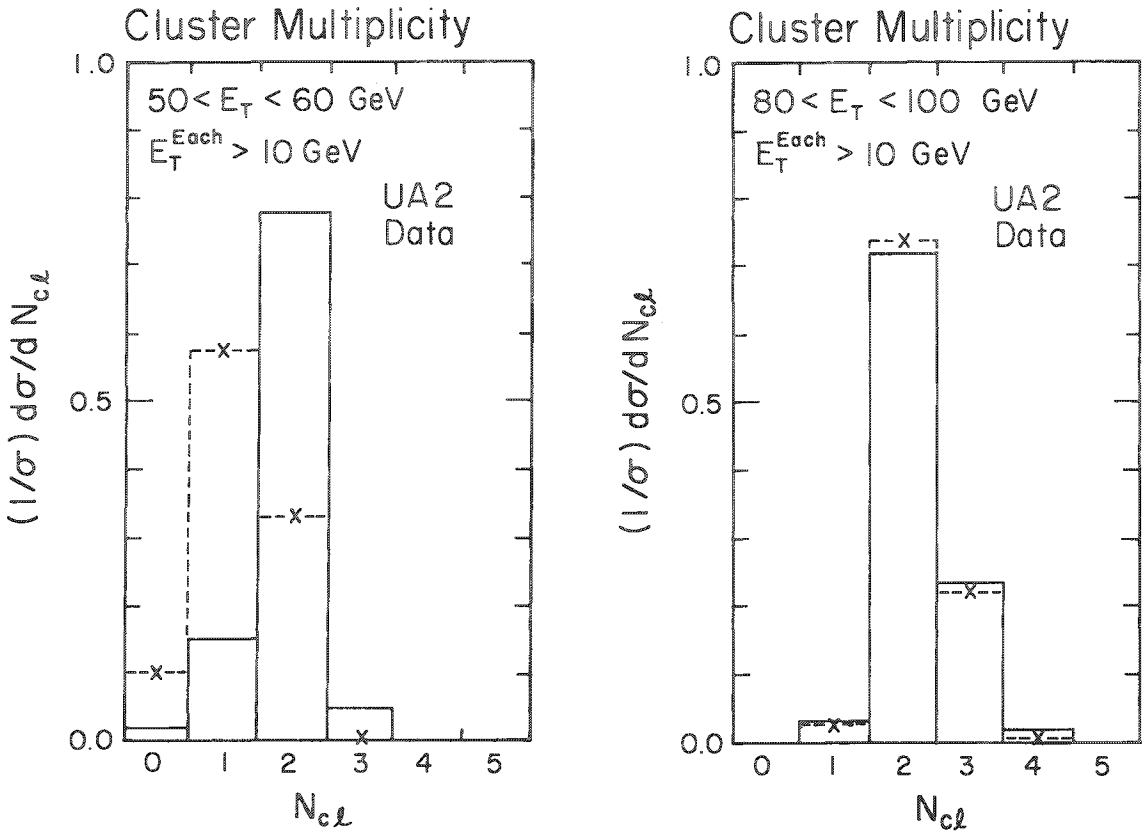

Fig. 20. Comparison of UA2 data [17] (solid lines) on the probability of finding $N_{c\ell}$ clusters each of which has transverse energy greater than 10 GeV in an event with total transverse energy in the range $50 < E_T < 60$ GeV (left) and $80 < E_T < 100$ GeV (right) for $\bar{p}p$ collisions at W=540 GeV with the QCD Monte-Carlo model (dashed lines). The pseudorapidity range is as in Fig. 11 ($|\eta| < 1.0$).

2). QCD perturbation theory tells us nothing about minimum bias events.

Complicated "jet finding" algorithms are not necessary in order to observe the rich topological structure of large p_T hadron-hadron scattering expected from QCD. One needs only to examine and identify the patterns of transverse energy deposition. This can be done by comparing the average transverse energy flow patterns for a variety of triggers or by defining a transverse energy grid and looking at the cluster patters. At large E_T the UA2 group at the CERN collider [17] find that the two highest transverse energy clusters carry most of the total transverse energy (80% for $E_T > 100$ GeV). However, I believe it is somewhat misleading to say that "two-jets" dominate since multicluster topologies occur at a sizeable rate.

One way to quantify the multicluster patterns is to examine the multiplicity of clusters each of which has a transverse energy greater than some value, E_T^{each}. Although the QCD Monte-Carlo produces events which contain less total transverse energy in the first and the first two clusters at, say, E_T=100 GeV, the model and data do agree on the probability of finding three clusters with $E_T^{each} > 10$ GeV (about 20% for $80 < E_T < 100$ GeV). Since I have not examined the sensitivity of the QCD Monte-Carlo to changes in the fragmentation scheme or to changes in the QCD perturbative parameter Λ [18], it is difficult to judge the significance of the disagreement (and the agreement) with the UA2 data. Also, I do not know how well models without initial state gluon Bremsstrahlung (such as Isajet [19]) fit the CERN collider data. Nevertheless, I believe that the QCD Monte-Carlo model presented here is telling us something interesting about the dynamical interplay between what has previously been referred to as "background" and the what has previously been referred to has "high p_T jets". In addition, multicluster topologies with $N_{cl} > 2$ must occur in nature if QCD is correct (although they may not

occur at precisely the rate I have predicted here). It is important to quantify and examine these multicluster patterns experimentally. Hadron-hadron collisions provide an excellent place to study the dynamics of QCD.

ACKNOWLEDGEMENTS

Much of this paper could not have been presented without the cooperation of the UA2 group which allowed me access to unpublished data. In particular, I wish to thank Peter Jenni for providing me the UA2 results on cluster multiplicities. I gratefully acknowledge useful discussions with P. Darriulat of UA2; G. Thompson and J. Rohlf of UA1; and K. Hansen, H. Boggild, and R. Moller of AFS concerning the data. In addition, I would like to thank K. Hansen, the Niels Bohr Institute, and Nordita for the hospitality shown to me during the summer of 1983 where the analysis of the AFS data was carried out. Finally, I congratulate B. Hahn and P. Minkowski on a most enjoyable and stimulating workshop.

FOOTNOTES AND REFERENCES

1. G. Altarelli and G. Parisi, Nucl. Phys. B126, 298 (1977).

2. G. C. Fox and R. L. Kelly, Caltech preprint CALT-68-890 and AIP Conference Proceedings No. 85, "Proton-Antiproton Collider Physics (1981).

3. R. D. Field, G. C. Fox, and R. L. Kelly, Phys. Letters 119B, 439 (1982).

4. R. Odorico, Nucl. Phys. B199, 189 (1982); Phys. Letters 118B, 151 (1982); University of Bologna preprint IFUB 82120 (1982).

5. G. C. Fox and S. Wolfram, Nucl. Phys. B168, 285 (1980); G. C. Fox and S. Wolfram, "A Gallimaufry of e+e- Annihilation Shapes", Caltech preprint CALT-68-723 (1979), unpublished. G. C. Fox, lectures presented at the 1981 SLAC Summer School, CALT-68-863.

6. R. D. Field, "Jet Formation in QCD", invited talk presented at the XIII International Symposium on Multiparticle Dynamics, Volendam, The Netherlands, 6-11 June 1982, University of Florida preprint UFTP-82-28 (1982).

7. G. Marchesini and B. R. Webber, CERN preprint TH-3525 (1983); B. R. Webber, CERN preprint TH-3569 (1983). Marchesini and Webber have improved the parton shower generation method to include, in an approximate way, higher order perturbative effects.

8. To leading order, there is an ambiguity in the choice of the energy scale, Q. All choices that increase linearly with the parton-parton transverse momentum, $\hat{p}_T$, are equivalent. This choice of Q saves a considerable amount of computer time as is discussed in Ref. [2].

9. R. D. Field and S. Wolfram, Nucl. Phys. B213, 65 (1983). R. D. Field, "The Production of Partons and Hadrons in e+e- Annihilations - Quark and Gluon Jet Models", University of Florida preprint UFTP-81-12 and proc. conf. on perturbative QCD, Florida State University (March 1981), AIP Conference Proceedings No. 74 (Particle and Fields Subseries No. 24).

10. R. D. Field and G. C. Fox, "QCD Monte-Carlo Models for e+e- Annihilations and Hadron-Hadron Collisions", invited talks presented at the Europhysics Study Conference on Jet Dynamics in Quark and Lepton Interactions, Erice, Sicily, 12-17 Sept. 1982, CALT-68-965 and UFTP-82-30.

11. R. D. Field and R. P. Feynman, Phys. Rev. D15, 2590 (1977); Nucl. Phys. B138, 1 (1978).

12. T. Akesson et al. (AFS Collaboration), "The Dominance of Jets at Large Transverse Energy in a Full-Azimuth Hadron Calorimeter at ISR Energies", CERN preprint CERN-EP/83-71.

13. The circularity, C, is a measure of the event shape. It is equal to 1-P where P is the planarity (two dimensional analogue of sphericity) defined by $P = \left(\Sigma(\max)-\Sigma(\min)\right)/\left(\Sigma(\max)+\Sigma(\min)\right)$, where $\Sigma(\max)$ and $\Sigma(\min)$ maximize and minimize, respectively the sum of p_T^2 in the transverse $(p_T)_x$ and $(p_T)_y$ plane.

14. G. Arnison et al. (UA1 Collaboration), "Hadronic Jet Production at the CERN Proton-Antiproton Collider", CERN preprint CERN-EP/83-118.

15. M. Jacob, "Collider Physics - Present and Prospects", talk presented at the SLAC Topical Conference, 27-29 July 1983, CERN preprint TH-3693.

16. I apologize for not being able to produce the usual three dimensional "lego plots", but at present my computer graphic capabilities are limited.

17. P. Bagnaia et al. (UA2 Collaboration), "Measurement of Very Large Transverse Momentum Jet Production at the CERN $p\bar{p}$ Collider", CERN preprint CERN-EP/84-12; and P. Jenni private communication.

18. To leading order the choice of the QCD perturbative parameter Λ is arbitrary and no one knows the best leading order effective Λ to use in hadron-hadron collisions. Reducing Λ would reduce the overall amount of wide-angle gluon Bremsstrahlung. If it indeed turns out that the CERN collider data at high transverse energy is "cleaner" than the QCD Monte-Carlo (i.e. more two-jet like) than it may simply be an indication that one should use a smaller effective Λ.

19. F. E. Paige and S. D. Protopropescu, BNL 29777 (1980).

Comparison of Quark and Gluon Jets

by

G. Schierholz

Deutsches Elektronen-Synchrotron DESY, Hamburg

Abstract

If QCD is the underlying theory of the strong interactions, quark and gluon jets should appear to be rather different in nature. In this talk I shall discuss the (theoretical) roots of this difference and to what extent it has been borne out experimentally.

1. Introduction

Quarks and gluons play quite a different role in QCD. While quarks are mainly flavour labels and sources of colour perturbation in the vacuum, gluons are largely responsible for confinement, i.e. the QCD vacuum, and dominate the particle production mechanism. This leads us to expect the fragmentation patterns of quark and gluon jets to be rather diverse.

The purpose of my talk is to illuminate this issue. So far we are not able to derive the fragmentation functions from first principles. But in the last years a vast amount of experimental information on the fragmentation mechanisms of quark and gluon jets has accumulated (and I believe there is a lot more to come from the $p\bar{p}$ collider) which will compensate for this weakness.

2. Space-Time Picture of Quark and Gluon Jets

To begin with let me review our current understanding of the process of hadronization in quark and gluon jets.

Quark Jets

As a quark leaves the interaction region it trails behind it a colour (triplet) flux tube. At some point the gain in diminishing the flux tube length outweighs the cost of exciting a $q\bar{q}$ pair from the vacuum, and the flux tube will break into a string bit of perhaps a mass of ≈ 1 GeV (length ≈ 1 fermi, given a string tension of 1 GeV/fermi) and a "heavy" string consisting of the original (energetic) quark and the newly created antiquark. As the leading quark and the antiquark move apart, the "heavy" string will break repeatedly until eventually the system has totally decayed into string bits of the aforementioned size:

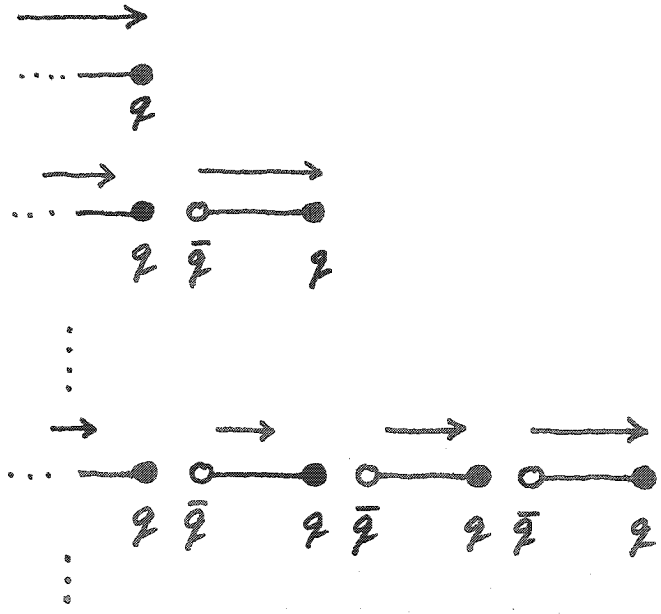

The string bits are strongly ordered in rapidity. The lengths of the arrows represent (pictorially) the velocities of the bits. If not originally so, the string bits will evolve into strongly interacting systems, bags, containing a $q\bar{q}$ pair:

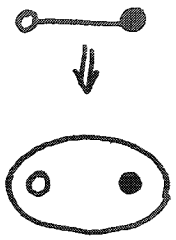

The (Feynman) graphical description of the quark jet evolution

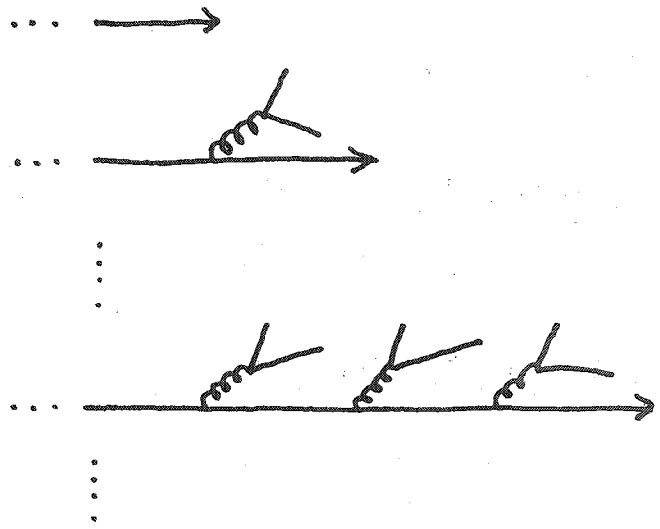

leads in the limit N_c = large to more or less the same strong ordering in rapidity. In the following I shall employ both notations.

The validity of the string picture has only recently been verified experimentally by comparing the fragmentation properties of charm jets with those of the average jet. According to this picture the two jets should only differ in the leading particle spectrum, and that is exactly what has been found [1].

Gluon Jet

An energetic isolated gluon will trail a colour (octet) flux tube behind it. In a world without dynamical triplets of colour the flux tube would break up into a sequence of gluon-string bits in the same way the quark flux tube decays into string bits. The masses of the lowest-lying glueball states range from [2] 0.7 to $\gtrsim$ 2 GeV, and hence the mass of a gluon-string bit is expected to follow some distribution centered on a mean in the range 1.5 to 2 GeV (length $\lesssim$ 1 fermi,

given a string tension more than twice that of the triplet flux). Including dynamical quark triplets is not expected to alter these numbers very much.
In the real world with quarks the flux tube may, however, also break by exciting two $q\bar{q}$ pairs (in the octet representation) from the vacuum as shown (e.g.) below:

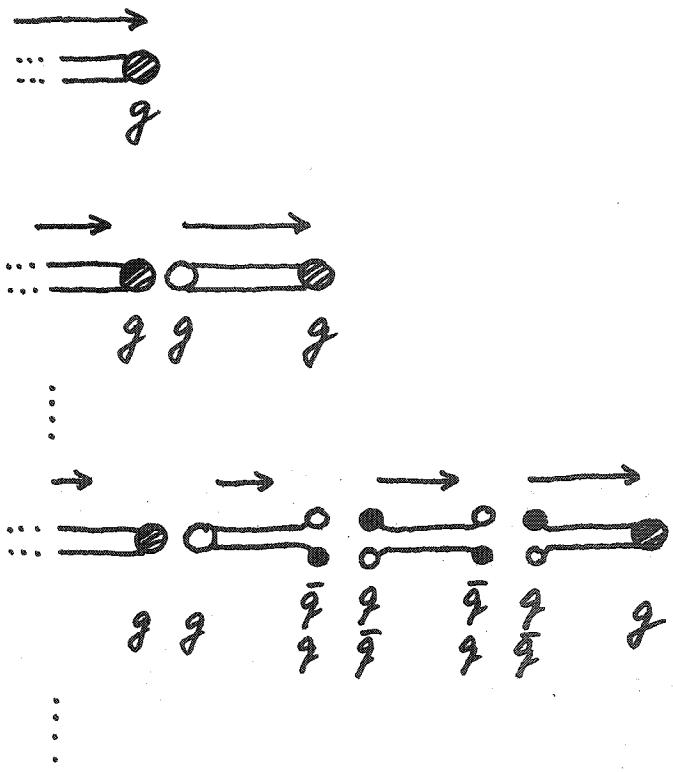

The gluon-, mixed- and diquark-string bits will evolve into three topologically distinct physical systems:

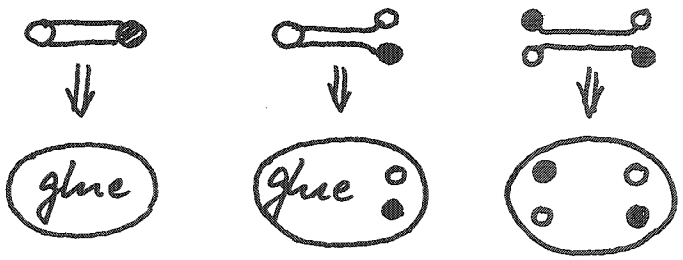

giving rise to glueballs, so-called mixed ($q\bar{q}g$) states and four-quark resonances, respectively. The masses of the lowest-lying mixed states are expected to lie in the range [3] 1.5-2 GeV.

The (Feynman) graphical description of the gluon jet evolution

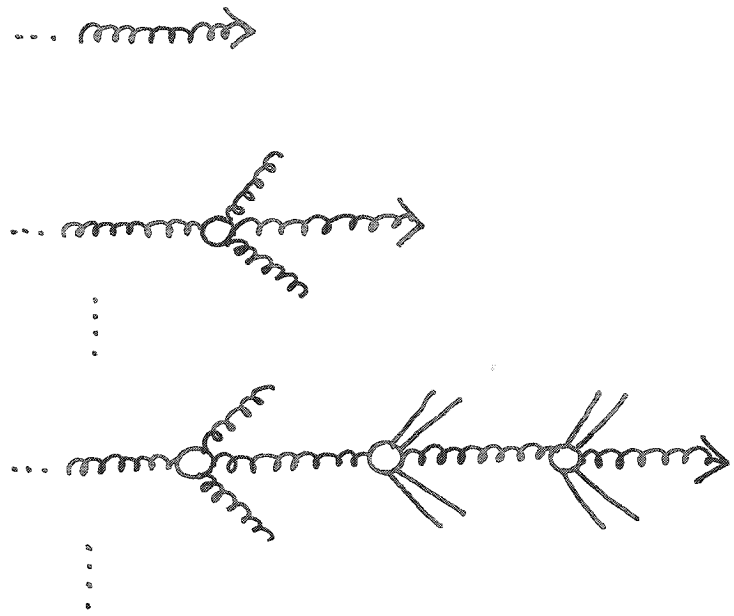

loes not obviously agree with the string picture. Presumably this can be ıchieved to some extent by taking proper care of quantum interference phenomena.

:opological Properties

'rom the discussion so far it is apparent that the gluon jet has a much richer ıarticle spectrum than the quark jet. But more about this later. A further ;triking difference is that the particle flow in the gluon jet depends crucially on its history, while in the quark jet it appears to be more universal. To give an example consider (i) two back-to-back gluon jets as they arise (e.g.) from heavy para-quarkonium decays or $p\bar{p} \rightarrow gg + X$

(i)

and (ii) a $q\bar{q}g$ three-jet event as it appears (e.g.) in e^+e^- annihilation

(ii)

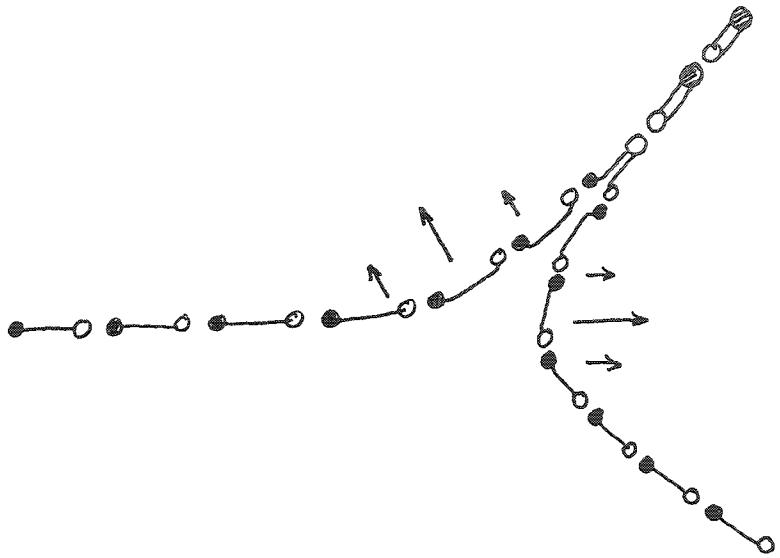

The three-jet configuration shown is only one of many possible final states. Its particular feature is that the gluon (colour octet) flux tube has broken initially and repeatedly by $q\bar{q}$ pair creation. Furthermore, it assumes that the interaction between overlapping string bits is small so that the two resulting triplet flux tubes evolve more or less independently (as indicated). Accordingly the gluon jet here will be oblate and much broader (in the event plane) than in case of the back-to-back jet (i).

The JADE group has confirmed that the fragmentation proceeds to some extent along the colour flux lines rather than strictly along the parton axes. Below I have transcribed their data [4] into an "event-shape" plot

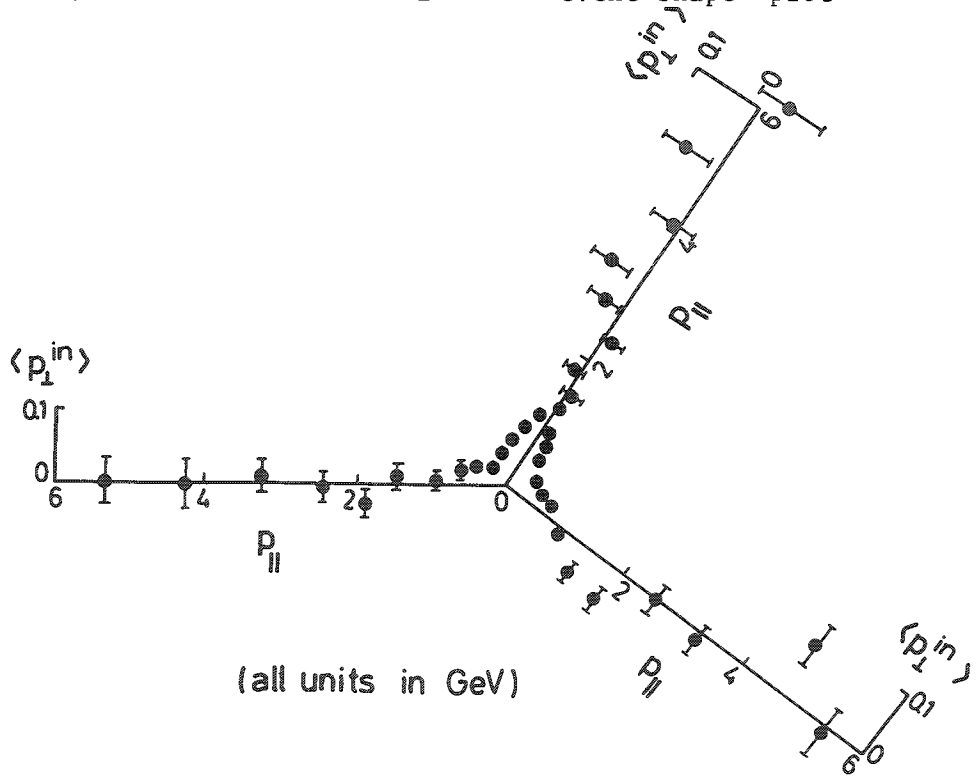

which clearly shows the effect. (In this plot $\langle p_\perp^{in} \rangle$ is zero when the particles fall on the jet axes.)

In general the gluon flux tube may also break by forming gluon-string bits

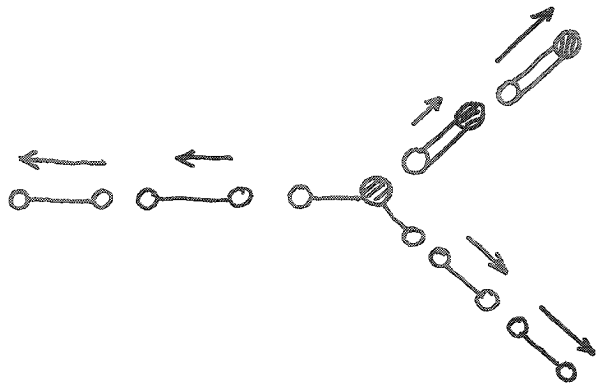

and the overlapping string bits in (ii) may interact (e.g. to give baryons as I will discuss later on), which then will fragment more or less along the parton axes. How much this is so can only be answered by the experimentalists at the moment. But it is conceivable that the Lund fragmentation model [5], which treats the gluon string as a superposition of two noninteracting quark strings, is as far from the truth as the independent parton fragmentation models.

It is interesting to note that Webber's model [6] for jet fragmentation, which follows the graphical description including some soft-gluon interference, also reproduces the string effects, and I am sure that this will shed some more light on this issue.

3. Longitudinal Evolution

I like to discuss now the single particle distributions in quark and gluon jets. Let me begin (for a change) with the perturbative aspects of it.

(a) Perturbative

The longitudinal development of quark and gluon jets is believed to be governed by the evolution equations [7]:

$$\partial_t D_q^h(z,t) = \frac{6}{33-2N_f} \int_z^1 \frac{dx}{x} \left[P_q^q(x)\, D_q^h\left(\frac{z}{x},t'\right) + P_q^g(x)\, D_g^h\left(\frac{z}{x},t'\right) \right],$$

$$\partial_t D_g^h(z,t) = \frac{6}{33-2N_f} \int_z^1 \frac{dx}{x} \left[P_g^g(x) D_g^h\left(\frac{z}{x},t'\right) + N_f \left(P_g^q(x) D_q^h\left(\frac{z}{x},t'\right) + P_g^{\bar{q}}(x) D_{\bar{q}}^h\left(\frac{z}{x},t'\right) \right) \right],$$

where $t = \ln [\alpha_s(Q_0^2)/\alpha_s(Q^2)]$, $t' = \ln [\alpha_s(Q_0^2)/\alpha_s(\tilde{Q}^2)]$.

$z \to 1$

This set of coupled equations can be solved for $z \approx 1$, and we obtain [8]

$$D_q^h(z,t) \underset{z\to 1}{\simeq} \text{const.} \, [\alpha_s(Q^2)]^{-(\frac{3}{4}-\gamma_E)\frac{16}{33-2N_f}} (1-z)^{c_q(t)},$$

$$c_q(t) = c_q(0) + \frac{16}{33-2N_f} t$$

for the fragmentation function of the quark and

$$D_g^h(z,t) \underset{z\to 1}{\simeq} \text{const.} \, [\alpha_s(Q^2)]^{-(\frac{11}{12}-\frac{N_f}{8}-\gamma_E)\frac{9}{4}\frac{16}{33-2N_f}} (1-z)^{c_g(t)},$$

$$c_g(t) = c_g(0) + \frac{9}{4}\frac{16}{33-2N_f} t$$

for the fragmentation function of the gluon (γ_E is Euler's constant). The derivation assumes that $c_q < c_g - 1$ which, if not originally so, will become true at least at large t.

Because quark and gluon jets lose momentum by gluon bremsstrahlung, the single particle distribution in the jets becomes softer as Q^2 increases. Moreover, we see that the ratio between the rate of softening of gluon and quark jets is $9/4 = N_c/C_F$, which is a consequence of the higher colour charge of the gluon. For Q_o = 10 GeV, Q = 100 GeV and N_f = 5 we obtain ($\Lambda_{\overline{MS}}$ = 200 MeV)

$$c_q(t) = c_q(o) + 0.30,$$

$$c_g(t) = c_g(o) + 0.68$$

which might be just enough of a change to be detectable experimentally. To draw any firm conclusions one will, however, have to know $c_q(o)$, $c_g(o)$ (e.g. from measurements on and off the Υ resonance) rather accurately.

I shall discuss the experimental situation after I have presented the nonperturbative aspects of the longitudinal distributions at the end of this section.

Multiplicities

The zeroth moments of the quark and gluon fragmentation functions give the mean multiplicities in quark and gluon jets

$$n_q^h(t) = \int_0^1 dz\, D_q^h(z,t),$$

$$n_g^h(t) = \int_0^1 dz\, D_g^h(z,t).$$

The evolution equations for the zeroth moments develop, as they stand, some divergences associated with the emission of a divergent number of soft gluons. But if the gluon is very soft it cannot fragment into hadrons. So we integrate only over those gluons $t' \geq t_0$ which are capable of fragmenting [8]. This gives

$$\partial_t n_q^h(t) \simeq \frac{16}{33-2N_f} e^t \int_{t_0}^t dt'\, e^{-t'} n_g^h(t'),$$

$$\partial_t n_g^h(t) \simeq \frac{9}{4} \frac{16}{33-2N_f} e^t \int_{t_0}^t dt'\, e^{-t'} n_g^h(t'),$$

which has the asymptotic solution

$$n_g^h(t) \simeq \frac{9}{4} n_q^h(t),$$

$$n_g^h(t) \simeq \text{const.}\; e^{-2\sqrt{\frac{36}{33-2N_f} \ln Q^2/\Lambda^2}}.$$

Again there is a factor 9/4 between the asymptotic multiplicities in gluon and quark jets due to the greater colour charge of the gluon.

To tell how far we are from asymptotic one has to go beyond the presentation given here. Webber has done this and he finds for the ratio $\langle n_g \rangle / \langle n_q \rangle$ (which is of most interest to us here) the following energy dependence [6]:

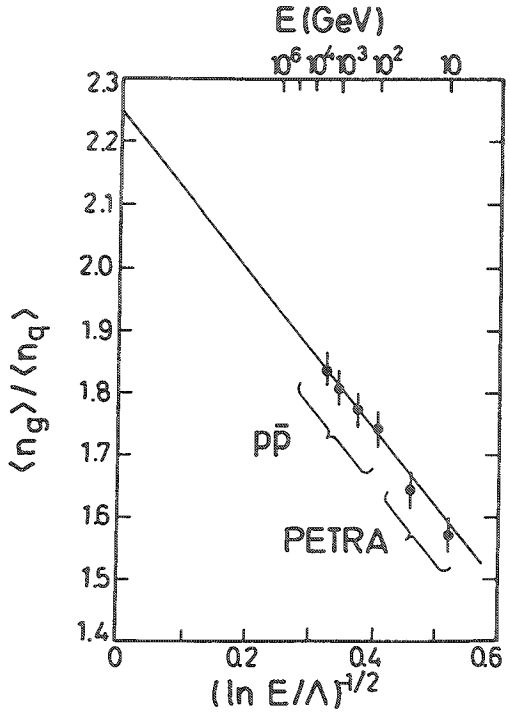

(the points show the Monte Carlo results and the line is a linear fit). The outcome is that the asymptotic predictions are so asymptotic as to be useless. But the difference of quark and gluon jet multiplicities is still big enough to be conclusive.

The experimental data and the (Monte Carlo) predictions are summarized in the figure below

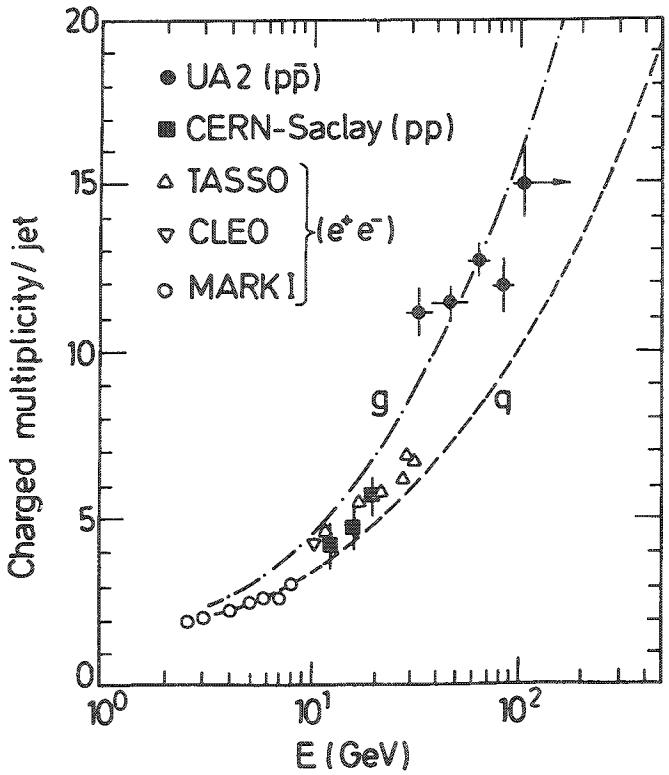

where E is the c.m. energy of the two-jet system. The dashed line is the prediction for the quark jet multiplicities, the dashed-dotted line that for the gluon jet multiplicities [6]. The TASSO data [9], which proceed dominantly from quark jets, fall (at their highest energies) close to the quark curve while the UA2 data [10], which are dominated by gluon jets, fall on the gluon curve. This nicely confirms the predictions. One can also say that the QCD prediction of a rapidly increasing multiplicity is in accord with the data.

(b) Nonperturbative

According to the string picture the fragmentation function of the quark is given by the iterative equation

$$D_q^h(z) = \int_0^{1-z} dy \frac{dP}{dy} \left[\frac{1}{1-y} D_q^h\left(\frac{z}{1-y}\right) + \delta(y+z-1) \right],$$

where dP/dy is the probability to find a meson containing the original quark at $1-y$. The most natural choice for the probability function is $dP/dy = 1$, apart from may be the boundaries. This implies the large-z behaviour $D_q^h(z) \sim$ const. For the fragmentation function of the gluon we find analogously

$$D_g^h(z) = \int_0^{\frac{1}{2}} dy_1 \int_0^{\frac{1}{2}} dy_2 \frac{d^2P}{dy_1 dy_2} \left[\frac{\Theta(\frac{1}{2}-y_1-z)}{\frac{1}{2}-y_1} D_g^h\left(\frac{z}{\frac{1}{2}-y_1}\right) + \frac{\Theta(\frac{1}{2}-y_2-z)}{\frac{1}{2}-y_2} D_g^h\left(\frac{z}{\frac{1}{2}-y_2}\right) + \delta(y_1+y_2-z) \right].$$

In case the gluon flux tube breaks into a sequence of noninteracting (triplet) string bits

we expect, except perhaps for $y_1, y_2 \approx 0$,

$$\frac{d^2P}{dy_1 dy_2} = \frac{dP}{dy_1} \frac{dP}{dy_2} = 1.$$

At large z this gives $D_g^h(z) \sim (1-z)$, which has an extra power of $(1-z)$. Note also that $\langle n_g \rangle \approx 2 \langle n_q \rangle$ in this picture.

The Lund group has studied the quark and gluon fragmentation functions in the context of this simplified model in great details. The result of their cal-

culation is given below [5]

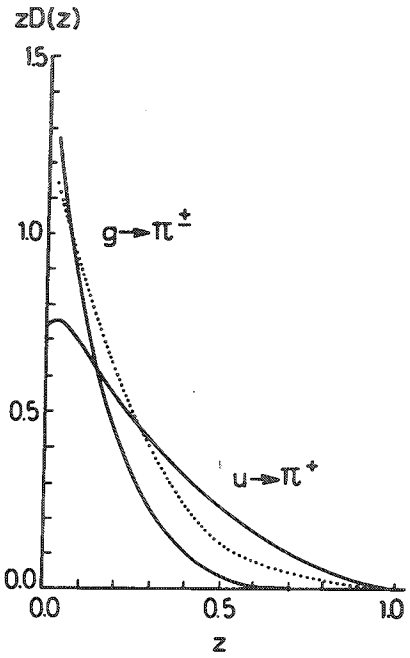

We see that the gluon fragmentation function comes out to be very much softer than that of the quark.

This difference (if true) should become visible if we compare the jet fragmentation at PETRA (mostly quark jets) to that of the $p\bar{p}$ collider (mostly gluon jets) what I have done below

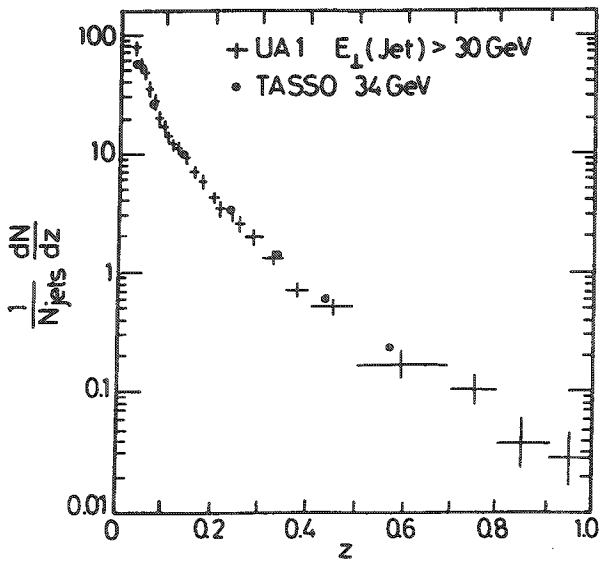

It looks as if the quark and gluon fragmentation functions are almost the same contrary to the model. This appearance is, however, deceptive. In the UA2 data [11] events with $z \leqslant 0.05$ have been discarded. If one applies the same cut to the

Lund gluon fragmentation function (and rescales) one obtains the dotted curve in the figure before [12], and a lot of the difference has gone away. This will be further washed out by also including charm quark jets (which at PETRA energies are much softer than u and d quark jets [1]) in the model calculations. But there is also the possibility, as I said before, that the gluon flux tube decays into glueballs and that the overlapping (triplet) string bits interact which will obviously modify the predictions for the quark and gluon fragmentation functions.

4. Transversal Evolution

The intrinsic transverse momenta in jets are proportional to Λ, the only scale parameter in QCD (in the chiral limit), and hence they are nonperturbative in origin.

Let us consider now (e.g.) two back-to-back quark-antiquark and gluon jets, respectively. As the quark and antiquark (the two gluons) separate the transversal width of the field energy distribution (flux tube) increases due to quantum fluctuations [13]:

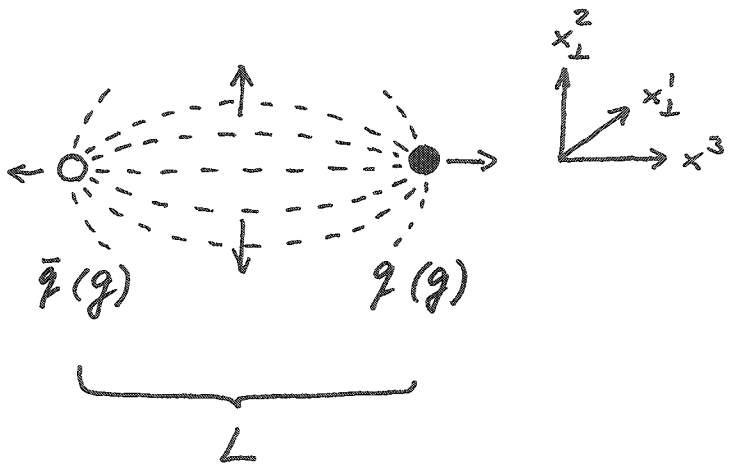

(It increases without bound when the $q\bar{q}$ (gg) separation goes to infinity.) The chromo-electric field energy density above the vacuum is [13]

$$\mathcal{E}_{q(g)}(x) \sim e^{-\sigma_{q(g)} \frac{\pi x_\perp^2}{\ln L/\lambda}} ,$$

where $\sigma_{q(g)}$ is the string tension and λ is some constant. In momentum space this gives

$$\mathcal{E}_{q(g)}(p_\perp) = \int d^2x_\perp \, e^{i p_\perp x_\perp} \mathcal{E}_{q(g)}(x) \sim e^{-\frac{\pi L/\lambda}{\pi \sigma_{q(g)}} p_\perp^2}.$$

The partons that break the flux tube (while expanding) will now be created with an intrinsic transverse momentum

$$\langle p_\perp q(g) \rangle = \int dp_\perp \, p_\perp \, \mathcal{E}_{q(g)}(p_\perp),$$

so that the mean transverse momentum of hadrons in quark and gluon jets is

$$\langle p_\perp^4 q(g) \rangle \cong \frac{4}{3} \langle p_\perp q(g) \rangle \sim \sigma_{q(g)}.$$

The string tensions σ_q and σ_g can and have been calculated on the lattice. What will interest us here is only the ratio σ_g / σ_q. By dimensional reduction techniques [15] (which have been verified in SU(2) by lattice Monte Carlo calculations [15]) we arrive at $\sigma_g / \sigma_q = 9/4$, so that

$$\langle p_\perp^4 g \rangle / \langle p_\perp^4 q \rangle = 9/4.$$

The JADE group finds a significant difference in the mean transverse momentum out of the three-jet plane [4]:

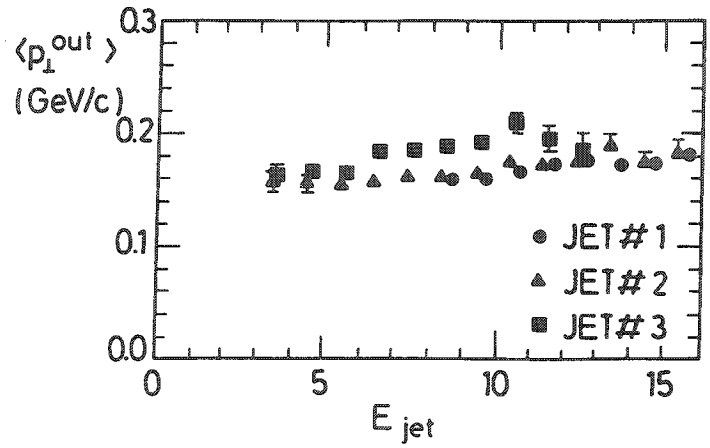

The probability that the fastest jet (# 1) is the quark or antiquark is 88 % and that the least energetic jet (# 3) is the gluon is 51 %. Taking this into account I obtain (at E_{jet} = 10 GeV)

$$\langle p_{\perp q}^{out} \rangle \approx 130 \text{ MeV}, \quad \langle p_{\perp g}^{out} \rangle \approx 260 \text{ MeV},$$

which gives for the ratio

$$\langle p_{\perp g}^{out} \rangle / \langle p_{\perp q}^{out} \rangle \approx 2,$$

which is close to what one expects.

5. Particle Yields

In the gluon jet (at least) the leading string bits should remember that they are fragments of a (iso-singlet) gluon. This is to say that we expect glueballs, mixed ($q\bar{q}g$) states, η, η', ω, ϕ, etc. to be produced abundantly (for a model calculation involving the conventional mesons see (e.g.) ref. 16). So far the JADE group has found some evidence [17] that the η yield is larger for three-jet events than for two-jet events supporting this picture. For a further test and for our further understanding of the fragmentation mechanism it is important now to also trace the glueballs and mixed states.

The four-quark states in the gluon jet, having a mean mass of O(2 GeV), may decay in two basic modes [18]

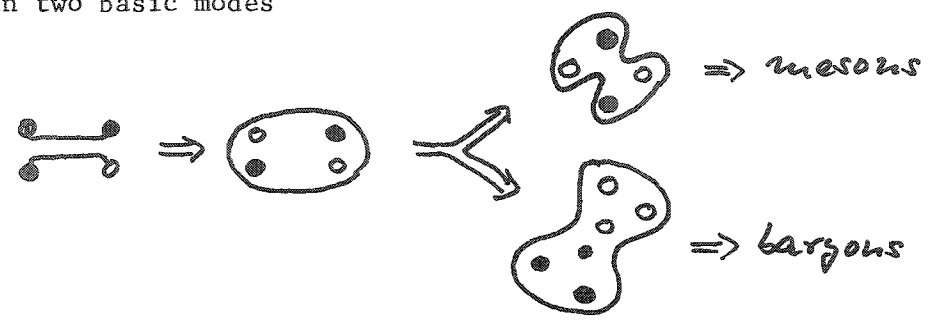

In case the two (triplet) string bits would not interact (Lund model) only the top mode would be present. To gain some insight into the dynamics of the decay one may look at low energy $p\bar{p}$ annihilations. At $\sqrt{s} \approx 2$ GeV the relative kinetic energy is low enough that the intermediate state will at some point consist of

two quarks and two antiquarks mixed together in a strongly interacting region of total mass $\approx$ 2 GeV. The annihilations correspond to the case when this system decays into mesons. The cross section is 77 ± 3 mb [19]. The cross section for producing a baryon-antibaryon pair may be estimated by taking $p\bar{p} \rightarrow p\bar{p}$ or $n\bar{n}$ and subtracting the pp value. This gives $\approx$ 38 mb [19]. Thus there appears to be no particular suppression of this mode, and our best guess is that the decay of the gluon flux tube into baryon, antibaryon will also not exhibit any marked dynamical suppression. This contradicts obviously the (naive) Lund model to the extent that we observe abundant baryon production in gluon jets. (But at present we can also not totally deny that there are other mechanisms within the context of QCD that might lead to substantial baryon production in jets. For a further discussion see ref. 18).

Let me now turn to the data. The DASP II group has found that antiprotons on the Υ (presumably three gluon jets) are produced at a rate about six times higher than on the neighbouring continuum [20]. At PETRA [21] the $\bar{p}$/meson and Λ/meson ratios increase with x and become large. In deep inelastic processes, and in particular the EMC data [22], the ratio of protons to mesons increases with increasing $p_\perp$ (three-jettiness) as shown below:

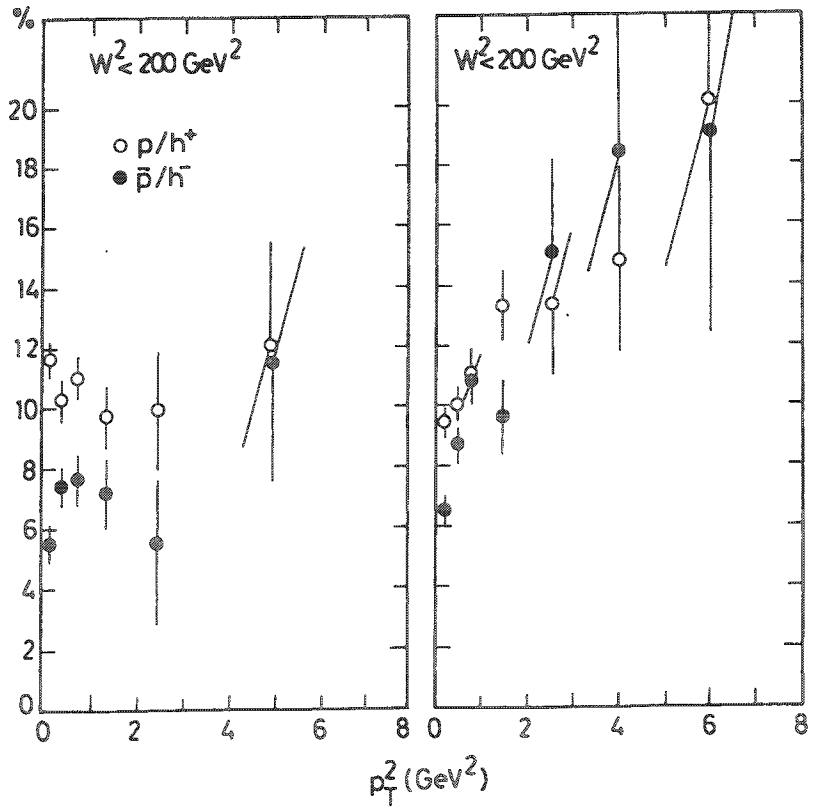

We conclude that the recent high-energy data does not only reveal substantial baryon production but also indicates that the (dominant) source of all these baryons is glue.

6. Miscellaneous

In this last section I like to mention very briefly a couple of other features that further mark the different nature of quark and gluon jets.

KNO Scaling

We expect the shape of the KNO scaling curve $(\langle n_{ch}\rangle P(n_{ch})$ versus $n_{ch}/\langle n_{ch}\rangle)$ for gluon jets at large $n_{ch}/\langle n_{ch}\rangle$ to be much flatter than for quark jets. This follows naturally from the (simplified) Lund model and should be true in general, though maybe in a weaker form. Experimentally there are some indications that this is indeed the case.

Prompt Photons

The QCD vacuum is a highly nontrivial setup of fluctuating colour fields. Nachtmann and Reiter have put forward the idea that energetic quarks traversing these fields will produce soft photons [23] (and soft gluons) similar to synchrotron radiation of energetic electrons passing through a magnetic field. This would lead us to expect more prompt photons in quark jets than in gluon jets.

Charge Retention

Measurements of the net charges of quark jets in neutrino and antineutrino interactions have appeared recently [24]. It has been found that the net charge of the jet closely reflects the charge of the parent quark. Moreover, it has been shown that the energy dependence of the net charge of the quark jets bears some information about the charge exchange properties of "isolated" quarks [25]. It will be important now to repeat the analysis for gluon jets at the $p\bar{p}$ collider.

7. Conclusions

Quark and gluon jets, that seems to be established, are different. As far as one can tell, the differences are in qualitative (and in some cases even semi-quantitative) agreement with our theoretical expectations based on QCD. However, we cannot make precise tests of QCD yet because of substantial uncertainties in the theoretical calculations.

References

1. TASSO Collaboration, M. Althoff et al.: DESY preprint 83-114 (1983).
2. K. Ishikawa, A. Sato, G. Schierholz, M. Teper: Zeitschr. f. Physik C21, 167 (1983); B. Berg: DESY preprint 84-012 (1984).
3. F. Close in Few Body Problems in Physics, Proceedings of the Tenth International Conference on Few Body Problems in Physics, 1983, ed. B. Zeitnitz, Vol. 1, p. 55c (North-Holland, 1984).
4. JADE Collaboration, W. Bartel et al.: Zeitschr. f. Physik C21, 37 (1983).
5. B. Andersson, G. Gustafson, G. Ingelman, T. Sjöstrand: Phys. Reports 97, 31 (1983).
6. B.R. Webber: CERN preprint TH.3713 (1983).
7. J.F. Owens: Phys. Lett. 76B, 85 (1978); T. Uematsu: Phys. Lett. 79B, 97 (1978).
8. E.g. B.R. Webber: Phys. Scripta 25, 198 (1982).
9. TASSO Collaboration, R. Brandelik et al.: Phys. Lett. 89B, 418 (1980).
10. UA2 Collaboration, P. Bagnaia et al.: CERN preprint EP/83-94 (1983).
11. UA1 Collaboration, G. Arnison et al.: Phys. Lett. 132B, 223 (1983).
12. T. Sjöstrand, private communication.
13. M. Lüscher, K. Symanzik, P. Weisz: Nucl. Phys. B173, 365 (1980).
14. M. Lüscher, G. Münster, P. Weisz: Nucl. Phys. B180, 1 (1981).
15. J. Ambjørn, P. Olesen, C. Peterson: Niels Bohr Institute preprint NBI-HE-84-06 (1984).
16. C. Peterson, T.F. Walsh: Phys. Lett. 91B, 455 (1980).
17. JADE Collaboration, W. Bartel et al.: DESY preprint 83-063 (1983).
18. G. Schierholz, M. Teper: Zeitschr. f. Physik C13, 53 (1982).
19. V. Flaminia et al.: CERN-HERA 79-03 (1979); O. Benary et al.: UCRL-20000 NN (1970).
20. DASP II Collaboration, H. Albrecht et al.: Phys. Lett. 102B, 291 (1981).
21. TASSO Collaboration, R. Brandelik et al.: Phys. Lett. 94B, 444 (1980); JADE Collaboration, W. Bartel et al.: Phys. Lett. 104B, 325 (1981).
22. European Muon Collaboration, J.J. Aubert et al.: CERN preprint EP/83-164 (1983).
23. O. Nachtmann, A. Reiter: Heidelberg preprint THEP-83-28 (1983).
24. J.P. Berge et al.: Phys. Lett. 91B, 311 (1980); N. Schmitz: Lectures at the XX Krakow School, Zakopane, 1980.
25. M. Teper: DESY preprint 81-007 (1981).

TRIPLE AND QUADRUPLE JETS

Z. Kunszt *

Institut für Theoretische Physik
Universität Bern
Sidlerstrasse 5, CH-BERN, Switzerland

Abstract: The parton model description of three and four jet production in proton-antiproton collisions is shortly reviewed. Four heavy quark production is also discussed.

1. THREE JET PRODUCTION

The very large rate of jet production[1)-4)] in proton-antiproton collisions requires the quantitative study of multijet production rates.

In e^+e^- annihilation [5)] triple and quadruple jets have been studied by calculating the cross sections of the parton processes $e^+e^- \to q\bar{q}g$, $e^+e^- \to q\bar{q}gg + q\bar{q}q'\bar{q}'$. These cross sections are singular when the final partons have collinear or soft momenta, therefore they can be compared with the data only for well separated hard jets. Such a comparison can be performed either with the application of a jet-finding algorithm to the data or using a model to hadronize the final jets. Experience at PETRA and PEP has shown that both

---

*Permanent address: Central Research Institute for Physics,
Budapest, Hungary

methods are practical and their inherent ambiguities are comparable. The first method has the advantage of simplicity, the second method is capable to accommodate more detailed features of the final state hadrons.

In hadron collisions we can proceed similarly, however, the calculations are more complicated. E.g. the $2 \to 3$ subprocesses are described by more than 50 Feynman diagrams. Nevertheless this calculation has been performed[6] and Berends et al.[7] have succeeded to find surprisingly short formulae for the original quite lengthy expressions.

UA1 has analyzed three jet events[1]. They measured p_{out} distribution and compared it with theoretical prediction[8] in the large p_{out} region where a simple two jet model clearly fails to describe the data. p_{out} is the transverse momentum out of the plane given by directions of the three momenta of a trigger jet and the beam:

$$p_{out} = \frac{1}{2} \sum_i | p_{i,out} | \qquad (1)$$

As we can see on Fig. 1 the agreement between the measured distribution and the QCD calculation is remarkably good, although 4-jet production and hadronization effects have not been included.

Fox and Wolfram have proposed a branching approximation[9] in which an arbitrary number of jets are produced but the matrix elements are approximated by the leading log summation of the collinear singularities. In this approximation multijet production can be implemented by Monte Carlo method naturally, since both the multiparticle phase space and the matrix elements are calculated by a branching procedure.

The p_{out} distribution as measured by the UA1 experiment has been calculated also in this approximation[10]. Again the agreement is acceptable although the theoretical value is slightly above the data.

At very high energy the branching approximation tends to produce large jet multiplicity[11] which may indicate that the model tends to overestimate the multijet production rates.

2. FOUR JET PRODUCTION

An explicit calculation of 4-jet production is straightforward but very lengthy. The number of Feynman diagrams of the various subprocesses are as follows:

$gggggg$	205 diagrams	(2a)
$ggggq\bar{q}$	123 diagrams	(2b)
$ggq\bar{q}q\bar{q}$	72 diagrams	(2c)
$ggq\bar{q}Q\bar{Q}$	36 diagrams	(2d)
$qq\bar{q}q\bar{q}$	42 diagrams	(2e)
$qq\bar{q}Q\bar{Q}$	14 diagrams	(2f)
$qq\bar{Q}Q'\bar{Q}'$	7 diagrams	(2g)

The calculation of these diagrams appears to be feasible with a completely numerical procedure, although the computer time becomes non-negligible. However, a reasonable estimate of the 4-jet production rates can be obtained also with a partial calculation. It is well known that both for two and three-jet production the dominant subprocesses are of the scattering processes

$gg \to gg$	$gg \to ggg + gq\bar{q}$	(3a)
$gq \to gq$	$gq \to ggq + Q\bar{Q}q$	(3b)
$qq' \to qq'$	$qq' \to qq'g$	(3c)

It has been found numerically that when flavour blind jet properties are calculated the subprocesses (3a)-(3c) give very similar distributions[6]. Furthermore their normalizations satisfy approximately the relation[12]

$$d\sigma_{qq} : d\sigma_{gq} : d\sigma_{gg} \quad 4/9 : 1 : 9/4. \tag{4}$$

The advantage of this relation has been recently emphasized[12]. Also it has been extensively used by the UA1 experiment[2] in the analysis of the jet data.

It has also been found that identical flavour effects in flavour blind jet production are always negligible.

It seems natural to assume that the relation (4) will hold approximately also in case of 4-jet production and that idential flavour effects remain negligible. With this assumption it is sufficient to calculate only the 36 diagrams of type (2d) and the 7 diagrams of type (2g). I have performed this calculation[13] *.

To illustrate the size of 4-jet rates (see Fig. 2) I plotted p_{out} distributions for 3-jet and 4-jet production in the rapidity interval $|\eta| < 1.5$. The jets have been required to be well separated in the lego plot and to have

---

* The cross section of the six quark subprocess has been calculated both by a completely numerical program and by REDUCE. The matrix elements of the 4q2g subprocesses have been calculated only numerically.

reasonably large transverse momenta. The size of the 4-jet rate is non-negligible but it remains a reasonable radiative correction. With the cuts applied the 4-jet rate is larger at higher energy.

3. PRODUCTION OF TWO PAIRS OF HEAVY QUARKS

The subprocesses of type (2d) and (2g) represent also the leading order QCD processes for the production of two heavy quark pairs[13]. Four heavy flavour production e.g. gives the background to the associated production of heavy ($m_H \lesssim 30$ - 150 GeV) standard Higgs boson with a pair of heavy quarks[14]. In order to illustrate the magnitude of the background I summarized some cross section values in Table 1. The result is negative, the direct QCD production of four heavy quarks has overwhelmingly ($\gtrsim$ 100 times) larger cross section than the associated production of two heavy quarks and a heavy standard Higgs boson which decays predominantly into the heaviest quark pair allowed by the kinematics.

References

1) UA1 Collaboration, G. Arnison et al., Phys.Lett. 132B (1983) 214.

2) UA1 Collaboration, G. Arnison et al., Phys.Lett. 132B (1983) 294.

3) UA2 Collaboration, P. Bagnaia et al., Z.Phys. C20 (1983) 117.

4) UA2 Collaboration, P. Bagnaia et al., CERN-EP/84-12 (1984).

5) G. Wolf, talk given at the XIV International Symposium on Multiparticle Dynamics, Granlibakken, Lake Tahoe, USA, DESY-83-096 (1983).

6) Z. Kunszt and E. Pietarinen, Z.Phys. C2 (1979) 355 and Nucl.Phys. B164 (1980) 45.
T. Gottschalk and D. Sivers, Phys.Rev. D21 (1980) 102.

7) F.A. Berends, R. Kleiss, P. De Causmaecker, R. Gastmans and T.T. Wu, Phys. Lett. 103B (1981) 124.

8) Z. Kunszt and E. Pietarinen, Phys.Lett. 132B (1983) 453.

9) G.C. Fox and S. Wolfram, Nucl.Phys. B168 (1980) 287.

10) R. Odorico, Ref.Th.3744-CERN (1983).

11) F.E. Paige, preprint BNL-33952 (1983).

12) G. Cohen-Tannoudji et al., preprint SPh. T/70 (1983).
B. Combridge and C. Maxwell, preprint RL-83-095 (1983).
F. Halzen and P. Hoyer, Phys.Lett. 130B (1983) 326.

13) Z. Kunszt, to be published.

14) J. Ellis and H. Kowalski, private communication.

Table 1: Cross section values for $t\bar{t}t\bar{t}$ production and $t\bar{t}H$ production, with m_t = 35 GeV and m_H = 120 GeV

$\sqrt{s}$ (TeV)	σ(tttt) (pbarn)	σ(Htt) (pbarn)
2	17	0.014
5	26	0.21
10	130	1
20	620	3.6
40	1700	11

Figure Captions

Fig. 1: p_{out} distribution measured by the UA1 experiment and its comparison by a 2-jet model and a perturbative QCD calculation.

Fig. 2: p_{out} distributions given by 3-jet and 4-jet final states at three different energies, and with suitable cut-off to match experimental jet resolution and avoid collinear and soft singularities. $\sqrt{s}$ denotes the centre of mass energy of the proton antiproton collisions, η is the pseudorapidity

$$\eta = 0.5 \ln \frac{|\vec{p}| - p_{\parallel}}{|\vec{p}| + p_{\parallel}}$$

$p_{TR}^{(i)}$ is the absolute value of the transverse moment of the final jet (i), E_{TR} is the transverse energy $E_{TR} = \Sigma\, p_{TR}^{(i)}$, Δ is the distance in the Lego-plot $\Delta_{ij} = |(\Delta\eta_{ij})^2 + (\Delta\phi_{ij})|^{1/2}$, where $\Delta\phi_{ij}$ denotes the azimuthal angle difference between the transverse momenta of the jets i and j.

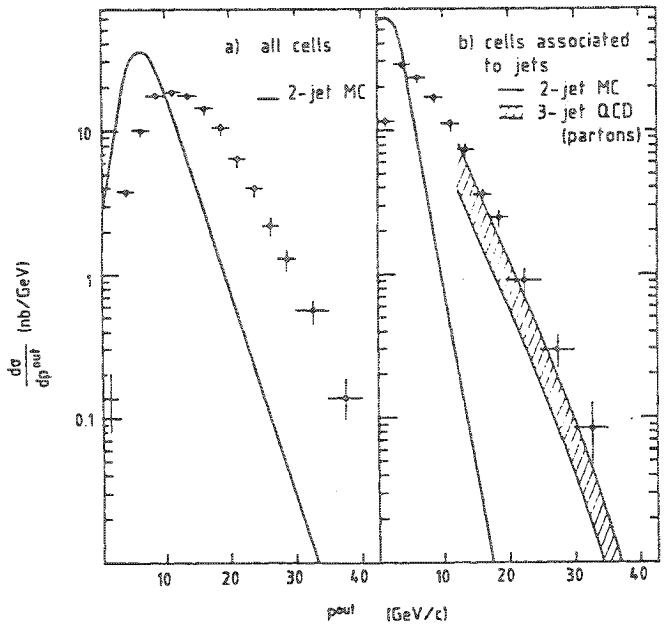
a) all cells
2-jet MC
b) cells associated to jets
2-jet MC
3-jet QCD (partons)
$\frac{d\sigma}{dp^{out}}$ (nb/GeV)
p^{out} (GeV/c)

Fig. 1

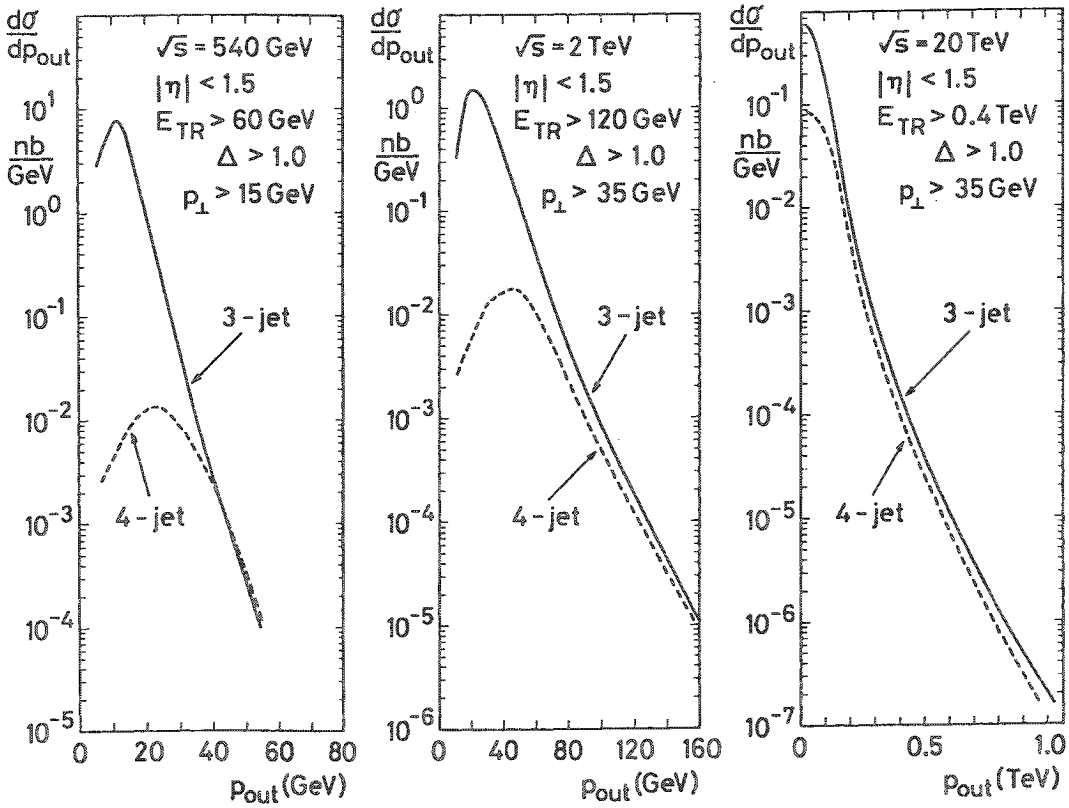
$\frac{d\sigma}{dp_{out}}$
$\sqrt{s}$ = 540 GeV
$|\eta| < 1.5$
$E_{TR} > 60$ GeV
$\Delta > 1.0$
$p_\perp > 15$ GeV
3-jet
4-jet
p_{out} (GeV)
$\sqrt{s}$ = 2 TeV
$|\eta| < 1.5$
$E_{TR} > 120$ GeV
$\Delta > 1.0$
$p_\perp > 35$ GeV
3-jet
4-jet
p_{out} (GeV)
$\sqrt{s}$ = 20 TeV
$|\eta| < 1.5$
$E_{TR} > 0.4$ TeV
$\Delta > 1.0$
$p_\perp > 35$ GeV
3-jet
4-jet
p_{out} (TeV)

Fig. 2

JETS: WHAT WE CAN STILL LEARN ...

B. Humpert*)
Institut de Physique Nucléaire
Université de Lausanne
CH-1000 LAUSANNE

and

R. Odorico
Dipartimento di Fisica dell' Università di Bologna
I.N.F.N., Sezione di Bologna
I-40126 BOLOGNA

Geneva, April 27, 1984

Abstract: A short overview is given about ongoing theoretical analyses concerning large- and low-p_t jet (j) production. A new class of (4-parton) processes, with two short-distance processes taking place simultaneously, is introduced, and cross-section estimates are given for: (4j)-, (W^+jj)-, and (WW)-production. The size of the (2-parton) 2j-,..,6j- cross sections (also with W,Z) is determined. The importance of coincidence measurements between large- and low-p_t jets is stressed.

*) The author thanks the CERN Theoretical Physics Division for its kind hospitality.

Jets result either from large-p_t hard scattering or from a less understood low-p_t interaction process. In this paper we present ongoing developments. We first give details on the large-p_t jet-jet invariant mass distribution. Allowing for the simultaneous interaction of two parton pairs, we are led to a new class of processes contributing to (4j)-,(W^+jj)- and (WW)-production. In the second part, we evaluate their integrated cross-sections, and we determine the size of similar (2-parton) multi-jet contributions (without/with W,Z). Finally, coincidence measurements between large-p_t and low-p_t jets can give new insights into the low-p_t dynamics.

Large-p_t jet-jet production has in the recent past been studied by the $p\bar{p}$ collider experiments UA2 [1] and UA1 [2], and a systematic analysis of the theoretical expectations [3] was completed. In Fig.1 we show $d\sigma/dM$ (fat solid curve) and indicate the size of the relevant subprocesses (solid curves with subprocess numbers). For calculation details we refer to Ref.[3]. At smaller (larger) M values qg(7) (qq(1),$q\bar{q}$(4)) scattering dominates whereas the gg(8) process is of negligible influence. We have also limited the rapidity region to $|y|\leq 0.85$, as is at present the case for the UA2 detector, and show the enormous loss in rate (fat dashed line). How sensitive are these results if the QCD parameters are changed ? Using a variety of scale dependent momentum distributions, we notice a factor ~2 spread in the mass spectrum if parametrizations with an excessively 'hard' gluon spectrum are ignored [3]. At large M values, the gluon (quark) subprocesses reveal a cross-section spread of several orders of magnitude (of a factor 2-5) which,at small M values, is however much less. Since in the former energy region the quark subprocesses dominate, the cross-section spread in the total sum is moderate. Varying the scale parameter within $0.1\ \text{GeV}\leq\Lambda\leq 0.7\ \text{GeV}$ reveals at small (large) M values almost no (a factor ~3) cross-section variation,mainly due to the structure functions. Similar features are observed in the single-jet q_t distribution [3].

Allowing for the possibility of two simultaneous short-distance processes [4], we are led to a new class of processes

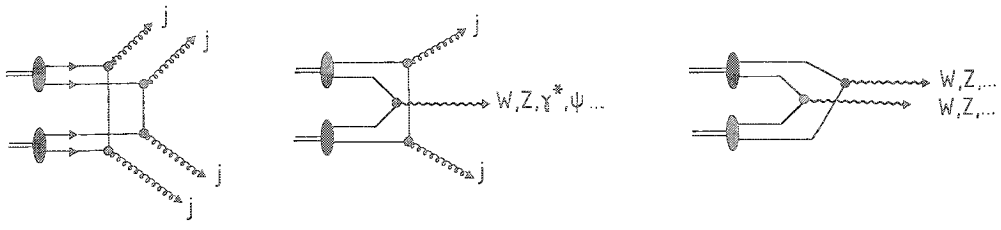

which contribute to (4j)-, (W^+jj)- and (WW)-production. The cross- section reads

$$d\sigma = \sum_{q/g} \frac{\hat{d\sigma}_{12}\,\hat{d\sigma}_{34}}{\pi R^2} \cdot V(x_1,x_3) \cdot \bar{V}(x_2,x_4)$$

$\hat{d\sigma}_{ij}$ is the differential parton cross-section. $\pi\cdot R^2=\sigma_{el}$ ~40mb estimates the flux of partons in a hadron, and $V(x_1,x_3)$ is the two-parton momentum distribution. For further details we refer to Refs. [4].

There is little theoretical understanding of the single- or multi- parton momentum distibutions. The earliest attempt dates back to 1971 [5], and since then - almost no progress !

$$u(x_1 \ldots x_N) = \prod_j^N \frac{f(x_j)}{x_j}(1-X)^{\gamma} C(X) \approx \prod_j^N u(x_j)\cdot(1-X)\cdot\theta(1-X)$$

The Kuti-Weisskopf model [5] assumes an infinity of partons in the nucleon, which, apart from momentum conservation (→ C(X), $X=x_1+..+x_N$), are uncorrelated; the confinement effects on each constituent type are described by the 'primitive' structure functions (→ $f(x_j)$). In the small x_j region , this form is well approximated by a product of the 'usual' single particle structure functions whereby the QCD corrections are also taken into account.

We have determined the influence of the analogous (2-parton) 'background' processes by using the Odorico Monte-Carlo program [6] for the multi-jet event generation. The incoming partons with primordial transverse momentum undergo a single 'hard' scattering process; initial and final (soft) gluon radiation does occur according to the Altarelli-Parisi (leading-log) splitting probabilities. The remaining energy is distributed among the spectator-jet hadrons according to a longitudinal phase-space model with a q_t cut-off and experimental information on the relative importance of the individual hadrons.

In Fig.2 we show the integrated cross-sections for 2-,...,6-jet production (solid lines). The transverse momentum of all jets is limited to $q_t \geq p_{cut}$=15 GeV. We have varied the QCD parameters and found little cross-section change. In the same figure we present the influence of the process: $p\bar{p}\rightarrow$(4 partons)→4-jets+X (dashed line). As p_{cut} increases its cross-section falls faster than the analogous 2-parton process. In Figs.3 and 4 the integrated cross-sections for W,Z+nj production (n=0,..,4) are shown (solid lines). The strong cross-section rise of the analogous 4-parton processes (dashed lines) is partially due to the W,Z threshold onset and partially follows from the simultaneous gluon scattering process. Above $\sqrt{s}$=2 TeV this mechanism dominates over the analogous 2-parton process. All these predictions, however, depend on the parton flux in the nucleon which implies a large (but well defined) uncertainty. In Fig.5 we compare the 2nd order SU_2xU_1 predictions involving only two initial state

partons [7], with the analogous 4-parton process. The strong discrepancy results from the large W,Z masses.

The production mechanism of the spectator-jets is far from being unanimously clear and several models for 'soft' hadron production have been proposed. The recombination model [8] assumes sea-q_v recombination to form a final state meson. In the DTU-model [9], tube-like color-singlet systems are created consisting of 3 and 3 colour charges which stretch the connecting colour flux-line and thus lead to hadron production. The Lund model [10] is based on the space-time picture of a 'YoYo', on the qq creation probability, and on an Ansatz for the quantum number distribution on the stretched string. Several other models exist [11].

In order to find more stringent distinction criteria between these schemes, we stress the importance of coincidence measurements among the large- and low-p_t jets; a possibility which so far has been mostly ignored. With such purposes in mind we have carried out a first analysis [12] of the process: $p\bar{p}\rightarrow\gamma j^{+}j_s{}^{+}X$ and present in Fig.6 the spectator-jet momentum (x_j) distribution for $y_\gamma=0$ and $q_t\geq 10$ GeV. Integration over all other kinematical variables has been carried out. Using 2-parton momentum distributions $V(x_2,x_j)$ at the lower vertex (of the close-by graph) we admit that part of the energy is distributed among the infinity of partons in the nucleon - therefore the rapid x_j-decrease. In the Lund model, instead, all energy at the lower vertex is distributed among the large-p_t parton (x_2) and the spectator-jet parton ($x_j=1-x_2$) resulting in the extended x_j- distribution (in Fig.6) .

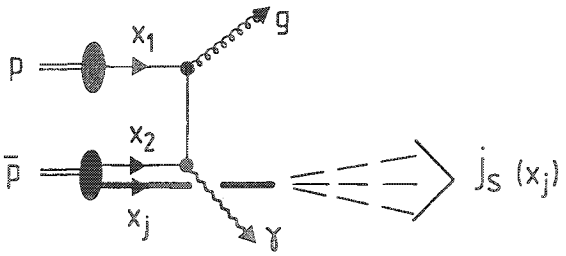

In this short note we have introduced new ideas in the field of jet-physics which await to be tested by experiment.

REFERENCES

[1] UA2 Collaboration, CERN: M.Banner et al., Phys.Lett. 118B (1982) 203; P.Bagnaia et al., Zeitschr.f.Physik C20 (1983) 117; P.Bagnaia et al., "Measurement of Very Large Transverse Momentum Jet Production at the CERN $p\bar{p}$ Collider", CERN-EP/84-12 (1984).

[2] UA1 Collaboration,CERN: G.Arnison et al., Phys.Lett. 123B (1983) 115; G.Arnison et al., Phys.Lett. 132B (1983) 214; G.Arnison et al., Phys.Lett. 132B (1983) 223.

[3] B.Humpert,"Two-Jet Production in $p\bar{p}$ Collisions"(to appear); Preprint,Ref.TH.3817-CERN(1984) (Phys.Lett,to be publ.) .

[4] B.Humpert,Phys.Lett.131B(1983)461;N.Paver and D.Treleani, Nuov.Cim.70A(1982)215; ibid.73A(1983)392; Preprint, ISAS-60/83/E.P., Trieste (1983).
Earlier references are:
P.Landshoff and J.Polkinghorne,Phys.Rev.D12(1975)3738; M.Jacob, Ref.TH.3515-CERN(1983);G.Goebel et al.,Phys.Rev.D22(1980)2789; F.Takagi,Phys.Rev.Lett.43(1979)1296.

[5] J.Kuti and V.F.Weisskopf,Phys.Rev.D4(1971)3418; H.R.Gerhold, Nuov.Cim.59A(1980)373; E.Takasugi et al.,Phys.Rev.D20(1979)211.

[6] R.Odorico,Nucl.Phys. B228(1983)381, Ref.TH.3760-CERN, Ref.TH. 3761-CERN(1983); B.Humpert and R.Odorico, in preparation.

[7] B.Humpert,Phys.Lett.135B(1984)179.

[8] K.P.Das and R.C.Hwa, Phys.Lett. 68B(1977)459.

[9] A.Capella,U.Sukhatme and J.Tran Thanh Van,Z.Phys.3(1980)329; P.Aurenche,F.W.Bopp and J.Ranft,Annecy Preprint LAPP-TH-83 (Z.Phys.,to be publ.) .

[10] B.Andersson et al.,Phys.Rep.97(1983)31; H.-U. Bengtsson and G.Ingelman,Preprint Ref.TH.3820-CERN (1984).

[11] W.Kittel,Nijmegen Univ.Report,HEW 203 (1981); B.Humpert,Proc. 4th Warsaw Symp. on Elem.Particle Physics,Kazimierz,1981 (eds.Z.Ajduk and K.Doroba,Warsaw Univ.Press,1981).

[12] B.Humpert and G.Ingelman,Int.Conf.'Hadron Structure '83', Smolenice,Czechoslovakia,1983; and in preparation .

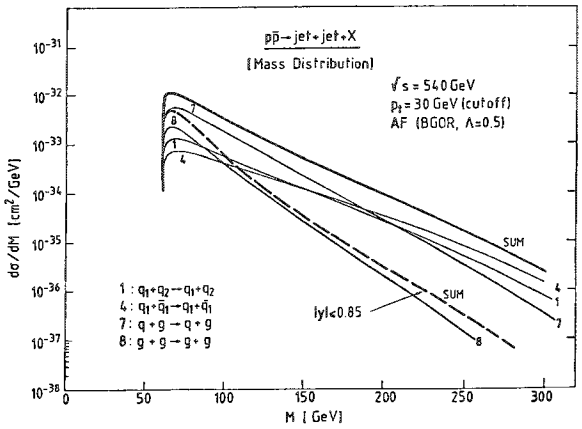

Fig.1

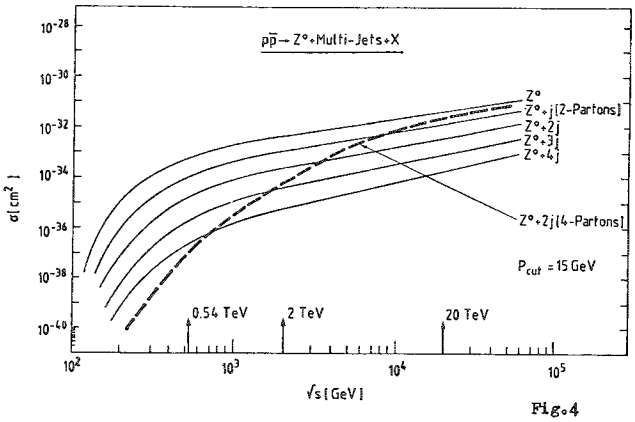

Fig.4

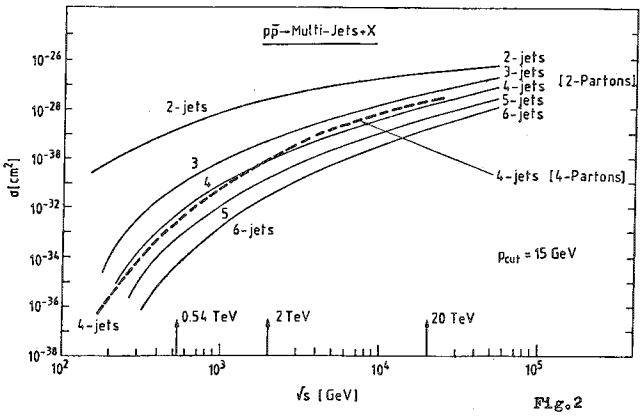

Fig.2

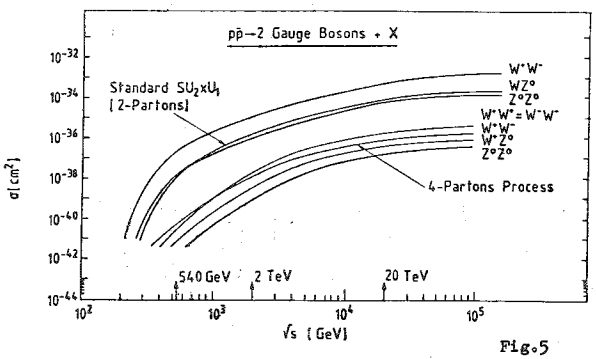

Fig.5

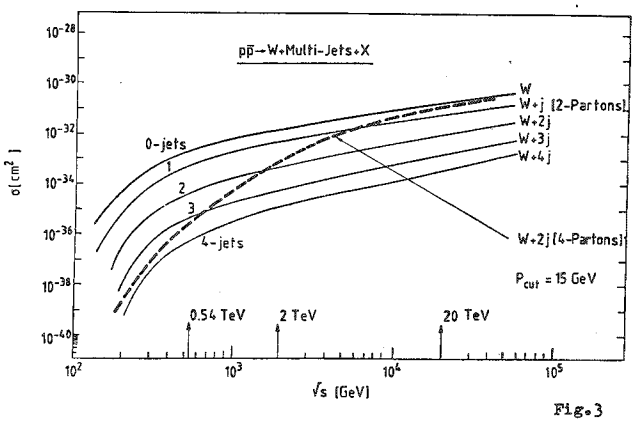

Fig.3

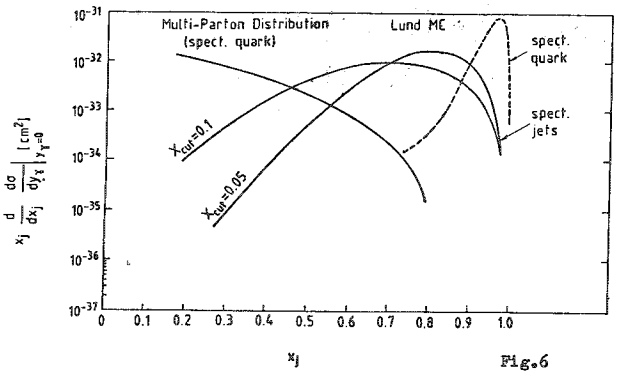

Fig.6

RECENT RESULTS FROM HIGH TRANSVERSE MOMENTUM PROCESSES AT THE ISR

W.M. Geist

CERN, Geneva, Switzerland

ABSTRACT

Various aspects of three ISR experiments on deep inelastic phenomena are discussed. New data on inclusive production at high transverse momentum of protons give first experimental evidence for hard diquark scattering. Measurements of deep inelastic production of single kaons and jets and rather detailed analyses of jet structures and of correlations between jets are presented. The experimental findings are consistently explained in terms of hard scattering of quarks and gluons. Finally, it is shown that a precise measurement of central particle production in these hard scattering events could reveal the prevailing fragmentation mechanism of systems of coloured partons.

1. INTRODUCTION

Experiments dealing with high transverse momentum phenomena in hadron-hadron collisions aim primarily at an understanding of parton scattering dynamics. The scattered colored partons fragment into two jets at large angles relative to the beam direction. The non-interacting colored constituents fragment into two longitudinal (spectator) jets. Hence the parton scattering mechanism can be inferred from detailed studies of all jets.

The rare 4-jet events are separated from the more numerous soft hadronic interactions by: (a) either triggering on a large transverse energy E_T detected in calorimeters (E_T trigger), or (b) by triggering on those sideways jets in which one single particle carries most of the jet energy (single particle trigger). Historically single particle trigger experiments at the ISR gave first evidence for strong interactions among partons. New results from an experiment of this type are given in sect. 2. Recent data from two E_T trigger experiments are presented in sect. 3. Measurements of central particle production in deep inelastic events are discussed in sect. 4.

2. INCLUSIVE SINGLE PARTICLE PRODUCTION AT HIGH p_T

The measurements presented in this section come from the ABCDHW Collaboration working at the Split Field Magnet (SFM) Detector. The data were taken with a single particle trigger at a polar angle Θ away from 90°.

It is known since quite some time that events with a single particle trigger of high transverse momentum p_T show the expected 4-jet structure [1]. A somewhat different representation of the results from ref. [1c] is given in fig. 1, where the ratio F of the transverse momentum flow in events with $p_T > 4$ GeV/c to the flow observed in normal inelastic events is displayed as function of c.m.s rapidity y and azimuthal angle (φ (trig) ~ 0). The trigger particle is not included. In addition to the longitudinal spectator jets, a jet of particles along the trigger particle is observed (trigger jet) as well as a large relative momentum flow due to the "away jet" at $\varphi \sim 180° \pm 30°$. No trigger requirement is imposed on the away jet.

More than 75% of the trigger jet energy [2], however, is carried by the trigger particles. One expects therefore that the trigger jet is slimmer than the away jets as observed in fig. 1. A more quantitative support of this reasoning comes from e^+e^- data in fig. 2 [3]. The inclusive yield of charged jet particles is shown as function of the fragmentation variable z in addition to the distributions for charged particles produced in those jets where the fastest charged particle (trigger) has z(trig) > 0.5 or z(trig) > 0.7. Also given are distributions for particles in trigger jets from pp collisions with p_T > 4 GeV/c and p_T > 6 GeV/c [4], i.e. $\langle z(trig) \rangle$ = 0.72 or 0.78 [2a]. Both sets of data exhibit consistent trends, i.e. the particle yield decreases with increasing z(trig). From neutrino interactions one knows [5] that ~ 80% of the pions produced at z > 0.7 contain the fragmenting quark. This suggests that in proton-proton collisions high -p_T $\pi^+(u\bar{d})$ and $K^+(u\bar{s})$ mesons are mainly produced as leading fragments of scattered u-quarks whereas $\pi^-(\bar{u}d)$ mesons come mainly from d-quarks. A recent detailed study [6] supports these simple ideas. K^- triggers on the other hand, which do not share any valence quarks with the protons, are shown to be predominantly leading fragments of flavourless, soft partons such as gluons [7]. A test of this simple picture is provided by the relative cross sections for inclusive $K^\pm$ and $\pi^\pm$ production shown in fig. 3 as function of $x_T = 2 \cdot p_T/\sqrt{s}$ [8]. The fact that both K^+ and π^+ are mainly produced by scattering and subsequent fragmentation of u-quarks translates into a constant ratio of cross sections. The decreasing ratio K^-/π^- in fig. 3 is consistent with K^- mesons being produced by gluons which have a softer structure function [9] than the d-quarks fragmenting into π^-. QCD predictions in fig. 3 also underline the need for a large gluon contribution to K^- production [8]. Whereas one has reached a consistent picture of meson production at high p_T the situation is less clear in case of (anti)baryon production. In fig. 4 recent measurements [10] of the inclusive ratios p/h^+ and $\bar{p}/h^-$ are displayed as functions of the polar angle Θ at p_T > 3.8 GeV/c. If both (anti)protons and mesons of the same charge are produced by fragmentation of the same type of scattered partons one expects inclusive ratios independent of kinematic variables. This expectation is borne out experimentally for $\bar{p}$ production only. The ratio p/h^+ does depend on p_T (not shown, [10]) and on Θ (fig. 4). This observation can be qualitatively explained by hard scattering of diquarks which should frequently fragment into baryons.

Since diquarks are extended objects a form factor $F(Q^2)$ in the hard process tends to suppress the cross section at fixed p_T as function of decreasing polar angle Θ, i.e. increasing momentum transfer Q. Further detailed correlation measurements will be done in order to verify this hypothesis. For a comparable kinematic configuration the EMC Collaboration has measured relative (anti)proton yields [11] in parton jets from deep inelastic muon interactions. A comparison of the data of ref. [11] with those of fig. 4 ($\Theta \sim 50°$) is given in fig. 5, good agreement is found.

3. INCLUSIVE JET PRODUCTION AND JET PROPERTIES

At the ISR two experiments made use of E_T triggers to select jet-like events. The transverse energy was measured in a solid angle $\Delta\Omega = \Delta y.\Delta\varphi \sim 2 * 2\pi$. The CMOR Collaboration triggers on large electromagnetic energy E_T^o which is mainly due to the "neutral" jet component (i.e. π^o) [12]. The relative event yields in $p\bar{p}$ and pp interactions are shown in fig. 6 as function of E_T^o at $\sqrt{s}$ = 52.4 GeV/c. The value of the ratio is close to 1 and does not strongly depend on the "jettiness" of the events [13]. The AFS Collaboration uses a large total energy E_T as signature for jet production. They determine the invariant jet cross sections at $\sqrt{s}$ = 63 and 45 GeV from an analysis of event shapes measured in one quadrant of the full calorimeter. The invariant cross section [14] is displayed in fig. 7 as function of $x_T = 2p_T/\sqrt{s}$. It was multiplied by $p_T^{-5.3}$ assuming that $E * d\sigma/dp \propto p_T^{-n} * f(x_T, \Theta)$. The UA1 data [15] are in reasonable agreement with the AFS measurements and justify thus a posteriori the assumed factorizable form. A compilation of measurements of the power n for inclusive production of jets, pions [16] and protons [17] is given in fig. 8. Pointlike scattering corresponds to n = 4. Any dependence of the cross section on a length or momentum scale tends to raise n. In case of jet production there is a dependence on the intrinsic transverse momentum of partons and on Q^2 due to structure functions [9] and $\alpha_s(Q^2)$; for pion production one expects in addition Q^2 dependent fragmentation functions and, finally, for proton production a further Q^2 dependence is caused by the diquark form factor.

For a more complete understanding of hard processes a detailed study of jet properties was performed. It should be noted here that the jet energy E_{jet} is roughly given by $E_{jet} \leq 0.5 * E_T$; $E_T \sim E_T^o + 7$ GeV for the CMOR data [22]. Both experiments state that only for $E_T \geq 30$ GeV more than 50% of all events are jet-like [18,19,22]. First, the jet axes were determined from charged and neutral particles in both experiments [12,18]. The AFS Collaboration then measured for charged particles the average transverse momentum q_T relative to the jet axis as function of z. The data are shown in fig. 9(a) for $E_T > 33$ GeV [18,19]. Good agreement is found with a Monte-Carlo calculation using $\langle q_T \rangle \sim 0.65$ GeV/c and including detector simulation. Similar results were obtained by the UA1 Collaboration [21]. Measurements of $\langle |j_T| \rangle = \langle q_T \rangle$ by the CMOR Collaboration are given as function of z and E_{jet} in fig. 9(b) [22]. In fig. 9(b) $\langle |j_T| \rangle$ is significantly smaller than in fig. 9(a) but is in rough agreement with e^+e^- results at $\sqrt{s} \sim 2 * E_{jet}$ [23]. The large difference between the two sets of ISR data can hardly be attributed to instrumental effects or to the different method of determining the jet axes [12,18]. It may be a consequence of the fact that ~ 70% of E_{jet} recorded in the CMOR experiment is carried by the neutral jet component [22] triggered upon. This large percentage happens to be similar to $\langle z(trig) \rangle$ in the single particle experiment of sect. 2 such that in both cases only ~ 30% of E_{jet} is available to produce additional charged particles. For charged trigger jet secondaries fig. 9(c) shows $\langle p_{perp} \rangle = \langle q_T \rangle$ versus $p_{\parallel}$ ($z = p_{\parallel}/E_{jet}$), the momentum component parallel to the jet axis. The data were obtained by the ABCDHW Collaboration with a single particle trigger [4]. Agreement with the CMOR data is found.

The longitudinal jet structure was investigated by the AFS Group. For charged jet particles the distribution in $x_p = 2 * p/W$ was determined. The invariant two-jet energy W was calculated from all particles associated to the jets. The resulting distribution is at variance with e^+e^- results [23] (not shown [24]). A refined determination of W based upon Monte-Carlo corrections to truncated jets gives rise to the modified distribution in fig. 10 [18,19]. It is now consistent with UA1 data [21] and also with e^+e^- data [23] except for an excess at $x_p < 0.10$ (sect. 4).

One may anticipate dissimilar jets due to their different parton composition in e^+e^- interactions (u,c,d,s,b) and in proton-proton collisions (probably u, d, gluons). Experimental evidence for the expected parton composition of jets from pp interactions, i.e. for valence quarks and gluons, was already found in sect. 2. Charge ratios in jets which are not affected by the presence of a leading (trigger) particle support this picture as demonstrated below. Fig. 11 shows the ratios of positive to negative particles as function of z from jets obtained by the AFS [18] and CMOR [22] Collaborations. The ABCDHW charge ratios as function of $x_E \sim z * \langle z(trig) \rangle$ obtained from away jets recoiling against a single charged trigger particle are given as well [6,7]. Jet particles with $z > 0.7$ are potential candidates for single particle triggers (sect. 2), hence it is justified to include in fig. 11 the measured inclusive ratio of positive and negative hadrons, i.e. the ratio $[\sigma(\pi^+) + \sigma(K^+) + \sigma(p)]/[\sigma(\pi^-) + \sigma(K^-) + \sigma(\bar{p})]$ [8,10,16] as function of z (where $z = z(trig) = f(p_T)$ [2a]). All sets of data are consistent. A ratio bigger than 1 and rising with z (x_E) supports the idea of a large contribution of u quarks as expected from the proton composition.

Making use of the asymmetric trigger configuration (θ (trig) ~ 50°) the ABCDHW Collaboration has obtained evidence for jets from neutral partons in the following way. Consider first quark-quark scattering for which the momenta of the scattered quarks are equal and opposite on the average in the pp rest system. In this case the trigger particle and the away jet should be collinear (back-to-back). This is supported by fig. 12 [8] where a large charge ratio for the away jets (from valence quarks) is found in the back-to-back configuration for π^+ and K^+ triggers. Note that the K^+ and π^+ triggers come dominantly from u-quark fragmentation (sect. 2). If, however, (hard) u-quarks yielding π^+ and K^+ triggers scatter off (soft) gluons, the fragments of the gluons should frequently populate the same longitudinal hemisphere as the trigger particle (back-to-antiback) due to a boost from the quark-gluon c.m.s to the proton-proton c.m.s. This expectation is supported by the small charge ratio [10] for this configuration in fig. 12. For K^- triggers, however, the charge ratio in the back-to- antiback configuration is much larger than for π^+ and K^+ triggers (fig. 12). This is expected if gluons yield the K^- triggers (sect. 2) such that the away jets are dominantly due to valence quark jets.

4. CENTRAL PARTICLE PRODUCTION

The transverse energy flow in jet events obtained by the AFS Collaboration [18,19] at $\sqrt{s}$ = 63 GeV is shown in fig. 13 for $|y| < 1$ as function of the azimuthal angle $\Delta\varphi$ relative to one jet axis; an estimate of the flow in normal inelastic events (minimum bias) is included. In addition to the clear jet structures at $\Delta\varphi \sim 0°$ and 180° one notices an increase of a factor $R \sim 3.0$ of the flow at $\Delta\varphi \sim 90°$ in jet events relative to inelastic events. Similar results were obtained by the UA2 Collaboration [25]. In fig. 14 the measured ratio R' of particle densities in events triggered by a single particle with $p_T > 4$ and Θ (trig) ~ 50° GeV/c to normal inelastic events is given as function of y for $\Delta\varphi = 90° \pm 20°$ [26]. For $|y| < 1$ the yield in high p_T events is again larger (by a factor $R' \sim 2$). The observed effects may be caused by a superposition of two jet-jet systems with particle densities $\rho_j\ (2E_{jet})$ from the system of sideways jets and $\rho_s\ (\sqrt{s'} = \sqrt{s} - 2E_{jet})$ from the spectator jets. Approximating $\rho_j\ (2E_{jet})$ by $\frac{d\sigma}{dy}\ (y \sim o)$ from e^+e^- collisions at $W = 2E_{jet}$ [27] and $\rho_s\ (\sqrt{s'})$ by $\frac{d\sigma}{dy}\ (y \sim o)$ from non-diffractive pp collisions at $\sqrt{s'}$, one finds $R'\ (E_{jet}) = (\rho_j\ (2E_{jet}) + \rho_s\ (\sqrt{s'}))/\rho\ (\sqrt{s}) \sim 2 - 2.5$, where $\rho\ (\sqrt{s})$ is taken from inelastic pp collisions (*). The ratio R' should be close to the ratio R of energy flows, hence the data in fig. 3 and 4 are roughly consistent with a superposition of (at least) two fragmenting jet-jet systems.

Possible superpositions of two or more jet-jet systems are being studied in more detail by the ABCDHW Collaboration [28]. The idea is the following: the four coloured partons or parton systems emerging from a hard interaction may fragment e.g. either independently or the fragmentation may occur along strings connecting the coloured parton (system)s. In the latter case one expects a rather large particle density at medium transverse momentum relative to both neighbouring jet axes due to a Lorentz boost from the string c.m.s. to the proton-proton c.m.s (see sketch).

(*) ρ (non-diffr.) ~ 1.25 ρ (inelastic) at y ~ 0.

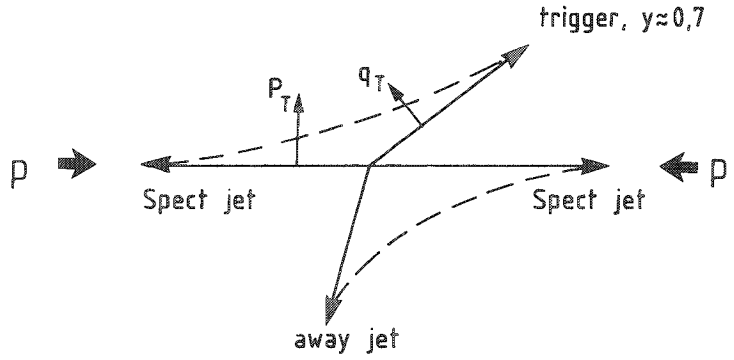

The secondary particle density $\varphi = 0° \pm 20°$ (φ(trig) = 0°) and p_T(sec) > 1 GeV/c was calculated for the string configuration given in the diagram which should occur mainly for quark-quark small angle scattering [29]. The calculated density was normalized to the density predicted for independent fragmentation and the ratio r is shown in fig. 15(a) as function of y. Fragmentation was generated in the respective rest system according to measured e^+e^- distributions. In fig. 15(a) one finds indeed a large relative yield from the string picture for $-3 < y < 0.0$ and p_T(sec) > 1 GeV/c, i.e. outside the 'cores' of the trigger and the spectator jets. The experimental rapidity distribution in fig. 15(b) for the cuts defined above indicates that the predicted effect is measurable with sufficient precision. This analysis is in progress. It should be pointed out, however, that more than one string configuration [29] contributes generally to a given experimental configuration.

5. CONCLUSIONS

Experimental evidence is found for a substantial contribution of hard diquark scattering to high p_T proton production. Data on inclusive production at high p_T of mesons and of jets, on jet structures and on correlations between jets are consistently described by quark and gluon scattering and fragmentation. A detailed study of particle production in a kinematical region where jets merge has been started. It should contribute to a better understanding of fragmentation mechanisms.

Acknowledgements

I am grateful to the organizers for inviting me to this very inspiring meeting. Thanks to my colleagues working at the ISR for discussions and, especially, to T. Akesson, T. Cox, H.G. Fischer, Ch. von Gagern and T. Lohse for supplying me with unpublished data.

REFERENCES

[1] (a) M. Della Negra et al., Nucl. Phys. B127 (1977) 1;
(b) M.G. Albrow et al., Nucl. Phys. B145 (1978) 305;
(c) A. Breakstone et al., CERN/EP 83-182, to be published in Zeitschr. für Phys. C.

[2] H.G. Fischer, Proc. of the EPS Conference, Lisbon (1981) 897;
C.D. Buchanan, Proc. XVIIth Rencontre de Moriond (1982) vol. II, 139;
J.L. Alonso et al., Zeitschr. für Phys. C6 (1980) 21.

[3] G. Hanson et al., Phys. Rev. D26 (1982) 991.

[4] A. Breakstone et al., CERN/EP 83-186, to be published in Zeitschr. für Phys. C.

[5] P. Allen et al., Nucl. Phys. B214 (1983) 369.

[6] A. Breakstone et al., CERN/EP 84-53, submitted to Zeitschr. für Phys. C.

[7] A. Breakstone et al., Gluon tagging in hard proton-proton interactions at the ISR, to be published.

[8] A. Breakstone et al., Phys. Lett 135B (1984) 510.

[9] H. Abramowicz et al., Zeitschr. für Phys. C12 (1982) 289;
F. Bergsma et al., Phys. Lett. 123B (1983) 269.

[10] A. Breakstone et al., CERN/EP 84-2, submitted to Phys. Rev. Letters.

[11] J.J. Aubert et al., Phys. Lett. 135B (1984) 225.

[12] A.L.S. Angelis et al., Phys. Lett. 126B (1983) 132.

[13] CMOR Collaboration, Ch. von Gagern, priv. communication.

REFERENCES (Cont'd)

[14] T. Akesson et al., Phys. Lett. 123B (1983) 133.

[15] M. Banner et al., Phys. Lett. 118B (1982) 203.

[16] A. Breakstone et al., Phys. Lett. 135B (1984) 505.

[17] ABCDHW Collaboration, T. Lohse, priv. communication.

[18] T. Akesson, CERN/EP 83-130 (1983).

[19] T. Akesson et al., CERN/EP 84-56 (1984).

[20] T. Akesson et al., Phys Lett. 128B (1983) 354.

[21] G. Arnison et al., Phys. Lett. 132B (1983) 223.

[22] A.L.S. Angelis et al., CERN/EP 84-46 and T. Cox, priv. communication.

[23] M. Althoff et al., DESY 83-130 (1983).

[24] T. Akesson et al., Contribution to the International Europhysics Conference on High Energy Physics, Brighton, England, July 1983.

[25] P. Bagnaia et al., CERN/EP 83-94 (1983).

[26] ABCHW Collaboration, unpublished.

[27] P. Söding, Proceedings of the International Europhysics Conference on High Energy Physics, Brighton, England, July 1983.

[28] ABCDHW Collaboration, to be published.

[29] e.g. H.U. Bengtsson and G. Ingelman, CERN/TH 3820 (1984).

FIGURE CAPTIONS

Fig. 1 Transverse momentum flow in events with a trigger particle with $p_T > 4$ GeV/c produced at $\theta \sim 50°$ relative to that in normal inelastic events.

Fig. 2 Inclusive z-distribution of charged jet particles obtained at $\sqrt{s} = 6.8$ GeV by MkI. Also given are z-distributions for charged particles in trigger jets from a SFM experiment using a single particle trigger at $\sqrt{s} = 62$ GeV.

Fig. 3 Relative cross sections for $K^{\pm}$ and $\pi^{\pm}$ production versus x_T; also given are QCD predictions with and without gluon contributions.

Fig. 4 Relative proton and antiproton yields versus θ at $\sqrt{s} = 62$ GeV.

Fig. 5 Relative proton and antiproton yields from EMC compared to SFM data obtained at $p_T \geq 4$ GeV/c and $\theta \sim 50°$ [10].

Fig. 6 Relative event yields versus E_T^o from pp and $p\bar{p}$ collisions.

Fig. 7 Invariant cross sections as functions of x_T from the AFS and UA1 experiments.

Fig. 8 Compilation of measurements of the power n of the p_T dependence of inclusive cross sections ($\propto p_T^{-n} \cdot f(x_T, \theta)$) for jets, pions and protons.

Fig. 9 Measurements of average transverse momenta relative to jet axes:
(a) data from the AFS Collaboration and a Monte-Carlo simulation;
(b) data from the CMOR Collaboration;
(c) trigger jet data obtained by the ABCDHW Collaboration.

Fig. 10 Inclusive distribution versus $x_p = 2p/W$ from jets obtained by the AFS Collaboration.

Fig. 11 Charge ratio (+/-) in jets from the AFS and CMOR Collaborations; the charge ratio in jets recoiling against a single charged high p_T particle and the ratio of inclusive cross section for positive and negative hadrons from the ABCDHW Collaboration are also shown.

Fig. 12 Charge ratio (+/-) from away jets in the back-to-back or back-to-antiback configuration for π^+/K^+ and K^- triggers with $p_T > 4$ GeV/c (ABCDHW Collaboration).

Fig. 13 Transverse energy distribution as function of the azimuthal angle $\Delta\varphi$ relative to one jet axis (AFS Collaboration, $\sqrt{s} = 63$ GeV).

Fig. 14 Ratio of particle densities in high p_T events ($p_T > 4$ GeV/c) and normal inelastic events for $\varphi = 90° \pm 20°$ as function of rapidity (ABCDHW Collaboration).

Fig. 15 (a) Ratio r of predicted particle densities from the string model and from the independent fragmentation model as function of rapidity.

(b) Measured rapidity distribution for particles produced with p_T (sec) > 1 GeV/c and with $\varphi = 0 \pm 20°$ in events with a single particle trigger with $p_T > 4$ GeV/c, $\varphi \sim 0°$ and $\theta \sim 50°$ (ABCDHW Collaboration).

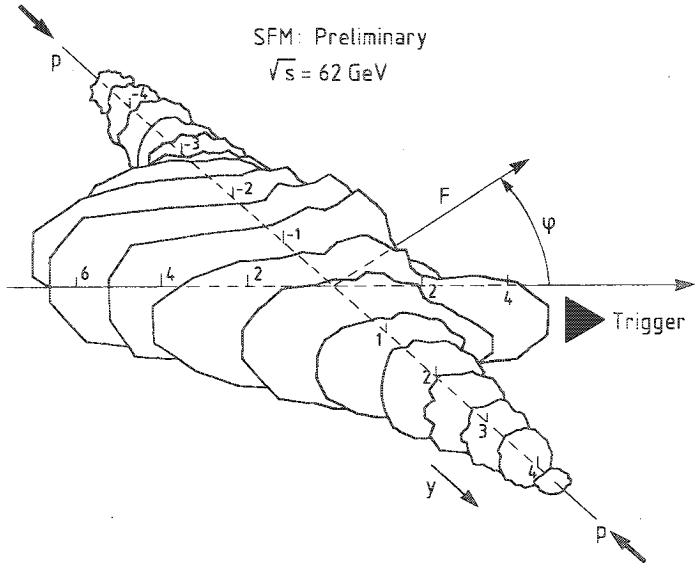
SFM: Preliminary
√s = 62 GeV
p
F
φ
Trigger
y
p

Fig. 1

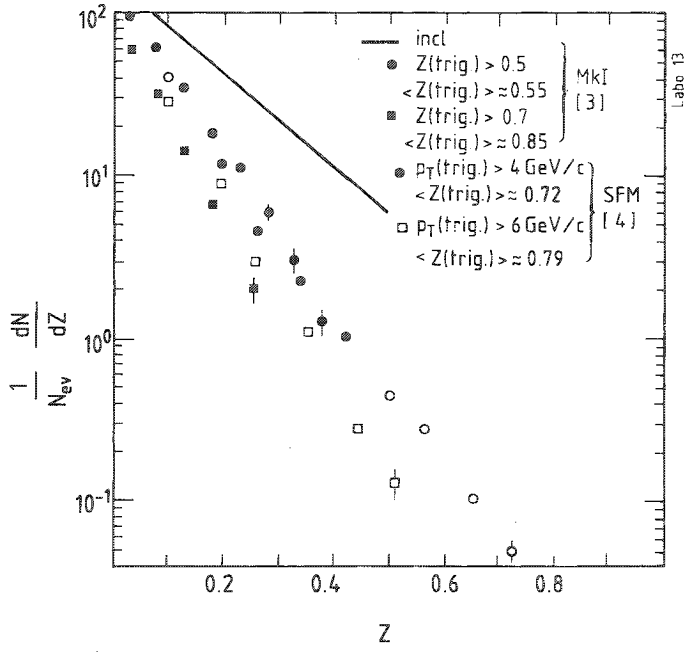
incl
Z(trig.) > 0.5
<Z(trig.)> ≈ 0.55
Z(trig.) > 0.7
<Z(trig.)> ≈ 0.85
MkI [3]
pT(trig.) > 4 GeV/c
<Z(trig.)> ≈ 0.72
pT(trig.) > 6 GeV/c
<Z(trig.)> ≈ 0.79
SFM [4]
Labo 13
1/Nev dN/dZ
Z

Fig. 2

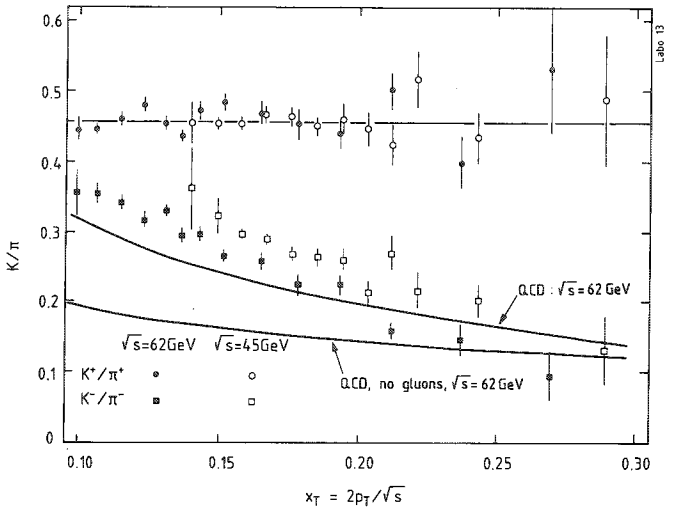

Fig. 3

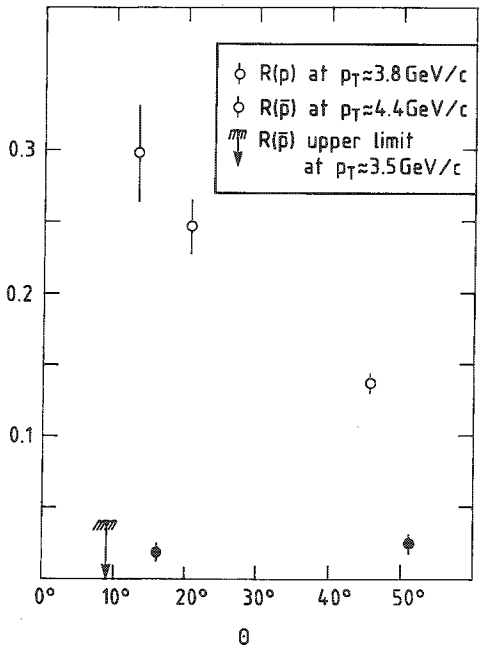

Fig. 4

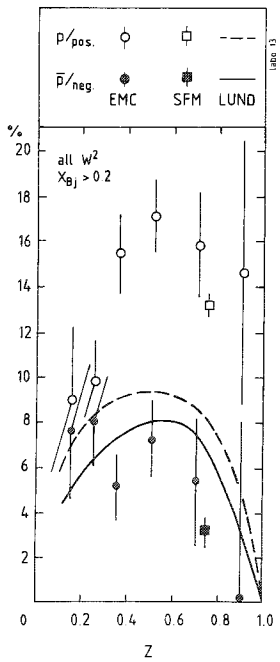

Fig. 5

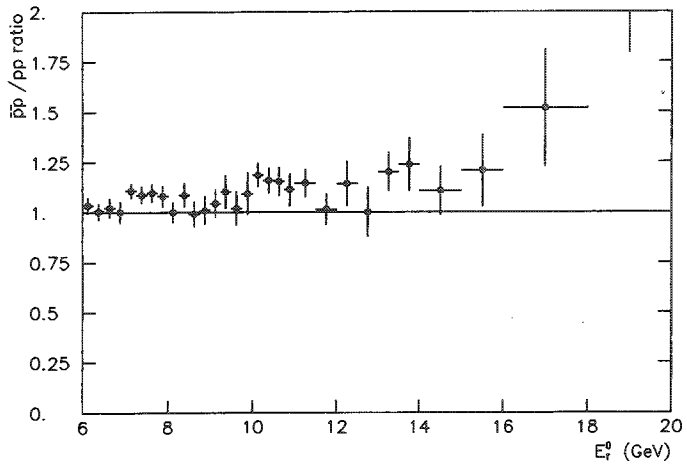

Fig. 6

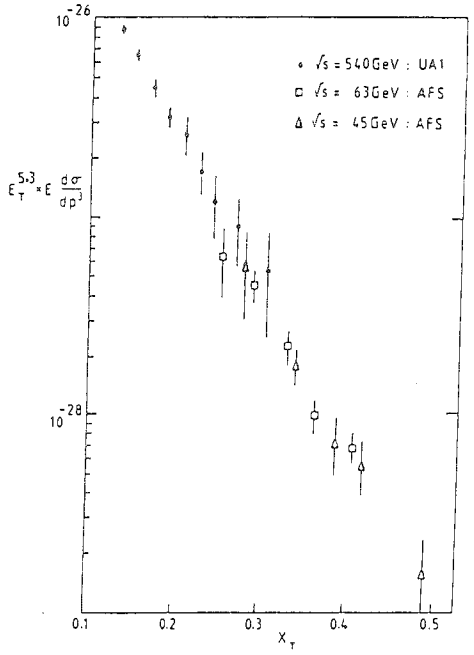

Fig. 7

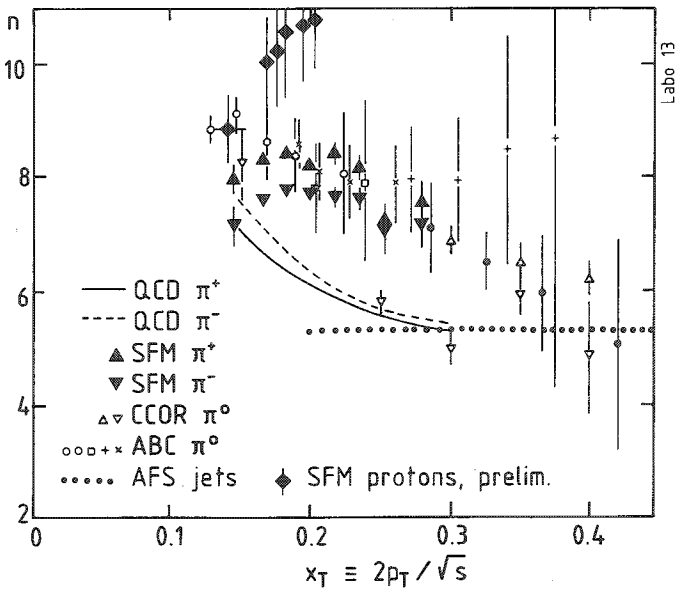

Fig. 8

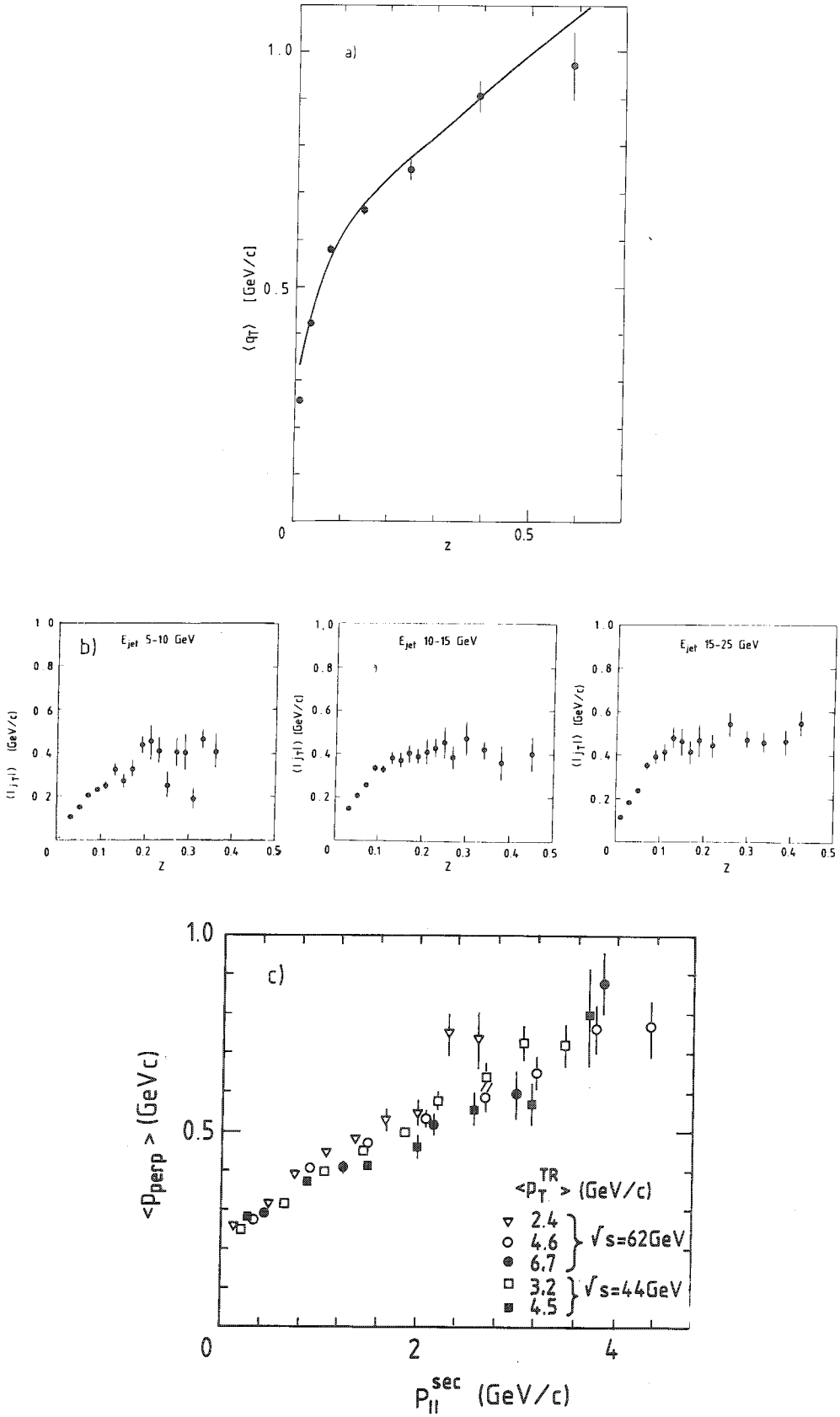
a)
1.0
0.5
0
0.5
z
⟨qT⟩ [GeV/c]
b)
Ejet 5-10 GeV
Ejet 10-15 GeV
Ejet 15-25 GeV
⟨|jT|⟩ (GeV/c)
z
c)
⟨pperp⟩ (GeV/c)
⟨pTTR⟩ (GeV/c)
2.4
4.6
6.7
√s=62GeV
3.2
4.5
√s=44GeV
psecll (GeV/c)

Fig. 9

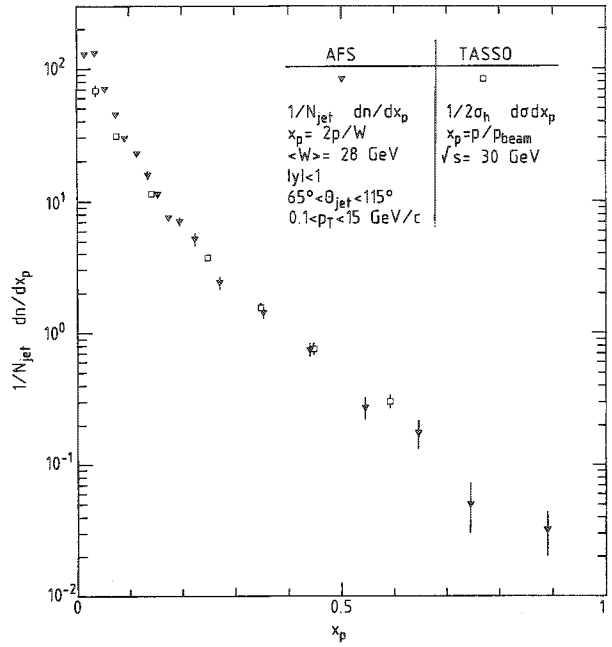

Fig. 10

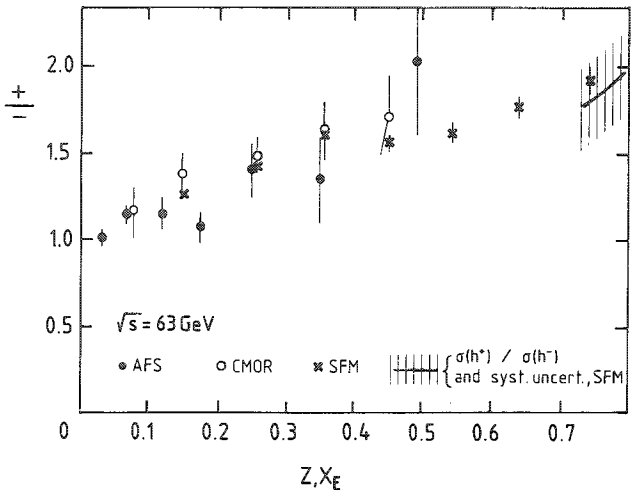

Fig. 11

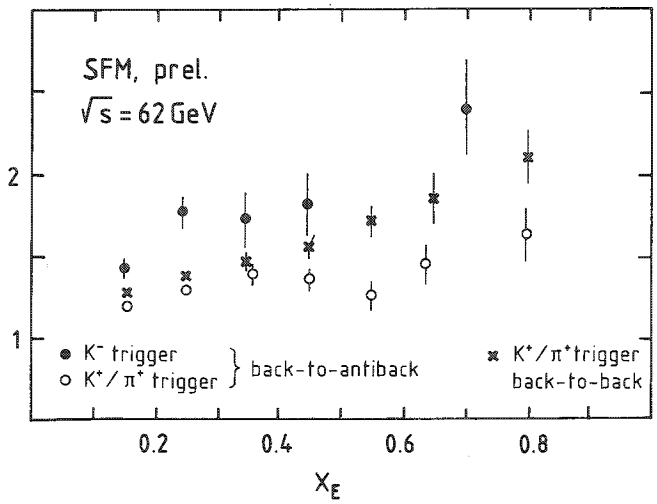

Fig. 12

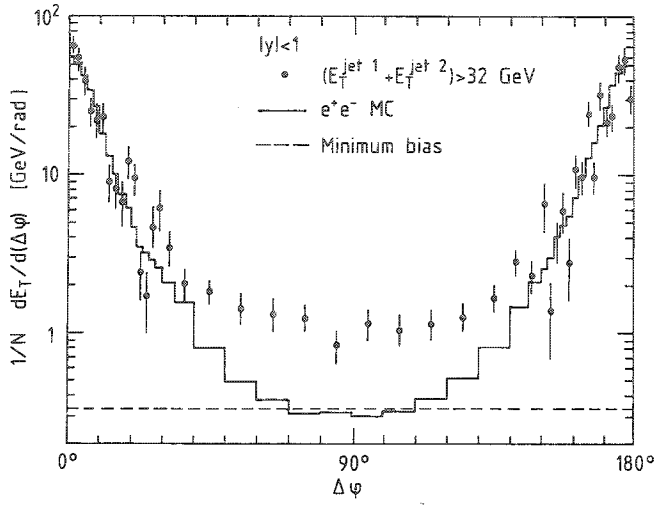

Fig. 13

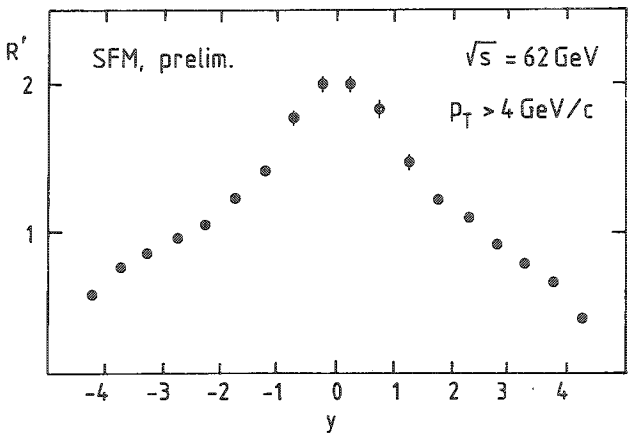

Fig. 14

SFM : preliminary, $\sqrt{s}$ = 62 GeV
trigger: p_T > 4 GeV/c, y≈0.7, φ≈0°
secondaries: p_T > 1 GeV/c, φ=0°±20°

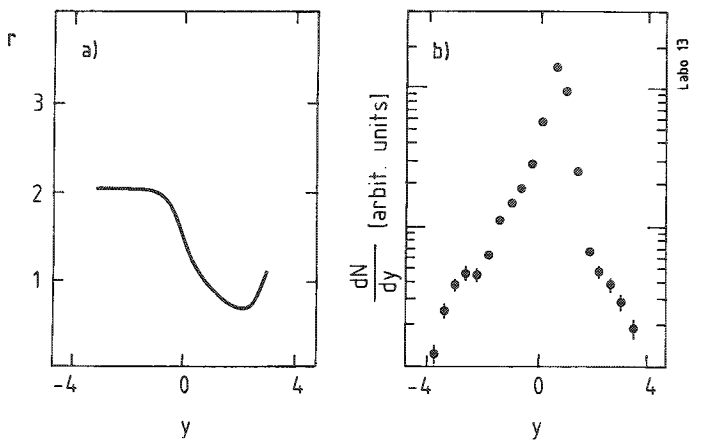

Fig. 15

Transverse Momentum Distributions of Jets and Weak Bosons.

R. K. Ellis

Fermi National Accelerator Laboratory, Batavia, IL. 60510

The theoretical description of processes leading to events at large transverse momentum is reviewed. Numerical estimates are given for jet cross-sections and for W and Z production cross-sections. The influence which uncertainties in the input parameters have on the theoretical predictions is also discussed.

1. Jet Cross-Sections

The observation of clearly identified jets at the CERN $S\bar{p}S$ collider[1,2] opens a new era in the study of hadron structure. For the first time using hadronic probes we have irrefutable evidence for the parton substructure of the proton. The observed constituents scatter as the quarks and gluons of QCD should. Of course, in the interactions of objects as complicated as protons there are uncertainties, both theoretical and experimental, some of which will be described below. But before entering into these details it is important to remember that the gross features of the data are clearly in agreement with QCD.

The jet cross-section observed at the collider is four or more orders of magnitude bigger than the large p_T cross-section at the ISR. Despite this big change, the predictions[3] of the QCD improved parton model describe the data well, both in shape and in normalisation. This agreement with data requires the inclusion of a scale breaking gluon distribution. In addition to the p_T spectrum, the angular distribution of the observed jets is consistent with the exchange of a single massless vector gluon in the t channel[4]. Apart from the scale breaking logarithms of QCD, the constituents of the proton appear to behave as point-like particles.

The cross-section for jet production is calculated using the parton model formula,

$$E\frac{d^3\sigma}{d^3p} = \sum_{i,j}\int dx_1\,dx_2\; f_i(x_1,Q^2)\,f_j(x_2,Q^2)\left[\frac{p^0 d^3\sigma}{d^3p}\right], \qquad (1)$$

where the sum on i,j runs over different types of partons. The parton cross-sections are calculable in perturbation theory and in lowest order are given by

$$\frac{p^0 d^3\sigma}{d^3p} = \left(\frac{\alpha_s(Q)}{s}\right)^2 \left|M^{ij}\right|^2, \qquad (2)$$

where M is the invariant matrix element. The contribution of the various sub-processes to the total cross-section is dependent on the size of the matrix element and the values of the distribution for the incoming partons. The influence of the former factor can be judged from Table 1 where the analytic forms of the matrix elements and their numerical values at 90° in the parton parton centre of mass are given. On the basis of the parton cross-sections alone it is clear that processes involving initial state gluons are favoured.

PARTON PROCESS	$\lvert M\rvert^2$	F_M
$q\underline{q}' \to q\underline{q}'$ $q\bar{q}' \to q\bar{q}'$	$\frac{4}{9}\frac{s^2+u^2}{t^2}$	2.22
$qq \to qq$	$\frac{4}{9}\left(\frac{s^2+u^2}{t^2} + \frac{s^2+t^2}{u^2}\right) - \frac{8}{27}\frac{u^2}{st}$	3.26
$q\bar{q} \to q'\bar{q}'$	$\frac{4}{9}\frac{t^2+u^2}{s^2}$	0.22
$q\bar{q} \to q\bar{q}$	$\frac{4}{9}\left(\frac{s^2+u^2}{t^2} + \frac{t^2+u^2}{s^2}\right) - \frac{8}{27}\frac{u^2}{st}$	2.59
$q\bar{q} \to gg$	$\frac{32}{27}\frac{u^2+t^2}{ut} - \frac{8}{3}\frac{u^2+t^2}{s^2}$	1.04
$gg \to q\bar{q}$	$\frac{1}{6}\frac{u^2+t^2}{ut} - \frac{3}{8}\frac{u^2+t^2}{s^2}$	0.15
$qg \to qg$	$-\frac{4}{9}\frac{u^2+s^2}{us} + \frac{u^2+s^2}{t^2}$	6.11
$gg \to gg$	$\frac{9}{2}\left(3 - \frac{ut}{s^2} - \frac{us}{t^2} - \frac{st}{u^2}\right)$	30.4

Table 1. Parton matrix elements [averaged (summed) over initial (final) colours and spins]. F_M is the value of $\lvert M\rvert^2$ in the parton parton centre of mass at 90°, $(s = -t/2 = -u/2)$.

Clean jets are observed at $\sqrt{S} = 540$ GeV for values of the transverse energy between 20 and 150 GeV. The parameter x_T therefore ranges between

$$\left[x_T = \frac{2E_T}{\sqrt{S}}\right] \qquad 0{\cdot}07 \leq x_T \leq 0{\cdot}56\ . \qquad (3)$$

The variable x_T provides a good estimate of the value of x at which the parton distributions are probed. At lower values of x_T even the softer parton distributions such as gluons or antiquarks are important. Fig.1, taken from ref.(5), shows the contribution of the various subprocesses to the total jet production cross-section. Below E_T of 80 GeV the dominant processes are gluon initiated. Above this value of E_T the harder valence quark distribution makes the quark-quark scattering diagrams dominate. Low x_T jets thus provide an ideal place to study gluon jets.

Ignorance of the gluon distribution function, which is poorly determined from deep-inelastic scattering, does not lead to a large uncertainty in the jet cross-section, because of a correlation between the shape of the measured gluon distribution and the value of Λ. This is illustrated in Fig.2 where two phenomenologically acceptable gluon distribution functions taken from ref.(6) are shown at $Q^2 = 4GeV^2$ and $Q^2 = 2000GeV^2$. The narrower gluon distribution function (denoted D01) has $\Lambda = .2$ GeV, whereas the broader gluon distribution (D02) has $\Lambda = .4$ GeV. Despite the large differences at low Q^2, at higher values (e.g. $Q^2 = 2000GeV^2$, the approximate scale relevant for high p_T jets) the two gluon distributions are practically identical. This is particularly true of the low x region in which the gluon distribution is most important.

A theoretical issue, related to the value of Λ, is the choice of Q, the scale in the parton distribution functions (eq.(1)) and in the running coupling constant (eq.(2)). In theory, this question could be resolved if an $O(\alpha_s^3)$ calculation had been performed. Different choices for the scale Q modify the form of the $O(\alpha_s^3)$ terms. Because the parton cross-section begins in order $O(\alpha_s^2)$ the truncated result without $O(\alpha_s^3)$ terms is quite sensitive to the choice of scale. Without an $O(\alpha_s^3)$ calculation we can at best make an educated guess of the correct scale using the only fragment of the complete calculation which has been performed[7,8].

$$q_i + q_j \rightarrow q_i + q_j + G \qquad (4)$$

This calculation suggests that the most appropriate scale is

$$Q^2 = p_T^2/2 \; . \qquad (5)$$

With this choice of scale the corrections to the process in eq.(4) are small for most values of x_T. The complexity of the calculation of the radiative corrections to other partonic sub-processes, especially gluon-gluon scattering,

makes it probable that eq.(5) is the best estimate we shall have for some time. Furthermore our information on the gluon distribution is gleaned from deep inelastic scattering where it first enters at $O(\alpha_s)$. This information is not sufficient to provide a meaningful determination of the gluon distribution function including the $O(\alpha_s)$ terms. It is precisely these correction terms which are needed to give meaning to the $O(\alpha_s^3)$ terms in gluon-gluon scattering. So even if the calculation of radiative corrections to gluon-gluon scattering were technically feasible, it would still be hard to interpret.

2. q_T Distributions of W and Z Bosons.

The production of W and Z bosons proceeds via the Drell-Yan quark anti-quark annihilation mechanism. The total cross-section is calculated from,

$$\sigma = N \int dx_1 dx_2 \left[H(x_1, x_2, Q^2)\, \delta(x_1 x_2 - \tau) \right] + O(\alpha_s) \qquad (6)$$

where N is an overall normalisation and H is the product of quark and anti-quark distribution functions evaluated at scale Q^2, and weighted with the appropriate coupling factors. The $O(\alpha_s)$ terms have been calculated and give rise to a positive correction of about 40% for both W and Z production at $\sqrt{S}$ = 540 GeV. Because the correction is large there is some uncertainty in the prediction for the total cross-section. However the $O(\alpha_s)$ correction is much smaller than it was for μ - pair production at lower energies, (because the coupling constant is smaller), and therefore the ambiguity in the overall normalisation of W and Z production (the so called K-factor) is reduced. The best theoretical values for the total production cross-sections at $\sqrt{S}$ = 540 GeV are[9],

$$\sigma^{W^+ + W^-} = 4.2 \,{}^{+1.3}_{-0.6}\ \text{nb} \quad , \quad \sigma^{Z} = 1.3 \,{}^{+0.4}_{-0.2}\ \text{nb} \qquad (7)$$

Multiplying these numbers by the branching ratios into electrons,

$$B^{W^\pm \to e^\pm} = .089 \quad , \quad B^{Z \to e^+e^-} = .032 \qquad (8)$$

corresponding to m_t = 40 GeV and α_s/π = .04 the predictions for the observed decay channels are,

$$(\sigma B)^{W^\pm \to e^\pm} = 370 \,{}^{+110}_{-60}\ \text{pb} \quad , \quad (\sigma B)^{Z \to e^+e^-} = 42 \,{}^{+12}_{-6}\ \text{pb}. \qquad (9)$$

The transverse momentum distribution of the intermediate vector bosons is theoretically more complicated than the total cross-section. In the limit in which the transverse momentum q_T is of the same order as the mass of the vector boson, Q, the transverse momentum should be well described by recoil against one

massless parton and the maximum transverse momentum A_T is controlled by the kinematics of the one parton emission diagrams.

$$A_T^2 = \frac{(S+Q^2)^2}{4S\cosh^2 y} - Q^2 \qquad (10)$$

Decreasing q_T introduces a second scale into the problem and for small q_T we find that large terms are generated and must be resummed if we are to have a valid perturbative prediction. The emission of many gluons changes the form of the q_T distribution but should leave the total cross-section, which is quite reliably calculated in $O(\alpha_s)$, unchanged. The resummation was first attempted by DDT[10] and subsequently modified and consolidated[11]. A consistent framework for going beyond the leading double logarithmic approximation has been indicated by Collins and Soper[12]. The work reported here[9] which was used to generate the numerical results has the following features.

a) At large q_T we automatically recover the $O(\alpha_s)$ perturbative distribution coming from one gluon emission, without ad hoc introduction of matching procedures between hard and soft radiation.

b) In the region $q_T << Q$ the soft gluon resummation is performed at leading double logarithmic accuracy.

c) Only terms corresponding to the emission of soft gluons for which the exponentiation can be theoretically justified are resummed.

d) The integral of the q_T distribution reproduces the well known results for the $O(\alpha_s)$ total cross-sections exactly.

e) The average value of q_T^2 is also identical with the perturbative result at $O(\alpha_s)$.

f) All quantities are expressed in terms of precisely defined quark distribution functions as measured in deep inelastic scattering.

g) The results constitute the first term in a systematic expansion.

The result contains a resummation of logarithmic terms in impact parameter space. This allows exact conservation of the transverse momentum of the emitted gluons. The form of the result is,

$$\frac{d^2\sigma}{dq_T^2 dy} = N\int \frac{d^2b}{(2\pi)^2} e^{-ib\cdot q_T}\left[R(b^2,Q^2)\exp S(b^2,Q^2)\right] + Y(q_T^2,Q^2) \qquad (11)$$

where the form factor (including only terms which can be deduced from an $O(\alpha_s)$ calculation), is

$$S(b^2,Q^2) = \int_0^{A_T^2} \frac{d\mu^2}{\mu^2}\left[J_0(b\mu) - 1\right]\frac{4}{3}\frac{\alpha_s(\mu)}{2\pi}\left(2\ln Q^2/\mu^2 - 3\right) \qquad (12)$$

The complete $O(\alpha_s)$ expressions for Y and R are given in ref.(9) and are too complicated to reproduce here. The zeroth order term in R involves the parton distribution functions evaluated at a b-dependent scale

$$R = H(x_1^0, \tau/x_1^0, B^2) + O(\alpha_s)\,, \quad x_1^0 = \sqrt{\tau}\,e^y\,, \quad B^2 \sim \frac{1.59}{b^2} \qquad (13)$$

The function Y is completely finite as q_T tends to zero.

This result for the form factor is in agreement with the general form of Collins and Soper. Their result is written in terms of arbitrary parameters c_1 and c_2 which be used to modify the scale at which the separation between hard and soft contributions is made. After some manipulation their result for the form factor can be written as,

$$S_{CS}(b^2,Q^2) = -\frac{8}{3\pi}\int_{c_1/b}^{c_2 Q}\frac{d\mu}{\mu}\left[\ln\left(\frac{c_2^2 Q^2}{\mu^2}\right)A(\mu) + B(\mu)\right] \qquad (14)$$

Making the natural choices for the parameters,

$$c_1 = 2\,e^{-\gamma_E}\,, \quad c_2 = A_T/Q \qquad (15)$$

we obtain in the $\overline{MS}$ scheme,

$$A(\mu) = \alpha_s(\mu) + D\,\alpha_s^2(\mu) + O(\alpha_s^3)\,, \quad B(\mu) = \alpha_s(\mu)\left\{-\frac{3}{2} - 2\ln c_2\right\} \qquad (16)$$

The term D is the higher order correction which is dominant in the low q_T region and is given by,[13,14]

$$D = \frac{1}{2\pi}\left\{\left(\frac{67}{18} - \frac{\pi^2}{6}\right)3 - \frac{10\,n_f}{18}\right\} \qquad (17)$$

Eq.(14) is readily shown to be in agreement with eq.(12) in the approximation in which we replace the Bessel function by a Θ function.[15]

The numerical consequences of eq.(11) are shown in Fig. 3 . Also shown is a histogram of the 52 UA1 W events suitably normalised. The parton distributions used are those of ref.(6), which have two different choices for Λ. Both sets are compatible with low energy data. The principal uncertainty in eq.(11) is associated with the choice of Λ. From Fig. 3 we see that this leads to a variation of about 15%. The form of the parton distribution functions leads to a small uncertainty, since quark distributions, well determined in deep inelastic scattering, are most important. The behaviour of the strong coupling

constant in the very low momentum region has only a minor effect above q_T of 2 GeV. The influence of higher order corrections can be estimated by including the only term which has been calculated (eq.(17)) in our numerical analysis. The effect of the inclusion of D is numerically approximately equivalent to a rescaling of Λ by a factor of about 2. Thus the effect of higher order corrections cannot be distinguished from the uncertainty in Λ.

The differential cross-section for $W^+ + W^-$ production at zero rapidity is,

$$\left.\frac{d\sigma}{dy}\right|_{y=0} \sim 2.3\,nb \tag{18}$$

The corresponding result for Z production is,

$$\left.\frac{d\sigma}{dy}\right|_{y=0} \sim .8\,nb \tag{19}$$

The shape of the q_T distribution for Z production is very similar to the plot for W production shown in Fig.3. Here again the main uncertainty comes from the choice of Λ.

3. References

1) G. Arnison et al., Phys. Lett. 123B (1983) 115.
2) M. Banner et al., Phys. Lett. 118 (198 2) 203.
   P. Bagnaia et al., Z. Phys. C20 (1983) 117.
3) R. Horgan and M. Jacob, Nucl. Phys. B179 (1981) 441.
4) W. Scott, these proceedings.
5) E. Eichten, I. Hinchliffe, K. Lane and C. Quigg, Fermilab preprint 84/17-T.
6) D. Duke and J.F. Owens, Florida preprint FSU-HEP-831115 (1983).
7) R.K. Ellis, M.A. Furman, H.E. Haber and I. Hinchliffe, Nucl. Phys. B173 (1980) 397.
8) W. Furmanski and W. Slominski, Krakow preprint TPJU 11/81 (1981).
9) G. Altarelli, R.K. Ellis, M. Greco and G. Martinelli, CERN preprint TH (1984).
10) Yu. L. Dokshitzer, D.I. Dyakonov and S.I. Troyan, Phys. Lett. 78B (1978) 290, Phys. Rep. 58 (1980) 269.
11) G. Parisi and R. Petronzio, Nucl. Phys. B154 (1979) 427.
    P. Chiappetta and M. Greco, Nucl. Phys. B221 (1983) 269 and references therein.
12) J.C. Collins and D.E. Soper, Nucl. Phys. B197 (1982) 446 and references therein.
13) J. Kodaira and L. Trentadue, Phys. Lett. 112B (1982) 335.
14) C.T.H. Davies and W.J. Stirling, CERN preprint TH3853 (1984).
15) S.D. Ellis, N. Fleishon and W.J. Stirling, Phys. Rev. D24 (1981) 1386.

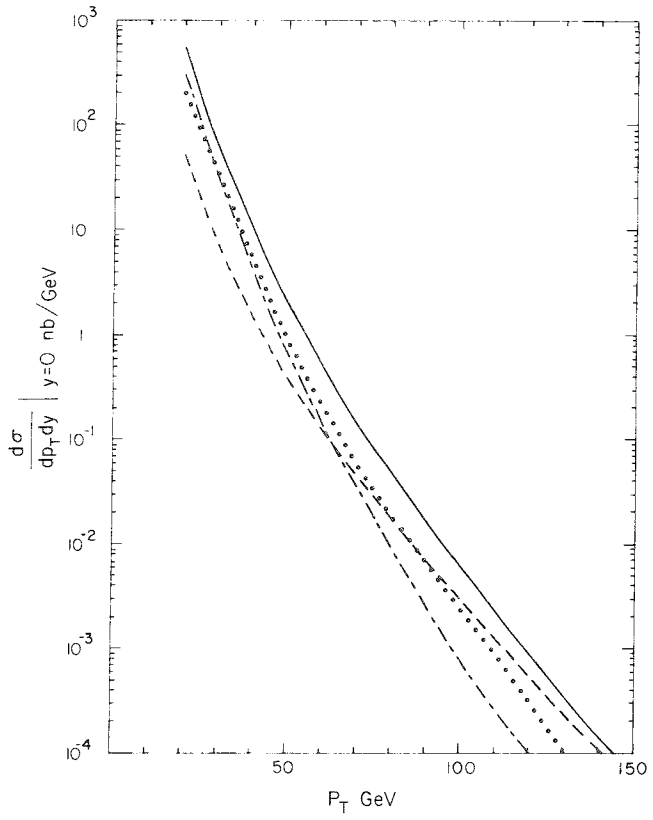

Fig. 1 Subprocess contributions to the jet cross-section (dashed line, qq scattering; dashed-dotted line, gg scattering; dotted line, qg scattering; solid line,total). The scale Q,(cf.eqs.(1,2)) is chosen so that $Q = p_T/2$ and $\Lambda = .2$ GeV.

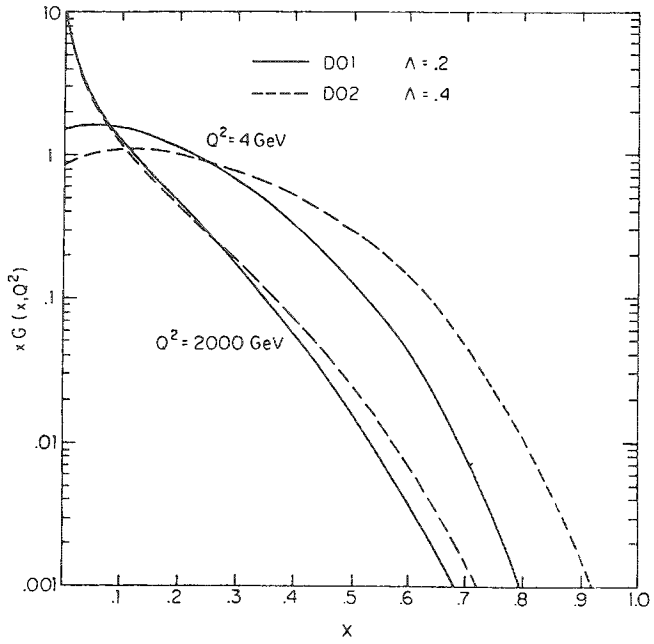

Fig. 2 Two parametrizations for the gluon distribution at $Q^2 = 4$ GeV^2 and $Q^2 = 2{,}000$ GeV^2.

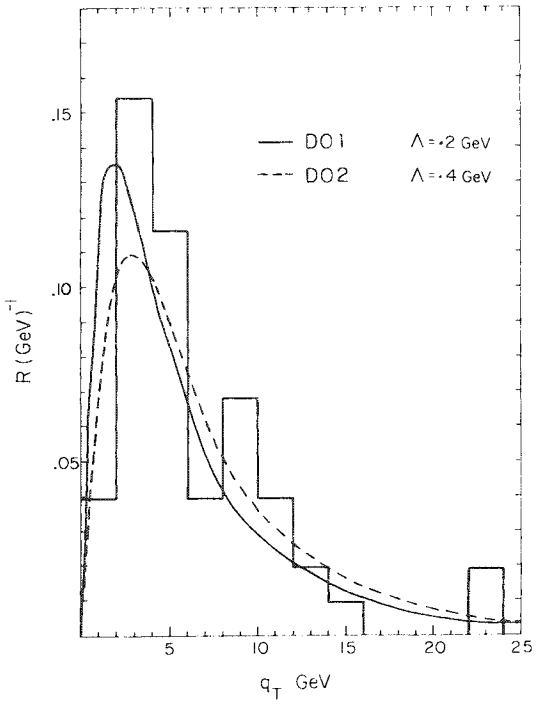

Fig. 3 The differential cross-section for the production of W bosons. The ratio

$$R = \frac{d\sigma}{dq_T dy} \Big/ \frac{d\sigma}{dy} \text{ at rapidity } y=0 \ .$$

W,Z Physics and Standard Model

PRODUCTION OF HIGH MASS ev AND e^+e^- PAIRS IN THE UA2 EXPERIMENT AT THE CERN $\bar{p}p$ COLLIDER

The UA2 Collaboration
(Berne, CERN, Copenhagen, Orsay, Pavia, Saclay)

presented by
J. SCHACHER
University of Berne, Switzerland

ABSTRACT

We present new results on intermediate vector boson production at the CERN $\bar{p}p$ collider. A comparison is made with the predictions of the standard model of the unified electroweak Glashow-Salam-Weinberg theory.

1. INTRODUCTION

We report here the results from a search for electrons with $p_T > 15$ GeV/c produced at the CERN $\bar{p}p$ collider ($\sqrt{s} = 540$ GeV) during its 1982 and 1983 periods of operation.

Following a general discussion of the topology of the events containing an electron candidate, we shall compare the data with expectations in the framework of the electroweak standard model [1] for the reactions

$$\bar{p} + p \rightarrow W^{\pm} + \text{anything} \qquad (1)$$
$$\rightarrow e^{\pm} + \nu\ (\bar{\nu})$$

$$\bar{p} + p \rightarrow Z^0 + \text{anything} \qquad (2)$$
$$\rightarrow e^+ + e^- \quad \text{or} \quad e^+ + e^- + \gamma$$

where $W^{\pm}$ and Z^0 are the postulated charged and neutral Intermediate Vector Bosons (IVB), respectively.

According to the amount of data collected we are now in the position to study some details of the IVB production, e.g. the influence of emission of gluon radiation on the distribution of the W transverse momentum (Fig.1).

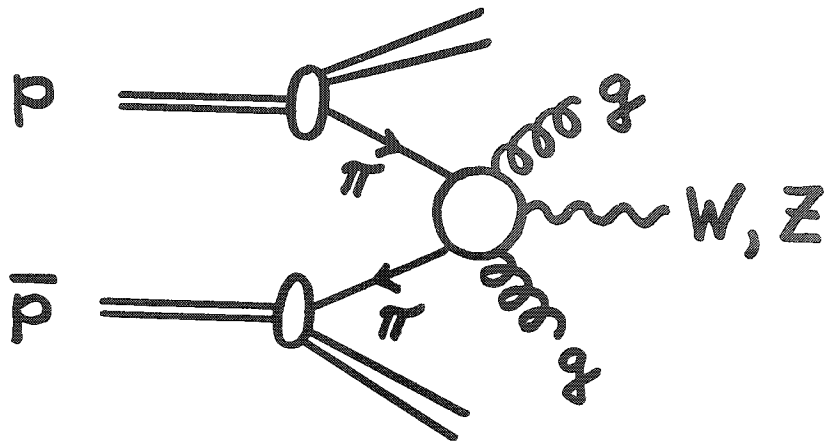

Fig.1 Typical diagram for W and Z production, taking into account emission of gluon (g) radiation. π : parton in p or $\bar{p}$.

Preliminary results from the study reported here have already been presented elsewhere [2] and a more complete discussion can be found in a recent publication [3].

2. THE DETECTOR

The experimental apparatus, shown in Fig.2, has been described in detail elsewhere [4]. At the centre of the apparatus a system of cylindrical chambers (the vertex detector [5]) measures charged particle trajectories in a region without magnetic field. The vertex detector consists of : a) four multi-wire proportional chambers, (C1 to C4), having cathode strips with pulse height read-out at ±45° to the wires ; b) two drift chambers with measurement of the charge division on a total of 12 wires per track. The drift chambers are used to obtain both tracking information and to evaluate the most likely ionisation I_0 associated with each track. From the reconstructed tracks the position of the event vertex is determined with a precision of ±1 mm in all directions.

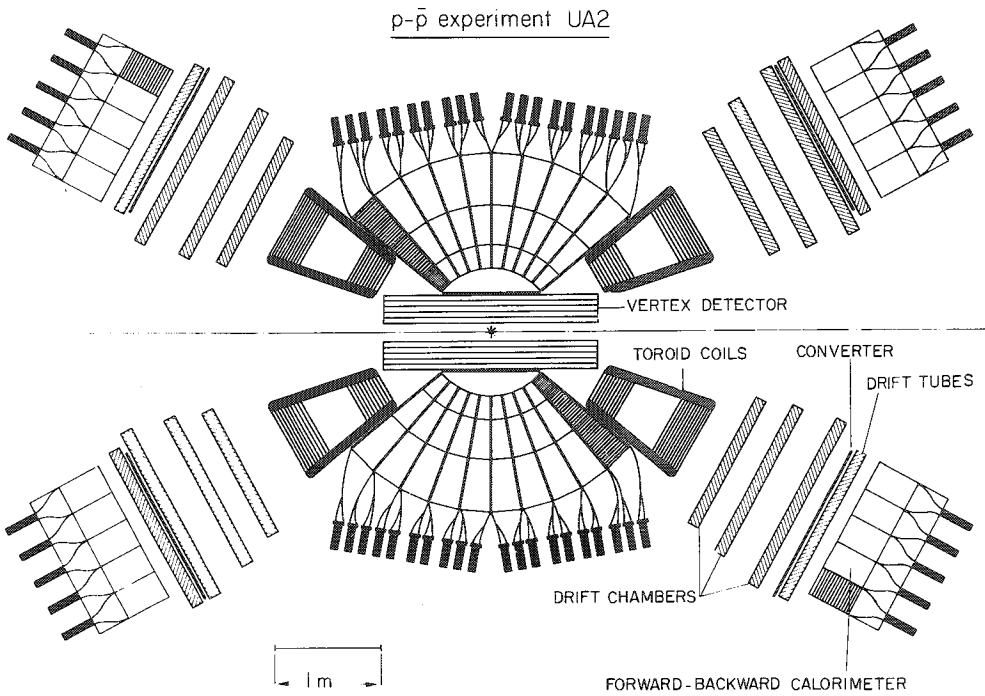

Fig.2 A view of the UA2 detector in a plane containing the beam line.

The vertex detector is surrounded by an electromagnetic and hadronic calorimeter (central calorimeter [6]), which covers the full azimuth and a polar angle interval $40° < \theta < 140°$. The calorimeter is segmented into 240 independent cells, each covering 10° in θ and 15° in ϕ and built in a tower structure pointing to the centre of the interaction region. The cells are segmented longitudinally into a 17 radiation lengths thick electromagnetic compartment (lead-scintillator) followed by two hadronic compartments (iron-scintillator) of $\approx$ 2 absorption lengths each.

In the angular region covered by the central calorimeter a cylindrical tungsten converter, 1.5 radiation lengths thick, followed by a cylindrical proportional chamber (C5), is located just after the vertex detector. This device localises electromagnetic showers initiated in the tungsten with a precision of ±3 mm, as verified using test-beam electrons.

For the first 15 nb^{-1} of integrated luminosity, collected during the Autumn of 1982, the azimuthal coverage of the central calorimeter was only 300°. The remaining interval (±30° around the horizontal plane) was covered by a magnetic spectrometer which included a lead-glass array to measure charged and neutral particle production [7].

The two forward regions ($20° < \theta < 37.5°$ and $142.5° < \theta < 160°$) are each equipped with twelve toroidal magnet sectors with an average bending power of .38 Tm. Each sector is instrumented with

a) three drift chambers [8] located after the magnetic field region. Each chamber contains three planes with wires at -7°, 0° and +7° with respect to the magnetic field direction.

b) a 1.4 radiation lengths thick lead-iron converter, followed by a preshower counter which consists of two pairs of layers of 20 mm diameter proportional tubes (MTPC), staggered by a tube radius and equipped with pulse height measurement [9]. This device localises electromagnetic showers initiated in the converter with a precision of ±6 mm.

c) an electromagnetic calorimeter consisting of lead-scintillator counters assembled in ten independent cells, each covering 15° in ϕ and 3.5° in θ. Each cell is subdivided into two independent longitudinal sections, 24 and 6 radiation lengths thick, respectively, the latter providing rejection against hadrons.

The systematic uncertainty in the energy calibration of the electromagnetic calorimeters for the data presented here amounts to an average value of ±1.5%. The cell-to-cell calibration has a distribution with a r.m.s. of 2.2%. The energy resolution for electrons is measured to be $\sigma_E/E = 0.14/\sqrt{E}$ [6] in the central calorimeter and $0.17/\sqrt{E}$ in the forward ones (E in GeV).

3. DATA TAKING AND DATA REDUCTION

In order to implement a trigger sensitive to electrons of high transverse momentum, the photomultiplier gains in all calorimeters were adjusted so that their signals were proportional to the transverse energy.

Because of the cell dimensions, electromagnetic showers initiated by electrons may be shared among adjacent cells. Trigger thresholds were applied, therefore, to linear sums of signals from matrices of 2 × 2 cells, rather than to individual cells. In the central calorimeter, all possible 2 × 2 matrices were considered; in the two forward ones, we included only those consisting of cells belonging to the same sector.

A W trigger signal (for Z^0 trigger: see Ref.12) was generated whenever the linear sum from at least one such matrix exceeded a threshold which was typically set at 8 GeV. To suppress background from sources other than $\bar{p}p$ collisions, we required a coincidence with two signals obtained from scintillator hodoscopes covering the polar angle interval 0.47° - 2.84° with respect to the beams on both sides of the collision region. These hodoscopes, which were part of an experiment to measure the $\bar{p}p$ total cross-section [10], gave a coincidence signal in more than 98% of all non-diffractive $\bar{p}p$ collisions.

Approximately 7×10^5 W triggers were recorded during the 1982 and 1983 runs, corresponding to an integrated luminosity $\mathcal{L} = 131\ nb^{-1}$.

A first data reduction is made by requiring the presence of an energy cluster with a transverse energy greater than 15 GeV. In the central calorimeter, clusters are obtained by joining all electromagnetic cells which share a side and contain at least 0.5 GeV. A halo contribution from the cells having at least one side in common with a cluster is also added. The forward calorimeter clusters consist of at most two adjacent cells having the same azimuth (the cells are far from the interaction point and are much larger than

the lateral extension of an electromagnetic shower - the dead region between cells at different azimuth does not allow clustering across it).

In the surviving events, a search is made for configurations consistent with the presence of a high-p_T electron among the collision products. An electron is identified from the observation of

a) the presence of a cluster of energy deposition in the first compartment (electromagnetic) of the calorimeters with a small lateral size and only a small energy leakage in the hadronic compartment.

b) the presence of a reconstructed charged particle track which points to the energy cluster. The pattern of energy deposition must agree with that expected from an isolated electron incident along the track direction.

c) the presence of a hit in the preshower counter with an associated pulse height larger than that of a minimum ionising particle (m.i.p.). The distance of the hit from the track must be consistent with the space resolution of the counter itself.

A set of cuts has been defined according these requirements. A detailed description of these cuts can be found in Ref.3.

The efficiencies of the simultaneous application of these cuts are 76% and 80% in the central and forward regions, respectively.

4. TOPOLOGY OF EVENTS CONTAINING AN ELECTRON CANDIDATE.

After application of the electron cuts the sample is reduced to 225 events, containing genuine electrons and still fake electrons resulting from misidentification of hadrons. The p_T distribution is shown in Fig.3.

The background of fake electrons can be shown to fall mainly into two categories. In approximately 70% of the cases we are dealing with "overlaps", i.e. jets fragmenting into a hard π^0 with a charged pion nearby in angle. The rest of the background results from π^0s undergoing Dalitz decays or conversions in the beam-pipe.

From studies of hadron jets [11] we expect the fake electrons to be accompagnied by other high-p_T jets at approximately opposite azimuth. We shall therefore search for high-p_T jets by grouping together adjacent cells with energy into clusters using an algorithm described elsewhere [11]. Clusters with more than 3 GeV of transverse energy are retained and called jets. For minimum bias triggers such clusters occur in only 15% of the events.

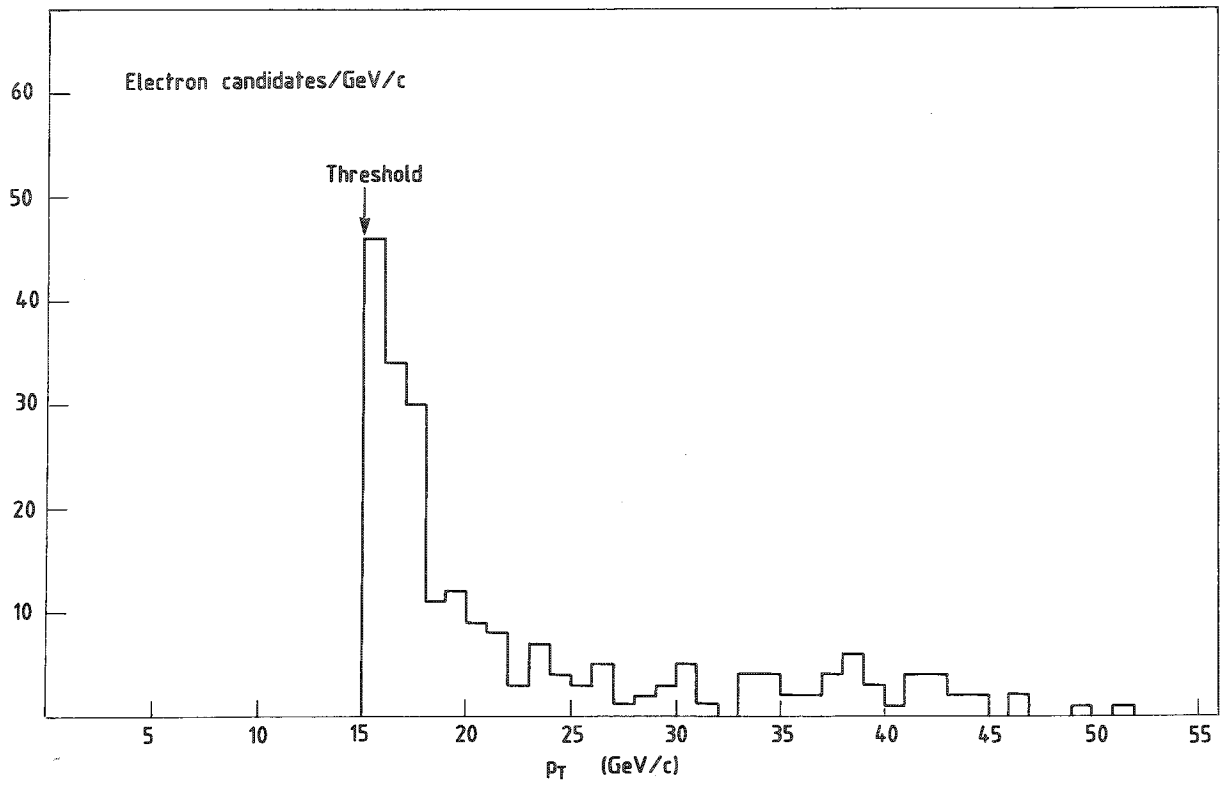

Fig.3 Transverse momentum distribution of the 225 electron candidates satisfying the electron cuts.

We find that 45 events contain no jet, the electron candidate being the only high-p_T particle observed. Their p_T distribution is shown in Fig.4a. Such events contain either a neutrino, as in the case of $W \rightarrow e\nu$ decay, or other high-p_T particles having escaped detection. In the latter case we would expect a rapidly falling p_T-spectrum typical of the jet p_T distribution [11].

The remaining 180 events contain at least one jet (according to our definition), and Fig.5 shows the azimuthal separation of the highest p_T jet from the electron candidate. The events in the peak at $\Delta\phi = 180°$ are likely to be background. Hence we sum all transverse momenta of clusters having $\Delta\phi > 120°$ and define

$$\rho_{opp} = -\vec{p}_T^{\,e} \cdot \Sigma\vec{p}_{T,jet} / |\vec{p}_T^{\,e}|^2 \qquad (3)$$

where $\vec{p}_T^{\,e}$ and $\vec{p}_{T,jet}$ are two-dimensional vectors obtained projecting $\vec{p}_e$ and $\vec{p}_{jet}$ on a plane perpendicular to the beams.

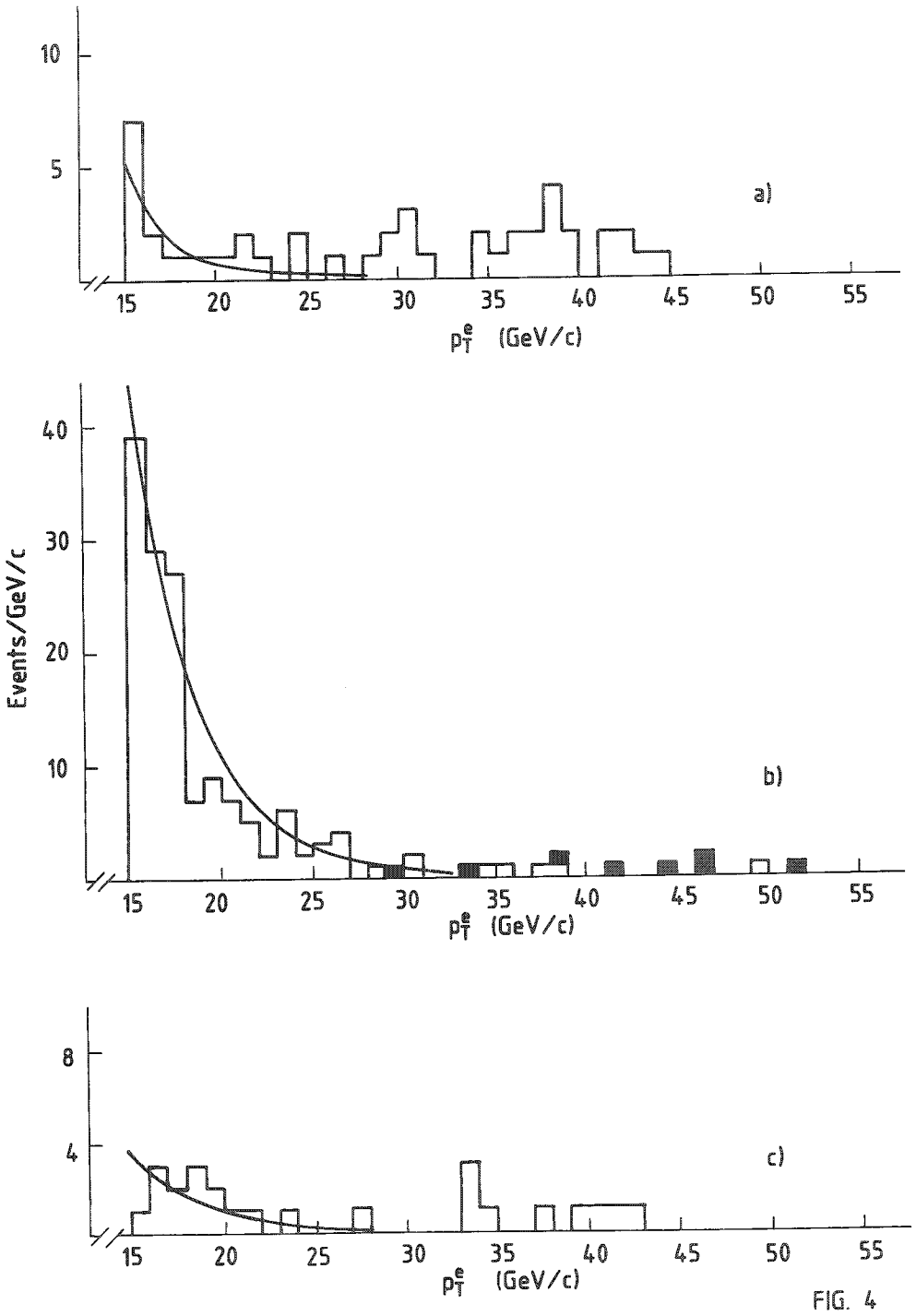

FIG. 4

Fig.4a) Transverse momentum distribution of the electron candidates in events with no additional jet. b) Transverse momentum distribution of the electron candidates in events having $\rho_{opp} > 0.2$. Dark points correspond to electrons from Z^0 decays. c) Transverse momentum distribution of electron candidates in events with additional jets having $\rho_{opp} < 0.2$.

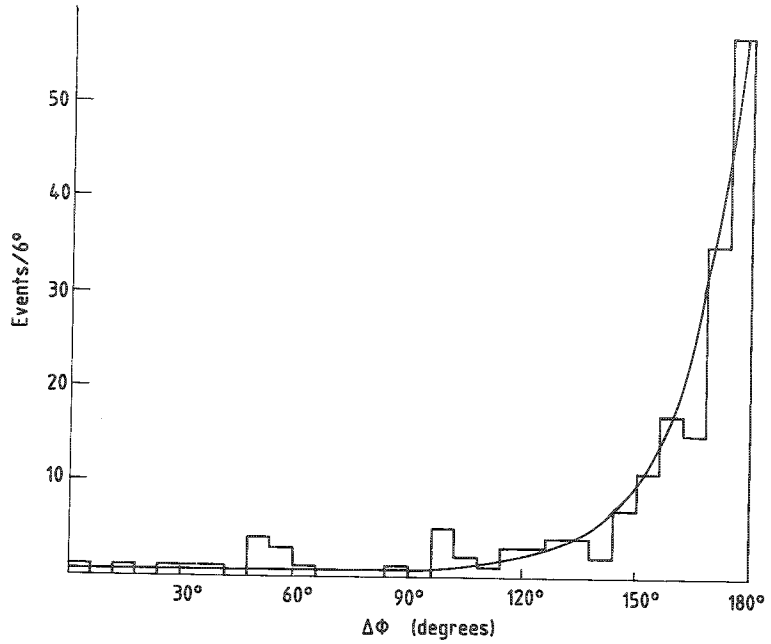

Fig.5 Distribution of the azimuthal separation $\Delta\phi$ between the electron candidate and the associated jet having the highest p_T. Curve: estimated background.

The distribution of ρ_{opp} is shown in Fig.6. We reject the 156 events having $\rho_{opp} > 0.2$. Their p_T^e distribution is shown in Fig.4b. This sample contains the eight $Z^0 \rightarrow e^+e^-$ (or $e^+e^-\gamma$) events recently reported [12].

The p_T^e distribution of the remaining 24 events is shown in Fig.4c. These events do contain, in addition to the electron candidate, jets which do not carry a significant transverse momentum in the direction opposite to the electron ($\rho_{opp} < 0.2$).

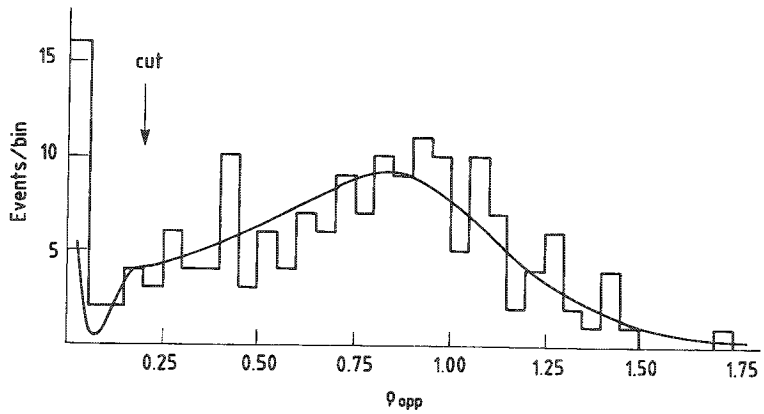

Fig.6 Distribution of ρ_{opp} for events containing an electron candidate and at least one associated jet. Curve: estimated background.

5. BACKGROUND TO THE ELECTRON SPECTRA

For the present we shall regard the 148 events containing a jet back to back with the electron candidate as a background sample of fake electrons (after removal of the eight Z^0 events).

These events occur at a rate lower than that of jet production by a factor of 3.6×10^4 for the central detector and 2.6×10^5 for the forward ones.

The backgrounds to the two event samples of Fig.4a and 4c are now estimated as follows. We consider a sample of events containing a manifestly fake electron not surviving the cuts. These events are now divided into three classes of different topologies, called samples A,B and C, corresponding to the three classes of electron candidates of Fig.4.

We assume that the p_T distributions of the samples A, B and C are similar to those of the background events contained in the corresponding electron samples. We can check this assumption for the 148 electron candidates with $\rho_{opp} > 0.2$ which, as mentioned above, are taken as a pure background sample, and we do indeed find that they have the same p_T distribution as the fake electrons of sample B. The background contributions to the 69 electron candidates in the other two topologies (45 with no additional jets and 24 with jets having $\rho_{opp} < 0.2$) are then estimated directly from the p_T distributions of samples A and C, multiplied by a factor equal to the ratio of the total number of electron candidates with $\rho_{opp} > 0.2$ (148 events) to the total number of events in sample B. These background estimates are shown as smooth curves in Fig. 4a and 4c.

6. THE W → eν EVENT SAMPLE

The combined p_T^e distribution of the 69 events from Fig.4a and Fig.4c is shown in Fig.7 together with the background estimate. The presence of a significant signal above the background is taken as evidence that most of the electron candidates shown here are indeed electrons and associated with a high-p_T neutrino ($\vec{p}_T^{\,\nu} = \vec{p}_T^{\,W} - \vec{p}_T^{\,e}$). There is a clear accumulation of events near $p_T^e = 40$ GeV/c, which is distinctive of the Jacobian peak as expected for W → eν decay. For $p_T^e > 25$ GeV/c the distribution contains 37 events with an estimated background of 1.5 ± 0.1 events.

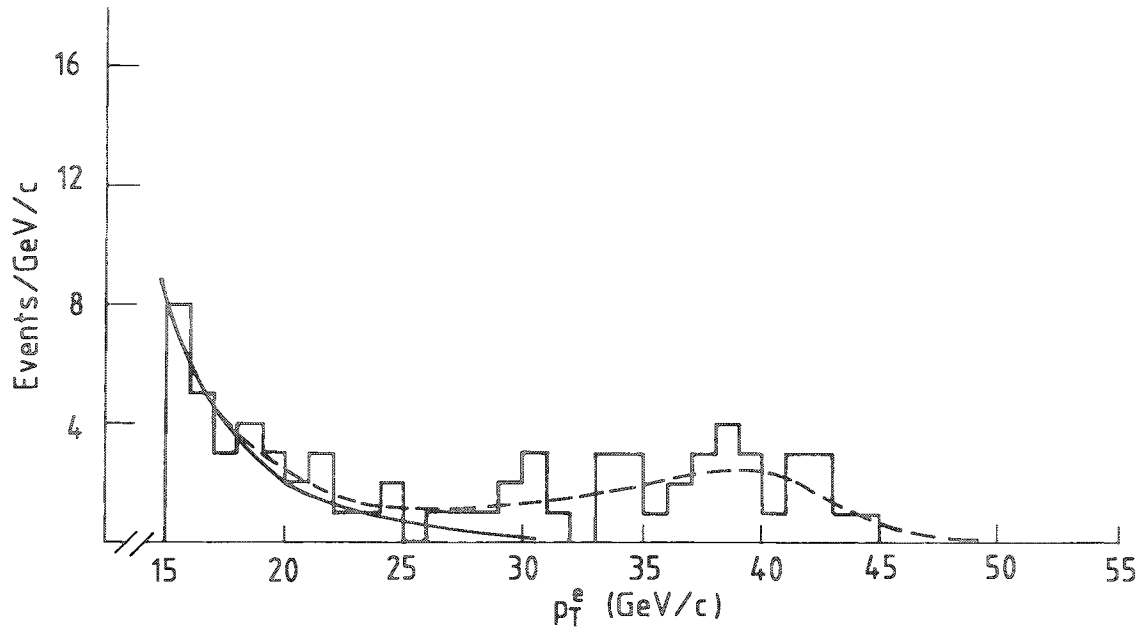

Fig.7 Transverse momentum distribution of the electron candidates in the W → ev event sample. Full curve : background estimate. Dashed curve : sum of all the contributions as discussed in Section 7.

We estimate the transverse momentum $\vec{p}_T^{\,W}$ of the W by

$$\vec{p}_T^{\,W} = -\left(\Sigma\, \vec{p}_{T,jet} + \xi\, \vec{P}_T^{\,sp} \right) \qquad (4)$$

where the sum extends over all observed jets and $\vec{P}_T^{\,sp}$ is the total p_T of all observed particles not belonging to jets. In an ideal detector the correction factor ξ would be 1. For an incomplete coverage some fraction of the particles in the event is lost (typically among the low transverse momentum particles). We estimate, using the eight Z^0 events, that ξ should be 2.2 ± 0.5 in order to satisfy Eq.(4) on the average.

The distribution of p_T^W is shown in Fig.8a and 8b, using $\xi = 1$ and $\xi = 2.2$, respectively. The mean value (for $\xi = 2.2$) is $\langle p_T^W \rangle = 6.9 \pm 1.0$ GeV/c. QCD predictions [13], illustrated by the curve in Fig.8, are consistent with the observed distribution. The event with the highest value of p_T^W, 29.6 GeV/c, is interpreted as a W recoiling against a high-p_T jet. Among the W candidates with $p_T^e < 25$ GeV/c we find two events

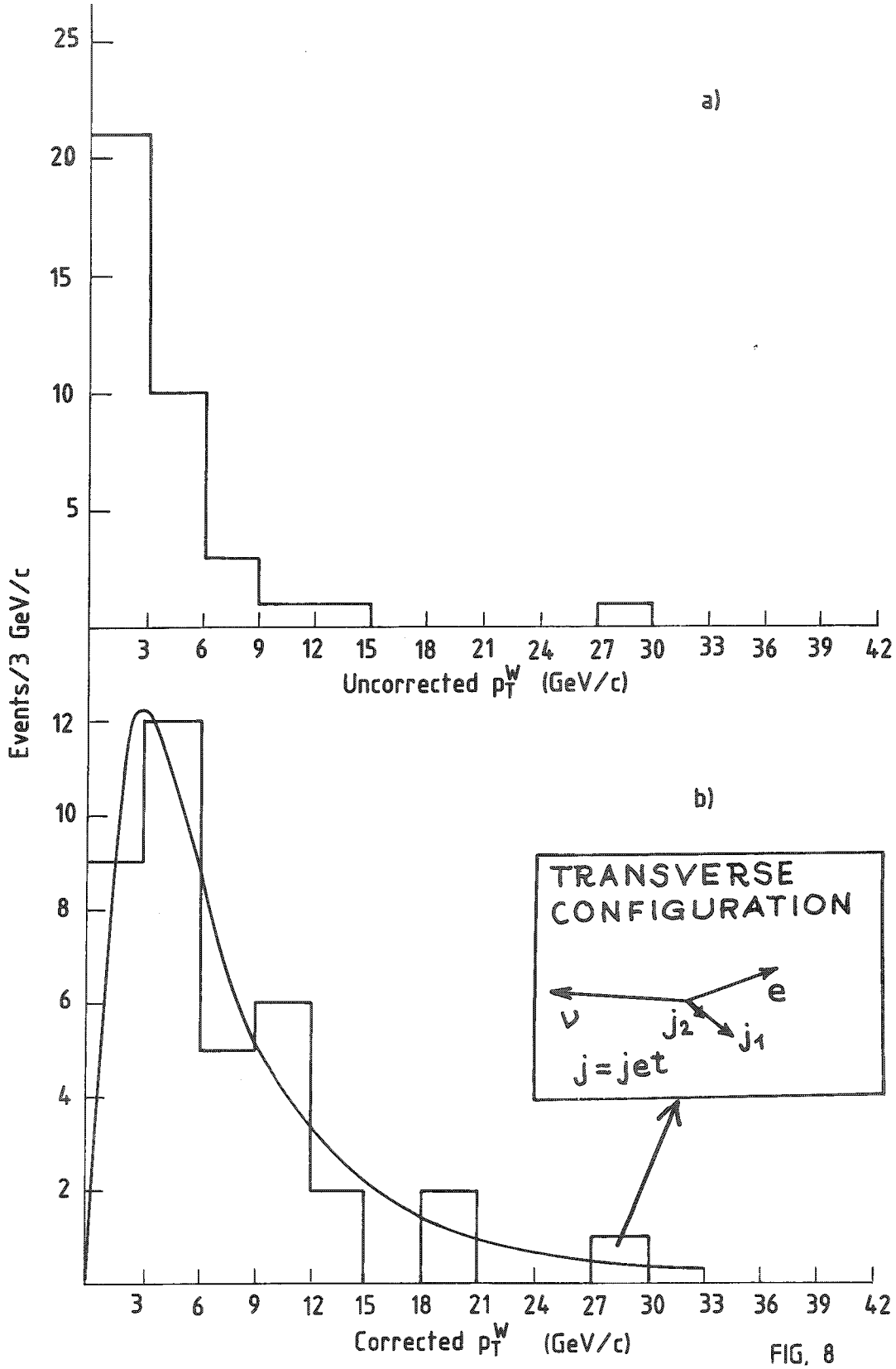

FIG. 8

a) Uncorrected distribution of the W transverse momentum (Eq.(4): ξ=1)
b) Corrected distribution (Eq.(4): ξ=2.2). Curve: QCD prediction [13].

with even higher values for p_T^W, clearly separated from the rest of the events. These events are discussed elsewhere [14].

We note that the level of activity in the W events is about twice as high as that in minimum bias events. This feature is reflected in the average observed sum of the transverse energies of all particles other than the electron and jets (if any) $\langle \Sigma E_T \rangle = 14.1 \pm 1.7$ GeV and the average value of the charged multiplicity $\langle n_{ch} \rangle = 19.3 \pm 1.9$ in the rest of the event. The corresponding values for minimum bias events are $\langle \Sigma E_T \rangle = 8.8$ GeV and $\langle n_{ch} \rangle = 14.7$.

7. DETERMINATION OF THE W MASS

The mass M_W of the W is determined from the $W \rightarrow e\nu$ candidates with $p_T^e > 25$ GeV/c by performing a maximum likelihood fit to their two-dimensional distribution $d^2n/dp_T^e d\theta_e$, where θ_e is the measured electron polar angle. In the Monte Carlo program which is used to generate the distribution $d^2n/dp_T^e d\theta_e$ for different values of M_W, we make the following assumptions:

a) the W longitudinal momentum distribution is obtained using the quark structure functions of the proton (antiproton) with scaling violation, as given by Glück et al. [15].

b) the p_T^W distribution is taken from Ref.13 allowing for variations of $\langle p_T^W \rangle$ in order to take into account uncertainties of QCD predictions.

c) the $W \rightarrow e\nu$ decay angular distribution is described by the standard V-A coupling.

d) the M_W distribution is generated according to a Breit-Wigner curve with a fixed value of the W width, $\Gamma_W = 2.7$ GeV/c² .

The detector response is taken into account.

The sample of 37 measured events with $p_T^e > 25$ GeV/c is contaminated by three background sources:

a) misidentified electrons from two jet background: 1.5 ± .1 events.

b) electrons from $Z^0 \rightarrow e^+e^-$ decay with one electron undetected: 2.5 ± .9 events. This contribution is evaluated by Monte Carlo technique normalizing the result to the total number of $Z^0 \rightarrow e^+e^-$ detected in this experiment (8 events, Ref.12).

c) electrons from $W \rightarrow \tau\nu, \tau \rightarrow e\bar{\nu}_e\nu_\tau$ decay chain : .9 ± .1 . The detector acceptance for electrons from $W \rightarrow \tau \rightarrow e$ decay chain has been evaluated by Monte Carlo technique, and we assume a branching ratio $B_\tau = 0.17$ for the decay $\tau \rightarrow e\bar{\nu}_e\nu_\tau$ [16].

The sum of all contributions is shown as a dashed curve in Fig.7. After subtraction of the background events, we are left with a sample of 32.1 ± 6.0 $W \rightarrow e\nu$ decays. The best fit to the experimental $d^2n/dp_T^e d\theta_e$ distribution including the mentioned background contributions gives

$$M_W = 83.1 \pm 1.9 \text{ (stat.)} \pm 1.3 \text{ (syst.) GeV/c}^2.$$

An uncertainty of ±1 GeV/c^2, which results from the effect of varying $\langle p_T^W \rangle$ between 4 and 10 GeV/c in the fit, is added in quadrature to the statistical error. The systematic error reflects the uncertainty in the overall mass scale arising from the absolute calibration of the calorimeter (±1.5%) and from small differences in the relative calibration of various cells of the calorimeter.

Within the quoted errors this value agrees with the result of the UA1 experiment [17], $M_W = 80.9 \pm 1.5\text{(stat.)} \pm 2.4\text{(syst.) GeV/c}^2$.

8. CROSS SECTION FOR INCLUSIVE W PRODUCTION

The cross section σ_W^e for the inclusive process $\bar{p} + p \rightarrow W^\pm +$ anything, followed by the decay $W \rightarrow e\nu$, at $\sqrt{s}$=540 GeV is obtained from the relation

$$N_W^e = \mathscr{L}\, \sigma_W^e\, \varepsilon\, \eta$$

where $N_W^e = 32.1 \pm 6.0$ is the number of $W \rightarrow e\nu$ decays obtained by subtracting from the electron sample the background events as described in the previous section, $\mathscr{L} = 131$ nb^{-1} is the integrated luminosity, $\varepsilon = .60 \pm .01$ is the detector acceptance which includes the effect of the p_T^e threshold and $\eta = .77 \pm .05$ is the overall efficiency of the electron identification criteria averaged over the central and forward detectors. The effect of the cut $p_{opp} < .2$ previously described is taken into account in the acceptance evaluation. We finally obtain

$$\sigma_W^e = .53 \pm .10 \text{ (stat.)} \pm .10 \text{ (syst.) nb}$$

where the systematic error reflects a ±20% uncertainty in the knowledge of $\mathcal{L}$. This value is in agreement with QCD predictions [13,18] and with the results of the UA1 experiment [17] .

9. CHARGE ASYMMETRY

It is known that, as a consequence of the V-A coupling, the W is always produced with full polarisation along the direction of the incident $\bar{p}$ beam and a distinctive charge asymmetry can be observed in the decay $W \rightarrow e\nu$. In the W rest frame the angular distribution has the form $(1 + \cos\theta^*)^2$ for electrons and $(1 - \cos\theta^*)^2$ for positrons, where θ^* is the angle between the momentum of the charged lepton and the direction of the incident protons. However, precisely the same configuration would result from V+A coupling because in this case all helicities change sign. In order to maintain full generality and allow for different amounts of V and A couplings, we write the angular distribution in the form

$$dn/d(\cos\theta^*) \propto (1-q\ \cos\theta^*)^2 + 2\ q\ \alpha\ \cos\theta^* \qquad (5)$$

where q is -1 for electrons and +1 for positrons and α depends on the ratio x between the A and V couplings (time reversal invariance requires x to be real). Under the assumption that x is the same for both $Wq\bar{q}$ and $We\nu$ couplings, α is given by

$$\alpha = [(1-x^2)/(1+x^2)]^2 \qquad (6)$$

which gives $\alpha = 0$ for $|x| = 1$.

In the UA2 detector a determination of the charge sign is only possible in the forward detectors where a magnetic field is present.

We consider the 8 events having an electron with $p_T^e > 20$ GeV/c in the forward detectors. The estimated background is 0.2 events. A comparison between the electron momentum p and energy E is made in Fig.9, which shows the position of these events in the plane $(\hat{p}^{-1}, E^{-1})$, where $\hat{p}$ is the electron momentum with the sign of the product $q \cos\theta_e$ (θ_e: laboratory angle of the electron momentum with respect to the proton direction). The horizontal error bars in Fig.9 represent the uncertainty on p^{-1}, which is 0.01 $(GeV/c)^{-1}$.

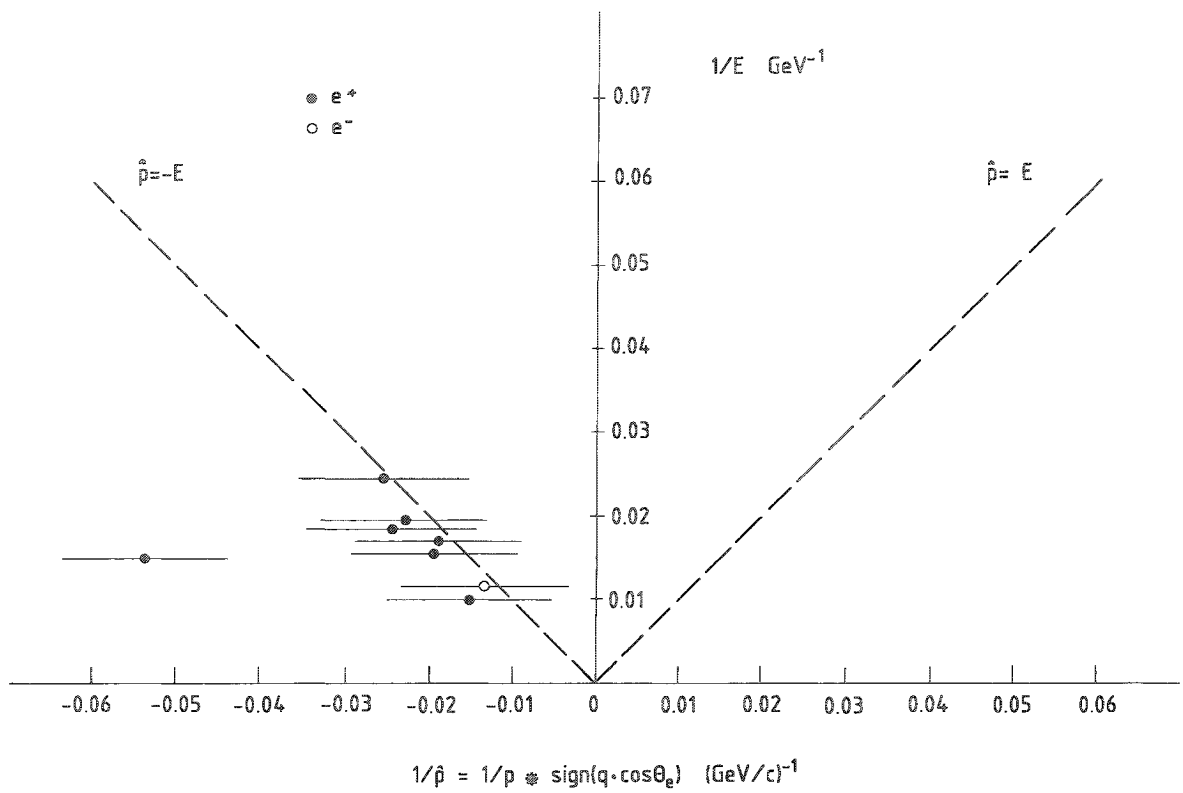

Fig.9 Plot of 1/E vs 1/$\hat{p}$ for the eight W → ev candidates with p_T^e > 20 GeV/c detected in the forward regions. The quantity $\hat{p}$ is the electron momentum with the sign of the product q cosθ [q=+1(-1) for $e^+(e^-)$].

A clear asymmetry is visible in Fig.9: all events lie on one side of the plot. In order to extract a value of x from these data we compute two-dimensional distributions $f^{\pm}(p_T^e, \theta_e)$ for positrons and electrons separately, using Eqs.(5) and (6) and taking into account the W longitudinal motion. To each event we assign a likelihood $Q_i = f^+\eta^+ + f^-\eta^-$, where $\eta^+(\eta^-)$ is the probability density that the observed particle was a positron (an electron) of momentum p. The functions $f^{\pm}$ are calculated at the observed values of p_T^e and θ_e. The probability densities $\eta^{\pm}$ reflect the uncertainty in the determination of the charge sign resulting from the error in the momentum measurement. Maximizing the likelihood $\Pi_i Q_i$ we obtain $|x| = 1.0^{+0.5}_{-0.3}$ for the ratio between the strengths of the A and V couplings.

We remark that our event sample consists of seven positrons detected in one hemisphere and one electron detected in the opposite one. The probability to observe no more than one electron in one of the two hemispheres is ≈ 7%.

10. THE DECAY $Z^0 \rightarrow e^+e^-$

The observation in this experiment of seven $Z^0 \rightarrow e^+e^-$ decays and one $Z^0 \rightarrow e^+e^-\gamma$ decay has already been reported [12]. Following a recent recalibration of the calorimeters, the invariant mass values of these events and their errors have been slightly modified. The updated value of the Z^0 mass based on a weighted average [3] is

$$M_Z = 92.7 \pm 1.7(\text{stat.}) \pm 1.4(\text{syst.}) \text{ GeV/c}^2. \qquad (7)$$

We recall that this value is obtained using only the four events for which the energy of both electrons (and that of the photon in the $e^+e^-\gamma$ event) is unambiguously determined. Within errors, this result agrees with the Z^0 mass value determined in the UA1 experiment [19].

In order to extract an estimate of the Z^0 width, Γ_Z, from these four events, we first note that the r.m.s. deviation of the four mass values from the value of M_Z given by Eq.(7) is 2.0 GeV/c², which is almost the same as the weighted average of the errors σ = 2.1 GeV/c². To obtain an upper limit to Γ_Z, we use a Monte Carlo program which generates a large number of event samples, each consisting of four $Z^0 \rightarrow e^+e^-$ decays, according to a Breit-Wigner shape and taking into account the energy resolution of the detector. As an estimate of the upper limit to Γ_Z at the 90% confidence level, we use the value which gives an r.m.s. of less than 2.0 GeV/c² in 10% of the event samples. This value is $\Gamma_Z < 6.5$ GeV/c² at the 90% confidence level.

Within the standard model, this upper limit can be related to the number of additional light neutrinos ΔN_ν. We find $\Delta N_\nu < 22$ at the 90% confidence level, assuming $\sin^2\theta_W = 0.22$ and a value of the t-quark mass $m_t > M_Z/2$.

An independent estimate of Γ_Z can be obtained within the standard model by measuring the ratio $R = \sigma_Z^e/\sigma_W^e$, where σ_Z^e is the cross-section for inclusive Z^0 production followed by the decay $Z^0 \rightarrow e^+e^-$ [20]. We obtain σ_Z^e after corrections which take into account the detector acceptance and the efficiency of the electron identification criteria. In this case we use all eight events, for which at least one electron passes all cuts, and we find

$$\sigma_Z^e = 0.11 \pm 0.04(\text{stat.}) \pm 0.02(\text{syst.}) \text{ nb} \qquad (8)$$

which is approximately twice as large as the value predicted by QCD [13,21]. For comparison, we quote the result found by the UA1 experiment: $\sigma_Z^e = 0.050 \pm 0.020(\text{stat.}) \pm 0.009(\text{syst.})$ nb [19].

The error on R is dominated by statistics, because the value of the total integrated luminosity cancels out. We find $R = 0.21 \pm 0.08$, and $R > 0.116$ at the 90% confidence level. QCD estimates of the ratio between Z^0 and W production cross-sections [20] provide a relation between R and the ratio Γ_W/Γ_Z :

$$\Gamma_W/\Gamma_Z = (9.3 \pm 0.9)\ R \qquad (9)$$

where the error reflects the uncertainty of the QCD calculations. Using the standard model value of Γ_W , $\Gamma_W = 2.77$ GeV/c² (which corresponds to a t-quark mass $m_t = M_Z/2$), we find $\Gamma_Z < 2.6$ GeV/c² at the 90% confidence level.

As before, we can extract upper limits to the number of additional light neutrinos ΔN_ν. We find $\Delta N_\nu \leq 0$ at the 90% confidence level (for more details, see Ref.3).

11. THE DECAY $Z^0 \rightarrow e^+e^-\gamma$

We have reported [12] a $Z^0 \rightarrow e^+e^-\gamma$ event containing a photon with an energy k = 24 GeV and an 11 GeV electron separated by an angle $\omega_{lab} = 31°$, excluding, therefore, external bremsstrahlung. In Ref.12 we estimated the probability to be $\approx 5 \times 10^{-3}$ per event, that in a $Z^0 \rightarrow e^+e^-$ decay a photon at least as hard as the observed one is emitted as a result of radiative corrections [22] and the e^+e^- opening angle is equal to or smaller than the measured one. This calculation, which was performed in the Z^0 rest frame, should not be considered as an estimate of the probability of such a $Z^0 \rightarrow e^+e^-\gamma$ decay because it does not take into consideration all configurations which are less likely than the observed one.

There are several possible ways to define the relative likelihood of $Z^0 \rightarrow e^+e^-\gamma$ configurations. For cases of non-collinear $e\gamma$ pairs, the event distribution in the Z^0 rest frame is given by the differential cross-section

$$\frac{d^2\sigma}{dx_1 dx_2} = \sigma_0 \frac{\alpha}{2\pi} \frac{x_1^2 + x_2^2}{(1-x_1)(1-x_2)} \qquad (10)$$

where σ_0 is the total cross-section for $Z^0 \rightarrow e^+e^-$ without radiative corrections and $x_i = 2E_i/M_Z$, E_i being the electron energies. We say that a configuration is less likely than the observed one if its differential cross-section is smaller than that calculated at the point corresponding to the observed $Z^0 \rightarrow e^+e^-\gamma$ event. Integrating Eq.(10) over all configurations which are less likely than the observed one we find a probability of 1.4% per event or 11% to observe at least one such event in a sample of eight. It should be noted that detectable $Z^0 \rightarrow e^+e^-\gamma$ decays can be divided into two classes of configurations, the first consisting of three clearly resolved energy clusters and the second containing unresolved $e\gamma$ pairs which result in energy clusters inconsistent with an isolated electron. The corresponding probabilities are $\approx$ 1.0% and $\approx$ 0.1% per event, respectively. The remaining $Z^0 \rightarrow e^+e^-\gamma$ decays correspond to configurations which are not detectable in the UA2 apparatus.

Further possibilities to calculate a probability for observing such an event are given in Ref.3.

12. SEARCH FOR THE DECAY $W \rightarrow e\nu\gamma$

Given the interest in unexpected decay modes of the Z^0 we have also looked for events compatible with the decay $W \rightarrow e\nu\gamma$ in the full data sample:

In the central detector, we search for events containing an electron candidate with $p_T^e > 8$ GeV/c, which passes the electron cuts, and an additional photon with a momentum k in excess of 8 GeV/c. A photon is defined as an energy cluster, which satisfies the same criteria on size and hadronic leakage as an electron, but has no charged particle track pointing to it. If also the photon cluster is seen in the central detector, we require an angular separation $\omega > 30°$ between the cluster centroids in order to resolve the $e\gamma$ pair. Six events satisfy these conditions. However, none of them survives the additional requirement of a transverse momentum imbalance compatible with the presence of a neutrino having $p_T^\nu > 10$ GeV/c. A Monte Carlo estimate of the number of $W \rightarrow e\nu\gamma$ decays, which are expected to satisfy all of these requirements as a result of radiative corrections, gives 0.1 event.

In the forward detectors we can identify eγ pairs with very small opening angles by releasing the condition, that the electron momentum p and the energy E agree within the measuring errors. In this case, however, we limit our search to electron transverse momenta in excess of 20 GeV/c (measured in the calorimeter), for which we expect a background contribution of 0.2 events. We find one event which contains a cluster of transverse energy E_T = 41 GeV (E = 86.2 GeV) and a track of 3.6 GeV/c momentum pointing to the cluster and satisfying all other electron identification criteria. Large missing p_T is detected in this event as expected in the case of an associated neutrino. The estimated background for $p_T^e > 35$ GeV/c is 0.01 events. Since the opening angle of this eγ pair is compatible with zero, we also consider the effect of external bremsstrahlung and we obtain a probability of 0.5% per $W \rightarrow e\nu$ decay or 4.5% to observe one such event in the sample of 9 $W \rightarrow e\nu$ and $e\nu\gamma$ candidates with $p_T^e > 20$ GeV/c detected in the forward detectors.

13. COMPARISON WITH THE SU(2)⊗U(1) MODEL

The IVB mass values predicted in the framework of the standard model taking into account radiative corrections are [23] $M_W = 83.0\ ^{+2.9}_{-2.7}$ GeV/c² and $M_Z = 93.8\ ^{+2.4}_{-2.2}$ GeV/c². These values are in excellent agreement with our experimental results.

We can extract a value of $\sin^2\theta_W$ from the definition $\sin^2\theta_W = 1-M_W^2/M_Z^2$, where the systematic errors on the mass scale resulting from the uncertainty in the calorimeter calibration cancel out. We find

$$\sin^2\theta_W = 0.196 \pm 0.047 \qquad (11)$$

in good agreement with the world average result of deep-inelastic neutrino experiments (including radiative corrections) $\sin^2\theta_W = 0.217 \pm 0.014$ [24].

We can also extract a more precise value of $\sin^2\theta_W$ from the relation $M_W = A/\sin\theta_W$, where the numerical value A = 38.65 ± 0.04 GeV/c² is obtained taking into account radiative corrections [23]. In this case we find

$$\sin^2\theta_W = 0.216 \pm 0.010(\text{stat.}) \pm 0.007(\text{syst.}). \qquad (12)$$

A test of the standard model is provided by the relationship $\rho = M_W^2/[M_Z^2(1-A^2/M_W^2)]$, which should be equal to 1 for the minimal Higgs structure. We find

$$\rho = 1.02 \pm 0.06. \qquad (13)$$

14. CONCLUSIONS

We have studied the production of electrons with very high transverse momentum at the CERN $\bar{p}p$ collider. From a sample of events containing an electron candidate with $p_T > 15$ GeV/c, we have extracted a clear signal resulting from the production of the charged intermediate vector boson $W^{\pm}$, which subsequently decays into an electron and a neutrino.

We have also given new and more refined results on the production and decay of the neutral vector boson Z^0.

Our experimental results show good agreement with the predictions of the standard model of the unified electroweak theory. Furthermore, the production cross section and the distributions of the transverse momentum of the intermediate vector bosons are within the predictions of QCD calculations.

REFERENCES

1) For a review see J. Ellis et al., Ann. Rev. Nucl. Part. Science 32 (1982), 443.

2) The UA2 Collaboration, presented by G. Sauvage and J. Schacher, Latest results from the UA2 experiment at the CERN $\bar{p}p$ Collider, Proc. of the Int. Europhysics Conf. on High Energy Physics, Brighton, July 1983, p. 472.
A.G. Clark, Results from the UA2 experiment at the CERN $\bar{p}p$ Collider, Proc. of the 1983 Int. Symp. on Lepton and Photon Interactions at High Energies, Cornell, August 1983, p. 53.

3) P.Bagnaia et al., A study of high transverse momentum electrons produced in $\bar{p}p$ collisions at 540 GeV, CERN-EP/84/39, submitted to Zeitschrift für Physik C.

4) B. Mansoulie, The UA2 apparatus at the CERN $\bar{p}p$ Collider, Proc. of the 3rd Moriond Workshop on $\bar{p}p$ physics (1983), p. 609 (editions Frontières).

5) M. Dialinas et al., The vertex detector of the UA2 experiment, LAL-RT/83-14 (1983).

6) A. Beer et al., The central calorimeter of the UA2 experiment at the CERN $\bar{p}p$ Collider, CERN-EP/83-175 (1983), to be published in Nucl. Instr. Meth.

7) M. Banner et al., Phys. Lett. 115B (1982), 59.
M. Banner et al., Phys. Lett. 122B (1983), 322.

8) C. Conta et al., The system of forward-backward drift chambers in the UA2 detector, CERN-EP/83-176 (1983), to be published in Nucl. Instr. Meth.

9) K. Borer et al., Multitube proportional chambers for the localization of electromagnetic showers in the UA2 detector, CERN-EP/83-177 (1983), to be published in Nucl. Instr. Meth.

10) R. Battiston et al., Phys. Lett. 117B (1982), 126.

11) P. Bagnaia et al., Z. Phys. C20 (1983), 117.
P. Bagnaia et al., Phys. Lett. 138B (1984), 430.

12) P. Bagnaia et al., Phys. Lett. 129B (1983), 130.

13) G. Altarelli, R.K. Ellis, M. Greco and G. Martinelli, Vector boson production at Colliders : a theoretical reappraisal, Ref. TH. 3851-CERN (1984).
F. Halzen and W. Scott, Phys. Lett. 78B (1978), 318.

14) P. Bagnaia et al., Phys. Lett. 139 (1984), 105.
A. Roussarie, these Proceedings.

15) M. Glück et al., Z. Phys. C13 (1982), 119.

16) Review of Particle Properties, Phys. Lett. 111B (1982).

17) G. Arnison et al., Phys. Lett. 129B (1983), 273.

18) P. Minkowski, Remarks on W production in $\bar{p}p$ collisions at $\sqrt{s}$ = 540 GeV, University of Bern preprint BUTP-83/22 (1984), to be published in Phys. Lett. B.

19) G. Arnison et al., Phys. Lett. 126B (1983), 398.

20) C. Jarlskog and F.J. Yndurain, Phys. Lett. 102B (1983), 361.
F. Halzen and K. Mursula, Limits to the number of neutrinos, a comment on Z^0 discovery, University of Helsinki preprint HU-TFT 83-36 (1983).
K. Hikasa, Counting neutrino species at high-energy proton-antiproton collisions, University of Wisconsin preprint MAD/PH/144 (Nov. 1983).

21) B. Humpert and W.L. van Neerven, Phys. Lett. 93B (1980), 456.

22) D. Albert, W.J. Marciano, D. Wyler and Z. Parsa, Nucl. Phys. B166 (1980), 460.
F.A. Berends and R. Kleiss, Hard Photon Effects in $W^{\pm}$ and Z^0 decay, University of Leiden, The Netherlands, Nov. 1983.

23) For a review see W.J. Marciano, Electroweak interactions, Proc. of the 1983 Int. Symp. on Lepton and Photon Interaction at High Energies, Cornell, August 1983, p.80.

24) A. Sirlin and W.J. Marciano, Nucl. Phys. B189 (1981), 442.
C.Llewellyn Smith and J. Wheater, Phys. Lett. 105B (1981), 486.

ELECTROWEAK INTERACTION PARAMETERS

William J. Marciano

Brookhaven National Laboratory
Upton, New York 11973

OUTLINE

1. Standard Model Parameters
2. $\sin^2\theta_W$
3. $W^{\pm}$, Z Masses and Widths
4. Radiative Z and W Decays
5. Higgs-Top Quark Mass Connection
6. Grand Unification and New Physics
7. Comments and Speculations (A 93 GeV Pseudoscalar?)

1. STANDARD MODEL PARAMETERS

Let me begin by listing the present "best" values of some standard $SU(3)_c \times SU(2)_L \times U(1)$ model parameters[1].

$$\Lambda^{(4)}_{\overline{MS}} = 100^{+100}_{-\ 50}\ \text{MeV} \tag{1.1}$$

$$\alpha^{-1}(m_W) = 127.70 \pm 0.30 + \frac{8}{9\pi}\,\ell n\left(\frac{m_t}{36\ \text{GeV}}\right) \tag{1.2}$$

$$\sin^2\hat{\theta}_W(m_W) = 0.219 \pm 0.006 \qquad (\overline{MS}\ \text{definition}) \tag{1.3}$$

$$m_W = 82.2 \pm 1.8\ \text{GeV} \tag{1.4}$$

$$m_Z = 93.2 \pm 1.5\ \text{GeV} \tag{1.5}$$

$$\rho = 1.01 \pm 0.02 \tag{1.6}$$

$$m_e = 0.511\times10^{-3}\ \text{GeV} \qquad m_d \simeq 9\times10^{-3}\ \text{GeV} \qquad m_u \simeq 5\times10^{-3}\ \text{GeV} \tag{1.7a}$$

$$m_\mu = 0.106\ \text{GeV} \qquad m_s \simeq 0.175\ \text{GeV} \qquad m_c \simeq 1.25\ \text{GeV} \tag{1.7b}$$

$$m_\tau = 1.78\ \text{GeV} \qquad m_b \simeq 4.5\ \text{GeV} \qquad m_t > 22\ \text{GeV} \tag{1.7c}$$

In addition to the above, there are 4 KM quark mixing parameters (see C. Jarlskog's talk for a detailed discussion[1]) and the mass of the Higgs scalar, m_H, which is bounded by theoretical arguments to lie in the range (see D. Wyler's talk[1]),

$$7 \text{ GeV} < m_H < 1 \text{ TeV} \tag{1.8}$$

Subsequent sections will discuss $\sin^2\theta_W$, m_W, m_Z and ρ in detail. Here, let me make a few remarks concerning some of the other parameters.

The determination of the QCD mass scale, $\Lambda^{(4)}_{\overline{MS}}$, in Eq. (1.1) comes from radiative upsilon decay[2] $T \to \gamma gg$. That parameter is defined by $\overline{MS}$ (modified minimal subtraction) through the relationship[3]

$$\Lambda^{(N_F)}_{\overline{MS}} = \mu \exp\left[\frac{1}{b_0 \alpha_s(\mu)} - \frac{b_1}{b_0^2} \ln\left(\frac{-2}{b_0 \alpha_s(\mu)}\right)\right] \tag{1.9a}$$

$$b_0 = -\frac{1}{2\pi}(11 - 2N_F/3) \tag{1.9b}$$

$$b_1 = -\frac{1}{4\pi^2}(51 - 19N_F/3) \tag{1.9c}$$

with $\alpha_s(\mu)$ the running $\overline{MS}$ QCD coupling and N_F the number of quark flavors with mass $\leq \mu$. Continuity of $\alpha_s(\mu)$ for all μ then leads to the approximate relationship[4] (for $m_t \simeq 36$ GeV)

$$\Lambda^{(6)}_{\overline{MS}} : \Lambda^{(5)}_{\overline{MS}} : \Lambda^{(4)}_{\overline{MS}} : \Lambda^{(3)}_{\overline{MS}} = 27 : 63 : 100 : 130 \tag{1.10}$$

A reduction in the $\Lambda^{(N_F)}_{\overline{MS}}$ uncertainties (now about a factor of 2) is important for testing QCD and grand unified theories (see section 6). Quarkonia spectroscopy and lattice calculations offer the best possibility of reducing the present errors.

The running electromagnetic coupling $\alpha(\mu) = e^2(\mu)/4\pi$, given in Eq. (1.2) for $\mu = m_W$, is obtained from the usual fine structure constant via the perturbative relationship[5]

$$\alpha^{-1}(\mu) = \alpha^{-1} - \frac{2}{3\pi}\sum_f Q_f^2 \ln(\mu/m_f) + \frac{1}{6\pi} + \ldots \tag{1.11}$$

where the summation is over all charged fermions with mass, $m_f \leq \mu$. To incorporate strong interaction effects, the light quark contribution to Eq. (1.11) is actually obtained from a dispersive analysis of $e^+e^- \to$ hadrons rather than the perturbative corrections[6]. Most of the uncertainty in Eq. (1.2) i.e. ± 0.30, stems from e^+e^- data uncertainties. The 7.3% increase in $\alpha(\mu)$ in going from $\mu = 0$ to m_W is very important. That effect is the dominant radiative correction to the $W^\pm$ and Z mass formulas[5] (see section 3). It

is, therefore, reassuring that QED tests at PEP and PETRA verify the running of $\alpha(\mu)$ by effectively measuring $\alpha(\sqrt{s})$. Indeed, I find from a cursory examination of PETRA data

$$\alpha^{-1}(34.5\ \text{GeV}) \simeq 130 \pm 2 \tag{1.12}$$

which is in agreement with the prediction in Eq. (1.11).

The quark masses in Eq. (7) are taken from the comprehensive review by Gasser and Leutwyler[7] while the bound on m_t comes from PETRA data. An important development is the long b-quark lifetime which was measured at PEP last year to be $\tau_b \simeq 10^{-12}$ sec. Combining τ_b, the branching ratio $r \equiv \Gamma(b\to uX)/\Gamma(b\to cX) < 0.05$ and the CP violating ε parameter, Ginsparg, Glashow and Wise[8] derived an interesting bound on m_t

$$m_t > 40 \sqrt{\frac{0.33}{B} \cdot \frac{0.05}{r}}\ \frac{\tau_b}{10^{-12}\ \text{sec}}\ \text{GeV} \tag{1.13}$$

where B is the K^0-$\bar{K}^0$ matrix element. Their result suggests a large m_t or a much larger value for B than the conventional 0.33. Some implications of large m_t ($> m_H/2$) will be discussed in section 5.

2. $\sin^2\theta_W$

There are two popular definitions of the renormalized weak mixing angle. The quantity $\sin^2\hat{\theta}_W(m_W)$ given in Eq. (1.3) is defined by $\overline{MS}$ (modified minimal subtraction) and evaluated at $\mu = m_W$. It is very useful for model independent discussions and analysis of grand unified theories[6]. Indeed, in the latter case it makes sense to define all couplings by the same renormalization prescription. A second definition[9]

$$\sin^2\theta_W \equiv 1 - m_W^2/m_Z^2 \tag{2.1}$$

is appropriate only for the standard model with $\rho = 1$. Nevertheless, by the very nature of its definition, it is well suited for discussions involving m_W and m_Z. These two definitions differ by $O(\alpha)$ corrections which for $m_H \simeq m_Z$ are numerically[10]

$$\sin^2\theta_W \simeq 1.006\ \sin^2\hat{\theta}_W(m_W) \tag{2.2}$$

(The exact relationship is given in Ref. 10.)

The $O(\alpha)$ radiative corrections to deep-inelastic ν_μ-N scattering and eD asymmetry experiments were calculated in 1981. They allowed a precise determination of $\sin^2\theta_W$,[9,11]

$$\sin^2\theta_W = 0.217 \pm 0.014 \qquad \text{(1981 } \nu N \text{ world average)} \tag{2.3}$$

$$\sin^2\theta_W = 0.218 \pm 0.020 \qquad \text{(eD asymmetry)} \tag{2.4}$$

Other more recent measurements of $\sin^2\theta_W$ from $\nu_\mu N$, $\nu_\mu e$, atomic parity violation, $e^+e^- \to \mu^+\mu^-$ etc. are all consistent with Eqs. (2.3) and (2.4) but they have larger errors.

Combining deep-inelastic neutrino and antineutrino data (R_ν and $R_{\bar\nu}$), one finds[12,13]

$$\rho = 1.02 \pm 0.02 \tag{2.5}$$

where $\rho \equiv m_W^2/m_Z^2\cos^2\theta_W$ should be exactly 1 in the standard model with minimal Higgs structure. This determination lends great support to the standard model. However, I should interject a word of caution. The small errors in Eq. (2.5) result from the extremely sensitive dependence of $R_{\bar\nu}$ on ρ. That sensitivity also pertains to QCD effects and sea quark contributions. Hence their theoretical error may add somewhat to the uncertainty in Eq. (2.5).

3. $W^\pm$ AND Z MASSES AND WIDTHS

With the discovery of the $W^\pm$ and Z now completed, it becomes important as a next step to test the standard model by precise measurements of their masses and decay properties. In that regard, radiative corrections to vector boson masses and widths are timely and interesting.

To obtain the $O(\alpha)$ corrections to the $W^\pm$ and Z mass formulas requires a complete one-loop calculation of the γ, $W^\pm$ and Z self-energies as well as the full $O(\alpha)$ corrections to muon decay. Combining those calculations gives[5,9,13,14]

$$m_W = \left[\frac{\pi\alpha}{\sqrt{2}\, G_\mu \sin^2\theta_W(1-\Delta r)}\right]^{1/2} \tag{3.1}$$

$$m_Z = m_W/\cos\theta_W \tag{3.2}$$

where Δr denotes the complete $O(\alpha)$ radiative corrections,

$$\alpha = 1/137.035963 \tag{3.3}$$

and G_μ is the muon decay constant which is conventionally defined by[15]

$$1/\tau_\mu = \frac{G_\mu^2 m_\mu^5}{192\pi^3}\left(1 - \frac{8m_e^2}{m_\mu^2}\right)\left(1 + \frac{3m_\mu^2}{5m_W^2}\right)\left[1 + \frac{\alpha}{2\pi}\left(\frac{25}{4} - \pi^2\right)\left(1 + \frac{2\alpha}{3\pi}\ln\frac{m_\mu}{m_e}\right)\right] \tag{3.4}$$

Recent measurement of the muon lifetime now yields a new (slightly higher) value[16)]

$$G_\mu = 1.16638 \pm 0.00002 \times 10^{-5}\ \text{GeV}^{-2} \tag{3.5}$$

From Eqs. (3.1)-(3.5) one obtains

$$m_W = \frac{37.2804 \pm 0.0003}{\sin\theta_W (1-\Delta r)^{1/2}} = m_Z \cos\theta_W \tag{3.6}$$

Setting $\Delta r = 0$ would give the uncorrected predictions for m_W and m_Z as functions of $\sin^2\theta_W$. Including the calculated Δr significantly shifts those predictions because Δr is quite large due to the vacuum polarization effects in Eq. (1.11) for $\mu = m_W$. The complete analytic expression for Δr is given in Ref. 9. Numerically, for $m_t \simeq 36$ GeV and $m_H \simeq m_Z$, one finds[13,15)]

$$\Delta r = 0.0696 \pm 0.0020 \tag{3.7}$$

where the uncertainty comes from hadronic vacuum polarization effects. Putting this value into Eq. (3.6) yields the "corrected" predictions

$$m_W = \frac{38.65 \pm 0.04\ \text{GeV}}{\sin\theta_W} \tag{3.8}$$

$$m_Z = \frac{77.30 \pm 0.08\ \text{GeV}}{\sin 2\theta_W} \tag{3.9}$$

Given a value for $\sin^2\theta_W$ one can predict m_W and m_Z; or inverting these formulas, a determination of m_W or m_Z yields $\sin^2\theta_W$.

Recently updated values[1,17)] for m_W and m_Z are given in Table I.

TABLE I. UA1 and UA2 Values for m_W and m_Z

	UA1	UA2	Average
m_W(GeV)	80.9±1.5±2.4	83.1±1.9±1.3	82.2±1.8
m_Z(GeV)	95.1±1.5±2.9	92.7±1.0±1.4	93.2±1.5

The average mass values in Table I when used in conjunction with Eqs. (3.8) and (3.9) yield (both m_W and m_Z give the same $\sin^2\theta_W$)

$$\sin^2\theta_W = 0.221 \pm 0.007 \tag{3.10}$$

which is in excellent agreement with the 1981 scattering results in Eqs. (2.3) and (2.4). The value for $\sin^2\hat{\theta}_W(m_W)$ given in Eq. (1.3) was obtained by computing the weighted average of these various independent determinations and dividing by 1.006 (see Eq. (2.2)).

One can also determine $\sin^2\theta_W = 1 - m_W^2/m_Z^2$ directly from m_W and m_Z without using Δr. From Table I, one finds

$$\sin^2\theta_W = 1 - m_W^2/m_Z^2 = 0.222 \pm 0.020 \tag{3.11}$$

The agreement between Eqs. (3.10) and (3.11) provides strong support for the standard model.

Alberto Sirlin and I recently examined how one could test the standard model by precise determinations of $W^{\pm}$ and Z masses. Eliminating θ_W by combining Eqs. (3.1) and (3.2), we obtained the following useful formulas[13]

$$m_W = m_Z \left[\frac{1 + \sqrt{1 - 4A^2/m_Z^2}}{2} \right]^{1/2} \tag{3.12}$$

$$m_Z - m_W = m_W \left[\frac{1}{\sqrt{1 - A^2/m_W^2}} - 1 \right] \tag{3.13}$$

$$m_Z - m_W = m_Z \left[1 - \left(\frac{1 + \sqrt{1 - 4A^2/m_Z^2}}{2} \right)^{1/2} \right] \tag{3.14}$$

$$\Delta r = 1 - \frac{(37.28 \text{ GeV})^2}{m_W^2 (1 - m_W^2/m_Z^2)} \tag{3.15}$$

$$\rho = \frac{m_W^2}{m_Z^2 \left(1 - A^2/m_W^2\right)} \tag{3.16}$$

$$A = \frac{37.280 \text{ GeV}}{(1-\Delta r)^{1/2}} = 38.65 \text{ GeV} \tag{3.17}$$

These formulas are used to compare the UA1 and UA2 results with theoretical expectations in Table II. (The ρ value in Eq. (1.6) was obtained by averaging the values in the table with Eq. (2.5).)

TABLE II. Comparison of the UA1 and UA2 results with standard model expectations for $\sin^2\theta_W = 0.220 \pm 0.006$. 100% correlation in the m_W and m_Z systematic uncertainties is assumed.

	UA1	UA2	Standard Model with $\sin^2\theta_W = 0.220 \pm 0.006$
m_W (GeV)	$80.9 \pm 1.5 \pm 2.4$	$83.1 \pm 1.9 \pm 1.3$	82.4 ± 1.1
m_Z (GeV)	$95.1 \pm 1.5 \pm 2.9$	$92.7 \pm 1.0 \pm 1.4$	93.3 ± 0.9
$m_Z - m_W$ (GeV)	$14.2 \pm 2.1 \pm 0.4$	$9.6 \pm 2.1 \pm 0.2$	10.9 ± 0.2
Δr	$0.232 \pm 0.079 \pm 0.045$	$-0.025 \pm 0.172 \pm 0.032$	0.0696 ± 0.0020
ρ	$0.938 \pm 0.038 \pm 0.016$	$1.025 \pm 0.040 \pm 0.009$	1
$\sin^2\theta_W = \left(\frac{38.65\ \text{GeV}}{m_W}\right)^2$	$0.228 \pm 0.008 \pm 0.014$	$0.216 \pm 0.010 \pm 0.007$	0.220 ± 0.006
$\sin^2\theta_W = 1 - m_W^2/m_Z^2$	0.276 ± 0.035	0.196 ± 0.040	0.220 ± 0.006

Deviations from the standard model predictions could signal new interesting physics or provide information regarding a very heavy t or H. Indeed, one finds[13] $\Delta r = 0.0696+\delta$ where

$$\delta \simeq \frac{-3\alpha}{16\pi} \frac{\cos^2\theta_W}{\sin^4\theta_W} \frac{m_t^2}{m_W^2} , \qquad m_t \gg 36 \text{ GeV} \tag{3.18}$$

$$\delta \simeq \frac{11\alpha}{48\pi} \frac{1}{\sin^2\theta_W} \ell n\ (m_H^2/m_Z^2) , \qquad m_H \gg m_Z \tag{3.19}$$

Such effects would also show up as a shift in ρ by $-\delta \tan^2\theta_W$.

Eventually, m_Z will be measured to within ± 0.1 GeV at LEP while the DO detector[18] at Tevatron (if approved) promises to measure m_W to within ± 0.05 GeV. Such measurements will determine $\sin^2\theta_W$ to within ± 0.0004! Using both masses as input will determine ρ to within ± 0.002 and the radiative correction Δr to within ± 0.003. At that level one is certainly probing radiative corrections. Indeed such measurements would be sensitive to new physics present only as loop effects.

Let me complete this section with an update of the predicted $W^{\pm}$ and Z decay widths. For $\sin^2\theta_W = 0.22$ and $m_t \simeq 36$ GeV, one expects (including radiative corrections and m_t effects)[19]

$$\Gamma(W \to \text{all}) \simeq \Gamma(Z \to \text{all}) \simeq 2.80 \text{ GeV} \tag{3.20}$$

Deviations from these predictions could signal new physics such as 4th generation mixing, larger m_t, additional neutrinos etc. For example, the number of neutrino species, N_ν, is given by[19]

$$N_\nu = 3 + \frac{\Gamma(Z\to\text{all}) - 2.8 \text{ GeV}}{0.178 \text{ GeV}} \tag{3.21}$$

The UA2 group[17] has already made a good determination of $\Gamma(W\to\text{all})/\Gamma(Z\to\text{all})$ which when combined with QCD gives $N_\nu < 6$ (90% CL). The DO detector[18] is capable of measuring that ratio to better than 10%.

4. RADIATIVE Z and $W^{\pm}$ DECAYS

Out of the 13 $Z \to e^+e^-$ or $\mu^+\mu^-$ candidate events in the UA1 and UA2 data, 3 have a distinct energetic photon in the decay products. That represents a 23% branching fraction for radiative events; much too large to be bremsstrahlung. Even more mysterious are new γ + missing energy events that could represent $Z \to \bar{\nu}\nu\gamma$.

A conservative view is that the first three events are merely bremsstrahlung and that the branching fraction will decrease as the statistics improve. To address that possibility, I will give a general branching ratio formula for the bremsstrahlung decays $B \to \bar{f}_1 f_2 \gamma$ where B is a generic gauge boson with electric charge Q_1+Q_2. The percentage of events in which the photon carries a fraction of the total energy $E_\gamma/m_B > \varepsilon$ and has an opening angle greater than 2δ relative to any charged fermion in the final state is given by (for $\delta, \varepsilon \ll 1$)[20]

$$\frac{\Gamma(B\to f_1\bar{f}_2\gamma)}{\Gamma(B\to f_1\bar{f}_2)+\Gamma(B\to f_1\bar{f}_2\gamma)} = \frac{\alpha}{\pi}\left\{\frac{Q_1^2+Q_2^2}{2}\left[(4\ \ell n\ 2\varepsilon+3)\ell n\delta+\frac{\pi^2}{3}-\frac{7}{4}\right]\right.$$

$$\left.+(Q_1+Q_2)^2\left[\ell n\ 2\varepsilon+5/6\right]+O(\delta)+O(\varepsilon)\right\} \qquad (4.1)$$

For $Z \to e^+e^-\gamma$ and $W \to e\nu\gamma$ this formula gives

$$\frac{\Gamma(Z\to e^+e^-\gamma)}{\Gamma(Z\to e^+e^-)+\Gamma(Z\to e^+e^-\gamma)} = \frac{\alpha}{\pi}\left[(4\ \ell n\ 2\varepsilon+3)\ \ell n\ \delta+\frac{\pi^2}{3}-\frac{7}{4}\right] \qquad (4.2)$$

$$\frac{\Gamma(W\to e\nu\gamma)}{\Gamma(W\to e\nu)+\Gamma(W\to e\nu\gamma)} = \frac{\alpha}{2\pi}\left[(4\ \ell n\ 2\varepsilon+3)\ \ell n\ \delta+2\ \ell n\ 2\varepsilon+\frac{\pi^2}{3}-\frac{1}{12}\right] \qquad (4.3)$$

If we take $\varepsilon = 0.1$ ($E_\gamma > 9$ GeV) and $2\delta > 10°$ (0.17 radians), these branching fractions are 0.023 and 0.01. The latter is consistent with the lack of observation of $W \to e\nu\gamma$ while the $Z \to e^+e^-\gamma$ prediction is about 1/10 of the observation. It will be interesting to see what happens with increased statistics.

5. HIGGS - TOP QUARK MASS CONNECTION

The Higgs scalar and top quark are the only missing particles of the standard model. In time, the top quark should be discovered either by $W\to t\bar{b}$ or $t\bar{t}$ production (unless it is very heavy). On the other hand, the Higgs scalar may be more elusive. If $m_H < 60$ GeV, it should be observable through the decays $Z \to H\mu^+\mu^-$ or $H\gamma$. Somewhat higher masses (up to $\simeq$ 100 GeV) may be detectable at LEP II via $e^+e^- \to ZH$ if high luminosity $\simeq 10^{32}$ cm^{-2} sec^{-1} is achieved. On the other end of the scale, for m_H very large, the Higgs scalar can be best produced by gluon-gluon fusion at a hadron-hadron collider. If $m_H > 2m_W$, then the decay $H \to W^+W^-$ should dominate and provide a distinct signal.

What if $m_W < m_H < 2m_W \simeq 166$ GeV? W.-Y. Keung and I recently considered that possibility[21]. We compared the rates for $H \to W^\pm X$ and $H \to q\bar{q}$ where X is anything and q is a generic heavy quark. Our result

$$\frac{\Gamma(H\to W^{\pm}X)}{\Gamma(H\to q\bar{q})} = \frac{\alpha}{4\pi\sin^2\theta_W}\left(\frac{m_W^2}{m_q^2}\right)\left(1-\frac{4m_q^2}{m_H^2}\right)^{-3/2}F(\varepsilon) \tag{5.1a}$$

$$F(\varepsilon) = \left\{\frac{3(1-8\varepsilon^2+20\varepsilon^4)}{\sqrt{4\varepsilon^2-1}}\arccos\left(\frac{3\varepsilon^2-1}{2\varepsilon^3}\right) - (1-\varepsilon^2)\left(\frac{47}{2}\varepsilon^2 - \frac{13}{2} + \frac{1}{\varepsilon^2}\right)\right.$$

$$\left. - 3(1-6\varepsilon^2+4\varepsilon^4)\,\ell n\,\varepsilon\right\} \tag{5.1b}$$

where $\varepsilon = m_W/m_H$. This ratio can be significant if ε is near 1/2 and m_q is not too large. If $m_q = m_t \simeq 36$ GeV, then this branching ratio exceeds 10% only for $m_H > 160$ GeV. On the other hand, if $m_t > m_H/2$, then we need only compare with $H \to b\bar{b}$. In that case $\Gamma(H \to W^{\pm}X)/\Gamma(H \to \text{all})$ exceeds 10% for $m_H > 125$ GeV and 50% for $m_H > 150$ GeV. This point is illustrated in Fig. 1. (For further details see Ref. 21.)

If the branching ratio for $H \to W^{\pm}X$ is significant, one could try to detect this mode via leptonic decays $W \to e\nu$ or $\mu\nu$ with X = 2 hadronic jets. Of course, one still needs a significant number of Higgs scalars. They can be best produced at a high-energy high-luminosity hadron collider.

Is the scenario $m_H > 125$ GeV and $m_t > m_H/2$ a realistic possibility? A recent analysis by Bég, Panagiotakopoulos and Sirlin[22] based on theoretical consistency in the standard model suggests that $m_H > 125$ GeV may actually require that m_t (or some more massive fermion) be greater than $m_H/2$.

Could a Higgs scalar with m_H in the range 80 ~ 160 GeV have been produced at the CERN $p\bar{p}$ collider? Unfortunately, the cross-section for $p\bar{p} \to H$ via gluon fusion is quite small at a $\sqrt{s} = 540$ GeV collider. The cross-section is given by[23]

$$\sigma(p\bar{p}\to H) = \frac{\pi^2}{8m_H^3}\Gamma(H\to gg)\int_{\ell n\sqrt{\tau}}^{-\ell n\sqrt{\tau}} dy\,\tau F_G(\sqrt{\tau}e^{y})F_G(\sqrt{\tau}e^{-y}) \tag{5.2}$$

$$\tau = m_H^2/s \quad , \quad F_G = \text{Gluon distribution function}$$

where $\Gamma(H\to gg)$ is the 2 gluon decay rate of the H. For the standard model this cross-section is approximated by[21]

$$\sigma \simeq 4\times10^{-36}\exp\left[-m_H/21\text{ GeV}\right]\text{cm}^2, \quad \text{for } 80\text{ GeV} < m_H < 160\text{ GeV} \tag{5.3}$$

(There may be a factor of 10 uncertainty in this formula due to uncertainties in F_G.) Given the total integrated luminosity at CERN[1] $\simeq 1.3\times10^{35}$ cm^{-2}, one

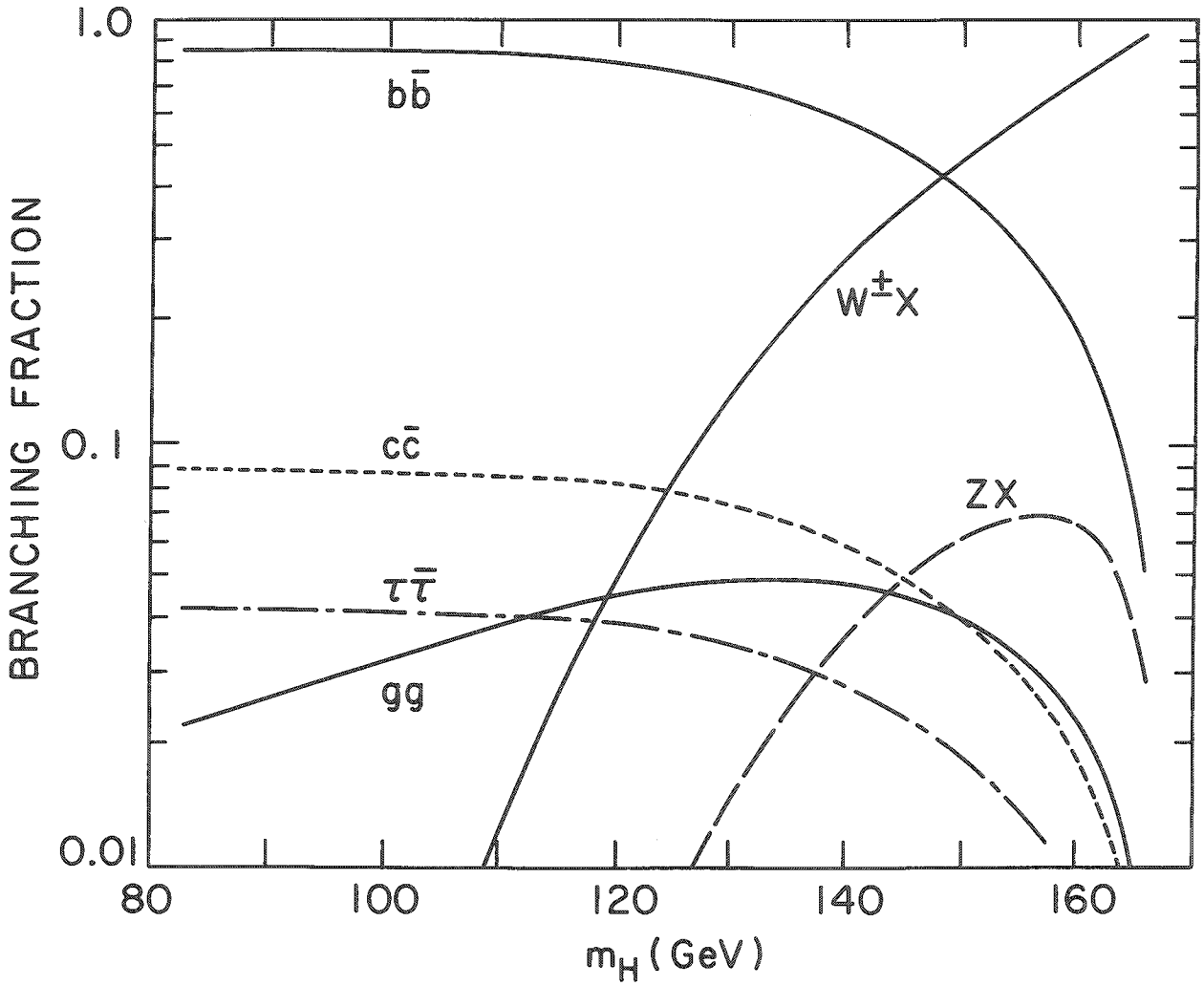

Fig. 1 Higgs decay branching ratios $m_t > m_H/2$.

expects about 0.01 events for $m_H \simeq 90$ GeV and 0.0004 events for $m_H \simeq 150$ GeV. If for some reason $\Gamma(H \to gg)$ is much greater than the standard model prediction, then the production cross-section can be enhanced. However, increasing it by a factor of 10^3 to make H production at present CERN luminosities viable would elevate $H \to gg$ to the dominant decay mode. That would still make its observation difficult, since one would have to find it in the 2 jet cross-section.

6. GRAND UNIFICATION AND NEW PHYSICS

Grand unified theories (GUTS) provide important motivation for precise measurements of the standard model parameters. To illustrate this point, I give in Table III predictions of the "minimal" SU(5) model[24] (assuming no new physics between m_W and the unification mass m_X).

TABLE III. Minimal SU(5) model predictions using $\alpha(m_W) = 1/127.7$ and values for $\Lambda^{(4)}_{\overline{MS}}$ as input.[25]

$\Lambda^{(4)}_{\overline{MS}}$ (MeV)	$\sin^2\theta_W$	m_W (GeV)	m_Z (GeV)	m_X (GeV)	τ_p (yr)
25	0.226	81.3	92.3	3×10^{13}	$3\times10^{26\pm1}$
50	0.222	82.0	92.8	6.2×10^{13}	$3\times10^{27\pm1}$
100	0.218	82.8	93.6	1.3×10^{14}	$5\times10^{28\pm1}$
200	0.214	83.5	94.3	2.7×10^{14}	$5\times10^{29\pm1}$
400	0.210	84.3	94.9	5.5×10^{14}	$1\times10^{31\pm1}$

For $\Lambda^{(4)}_{\overline{MS}} \simeq 100$ MeV, the $\sin^2\theta_W$, m_W and m_Z predictions are in good agreement with experiment. However, the predicted proton lifetime τ_p, is well below the experimental bound[26] $\tau_p > 10^{32}$ yr. That bound requires a unification mass $m_X \gtrsim 10^{15}$ GeV. The value of m_X can be increased only by appending new physics between m_W and m_X. (Of course one always anticipated new physics in that domain.) The new physics could be additional relatively light Higgs scalars, fermions, technicolor, supersymmetry, new gauge bosons, etc.

As new physics is uncovered above m_W, the GUT predictions will be modified. It is, therefore, important to have precise measurements of $\Lambda_{\overline{MS}}$,

$\sin^2\theta_W$ etc. available to test the altered GUT. Of course, it should be obvious that continued searches for proton decay must remain a very high priority.

7. COMMENTS AND SPECULATIONS (A 93 GeV Pseudoscalar?)

Discovery of the $W^{\pm}$ and Z has provided significant evidence in support of the standard model. Precise measurements of their masses and decay widths will next test the model at the level of its quantum radiative corrections, perhaps unveiling new physics along the way. What else is left? The top quark is certainly waiting to be found and the elusive Higgs scalar (or some alternative dynamics) will be the object of an intense search. But what other physics is on the horizon? Grand unified theories now require some new physics; but they don't specify what it should be. We will have to be guided by experiment.

At this meeting we have learned about exciting events found by the UA1 and UA2 collaborations[1] which do not seem to have a simple explanation in the framework of the standard model. The UA1 jet + missing energy and UA2 $W^{\pm}$ + jet events are suggestive of a new phenomenon opening up at $\simeq$ 150 GeV and manifesting itself with very large cross-sections. They seem to imply that the present generation of $p\bar{p}$ colliders will provide additional excitement. Hopefully, CERN and Fermilab (starting in 1986) will fully exploit the potential of their colliders.

Another interesting UA1 event has γ + missing energy at 100±10 GeV, (there are other candidates)[17]. Is it related to the anomalous $e^+e^-\gamma$ and $\mu^+\mu^-\gamma$ events previously uncovered? I would like to conclude this talk with a speculation by suggesting that these radiative events are not Z decays. Perhaps instead, there is a new pseudoscalar particle (I will call it P) which has a mass near m_Z i.e. at about 93 GeV.[27] The P could be produced by gluon-gluon fusion (the Pgg coupling must be large). It could then decay into $f\bar{f}\gamma$ via a virtual Z (see Fig. 2). ($P\to f\bar{f}$ is helicity suppressed.) For such decays to be competitive with P→gluon+gluon, the $PZ\gamma$ coupling must also be very big. The near degeneracy of the P and Z should enhance this vertex; however, such a scenario would most naturally occur in a composite model where the Z is a very tightly bound $Q\bar{Q}$ vector state and the P is a $^1S_0$ onium. (In that case I would rename P the η_Z.)

For radiative decays $P\to f\bar{f}\gamma$, dominated by the amplitude in Fig. 2, one expects a photon spectrum of the form (for $m_P \simeq m_Z$)[28]

$$\frac{1}{\Gamma(P\to f\bar{f}\gamma)}\frac{d\Gamma(P\to f\bar{f}\gamma)}{dx} = C(x-x^2)\left|F(x)\right|^2 , \quad 0 \le x \le 1 \qquad (7.1)$$

where $x = 2E_\gamma/m_P$, F(x) is a form factor that depends on the dynamics of the

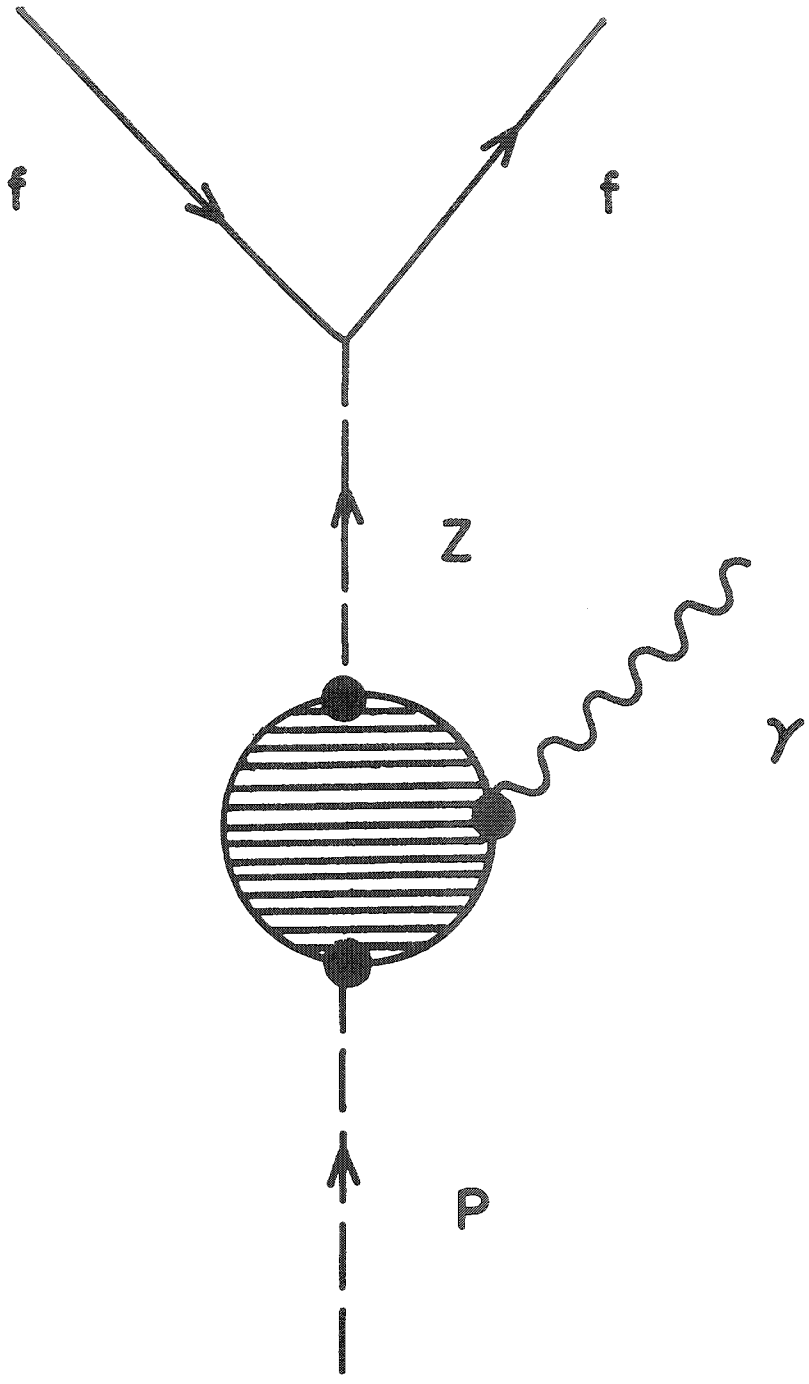

Fig. 2

$PZ\gamma$ vertex and C is a normalization constant

$$C^{-1} = \int_0^1 dx\ (x-x^2)\left|F(x)\right|^2 \qquad (7.2)$$

Approximating F(x) by a constant leads to a distribution symmetric about the $x = 1/2$ ($E_\gamma = m_P/4$) maximum. That would imply an average photon energy $\langle E_\gamma \rangle = m_P/4 \simeq 23$ GeV (in the P rest system) and an invariant mass for the $f\bar{f}$ pair at $m_P(1-x)^{1/2}$ which is peaked at $m_P/\sqrt{2} \simeq 66$ GeV. The characteristics of such decays closely resemble the UA1 and UA2 $e^+e^-\gamma$, $\mu^+\mu^-\gamma$ ($\nu\bar{\nu}\gamma$) events. They are very distinct from the 1/x bremsstrahlung spectrum which tends to be collinear with charged fermions.

The above speculation has several implications which can be used to test it. They are: 1) $\Gamma(P\to\mu^+\mu^-\gamma) = \Gamma(P\to e^+e^-\gamma) \simeq 1/6\Gamma(P\to\nu\bar{\nu}\gamma)$. 2) $\Gamma(P\to 2\text{ jets}+\gamma) \simeq 24\ \Gamma(P\to e^+e^-\gamma)$. 3) $P\to 2$ gluon jets should be prevalent in the 2 jet cross-section. The radiative events $\nu\bar{\nu}\gamma$ and 2 jets+γ should be looked for in the present data sample. The 2 jet decays would at present be difficult to separate from background.

It would be amusing if the P particle does exist. In that case history would be repeating itself. We would be experiencing a replay of the μ-π discovery as we disentangle the P and Z.

ACKNOWLEDGMENT

Work supported by Department of Energy Contract No. DE-AC02-76CH00016.

REFERENCES

1. Talks in these proceedings.

2. G.P. Lepage, Proc. of the 1983 Lepton-Photon Conf., Cornell University.

3. W.A. Bardeen, A. Buras, D. Duke and T. Muta, Phys. Rev. D18 3998 (1978).

4. W. Bernreuther and W. Wetzel, Nucl. Phys. B197, 228 (1983); W. Bernreuther, Ann. of Phys. 151, 127 (1983); W. Marciano, Phys. Rev. D29, 580 (1984).

5. W. Marciano, Phys. Rev. D20, 274 (1979).

6. W. Marciano and A. Sirlin in Proc. of the Second Workshop on Grand Unification, Ann Arbor, 1981, Eds. J. Leveille, L. Sulak and D. Unger, (Birkhauser, Boston); Phys. Rev. Lett. 46, 163 (1981).

7. J. Gasser and H. Leutwyler, Phys. Rep. 87, 77 (1982).

8. P. Ginsparg, S. Glashow and M. Wise, Phys. Rev. Lett. 50, 1415 (1983).

9. A. Sirlin, Phys. Rev. D22, 971 (1980); W. Marciano and A. Sirlin, Phys. Rev. D22, 2695 (1980).

10. S. Sarantakos, A. Sirlin and W. Marciano, Nucl. Phys. B217, 84 (1983).

11. A. Sirlin and W. Marciano, Nucl. Phys. B189, 442 (1981); C. Llewellyn Smith and J. Wheater, Phys. Lett. 105B, 486 (1981).

12. J. Kim, P. Langacker, M. Levine, and H. Williams, Rev. Mod. Phys. 53, 211 (1980).

13. W.J. Marciano and A. Sirlin, Phys. Rev. D29, 945 (1984).

14. F. Antonelli, M. Consoli and G. Corbo, Phys. Lett. 91B, 90 (1980); M. Veltman, ibid. 91B, 95 (1980); K. Aoki et al., Prog. Theor. Phys. 65, 1001 (1981); D. Bardin, P. Christova and O. Fedorenko, Nucl. Phys. B197, 1 (1982).

15. A. Sirlin, Phys. Rev. D29, 89 (1984).

16. K.L. Giovanetti et al., Phys. Rev. D29, 343 (1984).

17. Talks by C. Rubbia and J. Schacher in these proceedings.

18. Talk by M. Marx in these proceedings.

19. D. Albert, W. Marciano, D. Wyler and Z. Parsa, Nucl. Phys. B166, 460 (1980); W. Marciano and Z. Parsa, Proc. AIP DPF Summer Study, Snowmass, 1982, p155.

20. The formula in Eq. (4.1) is a simple extension of similar expressions in Ref. 19.

21. W.-Y. Keung and W. Marciano, BNL preprint 34578, 1984.

22. M.A.B. Bég, C. Panagiotakopoulos and A. Sirlin, Phys. Rev. Lett. 52, 883 (1984).

23. H. Georgi, S. Glashow, M. Machacek and D. Nanopoulos, Phys. Rev. Lett. 40, 692 (1978).

24. H. Georgi and S. Glashow, Phys. Rev. Lett. 32, 438 (1974); H. Georgi, H. Quinn and S. Weinberg, ibid. 33, 451 (1974).

25. W. Marciano, Proc. of the VPI Miniconference on Low Energy Tests of Conservation Laws, 1983.

26. IMB collaboration, R. Bionta et al., Phys. Rev. Lett. 51, 27 (1983); Published talks by IMB members.

27. W. Marciano, unpublished.

28. L. Arnellos, W. Marciano and Z. Parsa, Nucl. Phys. B196, 365 (1982).

$(W^{\pm}, Z)$: PRODUCTION FROM $p\bar{p}$ AND DECAY

Peter Minkowski

Institut für Theoretische Physik

Universität Bern

Sidlerstrasse 5, CH-BERN, Switzerland

Abstract: Electroweak parameters at the scale of 100 GeV are presented and put to work in the calculation of cross sections for W and Z production from $p\bar{p}$ collisions.

1. SETTING FOOT ON THE 100 GeV PLATEAU

We shall resume coupling constants and characteristic masses at a reference scale of $\mu \sim m_Z$ which we fix to the initial value of 100 GeV:

$$m_Z = \frac{e\left(1+\frac{\Delta r}{2}\right)}{\sin\vartheta_W \cos\vartheta_W}\left(\frac{1}{4\sqrt{2}\,G_F}\right)^{1/2} =$$

$$= (.30282)\cdot\frac{1+\frac{\Delta r}{2}}{\sin\vartheta_W\cos\vartheta_W}\left(4\sqrt{2}(1.16632)\cdot 10^{-5}\right)^{-1/2} \times \text{GeV}$$

$$e = \sqrt{4\pi\alpha} = .30282$$

$$m_Z = (.30282)(123.113)\,GeV \times \frac{1+\frac{\Delta r}{2}}{\sin\vartheta_W \cos\vartheta_W}$$

$$= (38.59\,GeV) \times \frac{1+\frac{\Delta r}{2}}{1.035} \quad \frac{1}{\sin\vartheta_W \cos\vartheta_W}$$

$$= (93.92\,GeV) \times \frac{1+\frac{\Delta r}{2}}{1.035} \quad \frac{\sin(27.62^\circ)\cos(27.62^\circ)}{\sin\vartheta_W \cos\vartheta_W}$$

$$\sin^2(27.62^\circ) = 0.215 \quad ^{1)} \qquad (1.1)$$

The Fermi constant is obtained from μ decay

$$\Gamma_{\mu^\pm} = (192\pi^3)^{-1} G_F^2 m_\mu^5 \left(1 - \frac{8m_e^2}{m_\mu^2} + \dots\right) \times$$

$$\times \left(1 + \frac{3}{5}\frac{m_\mu^2}{m_W^2} + \dots - \frac{\alpha}{2\pi}\left(\pi^2 - \frac{25}{4}\right)\right)$$

$$\rightarrow \quad G_F = (1.16632 \pm 0002) \cdot 10^{-5}\,GeV^{-2} \qquad (1.2)$$

The triad of coupling constants referring to the (standard) $SU3_c \times SU2_L \times U1$ gauge groups (g_s, g, g') are rescaled from their values at zero momentum transfer ($\alpha = \frac{e^2}{4\pi}$) to the 100 GeV scale as a consequence of radiative corrections through the vacuum polarization referring to W-W, Z-Z and γ-γ currents:

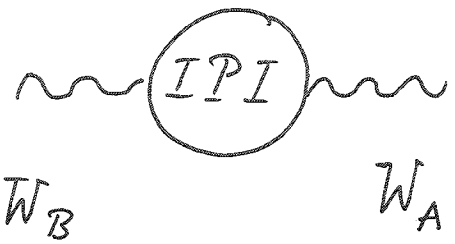

$$\left(-g_{\mu\nu}q^2+q_\mu q_\nu\right)\Pi^{tr}_{W_A W_B}$$

$$+\ \Pi^{long}_{\mu\nu\ W_A W_B}$$

$$g = e(\sin\vartheta_W)^{-1}\ ,\ g' = e\,(\cos\vartheta_W)^{-1},\ e=\sqrt{4\pi\alpha}$$

$$\downarrow \mu = 100\,GeV$$

$$\bar{g} = \bar{e}(\sin\vartheta_W)^{-1}\ ,\ \bar{g}' = \bar{e}\,(\cos\vartheta_W)^{-1},\ \bar{e} = \left(1+\frac{\Delta r}{2}\right)e$$

$$\left(\bar{g}\ ,\ \bar{g}'\ ,\ \bar{e}\right) = \left(1+\frac{\Delta r}{2}\right)(g\ ,\ g'\ ,\ e),\ \frac{m_W}{m_Z} \equiv \cos\vartheta_W$$

(1.3)

We rescale the strong coupling constant from a reference scale of 5 GeV to 100GeV using the effective four flavour formula to two loops.

$$\alpha_s(t) = 4\pi\ b_0^{-1}\ t^{-1}\left(1-\frac{b_1}{b_0^2}\frac{\log t}{t}+\cdots\right)$$

$$t=\log\left(\frac{\mu^2}{\Lambda^2_{\overline{MS}}}\right)\ ,\qquad b_0 = 11-\frac{2}{3}n_f \Longrightarrow \frac{25}{3}$$

$$b_1 = 102-\frac{38}{3}n_f \Longrightarrow \frac{154}{3}$$

$$\alpha_s(t) \simeq (1.508)\,t^{-1}\left(1-0.739\,\frac{\log t}{t}+\cdots\right)$$

(1.4)

In Table 1 we compare $\mu_o = 5$ GeV with $\mu = 100$ GeV for $\Lambda_{\overline{MS}} = 0.1$, 0.2 and 0.5 GeV respectively. The evolution of $\frac{1}{\alpha_s}$ according to eq. (1.4) is shown in Fig. 1.

		$\Lambda_{\overline{MS}} = 0.1$ GeV	$\Lambda = 0.2$ GeV	$\Lambda = 0.5$ GeV
$\bar{\alpha}_s$	$\mu = 100$ GeV	0.094	0.103	0.119
$\bar{g}_s$		1.09	1.14	1.22
α_s	$\mu = 5$ GeV	0.155	0.184	0.247
g_s		1.40	1.52	1.76

Table 1: Strong coupling constants α_s, $g_s = \sqrt{4\pi\alpha_s}$, for $\Lambda_{\overline{MS}} = 0.1$, 0.2, 0.5 GeV evolving for four effective flavours from $\mu = 5$ GeV to $\mu = 100$ GeV.

For $\sin^2\theta_W = 0.215$, $\Delta r = 0.07$ and $\mu = 100$ GeV, $\Lambda_{\overline{MS}} = 0.1$ GeV the coupling constants are shown in Table 2.

$SU3_c$	$SU2_L$	U1	e.m.
$\bar{\alpha}_s = \frac{1}{10}$	$\frac{\bar{g}^2}{4\pi} = \frac{1}{27.50}$	$\frac{5}{3}\frac{\bar{g}'^2}{4\pi} = \frac{1}{60.25}$	$\frac{8}{3}\bar{\alpha} = \frac{1}{47.97}$
$\bar{g}_s = 1.09$	$\bar{g} = 0.676$	$\bar{g}' = 0.354$	$\bar{e} = 0.313$

Table 2: Coupling constants relative to $SU3_c$, $SU2_L$, U1 at the 100 GeV reference scale

We note that $\bar{\alpha}_s$, $\frac{\bar{g}^2}{4\pi}$, $\frac{5}{3}\frac{\bar{g}'^2}{4\pi}$ and $\frac{8}{3}\bar{\alpha}$ are constrained to be equal in the symmetry limit of a unifying gauge group for which one fermion family is a complete representation (not necessarily irreducible)

$$\begin{pmatrix} u^1 u^2 u^3 \nu_e & \hat{u}^1 \hat{u}^2 \hat{u}^3 \\ d^1 d^2 d^3 e^- \; e^+ & \hat{d}^1 \hat{d}^2 \hat{d}^3 \end{pmatrix}^{\delta}_{I} \qquad \delta = 1,2 \text{ spin. index}, \quad I: \text{family index} \tag{1.5}$$

In eq. (1.5) we use the left handed fermion basis [2]

2. MASS, WIDTHS, BRANCHING FRACTIONS OF $W^{\pm}$, Z

a) $W^{\pm}$

Setting the electroweak parameter to the values given in Table 2 we have

$$m_W = (83.22)\,\text{GeV} \times \frac{1+\frac{\Delta r}{2}}{1.035}\left(\frac{0.215}{\sin^2\vartheta_W}\right)^{1/2} \tag{2.1}$$

For the hadronic decay channels $W^- \to d\bar{u}$, $s\bar{c}$, the width to order $\bar{\alpha}_s$ is calculated to be [3], neglecting all quark masses relative to m_W:

$$\Gamma\left(W^- \to \begin{matrix} d\bar{u} \\ s\bar{c} \end{matrix}\right) = \frac{\bar{g}^2}{16\pi} m_W \left(1+\frac{\bar{\alpha}_s}{\pi}\right) |KM|^2$$

$$= \frac{\bar{g}^3}{16\pi}\left(4\sqrt{2}\,G_F\right)^{-1/2}\left(1+\frac{\bar{\alpha}_s}{\pi}\right)|KM|^2$$

$$= 756\,\text{MeV}\left(1+\frac{\bar{\alpha}_s}{\pi}\right) = 780.7\,\text{MeV} \tag{2.2}$$

In the $t\bar{b}$ system the phase space is reduced significantly by the mass of the top quark

$$\Gamma\left(W^+ \to t\bar{b}\right) = \Gamma\left(W^+ \to u\bar{d}\right)\left(1+\frac{m_t^2}{2m_W^2}\right)\left(1-\frac{m_t^2}{m_W^2}\right)^2$$

$$\left(1+\frac{m_t^2}{2m_W^2}\right)\left(1-\frac{m_t^2}{m_W^2}\right)^2 = \begin{cases} .796 & m_t = 30\,\text{GeV} \\ .641 & m_t = 40\,\text{GeV} \end{cases} \tag{2.3}$$

We choose as representative reduction factor 0.7 and set

$$\Gamma(W^+ \to t\bar{b}) \lesssim 546.5 \text{ MeV}$$

$$\Gamma(W \to \text{hadrons}) = \begin{cases} 1561.4 \text{ MeV}, & m_t > m_W \\ 2107.9 \text{ MeV}, & m_t \simeq 35 \text{ GeV} \\ 2342.1 \text{ MeV}, & m_t \simeq 0 \end{cases} \tag{2.4}$$

For the three leptonic channels $e^-\bar{\nu}_e$, $\mu^-\bar{\nu}_\mu$, $\tau^-\bar{\nu}_\tau$ we obtain

$$\Gamma\left(W^- \to e^-\bar{\nu}_e + \begin{matrix} 0\gamma \\ 1\gamma \\ \vdots \end{matrix}\right) = \frac{\bar{g}^2}{16\pi}\frac{1}{3} m_W \left(1 + \frac{\alpha}{2\pi}\left(-\frac{2\pi^2}{3} + \frac{77}{12}\right)\right) =$$

$$\left(\text{and } e^-\bar{\nu}_e \to \mu^-\bar{\nu}_\mu \to \tau^-\bar{\nu}_\tau\right) \simeq 252.2 \text{ MeV}$$

$$\Gamma(W \to \text{leptons}) = 756.6 \text{ MeV} \tag{2.5}$$

The total width and branching fractions into $(e^-\bar{\nu}_e)$ then are

$$\Gamma_W^{\text{tot}} = \begin{cases} 2338.0 \text{ MeV} & m_t > m_W \\ 2864.5 \text{ MeV} & m_t \simeq 35 \text{ GeV} \\ 3098.7 \text{ MeV} & m_t \simeq 0 \end{cases}$$

$$Br(W^- \to e^-\bar{\nu}_e) = \begin{cases} 10.8\% & m_t > m_W \\ 8.8\% & m_t \simeq 35 \text{ GeV} \\ 8.1\% & m_t \simeq 0 \end{cases} \tag{2.6}$$

We note that the uncertainty in the mass range of the top quark brings a 20% uncertainty in the branching fraction into the $e^- \bar{\nu}_e$ mode and thus a corresponding uncertainty in the evaluation of the production cross section for the reaction

$$p\bar{p} \rightarrow W^- X \hookrightarrow e^- \bar{\nu}_e$$

b) Z

The mass of the Z boson for the electroweak parameters chosen is given by

$$m_Z = (93.92)\,\mathrm{GeV}\,\frac{1+\frac{\Delta r}{2}}{1.035}\left(\frac{0.215 \cdot 0.785}{\sin^2\vartheta_W \cos^2\vartheta_W}\right)^{1/2} \qquad (2.7)$$

For the hadronic decay channels we distinguish

$$(u\bar{u}),\ (c\bar{c}) \quad \left(\frac{m_u}{m_Z},\ \frac{m_c}{m_Z} \rightarrow 0\right)$$

$$(d\bar{d}),\ (s\bar{s}),\ (b\bar{b}) \quad \left(\frac{m_{d,s,b}}{m_Z} \rightarrow 0\right)$$

$$(t\bar{t}) \quad \left(\frac{m_t}{m_Z} \neq 0\right)$$

Trusting QCD perturbation theory at the gauge boson mass scale we obtain

$$\Gamma(Z \rightarrow \bar{u}u) = \frac{\bar{g}^2 \cdot m_Z}{32\pi \cos^2\vartheta_W}\cdot\left(1 - \frac{8}{3}s_W^2 + \frac{32}{9}s_W^4\right)\times \left(1+\frac{\bar{\alpha}_s}{\pi}\right) =$$

$(u \rightarrow c)$

$s_W = \sin\vartheta_W$

$$\Gamma(Z \to \bar{u}u) = (543.85\ \text{MeV}) \times \left(1 - \frac{8}{3} s_W^2 + \frac{32}{9} s_W^4\right) \times \left(1 + \frac{\bar{\alpha}_s}{\pi}\right) =$$

$$= (561.2\ \text{MeV}) \left(1 - \frac{8}{3} s_W^2 + \frac{32}{9} s_W^4\right) =$$

$$= (330.9)\ \text{MeV}$$

$\bar{u}u$ and $\bar{c}c$. (2.8)

Similarly we have for the $I_3^W = -1/2$ flavours d, s, b neglecting m_d, m_s, m_b relative to m_Z

$$\Gamma(Z \to \bar{d}d) = \frac{\bar{g}^2 m_Z}{32\pi \cos^2\vartheta_W} \left(1 - \frac{4}{3} s_W^2 + \frac{8}{9} s_W^4\right) \times \left(1 + \frac{\bar{\alpha}_s}{\pi}\right) \simeq$$

$d \to s \to b$

$$\simeq (423.4)\ \text{MeV} \qquad (2.9)$$

The reduction of the width for $m_t \neq 0$ relative to the flavours c, u is given by

$$\frac{\Gamma(Z \to \bar{t}t)}{\Gamma(Z \to \bar{u}u)} = \left(1 - \frac{4m_t^2}{m_Z^2}\right)^{1/2} \times \left\{1 - \frac{m_t^2}{m_Z^2} + \frac{6\,\mathrm{Re}\,\frac{a_R^t}{a_L^t}}{1 + \left|\frac{a_R^t}{a_L^t}\right|^2} \frac{m_t^2}{m_Z^2}\right\}$$

$$\frac{a_R^t}{a_L^t} = - \frac{\frac{2}{3} s_W^2}{\frac{1}{2} - \frac{2}{3} s_W^2} \simeq - 0.40 \qquad (2.10)$$

The suppression factor in eq. (2.10) for m_t = 30 and 40 GeV respectively amounts to

$$\frac{\Gamma(Z \to \bar{t} t)}{\Gamma(Z \to \bar{u} u)} = \begin{cases} 0.50 & m_t = 30\ GeV \\ 0.20 & m_t = 40\ GeV \end{cases} \qquad (2.11)$$

We obtain for the hadronic width of Z:

$$\Gamma_{Z \to hadrons} = \begin{cases} 1932.0\ MeV & m_t > m_Z/2 \\ 2047.8\ MeV & m_t \simeq 35\ GeV \\ 2262,9\ MeV & m_t \simeq 0 \end{cases} \qquad (2.12)$$

For the decay mode into charged leptons e^+e^-, $\mu^+\mu^-$, $\tau^+\tau^-$ we obtain

$$\Gamma(Z \to e^+e^-) = \frac{\bar{g}^2 m_Z}{96\pi \cos^2\vartheta_W} \left(1 - 4 s_W^2 + 8 s_W^4\right) \times \left(1 + \frac{3}{4} \frac{\alpha}{\pi}\right) =$$

$$= 92.4\ MeV$$

$$\Gamma\left(Z \to \begin{matrix} e^+e^- \\ +\mu^+\mu^- \\ +\tau^+\tau^- \end{matrix}\right) = 277.3\ \text{MeV}$$

$$\Gamma\left(Z \to \nu_e \bar{\nu}_e\right) = \frac{\bar{g}^2 m_Z}{96\pi \cos^2\vartheta_W} \cong 181.3\ \text{MeV}$$

$$\nu_e \to \nu_\mu \to \nu_\tau$$

$$\Gamma\left(Z \to \begin{matrix} \nu_e\bar{\nu}_e \\ +\nu_\mu\bar{\nu}_\mu \\ +\nu_\tau\bar{\nu}_\tau \end{matrix}\right) = 543.85\ \text{MeV} \qquad (2.13)$$

The total width and branching fractions into e^+e^- and into $\nu_e\bar{\nu} + \nu_\mu\bar{\nu}_\mu + \nu_\tau\bar{\nu}_\tau$ are

$$\Gamma_Z^{tot} = \begin{cases} 2753.2\ \text{MeV} & m_t > m_Z/2 \\ 2869.0\ \text{MeV} & m_t \simeq 35\ \text{GeV} \\ 3084.1\ \text{MeV} & m_t \simeq 0 \end{cases}$$

$$Br\left(Z \to e^+e^-\right) = \begin{cases} 3.3\,\% & m_t > m_Z/2 \\ 3.2\,\% & m_t \simeq 35\ \text{GeV} \\ 3.0\,\% & m_t \simeq 0 \end{cases}$$

$$Br\left(Z \to \begin{matrix} \nu_e\bar{\nu}_e \\ +\nu_\mu\bar{\nu}_\mu \\ +\nu_\tau\bar{\nu}_\tau \end{matrix}\right) = \begin{cases} 19.8\,\% & m_t > m_Z/2 \\ 18.9\,\% & m_t \simeq 35\ \text{GeV} \\ 17.6\,\% & m_t \simeq 0 \end{cases} \qquad (2.14)$$

3. PRODUCTION OF $W^{\pm}$ AND Z - CROSS SECTIONS AND DISTRIBUTIONS

The parameters which we determined from the reference values $\sin^2\theta_W = 0.215$, $m_W = 83.22$ GeV, $m_Z \tilde{=} 93.92$ GeV and $m_t \tilde{>} 35$ GeV imply $\Gamma_W^{tot} \tilde{=} 2.9$ GeV, $\Gamma_Z^{tot} \tilde{=} 2.9$ GeV.

We consider the cross sections for W and Z production from $p\bar{p}$ including QCD corrections of order $\alpha_s(Q^2 \tilde{>} m_Z^2) \tilde{>} 0.10$, fixing the $\Lambda_{\overline{MS}}$ (4 flavours) parameter to be 0.1 GeV [4].

For the $O(\alpha_s^0)$ W production cross section restricting ourselves to the subprocess $d + \bar{u} \to W^- \to e^- \bar{\nu}_e$

$$d\sigma_1 = \sigma_1 \cdot d\sigma_1^{red}$$

$$\sigma_1 = \frac{\bar{g}^4 \cos^2\vartheta_C}{192 m_W^2} \frac{m_W}{\Gamma_W^{tot}} = 1.604\ nb$$

$$d\sigma_1^{red} = f_1(x_e, x_1)\, x_e\, dx_e \frac{dz_e}{2} \times$$

$$\times \delta(x_1 x_2 - \tau)\ \delta\left(\tau - x_1 x_e \frac{1-z_e}{2} - x_2 x_e \frac{1+z_e}{2}\right) \times$$

$$\bar{u}_{p^-}(x_1, t)\ D_p(x_2, t)\, dx_1\, dx_2$$

$$t = \log\left(\frac{Q^2}{\Lambda^2_{\overline{MS}}}\right), \quad x_e = \frac{E_e}{E_{beam}}, \quad \tau = \frac{m_W^2}{s},$$

$$s = 4E^2_{beam}, \quad z_e = \cos\vartheta(e, \bar{p}) \qquad (3.1)$$

For $\Lambda = 0.1$ and 0.2 GeV we obtain using the structure functions of ref. 5

$$\sigma_{1\ W^+ + W^-}^{e^-\bar{\nu}_e + e^+\nu_e} = 2\int d\sigma_1 = \begin{cases} 386\ pb & \Lambda_{\overline{MS}} = 0.1\,GeV \\ 332\ pb & \Lambda_{\overline{MS}} = 0.2\,GeV \end{cases} \qquad (3.2)$$

Comparing with the results obtained in analytic form modulo the leptonic branching fraction of W by Altarelli, Ellis, Greco and Martinelli [4] we see that the difference in the resulting cross section is due to different rescaled structure functions. However in the subsequent evaluation of the $O(\alpha_s^1)$ correction we differ from the above work in that we do not define through that order the differential quark densities by the deep inelastic structure function F_2.

Although I differ in the choice of structure functions from Altarelli et al. with respect to their definition, their specific value as rescaled from deep inelastic scattering at small values of Q^2 is a matter of judicious approximation in the absence of measurement at the relevant Q^2 values, which are hopefully forthcoming at the HERA facility.

The process of hard gluon bremsstrahlung within specified kinematic limits for the emission of a gluon jet, which is understood as observable in principle refers to the subprocess

$$\bar{u} + d \rightarrow W^- + g \rightarrow e^- \bar{\nu}_e g$$

$$d\sigma_2 = \sigma_2 \, d\sigma_2^{red}$$

$$\sigma_2 = \frac{s}{m_W^2} \frac{1}{m_W^2} \frac{m_W}{\Gamma_W^{tot}} \frac{\bar{g}^4}{72} \omega_s^2 \vartheta_c \frac{\alpha_s(m_Z)}{4\pi} \widehat{=}$$

$$\widehat{=} 1.434 \text{ nb} \qquad (3.3)$$

The differential reduced cross section in eq. (3.3) contains infrared and collinear divergent terms and thus necessarily applies within a safe region to be defined only

$$d\sigma_2^{red} = d\omega_s \, f_2(\omega_s) \left(\frac{\tau}{x_1 x_2} \right)^2 / a\alpha - b\beta /^{-1} \times$$

$$\bar{u}_{\bar{p}} (x_1, t) \, D_p / x_2, t)$$

$$d\omega_s = x_e\, dx_e\, \frac{dx_g}{x_g}\, \frac{2\, dz_g}{1-z_g^2}\, \frac{dz_c}{2}\, \frac{d\phi_{eg}}{2\pi}$$

$$x_e = \frac{E_e}{E_{beam}}, \quad x_g = \frac{E_g}{E_{beam}}, \quad z_e = \cos\vartheta_e(e,\bar{p}), \quad z_g = \cos\vartheta(g,\bar{p})$$

$$f_2 = \left(x_1 x_e \frac{1-z_e}{2}\right)^2 + x_2^2 \left(x_1 - x_e \frac{1+z_e}{2} - x_g \frac{1+z_g}{2}\right)^2$$

$$a = x_1 - x_g \frac{1+z_g}{2}, \quad \alpha = x_e \frac{1-z_e}{2}$$

$$b = x_2 - x_g \frac{1+z_g}{2}, \quad \beta = x_e \frac{1+z_e}{2} \qquad (3.4)$$

$\phi_{eg} = \phi(e;g)$: azimuthal angle between the transverse momenta of e^- and the gluon jet.

The region of safe gluon jet momenta and angle we choose as follows

$$5^\circ \leq \vartheta(g,\bar{p})^{lab} \leq 175^\circ$$

$$(E_g)^{lab} \geq 5\,GeV \qquad (3.5)$$

The corrections due to virtual gluon contributions to σ_1 and the redefinition of quark structure functions can be discussed as dependent on the kinematic boundaries imposed in eq. (3.5) [4]. This discussion in fact justifies the above

boundaries since the remaining contributions cancel within the claimed accuracy of 20% relative to the hard gluon emission cross section. We obtain

$$\sigma_{p\bar{p}\to W^-+W^++g\to e^-\bar{\nu}_e g+e^+\nu_e g} = 2\int_{\text{kin. limits}} d\sigma_2$$

$$= \begin{cases} 190\ pb & \Lambda_{\overline{MS}} = 0.1\,GeV \\ 163\ pb & \Lambda_{\overline{MS}} = 0.2\,GeV \end{cases} \qquad (3.6)$$

for the ratio of $O(\alpha_s^0)$ Z to W production cross sections we find

$$\bar{p}p:\ \sigma_{0\ Z}^{e^+e^-} \Big/ \sigma_{0\ W^++W^-}^{e^+\ e^-} = 9.1 \pm 0.5 \qquad (3.7)$$

Thus we estimate

$$\sigma_{p\bar{p}}\left(\begin{matrix}e^+ & e^- \\ \uparrow & \uparrow \\ W^+ & W^-\end{matrix}\right) = \begin{cases} 576 & \Lambda_{\overline{MS}} = 0.1\,GeV \\ \pm 115\ pb & \\ 495 & \Lambda_{\overline{MS}} = 0.2\,GeV \end{cases}$$

$$\sigma_{p\bar{p}}\left(\begin{matrix}e^+e^- \\ Z\end{matrix}\right) = \begin{cases} 63 & \Lambda_{\overline{MS}} = 0.1\,GeV \\ \pm 13\ pb & \\ 54 & \Lambda_{\overline{MS}} = 0.2\,GeV \end{cases} \qquad (3.8)$$

These cross sections are to be compared with the experimental results [6), 7)]

$$\sigma_{p\bar{p}}\left(\begin{matrix}e^+ & e^- \\ \uparrow & \uparrow \\ W^+ & W^-\end{matrix}\right) = \begin{cases} 530 \pm 80 \pm 90\ pb & UA1 \\ 530 \pm 100 \pm 100\ pb & UA2 \end{cases}$$

$$\sigma_{p\bar{p}}\left(\begin{matrix}e^+e^- \\ Z\end{matrix}\right) = \begin{cases} 71 \pm 24 \pm 13\ pb & UA1 \\ 110 \pm 40 \pm 20\ pb & UA2 \end{cases} \qquad (3.9)$$

We calculate the number of events expected in the UA2 detector (forward and central detectors) given the avoce cross sections and the distributions in ref. 2 with the signature

$$\begin{Bmatrix} e^- \ '\bar{\nu}_e' \\ +e^+ \ '\nu_e' \end{Bmatrix} \qquad 20^\circ \leq \vartheta(e\,\bar{p}) \leq 160^\circ$$

$$|p_T^{e^\pm}| \geq 25\,\text{GeV}$$

$$N_{p\bar{p}}\left(\overset{e}{W^\pm W^-}\right)_{\text{restricted}} \cong (0.65)\,\sigma_{p\bar{p}}\left(\overset{e}{\uparrow} W^\pm W^-\right) \times \eta_{exp} \times \int \mathcal{L}\,dt \qquad (3.10)$$

In eq. (3.10) the distributions in transverse momentum and rapidity of the charged leptons as generated by a Monte Carlo program and yield for the kinematic constraints in angle and transverse momentum of the charged lepton above the reduction fractor 0.65. η_{exp} denotes the probability that within the given kinematic domain an electron (positron) is actually detected by the UA2 apparatus.

We take the average between the cross sections calculated for $\Lambda = 0.1$ and 0.2 GeV respectively and obtain [7]

$$N\left(\overset{e}{W}\right)_{\text{restricted}} = (0.65)\cdot(536 \pm 20\%) \times (0.131 \pm 20\%) \times 0.8 =$$

$$= (36.4 \pm 10)\ \text{events}$$

$$\eta_{exp} = 0.8 \qquad (3.11)$$

This is to be compared with the observed number of events which is 37 [7] with a background estimate of 1.5 events and of 2.5 events due to misinterpreted Z decay. Due to the similar decay distributions we also estimate the number of Z events for which one of the charged leptons falls within the kinematic region above.

$$N_0(e_1 \text{ from } Z) \simeq \left\{ 20^\circ \leq \vartheta(e_1, \bar{p}) \leq 160^\circ \;/\; p_T^{e_1} \geq 25\ \text{GeV} \right\}$$
$$\simeq (36.4 : 9.1) = (4 \pm 1) \qquad (3.12)$$

The probability that the second electron is not detected we denote by p_{veto}

$$P_{veto} = (1 - \eta_{exp})\ p(e_2 \text{ in accepted region; } + \text{ given } e_1 \text{ as in 3.12})$$
$$+ p(e_2 \text{ outside accepted region, given } e_1 \text{ as in 3.12})$$
$$\leq (0.2)/(0.65) + 0.35 \simeq 0.48 \qquad (3.13)$$

We expect however that the true p_{veto} is considerably smaller than the above estimate. From eq. (3.13) it follows

$$N(e^\pm \text{ from } Z;\ e_2 \text{ missed}) \leq (1.9 \pm 0.5) \text{ events}$$

We show the distribution of Monte Carlo generated events in transverse momentum of the gauge boson for W, Z production for $|p_T^{W,Z}| \geq 12$ GeV in Figs. 2 and 3.

Acknowledgements: I should like to thank the members of the UA2 group of Bern, in particular J. Schacher, H. Hänni and B. Hahn for many illuminating discussions. Thanks are also due to Z. Kunszt, I. Crewther-Rose and R. Stierlin for their critical suggestions and help with the numerical calculations.

References

1) A. Sirlin, Phys.Rev. D20 (1980) 971;
W.J. Marciano and A. Sirlin, Phys.Rev. D22 (1980) 2695;
see also
W.J. Marciano, contribution to these proceedings.

2) P. Minkowski, in "Theory of Fundamental Interactions 1982", LXXXI Corso, Soc. Italiana di Fisica, Bologna, Italy.

3) D. Albert, W.J. Marciano, D. Wyler and Z. Parsa, Nucl.Phys. B166 (1980) 460.

4) F. Paige ISA Jet program, BNL 2977-7 (1981);
P. Chiappetta and M. Perrottet, Marseille preprint CPT-83P-1525 (1983)
G. Altarelli, R.K. Ellis, M. Greco and G. Martinelli, CERN preprint TH.3851 (1984);
P. Minkowski, Bern preprint BUTP-83/22 (1984);
B. Humpert and W.L. van Neerven, Phys.lett. 93B (1980) 456;
B. Humpert, private communication.

5) P. Salati and J.C. Wallet, Annecy preprint LAPP-TH-64 (1982).

6) UA1 Collaboration, C. Rubbia, contribution to these proceedings.

7) UA2 Collaboration, J. Schacher, contribution to these proceedings.

8) R.K. Ellis, contribution to these proceedings.

9) D.W. Duke and J.F. Owens, Florida State Univ. preprint FSU-HEP 831115 (1984).

Figure captions

Fig. 1: Evolution of the inverse strong coupling constant $1/\alpha_s = 4\pi/g_s^2$ for four effective flavours for $\Lambda_{\overline{MS}} = 0.1$, 0.2 and 0.5 GeV from $\mu_o = 5$ GeV to $\mu = 100$ GeV.

Fig. 2: Differential cross section $\frac{d\sigma}{dp_T^W}$ for the proces $p + \bar{p} \to W^- + \text{jet} + X$ $\hookrightarrow e^- \bar{\nu}_e$ and (W^+) for $|p_T^W| \geq 12$ GeV taking into account the UA2 experimental limitation $20^o \leq \theta_e \leq 160^o$.
The dashed curve corresponds to the p_T^W distribution according to R.K. Ellis presented at this workshop [8] involving the structure functions of Duke and Owens [9]:

$$\left(\frac{d\sigma}{dy^W dp_T^W} \Big/ \frac{d\sigma}{dy^W} \right)_{y^W = 0}$$

Fig. 3: Differential cross section for jet production $\frac{d\sigma}{dp_T^Z}$ for the process $p + \bar{p} \to Z + \text{jet} + X$ $\hookrightarrow e^+e^-$ under the same kinematic constraints as in Fig. 2.

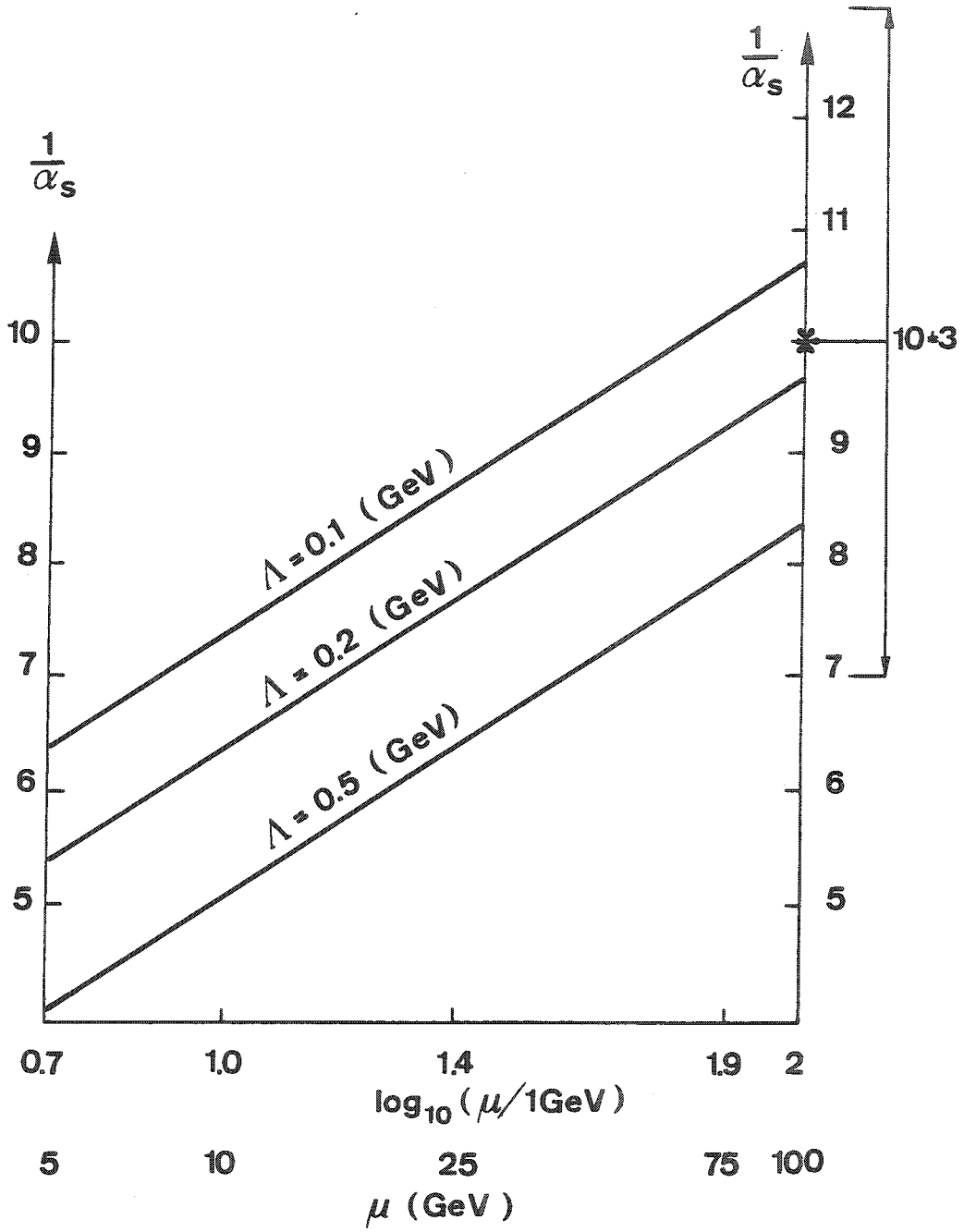
1/αs
12
11
10
9
8
7
6
5
10+3
Λ = 0.1 (GeV)
Λ = 0.2 (GeV)
Λ = 0.5 (GeV)
0.7
1.0
1.4
1.9
2
log10 (μ/1GeV)
5
10
25
75
100
μ (GeV)

FIG. 1

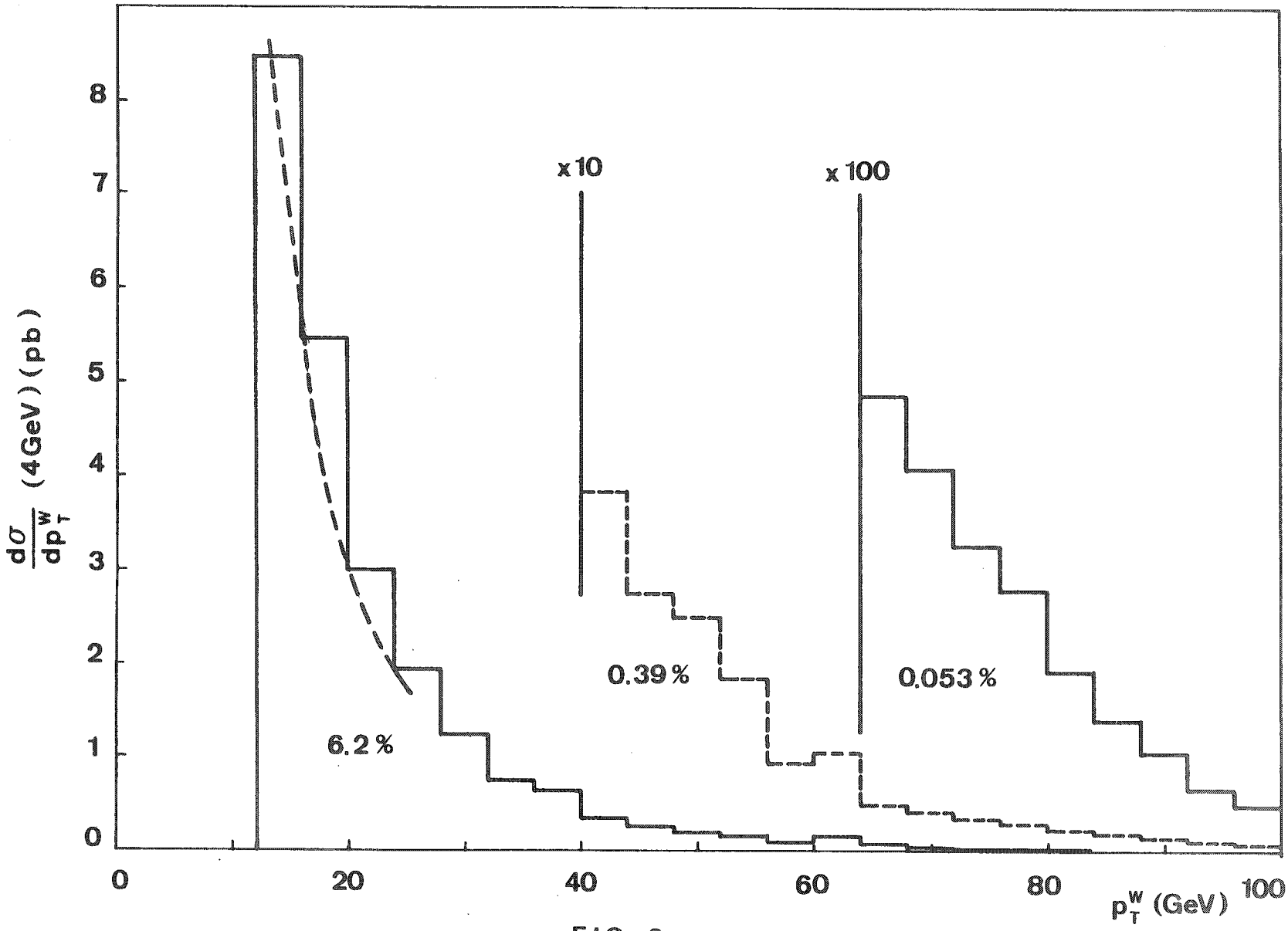
x 10
x 100
6.2 %
0.39 %
0.053 %
$\frac{d\sigma}{dp_T^W}$ (4GeV) (pb)
p_T^W (GeV)
0
1
2
3
4
5
6
7
8
0
20
40
60
80
100

FIG. 2

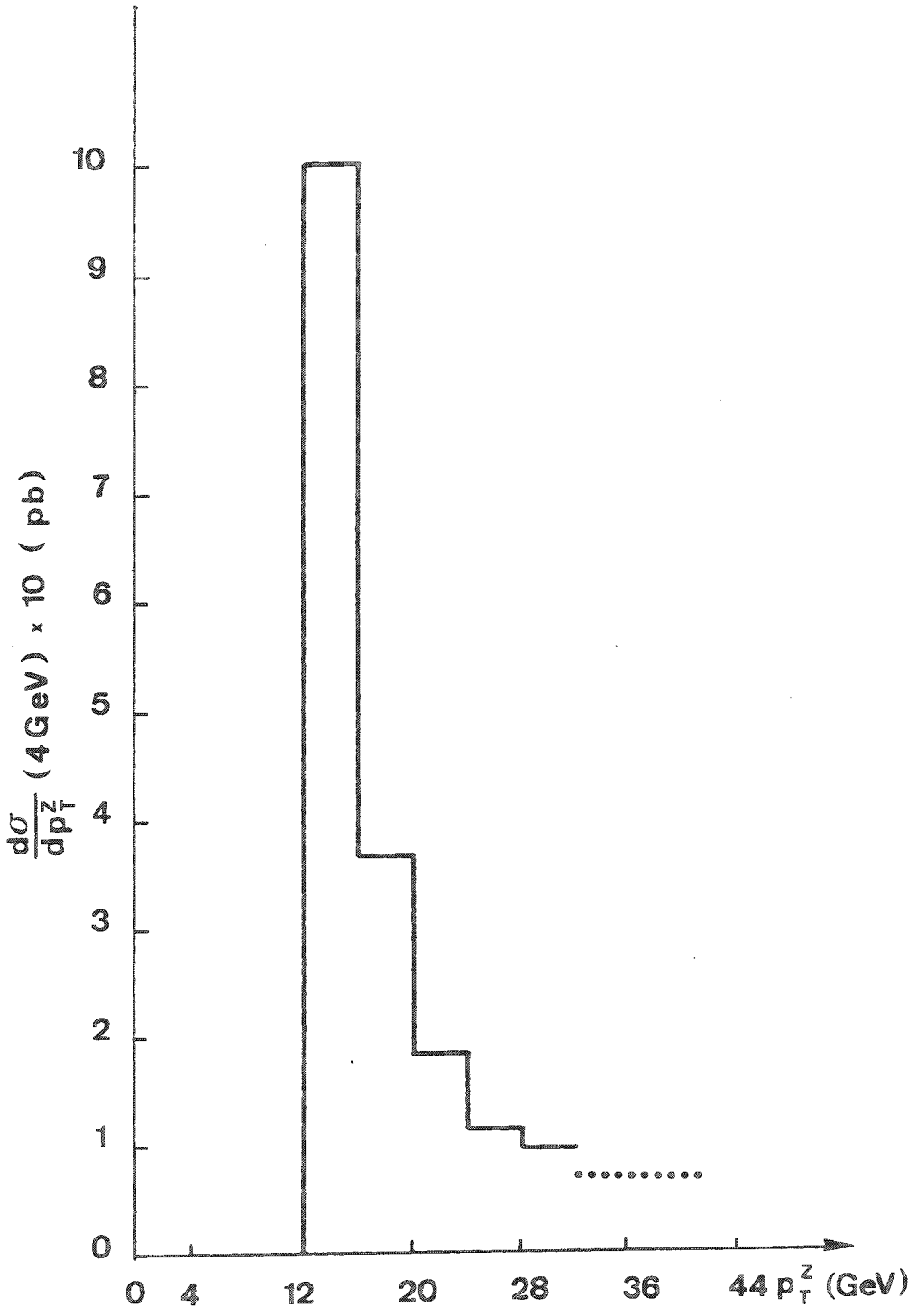
10
9
8
7
6
5
4
3
2
1
0
$\frac{d\sigma}{dp_T^Z}$ (4GeV) x 10 (pb)
0
4
12
20
28
36
44 p_T^Z (GeV)

FIG. 3

QCD p_T EFFECTS IN W/Z AND JET PRODUCTION

M. Greco
INFN - Laboratori Nazionali di Frascati, Frascati, Italy

Abstract

Theoretical aspects of transverse momentum distributions in QCD are discussed in connection to weak bosons and dijet production at Sp$\bar{p}$S collider energies.

The production of W and Z bosons[1] at the CERN Sp$\bar{p}$S collider allows a very important test of the Drell-Yan mechanism[2] in perturbative QCD in a completely new kinematical regime. The $O(\alpha_s)$ corrections to the total production cross section are of reduced size compared to fixed target energies and therefore the absolute production rates can be quite reliably predicted from perturbation theory[3].

On the other hand the transverse momentum distribution is probed in the soft region of $q_T \ll Q$, which, at lower energies, is not clearly separated from the "intrinsic q_T" ($q_T \sim \Lambda$) and large q_T ($q_T \sim Q$) regions, where non perturbative and $O(\alpha_s)$ effects respectively dominate the spectrum. Therefore one encounters here a unique opportunity to test those theoretical ideas which have been developed to resume to all orders the class of large logarithms of Q^2/q_T^2 arising from the emission of soft quanta. Conversely, a precise evaluation of these QCD effects is quite important for obtaining the accuracy desired to test the electroweak part of these process, referring in particular to the W mass, which is determined from the transverse spectrum of the decay lepton.

Much theoretical work has been recently dedicated to this subject[4]. In particular a very detailed analysis of the q_T spectrum has been recently performed[5], which authomatically combines the soft gluon resummation at $q_T \ll Q$ with the $O(\alpha_s)$ perturbative distribution at large q_T, without the ad hoc introduction of matching procedures between hard and soft radiation. The main formulae and the comparison with UA1 and UA2 experimental results have been already discussed by K. Ellis[6]. In the following I will first compare those

results with recent theoretical analyses[7] of the same problem in order to clarify the different approximations performed and the corresponding limits of validity. Next I will discuss the transverse momentum spectrum of the leptons produced in the decay of the weak bosons, which are closely related to the parent distribution and are of great importance for an accurate determination of the W boson's mass. Finally some transverse momentum effects in the production of dijets will be briefly discussed, showing possible evidence in favor of the three gluon coupling at collider energies.

The expression for the cross section for the production of a W^+ boson reads[5]

$$\frac{d\sigma}{dq_T^2 dy} = \frac{\pi^2 \alpha}{6S \sin^2\theta_W} \int b\,db\, J_o(b\,q_T)\, e^{S(b^2, Q^2, A_t^2)} R_q(b^2, Q^2, y) + \\ + Y_q(q_T^2, Q^2, y) + (\text{gluon terms}) , \tag{1}$$

where

$$R_q(b^2, Q^2, y) = H(x_1^o, x_2^o, P^2) \left[1 + \frac{\alpha_s C_F}{2\pi} \left(1 + \frac{5}{3}\pi^2 - \ln^2\left(\frac{A_t^2}{Q^2}\right) - \right.\right. \\ \left.\left. - 3\ln\left(\frac{A_t^2}{Q^2}\right)\right] + \frac{\alpha_s C_F}{2\pi} \left[\int_{x_1^o}^1 \frac{dz}{z} f_q(z) H\left(\frac{x_1^o}{z}, x_2^o, P^2\right) + \right. \tag{2}$$

$$\left. + \int_{x_2^o}^1 \frac{dz}{z} f_q(z) H\left(x_1^o, \frac{x_2^o}{z}, P^2\right)\right] ,$$

and $\tau = M^2/S$, $x_{1,2}^o = \sqrt{\tau}\exp(\pm y)$, $A_t^2 = \left[(S+Q^2)^2/4S\cosh^2 y - Q^2\right]$ is the kinematical bound of the transverse momentum squared for gluon emission, and $f_q(z) = 3/2\,(1-z)_+^{-1} - (1+z^2)\left[\ln(1-z)/(1-z)\right]_+ + (1+z^2)\ln z/(1-z) - 2 - 3z$. Furthermore the product of the parton distribution functions is defined

$$H(x_1, x_2, P^2) = \left\{ \left[u(x_1, P^2)\,\bar{d}(x_2, P^2) + c(x_1, P^2)\,\bar{s}(x_2, P^2)\right] \cos^2\theta_c + \right. \\ \left. + \left[u(x_1, P^2)\,\bar{s}(x_2, P^2) + c(x_1 P^2)\,\bar{d}(x_2 P^2)\right] \sin^2\theta_c \right\} + \left\{ 1 \leftrightarrow 2 \right\} , \tag{3}$$

where the scale P^2 at which the parton densities are probed is given by $P^2 \sim$ $\sim 4\,e^{-2\gamma_E}/b^2$ at large b.

The Sudakov form factor $S(b^2, Q^2, A_t^2)$, at the leading double and single logarithmic accuracy, is given by

$$S(b^2, Q^2, q^2_{Tmax}) = \frac{C_F}{\pi} \int_0^{q^2_{Tmax}} \frac{dq^2}{q^2}\, \alpha(q^2) \left[\ln\left(\frac{Q^2}{q^2}\right) - \frac{3}{2}\right] \left[J_o(bq) - 1\right], \quad (4)$$

with $q^2_{Tmax} = A_t^2$. The residual term Y_q in eq. (1) includes finite terms from annihilation graphs for $q_T \to 0$. Finally the gluon terms refer to the Compton scattering graphs, which give additive contributions to R_q and Y_q.

The bulk of the q_T distribution, where most of the data have been collected, comes from the soft part of eq. (1). Of course the residual finite terms play a major role for large q_T, say $q_T \gtrsim 30$ GeV where eq. (1) tends to the $O(\alpha_s)$ perturbative result. Then, for comparison with previous analyses of the soft contribution, it is useful to discuss some approximate forms of the Sudakov form factor (4).

First, taking $q^2_{Tmax} = Q^2$ as upper limit, the replacement can be made

$$\exp\left[S(b^2, Q^2, A_t^2)\right] \simeq \exp\left[S(b^2, Q^2, Q^2)\right] \left(1 + \int_{Q^2}^{A_t^2} \right), \quad (5)$$

with obvious notations. This is allowed because $\alpha(q^2)$ is small for $Q^2 \leq q^2 \leq A_t^2$. The resulting additional contribution to R cancels in this case the terms $\ln^2(A_t^2/Q^2) - 3\ln(A_t^2/Q^2)$ appearing in eq. (2) in the large b limit. A similar result holds approximately for $q^2_{Tmax} = Q^2/e^3 \sim (Q/4)^2$. Different choices of q_{Tmax}, with no compensating terms, would not agree with the exact result (1). Furthermore the next to leading constant term in integrand of eq. (4) is given by $(-3/2)$, and its presence is quite relevant for the falloff of the distribution $(d\sigma/dq_T dy)$ after the peak. In fact the so called "leading approximation", where one keeps only the logarithmic term $\ln(Q^2/q^2)$ in eq. (4) gives a very poor description of the weak boson distribution and consequently of the decay lepton spectrum, as discussed later. Finally no double counting between the soft and the hard finite contribution must be present, as in eq. (1).

The above discussion puts some doubts on the accuracy of previous analyses[7] of this problem and indeed only in a few cases[8] the answer is reasonably good up to $q_T \lesssim 20$ GeV, where however the treatment of hard effects is

unsatisfactory. In the other hand a detailed knowledge of the full q_T distribution, which is crucial to describe the QCD background for new phenomena at large q_T [9], can only be obtained from ref. 5.

We would like to discuss now the p_T distribution of the decay leptons from W/Z decays, which is relevant for an accurate determination of the charged boson's mass. The starting formula is given by [10]

$$E_p \frac{d\sigma}{d^3p} = \int \frac{d^3k}{E_k} \left(E_k \frac{d\sigma^W}{d^3k}\right) \frac{1}{2\pi} \delta\left(pk - \frac{M_W^2}{2}\right), \tag{6}$$

where $d\sigma^W$ is the invariant cross section for producing a W boson, times its leptonic branching ratio, see eq. (1), and the δ function reflects the two body decay kinematics. The technical details of integrating eq. (6) are given in ref. 11. We will give here only the main results, compared with the leading approximation analyses [10, 12]. In Fig. 1 we show [11] the invariant cross section at

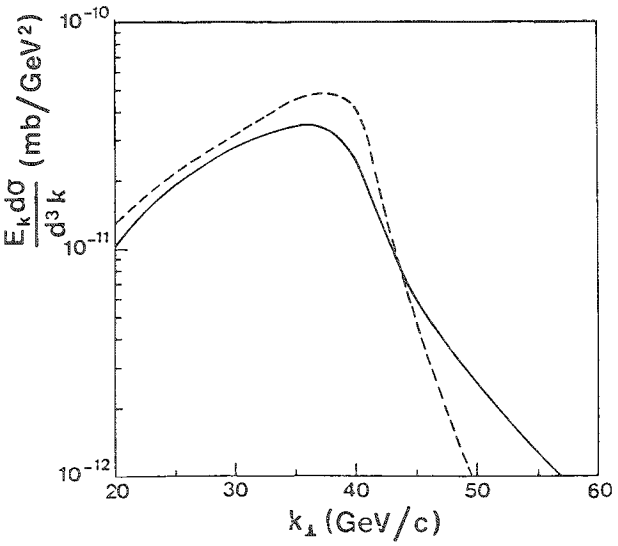

Fig. 1

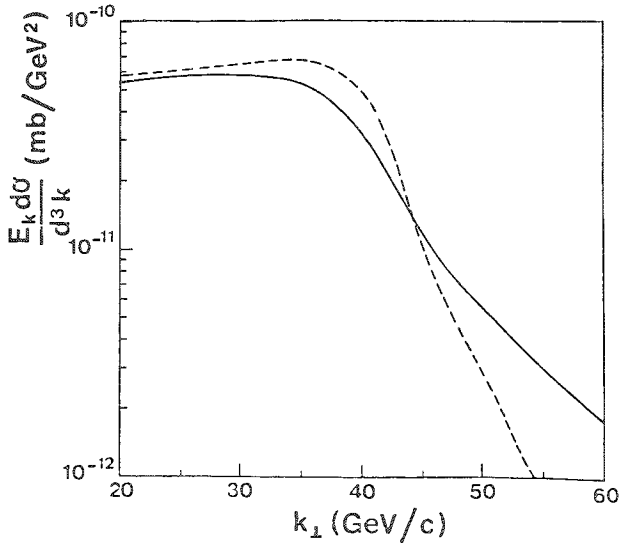

Fig. 2

a lepton angle $\theta = 90^o$, having used the Glück et al. [13] parametrization of the structure functions. A different choice of the parton densities, given for example, by Baier et al. [14], gives similar results. The leading approximation (solid curve), defined above, gives rise to a much broader p_T distribution than the one resulting from the inclusion of subleading terms (dashed curve) corresponding to eq. (1), which is reminescent of what observed for the q_T distribution of the W. Similar results are found [11] at $\sqrt{s} = 2000$ GeV (see Fig. 2), where however one observes an excess of events for small p_T com-

pared to $\sqrt{s}$ = 540 GeV, due to the much more sizeable effect of the sea when the energy increases. The relevant role played by the subleading terms is consistent with the UA1 data[15], which show no events for $p_\perp$ above 50 GeV.

As last topics, I would like to discuss now some transverse momentum effects in dijet production. The basic idea is the following[16,17]. At collider energies the subprocess of gluon-gluon scattering gives the dominant contribution to jet production, in contrast to the case of weak boson production, where only the quarks essentially play a role. The corresponding Sudakov form factors depends upon C_A instead of C_F, leading to a relative k_T dijet distribution which is regulated by the process of bremsstrahlung initiated by gluons instead of quarks. This observation provides a rather clean test of the three gluon coupling which can be easily studied by looking at the relative k_T distribution of two hard back-to-back jets. Then for k_T not very large, say $k_T \lesssim 20$ GeV, the distribution is dominated by soft gluon emission and is much broader than the corresponding quark case. This is shown in Fig. 3[17], where the k_T spectrum obtained by using a Glück at al.[13] parametrization of the gluon density (full line), is compared to the hypothetical case where gluons would radiate like quarks ($C_A = C_F$, dotted line). The theoretical uncertainty related to our poor knowledge of the gluon structure function is represented, in the same figure, by the dashed line which gives the analogous result for the CDHS gluon parametrization[18].

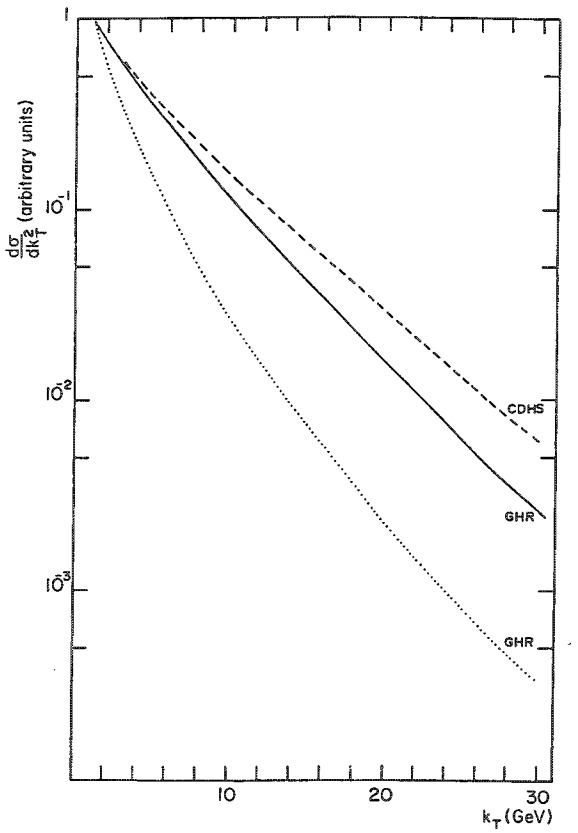

Fig. 3

Experimentally, it is better to define a projected k_T distribution perpendicularly to the trigger jet ($k_{T\perp}$). Then the UA1 preliminary data[19] are shown in Fig. 4 and compared to the theoretical predictions the two sets of gluon densities. An experimental resolution σ = 5 GeV is also included in the curves. There is a quite good agreement between theory and experiments for ($k_{T\perp}$) $\lesssim$

$\lesssim$ 20 GeV. At higher transverse momenta the theoretical predictions are not reliable, not including finite terms of order α_s coming from hard gluon bremsstrahlung and virtual one loop corrections, which have not been all computed. Finally, in Fig. 5 the hypothetical case of gluons radiating like quarks is also shown, clearly in a much poorer agreement with data.

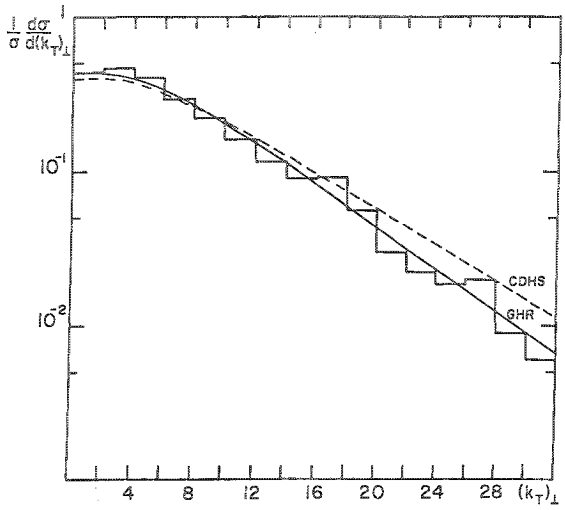

Fig. 4

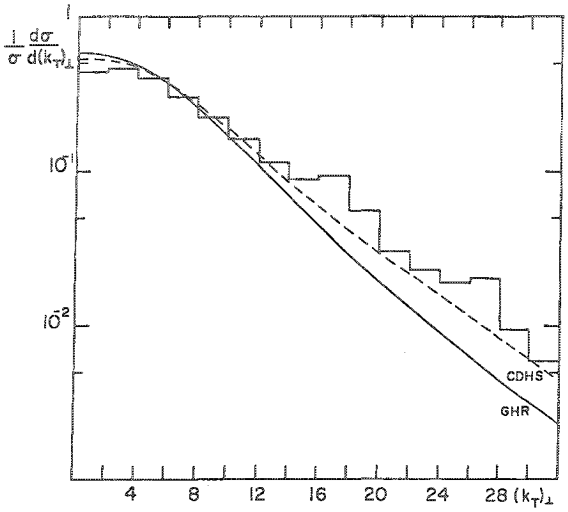

Fig. 5

In conclusion, we have discussed the relevance of detailed studies of p_T effects in W/Z production for precise tests of QCD as well as for the determination of the electroweak parameters. Similar effects observed in the production of back-to-back jets at collider energies are in good agreement with the expectations from the three gluon coupling.

References

1) UA1 Collab., G. Arnison et al., Phys. Letters 122B, 103 (1983); 126B, 392 (1983); UA2 Collab., G. Banner et al., Phys. Letters 122B, 476 (1983); 129B, 130 (1983).
2) S. D. Drell and T. M. Yan, Phys. Rev. 25, 316 (1970).
3) For a review, see G. Altarelli, Phys. Rep. 81, 1 (1982).
4) See, for example, P. Chiappetta and M. Greco, Nuclear Phys. B221, 269 (1983), and references therein.
5) G. Altarelli, R. K. Ellis, M. Greco and G. Martinelli, CERN preprint TH-3851 (1984).
6) R. K. Ellis, these Proceedings.
7) P. Aurenche and R. Kinnunen, Phys. Letters 135B, 493 (1984); P. Chiappetta and M. Greco, Phys. Letters 135B, 190 (1984); A. Nakamura, G. Pancheri and Y. Srivastava, submitted to Phys. Rev. Letters; L. Trentadue, Parma preprint (1983); F. Halzen, A. D. Martin and D. M. Scott, Phys. Rev. D25, 754 (1982).
8) P. Chiappetta and M. Greco, ref. (7); L. Trentadue, ref. (7).
9) C. Rubbia, these Proceedings; A. Roussarie, these Proceedings.
10) F. Halzen, A. D. Martin and D. M. Scott, ref. (7).
11) P. Chiapetta, M. Greco and J. Soffer, Frascati preprint LNF-84/14 (1984).
12) An analysis based on the proposal to exponentiate the whole first order contribution has been also carried out by F. Halzen, A. D. Martin and M. Scott, Phys. Letters 112B, 160 (1982).
13) M. Glück, E. Hoffmann and E. Reya, Z. Physik C13, 119 (1982).
14) R. Baier, J. Engels and B. Petersson, Z. Physik C2, 265 (1979).
15) UA1 Collab., G. Arnison et al., Phys. Letters 129B, 273 (1983).
16) M. Greco, Proceedings of the XVIII Rencontre de Moriond, La Plagne, 1983.
17) M. Greco, Frascati preprint LNF-84/21 (1984).
18) H. Abramowicz et al., Z. Physik C12, 289 (1982). The explicit parametrization used is given by M. Anselmino, P. Kroll and E. Leader, CERN preprint TH-3471 (1983).
19) M. Della Negra and W. Scott, private communication. We are grateful to M. Della Negra, C. Rubbia and W. Scott for providing us the UA1 preliminary information prior to publication and for several discussions.

TESTING THE WWγ COUPLING OF THE GLASHOW-SALAM-WEINBERG MODEL AT $p\bar{p}$ COLLIDERS

J. Cortés*, K. Hagiwara and F. Herzog

Physics Department, University of Wisconsin, Madison, Wisconsin 53706 USA
*CERN, Theory Division, CH-1211, Genéve 23, Switzerland

Presented by Franz Herzog

ABSTRACT

We propose methods to measure the anomalous magnetic moment κ of the W-boson, a quantity which is of foremost importance for testing the non-abelian structure of the electroweak gauge theory.

1. INTRODUCTION

The standard model[1] of the electroweak interaction is a renormalizable non-abelian, spontaneously broken gauge theory; an outstanding feature of such a theory is the self coupling of the gauge bosons. It is thus of great importance to test those vertices, and in the following we shall propose a method to probe the triple coupling of a photon (γ) with the charged intermediate vector bosons ($W^{\pm}$). We work in a minimally extended standard model where we attribute an anomalous magnetic moment κ to the W boson;[2] the magnetic moment of the W boson is then given by

$$\mu_W = \frac{e}{2m_W}(1+\kappa) \ . \tag{1}$$

Here e denotes the modulo of the electron charge and m_W the mass of the W. Every gauge theory, based on an arbitrary non-abelian group, predicts:

$$\kappa = 1 + O\left(\frac{e^2}{4\pi^2}\right) \ . \tag{2}$$

Any experiment that finds a substantial deviation from $\kappa = 1$ would thus disprove the gauge nature of the electroweak interaction.

2. THE PROCESS $p\bar{p} \to \gamma \ell \bar{\nu}_\ell X$

The process proton(p) + antiproton($\bar{p}$) → photon (γ) + charged lepton(ℓ) + antineutrino($\bar{\nu}_\ell$) + X takes place via a quark(d) - antiquark($\bar{u}$) annihilation; the corresponding tree level Feynman diagrams are

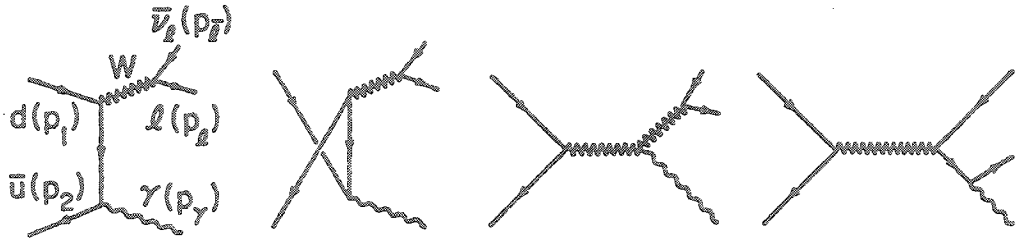

where we denote four-momenta in parentheses. By applying the zero width approximation to the W propagator, these diagrams can be split into two sets of diagrams, which we call M_P and M_D respectively:

M_P =

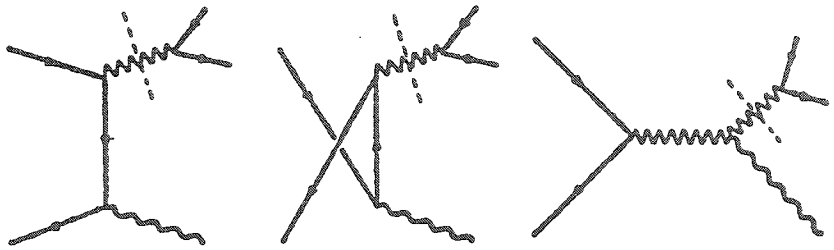

"production" process:
$d\bar{u} \to W\gamma$; $W \to \ell\bar{\nu}_\ell$

M_D =

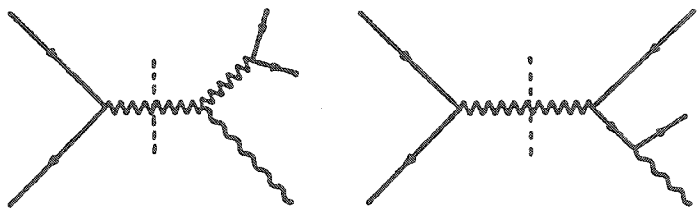

"decay" process:
$d\bar{u} \to W$; $W \to \gamma\ell\bar{\nu}_\ell$

The W propagators where we applied the zero-width approximation are cut by dashed lines. We shall treat the "production" and "decay" process separately, as they contribute in different regions of phase space; this can be seen in the distribution of the cluster transverse mass[3] defined as

$$m_T^2(\gamma\ell,\bar{\nu}_\ell) = (\sqrt{p_T^2(\gamma\ell)+m^2(\gamma\ell)} + p_T(\bar{\nu}_\ell))^2 - (\vec{p}_T(\gamma\ell) + \vec{p}_T(\bar{\nu}_\ell))^2 \,. \qquad (3a)$$

The cluster transverse mass is bound by the invariant mass,

$$m_T(\gamma\ell,\bar{\nu}_\ell) \leq m(\gamma\ell\bar{\nu}_\ell) \,. \qquad (3b)$$

In Fig. 1, we show the $m_T(\gamma\ell,\bar{\nu}_\ell)$ distribution.

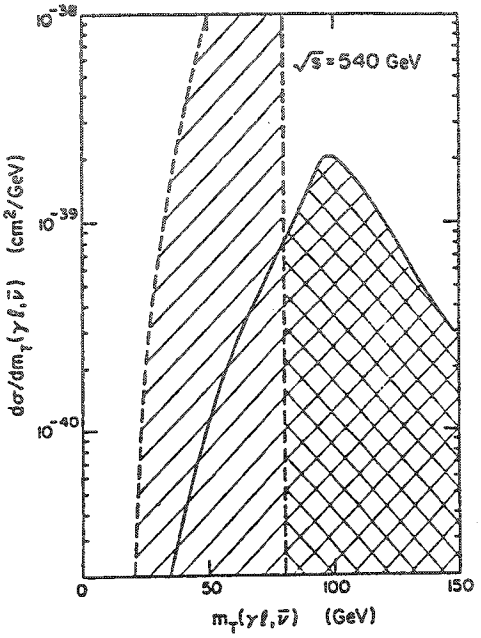

Fig. 1. Cluster transverse mass distribution of a process $p\bar{p} \to e\bar{\nu}\gamma + X$ at $\sqrt{s} = 540$ GeV. As a consequence of Eq. (3b) we can define two kinematical regions: 1) $m_T(\gamma\ell,\bar{\nu}_\ell) > m_W$: only the production process $p\bar{p} \to W\gamma X$; $W \to \ell\bar{\nu}_\ell$ is kinematically allowed. 2) $m_T(\gamma\ell,\bar{\nu}_\ell) < m_W$: the main contribution in this region comes from the decay process $p\bar{p} \to W$; $W \to \gamma\ell\bar{\nu}_\ell$. Note the Jacobian peak at $m_T(\gamma\ell,\bar{\nu}_\ell) = m_W$.

2.1 The production process $p\bar{p} \to W\gamma X$; $W \to \ell\bar{\nu}$ [4]

According to the theorem on radiation zeros [5] the amplitude M_p has a zero at

$$\frac{Q_d}{p_1 \cdot p_\gamma} = \frac{Q_{\bar{u}}}{p_2 \cdot p_\gamma} \tag{4a}$$

where $Q_d(Q_{\bar{u}})$ is the electric charge of the $d(\bar{u})$ quark. In the partonic c.m. frame this reads

$$\cos\theta^*_\gamma = \frac{1}{3} \quad , \quad \theta^*_\gamma \sphericalangle (\vec{p}_1, \vec{p}_\gamma) \; . \tag{4b}$$

To reconstruct this c.m. angle θ^*_γ from the final state we need to know the longitudinal momentum of the W boson (or equivalently the longitudinal momentum of the $\bar{\nu}_\ell$). In the zero width approximation there are two solutions for $\cos\theta^*_\gamma$ which we call $\cos\theta^*_\pm$; its explicit form can be found in Ref. 4. Because of the "V-A" structure of the W boson-fermion coupling and the tendency of the photon to follow the $\bar{u}$ quark rather than the d quark direction, the quantity θ^*_- is most of the time the true scattering angle. In Fig. 2 we show the $\cos\theta^*_-$ distributions at $\sqrt{s} = 2000$ GeV for different values of κ.

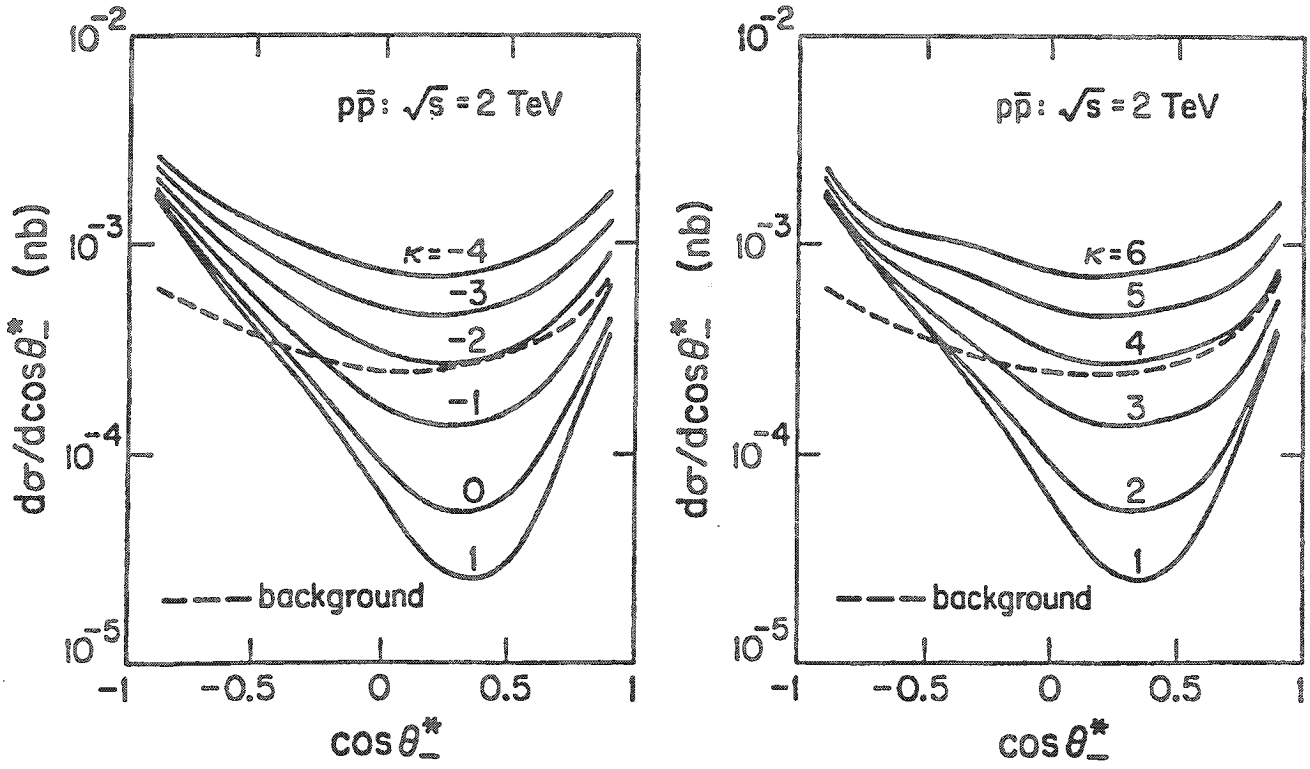

Fig. 2. $\cos\theta^*_-$ distribution for the process $p\bar{p} \to W\gamma X$; $W \to \ell\bar{\nu}_\ell$ at $\sqrt{s}$ = 2000 GeV for different values of the anomalous magnetic moment κ of the W boson. The following cuts are imposed: $|\vec{p}_{\gamma T}|, |\vec{p}_{\ell T}| > 10$ GeV; $m_T(\gamma\ell, \bar{\nu}_\ell) > 90$ GeV and $|y_\ell|, |y_\gamma| < 3$ where $y_\gamma(y_\ell)$ is the rapidity of the photon (charged lepton) in the $p\bar{p}$ c.m. frame. We used the distribution functions of Ref. 6 with $Q^2 = (p_1+p_2)^2 = \hat{s}$. The dashed lines denote the estimated background (to be discussed in Section 3) from $p\bar{p} \to W"\gamma"X$ where "γ" represents a jet that may fake photons.

2.2 The decay process $p\bar{p} \to WX$; $W \to \gamma\ell\bar{\nu}$ [7]

The theorem on radiation zeros [5] states that if we have a neutral and massless particle a zero appears in the amplitude when the photon is collinear to this neutral particle:

$$p_{\bar{\nu}} \cdot p_\gamma = 0 \to M_D = 0 \ . \tag{5a}$$

In the rest frame of the W boson the condition (5a) reads

$$\cos\theta^*_{\gamma\ell} = -1 \qquad \theta^*_{\gamma\ell} \measuredangle (\vec{p}_\ell, \vec{p}_\gamma) \ . \tag{5b}$$

Similar to the case of the production process, there are two solutions $\cos\theta^*_{\gamma\ell\pm}$ for the photon-lepton opening angle $\cos\theta^*_{\gamma\ell}$ in terms of the observable final state

variables; its explicit expressions can be found in Ref. 7. In Fig. 3 we present the $\cos\theta^*_{\gamma\ell^-}$ distribution.

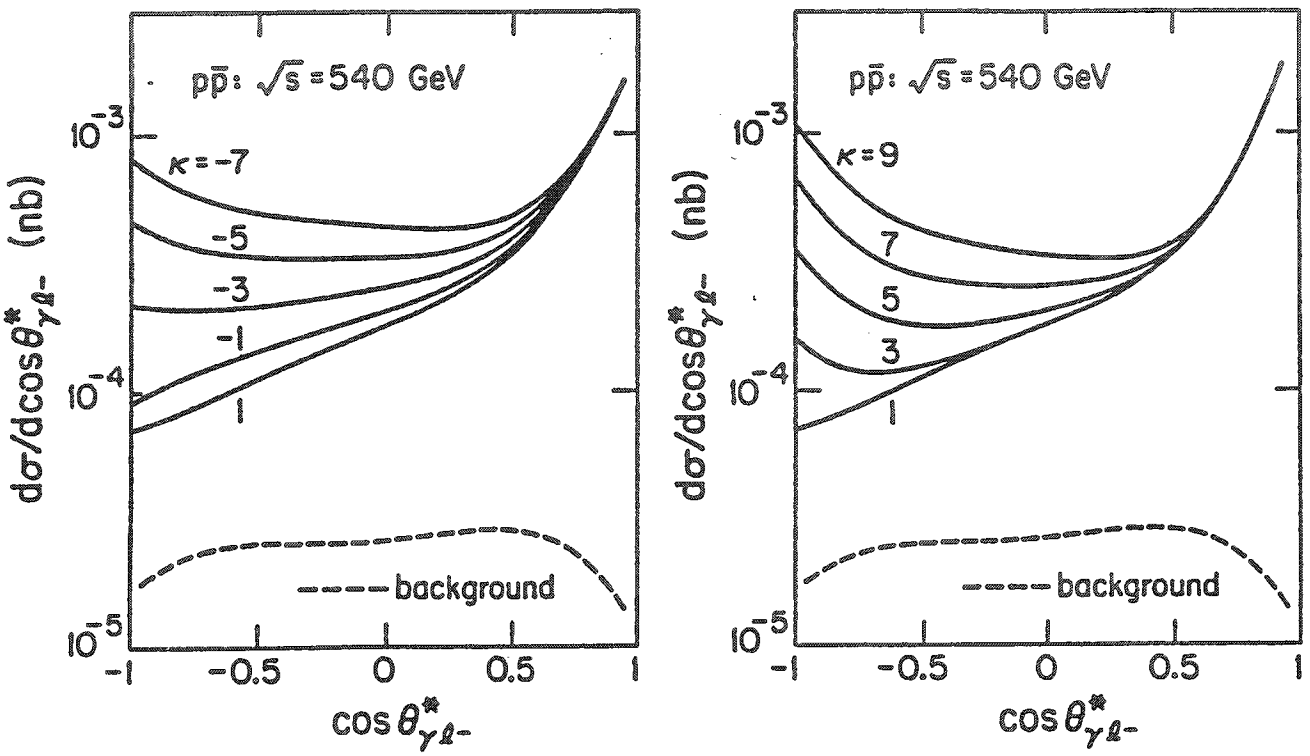

Fig. 3. $\cos\theta^*_{\gamma\ell^-}$ distribution for the process $p\bar{p} \to WX$, $W \to \gamma\ell\bar{\nu}_\ell$ at $\sqrt{s}$ = 540 GeV for different values of the anomalous magnetic moment κ of the W boson. The following cuts are imposed: $|\vec{p}_{\gamma T}|, |\vec{p}_{\ell T}| > 10$ GeV, 30 GeV $< m_T(\gamma\ell, \bar{\nu}_\ell) <$ 90 GeV, $|y_\ell|, |y_\gamma| < 3$ and $|\cos\theta_{\gamma\ell}| < .95$ where $\Theta_{\gamma\ell}$ is the photon-lepton opening angle in the $p\bar{p}$ c.m. frame. We used the distribution functions of Ref. 6 with $Q^2 = \hat{s}$. The dashed lines denote the estimated background (to be discussed below) from $p\bar{p} \to W$"γ" where "γ" stands for a jet that may fake photons.

3. BACKGROUNDS

To extract the signal from the bulk of data three requirements have to be met: i) high transverse momentum, isolated charged lepton, ii) large missing transverse momentum, and iii) high transverse momentum isolated photon. The successful identification of $W \to \ell\bar{\nu}$ events by UA1 and UA2 have demonstrated the effectiveness of the first two trigger conditions[8]; therefore we need to worry only about backgrounds that fake the third trigger condition. Main backgrounds will come from the process:

$$\begin{array}{ccccccc} p\bar{p} & \to & W & + & \text{jet} & + & X\,, \\ & & \hookrightarrow \ell\bar{\nu}_\ell & & \hookrightarrow \text{"}\gamma\text{"} & & \end{array} \qquad (6)$$

where a QCD jet fakes a photon. The contribution from the cascade process $p\bar{p} \to W + \text{jet} + X$; $W \to \tau\bar{\nu}$; $\tau \to \ell\bar{\nu}\nu$ turns out to be small, but we have included it in our analyses. Assuming a rejection rate $P_{"\gamma"/\text{jet}} = 1/200$, as suggested by Isajet analysis[10], we obtain the dashed lines given in Figs. 2 and 3 for the background estimate.

4. EFFECTS OF FINITE W-WIDTH AND HIGHER ORDER QCD CORRECTIONS

By dropping the zero width approximation for the W propagator, we have extra contributions such as an interference between "production" and "decay" amplitudes which destroy the separate radiation zeros at Eq. (4) and Eq. (5). We evaluated these $O(\alpha)$ effects since the $\cos\theta^*_-$ distribution in Fig. 2 shows a drop-off of a factor of 100 due to the radiation zero. We found[11] that the effect is numerically negligible in both the $\cos\theta^*_-$ as well as in the $\cos\theta^*_{\gamma\ell-}$ distributions.

The QCD higher-order corrections of $O(\alpha_s)$ may be more serious. In the case of the "decay" process, however, we expect small radiative corrections in $\cos\theta^*_{\gamma\ell-}$ distributions. This is because gluon emission in the initial state can only affect the polarization of the W boson. On one hand, this cannot influence the distribution near the zero at $\cos\theta^*_{\gamma\ell} = -1$ because every polarization amplitude has a zero at the same place. On the other hand, it has been shown[7] that the $\cos\theta^*_{\gamma\ell-}$ distribution for the decay of a longitudinally polarized W boson is almost identical to the $\cos\theta^*_{\gamma\ell}$ distribution for the decay of an unpolarized W boson in the entire $\cos\theta^*_{\gamma\ell}$ region.

In the case of "production" we find no heuristic argument about the size of higher-order corrections. It is a challenging task for theorists to study quantitatively the effects of higher-order corrections to the dip structure shown in Fig. 2.

5. CONCLUSIONS

Adding up all $e^{\pm}$, $\mu^{\pm}$ contributions, we show in Table 1 the expected event rates for $\kappa = 1$ at CERN and Fermilab colliders. We have not included the QCD motivated K-factor.

Table 1. Number of $(\gamma\ell\bar{\nu}_\ell)$ events expected at colliders by assuming an integrated luminosity $\int_{\text{year}} \mathcal{L}\, dt = 10^{37}\ \text{cm}^{-2}$. $\kappa = 1$.

$\sqrt{s} = 540$ GeV		$\sqrt{s} = 2$ TeV	
Production	Decay	Production	Decay
3 events	24 events	30 events	135 events

By considering rate, background, and effects of $O(\alpha_s)$ corrections, we find that the best place to probe the WWγ coupling at present-day $p\bar{p}$ colliders is the radiative decay process, $W \to \ell\bar{\nu}\gamma$. We urge experimentalists to look at this triple coupling that is of outstanding importance for any gauge theory of the electroweak interaction.

6. ACKNOWLEDGMENTS

This research was supported in part by the University of Wisconsin Research Committee with funds granted by the Wisconsin Alumni Research Foundation, and in part by the Department of Energy under contract DE-AC02-76ER00881.

7. REFERENCES

1. S. L. Glashow, Nucl. Phys. 22, 579 (1961); S. Weinberg, Phys. Rev. Lett. 19, 1264 (1967); A. Salam in Elementary Particle Theory, ed. by N. Svartholm (Almquist & Wiksell, Stockholm, 1968), p. 367.
2. T. D. Lee and C. N. Yang, Phys. Rev. D128, 885 (1962).
3. V. Barger, A. D. Martin and R.J.N. Phillips, Phys. Lett. 25B, 339 (1983).
4. J. Cortés, K. Hagiwara and F. Herzog, Madison preprint MAD/PH/102 (April, 1983).
5. C. J. Goebel, F. Halzen and J. P. Leveille, Phys. Rev. D23, 2682 (1981); Z. Dongpei, Phys. Rev. D22, 2266 (1980); S. J. Brodsky and R. W. Brown, Phys. Rev. Lett. 49, 966 (1982); R. W. Brown, K. L. Kowalski and S. J. Brodsky, Phys. Rev. 28, 264 (1983).
6. A. J. Buras and K.J.F. Gaemers, Nucl. Phys. B132, 249 (1978); J. F. Owens and E. Reya, Phys. Rev. D17, 3003 (1978).
7. J. Cortés, K. Hagiwara and F. Herzog, Madison preprint MAD/PH/108 (April, 1983).
8. UA1 collaboration, Phys. Lett. 122B, 103 (1983); UA2 collaboration, Phys. Lett. 122B, 476 (1983).
10. S. A. Kahn, T. J. Killian, M. J. Murtagh and F. E. Paige, "Monte Carlo study of $pp \to W^{\pm}\gamma X$ at CBA", BNL informal report 3/83 (1983).
11. J. Cortés, K. Hagiwara and F. Herzog, Madison preprint MAD/PH/164 (April, 1984).

The New Events

EXPERIMENTAL OBSERVATION OF EVENTS WITH LARGE MISSING TRANSVERSE ENERGY ACCOMPANIED BY A JET OR A PHOTON(S) IN $p\bar{p}$ COLLISIONS AT $\sqrt{s}$ = 540 GeV

UA1 Collaboration, CERN, Geneva, Switzerland

Presented by C. Rubbia, CERN

No written contribution received

Abstract from Physics Letters, 139B, 115 (1984)

We report the observation of five events in which a missing transverse energy larger than 40 GeV is associated with a narrow hadronic jet and of two similar events with a neutral electromagnetic cluster (either one or more closely spaced photons). We cannot find an explanation for such events in terms of backgrounds or within the expectations of the Standard Model.

OBSERVATION OF ELECTRONS PRODUCED IN ASSOCIATION WITH HARD JETS AND LARGE MISSING TRANSVERSE MOMENTUM IN $p\bar{p}$ COLLISIONS AT $\sqrt{s}$ = 540 GeV

The UA2 Collaboration

Bern - CERN - Copenhagen (NBI) -Orsay (LAL) - Pavia - Saclay (CEN) Collaboration

Presented by A.ROUSSARIE, SACLAY

ABSTRACT

Using a sample of events collected by UA2 and corresponding to an integrated luminosity of 116 nb^{-1}, we have searched for electron-"neutrino" pairs in which the tranverse momenta of the electron and of the "neutrino" exceed 15 GeV/c and 25 GeV/c respectively. A total of 35 events are observed in low background conditions. Most events can be interpreted in terms of W production from QCD processes. Four events in which the observation of hard jets makes this interpretation unlikely are described in detail. Possible sources of background contamination are considered.

1. INTRODUCTION

In a previous publication[1], we have studied a sample of events recorded by UA2 at the $Sp\bar{p}S$ collider, which contain an electron candidate in the final state with a transverse momentum $p_\perp$ (e) in excess of 15 GeV/c and no significant transverse energy detected at opposit azimuth. These events were analysed in terms of the production and decay of the electroweak bosons $W^\pm$.

The purpose of this presentation is to report on a systematic search for events containing an electron-"neutrino" pair in the final state, whatever the transverse energy at opposite azimuth to the electron may be. The loss of rejection power against background (mainly two-jet events) resulting from having relaxed this constraint, is compensated by the requirement that both the electron and the "neutrino" (observed missing transverse energy) have large transverse momenta.

Our detector does not distinguish between one or several neutrinos and other possible non-interacting particles, such as the photino postulated by supersymmetry theories. In the remainder of this presentation the word "neutrino" must therefore be understood in a broad sense.

2. APPARATUS

The UA2 detector has been described in detail elsewhere[2]. We briefly recall its main features.

Apart from two narrow cones along the beams, the detector provides full azimuthal coverage in three distinct regions of polar angles : $40° < \theta < 140°$, the central region, and $20° < \theta < 40°$, $140° < \theta < 160°$, the forward regions.

In the centre of the detector a set of coaxial cylindrical drift and proportionnal chambers detect the charged particles produced in the collision and measure the position of the event vertex.

An array of 480 calorimeter cells, each cell covering a similar domain of longitudinal phase-space (15° of azimuth and $\simeq$ 0.2 units of rapidity), measures electron energies E(e) to a good accuracy. Each cell is segmented longitudinally to provide electron-hadron separation. While hadron showers are usually contained in the 4.5 absorption lengths of the central calorimeter, providing a measurement of jet energies, they only deposit a fraction of their energy in the forward calorimeters which are $\simeq$ 1.0 absorption length thick. These forward regions are equipped with

magnetic spectrometers which provide additional rejection power against hadrons and converted photons when searching for electrons. In addition they measure the momenta of charged jet fragments, the energy of π^0's being measured in the calorimeter cells.

In both the central and forward regions electron identification is significantly improved by preshower counters which accurately measure the match between the observed incident track and the developing shower.

3. EVENT SELECTION

For this analysis we retain only the data collected during the 1983 period for which the azimuthal coverage of the UA2 detection was complete[2]. The corresponding integated luminosity is 116 nb^{-1}.

In each event we reduce the final state to a set of transverse energy clusters according to simple algorithms which have been described elsewhere[1)2)].

3.1 Electron selection

The electron identification criteria have been described in detail in table 1 of Ref.1. A first set of selection cuts is applied on the calorimeter data only (cluster radius, energy leakage in the hadronic compartment). Further refined criteria make use of the charged track trajectories and of the early shower positions, as measured by the vertex detector and the preshower detector respectively, and look for their compatibility with the calorimeter cluster. Furthermore in the forward regions, the magnetic spectrometer allows additional checks on the momentum-energy match and permits to remove electrons originating from γ conversions where the e^+e^- pair is observed. Altogether we have measured[1)] that the probability for a jet to simulate an electron candidate is $0.4 * 10^{-5}$ in the forward detectors and $2.8 * 10^{-5}$ in the central one, while the global detection efficiency of the electron criteria is estimated to be 80% and 76% respectively.

The present analysis deals with a sample of 200 events containing an electron candidate having $p_\perp(e) > 15$ GeV/c. We discard 10 events in which the electron candidate is observed near the interface between the central region and one of the forward regions and is associated with nearby calorimeter energy in each of the two regions.

The sample of event satisfying the first level of election criteria (calorimeter cuts) but not the complete set of cuts will be used to evaluate the background as described in reference 1. The background contained in the electron sample for a given

topology is obtained, very simply, by normalizing the background sample of the same topology by a given constant number (1/140 for the data considered hereafter).

3.2 "Neutrino" selection

Each of the calorimeter clusters not identified as electron are called "jets" if their transverse energy exceeds 3 GeV. For each event we calculate the momentum $\vec{p}$ (transverse component $p_\perp$ and longitudinal component $p_{//}$) and energy E of the electron candidate (e) and of each individual jet (j) assumed to be massless. We also evaluate the momentum $\vec{p}$, energy E and mass m of various sets of particles such as the system of all jets, (J) or the system of electron and jets, (Je). The quantity $p_\perp(Je)$ measures the missing transverse momentum in the set of all detected particles resulting in clusters having $E_\perp > 3$ GeV. In a typical event, the softer particles carry together only a small transverse momentum and, if no large transverse momentum particle has escaped detection, the observation of a large $p_\perp(Je)$ reveals the presence of a neutrino (ν) with $p_\perp(\nu) \simeq p_\perp(Je)$.

4. DATA ANALYSIS AND BACKGROUND EVALUATION

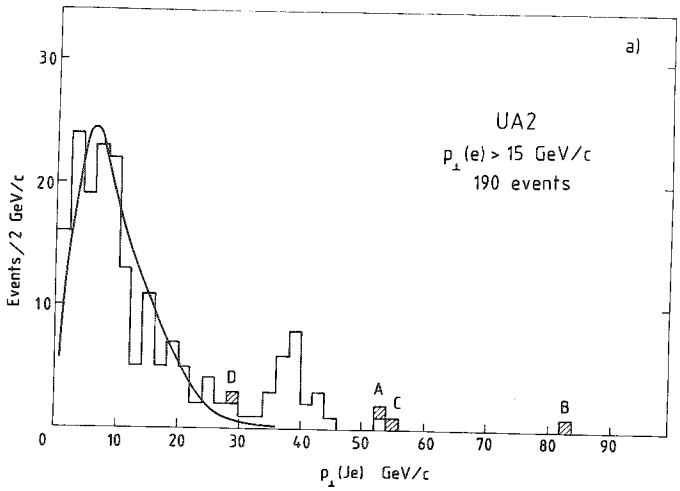

1.a)Transverse momentum distribution of the system of electron and jets in the initial sample of 190 events.

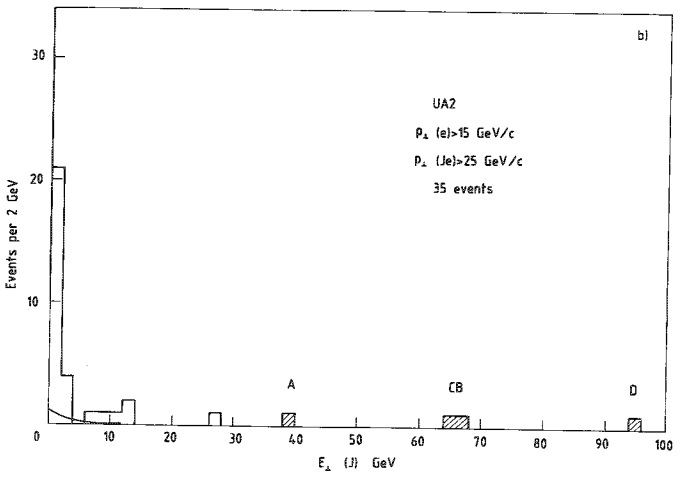

b)Transverse energy distribution of the system of jets in the sample of 35 events having $p_\perp(Je) > 25$ GeV/c. The lines correspond to the calculated background contaminations. The four events having $p_\perp(Je) > 25$ GeV/c, $E_\perp(J) > 30$ GeV, are cross-hatched.

The distribution of $p_\perp$(Je) is shown in Fig.1a. The background evaluation measures the probability that a mutijet event contains both a misidentified electron and an undetected jet (or jets) escaping the UA2 acceptance. Its distribution is shown as a curve superimposed on the data of Fig.1a.

In the remainder of this letter we restrict the analysis to the sample of 35 events which have $p_\perp$(Je) > 25 GeV/c, and which are therefore candidates for containing a large transverse momentum neutrino in the final state. The background contribution amounts to 3.4 ± 0.3 of these events.

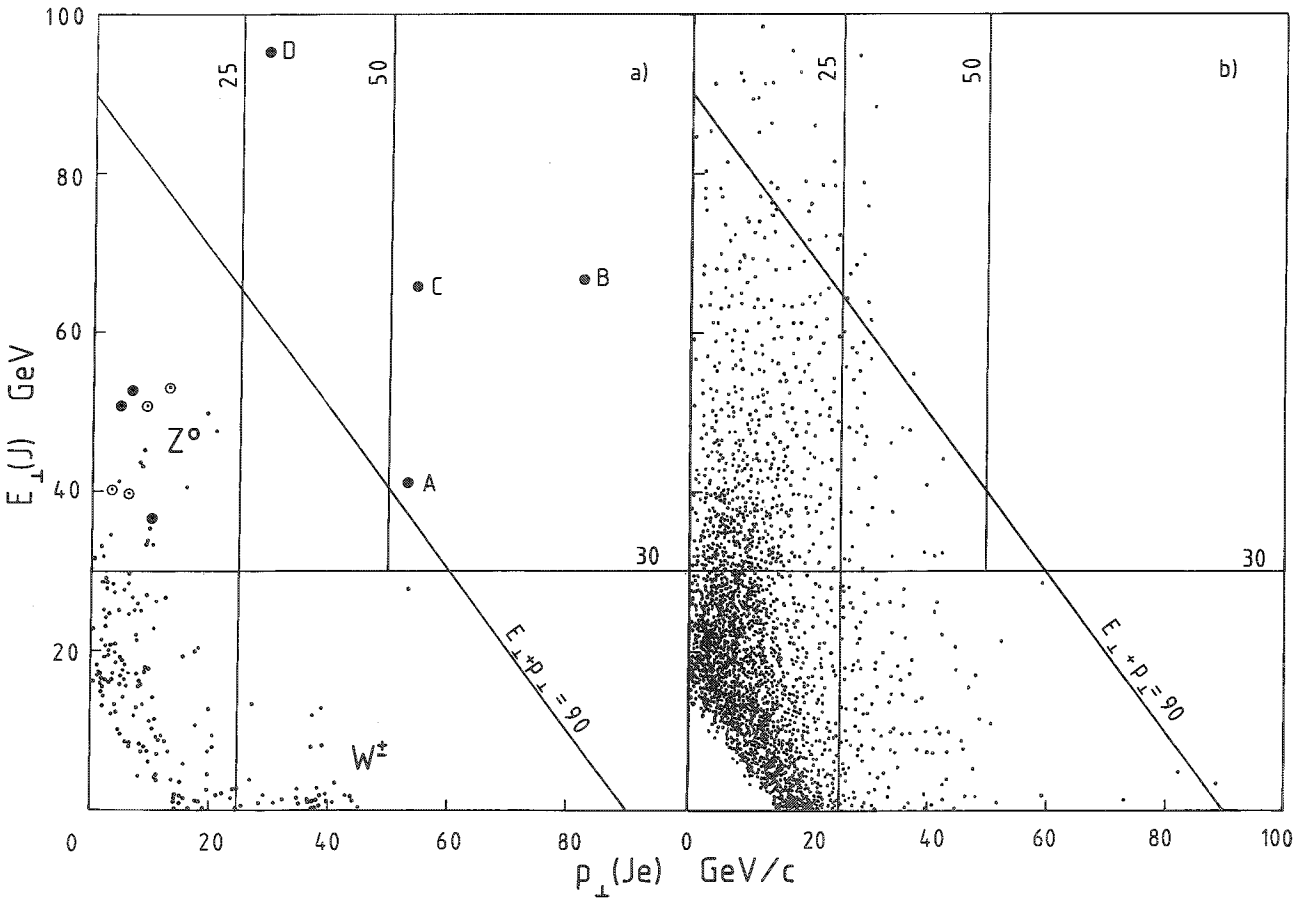

2.a)Distribution of the 190 events of the initial sample in the $p_\perp$(Je), $E_\perp$(J) plane. Seven Z° events are circled (the eighth one was collected during the 1982 period). The W region is indicated.

b)Distribution of the background sample in the $p_\perp$(Je), $E_\perp$(J) plane. A reduction factor of 141 must be applied to infer from this sample the background contamination to the sample of Fig.2a.

From the results of the analysis presented in Ref.1 we expect this sample to contain a number of events in which the observed electron carries most of the detected transverse energy, and is therefore accompanied by no jet or by jets having small transverse energies. The distribution of the sum of the jet transverse energies, $E_\perp(J)$, confirms this expectation (Fig.1b). The 31 events having $E_\perp(J) < 30$ GeV all belong to the samples of Figs. 4a and 4c in Ref.1, where they were interpreted in terms of $W \to e\nu$ decays. We do not comment further on these events. Instead we consider the four events having $E_\perp(J) > 30$ GeV. The distribution of the events in the $p_\perp(Je)$, $E_\perp(J)$ plane is shown in Fig. 2 for each of the signal and background samples. The background contamination expected in the region $p_\perp(Je) > 25$ GeV/c, $E_\perp(J) > 30$ GeV is $\simeq 0.45 \pm 0.04$ events. We first note how well the four events (labelled A,B,C and D) are isolated : remember that the background sample has to be normalized by $\sim 1/140$. In each of the four signal events the electron candidate is detected in the cental region of the UA2 detector. Their transverse momentum configurations are illustrated in Fig.3.

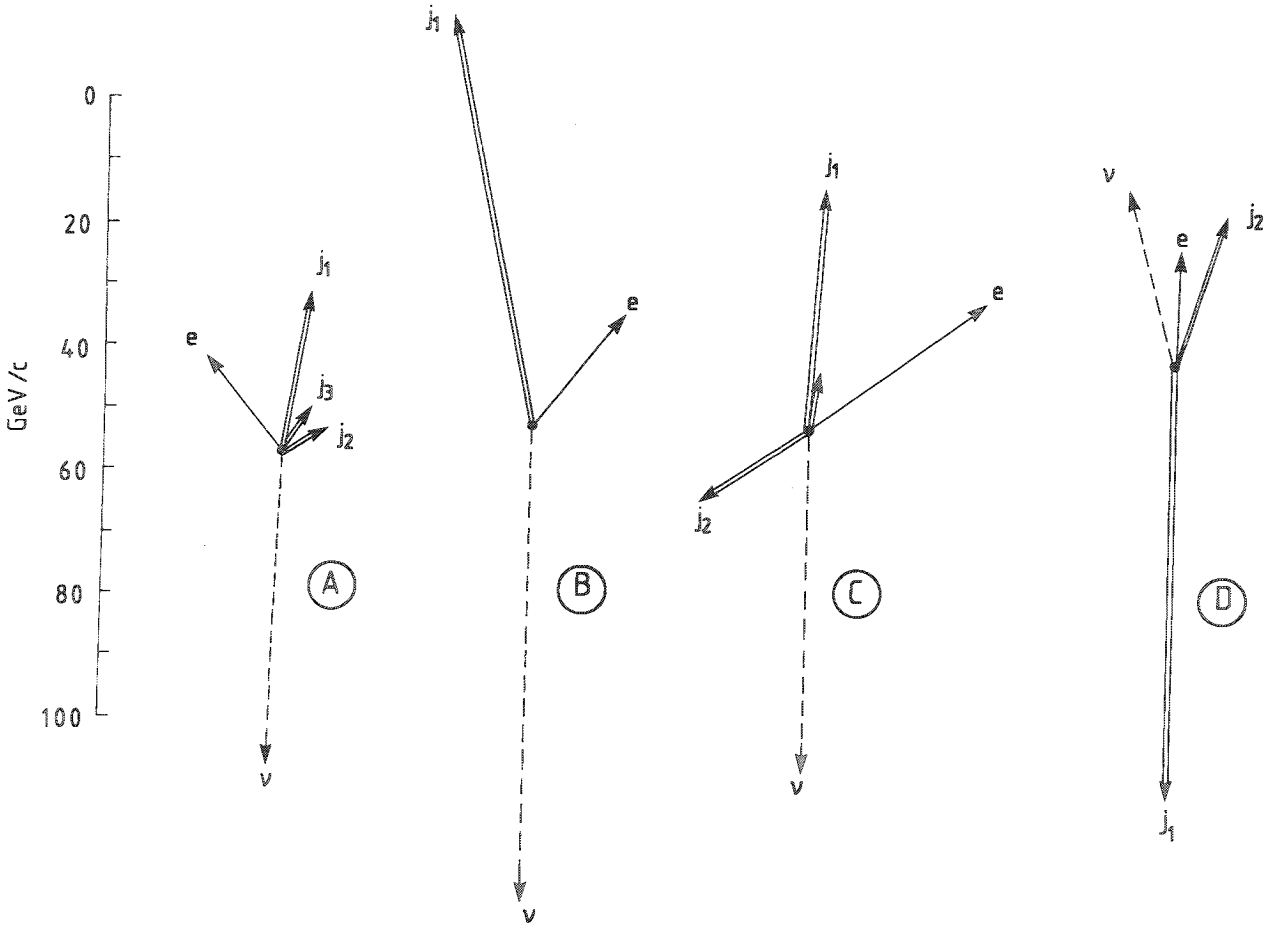

3. Transverse momentum configuration of the four events having $p_\perp(Je) > 25$ GeV/c and $E_\perp(J) > 30$ GeV. Their relative orientation is arbitrary.

For each event, in which $p_\perp(Je)$ and $E_\perp(J)$ take values p_0 and E_0 respectively, we evaluate the expected background contamination B_ν and B_J corresponding to the following configurations :

B_ν : $p_\perp(Je) > p_0$, $E_\perp(J) > 30$ GeV : (isolation along the $p_\perp(Je)$ axis)

B_J : $p_\perp(Je) > 25$ GeV/c, $E_\perp(J) > E_0$: (isolation along the $E_\perp(J)$ axis)

In each of the four events, either B_ν or B_J is always less than 0.02. Event D (B_J = 0.02, B_ν = 0.13) is mainly singular by the jet transverse energies. It is remarkable that there is no background event in the region $p_\perp(Je) > 50$ GeV/c, $E_\perp(J) > 30$ GeV, which contains events A to C. We infer from this a background contamination B_ν of at most 0.02 events (90% confidence level) in this region (see table 1).

The electron and neutrino misidentification is directly measured from the data themselves by the background evaluation. Nevertheless it is useful to add the following comments :

On the quality of the electron identification, we have checked that the characteristic parameters of the four events (see a few of them in table 1) agree well with the ones of the $W \to e\nu$ candidates. Each of the four events has been examined in detail with the help of a high resolution graphics display facility. The track multiplicity is of course higher here than in most of the $W \to e\nu$ events studied in Ref.1 and we cannot exclude that the increased complexity of the signal pattern in the central vertex detector could result in some deterioration of the electron identification power.

As far as neutrino identification is concerned, we have checked that in each of the four events there is no sign of large transverse momentum particle having hit passive parts of the UA2 detector, such as the magnet coils, in the azimuthal region where the neutrino is expected. However, in the case of event D which has an azimuthal configuration similar to that of a two-jet event (see Fig. 3), such an interpretation cannot be completely excluded. Jet j_2 lies close to the central-forward interface and lost energy may have generated the "neutrino". In the cases of events A to C, large transverse momentum particles may have escaped detection because they were produced at small angle to the beam line. We considered for each event the possibility that a jet having the same transverse momentum as the neutrino candidate be produced at θ = 15 ° (or 165 °). Under such an assumption we can calculate a lower limit for the invariant mass of the system of all large transverse momentum particles produced in the event, including the small angle undetected jet. In the case of events A to C they correspond to impossible or very unlikely kinematical configurations.

More generally we know that, for high mass two-jet events, the probability for one jet to escape detection in the UA2 detector, is smaller than 10%. If events A to C were such events, appearing at (p_0, E_0) in the $p_\perp(Je)$, $E_\perp(J)$ plane of Fig.2, we should observe at least ten times more events with the two jets being detected. They would have appeared in Fig.2 with $p_\perp(Je)$ small and $E_\perp(J) \simeq p_0 + E_0$.

But the only events having $p_\perp(Je) + E_\perp(J) > 90$ GeV are precisely the four events of Fig.3. The absence of other events in this region, even with low values of $p_\perp(Je)$, excludes such an interpretation.

A muon can in principle simulate a neutrino in the UA2 detector. Although we know of no mechanism which could produce a very massive electron-muon pair at a detectable rate, we looked, in each of the four events, for a track in the vertex detector near the neutrino azimuth and associated with calorimeter energy consistent with the response to a minimum ionizing particle. We found none.

In each of the four events in Fig.3 the sharing of the jet energies between the various calorimeters compartments[2] is consistent with expectation. Moreover, each jet contains several tracks having their origin at the event vertex. These observations exclude interpretations in terms of a cosmic ray or beam-gas background.

5. EVENT INTERPRETATION

In this section we study possible sources for events A to D, under the assumption that they contain a genuine $e\nu$ pair.

Event D contains a narrow $e\nu$ pair ($\Delta\Phi \simeq 17°$). It consists of a large transverse momentum jet ($p_\perp(j_1) = 70$ GeV/c) emitted at opposite azimuth to the electron-neutrino pair and to a smaller transverse momentum jet ($p_\perp(j_2) = 25$ GeV/c). The invariant mass of the $(e\nu j_2)$ system depends upon the unknown value of $p_{//}(\nu)$. It takes its minimum value, 25 ± 6 GeV/c^2, when the neutrino has the same rapidity as the (ej_2) system. In this case $m(e\nu j_1 j_2) = 145 \pm 15$ GeV/c^2. The configuration of this event suggests an interpretation in terms of a quark-antiquark pair, one member of which decays semileptonically. However, because of the restriction we have made before on the "neutrino" identification of event D, because of the absence of other events with similar topologies and because of the similarity of its configuration with that of a two-jet event, we prefer to defer such an interpretation until other events of the same kind have been observed.

In the three other events (A to C), the $e\nu$ pair has a large azimuthal opening ($\Delta\Phi > 120°$). The transverse mass of the $e\nu$ pair (Table 1) ranges between 56 GeV/c^2 and 82 GeV/c^2, suggesting an interpretation in terms of a $W \to e\nu$ decay, the W boson being the only known particle with a large enough mass. It is indeed possible to adjust the unknown value of $p_{//}(\nu)$ to obtain $m(e\nu) = m(W)$ and to describe the events in terms of associated W-jet(s) production. There are in general two solutions to this problem, associated with different values of $p_{//}(WJ) \equiv x_F(WJ)\sqrt{s}/2$ and of m(WJ). We retain the solution minimizing $|x_F(WJ)|$ (see Table 1).

The distribution of m(WJ) is shown in Fig.4 for all events having $p_\perp(Je) > 25$ GeV/c. While the 31 events having $E_\perp(J) < 30$ GeV cluster in the neighbourhood of $m(WJ) = m(W)$, the three events of Table 1 populate the region $160 \leq m(WJ) \leq 180$ GeV/c^2, which might suggest an interpretation in terms of a heavy object decaying into a W boson and a system J of other particles. However, the significance of this observation is weakened by the fact that the background events have a similar m(WJ) distribution (Fig.4) implying that the clustering in mass might simply result from kinematics. In addition such an interpretation should account for the fact that in events A and B, J consists essentially of a single jet, while in event C it consists of a large mass pair of jets.

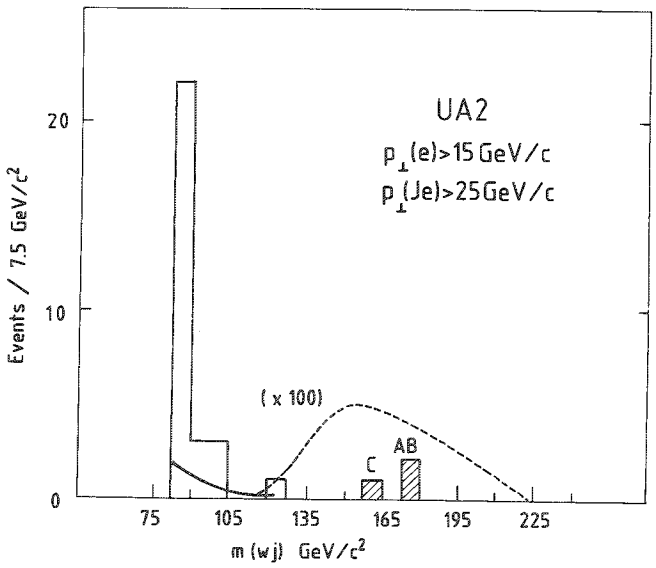

4.Distribution of m(WJ) for the 35 events having $p_\perp(Je) > 25$ GeV/c. Events having in addition $E_\perp(J) > 30$ GeV are cross-hatched. The smooth line corresponds to the calculated background. The dotted line is the background distribution (multiplied by 100) for events having $E_\perp(J) > 30$ GeV.

If these events are $W \to e\nu$ decays, we would like to know if the system of large transverse momentum jets associated to them is understandable in terms of a conventional known processes like QCD. What is the probability to produce these jets in association with the W? A reasonable upper limit can be obtained from UA2 multijet events[3] by measuring the probability to find , associated with a pair of jets $j_1 j_2$ (having the same configuration as the $e\nu$ pair ascribed to the W), a jet system (J). We state that

$$\frac{\sigma(p\bar{p} \to W + J + \ldots)}{\sigma(p\bar{p} \to W + \ldots)} \leq \frac{\sigma(p\bar{p} \to j_1 j_2 + J + \ldots)}{\sigma(p\bar{p} \to j_1 j_2 + \ldots)}$$

We evaluate such upper limits for events A to C from the sample of jet events described in Ref.3. We take as J any jet (jet pair) having a transverse momentum (invariant mass) at least as large as that of the corresponding jet (jet pair) in events A and B (C). From the total number of observed $W \to e\nu$ events (31), we compute N_{QCD}, upper limit to the number of events W + J expected to be produced via conventional QCD. The results, listed in Table 1, include the different acceptances of the UA2 apparatus to $e\nu$ pairs and to jet pairs. They indicate that events B and C, if they indeed contain a genuine $W \to e\nu$, are difficult to understand in terms of associated W-jet(s) production via known processes. Event A, on the other hand, has an unlikely high value of $x_F(WJ)$, corresponding to a W longitudinal momentum of nearly 150 GeV/c. The probability to find partons inside the beams to produce it, is only 6%.

In addition to the instrumental uncertainties quoted in Table 1, the measured jet energies are expected to be somewhat smaller than that of the parent partons (we neglect the jet mass and we do not include jet fragments which do not contribute to the transverse energy cluster). These effects are not corrected for in Table 1. Using the ISAJET programme[4] to simulate W decays into a pair of light quarks, we find that the two-cluster mass is measured $\simeq 15$ GeV/c^2 lower than m(W). Therefore the value m(J) = 63 ± 5 GeV/c^2 obtained for event C is not inconsistent with the hypothesis that J results from a W decay.

Finally we note that the interpretation of the $e\nu$ pair in terms of a W decay in events A to C is by no means mandatory because the missing transverse momentum does not need to be ascribed to a single neutrino but might be shared among several undetected particles.

6. CONCLUSION

A search of events containing an electron-neutrino pair having $p_\perp(e) > 15$ GeV/c and $p_\perp(\nu) > 25$ GeV/c has resulted in a sample of 35 events, the majority of which have been previously studied[1] and interpreted in terms of W production, with characteristic properties in agreement with QCD predictions.

Four events have been found, in which the $e\nu$ pair is produced in association with a jet, or a system of jets, having very large transverse energies. We have given a detailed description of these events and we have considered possible sources of background contaminations.

Three of these events contain a large transverse mass $e\nu$ pair and have been interpreted in terms of W-jet(s) associated production. However, their configurations are such that their production via known processes is very unlikely for at least two of them. In each of the three events the invariant mass of the w-jet(s) system is measured to be in the vicinity of 170 GeV/c^2, but the significance of this observation is weakened by the fact that this mass region is kinematically favoured by the selection criteria.

Interpretations in terms of new processes, including the possibility of ascribing the observed missing transverse energy to particles other than a single neutrino, have not been explicitely considered.

While the present study indicates that we have observed events corresponding to a genuine signal and suggests the existence of a new phenomenon, more data need to be collected in order to place this result on firmer ground.

REFERENCES

1. P. Bagnaia et al., UA2 Coll., A study of high transverse momentum electrons produced in pp collisions at 540 GeV, CERN-EP/84-39, March 26 1984, submitted to Z. Phys. C.

2. B. Mansoulié, The UA2 apparatus at the CERN pp Collider, Proceedings 3rd MOriond workshop on pp physics, editions Frontières, 1983, p. 609.

3. P. Bagnaia et al., UA2 Coll., Measurement of very large transverse momentum jet production at the CERN pp Collider, CERN-EP/84-12, February 2nd 1984, submitted for publication in Phys.Lett. B.

4. F. Paige and s. Protopopescu, ISAJET, BNL report 31987 (1981).

Table 1 : Event parameters

Events		A	B	C	Units
Electron	$p_T(e)$	18.3 ± 0.8	22.0 ± 0.9	34.4 ± 3.2	GeV/c
	η (e) a)	0.02	-0.23	0.24	
	$P(\chi^2)$ b)	0.97	0.76	0.002	
	d^2 b)	13	7	14	mm^2
	q_s b)	10	8	22	mip
Jets f)	$p_T(j_1)$	27 ± 3	67 ± 7	38 ± 5	GeV/c
	η (j_1) a)	-0.59	-0.26	0.07	
	$\Delta\phi(j_1)$ c)	50	310	311	degrees
	$p_T(j_2)$	6 ± 1		21 ± 3	GeV/c
	η (j_2) a)	0.50		0.12	
	$\Delta\phi(j_2)$ c)	93		183	degrees
	$p_T(j_3)$	5 ± 1		7 ± 1	GeV/c
	η (j_3) a)	-1.09		-1.38	
	$\Delta\phi(j_3)$ c)	70		316	degrees
	$E_T(J)$	39 ± 4	67 ± 7	66 ± 6	GeV
	m (J)			63 ± 5	GeV/c^2
	$p_T(\nu)$	51 ± 4	86 ± 6	57 ± 5	GeV/c
	$\Delta\phi(\nu)$ c)	220	141	141	degrees
	$m_T(e\nu)$	56 ± 2	81 ± 3	82 ± 4	GeV/c^2
	m (WJ)	179 ± 7	176 ± 9	162 ± 8	GeV/c^2
	x_F(WJ)	0.45 ± 0.04	-0.01 ± 0.06	-0.04 ± 0.05	
	B_ν d)	<0.016(90%CL)	<0.016(90%CL)	<0.016(90%CL)	
	B_j d)	0.33 ± 0.03	0.06 ± 0.01	0.06 ± 0.01	
	N_{QCD} e)	0.4	$1.2\ 10^{-2}$	$7\ 10^{-3}$	

a) The pseudo-rapidity η is positive in the proton direction.

b) Electron quality parameters are defined in Ref. 1.

c) $\Delta\phi$ is the azimuth difference with respect to the electron (in degrees).

d) Background evaluations B_ν and B_j are described in the text (Section 4).

e) Number of W-jets events expected from known production processes (see text).

f) Jet energies are expected to be smaller than the parent parton energies (see text). This has not been corrected for and affects all parameters depending upon jet energies.

Heavy Flavours and Related Topics

$D^{*\pm}$ PRODUCTION AT THE CERN SPS COLLIDER
(UA1 Collaboration)

R. Frey
University of California
Riverside, California 92521

1. INTRODUCTION

We report evidence for the production of the charged D^* mesons in $\bar{p}p$ collisions at $\sqrt{s}$ = 540 GeV. The search was confined to the charged particle fragments of hadronic jets. Preliminary results for the fragmentation function and production rate for D^* are given.

The UA1 detector is described elsewhere [1]. We mention briefly the detector elements of importance for this study. The Central Detector, a large drift chamber immersed in a 0.7T dipole magnetic field, was used for momentum and ionization measurement of charged particles. The mean value of $\Delta p/p^2$ is $(0.9\times10^{-2})/(\text{GeV/c})$ for the data discussed here. Ionization accuracy is about ±10% for a track of 1m length. Total jet energy is measured with accuracy $\Delta E/E \simeq 20\%$ by electromagnetic and hadronic calorimetry consisting of lead/scintillator stacks followed by the instrumented iron of the magnet yoke used as a hadron calorimeter.

The work reported here is based upon the data sample recorded in 1983 with integrated luminosity 118 nb^{-1}. The following two simultaneously recorded triggers are relevant to this study:

i) An "electron trigger", namely at least 10 GeV of localized transverse energy deposited in the central electromagnetic calorimeters.

ii) A global "E_T trigger", requiring more than 60 GeV of total transverse energy in all calorimeters with $|\eta| < 1.5$.

The results presented here come from the 1.2×10^5 electron triggers having a localized electromagnetic cluster with transverse energy in excess of 15 GeV. These events were reconstructed for the W/Z search. However they also contain about 30% of all jets having $E_T > 20$ GeV. A subset (27%) of the trigger (i) events which also satisfied the global E_T trigger was selected for this study.

2. METHOD

Jets containing a minimum of three charged particles were identified by applying a clustering algorithm to charged particle tracks. The jets were required to satisfy the following conditions: $16 < p_T < 20$ GeV/c [2], $|\eta| < 1$ and $\phi > 45^\circ$ with respect to the horizontal plane. Jets closer to the horizontal plane were excluded because of the relatively poor momentum resolution in this region.

The search for D^* in jets of charged particles followed the now standard procedure of looking for evidence of the decay sequence $D^{*+} \to D^o\pi^+ \to K^-\pi^+\pi^+$ as well as the charge conjugate mode. (Both modes are implied by the mention of one throughout this paper.) $K\pi$ and $K\pi\pi$ mass combinations were formed from the charged tracks associated with the jets. No particle identification was used to distinguish between K and π, so both K and π assignments were considered for each track. However the central detector ionization measurement was used to identify $e^\pm$ arising from photon conversions in the beam pipe, delta rays, etc.; these slow electrons can mimic the π^+ from $D^{*+} \to D^o\pi^+$ which has a mean momentum of only about 0.4 GeV/c in the kinematic range under study.

Figures 1a,b show the mass difference $\Delta M \equiv M(K^-\pi_1^+\pi_2^+) - M(K^-\pi_1^+)$ for (a) all events, and (b) $1.83 < M(K^-\pi_1^+) < 1.92$ GeV/c. Figures 1c,d show the $K^-\pi_1^+$ invariant mass distribution for (c) all events and (d) $146 < \Delta M < 148$ MeV/c^2. A Gaussian fit to the peak in ΔM (fig. 1b) gives a mean of 147.0 MeV/c^2 and an rms deviation of 0.6 MeV/c^2, compatible with the estimated experimental resolution. The peak value is shifted by 1.6 MeV/c^2 from the canonical value of 145.4 ± 0.2 MeV/c^2 [3]. This effect is most likely associated with the traversal of the slow π^+ through the beam pipe. The fitted mass and width of the $K^-\pi^+$ peak in fig. 1d are 1.870 GeV/c^2 and 22 MeV/c^2, compatible with the known D^o mass and the estimated mass resolution.

3. RESULTS

3.1 Fragmentation Function

The peak at 147 MeV/c^2 in fig. 1b contains 22 events on a background of 7. We have investigated the distribution in $z \equiv \vec{p}_D^* \cdot \vec{p}_{jet}/(p_{jet})^2$ for these events. $\vec{p}_D^*$ is the D^* momentum measured in the central drift chamber and p_{jet} is the total jet momentum determined from the energy deposited in the calorimeter modules. When the total momentum of the charged particles in the jet was within 20^o of the vertical gap in calorimetry the event was excluded from consideration, and a visual scan was used to further eliminate events with acceptance related problems. The z distribution for the remaining 7 events is shown in fig. 2. The histogram shows the actual data; the points have been weighted to correct for inefficiency in detecting the slow pion in $D^* \to D\pi$ decay for D^* momentum below 6 GeV/c. This inefficiency increases rapidly below z of 0.1 and no attempt has been made here to extrapolate to $z < 0.1$. The values of p_{jet} for these events range from 25 to 45 GeV/c. The sensitivity of $\langle z \rangle$ to various alternative definitions of z is less than 10%.

3.2 Production Rate

We have observed 22 $D^{*\pm} \to K^{\mp}\pi^{\pm}\pi^{\pm}$ decays in a total of 3.4×10^3 jets meeting the conditions discussed in section 2. This number includes only jets with at least 3 tracks. The corresponding total number of jets (from calorimetry) in the same range of azimuth and rapidity is 4.0×10^3, with mean E_T of 27 GeV. The total number of $D^{*\pm}$ is obtained using $B(D^{*+} \to D^o\pi^+ \to K^-\pi^+\pi^+) = 1.3 \pm 0.4$ %, an efficiency for $z > 0.1$ of 0.42 ± 0.18, and a fraction of D^* events excluded by the mass cuts of 0.20 ± 0.13. Then $N(D^{*\pm})/N(\text{jet}) = 1.2 \pm 0.2 \pm 0.7$.

4. DISCUSSION AND CONCLUSION

Although the systematic error is large, the number of $D^{*\pm}$ per jet given above seems surprisingly high, and the number of D^{*o} could presumably be equal to $D^{*\pm}$. However we note that this measurement applies only to jets in events satisfying combined electron and global E_T triggers, and may well be different for an unbiased jet selection.

Several studies[4] of heavy quark production in e^+e^- annihilation indicate that jets initiated by the heavy quark fragment in such a way that the hadron carrying the heavy flavor takes a large fraction of the total jet momentum ($\langle z(D^*)\rangle \simeq 0.5$). However in $\bar{p}p$ interactions at $\sqrt{s}$ of 540 GeV, gluon rather than quark initiated jets are expected to dominate for jet E_T values below about 50 GeV[5,6]. Indeed the rate of charm production observed here is about a factor of 10^2 higher than predicted for c-quark initiated jets [5]; in addition the D^* fragmentation function (fig. 2) is much softer than those measured for c-quark initiated jets. A likely conclusion concerning the charm production reported here is then that it results from the fragmentation of gluon initiated jets, although production via the decay of a copiously produced heavy object can not be ruled out at this point. A gluon jet would give rise to production of charmed particles in pairs, each pair residing within the jet. Even so, the large charm content of jets observed here is perhaps a consequence of the flavor independence of the gluon-quark coupling.

REFERENCES AND FOOTNOTES

1. UA1 Collab., G. Arnison et al., Phys. Lett. 122B (1983) 103.
2. The lower limit is imposed due to low reconstruction efficiency of the π^+ from $D^{*+} \to D^o\pi^+$ at low momentum. Because of steeply falling spectra in p_T few $D^{*+} \to K^-\pi^+\pi^+$ are lost by imposing the upper limit, thus leaving a narrow range of p_T for the fragmentation function study.
3. Particle Data Group, Phys. Lett. 111B (1982).
4. See for instance, J. Dorfan, Proc. 1983 Symposium on Lepton and Photon Interactions at High Energy, Cornell, (Cornell University, 1983), p. 686.
5. R. Horgan and M. Jacob, Nucl. Phys. B179 (1981) 441.
6. See contribution at this conference by R. K. Ellis.

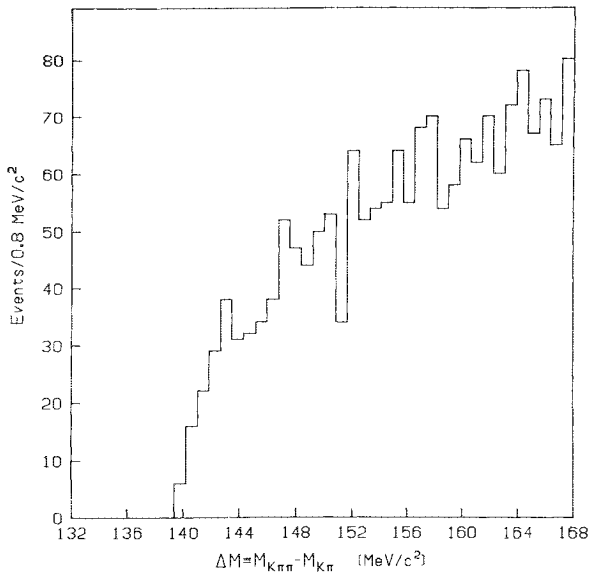

Fig. 1a. ΔM distribution in the region of $M(D^{*\pm})-M(D^{o})$ for all events.

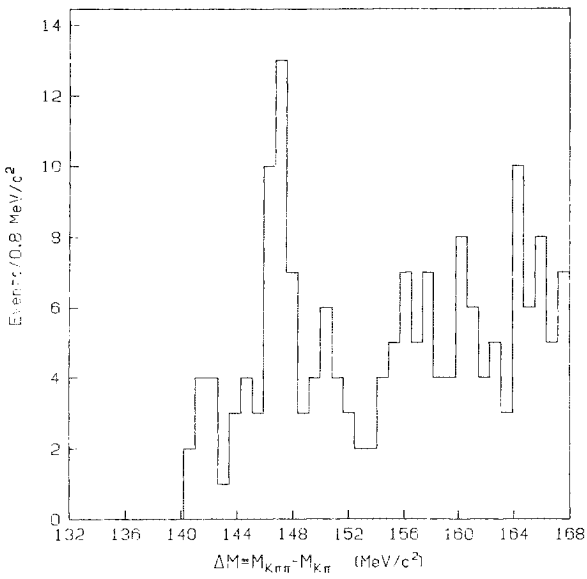

Fig. 1b. ΔM distribution for $1.83 < M(K\pi) < 1.92$ GeV/c^2.

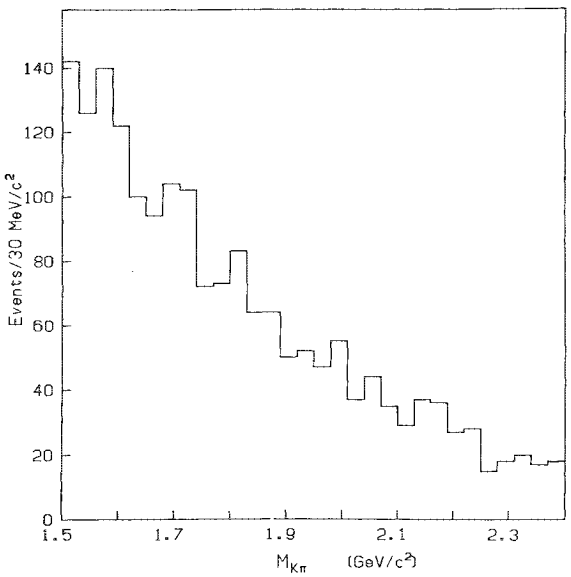

Fig. 1c. $M(K\pi)$ distribution in the region of $M(D^{o})$ for all events.

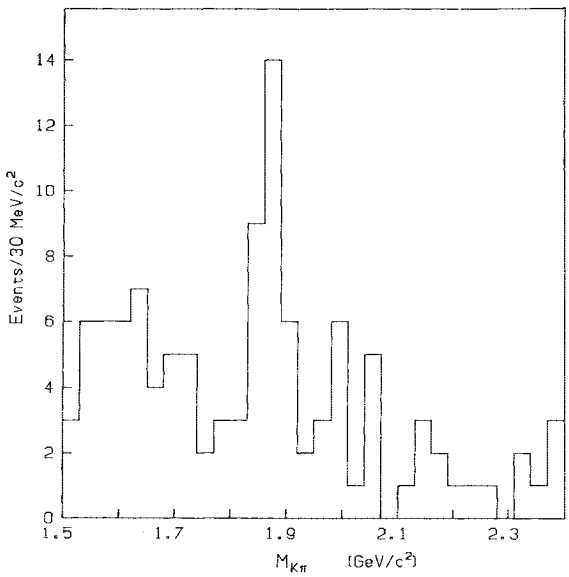

Fig. 1d. $M(K\pi)$ distribution for $146 < \Delta M < 148$ MeV/c^2.

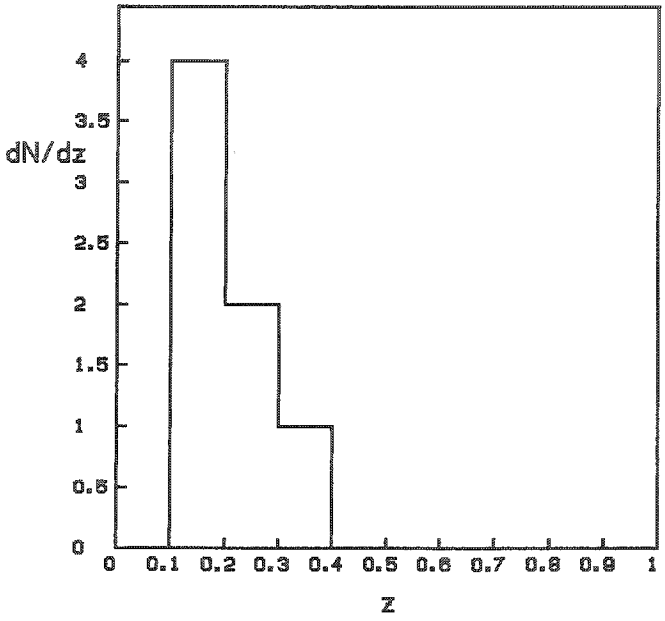

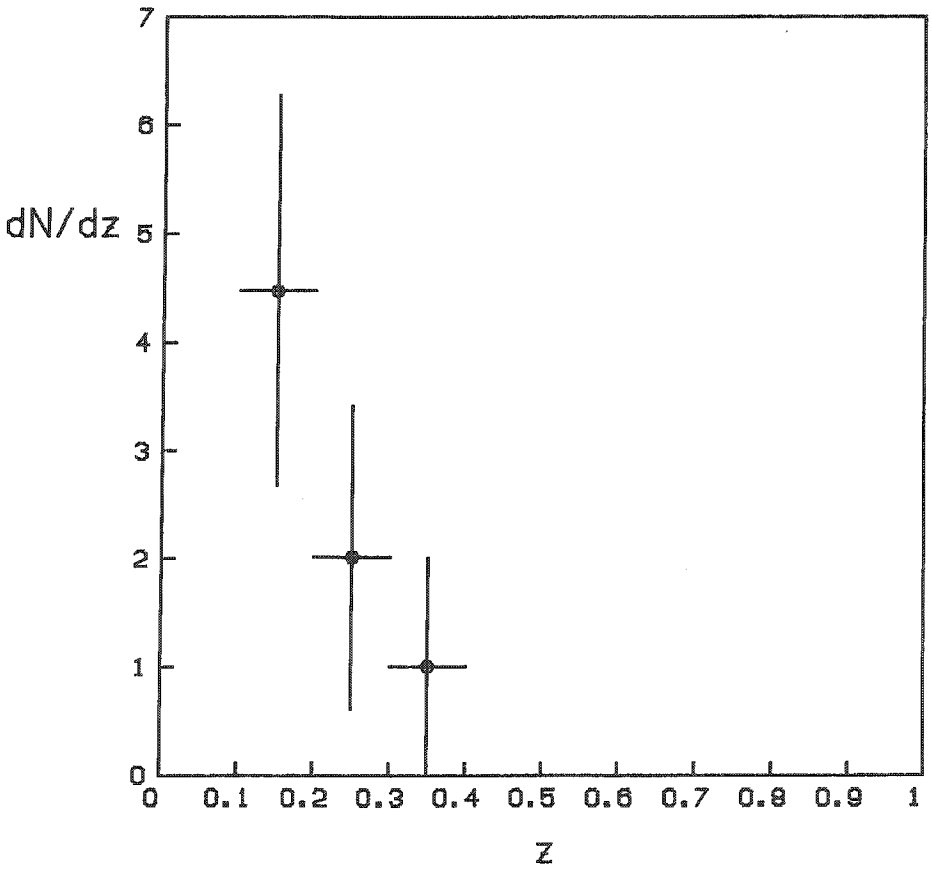

Fig. 2 $D^{*\pm}$ fragmentation function for $z > 0.1$. The histogram at top shows the uncorrected data. The bottom plot has been corrected for the track finding inefficiency of the $\pi^{\pm}$ from $D^{*\pm} \rightarrow D^{\circ}\pi^{\pm}$. The mean value of z for $z > 0.1$ is 0.2.

WEAK MIXING ANGLES AND HEAVY FLAVOURS

C. Jarlskog

Department of Physics
University of Stockholm
Stockholm, Sweden

ABSTRACT

The present status of the weak mixing angles, in the standard six quark model, is reviewed. The implications of the recent measurements of the beauty lifetime and branching ratios are discussed, in the framework of the Kobayashi-Maskawa and the Wolfenstein parametrizations. Expectations for $B^0 - \bar{B}^0$ mixing and consequences for the collider data are given. Other topics briefly reviewed are CP-violation, top quark mass and possible implications of the existence of a fourth family.

* On sabbatical leave from University of Bergen, Bergen, Norway.

The CERN Antiproton-Proton-Collider has, within the past couple of years, produced very beautiful data. Thanks to it the intermediate bosons $W^{\pm}$ and Z^{o} are no longer among the fictitions particles "only" required by the theory[1] but belong[2] to the real world.

During this Meeting we heard that the most recent collider data[3] may in fact be indicating that we are now entering into a new Era, the Post Standard Model Era. Indeed I was told by a great physicist (it is left to the reader to figure out who) this morning that "the standard model is finished". It may well turn out to be so, nevertheless, in this talk I shall assume that the standard model is still O.K. After all, no one expects the standard model to be the "Ultimate Theory", and indeed any deviation from the predictions of the standard model which could help us in a deeper understanding of Nature will be most welcome. No matter what happens, the standard model will always be remembered as one of the great steps in progress in physics.

In this talk I shall discuss the following topics:

1. Weak mixing angles in the standard model
2. What do we know about the V_{ij}
   - 2.1 The Cabibbo-sector
   - 2.2 The GIM-sector
   - 2.3 The KM-L-sector
3. The Wolfenstein parametrization
4. $M^{o} - \bar{M}^{o}$ systems, CP-violation and the top quark mass
   - 4.1 The box approach; Δm and $\Delta\Gamma$ for the neutral kaons
   - 4.2 CP-violation, ϵ and ϵ' for the K-system
5. $B^{o} - \bar{B}^{o}$ mixing
   - 5.1 Signatures of $B_s^{o} - \bar{B}_s^{o}$ mixing
6. Beyond three families
7. Concluding remarks

References

1. WEAK MIXING ANGLES IN THE STANDARD MODEL

The weak mixing, which I was asked to discuss, is related to the coupling constants of $W \Rightarrow f\bar{f}'$, where (f, f') denote a pair of quarks or leptons (Fig. 1).

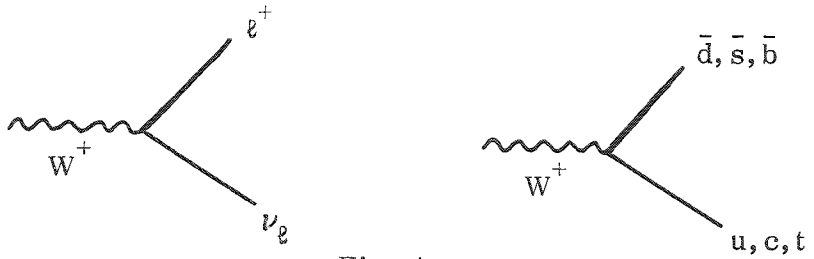

Fig. 1

It is important to keep in mind that the vertices in Fig. 1 (as well as those for W^-) account for all the observed flavour-changing phenomena in Nature. Moreover, there seems to be a major difference between the leptonic and hadronic transitions in Fig. 1. The leptons produced belong to the same family whereas the quarks may either belong to the same family (e.g., $W \Rightarrow \bar{d}u$) or to two different families (e.g., $W \Rightarrow \bar{d}c$). Thus, in the leptonic sector the (family) mixing angles are all consistent with zero and I shall not discuss them here (for a review of the present situation see, for example, Ref. 4.)

The Lagrangian responsible for the hadronic transitions in Fig. 1 has the form

$$\mathcal{L} = \frac{g}{\sqrt{2}} \overline{(u,c,t)}_L \gamma^\lambda \begin{pmatrix} V_{ud} & V_{us} & V_{ub} \\ V_{cd} & V_{cs} & V_{cb} \\ V_{td} & V_{ts} & V_{tb} \end{pmatrix} \begin{pmatrix} d \\ s \\ b \end{pmatrix}_L W_\lambda + \text{h.c.} \qquad (1)$$

where the V's are coupling constants; the notations are explained in detail in Refs. 5 and 6. With arbitrary V's, the above Lagrangian is a simple generalization of the Feynman-Gell-Mann[7] W-mediated V-A Lagrangian of the year 1958. As the V's are, in general, complex numbers it would seem that in Eq. (1) there are $2 \times 9 - 1 = 17$ (an overall phase is irrelevant) real parameters to be determined by experiment. However, in the standard model the 3 by 3 matrix in (1), hereafter denoted by V, is unitary and moreover, as shown[8] by Kobayashi and Maskawa (KM), depends on only 4 real parameters, 3 rotation angles $\theta_{1,2,3}$ and a phase angle δ. The KM parametrization[8] is reproduced[6] by the following product of 3 rotation matrices and a phase matrix

$$V = \begin{pmatrix} 1 & 0 & 0 \\ 0 & c_2 & s_2 \\ 0 & -s_2 & c_2 \end{pmatrix} \begin{pmatrix} c_1 & s_1 & 0 \\ -s_1 & c_1 & 0 \\ 0 & 0 & 1 \end{pmatrix} \begin{pmatrix} 1 & 0 & 0 \\ 0 & 1 & 0 \\ 0 & 0 & e^{i\delta} \end{pmatrix} \begin{pmatrix} 1 & 0 & 0 \\ 0 & c_3 & s_3 \\ 0 & -s_3 & c_3 \end{pmatrix} \qquad (2)$$

$c_i = \cos\theta_i$, $s_i = \sin\theta_i$, $0 \le \theta_i \le \pi/2$, $0 \le \delta < 2\pi$.

The observed CP-violation implies that all four angles are nonzero. Life might seem complicated enough, but it could have been much worse! For example, if there were four families V would be a 4 by 4 matrix, obtained from the product of 6 rotation matrices and 3 phase matrices, and the degree of complication increases roughly quadratically with the increasing number of families ($n(n-1)/2$ rotation matrices and $(n-1)(n-2)/2$ phase matrices; n = number of families).

The standard model does not explain why Nature is left - right asymmetric. The left - right symmetric models do better in this respect, as the asymmetry is attributed to the spontaneous symmetry breaking. On the other hand, the simplest left - right symmetric model has three more gauge bosons and much more involved Higgs sector. The point I would like to emphasize here is that we don't understand the quark mixing phenomenon. The elements of the matrix cannot be predicted from "first principles". Indeed, as of today, "Susy does not attack the family problem"[9]. Composite people have no families[10], and so on. However, in some models[11], by making some assumptions about the general structure of the quark mass matrices, one finds interesting predictions for the coupling constants V_{ij}. Another interesting point is that if there are more families, because of the unitarity of the matrix V, by measuring the strength of the observed transitions one, in principle, obtains a measure of the "leakage" to the unobserved families, for example

$$\sum_{j=d,s,b} |V_{uj}|^2 + \sum_{k} |V_{uk}|^2 = 1, \qquad (3)$$

where k denotes the charge -1/3 quarks of the as yet unobserved families. The measured (long) b-lifetime is however indicating that the "leakage" is decreasing rapidly (at least for the third family) and it might be impossible to learn anything about the as yet unborn families, even if we could measure the coupling constants quite accurately, simply because the higher families are less communicative (see Section 6).

2. WHAT DO WE KNOW ABOUT THE V_{ij} ?

The V_{ij} are (fundamental ?) natural constants. In principle, the best way to determine them is to measure the strength of all hadronic decay channels of the W. However, as often happens, what can be done "in principle" seems to be orthogonal to what is feasible in practice. At the moment it is not clear whether we shall learn anything in the near future about the V's from the W's who are produced and decay at the CERN $p\bar{p}$-collider.

2.1 The Cabibbo[12] sector (V_{ud}, V_{us}).

V_{ud} has been known for a long time[13], however it used to be called G_V^{β}. It is determined from the ft-values of $O^+ - O^+$ nuclear beta transitions and from the neutron lifetime. In the modern language all these processes involve $u \to d + e^+ + \nu$, $d \to u + e^- + \bar{\nu}$. i.e., the beta decay of a virtual up or down quark. The strength of these transitions compared with that of the muon decay gives V_{ud}.

The constant V_{us} is determined from the reactions $s \to u + e + \bar{\nu}$, $s \to u + \mu + \bar{\nu}$ (and antireactions) which take place in a meson or a baryon. Recently the CERN WA2-Collaboration[14] has presented us with the most accurate value of V_{us} which is obtained from the study of several beta transitions, $B_i \to B_f\,(e\nu,\ \mu\nu)$, in the baryon octet, see (Fig. 2).

The WA2-Collaboration has also reanalyzed the present information on V_{ud}. They find, after applying radiative corrections,

$$|V_{ud}| = 0.9735 \pm 0.0015$$
$$|V_{us}| = 0.231 \pm 0.003 \qquad (4)$$

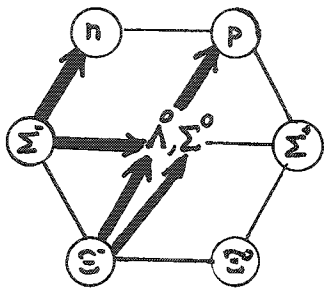

Fig. 2

It is gratifying that the value of V_{us} has been quite stable in the past. Actually, it is amusing to note that the very first estimate of V_{us} dates back to 1960 when Gell-Mann and Levy[15], in the framework of the Sakata Model[16] (which had no quarks but made hadrons out of p,n,Λ and their antiparticles) found $V_{p\Lambda} \approx 0.23$. Translating $p, n, \Lambda \to u, d, s$ gives $V_{us} \approx 0.23$ which happens to be what one finds now, Eq. (4). After the advent of the Cabibbo theory numerous determinations of V_{ud}, V_{us} have appeared in the literature[17], with results in the vicinity of the values in (4). Thus we don't expect V_{ud} and V_{us} to change much in the future.

2.2 The GIM[18]-sector

The coupling constants V_{cd} and V_{cs} are measured by studying dimuon production in neutrino and antineutrino interactions (Fig. 3)

Fig. 3

There are several uncertainties in such a determination. The double differential cross sections for charm production in neutrino and antineutrino charged current interactions in an isoscalar target are of the form

$$\nu: \quad \frac{d^2\sigma}{dx\,dy} = K\left[\,|V_{cd}|^2\underbrace{(u(x)+d(x))}_{\text{valence}} + |V_{cs}|^2\underbrace{(2s(x))}_{\text{sea}}\right],$$

$$\bar{\nu}: \quad \frac{d^2\sigma}{dx\,dy} = K\left[\,|V_{cd}|^2\underbrace{(\bar{u}(x)+\bar{d}(x))}_{\text{sea}} + |V_{cs}|^2\underbrace{(2\bar{s}(x))}_{\text{sea}}\right], \qquad (5)$$

$$K = \frac{G_F^2 M E x}{\pi}$$

where the notation is the standard one[19]; u(x) denotes the distribution function for the up quark in the proton which is assumed to be equal to that of the down quark in the neutron, etc. Thus the knowledge of the strange quark content of the nucleon is essential, especially for the antineutrino case, where the strange quark gives the dominant contribution. The parton distribution functions, in (5), are determined from the deep inelastic processes. One also needs to know the effective semileptonic branching ratio of the mixture of charm particles which is produced in neutrino interactions. For a more detailed discussion see, for example Refs. 20-22.

Before the last summer, there were several independent determinations of these coupling constants in the literature which all quoted a reasonably accurate value for V_{cd}. The value of V_{cs} was, however, because of the uncertainties mentioned above, very poorly determined. As an example the results found by three independent groups were

	V_{cd}	V_{cs}	
Paschos and Türke[20]	0.25 ± 0.04	> 0.81	(6a)
Chau et al.[21]	0.20 ± 0.03	$\geqslant 0.66$	(6b)
Kleinknecht and Renk[22]	0.24 ± 0.03	> 0.59	(6c)

As far as the determination of these coupling constants directly from data is concerned nothing has changed since the last summer. However, in the framework of the standard six-quark model, the V's are not independent. Using the recent information on beauty decay and the unitarity of V one may pin down the V_{cs} considerably, as I shall discuss below.

2.3 The KM-Lederman sector

Last summer, at the Brighton[23] and Cornell[24] Conferences, an amazingly long lifetime for the beauty was reported. In general one expected[25] the beauty lifetime to be shorter than the charm lifetime. The world-averaged D-lifetimes are[26]

$$\tau(D^0) = (4.4 \pm 0.6)\ 10^{-13}\text{s}$$
$$\tau(D^+) = (8.8 \pm 1.2)\ 10^{-13}\text{s}. \qquad (7)$$

The expected beauty lifetime was of the order of 10^{-14}s. The reason for expecting a shorter b-lifetime than the c-lifetime is due to the larger phase space available in the b-decay, specially if $b \to u$ would have been the dominant mode, $(m_b/m_c)^5 \approx (5/1.5)^5 \approx 400$. On the other hand, the $c \to s$ is a transition within the family while $b \to u, c$ necessarily involves a family "jump" (see Fig. 4).

Fig. 4

Thus some suppression, in the transition rate, was expected. A reasonable guess was $\theta_c^2 \sim 1/20$. Thus if the measurements would have found $\tau(b)/\tau(c) \approx 1/20$ nobody would have been surprised. But the results reported by the MAC and MARK-II Collaborations came as a real surprise. The published values of the b-lifetime are

$$\text{MAC-Coll.}^{27)} \qquad \tau(b) = (1.8 \pm 0.6 \pm 0.4)\ 10^{-12}\text{s}$$
$$\text{MARK-II-Coll.}^{28)} \qquad = (1.20\ ^{+0.45}_{-0.36} \pm 0.30)\ 10^{-12}\text{s} \qquad (8)$$

This year the MAC-Collaboration has obtained a new value[29)]

$$\tau(b) = (1.6 \pm 0.4 \pm 0.3)\ 10^{-12}\text{s} \qquad (9)$$

and MARK-II will also soon quote an improved result[29)].

The long b-lifetime implies that <u>both</u> $|V_{cb}|$ and $|V_{ub}|$ are small ($\lesssim \mathcal{O}(\theta_c^2)$, where θ_c = Cabibbo angle). Furthermore, it has been known for some time that the b decays preferentially to c. From comparing the shape of the energy spectrum of the leptons produced in the semileptonic b-decay with the theoretical expectations for $b \to u\,\ell\nu$ and $b \to c\,\ell\nu$ one finds

$$R = \frac{\text{Br}(b \to u\,\ell\nu)}{\text{Br}(b \to c\,\ell\nu)} \equiv \frac{b \to u}{b \to c} \qquad (10)$$

is much smaller than one. The present upper limit reads[30)]

$$R \lesssim 0.03 \qquad 90\%\ \text{c.l.}$$
$$\lesssim 0.04 \qquad 95\%\ \text{c.l.} \qquad (11)$$

obtained from combining the CLEO[31)] and CUSP data, from CESR. The above information

gives (for details and formulae see, for example Ref. 26)

$$\left|\frac{V_{ub}}{V_{cb}}\right| < 0.11, \tag{12}$$

$$|V_{cb}| = 0.05 \pm 0.01 \tag{13}$$

Thus the coupling constant for the transition from the third to the second family is approximately equal to the square of the coupling constant for the transition between the second and the first families. For the rates that matters a lot as the square of the coupling constant enters. The above results indicate that whereas the transitions between the first and the second families are only "first forbidden" (Cabibbo-suppressed) those among the second and the third are "second forbidden" (doubly Cabibbo-suppressed).

There have been several recent determinations of the V's inspired by the long b-lifetime. Unfortunately I can't quote all of them here because then I would violate the (page) unitarity limit imposed by the organizers. A few of the papers are, however, quoted in Refs. 32 and 33. These determinations use the old value of R, $R \leq 0.05$. With the new limit, $R \lesssim 0.03$, the analysis needs be redone, as the V's are somewhat affected. In summary, the V's, as of today, are

$$\begin{array}{lll} |V_{ud}| = 0.9735 \pm 0.0015, & |V_{us}| = 0.231 \pm 0.003, & |V_{ub}| < 0.006 \\ |V_{cd}| = 0.24 \pm 0.03 & |V_{cs}| \geq 0.96 & |V_{cb}| = 0.05 \pm 0.01 \\ |V_{td}| \lesssim 0.06 & |V_{ts}| \lesssim 0.06 & |V_{tb}| \geq 0.998 \end{array} \tag{14}$$

where I have taken the experimental values (Eqs. (4), (6c)) and have used the results (12) and (13). The remaining entries in (14) follow from unitarity. Note that the limit on $|V_{cs}|$, from unitarity is now by far superior to the measured value, Eq. (6). Actually, one gets a much better feeling for the above coupling constants in the Wolfenstein approach which is reviewed in the next section.

3. THE WOLFENSTEIN PARAMETRIZATION[33)]

The above structure of the elements of the family mixing matrix V is very nicely summarized in a transparent and easy to remember parametrization by Wolfenstein, as I shall describe now.

We know from experiment that the coupling constant $|V_{us}|$ is a rather small number. Let us, following Wolfenstein, define $V_{us} = \lambda$ and expand the matrix V in powers of λ, $\lambda \approx 0.23$. This is possible to do if we use the available experimental information (Eqs. (4), (12) and (13)) to fix three of the nine elements of V. We put

$$V_{us} \equiv \lambda, \qquad V_{ud} = 1 + \mathcal{O}(\lambda^2), \qquad V_{cb} = A\lambda^2 + \mathcal{O}(\lambda^3), \tag{15}$$

where $\lambda \approx 0.23$ and $A \approx 1.0$ follow from Eqs. (4) and (13). Furthermore, the limit $|V_{ub}/V_{cb}| < 0.11$ tells us that

$$|V_{ub}| = \mathcal{O}(\lambda^3). \tag{15a}$$

The remaining elements of V are now easily accessible, through unitarity of the matrix V which provides extremely powerful constraints, $\overline{\text{row}}^{*}_{(i)} \cdot \overline{\text{row}}_{(j)} = \delta_{ij}$, $\overline{\text{col}}^{*}_{(i)} \cdot \overline{\text{col}}_{(j)} = \delta_{ij}$. For example, the constraint $|\overline{\text{col}}(3)|^2 = 1$ yields immediately that

$$\begin{aligned} &|V_{tb}|^2 + A^2\lambda^4 + \mathcal{O}(\lambda^6) = 1, \\ &|V_{tb}| = 1 - \frac{A^2}{2}\lambda^4 + \text{ higher orders} \end{aligned} \tag{16}$$

Thus the coupling constant for $t \leftrightarrow b$ is even closer to 1 than that of $u \leftrightarrow d$, which from $|\overline{\text{row}}(1)|^2 = 1$, is $|V_{ud}| = 1 - \frac{\lambda^2}{2}$ + higher orders. Repeated use of the unitarity constraints yields, to order λ^3,

$$V = \begin{pmatrix} 1 - \frac{\lambda^2}{2} & \lambda & A\lambda^3(\rho - i\eta) \\ -\lambda & 1 - \frac{\lambda^2}{2} & A\lambda^2 \\ A\lambda^3(1 - \rho - i\eta) & -\lambda^2 A & 1 \end{pmatrix} + \mathcal{O}(\lambda^4) \tag{17}$$

where ρ and η are two real constants restricted by $\rho^2 + \eta^2 \leq 0.23$, a relation which follows from the upper limit $|V_{ub}/V_{cb}| < 0.11$. Note that η plays the role of δ, of the KM-parametrization, as the origin of the CP-violation. The KM and Wolfenstein parameters are related, to order λ^3, via

$$\begin{aligned} s_1 &= \lambda \\ s_2 &= A\lambda^2\left((1-\rho)^2 + \eta^2\right)^{1/2} \\ s_3 &= A\lambda^2(\rho^2 + \eta^2)^{1/2} \\ s_2 s_3 \sin\delta &= A^2\lambda^4\eta . \end{aligned} \tag{18}$$

As $\eta^2 \leq 0.23$ one immediately finds $s_2 s_3 \sin\delta \lesssim 10^{-3}$; this combination appears in CP-violation calculations (see section 4.2). It is now easy to use (18) and $\rho^2 + \eta^2 \leq 0.23$ to give the range of the KM-parameters

$$\begin{aligned} &s_1 = 0.231 \pm 0.003, \qquad 0.03 \lesssim s_2 \lesssim 0.07, \qquad s_3 < 0.02 \\ &s_2 s_3 \sin\delta \lesssim 10^{-3} . \end{aligned} \tag{19}$$

If the upper limit on ratio R, Eqs. (10) and (11), should decrease further the upper limit on η will also go down and the six quark model, as the origin of the CP-violation, will be ruled out. What an irony of fate! The six quark model was invented[8], prior to the discovery[34] of the b-quark, in order to explain the observed CP-violation and it may well turn out that just the observed CP-violation will cause the fall of the six quark model.

4. $M^0 - \bar{M}^0$ SYSTEMS, CP-VIOLATION AND THE TOP QUARK MASS

In the following M^0 denotes a neutral spinless boson such as K^0, D^0, B^0_d, B^0_s, ...

In the previous sections the values of the coupling constants quoted (i.e., Eqs. (14) and (19)) were rather model independent. Of course the treatment of the phase space, quark masses, etc. do matter in determining the coupling constants but these don't involve any "deep theoretical prejudices. If one wishes to go further (and as theorists we usually like to go as far as we can, perhaps sometimes a bit too far) one must make assumptions. The short distance (box diagram) approach in describing the $K^0 - \bar{K}^0$ system (and later on also $D^0 - \bar{D}^0$ and $B^0 - \bar{B}^0$) has been very popular, within the past 10 years. The reason is that, in a pioneering work, Gaillard and Lee[35] used the box diagram and predicted that the charm quark could not be too heavy. Actually their limits were very generous, $m_u \ll m_c \ll m_W$. The subsequent discovery[36] of the charm quark turned the box-approach into a "religion", which was employed not just as a framework for an order of magnitude estimate but for a precision calculation. For the latter purpose the box-approach is simply unreliable. For systems consisting of heavier quarks, however, the short distance approximation and thereby the box-approach is expected to do a better job. Nevertheless I shall review the box-approach, even for the kaons, just because it is so widely used. Furthermore, one may easily generalize the results to describe the neutral D and B-mesons.

4.1 The box-approach; Δm and $\Delta\Gamma$ for the neutral kaons

The $K^0 - \bar{K}^0$ mixing, in the short distance (box) approach, is given by the diagrams of Fig. 5

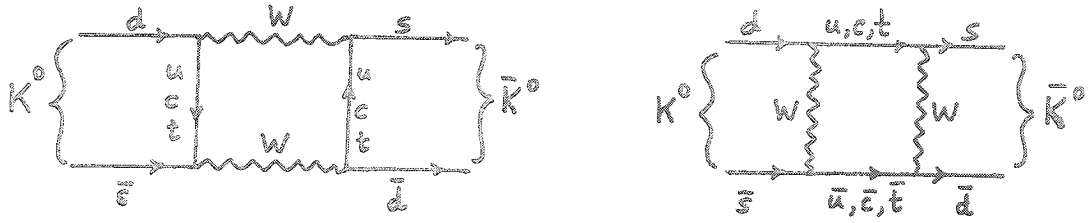

Fig. 5

For the $B^0 - \bar{B}^0$ system the corresponding diagrams are obtained by just letting either $d \to b$, $\bar{d} \to \bar{b}$ or $s \to b$, $\bar{s} \to \bar{b}$, in Fig. 5. However in the $D^0 - \bar{D}^0$ system, the external quarks are (u, c) and those in the loop d, s and b.

These diagrams may be used to calculate the $M^0 - \bar{M}^0$ mass matrix[37]

$$i\frac{\partial}{\partial t}\begin{pmatrix} M^0 \\ \bar{M}^0 \end{pmatrix} = \begin{pmatrix} M - \frac{i}{2}\Gamma & M_{12} - \frac{i}{2}\Gamma_{12} \\ M_{12}^* - \frac{i}{2}\Gamma_{12}^* & M - \frac{i}{2}\Gamma \end{pmatrix}\begin{pmatrix} M^0 \\ \bar{M}^0 \end{pmatrix}. \tag{20}$$

The physical states, with well defined masses will be denoted by H (heavy) and L (light), although in general the mass difference between them is minute. The measurables originating from the mass matrix are

$$\begin{aligned} \Delta m &= m(H) - m(L) \\ \Delta\Gamma &= \Gamma(H) - \Gamma(L) \\ \Gamma &= \tfrac{1}{2}(\Gamma(H) + \Gamma(L)), \end{aligned} \tag{21}$$

($m \equiv$ mass, $\Gamma \equiv$ width) as well as the parameter ϵ which gives the CP-impurity of the mass eigenstates. Diagonalization of the mass matrix gives immediately that

$$\begin{pmatrix} \Delta m \\ \Delta\Gamma \end{pmatrix} = \begin{pmatrix} 2\,\mathrm{Re} \\ -4\,\mathrm{Im} \end{pmatrix}\left[\left(M_{12} - \tfrac{i}{2}\Gamma_{12}\right)\left(M_{12}^* - \tfrac{i}{2}\Gamma_{12}^*\right)\right]^{1/2}, \tag{22}$$

$$\frac{1-\epsilon}{1+\epsilon} = \left(\frac{M_{12}^* - \frac{i}{2}\Gamma_{12}^*}{M_{12} - \frac{i}{2}\Gamma_{12}}\right)^{1/2}. \tag{23}$$

A quantity of great interest is the degree of mixing, denoted by Δ,

$$\begin{aligned} \Delta &= \frac{\mu + \gamma}{2 + \mu - \gamma}, \\ \mu &\equiv \left(\frac{\Delta m}{\Gamma}\right)^2, \qquad \gamma \equiv \left(\frac{\Delta\Gamma}{2\Gamma}\right)^2, \end{aligned} \tag{24}$$

where from $0 \leq \gamma < 1$ follows that $0 \leq \Delta \leq 1$.

In the case of $K^0 - \bar{K}^0$ system $\Gamma(K_S) \gg \Gamma(K_L)$ whereby $\gamma \approx 1$ and mixing is complete, i.e., the physical states are essentially "half K^0 and half $\bar{K}^0$". This is a fortunate coincidence which happens due to the small phase space available to $K_L \to 3\pi$ decays. For all other known $M^0 - \bar{M}^0$ systems such a fortunate circumstance is not expected, because the available phase space in both H and L decays is large. In general the widths of the H

and the L will be comparable and $\gamma \ll 1$. A second case where Δ can be large is if $\mu \gg 1$. In the box approach, the present values of the coupling constants indicate that this is expected to happen in the $B_s^o - \bar{B}_s^o$ system, where μ is expected to be appreciable, however not much larger than unity.

The box diagrams provide us with M_{12} and Γ_{12} and thus we can calculate all the quantities in Eqs. (22) - (24). For example, for the mass difference Δm $\Delta m = m(K_L) - m(K_S)$, in the limit $m_u \ll m_c, m_t$ and $m_c^2, m_t^2 \ll M_w^2$, is given by

$$\Delta m = C_K \cdot B_K \left[\eta_1 + \eta_2 \left(\frac{m_t}{m_c} s_2^2 \right)^2 + 4 \eta_3 s_2^2 \ln \left(\frac{m_t}{m_c} \right) \right],$$
$$C_K = \frac{1}{2} \left(\frac{G_F f_K m_c s_1}{2\pi} \right)^2 \cdot M_K \qquad (25)$$

Here the η's are[38] QCD correction factors of order 1 and B_K is the "infamous" bag parameter which measures the renormalization of the relevant $|\Delta s| = 2$ operator when one goes from quarks to hadrons

$$\langle K^o | (\bar{d} \gamma_\lambda (1-\gamma_5) s)^2 | \bar{K}^o \rangle = -\frac{4}{3} f_K^2 m_K B_K , \qquad (26)$$

f_K is the kaon decay constant and m_K refers to the mass. The value of the constant B is not known from first principles and the largest uncertainty in the box approach is due to this unknown B. For other systems, there is an additional uncertainty due to the fact that the decay constants f_M, $M = D^o$, B_d^o, ..., have not been measured. In (25) the first term is due to two charm quarks in the loop (see Fig. 5); the second term comes from two t-quarks and the last one is the contribution of the pair c, t. The numerical value of Δm for canonical values of B, $0 < B < 1$, comes out to be too small and increasing the top quark mass doesn't help much because $m_t s_2^2 / m_c \gtrsim 1$ already requires $m_t \gtrsim m_c / s_2^2 \gtrsim 1.5/(0.07)^2$ GeV $\approx$ 300 GeV which is a huge value and violates the assumption $m_t \ll m_w$. Even using the exact formulae[39] doesn't help and Δm is not reproduced. The reason is simply that the coupling constants V_{td} and V_{ts} are small, order λ^3 and λ^2 respectively. Thus one believes that there is a substantial long distance contribution to Δm from diagrams in Fig. 6

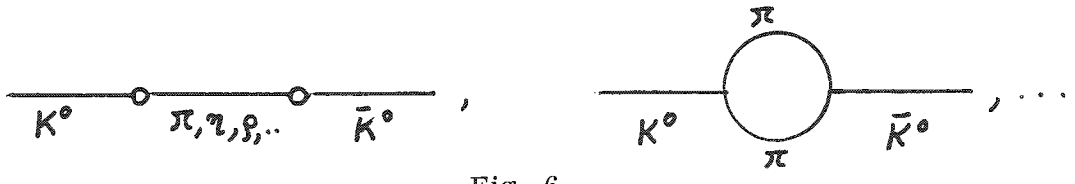

Fig. 6

Such one-particle, two-particle and more-particle intermediate states have been considered since a long time ago[40]. There are huge cancellations between such contributions[40] and the unknown hadronic form factors make the calculations tough and unreliable. In conclusion, the mass difference between K_L and K_S is not naturally reproduced in the six quark model if only the short distance (box) contribution is taken into account.

4.2 CP-violation, ϵ and ϵ' for the K-system

The Fitch-Cronin[41] parameter ϵ, in the box approximation, is given by

$$|\epsilon| = C'_K \cdot B_K \, s_2 s_3 \sin\delta \left| \eta_1 - \eta_2 \left(\frac{m_t}{m_c} s_2\right)^2 - 2\eta_3 \ln\left(\frac{m_t}{m_c}\right) \right| ,$$

$$C'_K = \left(\frac{G_F f_K m_c s_1}{\pi}\right)^2 \frac{m_K}{6\sqrt{2}\,\Delta m} . \qquad (27)$$

As we saw before, Eq. (19), the "KM-coefficient" in (27) is small. Again the quantity in $|\ldots|$ needs to be large in order to explain the experimental value of $|\epsilon|$. Here a large top quark mass can help to give agreement, because the coefficient of $(m_t/m_c)^2$ could be as much as 50 times larger than it was in the case of Δm, Eq. (25), viz., $(s_2)^2 \lesssim (0.07)^2$. The formula (27) was used last year by Ginsparg et al.[42] who obtained a lower limit on the top quark mass. The new value of R will increase their lower bound. Again the largest uncertainty comes from the unknown bag parameter B. So one usually quotes the limit on m_t together with the assumed value of B. Taking a larger value of B allows a smaller lower limit on m_t. Many authors[32] have recently provided graphs of the lower limit on m_t as a function of δ, B, etc. The general conclusion of such studies is that the value of $|\epsilon|$ is reproduced provided m_t is larger than 30(90) GeV for B equal to 1 (1/3).

Another interesting result in the K-sector is a lower bound on $|\epsilon'/\epsilon|$, which has been obtained by Gilman and Hagelin[43]. Here ϵ' is the (non-superweak) CP-impurity in the transition. One defines

$$\eta_{+-} = \frac{A(K_L \to \pi^+\pi^-)}{A(K_S \to \pi^+\pi^-)} \approx \epsilon - 2\epsilon' ,$$

$$\eta_{00} = \frac{A(K_L \to \pi^0\pi^0)}{A(K_S \to \pi^0\pi^0)} \approx \epsilon + \epsilon' .$$

Here A ≡ amplitude. Gilman and Hagelin were able to relate

$$|\epsilon'/\epsilon| = s_2\, s_3 \sin\delta \cdot (\text{known quantity})$$

where the quantity in the parenthesis can be extracted from experiment. Moreover, since we know the empirical value of ϵ, we may use Eq. (27) to calculate $s_2 s_3 \sin\delta$, for any given value of B and m_t. Actually this calculation gives a lower bound on $s_2 s_3 \sin\delta$, as we have neglected a small contribution[43] (with a negative sign) in the RHS of Eq. (27). The lower limit on $s_2 s_3 \sin\delta$ can then be translated into a lower limit on $|\epsilon'/\epsilon|$ which has approximately the functional form

$$|\epsilon'/\epsilon| \gtrsim \frac{\text{constant}}{B_K\left[(m_t/m_c)^2 + \cdots\right]} \tag{28}$$

for $m_t \ll m_W$. For larger m_t the expression, which replaces the square bracket in the denominator is known[39] and has been used[43] in the bound. The general conclusion of Ref. 43 is that $|\epsilon'|$ cannot be too small, for "reasonable" values of m_t and B. Typically $|\epsilon'/\epsilon| \gtrsim 0.01$ for $m_t \lesssim 30$ GeV and $B \lesssim 2/3$. Of course for larger m_t and/or B the lower bound becomes smaller and less interesting. The present experimental limit reads[44] $|\epsilon'/\epsilon| \lesssim 1/20$ but the ongoing generation of CP-experiments aim to explore[45] the region $|\epsilon'/\epsilon| \gtrsim 0.001$. Thus one should observe $|\epsilon'| \neq 0$ soon, if the box approach makes sense and B as well as m_t have "reasonable" values. It is going to be very interesting to see what the verdict, from the ongoing low energy CP-experiments and the high energy $\bar{p}p$-collider, is going to be. The lower bound on $|\epsilon'/\epsilon|$ is already a bit uncomfortable[43] and could easily be violated.

5. $B^0 - \bar{B}^0$ MIXING

The short distance (box) approach, described in the previous section, is expected to be much more reliable in describing the neutral $D - \bar{D}$ and $B - \bar{B}$ systems, as these contain heavy quarks. The relevant diagrams are shown in Fig. 7.

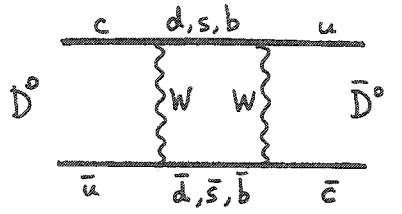

$$\Rightarrow \sum_{\substack{j,k= \\ d,s,b}} (V_{uj} V_{cj}^*)(V_{uk} V_{ck}^*) F_{jk}\,, \tag{29a}$$

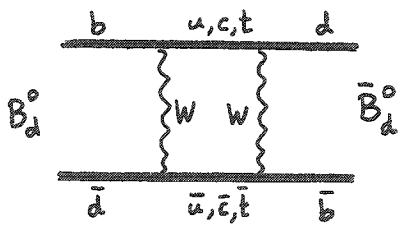

$$\Rightarrow \sum_{\substack{j,k= \\ u,c,t}} (V_{jd}^* V_{jb})(V_{kd}^* V_{kb}) \tilde{F}_{jk}\,, \tag{29b}$$

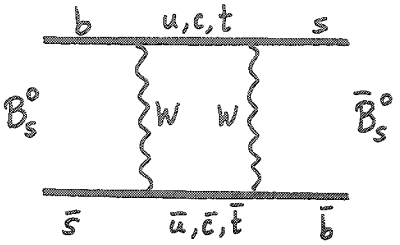

$$\Rightarrow \sum_{\substack{j,k= \\ u,c,t}} (V_{js}^* V_{jb})(V_{ks}^* V_{kb})\, \hat{F}_{jk} \,. \quad (29c)$$

Fig. 7

Note that the crossed diagrams (see Fig. 5) have not been depicted because they have the same general structure as the diagrams which are shown and thus don't modify the conclusion drawn below. In Eq. (29) the F's are functions of quark masses, decay constants, etc. Their general form is similar to the quantities we had in Eqs. (25) and (26). From the general structure of the diagrams in Fig. 7 we may immediately conclude that the mixing in the D system is much suppressed, as compared to the B, because the heaviest internal quark is the b. However the coefficient of m_b^2 is very small, viz.

$$|V_{ub} V_{cb}^*|^2 \lesssim \mathcal{O}((\lambda^5)^2) \,, \quad \lambda \approx 0.23 \,.$$

For the B's the situation is much more promising, because the heavy t quark contributes. Furthermore the strange-beauty looks more promising than the down-beauty. Both have a term (in $\tilde{F}$ and $\hat{F}$) which goes as m_t^2, for $m_t^2 \ll M_W^2$. However, the coefficient of this contribution is much larger for the B_s system than for the B_d, viz.

$$|V_{td} V_{tb}|^2 \approx |V_{td}|^2 \sim \mathcal{O}((\lambda^3)^2)$$

$$|V_{ts} V_{tb}|^2 \approx |V_{ts}|^2 \sim \mathcal{O}((\lambda^2)^2) \quad (30)$$

and $\lambda^2 \approx 0.05$. Thus among the heavy systems the mixing is expected to be largest for the $B_s^0 - \bar{B}_s^0$ system, on which I shall concentrate from now on.

There are, as for the K-system, several uncertainties in the calculation of the mixing in question. Again the parameter B is not known. Moreover the B_s-meson decay constant f_B has not been measured, and the t-quark mass is also unknown. Many authors[46] have computed the relevant quantities needed to predict the $B - \bar{B}$ mixing. As an order of magnitude estimate, it is perfectly O.K. to take the limit $m_b^2 \ll m_t^2 \ll m_W^2$. Then

$$M_{12} \approx G_F^2 \frac{f_B^2 \cdot B \cdot m}{12\pi^2} (V_{ts})^2 m_t^2 \,,$$

$$\left|\frac{\Gamma_{12}}{M_{12}}\right| \approx \frac{3\pi}{2} \frac{m^2}{m_t^2} \,, \quad (31)$$

where the quantities f, B and m denote respectively the B-meson decay constant, "bag parameter" and mass. These are, of course, the analogs of their namesakes, introduced after Eq. (25), for the K-system. In order to proceed further and calculate the degree of mixing Δ, Eq. (24), one must make some "reasonable" assumptions about the above unknown quantities. Furthermore the width, Γ, is calculated from the measured b-lifetime. Several such estimates of the mixing exist in the literature and the conclusion is that the mixing could be substantial, perhaps even almost complete. Typically, Δ is found to lie in the range 0.2 - 0.9. Although we don't know how good the assumptions made are there is nevertheless a good chance that Δ may well be large. For the sake of simplicity I shall assume that the mixing is complete in the $B_s^o - \bar{B}_s^o$ system and discuss its consequences for the $\bar{p}p$-collider experiments.

5.1 Signatures of $B_s^o - \bar{B}_s^o$ mixing

The signatures of mixing and CP-violation in $M^o - \bar{M}^o$ systems were discussed[47] in detail after the discovery of charmed particles. Experimentally, the $D^o - \bar{D}^o$ mixing is known to be small and that is no surprise, according to our estimates above. Since then the theoretical formalism developed in mid seventies has been repeatedly applied[48] to the $B - \bar{B}$ system. The most spectacular signature of such mixing is perhaps the so-called same sign dilepton phenomenon[47]. The semileptonic decay $b(\bar{b})$ produces a charged lepton (antilepton) as shown in Fig. 8.

Fig. 8

If mixing takes place, however, the b inside a neutral meson may turn into a $\bar{b}$ and thereby produce positively charged leptons as well. Thus at the CERN $p\bar{p}$-collider the following sequence of events may happen

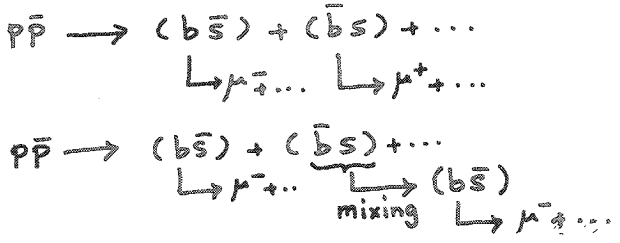

A rough estimate of the expected ratio of the number of same sign (SS) and opposite (OS) dileptons, say dimuons, may be obtained as follows. Assume that the produced b-quark has equal probability of picking up a $\bar{u}$, $\bar{d}$ or $\bar{s}$ from the sea. Then neglecting the beautiful baryons, a produced b quark will end up as the mesons B_u^-, B_d^0 or B_s^0 with equal probabilities (1/3 each). Furthermore the probabilities of finding the produced B_s^0 as B_s^0 or as $\bar{B}_s^0$ are equal (1/2 each), by our assumption of complete mixing. Thus the "probability chart" looks as follows

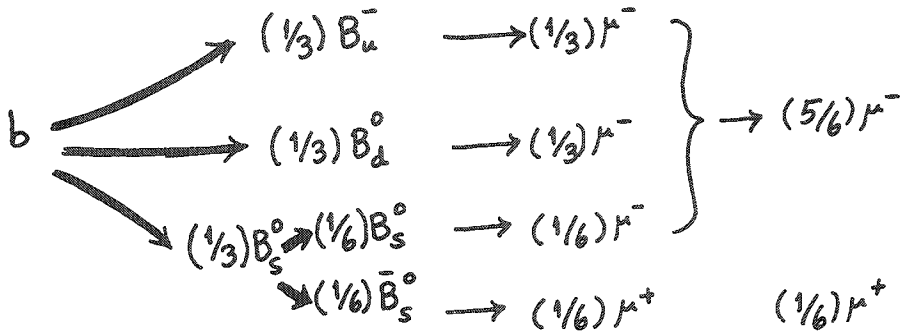

and similarly for the $\bar{b}$

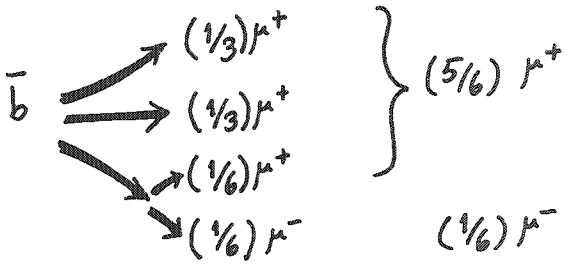

The ratio of the opposite sign and the same sign dimuons is given by

$$\frac{SS}{OS} = \frac{2\cdot(1/6)\cdot(5/6)}{(1/6)^2+(5/6)^2} = \frac{10}{26} \approx 0.4,$$

which is quite a substantial number. Furthermore the mixing being in the $B_s^0 - \bar{B}_s^0$ sector, when the $\bar{b}$-picks up a strange quark from the $(s\bar{s})$ in the sea the $\bar{s}$ is left behind and may produce strange particles, viz.

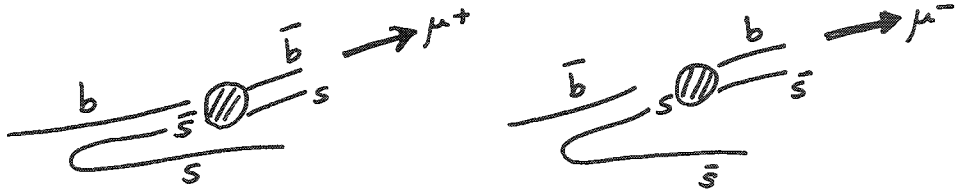

Fig. 9

Thus the sign of the lepton and the strangeness quantum number of the produced hadrons are correlated. One expects

$$p\bar{p} \to \mu^+\mu^+ (\Lambda^0, \bar{K}^0, \ldots)$$
$$p\bar{p} \to \mu^-\mu^- (\bar{\Lambda}^0, K^0, \ldots).$$

Of course the above discussion has been on purpose much simplified in order to explain the underlying ideas. However we[49] have done a more detailed realistic calculation, taking into account backgrounds, etc. and have compared our results with the UA1 dimuon data. The conclusion is that the same sign dimuons[50] could be due to $B_s^0 - \bar{B}_s^0$ mixing phenomenon. If so, this would be quite remarkable in view of the fact that the strange beautiful meson has not been seen yet! She certainly deserves her name "the strange beauty".

I have not discussed CP-violation in the $B - \bar{B}$ system which would have as a signature, for example, that the number of $\mu^+\mu^+$ and $\mu^-\mu^-$, produced due to mixing, are not equal. Unfortunately, the very same theory which predicts large mixing (at least for $B_s^0 - \bar{B}_s^0$) also tells us that essentially all CP-violating effects (such as for the same sign dimuons) will be very small. Thus it is extremely interesting to test this strong prediction of the standard model.

In conclusion the B-physics which so far has supplied us with surprises and taught us lessons may well continue to do so also in the future.

6. BEYOND THREE FAMILIES?

I was asked by the organizers of this workshop to talk also about heavy flavours. I have already discussed some aspects of the b-physics and possible signatures at the Collider. The theoretical aspects of the b and t-physics at the Collider are also reviewed by Francis Halzen[51] and Allan Martin[52]. Therefore, in the remaining few minutes I shall speculate a little about a hypothetical fourth family[53].

We have seen already that the degree of family mixing seems to decrease with the increasing family number. Thus the third and second families mix much less than the second and the first do. This pattern may continue on, if there are more families, so that the new families become less and less "communicative". So far, there is neither an urgent need nor any serious objection against the existence of a fourth family. The magnitude of the CP-violating parameter ϵ, in the K system, is somewhat problematic in the short distance approach. Of course one has the freedom of blaming the disagreement on the unknown bag parameter B and the t-quark mass. Another possibility is, however, to

have more families. Although there are restrictions on the number of neutrinos (and thus on the number of families) from the BIG-BANG nucleosynthesis, I believe that if a new family is discovered it will be accomodated. Much more powerful restrictions are expected to come from the measurement of the ratio of widths of the Z and W at the CERN $p\bar{p}$-collider.

Suppose that there is a fourth family with the quarks (a, r) having charges 2/3 and - 1/3 respectively. Then it follows from Veltman's calculation[54], of the corrections to the W and Z propagators, that the mass difference $|m_a - m_r|$ cannot be too large, $|m_a - m_r| \lesssim 300$ GeV. Furthermore the most recent data from DESY show[55] that there are no such quarks with masses below 20 GeV.

We don't know how the fourth family will communicate with the other three. One suggestive pattern is as shown in Fig. 10.

The most amusing situation occurs if $m_r < m_t$ and m_W. Then the r will presumably decay predominantly to the c-quark (Fig. 10).

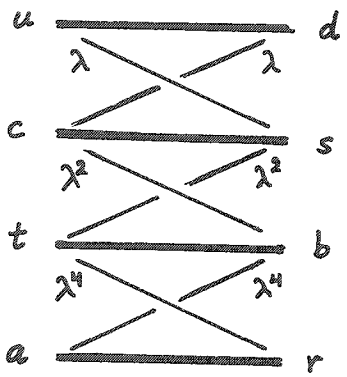

Fig. 10

We don't know the coupling constant for the $r \leftrightarrow c$ transitions. A "good" guess is $V_{cr} \approx \lambda^4 \cdot \lambda^2 = \lambda^6$. If so the r-quark could be remarkably long lived,

$$\tau_r \approx \frac{1}{9}\left(\frac{m_\mu}{m_r}\right)^5 \cdot (\lambda^{-12})\,\tau_\mu ,$$

where the factor 1/9, from the number of decay channels, could be 1/10 if there is a new heavy lepton with mass smaller than m_r. Putting $m_r \sim 40$ GeV gives $\tau_r \approx 10^{-12}$ sec. which is a remarkably long lifetime for such a heavy object. The point here is that with the present pattern of family mixing unexpected things may happen and there could indeed be one or more very long lived heavy flavours.

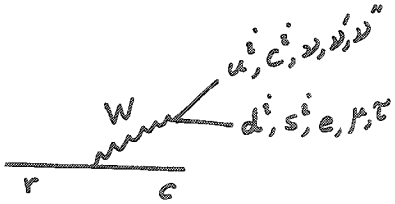

7. CONCLUDING REMARKS

In this talk I have reviewed the present status of the flavour mixing in the standard model. The standard six quark model has no serious difficulties in accomodating the observed pattern of family mixing. However the simple short distance approach does not

work as well as it did before. Furthermore, the Collider may turn out to be an ideal instrument for studying $B^0 - \bar{B}^0$ mixing. This year marks the 20th anniversary of the discovery[41] of the CP-violation and yet there is no sign of CP-violation anywhere except in the mass matrix of the $K^0 - \bar{K}^0$ system. The ongoing experiments looking for $|\epsilon'/\epsilon|$ may supply us with the first indication of CP-violation in a transition. For heavy quark systems, the standard model gives little hope of seeing any effect. A few years ago the situation looked very promising[56] for the charged B decays. Since then we have learned, from experiment, that it is unlikely that there will be, in such decays, two opposite CP amplitudes with comparable strengths. Within the standard model such CP-effects are hopelessly small.

Perhaps the standard model has already done its job, as the link to the next Era in front of us? Some observed phenomena may be just the first indications in this respect. Putting aside such deep questions as why families, masses, etc., let us remember that we don't understand

- the same sign dimuons observed in neutrino interactions[57]
- $Z \to e^+e^-\gamma$, $\mu^+\mu^-\gamma$ observed[58] at the Collider
- some of the phenomena observed by UA1 and UA2 as reported[3] as this Workshop.

I rather not quote these effects here, as the results were stamped "preliminary".

REFERENCES

1. O. Klein in "Les Nouvelles Théories de la Physique", Editions Frontières (Paris 1938) p. 81.
   S.L. Glashow, Nucl. Phys. 22 (1961) 579
   S. Weinberg, Phys. Rev. Lett. 19 (1967) 1264
   A. Salam in Elementary Particle Theory, Ed. N. Svartholm, Almqvist and Wiksell, Stockholm 1968
   A. Salam and J.C. Ward, Phys. Lett. 13 (1964) 168.
2. G. Arnison et al., Phys. Lett. 122B (1983) 103, 129B (1983) 273; 126B (1983) 398, 134B (1984) 469
   G. Banner et al., Phys. Lett. 122B (1983) 476
   P. Bagnaia et al., Phys. Lett. 129B (1983) 130.
3. J.R. Hansen (UA2-Collaboration), these Proceedings
   C. Rubbia (UA1-Collaboration), these Proceedings.
4. For a recent review see, for example,
   K. Winter, Proceedings of the 1983 International Symposium on Lepton and Photon Interactions at High Energies, Cornell 1983, Ed. D.G. Cassel and D.L. Kreinick, p. 177;
   M.H. Shaevitz, ibid., p. 132.
5. C. Jarlskog, Proceedings of the 1981 CERN-JINR School of Physics (Hanko, Finland), CERN Yellow Report 82-04, p. 63.

6. C. Jarlskog, in Proceedings of the 1978 Nato Advanced Study Institute on New Phenomena in Lepton-Hadron Physics, Ed. D.E.C. Fries and J. Wess.

7. R.P. Feynman and M. Gell-Mann, Phys. Rev. 109 (1958) 193 (especially page 197, discussions concerning a heavy charged W-boson).

8. M. Kobayashi and T. Maskawa, Prog. Theor. Phys. 49 (1973) 652

9. This master remark is due to Guido Altarelli.

10. For a review of composite model see R. Peccei, these Proceedings.

11. For a review see, for example, B. Stech, Heidelberg Preprint HD-THEP-83-31, to be published in the Proceedings of the 1983 Advanced Summer Institute, Munich.

12. N. Cabibbo, Phys. Rev. Lett. 10 (1963) 531.

13. For a review see for example, D.H. Wilkinson, Prog. in Particle and Nuclear Phys. 6 (1980) 325.

14. WA2 Collaboration, M. Bourquin et al., Z. Phys. C12 (1982) 307; C21 (1983) 1, 17, 27.

15. M. Gell-Mann and M. Levy, Nuovo Cimento 16 (1960) 705.

16. S. Sakata. Prog. Theor. Phys. 16 (1956) 686.

17. See, for example, L.M. Chounet, J.M. Gaillard and M.K. Gaillard, Phys. Rep. 4C (1972) 199.

18. S.L. Glashow, J. Iliopoulos and L. Maiani, Phys. Rev. D2 (1970) 1285.

19. See for example
C.H. Llewellyn Smith, Phys. Reports 3C (1974) 264
F.E. Close, An Introduction to Quarks and Partons (Academic Press 1979), Chap. 11.

20. E.A. Paschos and U. Türke, Phys. Lett. 116B (1982) 360.

21. L. Chau, W. Keung and M.D. Tran, Phys. Rev. D27 (1983) 2145.

22. K. Kleinknecht and B. Renk, Z. f. Physik C16 (1982) 7.

23. G. Hanson, Proceedings of the Internationel Europhysics Conference on High Energy Physics, (Brighton 1983), Eds. J. Guy and C. Costain, p. 330;
G. Chadwick, ibid. 333.

24. N.W. Reay, Proceedings of the 1983 International Symposium on Lepton and Photon Interactions at High Energies (Cornell 1983), Eds. D.G. Cassel and D.L. Kreinick, p. 244.

25. For a review see, for example, L. Chau, Phys. Reports 95 (1983) 1-94, see especially p. 59.

26. See, for example, C. Jarlskog, Proceedings of the International Europhysics Conference on High Energy Physics (Brighton 1983), Eds. J. Guy and C. Costain, p. 768.

27. E. Fernandez et al., Phys. Rev. Lett. 51 (1983) 1022.

28. N.S. Lockyer et al., Phys. Rev. Lett. 51 (1983) 1316.

29. Talk presented by Y. Yelton at the 19th Rencontre de Moriond, La Plagne, Feb. 26 - March 4, 1984; to appear in the Proceedings.

30. Talk presented by J. Lee-Franzini at the 19th Rencontre de Moriond, La Plagne, Feb. 26 - March 4, 1984; to appear in the Proceedings.

31. A. Chen et al., Preprint CLNS-84/597 = CLEO - 84-1.

32. K. Kleinknecht and B. Renk, Phys. Lett. 130B (1983) 459.
X. Pham and X. Vu, Preprint PAR LPTHE 83/28
E.A. Paschos and U. Türke, Preprint NSF-ITP-83-168.
L. Chau and W. Keung, Phys. Rev. D29 (1984) 592.
A.J. Buras, W. Słominski and H. Steger, Preprint MPI-PAE/PTh 77/83.
See also Ref. 26.

33. L. Wolfenstein, Phys. Rev. Lett. 51 (1983) 1945.

34. S.W. Herb et al., Phys. Rev. Lett. 39 (1977) 252.

35. M.K. Gaillard and B.W. Lee, Phys. Rev. D10 (1974) 897.

36. J.J. Aubert et al., Phys. Rev. Lett. 33 (1974) 1404.
J.E. Augustin et al., ibid. 1406.

37. See, for example
J.S. Bell and J. Steinberger, Proceedings of the International Conference on Elementary Particles, Oxford 1965, p. 195 (1966).

38. F.J. Gilman and M.B. Wise, Phys. Rev. D20 (1979) 2392; D27 (1983) 1128.

39. T. Inami and C.S. Lim, Prog. Theor. Phys. 65 (1981) 297.

40. C. Itzykson, M. Jacob and G. Mahoux, Nuovo Cimento Supp. 5 (1967) 978.
For a recent review see Ref. 25.

41. J.H. Christenson, J.W. Cronin, V.L. Fitch and R. Turlay, Phys. Rev. Lett. 13 (1964) 138.

42. P.H. Ginsparg, S.L. Glashow and M.B. Wise, Phys. Rev. Lett. 50 (1983) 1415.

43. F.J. Gilman and J.S. Hagelin, Phys. Lett. 126B (1983) 111; Preprint SLAC-PUB-3226

44. For a review see K. Kleinknecht, Proceedings of the XVIIth International Conference on High Energy Physics, London 1974, Eds. J.R. Smith, p. III-23.

45. K. Kleinknecht, talk presented at the 19th Rencontre de Moriond, La Plagne, Feb. 26 - March 4, 1984, to appear in the Proceedings.

46. J. Ellis et al., Nucl. Phys. B131 (1977) 285
A. Ali and Z.Z. Aydin, Nucl. Phys. B148 (1978) 165,
See also Ref. 25, and References therein.

47. A. Pais and S.B. Treiman, Phys. Rev. D12 (1975) 2744
L.B. Okun, V.I. Zakharov and B.M. Pontecorvo, Lett. Nuovo Cimento 13 (1975) 218.

48. J.S. Hagelin, Phys. Rev. D20 (1979) 2893
A.B. Carter and A.I. Sanda Phys. Rev. D23 (1981) 1567.
J.S. Hagelin, Nucl. Phys. B193 (1981) 123
See also Refs. 32 and 46 cited above.

49. A. Ali and C. Jarlskog, Stockholm Preprint, ITP-84-1 (CERN Preprint TH-3896).

50. For further theoretical explanations of the UA1 dimuons see, for example,
V. Barger and R. Phillips, Madison Prepr. PH/155
E.W.N. Glover, F. Halzen and A.D. Martin, Durham Report DTP 84/2
R. Kinnunen, CERN-EP-84-19.

51. F. Halzen, these Proceedings.

52. A.D. Martin, ibid.

53. See also V. Barger et al., Madison Preprint PH/150.

54. M. Veltman, Nucl. Phys. B123 (1977) 89.

55. M. Althoff et al., DESY Report 84-001.

56. J. Bernabeu and C. Jarlskog, Z. f. Physik C8 (1981) 233.

57. For a review see F. Halzen, Journal de Physique 43 Colloque C3-381 (Proceedings of the 1982 International Conference, Paris).

58. G. Arnison et al., Phys. Lett. 126B (1983) 398.
P. Bagnaia et al., Phys. Lett. 129B (1983) 130.

THE SEARCH FOR NEW FLAVOURS

F. Halzen* and A.D. Martin †

*Physics Department, University of Wisconsin, Madison, USA
†Physics Department, University of Durham, ENGLAND

ABSTRACT

We discuss the search for new quark flavours with $\bar{p}p$ colliders. We emphasize the following subjects: (a) production cross sections: central and "diffractive" production, heavy flavours in jets, (b) production of same and opposite sign dileptons, (c) signatures of heavy flavour production.

1. EVENT RATES FOR HEAVY FLAVOUR PRODUCTION

Event rates for $\bar{p}p \to Q\bar{Q}X$ (with Q = c,b,t,...) are routinely[1] calculated from the $q\bar{q} \to Q\bar{Q}$ and $gg \to Q\bar{Q}$ QCD fusion diagrams shown in Fig. 1. One should be aware however of other sources of heavy quarks: (i) "diffractive" production of $\Lambda_Q M_{\bar{Q}}$ (Λ=Qud, $M_{\bar{Q}} = \bar{Q}u$), (ii) heavy quarks in jets and (iii) weak production, e.g. $\bar{p}p \to WX$ followed by $W \to t\bar{b}$. Sources (i), (ii) could be potentially more copious than heavy quark production via the standard fusion mechanism and, although this is certainly not the case for (iii), $W \to t\bar{b}$ could be a preferable experimental trigger because of its clean signature.

That fusion is only part of the story is clearly illustrated by glancing back at the production of charm at lower energies; see Figs. 2, 3. Absolute cross sections seem to be in excess of those computed from the fusion diagrams (Fig. 2). Finding excuses for this is a useless effort as the fusion mechanism does not yield charmed particles with large longitudinal momentum (say $x_L > 0.2$) contrary to observation; see Fig. 3. As $m_Q/\sqrt{s}$ is likely to be the crucial variable in the problem, t-quark production at the $\bar{p}p$ collider could be qualitatively similar to c-quark production at the ISR as we might guess that, to within a factor of three or so, $(m_t/540) \simeq (m_c/63)$. One might also expect that the "diffractive" cross section has a logarithmic energy dependence and varies with the quark mass as $(m_Q)^{-2}$. This behaviour however cannot be correct: it predicts that $\sigma_b/\sigma_c \simeq 1/8$ which disagreees with ISR experiments, as the leptonic decays associated with such a large b-cross section are inconsistent[2] with the experimental fact that $(e,\mu)/\pi \simeq 10^{-4}$.

A three-step scenario for producing diffractive $\Lambda_Q M_{\bar{Q}}$ pairs is depicted in Fig. 4. When the QCD-evolved proton is in a state $uudQ\bar{Q}$ (step A), one of the heavy quarks ($\bar{Q}$ in Fig. 4) interacts with the colliding $\bar{p}$ (step B) and finally the interacting $\bar{Q}$ recombines with a valence u quark to form $M_{\bar{Q}}$ while the spectator Q recombines with the other u,d valence quarks to form Λ_Q (step C). The $Q,\bar{Q}$ which originate with low x from gluon emission, nevertheless emerge in particles with large Feynman x. As indicated in Fig. 4, the Λ_Q emerges at large x because the heavy quark Q combines with two valence quarks, whereas the $M_{\bar{Q}}$ containing one valence quark has intermediate x.

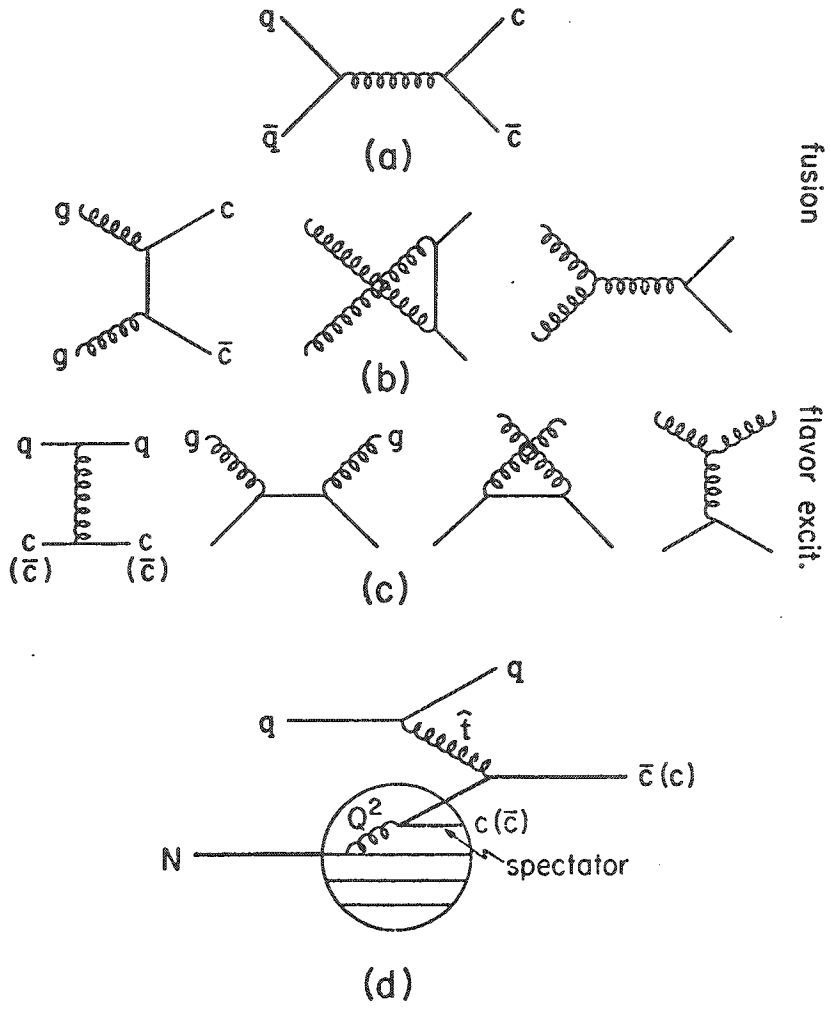

Fig. 1: Order α_s^2 diagrams for charm production. The production via flavour excitation is sketched in (d).

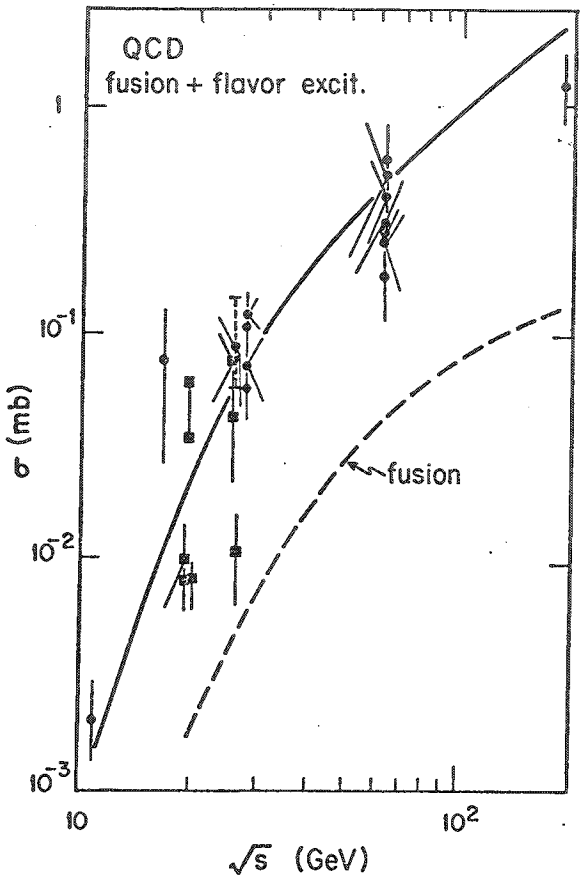

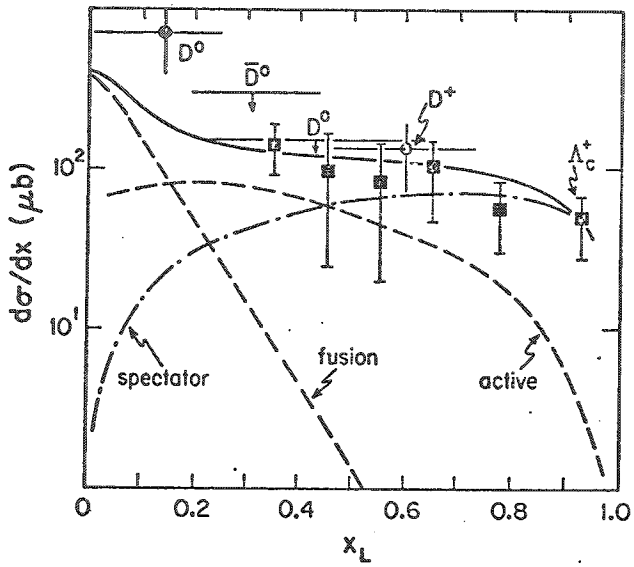

Figs 2, 3:
Data on the hadroproduction of charm compared with calculations based on the diagrams of Fig. 1.

Reliable predictions cannot be made because of the severe ambiguities associated with each of the steps in such a calculation. Barger et al.[3] perturbatively compute the $Q(\bar{Q})$-hadron cross section (step B) from the "flavour excitation" diagrams shown in Fig. 1. They lump the structure functions of steps A, C into one and basically let the charm data determine it. Such a model can then be scaled in m_Q. The prediction for the "diffractive" production of heavy quarks is shown in Fig. 5, where it is compared to the standard fusion calculation. In the m_Q range where the t quark is expected, an increase of the yield by roughly a factor 10 is predicted.[3] Collins and Spiller[4] on the other hand perturbatively compute step A, explicitly incorporate the recombination in step C, and guess (in one version of their calculation) that $\sigma(Qp) \sim (m_Q)^{-2}$ in step B. This is reasonable: one determines $\sigma(Qp)$ by the additive quark model and the $(m_Q)^{-2}$ suppression reflects the fact that the $Q\bar{Q}$ scattering state is a short-time fluctuation (or alternatively that the scattering $\bar{Q}$ is off-shell because of its large mass m_Q). Their predictions for m_t = 25, 35, 45 GeV are also shown in Fig. 5.

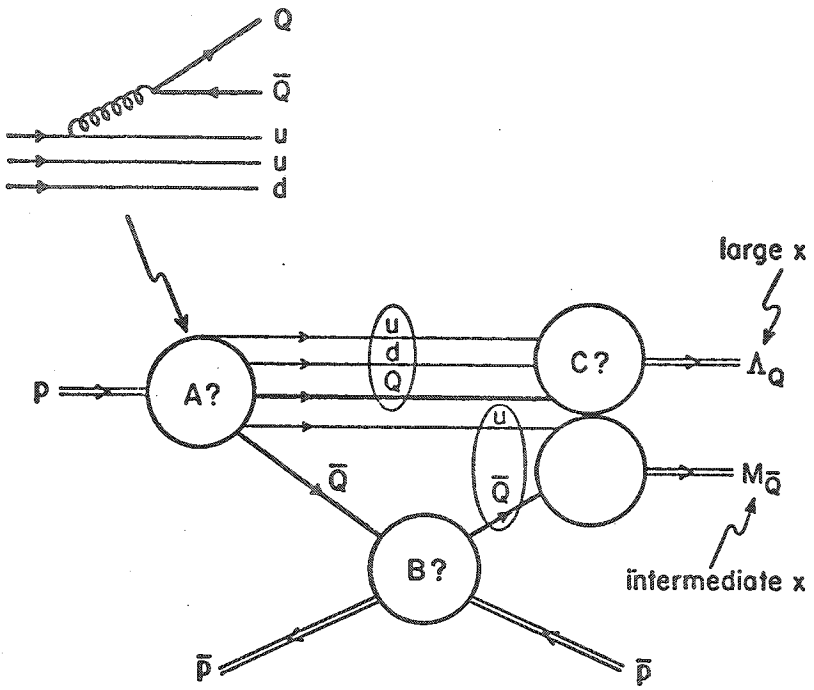

Fig. 4: A sketch of the mechanism for diffractive $\Lambda_Q M_{\bar{Q}}$ production. The three stages A, B and C are discussed in the text.

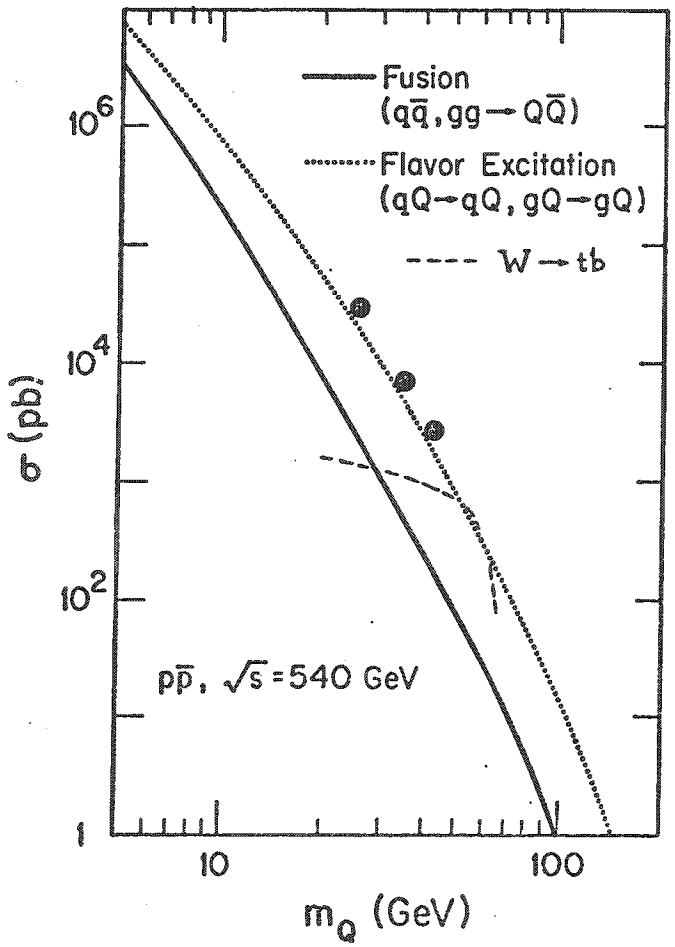

Fig. 5:
The m_Q dependence of the three mechanisms for heavy quark production. Note that weak production exceeds QCD fusion for $30 < m_t \lesssim 70$ GeV.

These calculations are able to describe the diffractive production of strange and charm quarks (see Figs. 2, 3 and Refs. 1, 3, 4, 5) and to the extent that the predictions in Fig. 5 represent an extrapolation in $m_Q/\sqrt{s}$ of data, they might well be a reliable guide to top production. In a collider experiment when the proton dissociates into $\Lambda_t\bar{T}$ the forward going Λ_t is presumably not detected, but, as emphasized by Horgan and Jacob,[6] the $\bar{T}$ meson produced at intermediate x (and low p_T) may be observed by its semileptonic decay $\bar{T} \to \ell^- \bar{\nu} X$. The transverse momentum distribution of the ℓ^- should peak at $p_{\ell T} \approx m_t/4$. A lepton charge asymmetry should result, since when alternatively the incoming antiproton dissociates into $\bar{\Lambda}_t T$ the $\bar{\Lambda}_t$ goes undetected and the ℓ^+ from $T \to \ell^+ \nu X$ may be observed. If the X jet can be identified then the "cluster" transverse mass (see section 3.2) may be exploited to estimate the mass of the T meson.

Notice that this hierarchical structure in x (Λ_t at large x, $\bar{T}$ at intermediate x, $t\bar{t}$ pairs at low x; compare Fig. 3) does not exist in the intrinsic heavy quark model.[7] Here the $t,\bar{t}$ themselves have large x and an intrinsic $t\bar{t}$ pair would be hardly separated by the recombination with light u,d quarks. No lepton asymmetry is expected. Finally it is interesting to speculate that a "diffractive" mechanism could be an unexpectedly abundant source of Higgs,[8] gluinos, ... and everything else that is routinely calculated from $q\bar{q}$, gg fusion.

We also draw attention to an intriguing result[9] presented at this conference: roughly 30% of the (mostly gluon) jets observed in $\bar{p}p$ collisions contain a charmed D particle which is observed through the $D^* \to D$ transition. This means that almost every jet could contain some type of charmed particle. The jets are preferentially produced at small angles as they approximately follow a $\sin^{-4}\frac{\theta}{2}$ Rutherford angular distribution. This source of charm is therefore also expected to preferentially populate the forward direction. The occurrence of such a "boring" production mechanism of new flavours could force us to completely reconsider the heavy flavour situation at the collider.

2. DILEPTONS: THE KEY TO HEAVY QUARKS?

The intimate connection between $Q\bar{Q}$ and $\ell\bar{\ell}$ production is well illustrated by some typical processes which lead to dimuons from $b\bar{b}$ production and decay:

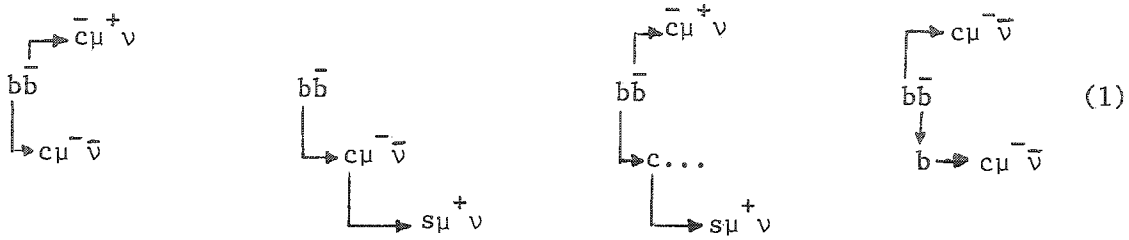

unlike sign, opposite sides | unlike sign, same side | like sign, opposite sides | like sign from B^o-$\bar{B}^o$ mixing

A calculation[10] of the production cross section of opposite sign dileptons from $c\bar{c}$, $b\bar{b}$ and $t\bar{t}$ origin is shown in Fig. 6 as a function of the dilepton invariant mass (assuming m_t = 35 GeV). Also shown is the production of large mass lepton pairs by the Drell-Yan mechanism $q\bar{q} \to \gamma^*(Z) \to \ell^+\ell^-$. Figure 7 shows the results of the same calculation after imposing cuts on the transverse momentum of the lepton. In the real world such cuts are required to identify the lepton in the detectors. In the mass range M ≃ 10 GeV where the dimuon signal peaks (for $p_{\mu T}$ > 5 GeV) the Drell-Yan and $b\bar{b}$ sources of dileptons closely compete. Dileptons of $b\bar{b}$ origin can however be separated by the following distinctive features: (i) presence of charm jets, (ii) presence of strange particles, (iii) the possible production of same sign dileptons.

In Table 1 we give the total event rate for dimuon production from various sources, including those of eq. (1). We see that $b\bar{b}$ production dominates at low $p_{\mu T}$ but is soon overtaken by Drell-Yan production. The table also shows the effect of B^o-$\bar{B}^o$ mixing on the relative number of like-and unlike-sign muon pairs. Our understanding of the $b\bar{b}$ dilepton signal should be a very high priority in two respects: it is the background to the "anomalous" and puzzling dimuon events presented at this conference[13] (or is it really the origin of these events?) and it is also the background in the t-quark search using the dilepton signal (see Figs. 6, 7 and Section 4).

We suggest[14] using ψ's as a tag for b mesons through the decay $b \to \psi X$. This decay of b-flavoured mesons has been observed[15] with the theoretically expected branching ratio of order 1%. For $B(B \to \psi X) = 0.01$ the production of ψ's via b decay dominates (at least at large p_T where the $\psi \to \mu^+\mu^-$ can be experimentally identified) the production of ψ's via the conventional QCD mechanisms $gg \to g\psi$ and $gg \to \chi_J g$ followed by $\chi_J \to \psi\gamma$ (J = 0, 1, 2).

Fig. 6:
The cross section for dilepton production (as a function of the invariant mass of the lepton pair) in $p\bar{p}$ collisions at $\sqrt{s}$ = 540 GeV, taken from ref.10. No K factor is included, that is K=1.

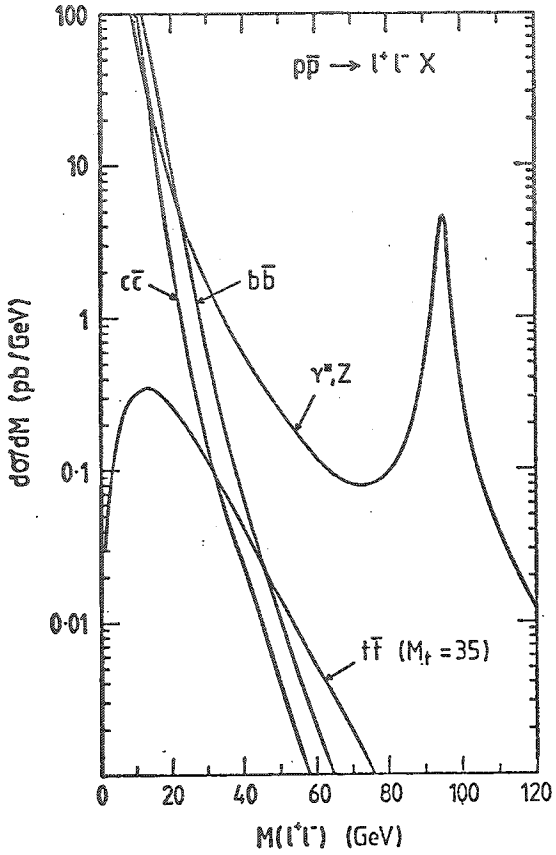

Fig. 7:
The same as Fig. 6 but with minimum p_T cuts imposed on the leptons.

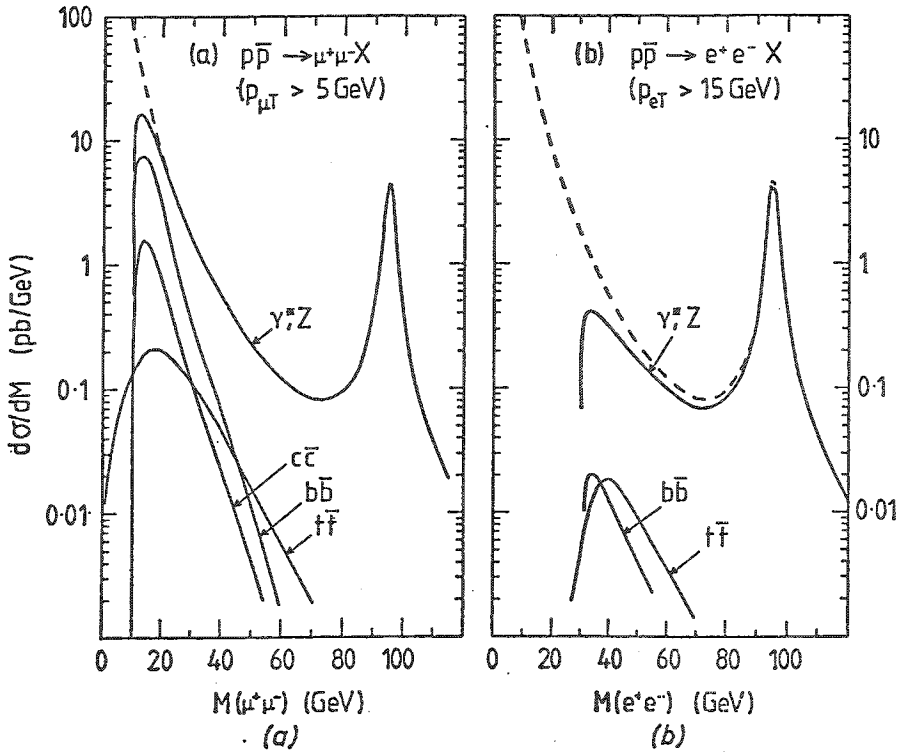

Table 1.

The number of dimuon events expected[11] in $\bar{p}p$ collisions at $\sqrt{s}$ = 540 GeV from various production mechanisms for different minimum p_T cuts on the muons ($p_{\mu T}$ shown in GeV/c). The event rate is shown for an integrated luminosity of 100 nb^{-1}: that is, the table entries multiplied by 10 give the cross sections in pb. The figures in brackets show the effect of the maximal expected B^o-$\bar{B}^o$ mixing, that is a mixing parameter ε = 0.15 in the notation of ref. 12. Dimuons from $t\bar{t}$, $t\bar{b}$ and $\bar{t}b$ cascades may compete at high $p_{\mu T}$ and are considered further in section 4 (see, in particular, Fig. 13). No K factor is included (K=1).

mechanism for dimuon production	$p_{\mu T} > 3$	$p_{\mu T} > 5$	$p_{\mu T} > 10$
$b\bar{b}$ decays:			
$\mu^+\mu^-$, opposite sides	143 (118)	12 (10)	0.4 (0.3)
$\mu^+\mu^-$, same side	15	1	0.01
$\mu^+\mu^+$, $\mu^-\mu^-$	42 (67)	3 (5)	0.04 (0.1)
$c\bar{c} \to \mu^+\mu^-$	23	2	0.1
$b \to \psi \to \mu^+\mu^-$	16	3	0.2
Drell-Yan $\gamma^*(Z) \to \mu^+\mu^-$	58	19	5

This is shown in Fig. 8. ψ's could provide us with a good measurement of the b-quark cross section. The "background" QCD process, dominated by $gg \to \chi_J g$ ($\chi_J \to \psi\gamma$) is also interesting. It is a sensitive measure of the gluon structure function at $\sqrt{s}$ = 540 GeV. Its determination at $\sqrt{s}$ = 540 GeV would be invaluable to help us control perturbative calculations in the small x ($x = m_\psi/\sqrt{s}$) range that is so important for making predictions[16] for TeV energies (SSC, Juratron). For example, cross sections for ψ production via χ's are increased by one order of magnitude if we replace the structure functions of Ref. 17, used in calculating the results shown in Fig. 8, by a scaling $3(1-x)^5$ gluon distribution.

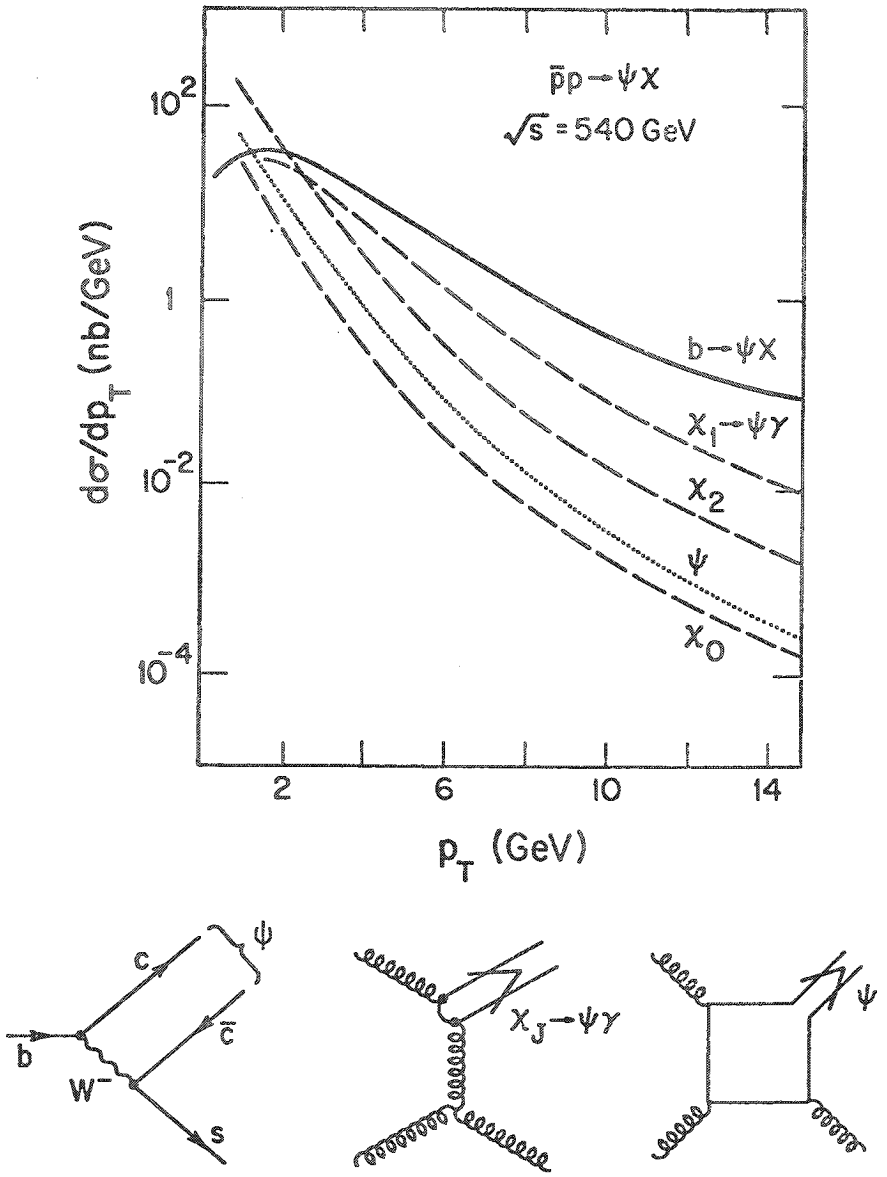

Fig. 8: The p_T distribution of J/ψ production in $\bar{p}p$ collisions at $\sqrt{s}$ = 540 GeV, together with some of the basic diagrams.

3. SIGNATURES FOR TOP

There are systematic procedures for isolating a t quark from the observation of its semileptonic decay products, $t \to b\ell\nu$, regardless of the way in which it is produced. We are concerned with events in which there is a charged lepton, jet activity and (provided the detector is hermetic) missing momentum transverse to the beam directions ($\vec{p}_{\nu T}$). The major problem is to distinguish such a t decay from the large background of $b \to c\ell\nu$ decays arising from the much more numerous $b\bar{b}$ pairs produced at the collider (see Fig. 5).

3.1 $\ell\nu$ transverse mass

If only the charged lepton and the missing transverse momentum are identified then it is appropriate to form the transverse mass, $M_T(\ell\nu)$, of the $\ell\nu$ system, defined by

$$M_T^2\ (\ell\nu) = (E_{\ell T} + E_{\nu T})^2 - (\vec{p}_{\ell T} + \vec{p}_{\nu T})^2 \qquad (2)$$

where $E_T^2 \equiv m^2 + p_T^2$. For the semileptonic decay of a heavy quark ($Q \to q\ell\nu$) M_T is restricted to the range

$$0 \leq M_T(\ell\nu) \leq m_Q - m_q . \qquad (3)$$

Fig. 9 shows the "idealized" M_T distributions expected from t and b semileptonic decays, together with that from the W leptonic decays[18]. The heavy quark decays may be distinguished from the W decays by their accompanying jet activity. The difference in the kinematic end-points of the distributions can be exploited to separate the t from the b (and c) decays. In practice the sharp cut-offs at $m_Q - m_q$ only occur when ℓ and ν result from the same primary decay; cascade semileptonic decays lead[20] to tails above the end-points (see Fig. 12 (a)). Moreover uncertainties in the observed values of $\vec{p}_{\nu T}$ smear the distributions and, in particular, there is a tendency of the M_T distribution of the much more numerous b decays to spill over to large M_T and to mask the t signal[21]. Therefore other criteria need to be invoked to convincingly isolate a t quark signal. We discuss these below.

3.2 Cluster transverse mass

In $t \to b\ell\nu$ events in which the b decay jet is also identified and measured we can form a much more selective transverse mass distribution. We treat the $b\ell$ system as a cluster with

$$\vec{p}_T = \vec{p}_{bT} + \vec{p}_{\ell T}$$
$$M^2 = (p_b + p_\ell)^2$$
$$E_T^2 = M^2 + p_T^2$$

and form a "cluster transverse mass"[18]

$$M_T^2\ (b\ell;\nu) = (E_T + E_{\nu T})^2 - (\vec{p}_T + \vec{p}_{\nu T})^2 \qquad (4)$$

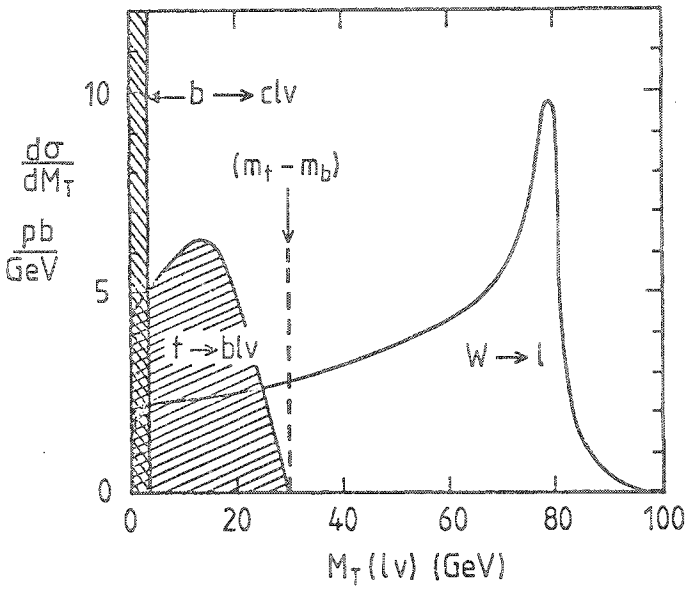

Fig. 9: The transverse $\ell\nu$ mass distributions[18,19] resulting from $t \to b\ell\nu$ and $b \to c\ell\nu$ decays, compared to that from the sum of the W leptonic decays: $W \to \ell\nu$ and $W \to \tau\nu \to \ell\nu\nu$, where ℓ = e or μ. It is assumed that m_t = 35 GeV and that $(B\sigma)_W = 2(B\sigma)_t$. With perfect resolution $M_T(\ell\nu)$ for $b \to c\ell\nu$ is confined to the region $M_T < m_b - m_c \simeq 3$ GeV.

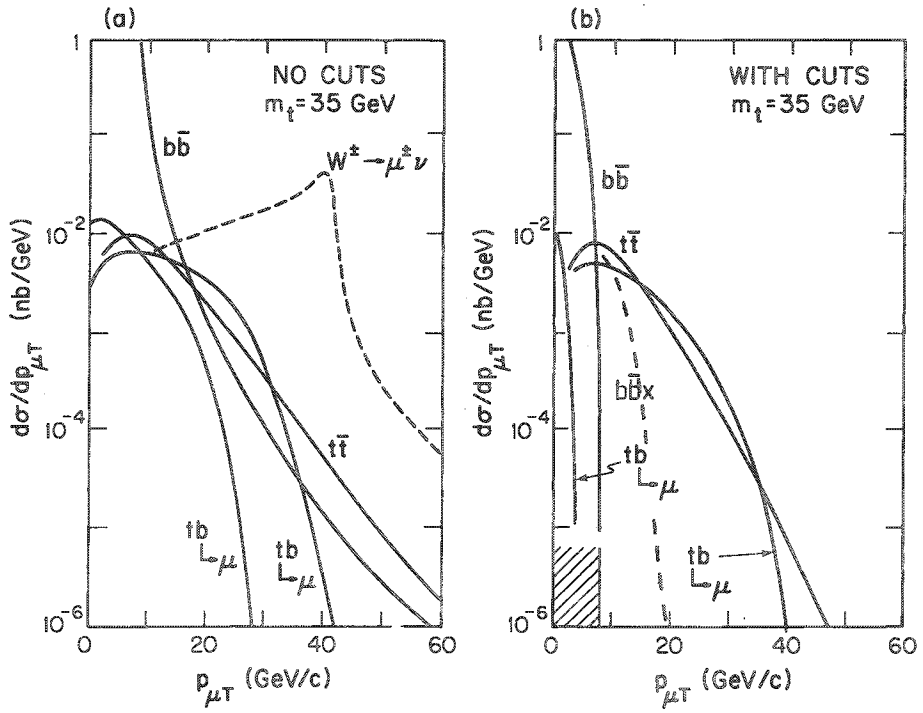

Fig. 10: The predicted muon p_T distributions from heavy quark production and decay in $p\bar{p}$ collisions at $\sqrt{s}$ = 540 GeV: (a) without cuts and (b) with the requirement that each event contains two p_T > 8 GeV jets, together with an isolated muon such that the summed hadronic $|p_T|$ is less than 3 GeV in a 30° cone about its direction. Only events from QCD fusion or W decay are shown; diffractive $t\bar{t}$ production is not included. For comparison the $\mu^{\pm}$ spectrum from $W \to \mu\nu$ decay is also shown. The figure is taken from refs. 22 and 23.

This leads to an effective two body ($t \to b\ell + \nu$) decay distribution with a sharp Jacobian peak at $M_T(b\ell;\nu) = m_t$ (see Fig. 3 of ref. 18). Realistic calculations[22,23], including missing p_T uncertainties and full cascade decays, smear the sharp peak (see Fig. 12) but leave a very pronounced t signal at m_t. A further discussion of this variable is given by Stirling[24].

3.3. Lepton isolation

The heavy quarks produced by QCD fusion ($t\bar{t}$,$b\bar{b}$) or by W decays ($t\bar{b}$,$\bar{t}b$) will lead to two jets which are approximately back-to-back in the transverse plane. The more massive the heavy quark the broader will be the jet of its decay fragments. Indeed for a massive t quark the t and $\bar{t}$ decay jets may overlap and even three subjets from a hadronic t decay may be visible. If we sum the moduli of the transverse momenta relative to the jet axis of the eventual light decay fragments of a Q decay jet we find[22] $\Sigma|\vec{p}_{i\perp}| \simeq \pi m_Q/4$, which is about 30 GeV for a t quark of mass 40 GeV, but only about 4 GeV for b decay. Moreover when concentrating on a decay lepton at fixed large p_T to the beam axis a relatively light quark like a b is itself inevitably produced at large p_T and so its decay products will appear collimated. Such a collimation need not occur for the decay of the massive t quark. We conclude that leptons at high p_T which result from b decay will belong to narrow jets containing hadronic decay debris, whilst those from t decay have a good chance of being isolated. However the lepton in $b \to c\ell\nu$ may appear isolated if the accompanying c jet has low p_T. An effective way of removing the large $b\bar{b}$ (and also $c\bar{c}$) background from $t\bar{t}$ or $t\bar{b}$, $\bar{t}b$ events is therefore to select events with an "isolated" lepton[22,25,26], together with two large p_T hadronic jets. This is well illustrated by the muon p_T distributions shown in Fig. 10, which assume m_t = 35 GeV. Although muons from $b\bar{b}$ decays dominate the spectrum (figure (a)), they can be eliminated at large $p_{\mu T}$ by criteria requiring muon isolation and two energetic jets (figure (b)). Indeed if m_t = 35 GeV, figure (b) predicts that in the present data sample (integrated luminosity of 136 nb^{-1}) there should be about 10 "clean" t quark events with $p_{\mu T} > 8$ GeV/c, about half coming from $W \to t\bar{b}$, $\bar{t}b$ decays and half from the $t\bar{t}$ produced by QCD fusion.

There is still a chance of events arising from higher-order QCD processes[23,26,27], such as $gg \to b\bar{b}g$ escaping the acceptance cut, see Fig. 11. An upper limit[23] to these contributions is shown by the $b\bar{b}x$ curve on Fig.10(b). This residual background may be eliminated by exploiting transverse mass techniques, as can be seen in Fig. 12.

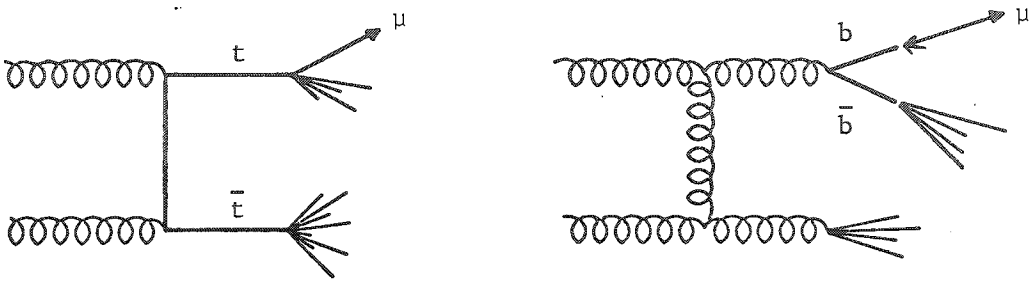

Fig. 11: The t signal of an isolated muon and two high p_T jets and a higher-order QCD background contribution in which one b decay fakes an isolated muon.

Finally, a nice property[28] of the $W \to t\bar{b}$ events is that the p_T distribution of the $\bar{b}$ jet has a Jacobian peak at

$$p_T(\bar{b}) \simeq (M_W^2 - m_t^2)/2M_W,$$

and so the indentification of a few events of this type would give an estimate of the t quark mass. Indeed one UA1 event[29] in the 1982 data sample has all the characteristics of $W \to t\bar{b}$ although the decay electron is more energetic than expected: an isolated electron of E_T = 30 GeV which recoils against a 29 GeV jet containing a reconstructed charm particle. Taking this event seriously would give $m_t \simeq 40$ GeV.

4. OTHER TOP SIGNALS

4.1 Multileptons

In many ways the multilepton signatures[30,10,12] of t quark production are superior to the single lepton events. The main disadvantage is that the event rate is an order of magnitude smaller. Possible signals from primary semileptonic decays are

$$gg, q\bar{q} \to t\bar{t} \to \ell^+\ell^- X$$

$$q\bar{q}' \to W \to t\bar{b} \to \ell^+\ell^+ X$$

where ℓ = e or μ. The results of a full cascade calculation[12] are shown in Fig. 13. For $p_{\ell T} > 5$ GeV/c the dilepton t signals are of the order of 10pb and so the signals are just beyond the present data sample. The $b\bar{b}$ background (discussed in detail in section 2) can be greatly suppressed because isolation criteria can now be imposed on two leptons. Such data will be of immense interest as the luminosity increases.

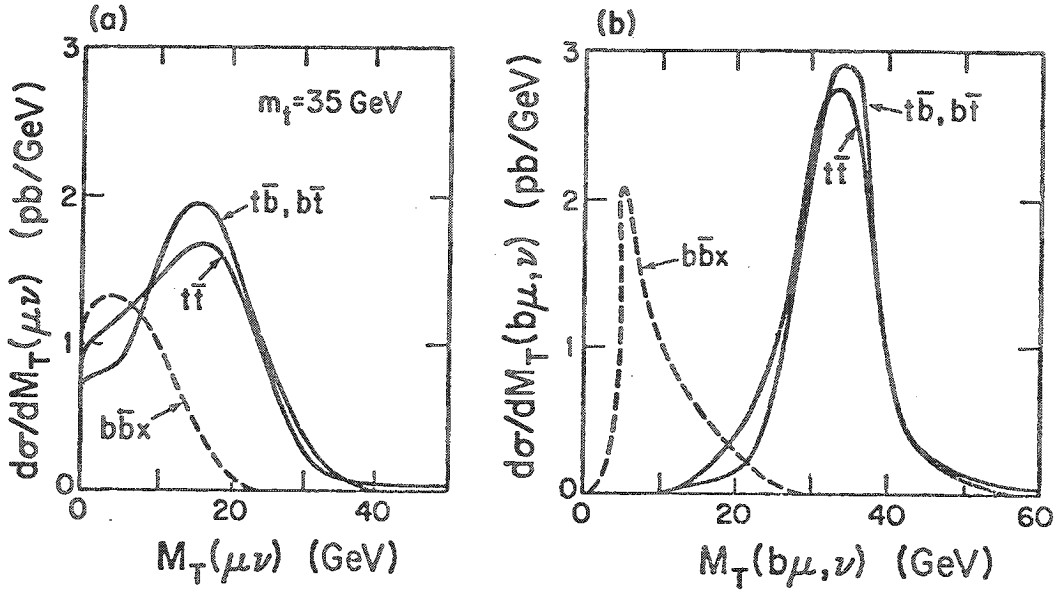

Fig. 12: The μν and cluster transverse mass distributions calculated from complete cascade decays with possible multiple neutrinos and including resolution smearing. The $b\bar{b}x$ backgrounds (dashed curves) are due to higher-order QCD processes which partially survive the $p_{\mu T} > 8$ GeV/c and muon isolation cuts imposed in Fig. 10(b). The figure is taken from ref. 23.

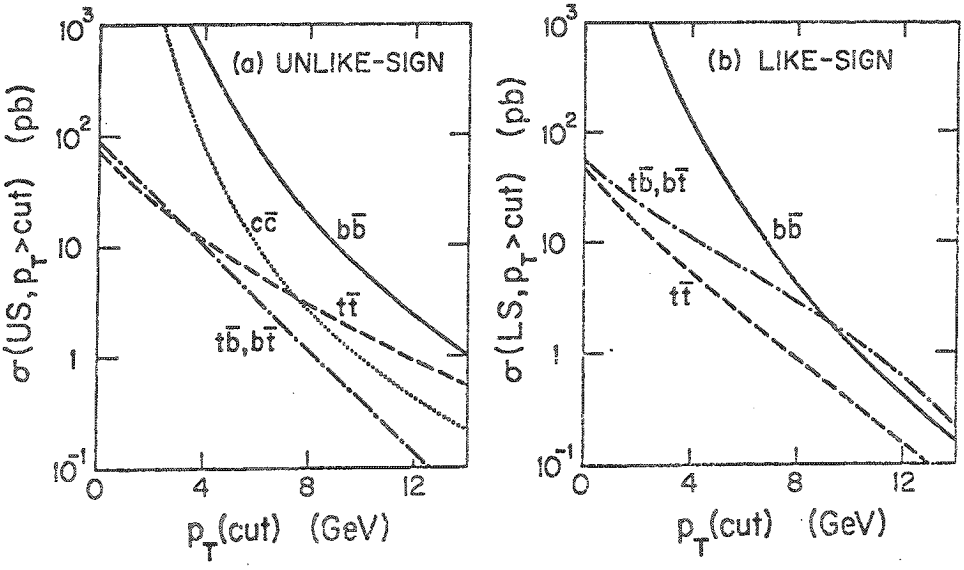

Fig. 13: Dependence of the cross section for dilepton production on the lepton p_T cut at $\sqrt{s}$ = 540 GeV, with m_t = 35 GeV. The figure is from ref. 12 and includes leptons from the full $t \to b \to c \to s$ cascades.

4.2 T production?

Just as ψ production may act as a trigger[14] for b quark production via the decay $B \to \psi X$, can $T \to \mu^+\mu^-$ be used to indicate t quark production via $T \to TX$? Unfortunately the $T \to TX$ branching ratio is much too small and T production is dominated by the subprocess $gg \to Tg$.

4.3 Toponium

The most frequently produced toponium state is predicted[31] to be η_t (^1S_o). If m_{η_t} = 70 GeV then the cross section, calculated from gg fusion, is about 5 pb at $\sqrt{s}$ = 540 GeV rising to 0.1 nb at $\sqrt{s}$ = 2 TeV. These estimates use a scale breaking gluon distribution, no K factor (K = 1) and assume $|\psi(0)|^2 \sim m_Q^2$. On each count they therefore represent a lower limit to η_t production. However the best signature is the decay mode $\eta_t \to \gamma\gamma$ which is expected to have a branching ratio of only about 1%.

ACKNOWLEDGEMENTS

We wish to thank B. Hahn and his colleagues at the University of Bern for arranging an excellent Workshop and to thank H. Baer, V. Barger, E.W.N. Glover, F. Herzog and R.J.N. Phillips for enjoyable collaborations which led to many of the results presented here.

REFERENCES

1. F. Halzen, Rapporteur's talk at the 21st High Energy Physics Conference, Journal de Physique, supplement to 12, C3-381 (1982).
2. F. Halzen, A.D. Martin and D.M. Scott, Zeit. für Phy. C13, 291 (1982).
3. V. Barger, F. Halzen and W.Y. Keung, Phys. Rev. D24, 1328 (1981) and D25, 112 (1982).
4. P.D.B. Collins and T. Spiller, Durham preprint DTP/84/4 (1984).
5. R. Odorico, Phys. Lett. 107B, 231 (1981) and in AIP Conf. Proc. No. 85, p. 100 (1981).
6. R. Horgan and M. Jacob, Phys. Lett. 107B, 395 (1981).
7. S.J. Brodsky, P. Hoyer, C. Peterson and N. Sakai, Phys. Lett. 93B, 451 (1980).
8. V. Barger, F. Halzen and W.Y. Keung, Phys. Rev. D25, 1838 (1982).
9. C. Frey, UA1 Collaboration, these proceedings.
10. E.W.N. Glover, F. Halzen and A.D. Martin, Durham preprint DTP/84/2, Phys. Lett. B (to be published).
11. We thank E.W.N. Glover for preparing table 1.
12. V. Barger and R.J.N. Phillips, Madison preprint MAD/PH/155 (1984).
13. C. Rubbia, UA1 Collaboration, these proceedings.
14. F. Halzen , F. Herzog, E.W.N. Glover and A.D. Martin, Durham preprint DTP/84/8.
15. S. Stone, CLEO collaboration, Proc. of the Int. Symp. on Lepton and Photon Interactions at High Energies, Cornell (1983).
16. See, e.g., I. Hinchliffe, these proceedings.
17. M. Glück, E. Hoffman and E. Reya,Z. Phys. C13, 119 (1982).

18. V. Barger, A.D. Martin and R.J.N. Phillips, Phys. Lett. 125B, 339 (1983).
19. V. Barger, Madison preprint MAD/PH/165, to be published in Proc. of Physics of 21st Century Conference, Tuscon (1983).
20. V. Barger, A.D. Martin and R.J.N. Phillips, Phys.Rev. D28, 145 (1983).
21. F. Halzen and D.M. Scott, Phys. Lett. 129B, 341 (1983); G. Ballocchi and R. Odorico, Bologna report IFUB 83/11.
22. V. Barger, H. Baer, A.D. Martin and R.J.N. Phillips, Phys. Rev. D29, 887 (1984).
23. V. Barger, H. Baer, K. Hagiwara, A.D. Martin and R.J.N. Phillips, Phys. Rev. (in press).
24. W.J. Stirling, these proceedings.
25. R. Odorico, CERN preprint TH 3678
26. S. Aronson, F. Paige, S. Protopopescu and D. Weygand, reported at the Gordon Conference, Aug. 1983.
27. I. Schmitt, L.M. Sehgal, H. Tholl and P.M. Zerwas, Aachen preprint PITHA 83/26.
28. V. Barger, A.D. Martin and R.J.N. Phillips, Phys. Lett. 125B,343 (1983).
29. D. DiBitonto, Proc. of Third Moriond Workshop on $\bar{p}p$ Physics p.473 (1983).
30. M. Abud, R. Gatto and C.A. Savoy, Phys. Lett. 79B, 435 (1978); S. Pakvasa, M. Dechantsreiter, F. Halzen and D.M. Scott, Phys. Rev. D20, 2869 (1979); N. Cabibbo and L. Maiani, Phys. Lett. 87B, 366 (1979); L.L. Chau, W.Y. Keung and S.C.C. Ting, Phys. Rev. D24, 2862 (1981); F.E. Paige, AIP Conf. Proc. 85, 168 (1981).
31. R. Baier and R. Rückl, Nucl. Phys. B208, 381 (1982).

THE MINIMUM MASS TECHNIQUE FOR DETECTING NEW HEAVY STATES IN HIGH ENERGY HADRON COLLISIONS

W.J. Stirling

CERN, Geneva, Switzerland

ABSTRACT

Many predicted heavy states are expected to decay frequently into three or more body final states in which at least one particle, such as a neutrino or photino, is non-interacting. A method is described for obtaining estimates of both the mass and the longitudinal momentum of the parent state. Two applications - the decay of top quark hadrons and gluinos (in the R symmetry scheme) - are discussed in detail.

1. INTRODUCTION

In recent years there has been a proliferation of theoretical predictions for new heavy states. Examples include the top quark and Higgs boson of the standard model, and more exotic 'constructs' such as supersymmetric particles, technicolour particles and excited quarks, leptons and weak bosons. A characteristic feature of many of these states is their frequent decay into multiparticle (or multi-jet) channels in which at least one particle is non-interacting. For example,

$$\begin{aligned} T &\rightarrow \mu \nu B \\ \tilde{g} &\rightarrow q \bar{q} \tilde{\gamma} \\ H &\rightarrow \mu \nu q \bar{q} \end{aligned} \qquad (1)$$

where T, B denote hadrons containing top, bottom quarks, $\tilde{g}$ and $\tilde{\gamma}$ denote the supersymmetric gluino and photino, and H is either the Higgs boson or a (WW) bound state. Here we are adopting the usual assumption that the photino is the lightest supersymmetric particle and that the theory is R invariant, i.e., the lightest (stable) supersymmetric particle has to be found at the end of the decay chain.

While the observation of missing energy in the final state is a useful signature for such processes, the mass and momentum of the parent cannot be determined directly from the data since one of the four-momenta in the final

state is not measured. It is important therefore to search for techniques which provide good estimates of these quantities. This talk will summarize the "minimum invariant mass" approach emphasized recently in Ref. 1). This method uses the four-momenta of the observed final state particles to construct invariant mass and longitudinal momentum distributions for the parent which are sharply peaked at their true values. Section 2 contains a general discussion of the method and two applications are considered in Section 3.

2. THE MINIMIZATION PROCEDURE

Consider a heavy state Q (=top meson, gluino,...) of mass M produced predominantly at small transverse momentum in a high energy process. Suppose that Q decays into n+1 (effectively massless) particles or jets, n of which are observed and their four-momenta measured. The missing transverse momentum is ascribed to the non-interacting particle, and so the four-momenta of the decay products can be written

$$p_i^\mu = (E_i, \vec{p}_{T_i}, p_{L_i}) \qquad i = 1, \ldots n$$

$$p_{n+1}^\mu = (\sqrt{z^2 + p_T^2}, \vec{p}_T, z) \qquad \vec{p}_T = -\sum_{i=1}^{n} \vec{p}_{T_i} \tag{2}$$

where z labels the unknown longitudinal momentum of the missing particle. As a function of z the invariant mass of the system M(z) has a unique positive minimum, i.e.,

$$\left.\frac{dM}{dz}\right|_{z=z_0} = 0$$

$$z_0 = \left(\sum_{i=1}^{n} p_{L_i}\right) \left|\sum_{i=1}^{n} \vec{p}_{T_i}\right| \left\{\left(\sum_{i=1}^{n} E_i\right)^2 - \left(\sum_{i=1}^{n} p_{L_i}\right)^2\right\}^{-\frac{1}{2}} \tag{3}$$

The minimum mass M* is defined to be the minimum invariant mass which can be constructed for the system, i.e., $M^* = M(z_0)$. A corresponding longitudinal momentum $P^*_L = \Sigma_{i=1}^{n} P_{L_i} + z_0$ can also be defined. Explicitly[1],

$$M^* = \left\{ \left(\sum_{i=1}^{n} E_i \right)^2 - \left(\sum_{i=1}^{n} P_{L_i} \right)^2 \right\}^{\frac{1}{2}} + \left| \sum_{i=1}^{n} \vec{P}_{T_i} \right|$$

$$P_L^* = \left(\sum_{i=1}^{n} P_{L_i} \right) \left[1 + \left| \sum_{i=1}^{n} \vec{P}_{T_i} \right| \left\{ \left(\sum_{i=1}^{n} E_i \right)^2 - \left(\sum_{i=1}^{n} P_{L_i} \right)^2 \right\}^{-\frac{1}{2}} \right] \qquad (4)$$

(Note that both these quantities are functions of the measured parameters only.) The assertion is that the decay distributions $d\Gamma/dM^*$ and $d\Gamma/dP_L^*$ are sharply peaked at the true values M and P_L. Thus the method allows an accurate determination of the mass and longitudinal momentum (more generally, the longitudinal momentum distribution) of the heavy state Q.

To see this explicitly, consider a simple phase space model for the decay $Q \to \Sigma_{i=1}^{n+1} P_i$. For this, the M* distribution can be calculated analytically. Defining a dimensionless variable $\xi = M^*/M$, the result is

$$\frac{1}{\Gamma} \frac{d\Gamma}{d\xi} = \frac{2n}{n+1} \frac{\xi^{2n-1}}{\sqrt{1-\xi^2}} F\left(\frac{1}{2}, \frac{n-1}{2}, \frac{n+3}{2}; \xi^2 \right) \qquad (5)$$

where F is the hypergeometric function. The distributions for n = 2 and n = 4 are shown in Fig. 1 - the sharp peak at $\xi = 1$ is evident. Taking the $\xi \to 1$ limit of Eq. (5) gives

$$\frac{1}{\Gamma} \frac{d\Gamma}{d\xi} \underset{\xi \to 1}{\sim} \frac{1}{\sqrt{1-\xi^2}} \left\{ \sqrt{\pi} \frac{\Gamma\left(\frac{n+1}{2}\right)}{\Gamma\left(\frac{n}{2}\right)} \right\} \qquad (6)$$

which shows that the singularity gets stronger as n increases. [The quantity in { } in Eq. (6) is a monotonically increasing function of n for $n \geq 0$.] This result is intuitively obvious, since as n increases a smaller fraction of the information about the true invariant mass is "lost" with the non-interacting particle. Similar remarks apply to the longitudinal momentum distribution $1/\Gamma\, d\Gamma/dP_L^*$. There is, however, no simple analytic analogue of Eq. (6) - the distribution corresponding to the particular case n = 2 is calculated numerically in the next Section.

Finally, it can be shown that the above distributions are quite insensitive to the inclusion of transverse momentum smearing for the heavy state Q and also final state particle masses, provided that $\langle P_T \rangle_Q$, $m_i \ll M$.

3. TWO APPLICATIONS

3.1 A process which appears ideally suited to the above analysis is the associated production and semi-leptonic decay of a top quark meson. Experience with the ISR shows that single large mass diffractive excitation is likely to give a particularly favourable signal to background ratio in such a case[2]:

$$\begin{aligned} \bar{p} + p &\longrightarrow X + p \\ X &\longrightarrow \bar{\Lambda}_t + T + X' \\ T &\longrightarrow \mu^+(e^+) + \nu + \text{jet}(b\bar{q}) \end{aligned} \qquad (7)$$

where $T = (t\bar{q})$, $\bar{\Lambda}_t = (\bar{t}qq)$. It is difficult to predict the cross-section from first principles, but the observation of a large diffractive charm signal at the ISR[2] suggests that the top quark rate may be sizeable[3)-6)]. Insofar as the baryon is expected to keep some leading role, the meson should be produced predominantly at smaller x_F (the Feynman scaling variable) and with a rather small transverse momentum. The T meson should therefore be more easily detected, and more often, since fragments of the $\bar{\Lambda}_t$ baryon are likely to be lost at very forward angles.

As pointed out in Ref. 6), there is a special charge correlation effect in the semi-leptonic decay which can provide an additional signature. When the antiproton "flares" the $\bar{t}$ quark stays with the antibaryon whereas the t quark forms a meson with eventual μ^+ production. The opposite is true when the proton flares. It will be assumed that in an experiment it is possible to isolate events in which only the top meson decay products - in the form of a single jet, a lepton of the appropriate charge and missing transverse energy - are observed. This separation of the two top quark hadrons is necessary since the missing transverse momentum has to be attributed to a single non-interacting particle.

The situation is summarized as follows: the top meson is produced with an a priori unknown (but assumed soft) x_F distribution, and with small p_T, and subsequently decays into a lepton, a neutrino and a hadronic jet. The four-momenta of the muon and jet are measured and the missing transverse momentum is ascribed to the neutrino. As described above, the minimum invariant mass method uses these parameters to determine (a) the mass and (b) the longitudinal momentum distribution of the top meson.

Top quark signatures have also been analyzed extensively by Barger, Martin and Philips[7]. Their "cluster transverse mass" defined in Ref. 7) is in fact identical to the minimum mass. The cluster transverse mass distribution for top quark decay has been presented in Ref. 7). Here the analysis is generalized to include the longitudinal momentum distribution, and to explore the sensitivity to experimental cuts[1].

Figure 2 (solid line) shows the $\xi = M^*/M$ distribution for top meson decay. The light quark spectator in the decay $T \to \mu\nu B$ has been ignored and the exact weak interaction matrix element for $t \to \mu\nu b$ has been used. Comparison with Fig. 1 ($n = 2$) shows that the inclusion of the matrix element has a negligible effect on the distribution. Note that by definition [Eq. (4)], the minimum mass distribution is invariant under longitudinal boosts and so the same curve obtains for any top meson x_F distribution.

Now consider the distribution in the "longitudinal momentum" P_L^*. It is again convenient to define a dimensionless variable $R^* = P_L^*/M$. Figure 3 shows the distributions $1/\Gamma\ d\Gamma/dR^*$ for various values of the top meson longitudinal momentum $P_L = RM$. The distributions are different for different R (unlike M^*, P_L^* is not boost invariant) but in each case the peak is close to the "true" value of R. Thus the P_L distribution can be unfolded from the experimental P_L^* spectrum.

The distributions shown in Fig. 3 are integrated over all values of M^*. Not surprisingly, the peaks can be made sharper by restricting the events to those which have M^* values close to M. This is illustrated in Fig. 3 by the hatched distribution (for $R = 2$) which has the additional constraint $M^* \geq 0.95M$.

The above calculations are, of course, rather naive in that the effects of detector geometry, experimental cuts, backgrounds, etc., have not been included. Ultimately, the utility of the method depends on its ability to survive these effects and still yield useful information. It turns out that the M^* and P_L^* distributions are in fact quite insensitive to restrictions on the decay phase space[1]. Examples of this are illustrated in Fig. 2. The dashed line shows the M^* distribution with the additional requirement that the jet, muon and neutrino each have a transverse momentum greater than some threshold value, p_T^{min}, chosen here to be $1/8M$. This presumably removes the contamination of leptons, neutrinos and jets from other (background) sources. Although some of the top meson signal is also lost, there is evidently little change in shape. A second type of cut relates more to the geometry of the detector. If the muons are required to be central in the laboratory, then the M^* distribution is no longer invariant under longitudinal boosts. In fact for top mesons with $\langle x_F \rangle \geq 0$, such an experimental restriction introduces a bias in

favour of events in which the muon is moving backwards in the meson centre-of-mass frame. Figure 2 (dotted line) shows the M* distribution for a meson of longitudinal momentum $P_L = 2M$, with the requirement that the (laboratory) pseudorapidity of the muon be between -1 and +1. Although the normalization is reduced by a factor of about 4, the characteristic shape is the same and the Jacobian peak at M* = M persists. The conclusion is therefore that the minimum mass is indeed a reliable indicator of the true invariant mass, even in the presence of quite severe cuts.

3.2 In the previous application, the fragments of the heavy state Q were assumed to be isolated in phase space from all other final state particles, thus allowing a precise determination of the mass and longitudinal momentum. If, however, the heavy states are produced in pairs which are <u>not</u> well separated in phase space, then there is clearly a difficulty in disentangling the appropriate decay fragments for each Q. An interesting example is provided by the pair production of supersymmetric gluinos. According to the usual ideas, these are expected to decay into a light $q\bar{q}$ pair with an unobserved "light" photino[8]. Consider, therefore, the process

$$p + \bar{p} \rightarrow \tilde{g} + \tilde{g} + X \qquad \tilde{g} \rightarrow q\bar{q}\tilde{\gamma} \qquad \tilde{g} \rightarrow q\bar{q}\tilde{\gamma} \qquad (8)$$

with the gluinos produced predominantly at small p_T but with arbitrary p_L. The signature is four large p_T hadron jets with missing transverse momentum.

A minimum mass M^*_{ij} can be constructed for each of the six possible pairings of the jets [Eq. (4), n=2]. Two of these pairings correctly identify the same gluino fragments and for these the M* distribution shows the usual peak at M* = M. The other four permutations correspond to wrong pairings and for these the M* distribution has of course no Jacobian peak - the wrong-pair distribution is broad over the range $0 \leq M^* \leq M$ with a maximum at M* = M. However, when all the different pairings are considered in total, the sharp peak at M* = M <u>does</u> dominate over the combinatoric background. A Monte Carlo calculation is shown in Fig. 4, for a phase-space-only model. Evidently the gluino mass can be readily determined from this minimum mass distribution. The method is particularly useful when, because of p_T threshold and rapidity cuts, not all the jets are observed. By simply extending the definition to include all <u>observed</u> jet pairs, the signal can again be shown to dominate over the background. By subsequently selecting those events which are in the vicinity of the peak, information can be obtained on the gluino p_L distribution, as described in the previous application.

ACKNOWLEDGEMENTS

The work presented here was done in collaboration with Edmond Berger, Daryl DiBitonto and Maurice Jacob. I am very grateful to them for many stimulating discussions. I would also like to thank Professor Hahn and his colleagues for organizing such an excellent workshop.

REFERENCES

1) E.L. Berger, D. DiBitonto, M. Jacob and W.J. Stirling - CERN Preprint TH. 3821 (1984), to be published in Phys.Lett.

2) D. DiBitonto - Proton-Antiproton Collider Physics, 1981 (Madison, WI), Eds. V. Barger, D. Cline and F. Halzen (AIP, N.Y., 1982), p. 26.

3) F. Halzen and A.D. Martin - These Proceedings.

4) S.J. Brodsky, C. Peterson and N. Sakai - Phys.Rev. D23 (1981) 2745.

5) P.D.B. Collins and T.P. Spiller, University of Durham Preprint DTP/84/4 (1984).

6) R. Horgan and M. Jacob - Phys.Lett. 107B (1981) 395.

7) V. Barger, A.D. Martin and R.J.N. Philips - Phys.Lett. 125B (1983) 339, 343; Phys.Rev. D28 (1983) 145.

8) D.V. Nanopoulos - These Proceedings.

FIGURE CAPTIONS

Figure 1 Minimum mass distributions ($\xi = M^*/M$) in a phase space model with two and four observed particles in the final state. Both curves have unit area.

Figure 2 Minimum mass distribution for the decay $t \to b\mu\nu$: (a) with no cuts (solid line), (b) with all final state transverse momenta $\geq M/8$ (dashed line), and (c) with $P_L = 2M$ and a cut on the muon pseudo-rapidity, $|\eta^\mu| \leq 1$ (dash-dotted line).

Figure 3 P_L^* ($= MR^*$) distributions for three different top meson longitudinal momenta, $P_L = 0, 2M, 4M$. The hatched distribution is obtained when the additional constraint $M^* > 0.95M$ is imposed.

Figure 4 Minimum mass distribution for double gluino decay, summed over all six possible pairings of the four jets. The dashed line is the background contribution from the four wrong pairings, and the normalization is such that $\int_0^2 d\xi \, dN/d\xi = 6$.

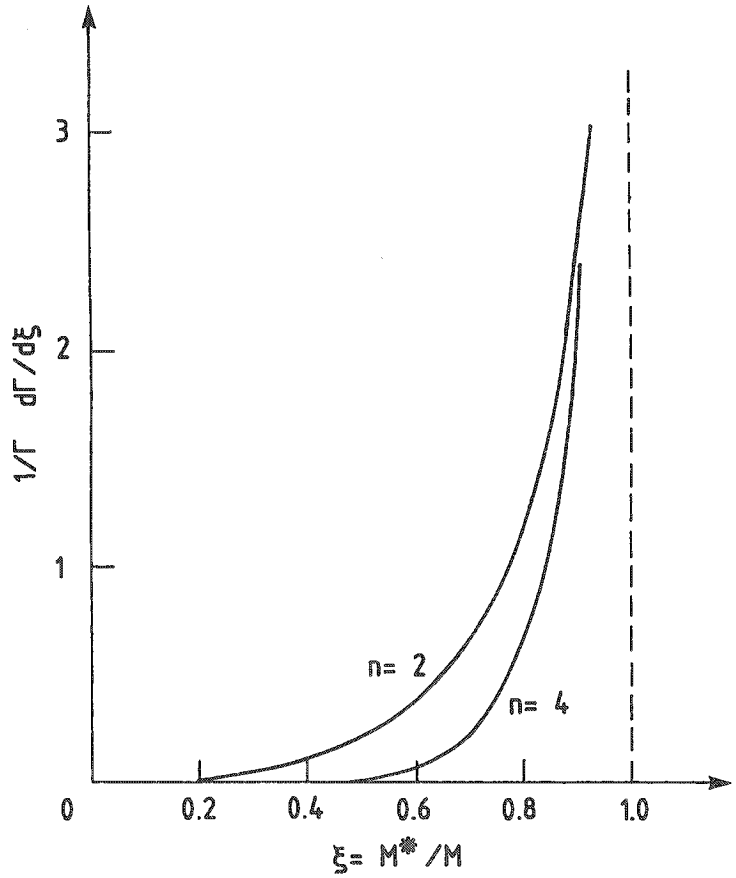
3
2
1
0
0.2
0.4
0.6
0.8
1.0
1/Γ dΓ/dξp
n= 2
n= 4
ξ= M* /M

Fig. 1

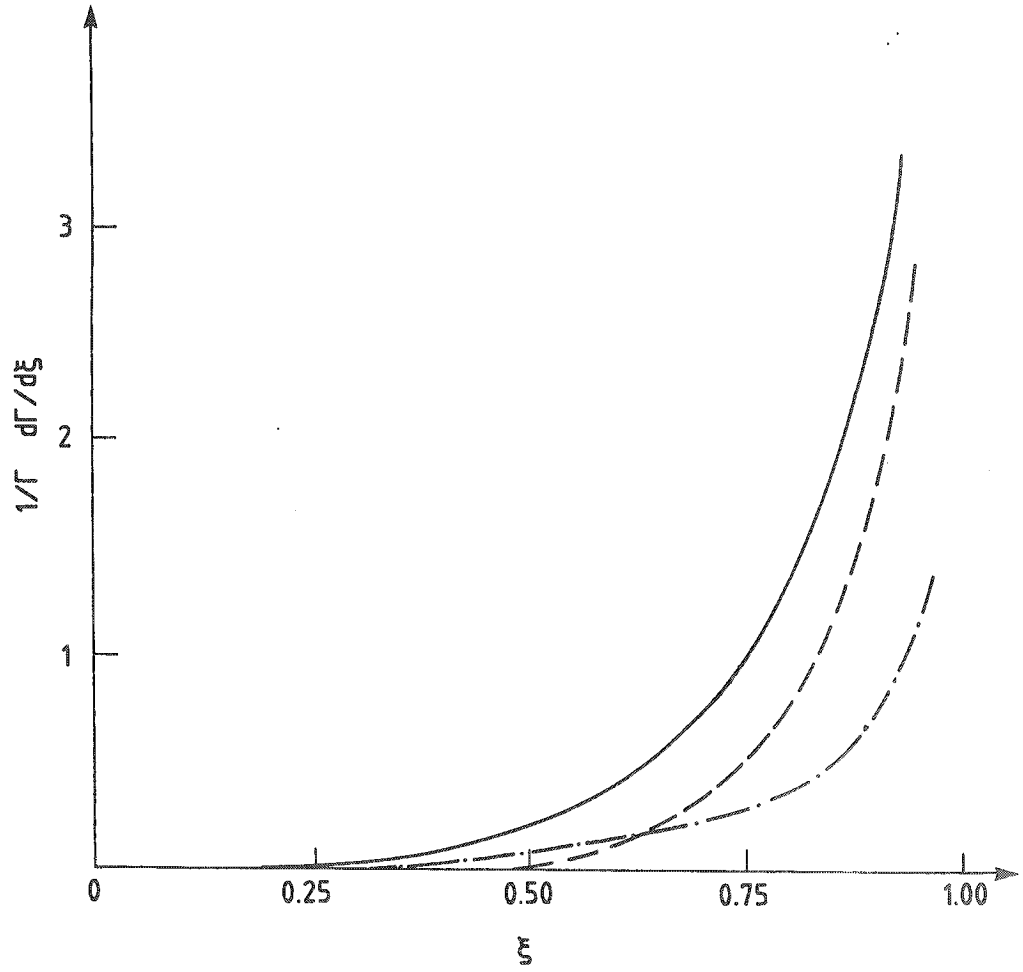
3
2
1
0
0.25
0.50
0.75
1.00
1/Γ dΓ/dξp
ξ

Fig. 2

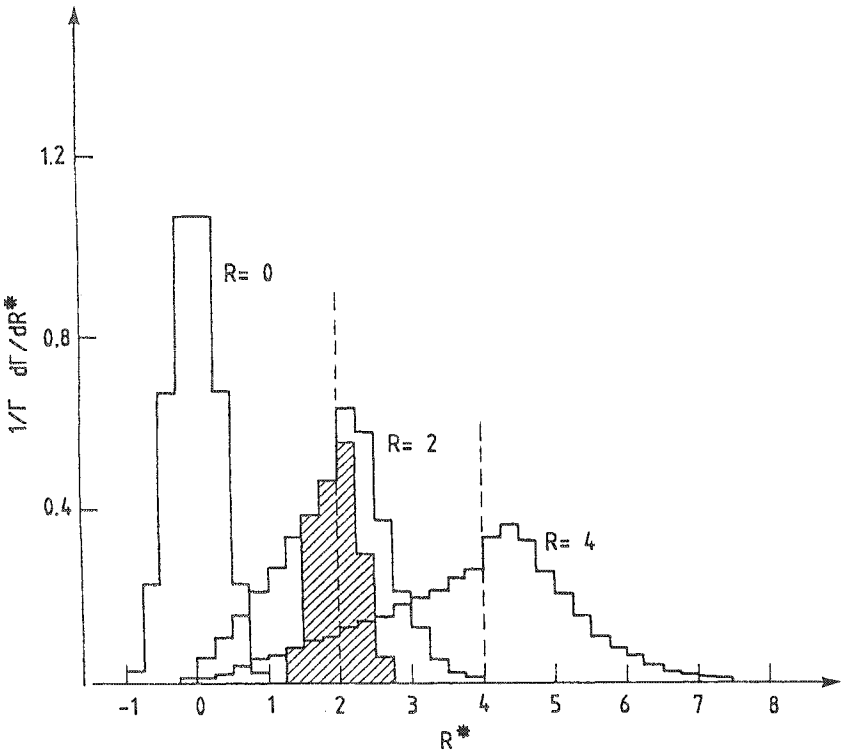
1.2
0.8
0.4
1/Γ dΓ/dR*
R= 0
R= 2
R= 4
-1
0
1
2
3
4
5
6
7
8
R*

Fig. 3

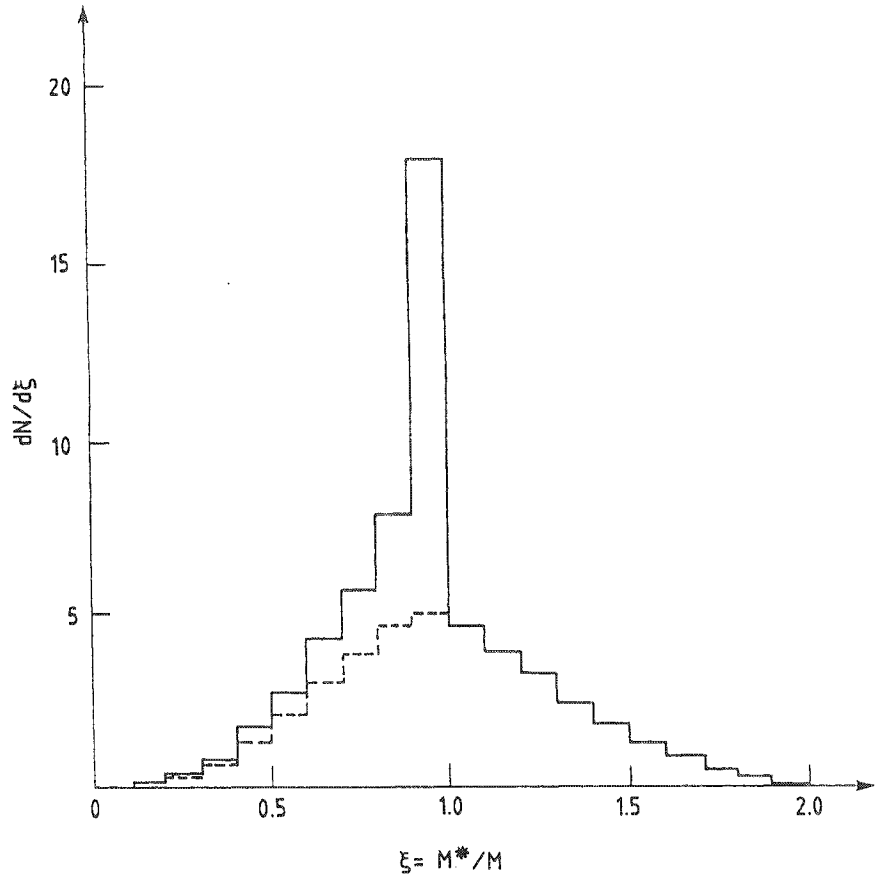
20
15
10
5
dN/dξ
0
0.5
1.0
1.5
2.0
ξ= M*/M

Fig. 4

UA5 Results

NEW RESULTS FROM UA5: STRANGE PARTICLE (K^o, Λ, Ξ^-) PRODUCTION AND LARGE FLUCTUATIONS IN MULTIPLICITIES

UA5 Collaboration

Bonn - Brussels - Cambridge - CERN - Stockholm

Presented by P. Carlson

ABSTRACT

Preliminary results are presented from about 6500 non single diffractive minimum bias events taken with the UA5 streamer chambers at the collider with a beryllium beam pipe. Significantly increased statistics on V^o production has permitted the first observation of Ξ^- as well as a more accurate estimate of the average transverse momentum of K^o_S and Λ. The non single diffractive multiplicity distribution has been studied in detail and revealed non scaling behaviour. In very narrow rapidity intervals large fluctuations, "spikes", in multiplicity occur.

1. INTRODUCTION

The UA5 detector, consisting of two large streamer chambers, was operated at the CERN $p\bar{p}$ collider during its first run in October 1981 and also during a run in September 1982. Some of the properties of the detector are given in Table 1. For further details, the reader is referred to published articles [1]. The new data that is presented here comes from the 1982 run, where a beryllium beam pipe was introduced in order to reduce the background from conversions. This data is henceforth called 1982 data as opposed to the 1981 data. The total number of non single - diffractive events used in the analysis presented here is about 6500.

Table 1. Properties of the UA5 detector

Streamer chamber visible volume (each)	$6 \times 1.25 \times 0.5\ m^3$
Streamer chamber separation	10 cm
Pseudorapidity acceptance	95% for $\|\eta\| < 3$ falling to 0% at $\|\eta\| = 5$
Range covered by trigger	$2 < \|\eta\| < 5.6$
Trigger acceptance (Monte Carlo estimate) for non single-diffractive events	95%
Collider luminosity	$10^{25}\ cm^{-2} s^{-1}$ (1981)
	$10^{26}\ cm^{-2} s^{-1}$ (1982)
Beam pipe	0.4 mm Fe (1981)
	2 mm Be (1982)

Results on the production of K^0_S and Λ from the 1981 data have been published [2]. The new 1982 data has given a five fold increase in statistics of V^0 production and the preliminary results given below include the first evidence for the production at the collider of $\bar{\Xi}$, for which a full kinematic fit can be made.

The 1982 data has permitted a more detailed study of the multiplicity distribution. Results showing the violation of KNO scaling (in the full rapidity range) favouring high multiplicity events at the collider have been published [3]. Results are given below from a systematic study of the multiplicity distribution in different rapidity regions. Very large fluctuations are observed in narrow rapidity intervals.

2. EVIDENCE FOR THE PRODUCTION OF Ξ^-

Fig. 1 shows a streamer chamber photograph of an event with a Ξ^- decaying into $\Lambda\pi^-$. *) 15 events of this type have been found. The analysis procedure for V's associated with the primary vertex are described in our published results from the 1981 data on strange particle production [2]. From the kinematics of the decays $K^0_S \to \pi^+\pi^-$ or $\Lambda \to p\pi^-$ the momentum of the neutral particle can be calculated. For the decay $\Xi^- \to \pi^- + \Lambda$ where the Λ points to the decay vertex and not to the primary vertex a 2 constraint fit can be made. All events with a Λ pointing to and coplanar with the decay vertex ("kink") give a good fit to the Ξ^- hypothesis. A few of the events are also consistent with the decay $\Omega^- \to K^- + \Lambda$. However, for this decay the acceptance is much smaller and furthermore the production of three strange quarks is very likely further suppressed. We therefore take the 15 events as Ξ^-, not Ω^-.

Background

A number of possible background reactions were studied by simulation, e.g.:

- random association of a V to a secondary vertex (kink)
- reactions in the streamer chamber gas of the type

$$K^+ n \to K^0 p$$
$$\hookrightarrow \pi^+\pi^-$$

- conversion of one photon from a π^0 decay:

$$\Sigma^+ \to p\pi^0$$
$$\hookrightarrow \gamma e^+ e^-$$

From 10 000 simulated events we conclude that less than one is expected as a background, and that the Ξ^- signal therefore is real.

Production rate

The acceptance of the streamer chambers to observe a Ξ^- decay is small and depends strongly on the Ξ^- transverse momentum p_T. The observed 15 events have fitted transverse momenta in the range 0.7 - 3.5 GeV/c and the production rate for $p_T > 1$ GeV/c in the pseudorapidity interval $|\eta| < 3.5$ is 0.04 ± 0.01 Ξ^- per event. A detailed account of the Ξ^- production, including an evaluation of the Ξ^-/Λ production ratio R, is under preparation [4]

---

*) Since there is no magnetic field we cannot distinguish Ξ^- from $\bar{\Xi}^+$ nor Λ from $\bar{\Lambda}$. We denote either of them with Ξ^- and Λ.

A measurement in e^+e^- collisions at $E_{c.m.}$ = 34 GeV gave as result $R = 0.09 \pm 0.03 \pm 0.03$ [5] (the last error is systematic), and in pp collisions a measurement at $E_{c.m.}$ = 63 GeV gave $R = 0.06 \pm 0.02$ for a p_T range of 1.2 - 2.4 GeV/c and for a rapidity range $|y| < 0.2$ [6].

3. INCLUSIVE K^o_S AND Λ PRODUCTION

The preliminary results based on 6500 minimum bias events are summarized in Table 2.

Table 2. Rates of K^o_S and Λ. Errors are statistical only.

		UA5 1982 data		UA5 1981 data [2]
		$\|\eta\| < 3.5$	$\|\eta\| < 3$	$\|\eta\| < 3$
Accepted events	K^o	344	318	92
	Λ	247	237	46
Correct number per event	K^o_S	1.1 ±0.1	1.0 ±0.1	1.0 ±0.2
	Λ	0.49 ±0.05	0.44 ±0.05	0.35 ±0.10
	K^o_S/Λ	2.15 ±0.3		2.9 ±1.0
	$K^o/\pi^\pm$	0.12 ±0.01		0.11 ±0.02

There is good agreement between the 1982 data and the published 1981 data. The additive quark model of Anisovich and Kobrinsky [7] gives $K^o/\Lambda = 2.16$, in excellent agreement with our measured value 2.15. The energy dependence of the K/π ratio is shown in Fig. 2 which illustrates the continous increase in this ratio.

p_T distribution

The p_T distribution for K^o_S is shown in Fig. 3 where it is compared to our published 1981 data and also to the published measurements of $K^{\pm}$ production by the UA2 collaboration for $|\eta| < 0.8$ [8]. The increased statistics reveals the deviation from an exponential behaviour, similar to the observation by the UA1 collaboration [9] for charged particles. The curve is a fit to the form [9]:

$$\frac{dN}{dp_T^2} = A\left[p_{T0}/(p_{T0} + p_T)\right]^n \qquad (1)$$

In calculating the average transverse momentum, $\langle p_T \rangle$, the form (1) is used for $p_T > 0.2$ GeV/c. However, the use of (1) for the region $p_T < 0.2$ GeV/c would underestimate $\langle p_T \rangle$ since the behaviour for small p_T is probably like $\exp(B \cdot m_T)$ where $m_T^2 = m^2 + p_T^2$ and m is the particle mass [10]. The results of the fit are given in Table 3.

Table 3. Preliminary results of the fit to the inclusive K^o_S p_T distribution.

Parameter	UA5 K^o_S	UA1 charged [9]
n	5.7	9.1
p_{T0}	0.73	1.3
$\langle p_T \rangle$ [a] (GeV/c)	0.56 ± .06	0.47 ± 0.01

a) Calculated assuming the form $\exp(-Bp_T)$ for the low p_T region that is unmeasured. The value of the parameter B was in this calculation taken to be $B = 4\ (\text{GeV/c})^{-1}$ for the UA5 data and $B = 5.7\ (\text{GeV/c})^{-1}$ for the UA1 data.

The inclusive p_T distribution for Λ is shown in Fig. 4 and is in good agreement with the published 1981 data [2]. The distribution is well described by an exponential. (The deviation from an exponential - as for the K^o distribution - probably sets in at a higher p_T for the heavier Λ). The average transverse momentum is $\langle p_T \rangle$ = 0.64 ± 0.07 GeV/c. Also shown in Fig. 4 are the inclusive p, $\bar{p}$ data from UA2 [8] which seems to obey the same p_T dependence with a ratio $\Lambda/p = 2.7$.

The energy variation of the average transvene momentum is shown in Fig. 5. There is a significant increase in $\langle p_T \rangle$ for all particle types at the collider.

Rapidity distribution

The K^o_S pseudorapidity and rapidity distributions are shown in Fig. 6a and b. The rapidity distribution is consistent with being flat out to $y \approx 2$, similar in shape to the 400 GeV/c data of Kichimi et al [12].

Multiplicity dependent effects

A possible signal of a quark gluon plasma is an increased production of strange quarks. At the same time the overall multiplicity is expected to increase. We have examined our sample of strange particles for multiplicity dependent effects. Fig. 7 shows the inclusive p_T distribution for K^o_S in two multiplicity bins, $n_{ch} \lesseqgtr 30$.

There is no significant difference between the distributions. Fig. 8 shows the number of coplanar V's (K^o or Λ) and the number of clean K^o_S per charged track as a function of the observed (uncorrected) multiplicity. There appears to be an increase with increasing n_{ch} though the distributions are consistent with being flat.

4. CHARGED PARTICLE MULTIPLICITY DISTRIBUTION

The lower background from conversions with the Be beam pipe has permitted a more detailed study of the multiplicity distribution. This is often done in terms of the KNO scaling concept [13], originally derived using Feynman scaling which is now known not to be valid. The framework of KNO scaling has still been found useful. If KNO scaling is valid, the multiplicity distribution scales in the variable $z = n/\langle n \rangle$:

$$\langle n \rangle \cdot \frac{\sigma_n}{\Sigma \sigma_n} \xrightarrow[s \to \infty]{} \psi(n/\langle n \rangle) = \psi(z)$$

where n is the (charged) multiplicity. $\psi(z)$ is a universal function, independent of energy.

In this paper we present results on three different aspects of the non single diffractive multiplicity distribution:

- the shape of the multiplicity distribution as a function of energy,
- the shape of the multiplicity distribution for different rapidity intervals at $E_{c.m.} = 540$ GeV, and
- the observation of individual events with locally very high density of tracks in rapidity.

The multiplicity distribution as a function of energy

Results in the $E_{c.m.}$ range from 10 to 50 GeV have suggested that the multiplicity distribution (full phase space) of non single diffractive events obey KNO scaling. Recent results from the UA5 experiment, however, show that there is a significant change of the shape of the multiplicity distribution favouring high multiplicities [3]. This is shown in Fig. 9 where the normalized multiplicity distribution $\langle n \rangle \sigma_n / \Sigma \sigma_n$, full phase space, is plotted as a function of the KNO variable z and compared to lower energy data [14, 15]. This change of shape is quantified in Fig. 10 where the C moments, defined as $C_k = \langle n^k \rangle / \langle n \rangle^k$, are shown as a function of energy. The data suggests a significant change in all moments at the collider.

The multiplicity distribution in a fixed limited range of rapidity $|\eta| < 1.3$ obeys KNO scaling if only events with at least one charged track in the region are included. This is shown in Fig. 11 where UA5 data [3] are compared with recent data from the ISR [16]. The exclusion of zero prong events (only reflecting triggering conditions), however, has no obvious physical justification and furthermore will - because of the variation of $\langle n \rangle$ with energy-change z in an energy dependent way.

The multiplicity distribution at $E_{c.m.} = 540$ GeV in different rapidity intervals

Models for particle production have been proposed that treat differently the "central region" from the two fragmentation regions [17]. In these models scaling is supposed to hold for the different regions separately. It is therefore of interest to study the corrected multiplicity distribution in a region $|\eta| < \eta_c$ where η_c is allowed to vary in small steps and look for scaling properties in these distributions.

Fig. 12 shows a sample of corrected multiplicity distributions with $\eta_c = 0.5$, 1.5, 3 and 5. The distributions are smooth and remembering that $dn/d\eta$ is approximately flat out to $|\eta| = 3$ one sees already that the relative fluctuations grow larger as the η-interval becomes more narrow. The same distributions now plotted as a function of the KNO variable z are shown in Fig. 13. Here the effect is very clear: for increasing η region the distribution becomes more narrow and the peak shifts outwards. The tail for $z > 1$ follows an exponential in z out to a larger value of z for a more narrow interval. The relative fluctuations observed are as high as $z = 7$ for $|\eta| < 0.5$ but reduces to $z < 4$ for $|\eta| < 5$. To illustrate this more quantitatively we show in Fig. 14 the C_3

moment as a function of η_C. For perfect scaling one would expect a constant C_3, but the measurements show a continous decrease of C_3 as η_C is increased from 0.5 to 5. We thus conclude that there is no evidence for a central region $\eta_C \geq 1$ that obeys scaling.

However, for different experimental reasons [16, 18] the zero prong events have often been excluded. Such a suppression would affect smaller regions more than larger ones since $\langle n \rangle$ changes more. Calculations show that such an effect is not important for $\eta_C > 2$ but reduces the value of C_3 for $\eta_C \leq 2$. The physics significance of this observation is not entirely certain, since the suppression of zero prongs affect the different regions in different ways.

Very large fluctuations in narrow rapidity intervals

We have searched in our data for signs of very high energy density which could possibly signal some new physics [19]. Fig. 15 shows three individual events from our data sample together with one Monte Carlo event. The events were selected to give a very high number of observed tracks in an interval $\Delta\eta = 0.5$ anywhere along the rapidity axis. There are as many as 15 tracks in $\Delta\eta = 0.5$ in the top event, corresponding to $dn/d\eta = 30$ (cf $\langle dn/d\eta \rangle \approx 3$). These events do not show any jetstructure, as shown in Fig. 16. The scatterplot in Fig. 17 shows as a function of the number of observed tracks the maximum number of tracks in $\Delta\eta = 0.5$ for each event. The straight line represents the arbitrary cut used to define the "spike" sample. The distribution looks rather smooth and the "spike" sample represents the tail of it. The properties of these selected "spike" events are summarized in Table 4 where also a comparison with Monte Carlo is made.

Table 4. Properties of "spike" events

	UA5 1982 data	UA5 Monte Carlo
Passing cut	0.7%	0.5%
$\langle n_{ch} \rangle$	47	41
$\langle N_{max} \rangle$ in $\Delta\eta = 0.5$	12.9	12.2
2 - D spericity (Disc 1, jet 0)	0.73	0.73

The arbitrary cut corresponds to $z \approx 5$, whereas we do observe fluctuations as large as $z = 10$. The fluctuations occur with approximately the same frequency in our data sample as in our Monte Carlo simulated events. In fact the UA5 'cluster' Monte Carlo [20, 21] suggests that the fluctuations might occur from random superposition of clusters.

The corrected multiplicity distribution in $\Delta\eta_l = 1$ (centered at $\eta = 0$) shown in Fig. 13 obeyed fluctuations up to $z \simeq 7$. To illustrate the effect of even further reducing the interval we show in Fig. 18 superimposed uncorrected multiplicity distributions in an interval $\Delta\eta = 0.5$. Fluctuations of $z > 3$, 6 and 8 occur with frequencies of 6%, 2×10^{-3} and 2×10^{-4}. The distribution is smooth and there is no structure for high z. Also shown for comparison are a simple and a compound Poisson. Although the latter is much wider, the data shows significantly larger tail.

5. CONCLUSIONS

From a detailed study of the UA5 1982 data at $E_{c.m.} = 540$ GeV we made the following preliminary conclusions

- first evidence for the production of Ξ has been found,
- the average transverse momentum for inclusive K^0_S and Λ production has increased to 0.56 ± 0.06 GeV/c and 0.64 ± 0.07 GeV/c respectively and the K/π ratio has increased to $12 \pm 1\%$,
- the non single diffractive multiplicity distribution in full phase space is much wider than at $E_{c.m.} = 53$ GeV and
- the non single diffractive multiplicity distribution, when shown as a function of the KNO scaling variable $z = n/\langle n \rangle$, widens continously when the rapidity interval gets more narrow, and in a narrow interval $\Delta\eta = 0.5$ fluctuations as large as $z = 10$ occur; these events appear like spikes where in this narrow interval as much as 15 tracks are observed without jet structure.

REFERENCES

[1] K. Alpgard et al., Phys. Lett. 107B (1981) 310, 315, Phys. Scr. 23 (1981) 642.

[2] K. Alpgard et al., Phys. Lett. 115B (1982) 65.

[3] J. Alner et al., Phys. Lett. 138B (1984) 304.

[4] UA5 Collaboration, J.G. Alner et al.: "Observation of $\bar{\Xi}^-$ production in $p\bar{p}$ interactions at $\sqrt{s} = 540$ GeV", to appear.

[5] M. Althoff et al., Phys. Lett. 130B (1983)340.

[6] T. Akesson et al., CERN-EP/84-26 (to be published).

[7] V.V. Anisovich and M.N. Kobrinsky, Phys. Lett. 52B (1974) 217 give the ratio $K^0/\Lambda = 2.4 + 0.6\lambda$ where λ is the strange quark suppression. We used the value $\lambda = 0.38 \pm 0.07$ as determined by K. Böckmann: "Particle production in $p\bar{p}$ interactions at 540 GeV and strange quark suppression", Proceedings of the VI Warsaw Symposium on Elementary Particle Physics, Kazimierz, May 1983 (to appear) and Th. Müller: "Strangeness suppression at collider energy", Proceedings of the XV International Symposium on Multiparticle Dynamics, Lake Tahoe, 22-27 June, 1983 (to appear).

[8] M. Banner et al., Phys. Lett. 122 B (1983) 322.

[9] G. Arnison et al., Phys. Lett. 118B (1982) 167.

[10] K. Guettler et al., Nucl. Phys. B116 (1976) 77.

[11] A.M. Rossi et al., Nucl. Phys. B84 (1975) 269.

[12] H. Kichimi et al., Phys. Rev. D20 (1979) 37.

[13] Z. Koba et al., Nucl. Phys. B40 (1972) 317.

[14] V.V. Ammosov et al., Phys. Lett. 42B (1972) 519;
H.B. Bialkowska et al., Nucl. Phys. B110 (1976) 300;
W.M. Morse et al., Phys. Rev. D15 (1977) 66;
S. Barish et al., Phys. Rev. D9 (1974) 2689;
A. Firestone et al., Phys. Rev. D10 (1974) 2080;
C. Bromberg et al., Phys. Rev. Lett. 31 (1974) 1563;
J. Whitmore et al., Phys. Rep. 10C (1974) 273.

[15] A. Breakstone et al., CERN-EP/83-165.

[16] A. Breakstone et al., Phys. Lett. 132B (1983) 458.

[17] See e.g. Liu Lian-Sou and Meng Ta-Chung, Phys. Rev. D27 (1983) 2640.

[18] W. Thomé et al., Nucl. Phys. B129 (1977) 365.

[19] See J.G. Rushbrooke: "Inelastic hadron-hadron-hadron processes at c.m. energies up to 40 TeV" and references therein, CERN EP/84-34 to appear in Proceedings of the workshop on $p\bar{p}$ options for the supercollider, 13-17 February, 1984, University of Chicago.

[20] UA5 Collaboration, Physics Reports to be published.

[21] K. Alpgard et al., Phys. Lett. 123B (1983) 361.

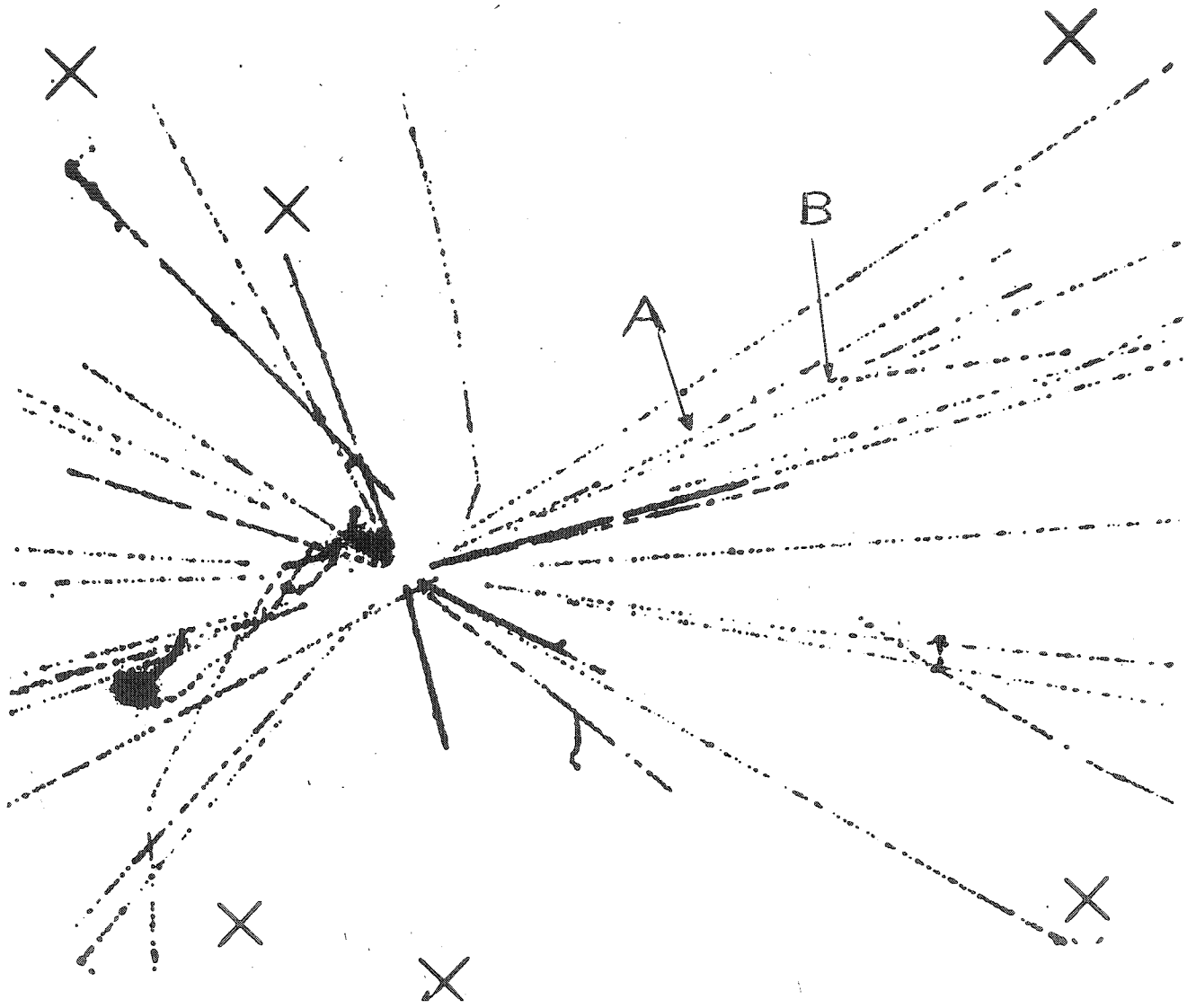

Fig. 1 A photograph of an event with a $\Xi^- \rightarrow \Lambda\pi^-$ decay. The decay point is at A and the $\Lambda \rightarrow p\pi^-$ decay at B. The kink at A is most easily visible if one looks along the π^- track in the plane of the photograph.

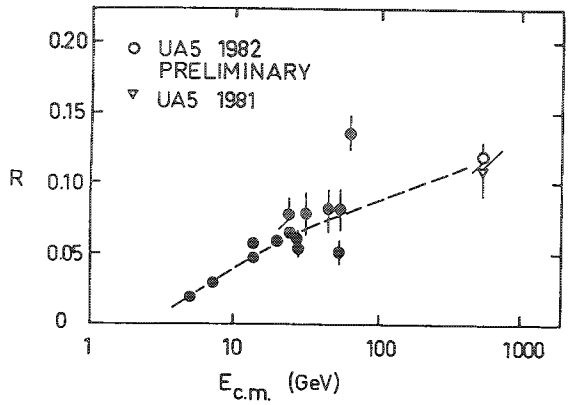

Fig. 2 The energy variation of the K/π ratio R. Data at lower energies are taken from [2].

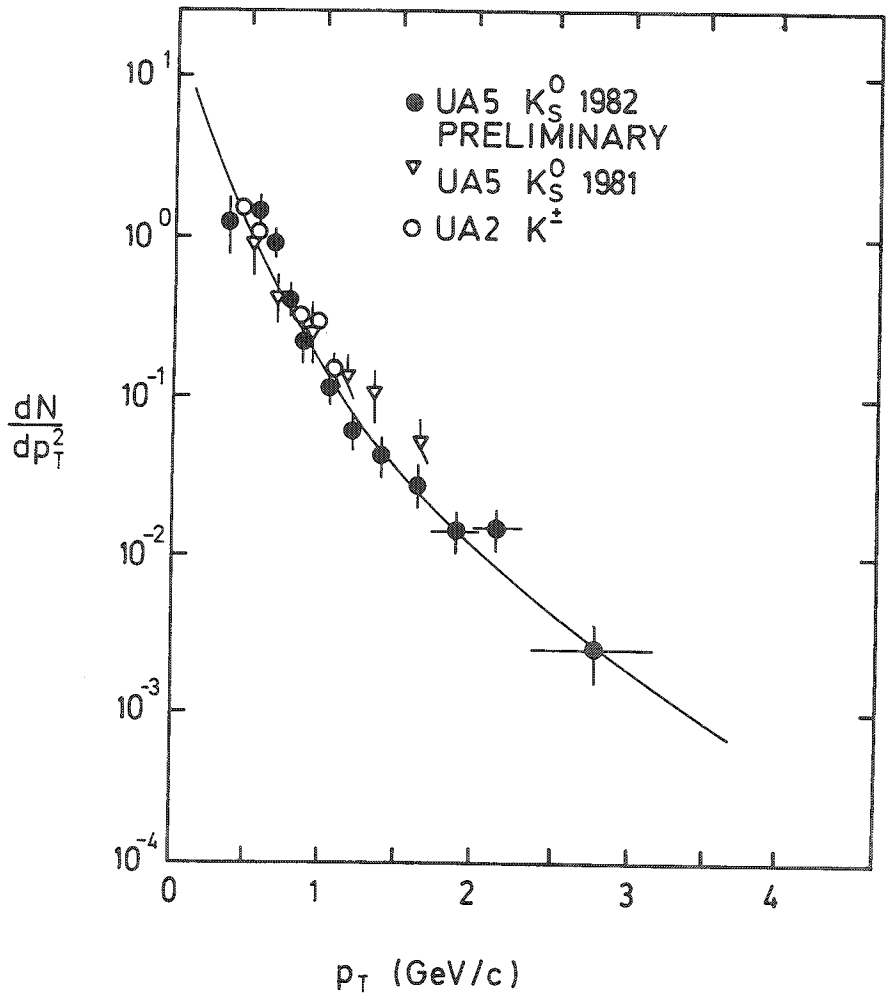

Fig. 3 The p_T distribution for K^0_S from from the UA5 1982 data compared to the published 1981 data [2] and to the UA2 $K^{\pm}$ data [8]. The full line is a fit discussed in the text.

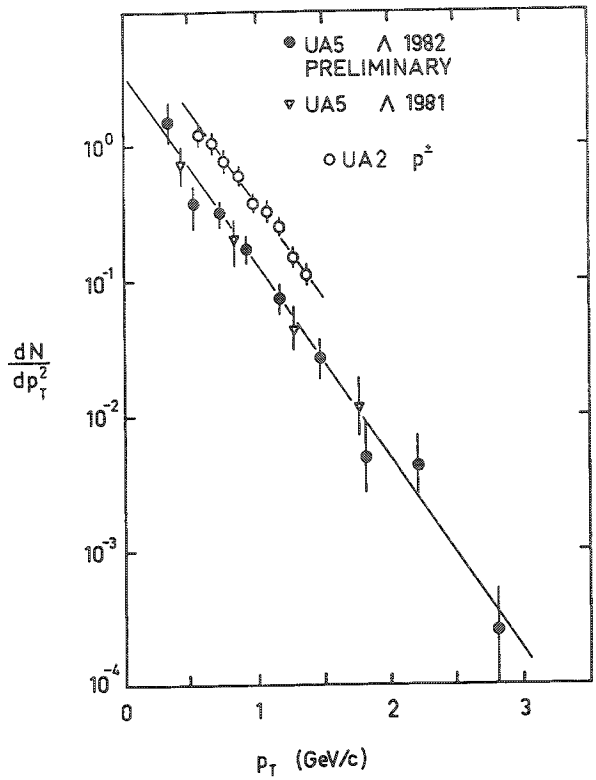

Fig. 4 The p_T distribution for Λ from the UA5 1982 data compared to the published 1981 data [2]. Also shown are the proton data from the UA2 experiment [8]. The straight line is a fit discussed in the text.

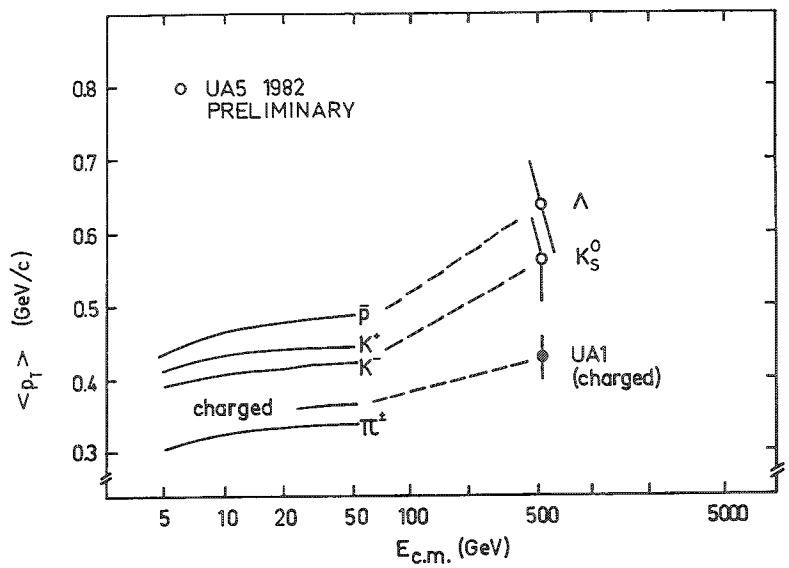

Fig. 5 The average transverse momentum as a function of $E_{c.m.}$ Low energy data is taken from Ref. [11]. The UA1 value is the published value 0.43 GeV/c [9], not the value 0.47 GeV/c given in Table 3.

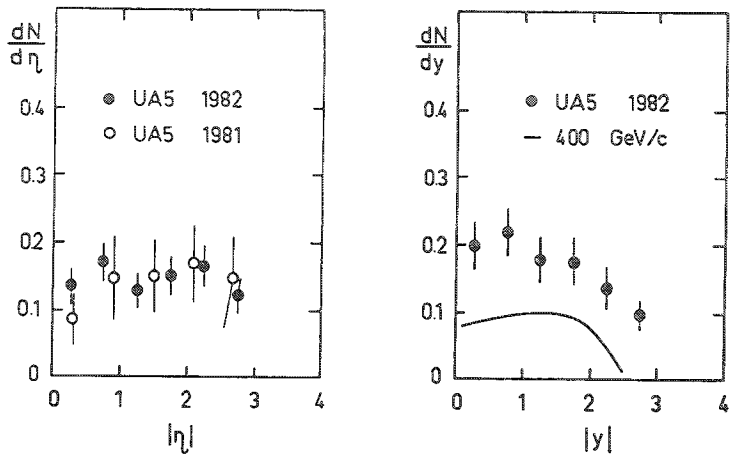

Fig. 6 The K^0_S pseudorapidity distribution compared to the published 1981 data [2] and the rapidity distribution compared to results at 405 GeV/c ($E_{c.m.}$ = 28 GeV) [12].

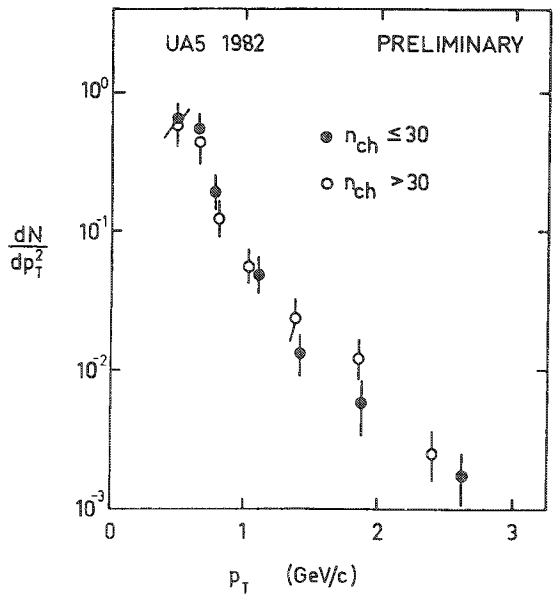

Fig. 7 The p_T distribution for K^0_S for two bands in observed event multiplicity.

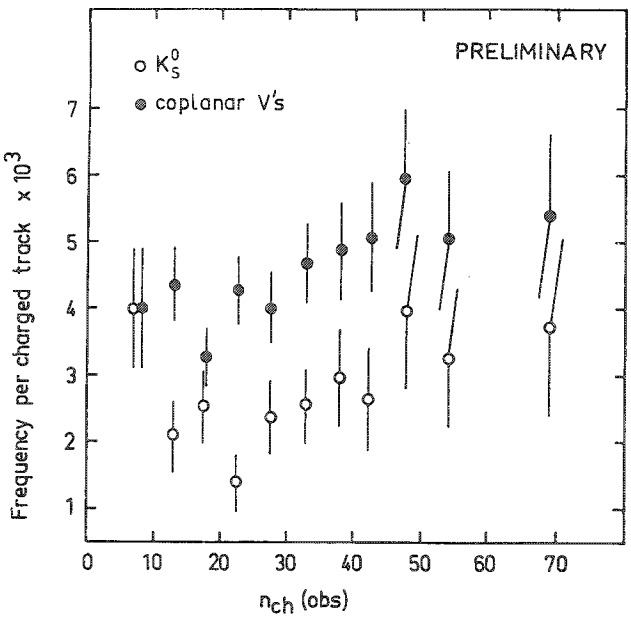

Fig. 8 The number of coplanar V's (K^0_S and Λ) and the number of K^0_S per charged track as a function of overall observed event multiplicity.

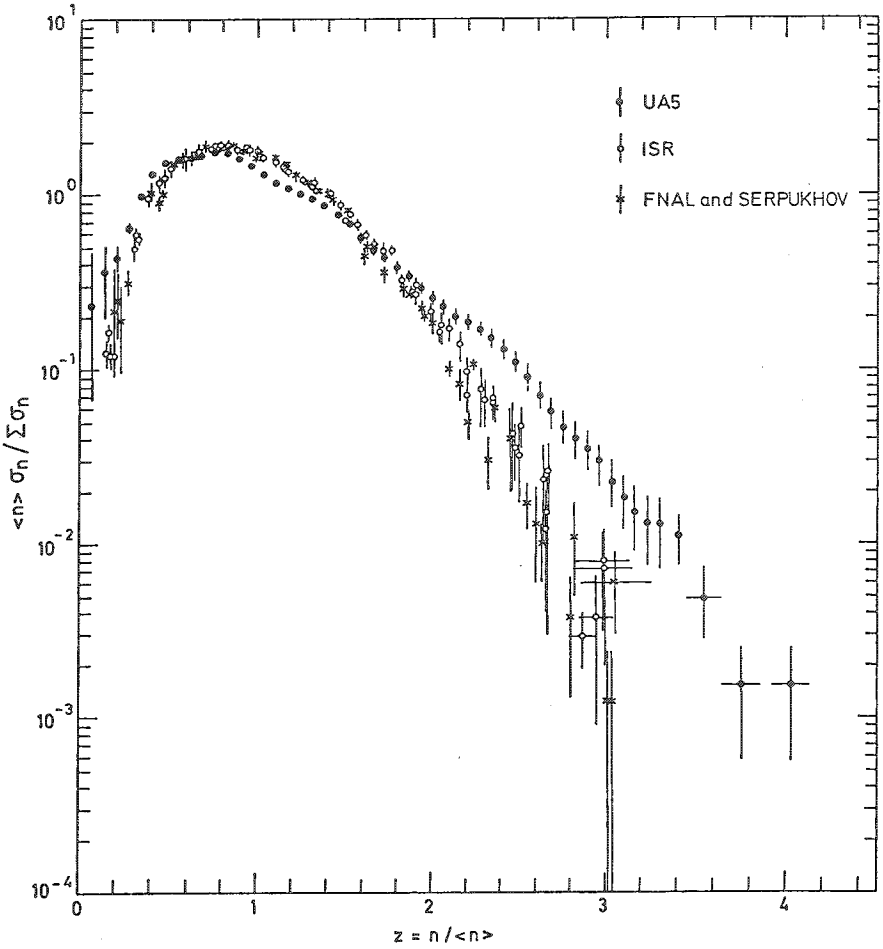

Fig. 9 The normalized non single diffractive multiplicity distribution as a function of the KNO scaling variable z. The UA5 data is the published joint 1981 and 1982 data [3]. Lower energy data is from Refs. [14, 15]. From [3].

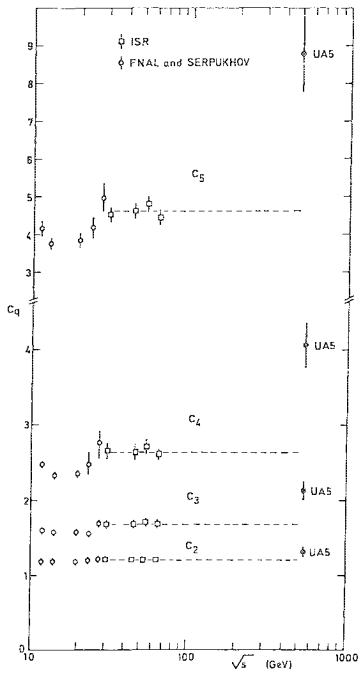

Fig. 10 The C moments of the non single diffractive multiplicity distributions as a function of energy. From [3].

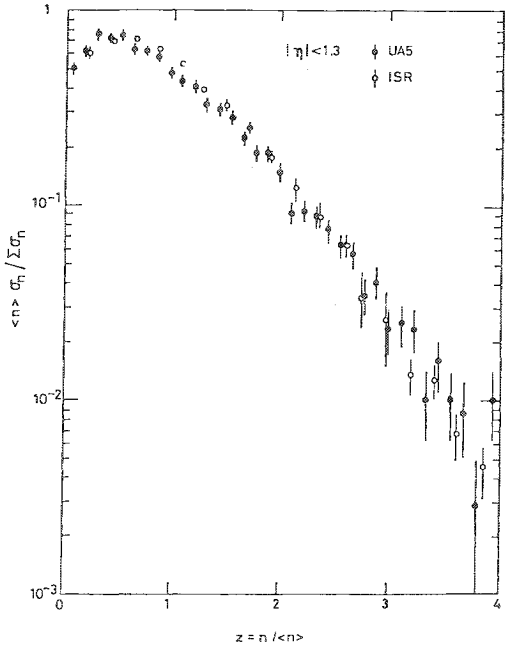

Fig. 11 The multiplicity distribution for non single diffractive events in the rapidity region $|\eta| < 1.3$. Only events with at least one track in this region are included. From [3].

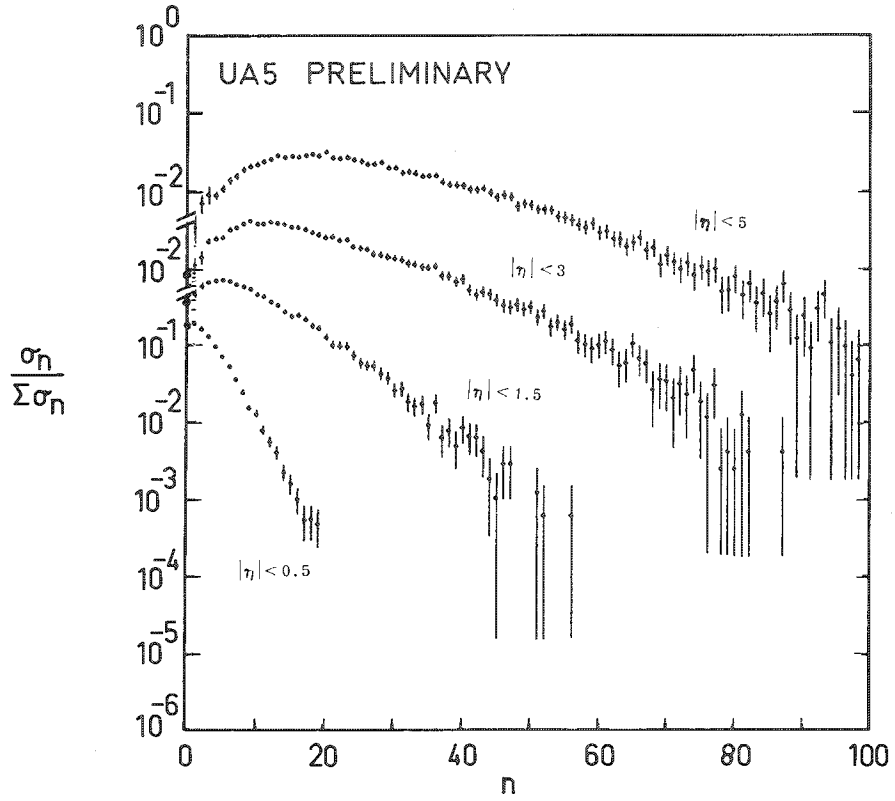

Fig. 12 Corrected non single diffractive multiplicity distributions for four different η regions: $|\eta| < 0.5$, 1.5, 3, 5. 1982 data.

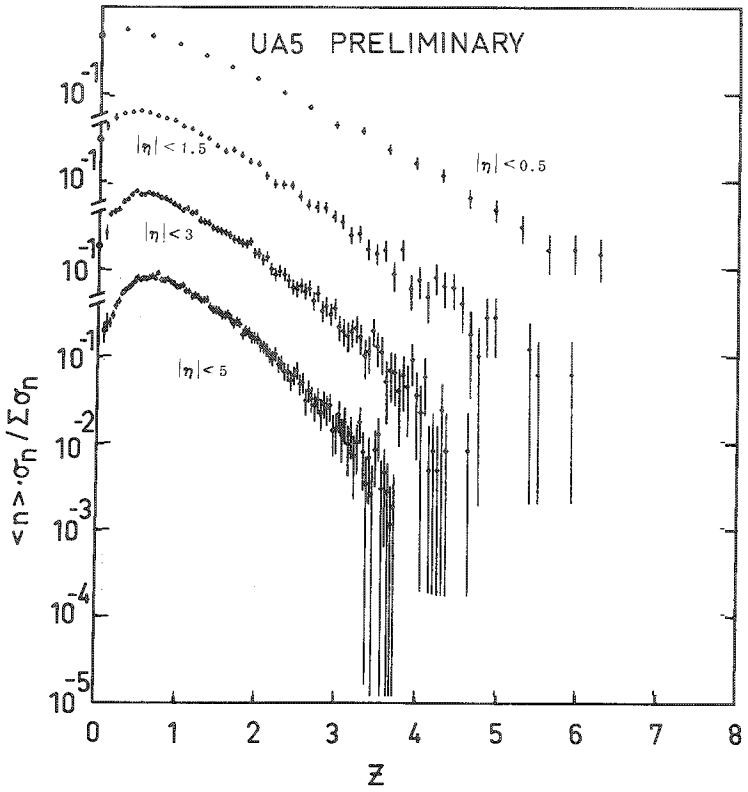

Fig. 13 Corrected non single diffractive multiplicity distributions plotted as a function of $z = n / \langle n_{ch} \rangle$ for the same η regions as in Fig. 12: $|\eta| < 0.5$, 1.5, 3, 5. 1982 data.

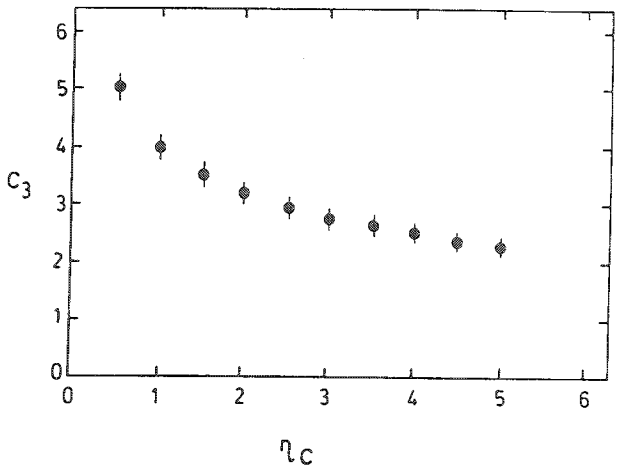

Fig. 14 The C_3 moment of the corrected non single diffractive multiplicity distribution in a region $|\eta| < \eta_C$ as a function of η_C. C_3 is defined as $C_3 = \langle n^3 \rangle / \langle n \rangle^3$.

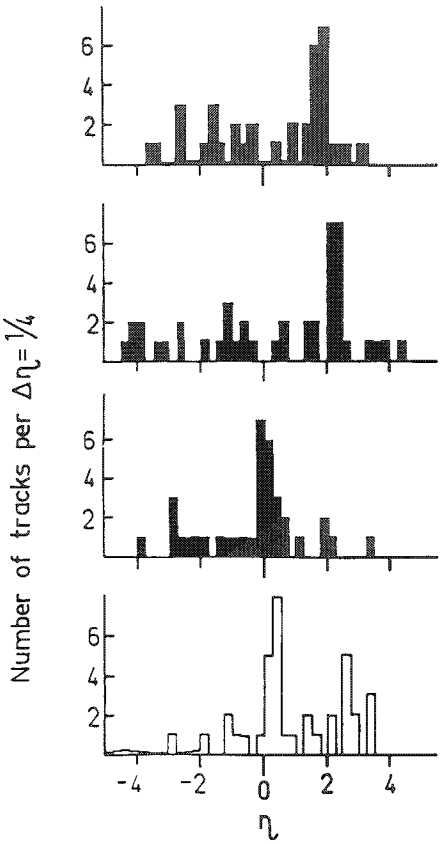

Fig. 15 Track density for three events from the data sample and one event (bottom) from the Monte Carlo simulation. The events were found in a scan where the maximum number of tracks in an interval $\Delta\eta = 0.5$ was searched for.

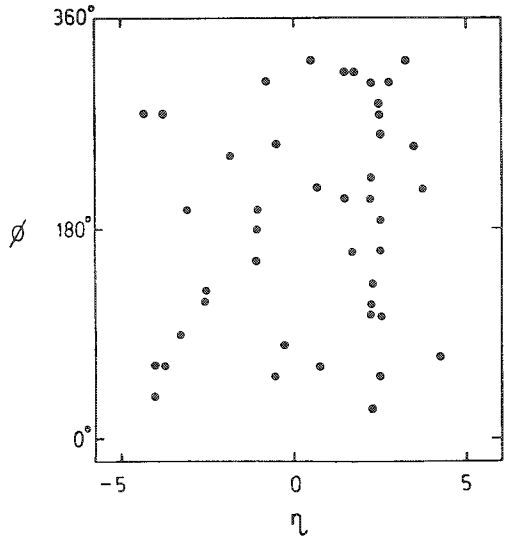

Fig. 16 η, ϕ distribution for the top event in Fig. 15. ϕ is the azimuthal angle around the beam pipe.

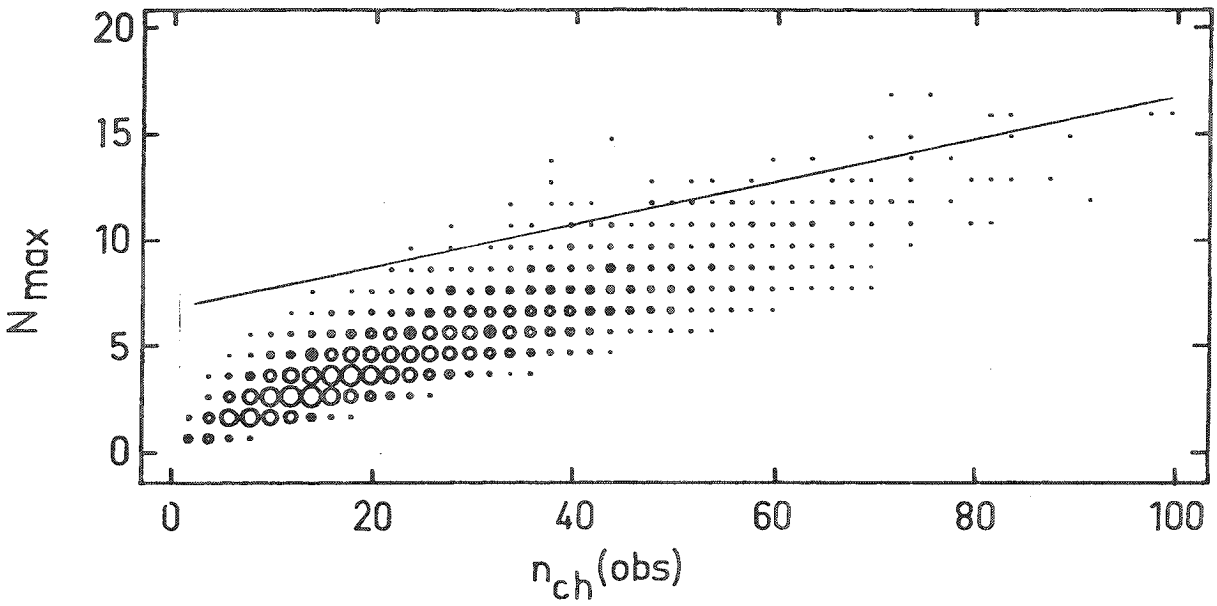

Fig. 17 The maximum number of tracks in $\Delta\eta = 0.5$ in each event as a function of the observed event multiplicity. The area of each small circle is proportional to the number of events with that combination. The straight line is $N_{max} = 0.1 \times n_{ch}$ (obs) + 7 and represents an arbitrary cut used to get the "spike" sample.

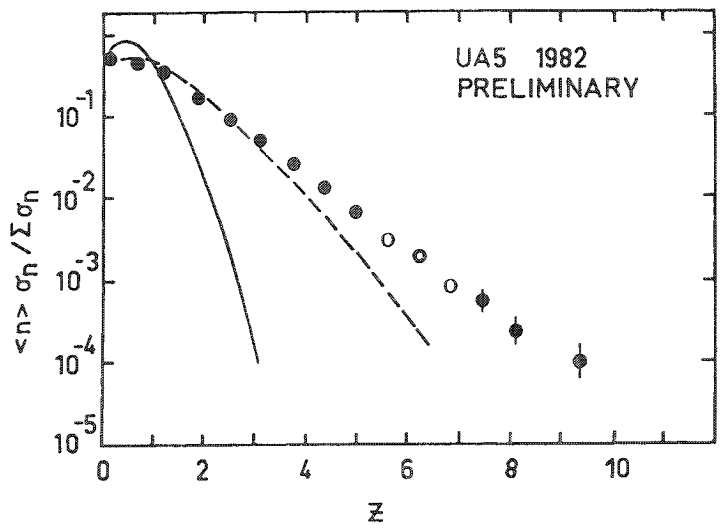

Fig. 18 The uncorrected (for acceptance) multiplicity distribution in an interval $\Delta\eta = 0.5$. All possible windows of interval $\Delta\eta = 0.5$ in the range $-2 < \eta < 2$ were superimposed. The straight and dashed lines represent a Poisson and a compound Poisson distributions having the observed mean (Poisson) and mean and dispersion (compound Poisson).

$p\bar{p}$ and pp Elastic Scattering

ELASTIC SCATTERING

A. Martin

Theoretical Physics Division, CERN
CH-1211 Geneva 23

What I want to present here should perhaps better be called "theoretical comments on experiments". Let me remind you that 14 months ago, in Rome[1], I indicated - somewhat arbitrarily - three possibilities for the high-energy behaviour of proton-antiproton scattering at collider energies.

1) The Froissart bound is not saturated, i.e., $\sigma_T/(\log s)^2 \to 0$. The simplest situation would be that σ_T tends to a constant sufficiently large to avoid contradiction with existing data[2]. Another interesting special case is that of the "critical Pomeron" for which σ_{tot} behaves like $(\log s)^{0.3}$ asymptotically and σ_{el}/σ_{tot} decreases.

2) The Froissart bound is saturated and we are already in the asymptotic regime at present energies, which means:

$$\frac{\sigma_{elastic}}{\sigma_{total}} = \text{const} \qquad \frac{b(s,t=0)}{\sigma_{total}} = \text{const}$$

where $b = d/dt\,(\log(d\sigma/d\Omega))$ is the slope of the diffraction peak, and $d\sigma/dt = F(t\sigma_t)$, where $F(z)$ is an entire function of order ½. Supporters of this point of view are, for instance, P. Kroll and J. Dias de Deus[3].

3) The Froissart bound <u>is</u> saturated, but we are still far away in energy from the asymptotic regime and, in particular, the opacity of the nucleon is still increasing. This is realized in some eikonal models like the Chou-Yang model[4] (in which what is given is the imaginary part of the amplitude, the real part being obtained from dispersion relations) and the Bourrely-Soffer-Wu model[5] which has a field theoretical origin and incorporates a priori real part effects and Regge pole effects. In these two models, the nucleon becomes "black" at infinite energy and therefore $\sigma_{el}/\sigma_{tot} \to \frac{1}{2}$. The supercritical string model, of Kaidalov and Ter Martyrosian[6], has similar features.

In Rome I favoured possibility N° 2, which was a priori appealing since Kroll and Dias de Deus[3] had succeeded in explaining nicely the ISR data and in particular the motion of the dip in pp scattering, given by $t_{dip} \times \sigma_T = 56\ \text{mb} \times (\text{GeV})^2$, and the depth of the dip by real part effects. However, the

situation has changed, as you have heard. Let me summarize the situation in the following Table. The first column contains ISR data at the arbitrarily chosen energy of 52 GeV cm; however, the ratio of elastic to total cross-sections shows no definite energy dependence in the whole ISR range, from 30 to 60 GeV. The second column contains a summary of the "old" data from UA4 at the nominal energy of 540 GeV/cm. The last column contains the main new results of UA4.

	ISR 52 GeV	SPPS 1982 "540" GeV	SPPS 1983 546 GeV
$\sigma_T^{\pm}$	43 mb	65-70 mb	62-63 mb
σ_{el}/σ_T	0.175 ±0.005	0.2±0.02	0.213 ±0.006±0.002
b(t=0)	13 GeV^{-2}	17.2±1	15.7±0.2*)
b($\|t\|$ =0.4)	10.5	13.6±0.2	13.3±0.2

*) In the Appendix I explain why I prefer this value obtained by UA4 from a quadratic fit.

This Table shows very clearly that it is no longer more possible to say that the asymptotic regime of the saturation of the Froissart bound has been reached (possibility N° 2), or more exactly that it was certainly not reached at the ISR, for the ratio σ_{el}/σ_{tot} is definitely increasing from the ISR to the collider, and the ratio of the slope to the total cross-section is definitely decreasing. Still the cross-section is rising and in fact compatible with the extrapolation of Amaldi et al.[7], based on measurements of real parts and total cross-sections at the ISR, so that case N° 1 does not seem very likely. In particular, it seems extremely difficult to believe that the Pomeron is "critical" because this would lead to a decreasing ratio of elastic to total cross-sections.

At present, models of type N° 3 are clearly favoured, i.e., models in which opacity increases. Not only opacity but also sharpness, because the shoulder observed at $t \simeq -0.8$ GeV^2 (which is understood to be a shoulder and not a dip because of real part effects) is too high compared to the predictions of geometrical scaling. In fact, Bourrely[8] has refitted the parameters of the Bourrely-Soffer-Wu model[5] and found that he can fit all pp and $p\bar{p}$ data, from ISR to collider, with the six parameters contained in their

model. The only problem they have is that b is a very rapidly varying function of t in the interval $-0.2 \leq t \leq 0$. Though there is no indication for such a fact, it is not clear that it really contradicts experiment. This model predicts $\sigma_{el}/\sigma_{tot} = 0.27$ at 10 TeV c.m., and 0.29 at 20 TeV c.m.

Now I would like to say a few words about the problem of the dip. The dip has been seen in pp scattering at the ISR and its depth explained by real part effects. Now, recent experiments on $p\bar{p}$ scattering at the ISR give results with relatively large errors which might indicate that a shoulder, in the case of $p\bar{p}$, is preferred to a dip[9]. The trouble is that we shall never know the truth for the ISR will be closed and this is very sad (not that they are closed one day but that they are closed so early!). There is a model, by Donnachie and Landshoff[10] in which the three-gluon exchange term acts as an effective odderon, i.e., a real contribution to the pp and $p\bar{p}$ amplitude which changes sign when one goes from pp to $p\bar{p}$. In pp it cancels the real part of the even signature amplitude while it does the contrary for $p\bar{p}$, thus eliminating the dip. This is possible, but let me stress that it is a non-asymptotic situation. As the energy goes to infinity either both the pp and $p\bar{p}$ dips will survive or they will disappear. This is the content of the theorem that Cornille and I obtained some years ago[11]. The only weak point of this theorem is connected with spin effects. So one could violate the theorem by having non-diagonal helicity amplitudes with a phase which increases to infinity. However, none of the existing models, including that of Donnachie and Landshoff, possess this property.

Finally, I would like to stress the importance of forward real part measurements (such a measurement is being planned in March 1985 by the UA4 group). We have already seen that the real part measurement was very effective in the past since it allowed the successful prediction of the cross-section at 540 GeV cm energy. Now that we know that we are far from the asymptotic regime, we have doubts on the $(\log s)^2$ behaviour of the cross-section and, furthermore, we want to know this cross-section at 10, 20 and 40 TeV c.m. energies at which machines might be built.

With Bourrely, we have made a little exercise, which is similar to the one made by Block and Cahn[2] some time ago. We take an explicitly analytic and crossing symmetric form of the even signature amplitude:

$$F^+ = is \frac{A + B\left(\log \frac{s}{s_0} - i\frac{\pi}{2}\right)^2}{1 + C\left(\log \frac{s}{s_0} - i\frac{\pi}{2}\right)^2} ,$$

and make a fit (not a best fit in the mathematical sense) to the ISR data (ρ and σ_T^+) with the constraint

$$(1+\rho^2)\,\sigma_T^+ = 64 \text{ mb at } E_{c.m.} = 546 \text{ GeV}$$

In the first fit we take C = 0, and we saturate the Froissart bound. In the second fit we try to take C as large as possible without spoiling the agreement with experiment. The parameters are the following.

	I Froissart saturated	II $\sigma_T \to$ const.
A	41.695	41.824
B	0.43	0.815
C	0	0.006
s_o	243.6	277.7

and we get

E_{cm} GeV	I		II	
	σ_T^+	ρ^+	σ_T^+	ρ^+
30	41.4	0.043	41.2	0.051
52	43.1	0.075	43.5	0.089
62	43.9	0.085	44.5	0.099
550	62.4	0.154	63.1	0.119
2 000	81.1	0.161	75.4	0.094
10 000	112.5	0.155	88.7	0.065
20 000	128.8	0.152	92.9	0.058
40 000	146.6	0.145	97.8	0.047

This Table shows that there is a big variation of ρ at the collider energy from 0.154 to 0.119. If the experimentalists can really measure ρ with an accuracy of 0.1 they will be able to separate these two possibilities and obtain precious indications on the trend of σ_T.

APPENDIX

I want to explain why I prefer the value $b(t=0) = 15.7 \pm 0.2$, obtained from the quadratic fit

$$\frac{d\sigma}{dt} \sim \exp(bt + ct^2)$$

$$b = 15.7 \pm 0.2 \text{ GeV}^{-2} \qquad c = 3.6 \pm 0.45 \text{ GeV}^{-4}$$

for $0.03 < -t < 0.5$ GeV^2 to the value

$$b = 15.3 \pm 0.2,$$

obtained from a linear fit to the data for $0.03 < -t < 0.15$ GeV^2.

First of all, the differential cross-section is analytic inside an ellipse in the t plane. The right extremity of this ellipse is at $t = +0.08$ GeV^2. If $\log(d\sigma/dt)$ has a second derivative non-zero for $t < -0.15$ GeV^2, this should continue for $t > -0.15$ GeV^2. One can invent a more quantitative argument using the positivity of the absorptive part, more specifically the fact that the absorptive part is a sum of Legendre polynomials with positive coefficients. In the limit of $|t_1 - t_2| \ll |t_1|$ or $|t_2|$ one can prove

$$\left| \frac{d^2A}{dt^2}(t_1) - \frac{d^2A}{dt^2}(t_2) \right| < 0.68 \frac{|t_1 - t_2|^{1/2}}{|t_1|^{3/2}} \frac{dA}{dt}(t=0)$$

This inequality would be constraining if the accuracy was very great, because it shows that by taking $t_1 - t_2$ small enough, one gets a contradiction if d^2A/dt^2 vanishes at t_1 and not at t_2. In fact a complete set of unitarity constraints has been obtained by S.M. Roy[12], but some work is necessary in order to confront them with experiment.

REFERENCES

1) A. Martin - Third Topical Workshop on Proton-Antiproton Collider Physics, Rome (January 1983), CERN Yellow Report 83-04 (1983) 351, Eds. C. Bacci and G. Salvini.
2) M.M. Block and A. Cahn - Phys.Lett. 120B (1983) 224.
3) J. Dias De Deus and P. Kroll - Acta Phys.Polon. B9 (1978) 159.
4) T.T. Chou and C.N. Yang - Phys.Rev. D19 (1979) 3268; Phys.Rev.Lett. 46 (1981) 764; Phys.Lett. 128B (1983) 457.
5) C. Bourrely, J. Soffer and T.T. Wu - Phys.Lett. 76B (1978) 481; Phys.Rev. D19 (1979) 3249.
6) A.B. Kaidalov and K.A. Ter Martyrosian - Moscow Preprint ITEP-51 (1982).
7) U. Amaldi et al. - Phys.Lett. 66B (1977) 390.
8) C. Bourrely - Private communication, to be published.
9) Experiment R420, preliminary result (1983).
10) A. Donnachie and P. Landshoff - Preprint DAMTP 84/6, M/C-TH 84-8; See also: M. Fukujita and J. Kwiecinsky - Phys.Lett. 83B (1979) 119.
11) H. Cornille and A. Martin - Phys.Lett. 40B (1972) 671.
12) S.M. Roy - Phys.Lett. 135B (1984) 191.

NEW SHAPE-EFFECTS IN PROTON-ANTIPROTON ELASTIC SCATTERING

Roland Henzi
McGill University

Following a series of startling CERN discoveries in the measurement of the proton-proton and the proton-antiproton elastic scatterings and total cross sections, among them the one-dip diffraction pattern and the total-cross-section rise, both not yet fully understood, new surprising features in the evolution of the diffraction pattern with increasing energy have been observed in the recent CERN experiments done by the UA4 group at the $p\bar{p}$ collider[1]. Especially a rise of σ_{el}/σ_{tot} and an evolution of the dip-bump structure into a relatively high shoulder. This energy evolution of the diffraction pattern can be traced back[2] to a behaviour of the proton which is more dynamical than previously thought, it becomes Blacker, Edgier, and Larger - BEL. In a sense, we are approaching even closer the step-function profile of the famous Froissart-Martin bound[3]. Here, I am going to summarize the arguments leading to the discovery of this BEL effect, and present some diffraction-theoretical predictions for future measurements, especially at supercolliders. The work reported here was done in collaboration with P. Valin.

Before going into details, I cannot resist saying that the story of elastic scattering and total cross sections reminds me of my last visit to the Bear Pit in Berne. I grew up near Berne, have a special relationship to the Bear Pit from my childhood on, and the bear keeper is a good friend of mine. Well, he took me to the Bear Pit. A huge crowd was there - all excited. I looked down. I didn't trust my eyes - a bear and a sheep sitting together. "Fantastic, how did you do it?", I turned to the bear keeper. Said he, "No problem. We change the sheep every day!"

1. TOOLS OF DIFFRACTION THEORY

The scattering amplitude normalized by $d\sigma/dt = \pi|f|^2$ is given by a Fourier-Bessel integral over the impact parameter b,

$$f(s,t) = \int_0^\infty h(b,s)\ J_0(b\sqrt{-t})\ b\ db \tag{1}$$

where J_0 is the famous Bessel function. The impact-parameter amplitude $h(b,s)$ is related to the partial-wave amplitude $f_\ell(s)$ by $h(b,s) = f_\ell(s)$ where $\ell = b\sqrt{s}/2 - 1/2$ hence, if we introduce the blackness $G(b,s)$, where $0 \leq G(b,s) \leq 1$, h satisfies the s-channel unitarity condition

$$\{\mathrm{Re}\ h(b,s)\}^2 + \{\mathrm{Im}\ h(b,s) - 1\}^2 = 1 - G(b,s) \leq 1 \tag{2}$$

The blackness G equals the inelasticity of the colliding particles, more precisely, the differential inelastic reaction rate, as a function of the impact parameter, and is also sometimes called the inelastic overlap function. We use these formulae for the elastic scattering at ISR and Collider energies by making two assumptions: dominance of the crossing-even amplitude, and neglect of spin. Both are compatible[3] with the presently available information (but keep in mind the Bear Pit saga!).

Crossing-even dominance entails that at the same energy the pp and $p\bar{p}$ diffraction patterns are identical so that one single blackness G controls both scatterings. Hence, an ISR measurement (say at $\sqrt{s}$ = 53 GeV) of the pp blackness and the Sp$\bar{p}$pS measurement (at $\sqrt{s}$ = 540 GeV) of the $p\bar{p}$ blackness translate into a measurement of the evolution of the pp (or $p\bar{p}$) blackness with increasing energy. The outcome is the BEL proton, its shape and the new effects resulting from the latter's dynamical behaviour being described in terms of the blackness G(b,s). Crossing-even dominance also determines Re h in terms of Im h through

$$\text{Re } h(b,s) = \frac{\pi}{2} \frac{\partial}{\partial \ell n\, s} \text{Im } h(b,s) \tag{3}$$

which is a generalization of Martin's 1973 method[4] for dealing, at high energy, in a good approximation with the dispersion relation for the crossing-even amplitude. Upon substituting Re h given by the Eq.(3) into the Eq.(2), we get an inhomogenous differential equation for Im h whose source term is the blackness G. This equation determines Im h, and with it Re h through the Eq.(3), in terms of G. We have therefore established that, as was already mentioned above, the blackness G indeed controls the scattering amplitude and vice versa.

In practice we solve (in a good approximation) this differential equation, and with it our scattering problem, by the following four-step procedure: (1) we solve the Eq.(2) for h_o with Re h_o = 0 and get $h_o = i\{1-\sqrt{1-G(b,s)}\}$, which does however not satisfy the Eq.(3) if G is energy dependent; (2) we take

$$h = i\{1-\sqrt{1-G(b,se^{-i\pi/2})}\} \simeq (i + \frac{\pi}{2} \frac{\partial}{\partial \ell n\, s}) \{1-\sqrt{1-G(b,s)}\} \tag{4}$$

which is obtained from h_o by replacing[4] s by $se^{-i\pi/2}$, satisfies the Eq.(3) in a good approximation (in fact, crossing symmetry exactly), and yields

$$f(s,t) = f_o(se^{-i\pi/2},t) \simeq (i + \frac{\pi}{2} \frac{\partial}{\partial \ell n\, s}) \text{ Im } f_o(s,t) \tag{5}$$

where f_o is given by the Eq.(1) with $h_o(b,s)$ as input; (3) we generate a modified blackness $G_1(b,s)$ by putting h into the Eq.(2); (4) if $G_1 \simeq G$ we have found in h a good approximation to the solution of the differential equation and, there-

fore, in f given by Eq.(5) a good approximation to our scattering amplitude. This procedure works well for ($\ell n\, s$)-physics, that is, when the blackness G considered as a function of $\ell n\, s$ varies slowly with the energy. Then, the Eq.(3) of course implies that Re h is small, while $G_1 \simeq G - (\mathrm{Re}\, h)^2$.

The SPS and ISR curves in the Argand diagram of Fig. 1 summarize the results of our analysis based on the above method, which will be further detailed in Section 2. The Tevatron and SSC curves are predictions (see below). ($\ell n\, s$)-physics is apparent, esp. Re h << Im h. The BEL effect in the blackness G is illustrated by the various sequences of equal-fermi-points on the curves: with increasing energy, each sequence converges toward the center (h = i) of the unitarity circle, that is, toward increasing blackness G.

2. THE ACTUAL BLACKNESS-PROFILE : THE BEL EFFECT

For a detailed analysis, one needs an explicit expression for the blackness G, which we take as[2)]

$$G(b,s) = G(0,s)\, e^{-\frac{b^2}{4B}} \{1 + \delta_2 \xi + \delta_4 \xi^2\} \tag{6}$$

$$\xi = e\gamma^2 \frac{b^2}{2B} e^{-\gamma^2 \frac{b^2}{2B}} \tag{7}$$

Jet physics provides one possible justification[5)] for this form which we call BEL ansatz. The central blackness G(0,s), the edginess parameters δ_2 and δ_4, the largeness parameter B, and the parameter γ may depend only on s. The impact parameter b and the largeness parameter B occur in the combination $b/\sqrt{B}$ which, through Fourier-Bessel transformation, leads to the combination $\sqrt{-t\,B}$ for the square of momentum transfer t and the largeness B. Hence, built into the BEL ansatz, if B depends on s, is a scaling variable t B(s) whose presence is desirable on the grounds of the studies on qualitative saturation[3)], connected to geometrical scaling[6)], of the Froissart-Martin bound : a scaling property $d\sigma/dt = \pi B^2 \{[\mathrm{Im}\, f(tB)]^2 + \rho^2(s,0)[d/dt(\mathrm{Im}\, f(t\,B)t)]^2\}$, where $\rho(s,0) = \mathrm{Re}\, f(s,0) / \mathrm{Im}\, f(s,0)$, exists if and only if for sufficiently large energy G(0,s), δ_2, δ_4, and γ do not depend on s.

The following energy dependences very precisely describe the $p\bar{p}$ diffraction at the Collider, assumed to equal the pp diffraction, and the pp diffraction at the ISR:

$$G(0,s) = \frac{.92 + .0264\ \ell n^2(s/s_0)}{1 + .0264\ \ell n^2(s/s_0)} \tag{8}$$

$$\delta_2 = .12 + .00086\ \ell n^2(s/s_0) \quad ; \quad \delta_4 = \tfrac{1}{4}\delta_2^2 \tag{9}$$

$$B = 6.6 + .051\ \ell n^2(s/s_0)\ \ \text{GeV}^{-2} \qquad ;\ \ \gamma^2 = .78 \tag{10}$$

where $s_0 = 100\ \text{GeV}^2$ and the relation between δ_4 and δ_2 follows[5] from jet physics. We call this parametrization BEL II; it improves our original BEL I parametrization[2]. These parametrizations entail $G_I \simeq G$; hence, our fundamental criterion of the step (4) of the process described in the previous section is satisfied, and G describes the actual blackness. The central blackness G(0,s), the edginess' δ_2 and δ_4, and the largeness B all increase with increasing energy: the BEL effect! No scaling in the above sense occurs (it may however approximately hold in some limited t-intervals). δ_2 will asymptotically also have to be of a form similar to G(0,s), to avoid a violation of the unitarity limit $G \leq 1$.

Fig. 1 shows the impact parameter amplitude h at various energies calculated on the basis of the Eq.(4) with the Eqs.(6-10) as input: ISR and SPS are data-reproducing, Tevatron and SSC are predictions. The dotted line is a calculation of the SPS curve based on scaling in the above sense the ISR data up to the SPS. The deviation of this line from the actual SPS curve, on the one hand, illustrates again the absence of scaling (as the deviation becomes more pronounced as b decreases, scaling "violation" should become more pronounced as $|t|$ increases) and, on the other hand, once more the BEL effect: relatively to scaling, Re h is larger, hence, according to Eq.(3) the variation of Im h with energy, and with it of G, stronger. Fig. 2 illustrates the "blacker-and-edgier" component of the BEL effect in a plot of the difference ΔG of two scaling functions G_H and G_L,

$$\Delta G(\tfrac{b}{R}) = G_H(\tfrac{b}{R}) - G_L(\tfrac{b}{R}) \tag{11}$$

where H and L refer to two selected higher and lower energies $\sqrt{s_H}$ and $\sqrt{s_L}$, and the scaling parameter R is a function of s, $R(s) = \sqrt{B(s)/B(s_H)}$. With the definition $G(b,s) \equiv \Gamma(b/R,s)$, the two scaling functions G_H and G_L are given by $G_H = \Gamma(b/R,s_H)$ and $G_L = \Gamma(b/R,s_L)$. If G scales, that is, depends on b/R only, then G_H equals G_L, and we get a zero ΔG-signal for any energy $\sqrt{s}$. For $s = s_H$, we have $\Delta G = G(b,s_H) - G_L(b)$, that is, ΔG equals the difference between the actual blackness G at $s = s_H$ and a fictitious blackness G_L scaled up to $s = s_H$ from $s = s_L$; the "larger" component of the BEL effect has been subtracted out. Its "blacker-and-edgier" component is now isolated in terms of ΔG evaluated at $s = s_H$, and displayed in the Fig. 2. The upper curve details the effect in going from the ISR to the SPS. It peaks near .7 fm and is distinctly present at 0 fm. The lower curve comes from our 1979 pp analysis[7] which unveiled

a similar albeit much smaller effect in the ISR range. Although our 1979 curve is outside the error bars of the Amaldi-Schubert analysis[8], which favoured scaling, it is according to the standard-deviation criterion not inconsistent with their results: the BEL effect already signalled itself in the era of pre-Collider physics, though not conclusively!

Figure 3 illustrates the uncertainties of our analysis (BEL II) of the BEL effect. Here, $R = \sqrt{\sigma_{tot}(s)/\sigma_{tot}(s_H)}$, which assures that contrary to the previous choice the scaling functions G_H and G_L reproduce the total cross section exactly. The curve goes negative since σ_{tot} increases slightly more rapidly with s than B. The very generous errors originate from many sources: rescaling of $d\sigma/dt$, of b, and so on. This figure illustrates also the insignificant uncertainties due to the difference between G_1 and G. Note that according to Fig. 1 Re $h(0,s_{ISR}) >$ Re $h(0,s_{SPS})$ and, therefore, that $\Delta G_1(0) = \Delta\{G(0) - [\text{Re } h(0)]^2\} > \Delta G(0)$, as born out in the figure. We have further investigated the BEL effect by a method entirely independent from the one described here[2], which gave results in excellent agreement with the present results. In sum, the BEL effect is well established on the basis of our present knowledge.

3. ON $d\sigma/dt$: TOWARD SUPER-t AND SUPERCOLLIDERS

The BEL parametrization accurately describes the diffraction pattern, for instance BEL II, completed before the new data presented by Cervelli at this workshop were known, has excellent $\rho(s,0)$ and σ_{tot} down to FNAL energies. σ_{el}/σ_{tot} increases from .18 at the ISR to .21 at the Collider, a 17 % increase to be compared to the new value of $\simeq$ 20 % reported by Cervelli[1] at this workshop. This increase is due to the "blacker-and-edgier" component of the BEL effect. Near t = 0, BEL gives $d\sigma/dt \propto \exp(at+ct^2)$ with a = 16.6 GeV^{-2} and c = 4.43 GeV^{-4}, to be compared with a = 15.7±.2 GeV^{-2} and c = 3.6±.5 GeV^{-4} reported by Cervelli[1]. Fig. 4 illustrates the linearly decreasing logarithmic slope A = a+2ct of $d\sigma/dt$ near t = 0. This slope decrease is a diffraction-theoretical rescattering effect[5] due to the second term in the Eq. (4) rewritten as

$$h = \frac{i}{2}\{G + \frac{G^2}{(1+\sqrt{1-G})^2}\} \qquad (12)$$

This rescattering term, near t = 0, gives rise in f to a term whose slope is flatter (because of the G^2) than that of the f-term due to G; hence, the slope of their sum decreases because they interfere constructively. Fig. 5 illustrates how accurately BEL I (BEL II is similar) describes the diffraction patterns measured at the ISR and the Collider, and Fig. 6 compares BEL I's performance with some other models - only BEL seems to be able to describe the Collider pattern correctly.

Fig. 5 also shows the BEL I prediction for super-t at the Collider, that is,

the experimentally quite challenging range of momentum transfers beyond $|t| \simeq 1.5$ GeV^2. The uncertainty band for the prediction represents the propagation of the BEL uncertainty due to the errors of diffraction pattern measurement. Fig. 6 shows that BEL's prediction differs markedly from other models. BEL's predicted slope decrease for increasing super-t is again due to rescattering[5] (second term of Eq.(12)) which in this t-region gives rise to an exponential-in-$\sqrt{-t}$ law; plotted versus $|t|$, this entails the slope decrease just mentioned. Fig. 7, finally, takes us to the Tevatron and the SSC supercolliders: BEL II's predictions, under the assumption that the Eqs. (6)-(10) continue to hold, are shown together with the SPS curve, the uncertainty bands having the same meaning as that of Fig. 5 explained above. The forward peak continues to rise and to shrink, the dip comes back and continues to move inwards, super-t's continue to rise: relatively to the forward peak, the secondary-maximum/shoulder-to-forward-maximum ratio increases from $6\text{x}10^{-6}$ at the Collider to $2\text{x}10^{-5}$ at the Tevatron to $1.6\text{x}10^{-4}$ at the SSC. At the SSC, the proton has become sufficiently edgy to produce a second dip near $|t| = 3.4$ GeV^2. Quite striking predictions!

4. THE BEL EFFECT: ITS UNDERLYING DYNAMICS

Although jet physics is able to provide a certain dynamical basis for the BEL effect[5], the proton's blackness and its evolution with energy remain fundamentally unexplained. But the BEL effect is phenomenologically well established. Its predictions for super-t and supercolliders are intriguing and, hopefully, will be confronted with experiment in a not too distant future. I hope by that time the question of the dynamics underlying the proton-proton blackness, a central question of the strong interaction, would have been answered.

I thank the organizors for a splendidly run workshop.

REFERENCES

1. G. Matthiae, Plenary Talk in the Proceedings of the International Europhysics Conference on High Energy Physics, Brighton, July 1983, published 1983 by Rutherford Appleton Laboratory, pages 714-742; and F. Cervelli, Invited Talk in the Proceedings of this Fourth Proton-Antiproton Collider Physics Workshop.
2. R. Henzi and P. Valin, Phys. Lett. 132B(1983)443.
3. A. Martin, Invited Talk in the Proceedings of the Third Topical Workshop on Proton-Antiproton Collider Physics, Rome, January 1983, pages 351-371; and A. Martin, Invited Talk in the Proceedings of this Fourth Proton-Antiproton Collider Physics Workshop.
4. A. Martin, Nuovo Cimento Letters 7(1973)811.
5. R. Henzi and P. Valin, "What Is Elastic Scattering Past the Diffraction Dip Telling Us?", to be published in Zeitschrift für Physik C (1984).
6. For example, see P. Kroll, J. Phys. G9(1983)L81.
7. R. Henzi and P. Valin, Nucl. Phys. B148(1979)513.

8. U. Amaldi and K.R. Schubert, Nucl. Phys. B166(1980)301.

9. H. de Kerret et al., CERN-Hamburg-Heidelberg-Annecy-Vienna Collaboration, Phys. Lett. 68B(1977)374.

10. T.T. Chou and C.N. Yang, Phys. Lett. 128B(1983)457.

11. A. Donnachie and P.V. Landshoff, Phys. Lett. 123B(1983)345, and contribution 203 to the International Europhysics Conference on High Energy Physics, Brighton, July 1983.

FIGURE CAPTIONS

1. Argand diagram for the pp (or $p\bar{p}$) impact parameter amplitude h at the indicated facilities (BEL II). Each point on a curve corresponds to a given impact parameter b. The blackness G is related to the distance of h from h=i by $\sqrt{1-G}$. The unitarity circle corresponding to Eq.(2) for G = 0 is indicated. (Dashed line, see text.) ISR - Intersecting Storage Rings: pp($\sqrt{s}$=53GeV); SPS - Super Proton Synchrotron Collider: $p\bar{p}$($\sqrt{s}$=540); Tevatron: $p\bar{p}$($\sqrt{s}$=2000); SSC - Superconducting Super Collider: pp($\sqrt{s}$=40000).

2. The "blacker-and-edgier" component of the BEL effect shown in terms of $\Delta G = G(b,s_H) - G_L(b)$, the difference between the actual blackness G at the higher energy $\sqrt{s_H}$ and a fictitious blackness G_L scaled up with $R(s) = \sqrt{B(s)/B(s_H)}$ from the lower energy $\sqrt{s_L}$. The lower curve shows a result of our 1979 analysis[7] done in the days of pre-Collider physics. Upper Curve: BEL I.

3. Same as Fig. 2 upper curve, but for BEL II with errors (see text) and a scaling parameter $R(s) = \sqrt{\sigma_{tot}(s)/\sigma_{tot}(s_H)}$. Solid and dashed lines: calculated with G_1 and G, respectively.

4. Decrease of the logarithmic slope $A = a+2ct$ of $d\sigma/dt \simeq e^{at+ct^2}$ near $t = 0$. Curves: BEL I and BEL II. Data: old from Matthiae[1], new from Cervelli[1].

5. BEL description of the measured Collider($\sqrt{s}$=540)[1] and ISR($\sqrt{s}$=53)[9] diffraction patterns, and BEL prediction with uncertainty band for super-t at the Collider.

6. Comparison of the BEL description of the measured Collider[1] diffraction pattern and of the BEL prediction for Collider super-t with some models. Long-dash line: De Dias-Kroll[6], short-dash line: Chou-Yang[10], dash-dot line: Donnachie-Landshoff[11], solid line: BEL I.

7. BEL II predictions with uncertainty bands for the indicated facilities, at the energies detailed in the caption of Fig. 1. At the SSC, the proton has become sufficiently edgy to produce a second dip.

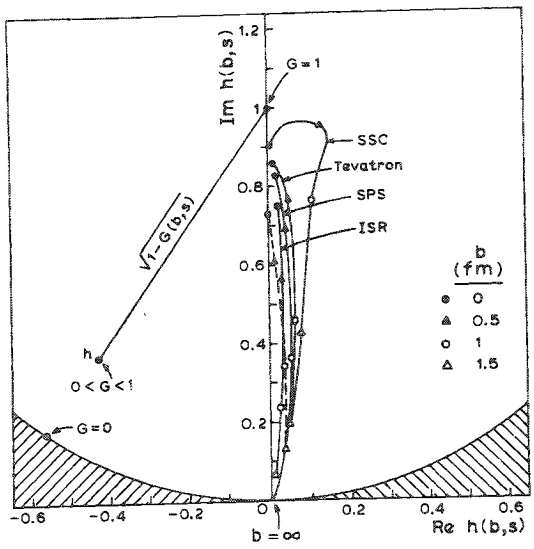

Fig. 1

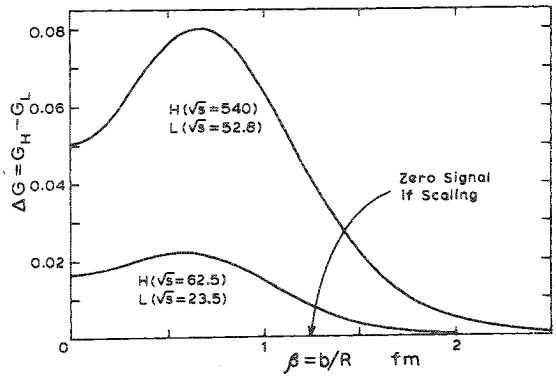

Fig. 2

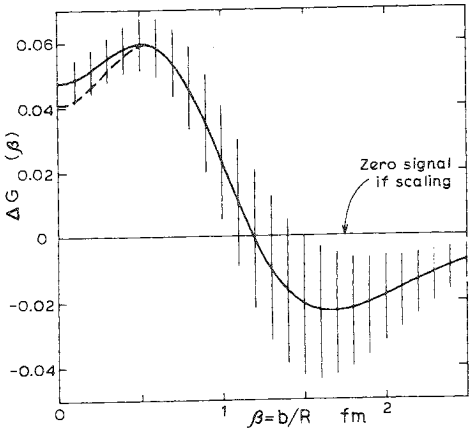

Fig. 3

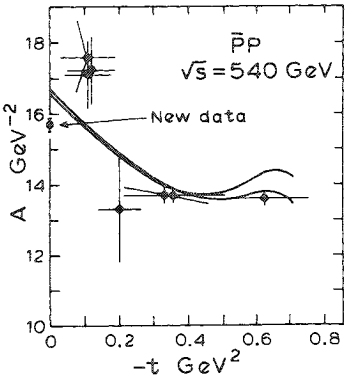

Fig. 4

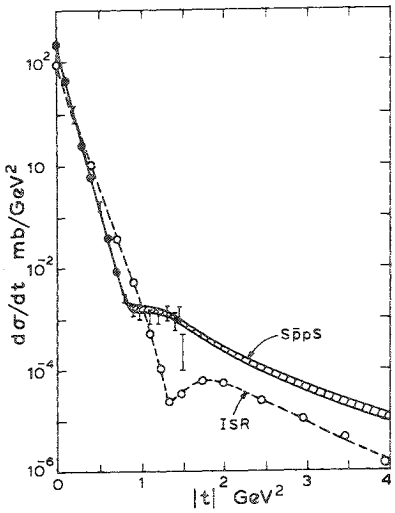

Fig. 5

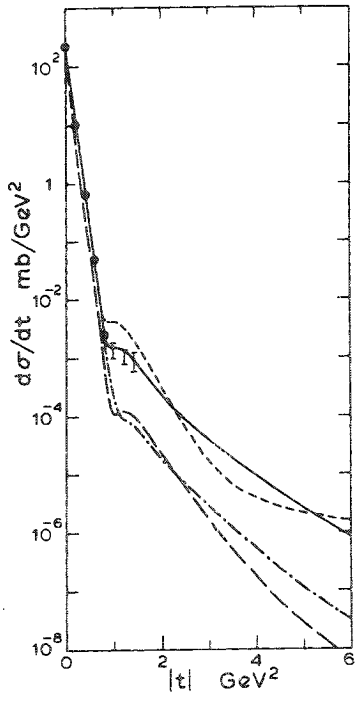

Fig. 6

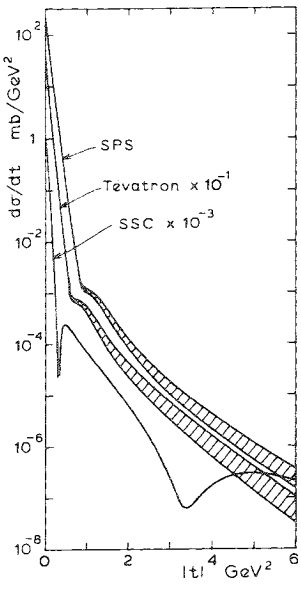

Fig. 7

NEW MEASUREMENT OF ELASTIC SCATTERING AND TOTAL CROSS SECTION AT THE CERN $p\bar{p}$ COLLIDER

UA4 Collaboration, CERN, Geneva, Switzerland

Presented by F. Cervelli, CERN and Pisa

No written contribution received

LEAR Physics

PHYSICS WITH ANTIPROTONS AT LEAR

Kurt KILIAN

CERN - EP Division CH-1211 Geneva 23

ABSTRACT

The low energy antiproton ring LEAR started to work at CERN in 1983. It provides clean $\bar{p}$ beams of much higher intensity and much better quality than available so far in the range from 0.1 to 2 GeV/c momentum. 16 of the 17 accepted experiments are installed and 14 of them took first data in 1983. After ≈ 240 hours of LEAR operation very first results are available. One can expect that exciting physics results be produced in many different domains provided LEAR gets enough $\bar{p}$ in the future.

1. INTRODUCTION

LEAR[1] is the low energy end of the CERN antiproton ($\bar{p}$) complex whose center is a $\bar{p}$ factory[2] consisting of the 26 GeV proton synchrotron (PS) and the antiproton accumulator (AA). During 1983 LEAR provided for ≈240 hours $\bar{p}$ beams at 300 and 600 MeV/c for physics experiments. Of course 16 newly installed experiments cannot all produce physics results in such a short running time. Therefore this report is mainly a preview. Nevertheless there are first results and indications how things may go in some experiments.

The present experimental program is well balanced and covers a wide range of physics. In order not to be lost in details it is worthwhile to ask: What is the most interesting aspect at the beginning of $\bar{p}$ LEAR physics ? It could be the chance to gain understanding of quark gluon dynamics in the low energy non-perturbative region and to develop on this basis a more microscopic description of low energy hadron interactions and hadron structure.

Hadrons are believed to be made from colored quarks (c-triplet) which interact by exchange of colored gluons (c-octet). Nature seems to restrict observable hadrons to overall c-singlets, which means that free colored quarks and gluons do not reach our detectors. This "explains" confinement and justifies the concept of bag models. The simplest c-singlets are three quark (qqq) fermions, the baryons and quark antiquark ($q\bar{q}$) bosons, the mesons. In the one boson exchange (OBE) models the color singlet baryons (B) and mesons (M) are taken as basic entities. In BB (and MB) interactions where the (3q) c-singlet baryon bags always come out again it has been shown that the simplifying assumption of c-singlet one boson exchange allows for a very successful parametrization of experimental data.

In the case of $B\bar{B}$ interaction where the unique process of hadronic annihilation comes into the game OBE models have problems. (A medium range absorptive potential has to be put in "by hand"). Here the original B (3q) and $\bar{B}$ ($3\bar{q}$) c-singlets can be dissolved. Valence quark pairs can be annihilated and created <u>at minimal</u> baryon <u>energy</u> in infrared slavery. The quarks and antiquarks can finally appear reshuffled, but now in ($q\bar{q}$) c-singlet mesons alone. All this occurs inside overlap regions of bags involving colored quarks and gluons rather than asymptotic c-singlet mesons or baryons.

Fig. 1 indicates how, for example, annihilation into two and three mesons could proceed. Only the extreme cases of re-arrangement and $q\bar{q}$ annihilation-recreation are shown. Theoretically $B\bar{B}$ interaction appears as a very complex manybody problem. Experimentally $B\bar{B}$ interactions at low energy are characterized by a correspondingly rich system of many different annihilation and reaction channels. It is a challenge for experimentalists at LEAR to do so many and so specific experiments that one finally can piece together sufficient information for a better understanding of the basic quark gluon dynamics.

An open question is to what extent one may isolate experimentally the effects of individual quark lines in diagrams like in Fig. 1. One alternative is for example to study the creation of a single $q\bar{q}$ pair (such as on the right side of Fig. 1b) under clean conditions by selecting a strange antistrange quark pair.

2. THE LEAR FACILITY

LEAR[1] is a small storage and stretcher synchrotron installed in the old PS South Hall (Fig. 2). It is a strongly focusing synchrotron with four laminated dipoles and a separate focusing structure with quadrupole doublets on either side of the dipoles. Some parameters are shown in Table 1. LEAR gets antiprotons from the CERN "antiproton factory"[1]. High density $\bar{p}$ batches, free of any contamination, are peeled off from the AA stack. They are injected into the PS, decelerated in the PS down to fixed momentum of 0.6 GeV/c, and then injected into LEAR. The batches can contain up to $\simeq 4.10^9$ $\bar{p}$ and they are transferred once every $\simeq$ 75 minutes. This is compatible with the accumulation in the AA and corresponds to an average $\bar{p}$ flux with $\simeq$ 100% duty cycle of $\simeq 10^6$ $\bar{p}$/s. A new scheme of ultraslow "stochastic" extraction[3] (normal resonance extraction with feeding via diffusion) has been developed for that purpose in LEAR. It provides the necessary spill out time of 1 hour. The $\bar{p}$ momentum can be tuned in LEAR (Finally from 100 MeV/c to 2000 MeV/c). Stochastic cooling[4] is used and provides very good beam quality.

Table 1: Some LEAR parameters

Momentum range:	0.1-2 GeV/c
Circumference:	78.54 m
Free length of long straight sections between quadrupoles:	8 m
Approximate working point:	Q_H=2.3; Q_V=2.7; γ_t^2=-(14.5)^2
Maximum acceptances (in πmm.mrad):	E_H=240; E_V=48; $\Delta p/p$=±1.1%

The stochastic extraction system feeds an external beam which is split into three simultaneously working branches[5]. The beam performance is : Emittance ε_H and ε_V (better than) $\simeq$ 3 to 5 πmm mrad and $\Delta p/p$ (better than) $\simeq 1.3 \cdot 10^{-3}$. (It is worthwhile to recall that in the "pre-LEAR time" normal secondary beams e.g. at 400 MeV/c had only $\simeq 10^{-3}$ of the intensity of LEAR, had a duty cycle of only $\simeq$ 0.1, had $\simeq$ 100 times more pions than $\bar{p}$'s, a momentum spread of $\Delta p/p \simeq \pm 1\%$ and emittances of about 100 πmm mrad). The extracted $\bar{p}$ intensity can be distributed freely on the 3 split branches. Each branch can be switched by a dipole into two experimental areas (Fig. 3).

3. A SHORT LOOK AT THE FIRST GENERATION OF EXPERIMENTS

The 17 approved experiments[6] are listed in Table 2. The majority of them (10) are addressed to studies in the $\bar{p}p$ system. Six others are related to $\bar{p}$ nucleus interactions. In one experiment (PS189) which is not yet installed the masses of $\bar{p}$ and p will be compared to an accuracy of 10^{-9} (CPT test) using a magnetic spectrometer with RF modulation.

At low LEAR energies short degraders with negligible hadronic losses can be used to slow down $\bar{p}$ and to stop them effectively with small energy straggling in thin targets. This is an obvious advantage for the $\bar{p}$ stop experiments (9 in total).

Eight experiments will do studies with transmission targets. Here the high beam quality ensures good angular resolution, the small momentum spread gives good energy resolution and the high $\bar{p}$ flux allows for statistical precision even with the thin targets which one needs if one wants to avoid energy smearing.

Table 2: LEAR - List of experiments

Exp.	Title	CERN Doc.	Spokesman (Contact.)
PS170	Precision measurements of the proton electromagnetic form factors in the time-like region and vector meson spectroscopy	PSCC/80-95	Dalpiaz (Pauli)
PS171	A study of $\bar{p}p$ interactions at rest in a H_2 gas target at LEAR	PSCC/80-101	Klempt (Gastaldi)
PS172	$\bar{p}p$ total cross-sections and spin effects in $\bar{p}p \to K^+K^-, \pi^+\pi^-, \bar{p}p$ above 200 MeV/C	PSCC/80-76	Bugg (Hess)
PS173	Measurement of $\bar{p}p$ cross-sections at low $\bar{p}$ momenta	PSCC/80-85	Walcher (Rasome)
PS174	Precision survey of X-rays from $\bar{p}p$ ($\bar{p}d$) atoms using the initial LEAR beam	PSCC/80-81	Davies (Welsh)
PS175	Measurement of the antiprotonic Lyman and Balmer X-rays of $\bar{p}H$ and $\bar{p}D$ atoms at very low target pressures	PSCC/80-99	Simons (Koch)
PS176	Study of X-ray and γ-ray spectra from antiprotonic atoms at the slowly extracted antiproton beam of LEAR	PSCC/80-103	Poth (Tauscher)
PS177	A search for heavy hypernuclei at LEAR	PSCC/80-74	Polikanov (Johansson)
PS178	Study of antineutron production at LEAR	PSCC/80-91	Voci
PS179	Study of the interaction of low-energy $\bar{p}$ and $\bar{n}$ with H, ^{2}H, ^{3}He, ^{4}He, Ne and ^{40}Ar nuclei using a streamer chamber in a magnetic field	PSCC/80-78	Piragino
PS182	Investigations on baryonium and other rare $\bar{p}p$ annihilation modes using high resolution π^0 spectrometers	PSCC/80-142	Tauscher
PS183	Search for bound $\bar{N}N$ states using a precision γ & charged pion spectrometer	PSSC/80-93	Smith (Armstrong)
PS184	Study of $\bar{p}$-nucleus interaction with a high resolution magnetic spectrometer	PSCC/80-140	Garreta
PS185	Study of threshold production of $\bar{Y}Y$ pairs in $\bar{p}p$ interactions at LEAR	PSCC/81-69	Kilian (Johansson)
PS186	Nuclear excitations by antiprotons and antiprotonic atoms	PSCC/80-83	von Egidy
PS187	A good statistics study of antiproton interactions with nuclei	PSCC/81-51	DiGiacomo
PS189	High precision mass measurements with a radiofrequency mass spectrometer - Application to the measurement of the $p\bar{p}$ mass difference	PSSC/81-84	Thibault

3.1 $\bar{p}$ stop experiments with hydrogen targets

The negatively charged $\bar{p}$ are captured in atomic orbits of "protonium" where they cascade down emitting an X-ray spectrum with a hydrogen like pattern but with $\approx 10^3$ times higher photon energy. From distortions in the X-ray spectrum (especially in the Lyman and Balmer series where annihilation effects become important) parameters of low energy $\bar{p}p$ interaction will be extracted.

Protonium has no atomic electrons and it is so small that it can reach the high electric field of neighbouring target protons. With increasing target density the Stark effect will therefore mix more and more S-wave strength into the atomic states which provokes fast annihilation from high n states owing to the increased hadronic overlap. Lyman transitions are therefore not observable with dense LH_2 targets. But variable target density is a tool to "select" experimentally S or P wave annihilation.

Three experiments (PS171, 174, 175, see Table 2) are studying protonium. In PS174 the stop target density is variable from normal pressure gas to liquid hydrogen and high resolution Si(Li) detectors are used. In PS175 $\bar{p}$ are degraded and stopped in low density hydrogen (400 mbar done, 15 mbar planned). The novel trick is to spiral $\bar{p}$ into the center of a focusing cyclotron field where they come to rest. High resolution semiconductor detectors are used here as well. There are first indications that Lyman transitions (K-X rays) in $\bar{p}p$ atoms have been seen in PS175[7]. In experiment PS171 (Asterix) the X-ray detector is a cylindrical drift chamber immediately surrounding a gaseous stop target. The resolution is moderate but ≈90% of the solid angle is covered. PS171 has two primary goals. The first is to disentangle the dependence of annihilation reactions on the quantum numbers of the $\bar{p}p$ system (S or P states etc.). These quantum numbers will be determined from the coincident X-ray transitions. The second is to identify multibody annihilation events with a large acceptance magnetic solenoid spectrometer (DM1 from Orsay). A search for resonances, glueballs or narrow baryonium states below threshold can be done this way.

There are two experiments (PS182, 183) which hunt for narrow bound states X, emphasizing high resolution. PS182 looks at $\bar{p}p \to \pi^\circ + X^\circ$ and also $\bar{p}p \to \gamma X^\circ$. The π° spectrum will be determined by reconstructing the $\pi^\circ \to \gamma\gamma$ kinematics with a pair of BGO spectrometers and also by looking at coincidence between one BGO detector and a lead glas array. PS183 searches for monoenergetic γ and $\pi^\pm$. The γ spectroscopy is done after a $\gamma \to e^+e^-$ conversion target. A large dipole magnet, filled with wire chambers is used as spectrometer (Fig. 4). Inclusive $\pi^\pm$ spectra measured in experiment PS183 show monochromatic pion lines (Fig. 5). While two lines in the π^+ spectra at 236 and 205 MeV/c can be explained by decays of stopped K^+ ($K^+ \to \mu^+\nu$ and $K^+ \to \pi^+\pi^\circ$) a line at 200 MeV/c which appears in both the π^+ and π^- spectrum is an indication for the existence of a narrow bound state baptized $G^\pm$ below threshold at a mass of 1620 MeV[8].

Baryonium[9] yes or no. That was one of the first controversies which stimulated the demand for a machine like LEAR. The results of PS183 supports evidence for bound narrow states. Are these elusive objects $\bar{B}B$ systems of nuclear physics type bound by OBE forces and stabilized by high angular momentum ? Or are they a manifestation of quark chemistry: color singlets with new substructures like for instance color triplet or color sextet diquark-antidiquark?

In experiment PS170 the rare annihilation channel $\bar{p}p \to e^+e^-$ will be measured. This reaction has its highest branching ratio at rest of only $\simeq 3.10^{-7}$. The necessary very good background rejection against hadron pairs is obtained with a magnetic dipole spectrometer combined with gas Cerenkov and shower counters. The electromagnetic form factor of the proton in the timelike region can be determined from $\bar{p}p \to e^+e^-$.

3.2 $\bar{p}$ experiments in flight with hydrogen targets

In PS170, e^+e^- production will also be studied in $\bar{p}$ interactions in flight. For the first time angular distributions can be obtained and one will get separately the electric and magnetic form factor G_E and G_M in the timelike region. The spectrum of vector mesons also and especially in the unphysical region (fig. 6) is strongly related to these form factors.

There are two experiments (PS172, 173) which look for resonances by measuring $\bar{p}p$ excitation functions down into the unknown region below 300 MeV/c momentum. So far $\bar{p}$ energy variation was done with degraders of variable thickness. This of course reduced the beam intensity drastically and limited the statistical precision. PS173 measures differential elastic and charge exchange (CEX) cross-sections with wire chambers and an $\bar{n}$ calorimeter array. A large spherical leadglass scintillator array also measures neutral and charged annihilation. PS172 first made a precision scan of σ_{total} and $\sigma_{pp\to neutral}$ in an absorption measurement and no indication of a narrow resonance was found between 600 MeV/c and 380 MeV/c[10]. Next $d\sigma/d\Omega$ and $P(\Theta)$ will be scanned in the charged two body channels $\bar{p}p \to \bar{p}p$, $\bar{p}p \to \pi^+\pi^-$ and $\bar{p}p \to K^+K^-$ with a polarized target. Narrow and also broad resonances may be disentangled with these data. The polarization of scattered protons (and possibly also $\bar{p}$) is determined by a polarimeter with carbon scatterer.

LEAR covers some interesting thresholds (Table 3). The CEX threshold is at $\simeq$100 MeV/c ($\simeq$5 MeV). Experiment PS178 studies the 0° production of $\bar{n}$ through $p\bar{p} \to \bar{n}n$ and the possibility of using $\bar{n}$ from this reaction for experiments. Above 1.43 GeV/c are the thresholds for strangeness 1 hyperon-antihyperon pairs $\bar{p}p \to \bar{Y}Y$. Experiment PS185 which investigates these reactions will be discussed in more detail in Section 4.

3.3 $\bar{p}$ stop experiments with nuclear targets

In experiments PS176 and PS186 antiprotonic atoms are studied. Measured X-ray yields, line shifts and widths tell something about $\bar{p}A$ hadronic interaction and also about $\bar{p}$ mass and magnetic moment. Nuclear γ ray measurements permit one to identify nuclear fragments after annihilation. The atomic quantum numbers before annihilation can be deduced from X-γ coincidences. The clean $\bar{p}$ beam allows for very low background. Fig. 7 shows as an example the high quality of antiprotonic X-ray spectra reached at LEAR.

PS177 is the smallest experiment at LEAR with the aim to measure the lifetime of a Λ particle in a heavy hypernucleus. This may give the "six quark in a bag" probability in a nucleus or could show whether the weak interaction is influenced by the extremely high electromagnetic field inside a heavy nucleus. $\bar{p}$ will be stopped on a very thin ($30\mu g/cm^2$) U or

Pu target. Annihilation on the nuclear surface produces $K\bar{K}+X$ in ≈7% of all cases. The $\bar{K}$ momentum distribution is optimally suited for recoilless $N(K,\pi)\Lambda$ strangeness exchange on nucleons in the same nucleus. Produced Λ can be bound and reach the hypernuclear ground state. During its lifetime the hypernucleus will leave the target foil (compare $\tau_{\Lambda} \simeq 2.6 \cdot 10^{-10}$s) and go into the vacuum with the Fermi recoil of the originally annihilated nucleon. The target will be choosen such that the weak decay of Λ leads to fission. Fission products can be measured free from any background in low pressure gas counters. The distance of the fission point from the target plane gives a measure for the hypernuclear lifetime. For that the well known "recoil distance method"[11] will be applied.

Table 3: Combinations of ≤ 4 Stable Particles which can be formed with Antiproton (& Proton) Beams from LEAR on a Proton Target.

Particle combinations with $\bar{p}$ beam	p beam	Threshold mass $\sqrt{s}$ (MeV/c^2)	Beam momentum with fixed p target (MeV/c)
$\bar{p}p$	pp	1876.559	0
$\bar{n}n$	-	1879.146	98.706
$K^+K^-K^+K^-$	-	1974.676	646.853
$K^+K^-K^0K^0$	-	1982.678	676.140
$4K^0$	-	1990.680	704.729
$\bar{p}p\pi^0$	$pp\pi^0$	2011.522	776.492
$\bar{n}n\pi^0$	-	2014.109	785.168
-	$d\pi^+$	2015.20	788.814
$\bar{p}n\pi^+$, $p\bar{n}\pi^-$	$pn\pi^+$	2017.420	796.207
$\bar{p}p\pi^0\pi^0$	$pp\pi^0\pi^0$	2146.484	1191.968
$\bar{n}n\pi^0\pi^0$	-	2149.071	1199.495
-	$d\pi^+\pi^0$	2150.162	1202.664
$\bar{p}n\pi^+\pi^0$, $p\bar{n}\pi^-\pi^0$	$pn\pi^+\pi^0$	2152.382	1209.116
$\bar{p}p\pi^+\pi^-$	$pp\pi^+\pi^-$	2155.693	1218.722
$\bar{n}n\pi^+\pi^-$	$nn\pi^+\pi^+$	2158.280	1226.219
$\bar{\Lambda}\Lambda$	-	2231.20	1435.070
$\bar{\Lambda}\Sigma^0$, $\Lambda\bar{\Sigma}^0$	-	2308.06	1652.736
$\bar{\Lambda}\Lambda\pi^0$	-	2366.163	1817.301
$\bar{\Sigma}^+\Sigma^+$	-	2378.720	1852.962
$\bar{\Sigma}^0\Sigma^0$	-	2384.920	1870.586
$\bar{\Sigma}^-\Sigma^-$	-	2394.68	1898.356

3.4 $\bar{p}$ experiments in flight with nuclear targets

There are three experiments in this field (PS179, 184 and 187) which took data at 300 and 600 MeV/c. Here $\bar{p}$ annihilation deposits a small momentum but ≈2 GeV of energy in a nucleus. In central collisions this energy deposit could give localized "hot spots" with characteristic decay properties. One expects that many nucleons and nuclear fragments are emitted, while for peripheral $\bar{p}A$ annihilation preferentially lower multiplicity mesonic reactions are expected.

In PS187 these differences have been seen[12]. This experiment uses a dipole magnet spectrometer with large acceptance which permits high statistical precision and capability to measure events with large multiplicity. High energy deposit in an active target was used as another good signature for central collisions. It was speculated that $\bar{p}$ might occupy narrow single particle-hole states in nuclei which could be the best seen in a recoilless forward knock on ($\bar{p}\rightarrow p$) reaction. No such effects are detected in the forward proton spectrum in PS187[12].

In PS179 a self shunted streamer chamber in a magnetic field is used with large acceptance and moderate momentum resolution. Fillings with H_2, D_2, ^3He, ^4He, ^{20}Ne, ^{40}Ar are foreseen. The experiment with ^4He filling could tell whether D and ^3He have been produced at the very beginning of the universe from $\bar{p}$ ^4He interactions. Several thousand high quality photos with ^4He and Neon filling have been taken.

PS184 uses a high resolution magnetic spectrometer (SPES II from Saclay). Emphasis lies on measurements of elastic and inelastic angular distributions and also on ($\bar{p}p$) knock-on reactions. This group has already published data on elastic and inelastic $\bar{p}$ scattering at 300 MeV/c on ^{12}C. Fig. 8 which is taken from the first LEAR publication[13] shows that $\bar{p}$ ^{12}C scattering has a pronounced dip in the angular distribution characteristic for a very strong imaginary potential.

4. STUDY OF $\bar{p}p \rightarrow \bar{\Lambda}\Lambda$

The more detailed discussion of PS185 which so far has only had parasitic test runs should be taken as an arbitrarily chosen example indicating the richness of physics in the LEAR experiments. The experimental set-up is sketched in Fig. 9. The $\bar{p}$ beam passes through a timing-counter S1 and a 2.5 mm polyethylene target T. The target length and the beam diameter (≈1mm) define the production vertex. Veto scintillators around the target identify beam $\bar{p}$, and prompt charged $\bar{p}$ interactions in the target. As signature for $\bar{\Lambda}\Lambda$, the appearance of delayed charged decays is used. Four hadronic decay combinations occur within typically 3 to 12 cm after the target.

$$\bar{p}p \rightarrow \bar{\Lambda}\Lambda \rightarrow \begin{cases} \bar{p}p\pi^+\pi^- & \text{four charged} & (41.2\%) \\ \bar{p}n\pi^+\pi^0, \bar{n}p\pi^0\pi^- & \text{two charged} & (23\% \text{ each}) \\ \bar{n}n\pi^0\pi^0 & \text{no charged} & (12.8\%) \end{cases}$$

The threshold kinematics permits small but fully efficient detectors since even the combined kinematics of the production $\bar{p}p \rightarrow \bar{\Lambda}\Lambda$ and of the decay $\Lambda \rightarrow p\pi$ confine the decay (anti)baryons into a rather small forward cone ($\lesssim 42^\circ$ half aperture for a 2 GeV/C $\bar{p}$ beam). The trigger for the delayed charged decays is obtained by requiring a hit in a forward scintillator hodoscope H ≈30 cm downstream of the target.

The kinematical details (decay vertices, decay planes) of an accepted event will be reconstructed from hits recorded in a stack of 23 planes of MWPCs and drift chambers. Which vertex belongs to $\bar{\Lambda}$ or Λ will be determined by the "baryon number identifier"(Fig. 9). Three drift chamber planes are used here in a solenoid type magnet. Left or right bending tells about the charge and therefore the particle type of the decay products. The decay products of $\bar{Y}$ and Y come from the field-free chamber stack and pass trough the aluminium coil of ≈1 cm thickness. This "low mass" solution keeps the main background from $\bar{n}$ annihilations low.

From the measured $\bar{\Lambda}$ and Λ production and decay vertices one can extract total and differential cross-sections. Since in the weak decay $\Lambda \to p\pi$ the proton goes preferentially in the direction of the Λ polarization vector, one can extract from the recorded decay tracks the Λ (similarly $\bar{\Lambda}$) polarizations and (for the 41% of decay combinations with four charged particles) even the $\bar{\Lambda}\Lambda$ spin correlations. The sensitivity for fully reconstructable "4 track" events will be with 10^6 $\bar{p}$/s ≃ 450 events per day and μbarn.

4.1 Quantum numbers of strange quark pair creation

The spin S and isospin I of a light diquark in the baryon 56-plet are related by a symmetry condition: a diquark (qq) has S = 0 (1) if I = 0 (1) For the isospin zero Λ with its single strange quark s of isospin zero (Fig. 10) this implies that the light (ud) diquark has isospin zero and therefore spin zero (similarly for $\bar{\Lambda}$. Note that for Σ the diquark has S=I=1). As a consequence the measurable $\bar{\Lambda}$ and Λ polarization vectors and spin correlations (singlet or triplet) are related to the $\bar{s}s$ loop. We get detailed information on the polarization behaviour of $\bar{s}s$ quark pair creation!

So far in $\bar{p}p \to \bar{\Lambda}\Lambda$ all experiments indicate large negative polarization for $|t'| \gtrsim 0.25$ (GeV/c)^2 for $\bar{\Lambda}$ and Λ[14]. If it is the $\bar{s}s$ quark loop which defines the polarization (Fig. 10) then we would predict strong negative Λ polarization in all reactions where an $\bar{s}s$ pair is created. Experiments support this assumption even in high-energy proton-induced inclusive Λ production where the same quark loop occurs. A model for $\bar{s}s$ pair creation via string dissociation in a $^3P_0$ state explains this effect[15].

There are experimental indication that $\bar{\Lambda}\Lambda$ pairs are only produced in triplet states[14] which means (if ud and $\bar{u}\bar{d}$ diquarks are perfect spin zero spectators) that the $\bar{s}s$ quark pairs are only made in triplet states.

Approaching threshold, the $\bar{\Lambda}\Lambda$ system is in an S-wave or P-wave at most. This can be determined from the shape of the differential cross-section and also from the energy dependence of $\sigma_{\bar{\Lambda}\Lambda}$ (Fig. 11). The three valence quarks in $\bar{\Lambda}$ and Λ are in a pure state of orbital angular momentum zero with the light diquark in a spin zero state. A relative S-wave or P-wave between $\bar{\Lambda}$ and Λ therefore implies a relative S-wave or P-wave, respectively, for the $\bar{s}s$ quark pair! What can we learn about the quantum numbers of $\bar{s}s$ pair creation ? If the quark pair is created with gluon quantum number 1^-, we have to find S-wave $\bar{\Lambda}\Lambda$ production and $\bar{\Lambda}\Lambda$ triplet spin correlation. On the other hand, quark pair creation in vacuum quantum numbers 0^+ implies that the $\bar{\Lambda}\Lambda$ system appears in the P-wave (in order to get positive parity) and again in a triplet state.

4.2 Final state interaction

Close to thresholds the newly produced particles appear with vanishing relative energy. In the laboratory system they go into a forward cone with very small aperture. For a long time they stay close to each other, so that there will be strong final-state interaction (f.s.i). If this f.s.i. can be sorted out then we can get information about low-energy interactions of interesting particle combinations which are not available so far[16] (Table 3). The detector shown in Fig. 9 is perfectly suited for such studies of forward confined multiparticle events.

The f.s.i. in the case of $\bar{p}p \to \bar{\Lambda}\Lambda$ will be predominantly annihilation. This should be a pronounced effect if the annihilation is of longer range than the production process. For $\bar{\Lambda}\Lambda$ production, in an OBE picture, strange mesons with at least kaon mass have to be exchanged, while annihilation might start at longer distance with pion exchange. The ratio of volumes that are characteristic for production and annihilation may then be as small as $(m_\pi/m_K)^3 \simeq 1/50$. (Note that in the case of $\bar{p}p \to \bar{n}n$ this ratio may be of the order of one owing to pion exchange in $\bar{n}n$ production).

In $\bar{\Lambda}\Lambda$ the expected strong annihilation effects in f.s.i. are likely to give a measured cross-section σ^{exp} which is reduced by a fraction d with respect to the phase-space behaviour σ^{ps} close to threshold : $\sigma^{exp} = \sigma^{ps}(1-d)$. In Fig. 11 the hatched area indicates where this deviation may be measured. In the simplest picture the depression d should be proportional (or at most equal) to the inelastic $\bar{\Lambda}\Lambda$ interaction probability

$$d \lesssim (\sigma_{inel})/(\sigma_{inel} + \sigma_{el})$$

Thus the energy dependence of f.s.i. effects gives information on the inelastic $\bar{\Lambda}\Lambda$ cross-section. Also the imaginary part of the $\bar{\Lambda}\Lambda$ scattering length could be extracted. Strong $\bar{\Lambda}\Lambda$ f.s.i. will create particularly strong cusp effects in channels with $\bar{K}K$ meson pairs if quark rearrangement is important in annihilation.

4.3 Resonances

With tunable $\bar{p}$ beams from LEAR one can easily look for narrow effects in the direct channel in $\bar{\Lambda}\Lambda$ production. If there are narrow baryonium states in $\bar{p}p$, then by analogy narrow baryonia could also appear in $\bar{\Lambda}\Lambda$. They could show up as spikes in the $\bar{p}p \to \bar{\Lambda}\Lambda$ cross section if they are above $2m_\Lambda$ mass and as spikes in typical $\bar{\Lambda}\Lambda$ annihilation channels e.g. $\bar{K}K$ if they are below $2m_\Lambda$.

Recently a narrow resonance ξ with a mass of 2220±15 MeV has been discovered with Mark III at SPEAR in radiative charmonium decays $J/\Psi \to \gamma + \xi$[17]. A peculiarity of ξ is its large decay branching ratio into K^+K^- and K_sK_s. The abundance of strange mesons in ξ decays has been taken as indication that ξ might be a glueball or a Higgs boson. It supports as well two other speculations : It could be a $\bar{\Lambda}\Lambda$ baryonium or a cusp effect as described above. The $\bar{\Lambda}\Lambda$ threshold is at 2231.2 MeV just within the mass range reported for the ξ. It is interesting to note that the detector of experiment PS185 is very well suited to measure $\bar{p}p \to \xi \to K_sK_s$. One can get angular distributions for K_s and determine width and mass of ξ with 0.5 MeV precision.

4.4 Scattering of polarized $\bar{\Lambda}$ and Λ

At high $\bar{p}$ momenta at LEAR (2 GeV/c) $\bar{\Lambda}$ and Λ are produced with momenta between 376 and 1624 MeV/c. The cross-section for $\bar{\Lambda}\Lambda$ production is about 100 μb. Already with a thin target this gives 6.10^4 $\bar{\Lambda}\Lambda$ pairs per day (with

10^6 $\bar{p}$/s) which decay into 4 charged decay particles. These events are full analyzable even if Λ or $\bar{\Lambda}$ undergo a secondary scattering.

A secondary scatterer can be installed close to the "production" target and one can use $\bar{\Lambda}$ and Λ mutually as tag for Λ and $\bar{\Lambda}$ scattering experiments. Energies, directions and polarizations before and after scattering can be determined both if Λ or $\bar{\Lambda}$ are scattered. We can then study e.g. with a secondary polyethylene target the elastic scattering of polarized Λ and $\bar{\Lambda}$ on protons and carbon. For 10^{-3} interaction length of the scatterer one gets $\simeq 50(\Lambda\uparrow p \to \Lambda\uparrow p)$ scattering events per day. Similarly it works for $\bar{\Sigma}^{\pm}$ and $\Sigma^{\pm}$.

Both the elementary and nuclear spin-orbit interaction can be determined by including the detection of the left-right asymmetry. In view of currently discussed models with different predictions of the spin-orbit interaction of hyperons in hypernuclei, particularly for the Σ case an improvement of the experimental value would be important.

For the understanding of the dynamics it is also of great value to be able to study the three channels related by crossing:

$$\bar{p}p \to \bar{\Lambda}\Lambda,\ \bar{\Lambda}p \to \bar{\Lambda}p,\ \Lambda p \to \Lambda p$$
$$\bar{p}p \to \bar{\Sigma}\Sigma,\ \bar{\Sigma}p \to \bar{\Sigma}p,\ \Sigma p \to \Sigma p$$

4.5 CP violation

CP violation effects in the partial hadronic decay ratio of $\bar{Y}$ and Y may occur. They are probably very small[18]. But an observation of CP violation in this field would be of extreme interest since it could allow to distinguish between different models for quark mixing in weak interaction. The experiment PS185 seems to be a necessary first step and already a good approach to check if such effects exist. A difference in the rates for $\{\bar{p}n\pi^+\pi^\circ\}$ and $\{\bar{n}p\pi^\circ\pi^-\}$ would be the signal for CP violation. The normalized difference

$$\Delta = \frac{\{\bar{p}n\pi^+\pi^\circ\} - \{\bar{n}p\pi^\circ\pi^-\}}{\{\bar{p}n\pi^+\pi^\circ\} + \{\bar{n}p\pi^\circ\pi^-\}}$$

can be determined to $\simeq 10^{-3}$ statistical precision within 5 to 10 days with 10^6 $\bar{p}$/s. The problem will be to get control of systematic errors. They occur mainly (besides "wrong" triggers) owing to asymmetries in the behaviour of $\bar{\Lambda}$ and Λ and their decay products. One can control the knowledge of systematic errors by performing the experiment at different $\bar{p}$ beam momenta. With some modifications a similar check of CP violation can be done for $\bar{p}p \to \bar{\Sigma}^+\Sigma^+$.

Another good test for CP violation effects should be a comparison of the decay asymmetries $\bar{\alpha}$ and α for $\bar{\Lambda}$ and Λ. Here $\bar{\alpha} + \alpha = 0$ has to be checked and one can reach a statistical precision of $\simeq 5.10^{-3}$ within 5 to 10 days with 10^6 $\bar{p}$/s in experiment PS185. (If $\bar{\alpha} + \alpha \neq 0$ this would simulate an apparent difference in $\bar{\Lambda}$ and Λ polarization).

5. CONCLUSION

It is not possible in a short paper to present all physics ideas around LEAR. Many other exciting subjects have been presented already at the Erice Workshop two years ago and earlier, for example ideas around the strong and weak CP violation effects in $\bar{K}K$ channels[19]. Despite the fact that LEAR will improve the experimental situation in the low energy range very substantially one has to face the fact that it is difficult to supply enough $\bar{p}$ beam time and $\bar{p}$ flux for these many interesting experiments. Therefore it is worthwhile to proceed with technical developments like ACOL[20] which increase the $\bar{p}$ flux, and with developments which allow to economize antiprotons.

Electron cooling for LEAR is under construction. It will further improve the efficiency of low energy scattering and stop experiments. Perfect cooling is needed for all projects which aim at further deceleration. Postdeceleration might be done with a radiofrequency quadrupole (RFQ) or with another small storage synchrotron (ELENA project). The "$\bar{p}$ economy" in high resolution transmission target experiments at LEAR can be improved to 100% efficient use once internal targets are operational. $\bar{p}p$ mini-collider operation and $\bar{p}H^-$ corotating beams may increase the efficiency in high resolution $\bar{p}p$ interaction studies at high energy and threshold respectively.

FOOTNOTES AND REFERENCES

1) The most complete collection of contributions to machine and physics aspects of LEAR can be found in the proceedings of the workshop on: Physics at LEAR with Low Energy Cooled Antiprotons, Erice, May 1982, Plenum Press, E. Majorana Int. Science series Nr. 17 Physical Sciences (U. Gastaldi & R. Klapisch Editors). We refer to these proceedings here as "Erice 82". LEAR is described in:
- P. Lefèvre "Erice 82", p.15
- W. Hardt, L. Hoffmann, P. Lefèvre, D. Möhl, G. Plass and D. Simon: Conceptual study of a facility for low-energy antiproton experiments, CERN/PS/DL/Note 79-1 (1979).

The idea to make something like LEAR at CERN was (to my knowledge) brought up and studied by D. Möhl in 1976.

2) R. Billinge: The CERN Antiproton source. These proceedings.

3) S. Van der Meer: CERN/PS/AA/78-6 (1978). R. Cappi and W. Hardt: Proc. of the XI International Conference on High Energy Accelerators, Geneva 1980. W. Hardt and R. Giannini "Erice 82",p. 49.

4) S. Van der Meer: Stochastic damping of betatron oscillations, CERN/ISR-PO/72-31 (1972). D. Möhl, G. Petrucci, L. Thorndahl and S. Van der Meer: Phys. Rep.,58,73(1980). D. Möhl, "Erice 82",p. 27.

5) D. Simon "Erice 82", p.55.

6) More information about the 17 LEAR experiments in:
- CERN Grey Book: "Experiments at CERN in 1983"
- Proposals (document numbers are given in Table 2)
- "Erice 82".

7) L. Simons, private communication and invited talk at Frühjahrstagung Kernphysik der DPG/ÖPG/SPG Innsbruck 1984

8) A. Angelopoulos et al. CERN-EP/84-47(1984) Submitted to Phys. lett.

9) L. Montanet, G.C. Rossi and G. Veneziano, Phys. Rep. 68 (1980) 149. See also contributions from the collaborations of PS173,182,183 in "Erice 82".

10) A. Clough et al., Evidence against the S-meson, Submitted to Phys. lett. and D. Bugg, private communication

11) V. Metag et al., Nucl. Instr. Meth. 114 (1974) 445.

12) N. DiGiacomo, private communication

13) D. Garreta et al., Phys. lett. 135 B (1984) 266

14) H.W. Atherton et al., Nucl. Phys. B 69 (1974)1. B. Jayet, Proc. 3rd Europ. Symposium on N-$\bar{N}$ Interactions, Stockholm 1976 (Pergamon Oxford 1977), p. 393. N. Kwak et al., Nuovo Cimento 23A (1974) 610. S.M. Jacobs et al., Phys. Rev. D17 (1978) 1187.

15) B. Andersson et al., Phys. lett. B 85 (1979) 417.

16) P.D. Barnes et al. "Erice 82" p. 843

17) K.F. Einsweiler et al. SLAC-P4B(1983)3202

18) L.L. Chau, Quark mixing in weak interactions. Phys. Rep. 95 Nr.1(1983)

19) E. Gabathuler and P. Pavlopoulos, "Erice 82", p. 747 and CERN/EP/82-118. J. Six "Erice 82", p. 739

20) Design study of an antiproton collector for the antiproton accumulator (ACOL). Yellow Report CERN/83-10 (1983). Editor E.J.N. Wilson.

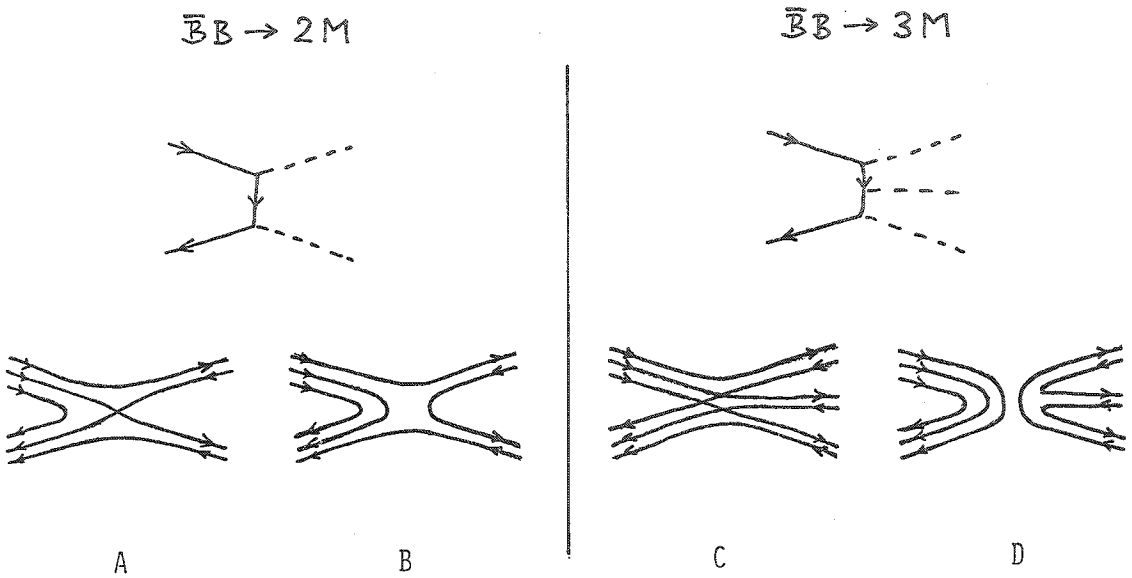

Fig. 1: Antibaryon-Baryon annihilation in terms of color singlets and more microscopically in terms of valence quark. Only few of the possible quark line diagrams are shown. In case b and d, quark pair creation is involved which is needed for $\bar{p}p$ annihilation into strange-antistrange mesons.

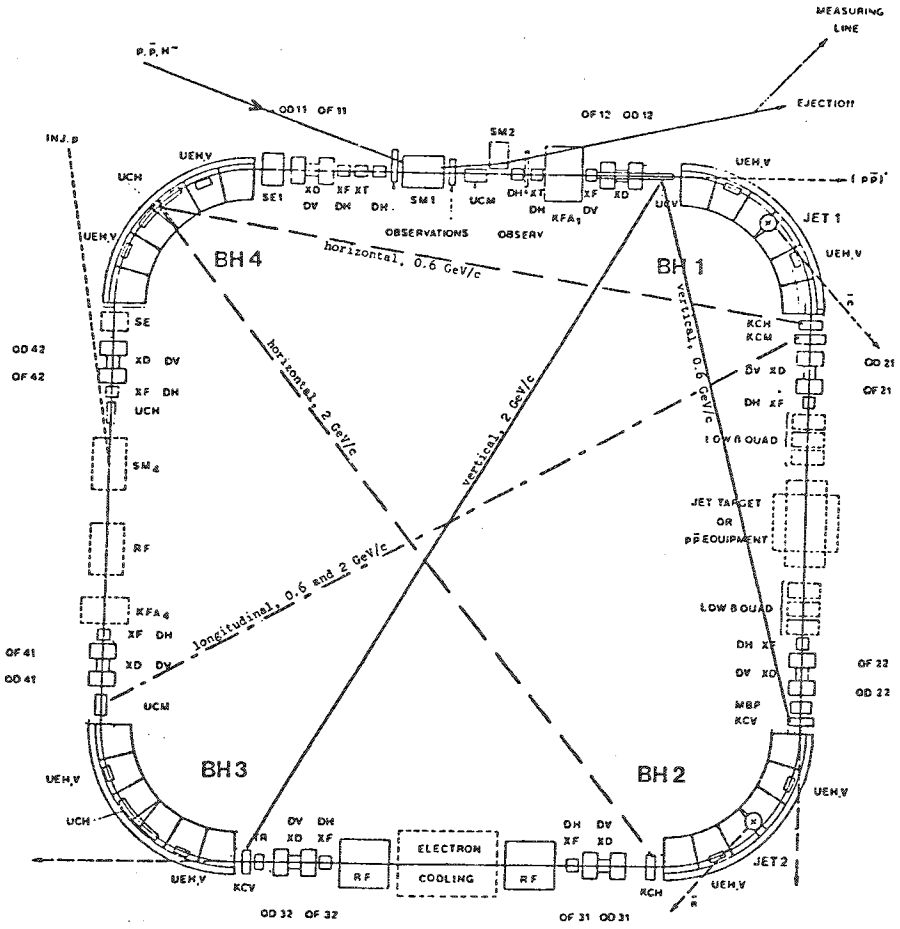

Fig. 2: General layout of the LEAR with magnet lattice and installations. The signal lines for the stochastic cooling systems are also shown.

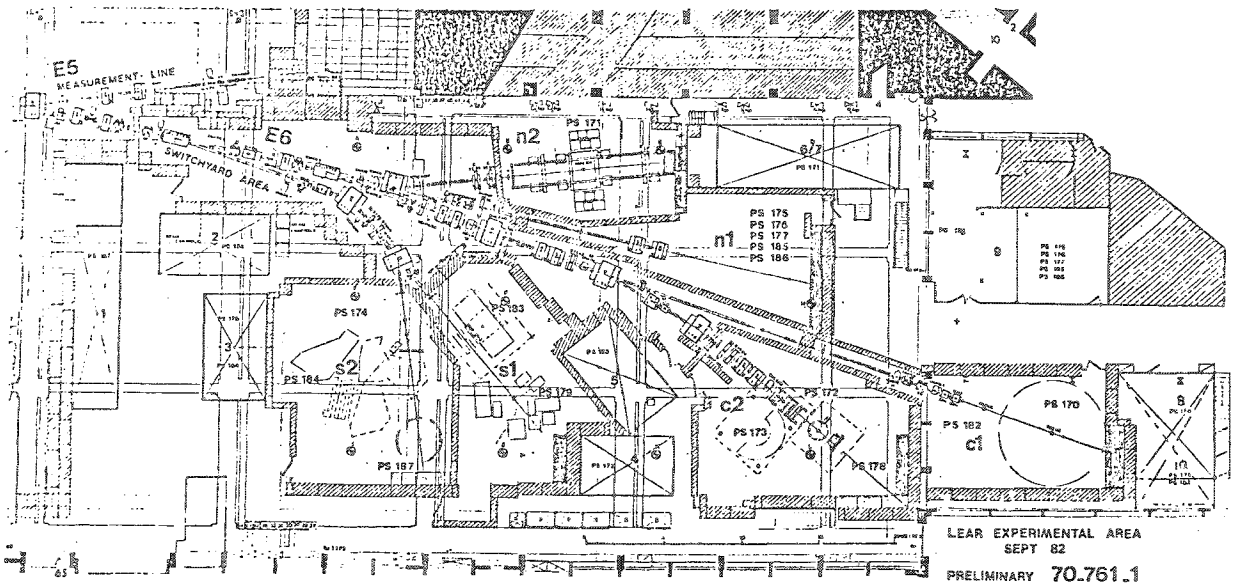

Fig. 3: LEAR experimental area.

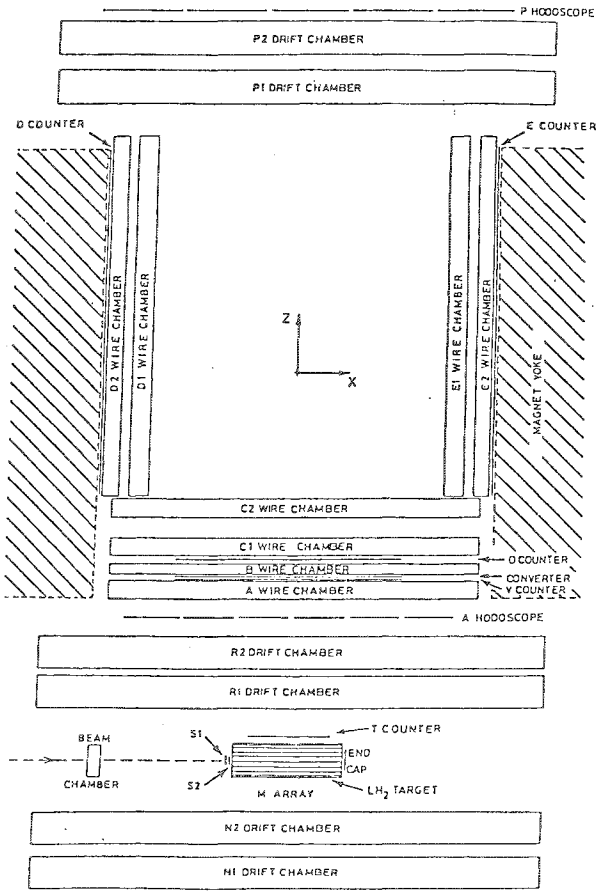

Fig. 4: Schematic layout of the PS183 apparatus at LEAR

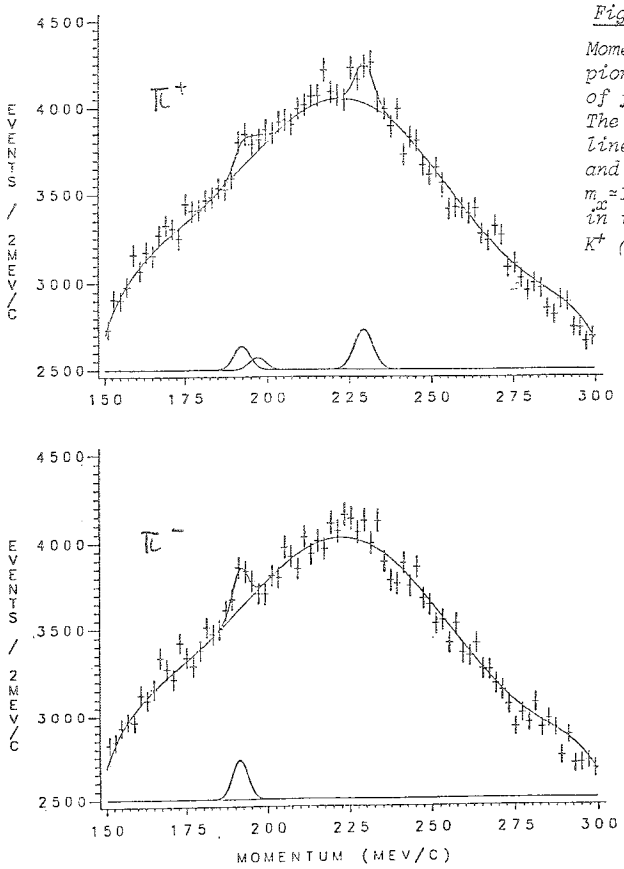

Fig. 5:

Momentum spectra of positive (top) and negative (bottom) pions measured in Expt. PS183. The curves show the results of fits to a smooth background plus Gaussian line shapes. The momentum scales are uncorrected for energy loss. The line at ∿190 MeV/c (∿200 MeV/c corrected) in the positive and negative spectrum corresponds to a missing mass m_x≃1620 MeV in $\bar{p}p \to \pi^{\pm} + X^{\mp}$. The two additional lines in the positive spectrum correspond to decays of stopped K^+ ($K^+ \to \mu^+\nu$ and $K^+ \to \pi^+\pi^0$).

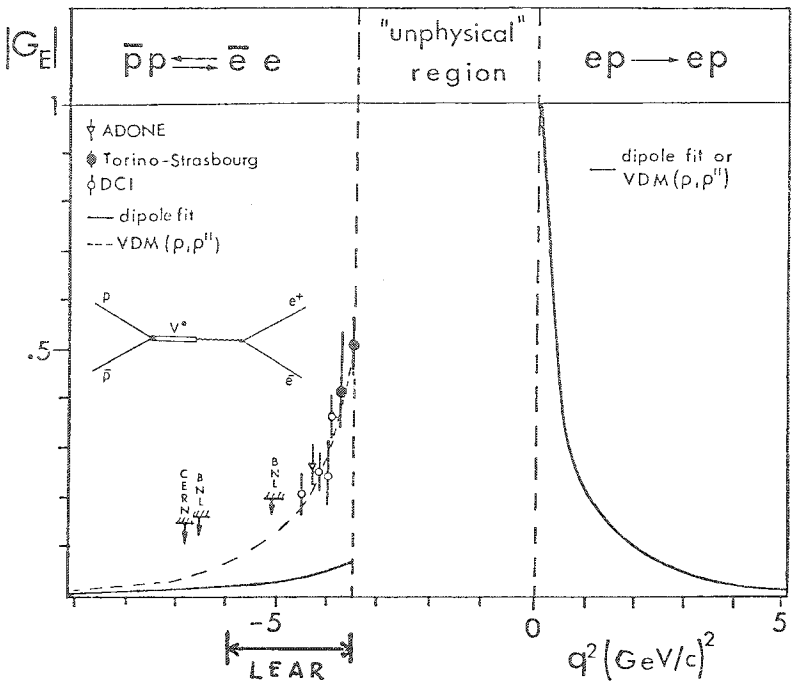

Fig. 6:

Experimental data on the electro-magnetic form factor of the proton. The time-like region will be scanned in Expt. PS170 at LEAR.

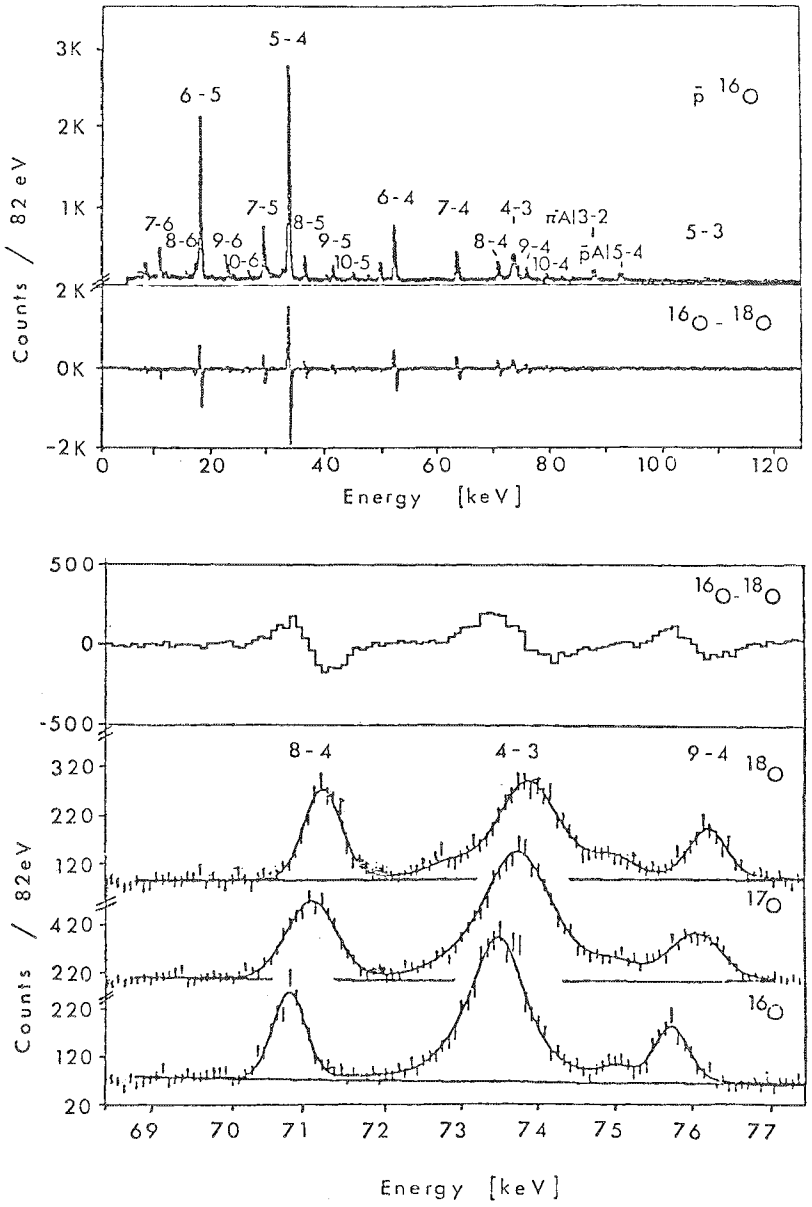

Fig. 7:

X ray spectrum from antiprotonic oxygen measured in Expt. PS176 (top) and comparison of a detail for 3 oxygen isotopes (bottom). The energy shifts for the isotopes result from a shift in reduced masses. The reduction of the strength of the 4→3 transition with increasing atomic weight corresponds to increasing hadronic absorption.

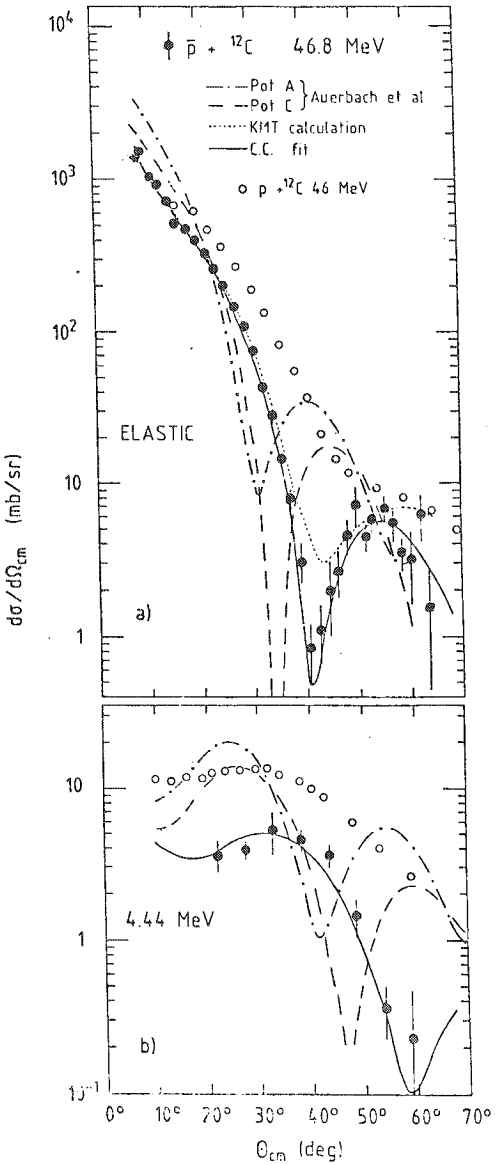

Fig. 8

Differential cross section for $\bar{p}$ ^{12}C elastic (a) and inelastic scattering to the 4.44 MeV state (b) measured in expt. PS184. Cross sections for p are shown for comparison. Curves are results of model calculations. For details see ref. 13.

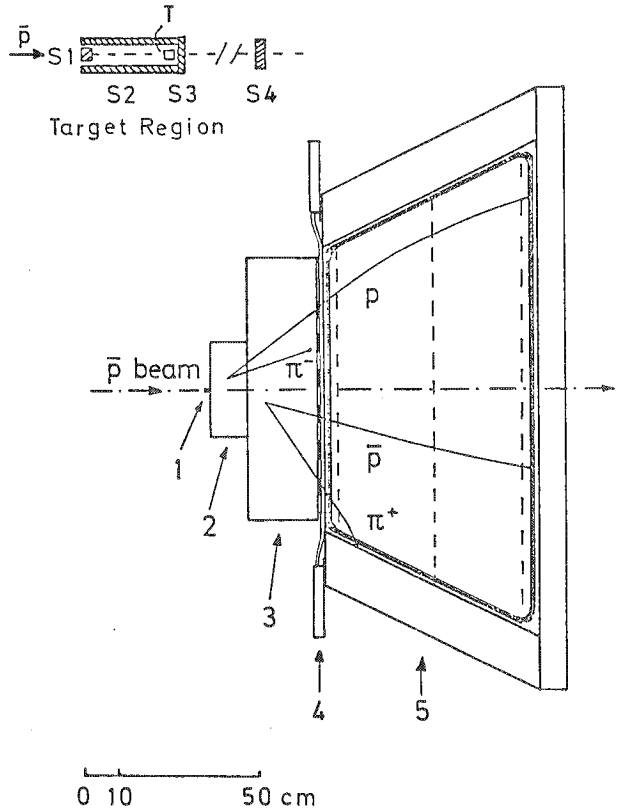

Experimental set-up with 1: target, 2: proportional wire chambers, 3: drift chambers, 4: hodoscope, 5: baryon number identifier. An example of a "perfect track event" is indicated.

The target region is given in a magnified view with T=target, S1-4: scintillation counters.

Fig. 9: Detector system for Expt. PS185 for a study of $\bar{p}p \to \bar{Y}Y$

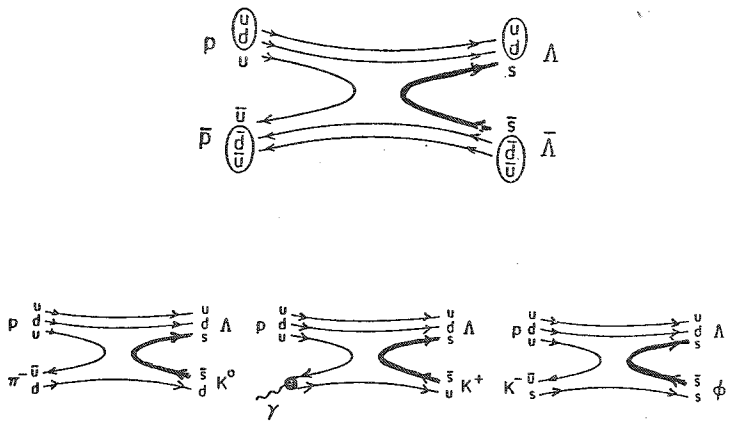

Fig. 10: Quark line diagram for the reaction $\bar{p}p \to \bar{\Lambda}\Lambda$ and some other reactions which also have a $s\bar{s}$ quark pair creation.

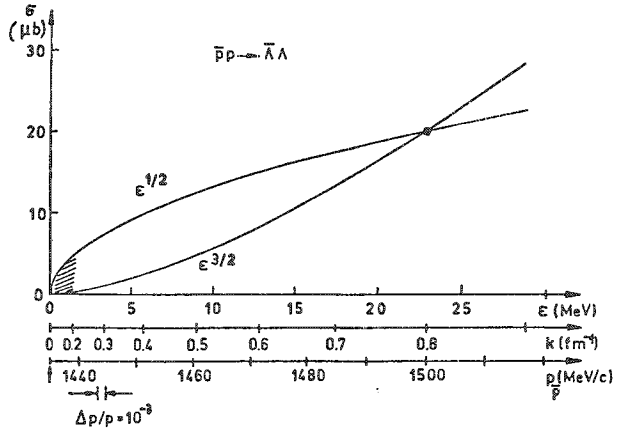

Fig. 11

Excitation function for the reaction $\bar{p}p \to \bar{\Lambda}\Lambda$ for pure S-wave ($\sigma \propto \varepsilon^{1/2}$) and P-wave ($\sigma \propto \varepsilon^{3/2}$), where the excess energy $\varepsilon = \sqrt{s} - 2m_\Lambda$. The hatched area indicates the region close to threshold where a final state interaction may be expected.

Upgrading of CERN $p\bar{p}$ Collider and Experiments

THE SPS p-pBAR COLLIDER, PRESENT PERFORMANCE AND FUTURE PROSPECTS

B. de Raad
CERN, Geneva, Switzerland.

1. INTRODUCTION

The SPS p-pbar collider has now operated for a total of 5 months and has delivered an integrated luminosity of 180 nb^{-1} to each of the two experiments UA1 and UA2. The operation of the accelerator complex is well mastered and the performances are steadily improving.

The peak luminosity reached in 1983 was $1.6 \times 10^{29} cm^{-2} s^{-1}$, with a luminosity life time of about 16 h, which is compatible with one refill per day, a typical production rate being 4 nb^{-1} per day,

The present peak luminosity is a factor 6 below the original design figure of $10^{30} cm^{-2} s^{-1}$ for the CERN p-pbar project, essentially since the antiproton collection rate is lower by about the same factor. The CERN p-pbar improvement program, which is centered around the construction of the antiproton collector ACOL, is aimed at increasing the production rate of the SPS collider up to 50 nb^{-1} per day.

This paper describes the present performance of the SPS and the developments which are in preparation to deal with higher antiproton intensities.

2. OPERATIONAL RESULTS

2.1 Review of past collider runs

The first proton-antiproton collisions at a center-of-mass energy of 540 GeV were observed in the SPS on the 10th July, 1981. The first physics run took place at the end of 1981 and produced a total integrated luminosity of

0.2 nb^{-1}. During the second run, from October to December 1982, the machine operated with 3 bunches of protons colliding against 3 bunches of antiprotons with beta values at both experiments of β^*_H= 2m, β^*_V = 1m. The proton bunch intensity reached its design value of 10^{11}p, whereas the antiproton bunch intensity was limited to around 1.3 × 10^{10} antiprotons. The peak luminosity reached 5.3 × $10^{28}cm^{-2}s^{-1}$ and the total integrated luminosity was 28 nb^{-1}.

From April to June 1983, the SPS operated in essentially the same configuration but the longer duration of this third run, an increased proton intensity, further reduced β^*'s, and better operational skill for all machines of the proton-antiproton complex resulted in a peak luminosity of 1.6 × $10^{29}cm^{-2}s^{-1}$ and an integrated luminosity delivered to each of the two experiments of 153 nb^{-1}.

2.2 Operation

Starting up a cold machine may take 24 hours, but a careful readjustment during routine operation is usually carried out in 4 to 6 hours. This happens two to three times a week, if possible during working hours when specialists are more easily available. During week-ends, one tries to profit from the better overall stability to have longer runs and faster refills. Filling times of down to one hour have been achieved.

Operational techniques have been developed to cope with the machine "mode" changes and with the requirement of reliable data-taking at injection and during the store. The first of these problems - for instance bringing the machine out of store and preparing for proton re-injection from the SPS back into the CPS to check the transfer line - was tackled using a multiprocessor job control structure[1] called the "sequencer". Using this, the execution of a list of up to 60 programs can be defined off-line, each such list is called a sequence. The most complex of these sequences controls the countdown to p-pbar injection. This switches some active equipment but mainly ensures that data-reading equipment is armed and that all beam measurements are saved for reference. Software structures have also been developed to gather and archive data during storage.

The success of the run owed much to the excellent reliability of the AA which on one occasion kept its beam for a record 30 days. The AA-SPS transfer

efficiency reached 80%, with 10% lost at extraction from the CPS and 10% at low energy in the SPS.

2.3 Performances for physics

Figure 1 shows the integrated luminosity for the 1983 collider run. After a laborious start-up characterized by low transfer efficiency and hectic overall conditions, a regular operation could be established producing an average of 2 nb^{-1} per day under conditions similar to those at the end of 1982. Through a number of improvements the performance increased steadily until after a short technical stop the production reached a record of 6 nb^{-1} per day. Towards the end, technical failures in the AA, CPS and SPS, and heavy daily storms reduced the production rate.

A short run was made in a high beta configuration ($\beta^*_H = \beta^*_V = 100$ m) to allow data-taking on elastic scattering at very small angles ($\geq$ 0.4 mrad).

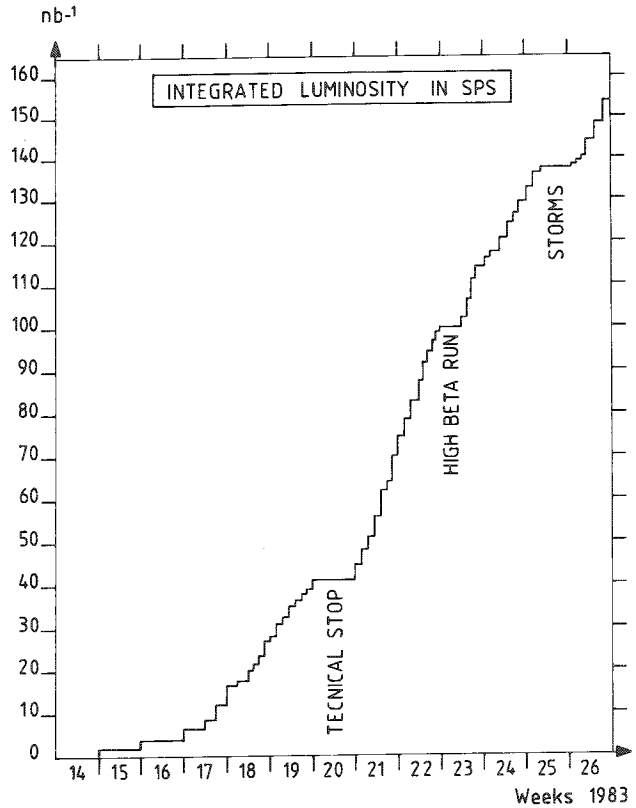

Fig 1.

Integrated SPS luminosity in the 1983 collider run.

Table 1 gives a comparison of the best results obtained in the collider runs of 1982 and 1983. The discussion of the performance limitations given below will be based on the 1983 column of this Table.

Table I.

Best Collider Performance in 1982 and 1983

	1982	1983
AA stacking rate (10^9pbar h^{-1})	5.5	6.6
Transfer efficiency	70%	75%
p intensity per bunch (10^{11})	1	1.4
pbar intensity per bunch (10^{11})	.13	.15
number of p and pbar bunches	3	3
Normalized emittances		
($\pi.10^{-6}$ rad.m) p	20	18
pbar	15	14
Beam-beam parameter ξ	0.0025	0.004
β^*_H (m), β^*_V (m)	2 x 1	1.3 x.065
Luminosity at start of coast ($10^{29}cm^{-2}s^{-1}$)	0.53	1.6
Luminosity lifetime (h)	18	16
Integrated luminosity (nb^{-1}) per day	2.2	6.2

3. BEAM PARAMETERS AND PERFORMANCE LIMITATIONS

3.1 Antiproton intensity

The maximum production rate of the AA is at present 6.6 x 10^9 pbar/hour and therefore a daily fill of the collider could ideally consume up to 1.6 x 10^{11} pbar. Unfortunately the AA is not always functioning at its optimum while breakdowns in the CPS, setting-up of the SPS with protons and the need to serve other users of the CPS decrease the number of protons available for pbar production. Furthermore, about 50% of the stores end prematurely by a technical fault in the SPS or too large a variation of the mains voltage, which reduces the available AA stacking time. As a consequence, the maximum intensity extracted from the AA in one fill has been 0.8 x 10^{11} pbar, with routine values around 0.6 x 10^{11} leading to 3 bunches of 1.5 x 10^{10} each stored in the SPS.

3.2 Proton intensity and emittances

The proton intensity is limited[2] to 1.4 x 10^{11} p/bunch by longitudinal instabilities during acceleration and by the Laslett space charge detuning at the injection energy of 26 GeV. The normalized transverse emit-

tance $\varepsilon^* = \varepsilon\beta\gamma$ of these intense proton bunches is usually about $18\pi \times 10^{-6}$ rad.m. (Emittances are defined at 2σ, i.e. $\varepsilon = 4\sigma^2/\text{beta}$).

3.3 Antiproton lifetime at 270 GeV

The SPS collider is operating in the weak-strong régime[3], in which the antiprotons are strongly perturbed by the crossings with the intense proton bunches while the protons are practically not affected by the weak antiproton beam.

The tune diagram at 270 GeV is shown in Fig. 2. All protons have approximately the same working point Q_p. The average tune shift experienced by a small amplitude antiproton at each crossing with a proton bunch is equal to the beam-beam parameter ξ, resulting in a total incoherent tune shift per turn of $\Delta Q = 6 \times 0.004 = 0.024$ in the present operation with 3 proton against 3 antiproton bunches. The small amplitude antiprotons therefore have the working point Qpbar.

Large amplitude antiprotons experience a smaller Q-shift because of the reduced particle density in the transverse tails of the proton bunches. The antiproton beam therefore occupies the cigar-shaped region shown in Fig. 2 extending from Q_p to Q_{pbar}, straddling the resonances of order 13 and 16 for the large amplitude antiprotons and some resonance lines of order 10 for the small amplitude antiprotons.

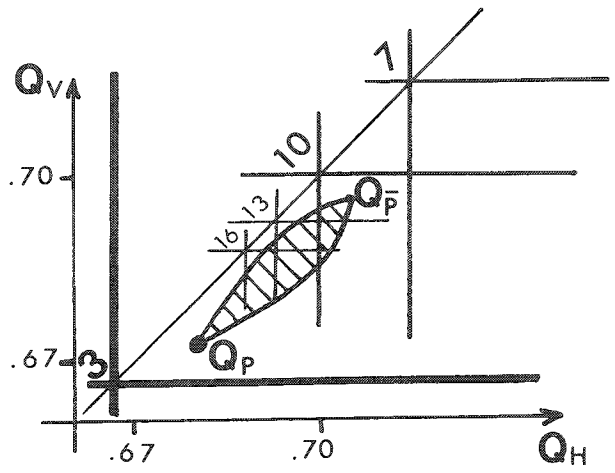

Fig. 2

The tune diagram at 270 GeV.

The rate of amplitude blowup of an antiproton caused by the repeated kicks in the strongly nonlinear field of the proton bunches is a rapidly increasing function of the antiproton amplitude. In the situation of Fig. 2 where only the small amplitude antiprotons touch the 10th order resonance, the beam-beam limited lifetime of the antiprotons is about 50 hrs. whereas an increase of 0.01 of the Q-value of the SPS decreases this lifetime to about 15h.

For this reason a large effort has been made to improve the stability of the machine parameters, which used to be a limiting factor for the antiproton lifetime. In particular the stability of the tunes which is essential for a good lifetime has been improved by a new current regulation system for the main magnet power supplies. Short-term variations, measured from the width of Schottky lines[4], are smaller than $\Delta Q = 3 \times 10^{-4}$. Long term drifts, possibly due to thermal effects, of a few times 10^{-3}, are corrected by programming the magnet currents.

The antiproton loss caused by the noise of the RF system corresponds to a lifetime of about 200h, so that the actual lifetime of the antiprotons in the SPS is 40 h (average value over a 20h. coast).

3.4 Antiproton emittances

The need for a good antiproton lifetime places a high premium on a small antiproton emittance. The design values of the cooled AA beam emittances are $\varepsilon^*_V = 3.7\pi \times 10^{-6}$, $\varepsilon^*_H = 5.2\pi \times 10^{-6}$ rad.m and the best performances achieved so far closely approach these values.

Great care must be taken in setting up the transfers between the machines to avoid emittance dilution due to injection errors. The CPS/SPS transfer is particularly critical because it must accept a beam of 0.6 % momentum spread. Early in the 1983 run the dispersion vector between the two machines was carefully matched. As a result the beam can now be transmitted in good conditions with a blow-up factor of the order of two, which gives in storage an emittance of $12\ \pi \times 10^{-6}$ rad.m. Unfortunately, deficiencies of the AA cooling system or badly adjusted transfers can result in a stored emittance as high as $18\ \pi \times 10^{-6}$ rad.m leading to a reduced lifetime of the antiproton bunches. This is illustrated in Fig. 3 where the loss rate of

three antiproton bunches of the same intensity but with different initial emittances are compared. Antiprotons whose amplitudes exceed the average dimension of the strong proton beam are rapidly peeled off, after which the decay rate approaches the same value for all three bunches.

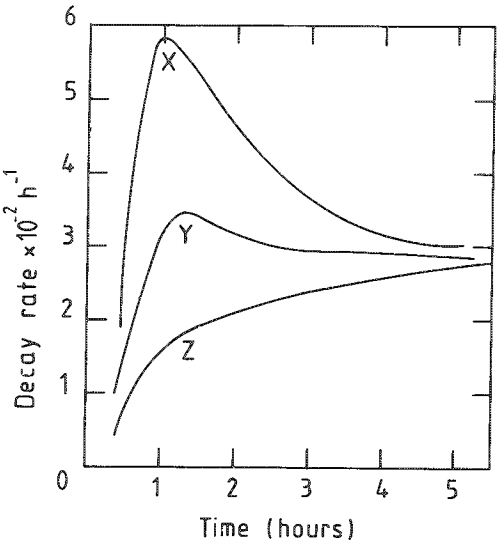

Fig. 3

Decay rate of pbar bunches with different emittances.
Emittance of the antiproton bunches $\varepsilon^*_x = 17\pi$,
$\varepsilon^*_y = 15\pi$, $\varepsilon^*_z = 12\pi$.
Emittance of protons 17π. Beam-beam parameter $\xi = 0.004$.

3.5 Proton lifetime at 270 GeV

The nitrogen equivalent gas pressure for multiple Coulomb scattering of 1.2×10^{-10} mbar in the SPS can only account for an emittance growth of the protons which is an order of magnitude lower than the measured value. In addition, the longitudinal emittance of the dense proton bunches grows considerably faster than that of the weak antiproton bunches.

All these features were pointing towards intra-beam scattering, i.e. multiple Coulomb scattering between protons in the same bunch. Careful measurements of longitudinal and transverse growth rates under different conditions of intensity and emittances were found in good agreement with the theory[5].

Longitudinally the high intensity bunches blow up until the tail of their distribution reaches the bucket separatrix. Thereafter protons start to leak out and an equilibrium distribution is established. Because of the dispersion in the machine and the coupling of horizontal and vertical betatron oscillations, intrabeam scattering also causes a growth of the transverse emittances. For the parameters of Table 1, the resulting proton lifetime is 60 h, while the e-folding time of the emittance growth is 50h. (average values over a 20h coast).

Combined with an antiproton lifetime of 40h. this leads to a luminosity lifetime of 16h.

3.6 Space charge effects at injection.

The tune spread of the antiprotons caused by the beam-beam effect at the injection energy of 26 GeV is the same as at 270 GeV, since the effects of the lower particle energy and the larger emittance at low energy cancel. However, the incoherent Laslett space charge detuning of the intense proton bunches, which is negligible at 270 GeV, is proportional to $1/\gamma^2$ and at 26 GeV amounts to $\Delta Q \approx -0.003$ for small amplitude protons. Similar to the case of the beam-beam effect, the large amplitude protons have a smaller ΔQ. By choosing $Q_H = 26.70$ and $Q_V = 26.71$ it is just possible to keep the protons above the third order resonance $Q_V = 26^{3}/_{3}$ and the antiprotons below the fourth order resonance $Q_V = 27^{3}/_{4}$. The injection of 3p + 3pbar bunches requires a "coast" at 26 GeV of 14.4 s and this duration is short enough for losses by resonances above the fourth order to be unimportant.

3.7 The low beta insertions

The design configuration[6] with $\beta^*_H = 2m$, $\beta^*_V = 1m$ in both experiments which had been commissioned in 1982 was used up to the middle of the 1983 run. After the technical stop it was pushed to $\beta^*_H = 1.3m$. $\beta^*_V = .65$ m with the expected gain in luminosity of a factor 1.5, which is apparent in Fig.1.

In an experiment at the end of the period the betas were further reduced to $\beta^*_H = 1m$, $\beta^*_V = 0.5m$. Even in this situation the chromatic aberrations could still be corrected and it is planned to use this low beta configuration during the 1984 run.

4. FUTURE DEVELOPMENTS

4.1 Collider operation at 310 GeV

During the winter shutdown at the beginning of 1984 the main power supplies have been upgraded and pumps have been added to the water cooling system of the magnets to permit collider operation at 310 GeV in the autumn of 1984. The gain in luminosity, because of the smaller beam cross-section at the higher energy, is about 15% but since the cross-sections increase rapidly with increasing energy, the production rates for W's and Z_o will be enhanced by a factor 1.5 and those for high p_T jets by a factor 2.

4.2 The low beta insertions

The existing low beta insertions were designed for $\beta^*_H \times \beta^*_V$ = 2m × 1m at 270 GeV and they will now be operated with $\beta^*_H \times \beta^*_V$ = 1m × 0.5 m at 310 GeV. This corresponds to the maximum strength of the existing low beta quadrupoles. Furthermore, the resulting large chromatic aberration, which is inversely proportional to β^* for a given quadrupole layout, is at the limit of what can be compensated with the 4 existing families of chromaticity sextupoles of the SPS.

To decrease the β^*-values further it is necessary to use stronger, smaller aperture low beta quadrupoles which are placed closer to the crossing point. Possible layouts are being studied and an increase in luminosity of about 20% seems possible.

4.3 Increased antiproton intensity

The order of magnitude increase of the available number of antiprotons resulting from the construction of ACOL will, of course, mainly be used to increase the antiproton intensity and therefore the peak luminosity, in the SPS. In addition, it will also give the possibility of more frequent refills of the SPS. This will increase the ratio of average to peak luminosity during a coast and will also improve the overall efficiency of the collider operation by allowing a more rapid refill after a technical fault.

At present the collider is optimized for a weak-strong régime and it is not clear whether the machine would work with the same beam-beam parameter ξ

in a strong-strong régime. Nevertheless, the present conditions, with the well-proven 3 bunch mode should remain valid up to about 6×10^{10} pbar/bunch, a factor 4 about the present pbar intensity.

4.4 Beam separation

To increase the luminosity further will require operation with 6 bunches in each beam. With the same proton intensity per bunch and therefore the same beam-beam parameter $\xi = 0.004$, the incoherent Q-shift per turn of the antiprotons then becomes $\Delta Q = 12 \times 0.004 = 0.048$ and inspection of Fig. 2 shows that this would place the antiproton beam right across the 10th order resonances. In an experiment where one pbar bunch was stored together with 6 dense p bunches, the pbar lifetime was reduced by a factor 4.

Therefore a scheme has been proposed[7] to separate beams of up to 6 bunches everywhere except in the detectors UA1 and UA2 and at one point in between. This reduces the total number of bunch crossings per turn to 3, i.e. even a factor 2 lower than in the present 3 bunch mode of operation. An accurate compensation of the deflections will be needed to make the beams collide head-on in the useful intersections. An experiment has shown that a difference in orbit of 0.2 rms beam size already halves the antiproton lifetime because of the appearance of all the nonlinear terms of order $(2n + 1)$ in the beam-beam force.

During the last winter shutdown, 4 existing separator tanks have been installed in the SPS to enable tests on beam separation to be made during the autumn 1984 run.

4.5 A 100 MHz RF system

The existing RF system of the SPS operates at a frequency of 200 MHz. A 100 MHz RF system[8] with a moderate voltage of 2MV would be adequate to hold the bunches at 310 GeV but since the bunch length would be twice as large, the intrabeam scattering of the protons would be reduced or alternatively a somewhat larger proton intensity would be tolerated. (The beam-beam effect remains unchanged since it is independent of the bunch length).

Also at injection the 100 MHz system has advantages. The longer proton bunches have a smaller incoherent Laslett space charge detuning, thus leaving more space in the tune diagram for the beam-beam induced Q-spread of the antiprotons. Alternatively, this could be used to increase the intensity of the injected proton bunches.

As the antiproton intensity in the AA increases, the longitudinal emittance of the extracted antiproton bunches may also increase. Also in this situation a 100 MHz system in the SPS has strong advantages since it permits to capture antiproton bunches which are twice as long, whereas the CPS extraction channel does not allow to increase the momentum spread above the present value $\Delta p/p = \pm 3 \times 10^{-3}$.

The 2MV of the proposed 100 MHz RF system are not sufficient for acceleration. The solution is, to adiabatically convert each single 100 MHz bunch into two bunches at 200 MHz, to accelerate with the 200 MHz system up to 310 GeV and then to recombine the two bunches again into a single one.

The small values of beta at the crossing point are associated with a strong beam divergence. Therefore the longer bunches of the 100 MHz system would reduce the luminosity for the UA1 detector by 7% while for the UA2 detector, which has a limited acceptance, this reduction becomes 18%.

In the case of stochastic cooling of the stored beams, which is being studied for the SPS[9], the cooling times are reduced by a factor two by doubling the bunch length and in the case of a 100 MHz RF system, the cooling times could just be made equal to the presently observed luminosity lifetime of 16h.

In general, a 100 MHz RF system provides a great flexibility to adapt the proton and antiproton bunches to the best operating conditions for maximum luminosity.

5. CONCLUSION

The SPS collider has now become an operational machine and its present luminosity has already led to very important physics results.

Its planned improvements should permit to transform the increased antiproton intensity resulting from the construction of ACOL into a tenfold increase in luminosity.

References

1. C. Saltmarsh, A multiprocessor, multi-task controls structure for the CERN SPS.
Conference on Computing in Accelerator Design and Operation, Berlin, 20-23 Sept. 1983.

2. J. Gareyte, The SPS p-pbar Collider, CERN SPS/84-3 (DI-MST), Lecture given at the CERN Accelerator School Course on Antiprotons for Colliding Beam Facilities, CERN, 11 - 21 October, 1983.

3. L.R. Evans, The Beam-Beam Interaction, CERN SPS/83-38 (DI-MST), Lectures given at the CERN Accelerator School Course on Antiprotons for Colliding Beam Facilities, CERN, 11 - 21 October, 1983.

4. T. Linnecar and W. Scandale, Continuous tune measurements using the Schottky detector, US Particle Accelerator Conference, Santa Fe, 21 - 23 March, 1983, IEEE Trans. Nucl. Sci. Vol. NS-30. No. 4 p. 2185-2187.

5. L.R. Evans, Intrabeam Scattering in the SPS Antiproton Collider, 12th Int. Conf. on High-Energy Proton-Accelerators, Fermilab, Batavia, Ill. U.S.A., 11 - 16 August, 1983.

6. P.E. Faugeras, A. Faugier, A. Hiliare and A. Warman, The Low Beta Insertions of the SPS Proton-Antiproton Collider, 12th Int. Conf. on High-Energy Accelerators, Fermilab, Batavia, Ill., U.S.A., 11 - 16 August, 1983.

7. L. Evans and A. Faugier, Beam-beam separation using electrostatic deflectors, CERN SPS/DI-MST/Note 83-1.

8. D. Boussard, A 100 MHz RF system in the SPS,
CERN SPS/ARF/Note/DB/gw/83-83.

9 D. Boussard, S. Chattopadhyay, G. Dôme and T. Linnecar, Feasibility Study of Stochastic Cooling of Bunches in the SPS. Lecture given at the CERN Accelerator School Course on Antiprotons for Colliding Beam Facilities, CERN, 11 - 21 October, 1983.

CERN'S $p\bar{p}$ SOURCE

R. Billinge
CERN, Geneva, Switzerland

1 INTRODUCTION

The intense bunches of protons and antiprotons needed for the SPS Collider are provided by the PS Complex as one of its many modes of operation. The PS Complex which began operation twenty-five years ago (November, 1959) consisted of a 200 m diameter proton synchrotron, fed by a 50 MeV Alvarez Linac (fig. 1). The same synchrotron is now the hub of a complex of ten interconnected machines (fig. 2), six of which are in operation and a further four under construction. To date in addition to beams of protons at a whole range of energies, intensities and spill times, antiprotons, H^- ions, deuterons and alpha particles have been provided and the list is shortly to be extended to include Oxygen ions, electrons and positrons. In what follows we shall describe how antiprotons are produced, accumulated, compacted by stochastic cooling then accelerated and shaped for transfer to the SPS.

2 OVERALL SCHEME

2.1 Antiproton Production

The antiprotons are produced by an intense beam (up to 1.5×10^{13} every 2.4 seconds) of protons at 26 GeV/c, which is focused onto a 3 mm diameter copper target. In order to match the circumference of the Antiproton Accumulator (AA) the production beam must occupy only a quarter of the PS machine circumference. To achieve this the four rings of the Booster Synchrotron are first filled by a 150 mA proton beam from Linac II. Following acceleration to 800 MeV the beams are extracted from two rings at a time and combined vertically for injection into the PS. This gives two sets of five double r.f. bunches of protons to be accelerated on harmonic number h=20. Once accelerated to 26 GeV, the r.f. system is divided in two operating on harmonic numbers 19 and 21 such that the two sets of five bunches approach each other azimuthally. When they ovelap, thus occupying 1/4th of the PS circumference, they are ejected and transported to the production target where pulsed quadrupoles focus the beam to a spot size of about 2 mm diameter.

2.2 Antiproton Collection

Antiprotons are collected around a momentum of 3.5 GeV/c, corresponding to the peak of the production spectrum. A pulsed magnetic focusing horn just after the target is used to capture a momentum bite of 1.5% at angles up to 50 mrad. This is then transported and matched into the AA machine (fig. 3). This machine is designed to accommodate widely separated orbits for a total momentum range of 6%.

The newly injected antiprotons occupy a momentum spread of 1.5% and transverse emittances of 100 π mm.mrads. In some of the locations where they are widely separated from previously stacked antiprotons, they are separated from the stack by moveable ferrite shutters, which form the inner side of single turn transformer-like structures. These constitute the stochastic Pre-Cooling System which detects and reduces the variations in revolution frequency such that the momentum spread is reduced from 1.5% to 0.2% in about 2 seconds. After this, the shutters are opened, and a conventional radio frequency system is used to capture the particles and move them inwards (deceleration) where they are deposited in the low density "tail" of the antiproton stack. From there, they are progressively cooled in transverse phase space and compacted in momentum towards the dense stack core. Each 2.4 seconds, a new pulse of a few million antiprotons is injected, pre-cooled and stacked, so that after about two days the dense stack reaches a few $\times 10^{11}$.

A dense bunch of antiprotons is then captured from the stack by the r.f. system, accelerated out to the injection/ejection orbit and extracted from the machine. It is transported to the PS and injected counter-clockwise, then accelerated from the accumulation momentum of 3.5 GeV/c to 26 GeV/c. At this stage, the bunch of antiprotons has a length of a few hundred nanoseconds - much too long to fit into a single 200 MHz bunch in the SPS. To achieve the latter, the PS r.f. system makes a phase jump to the unstable fixed point so that the bunch stretches out (fig. 4). Then the phase is returned to the stable point and with maximum available voltage, the long, thin bunch rotates until it occupies a momentum spread of $\pm$ 0.4% and a bunch length of 3 ns.

It is then transferred to the SPS and captured into a single bunch of the 200 MHz accelerating system. This process is repeated three times with antiprotons, having been preceded by three bunches of protons, similarly shortened, and the counter-rotating bunches of protons and antiprotons are then accelerated together up to the SPS collision energy of about 300 GeV.

3 PERFORMANCE AND FUTURE UPGRADING

The original design aims of the Antiproton Accumulator[1] corresponded to collecting 2.5×10^7 $\bar{p}$'s in a momentum range of 1.5% and transverse emittances of 100 π mm mrads, each 10^{13} protons on target and each 2.4 seconds. This, after 20 hours of stacking and cooling, was to give 6×10^{11} $\bar{p}$'s in 0.3% momentum and transverse emittances of 1.4 π x 1 π mm mrads. This corresponds to an increase in phase-space density given by

$$\frac{6 \times 10^{11}}{2.5 \times 10^{7}} \times \frac{1.5\%}{0.3\%} \times \frac{100\ \pi \times 100\ \pi}{1.4\ \pi \times 1\ \pi} = 8.6 \times 10^{8}$$

Subsequently, it was found that the assumed yield was optimistic by more than a factor 2 and the achieved cooling results in a density increase

$$\frac{3 \times 10^{11}}{1 \times 10^{7}} \times \frac{1.5\%}{0.3\%} \times \frac{90\ \pi \times 90\ \pi}{2\ \pi \times 1.5\ \pi} = 4.1 \times 10^{8}$$

after about 40 hours of accumulation.

It is now proposed[2] to increase the collection rate by about a factor 10. This improvement project has three main components: targetting, a collector ring (ACOL) and upgrading of the AA stochastic cooling systems to cope with the higher flux.

In the first component, it is intended to use powerful Lithium Lens focusing devices around a target through which a high current is pulsed. In this way it is hoped to capture a 6% momentum range and transverse emittances of 200 π mm mrads.

This beam will then be captured in the new ring being built around the AA (fig. 5) by a special r.f. system which will first rotate the short bunches in phase space, thus exchanging bunch length for momentum spread, and then adiabatically debunch the beam. In this way the momentum spread is reduced to 1.5%. Next, transverse cooling will be used to reduce the emittances from 200 π to about 10 π mm mrads and then the momentum is cooled from 1.5% to 0.2%.

This pre-cooled beam of about 10^8 $\bar{p}$'s is then transferred to the Accumulator, where cooling systems working up to 4 GHz will permit the accumulation of over 10^{12} antiprotons per day. With the stack densities already achieved, this would constitute an adequate $\bar{p}$ source to reach a luminosity of 10^{31} at 10 TeV.

REFERENCES

1. Design Study of a Proton-Antiproton Colliding Beam Facility. CERN/PS/AA 78-3.
2. Design Study of an Antiproton Collector for the Antiproton Accumulator (ACOL). CERN 83-10.

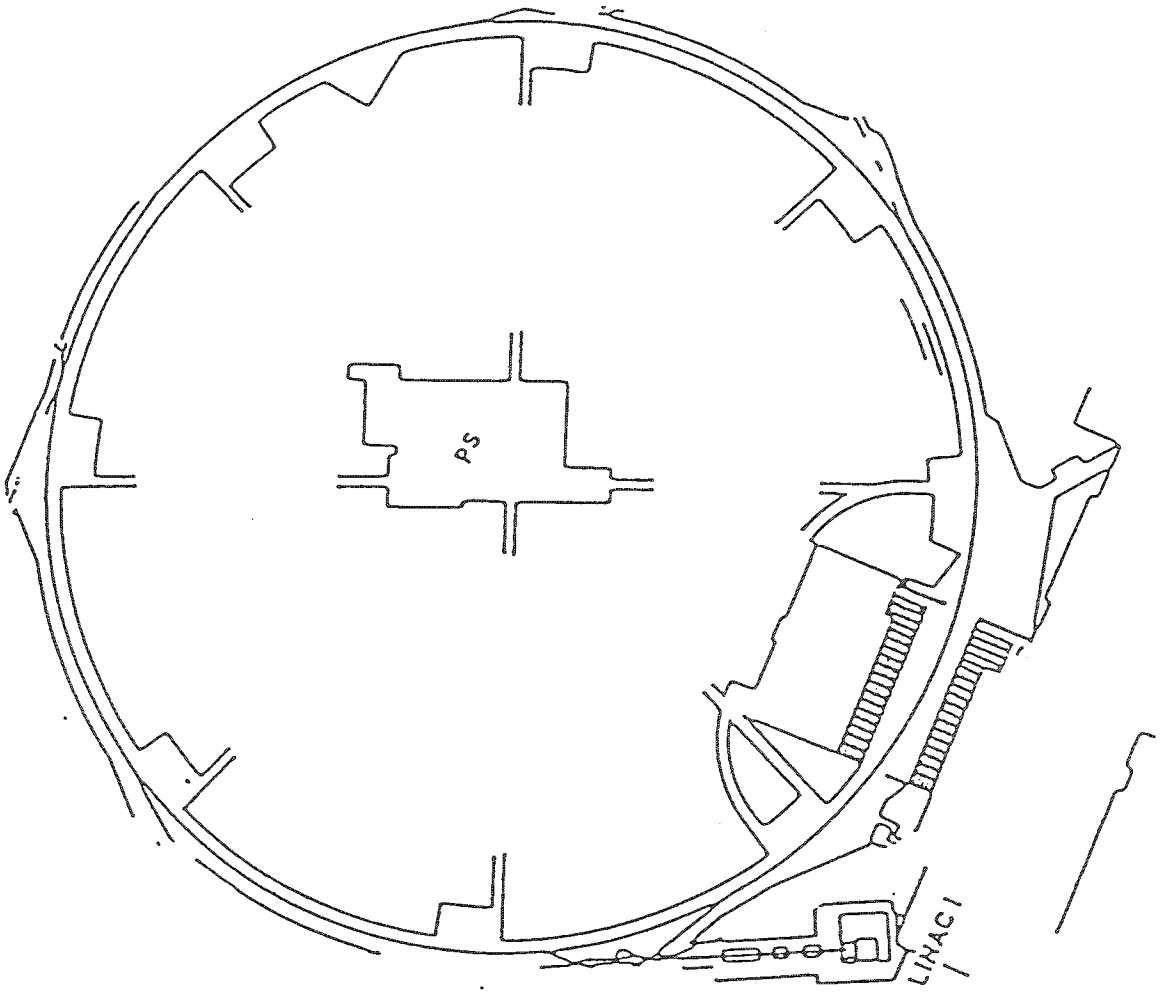

Fig. 1 : The CERN PS in 1959

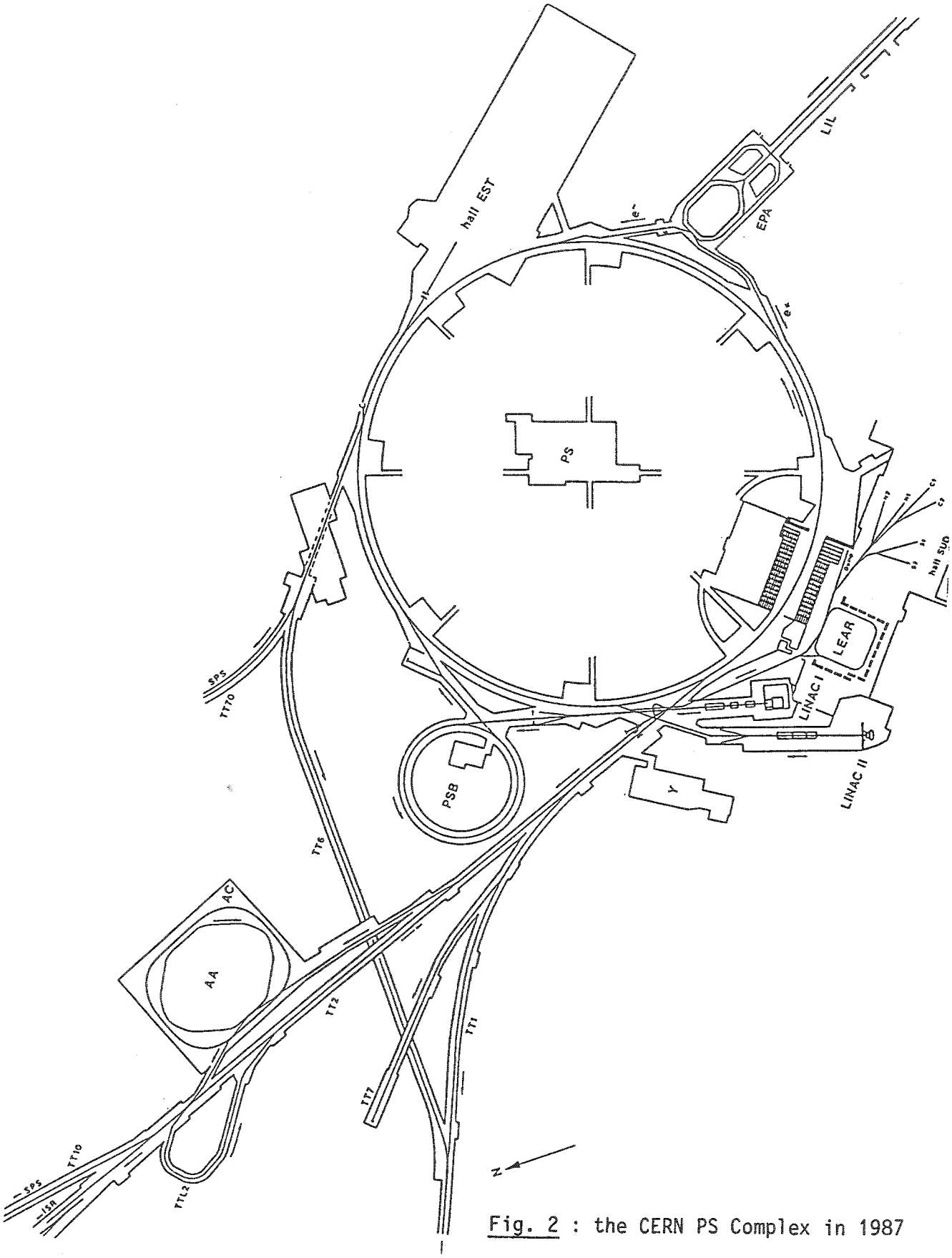

Fig. 2 : the CERN PS Complex in 1987

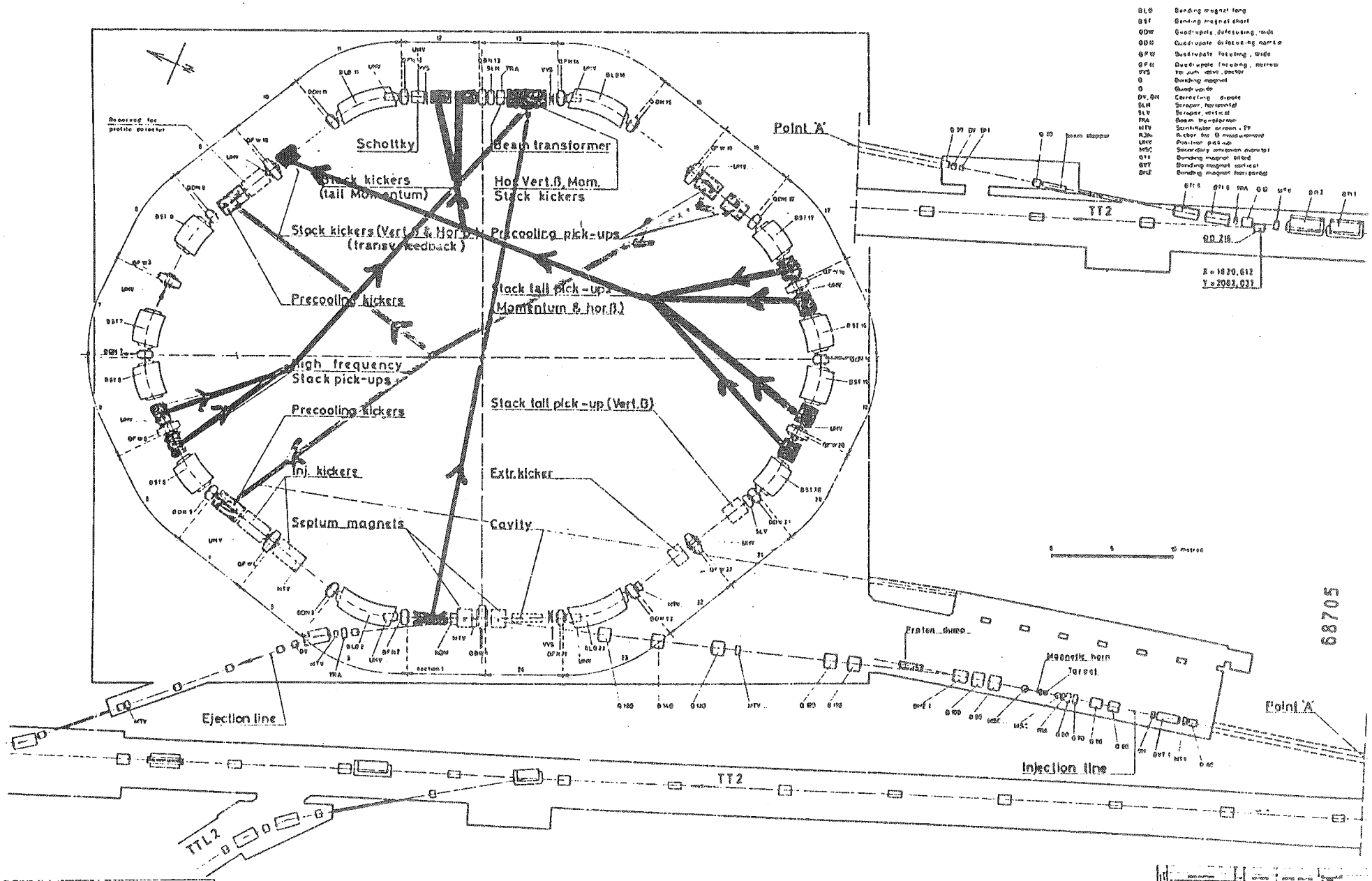

Fig. 3 : ANTIPROTON ACCUMULATOR GENERAL LAYOUT

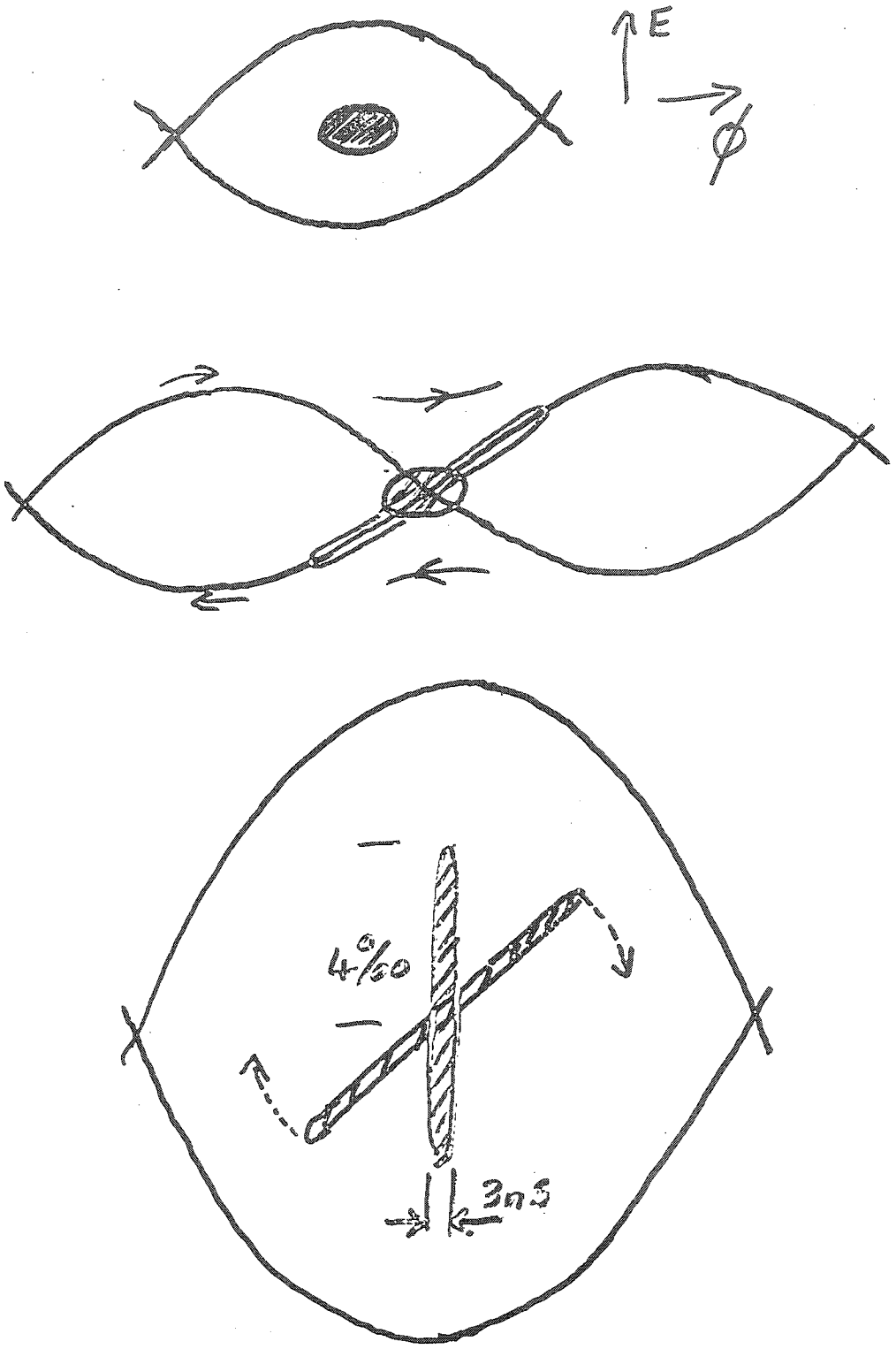

Fig. 4 : Bunch Compression

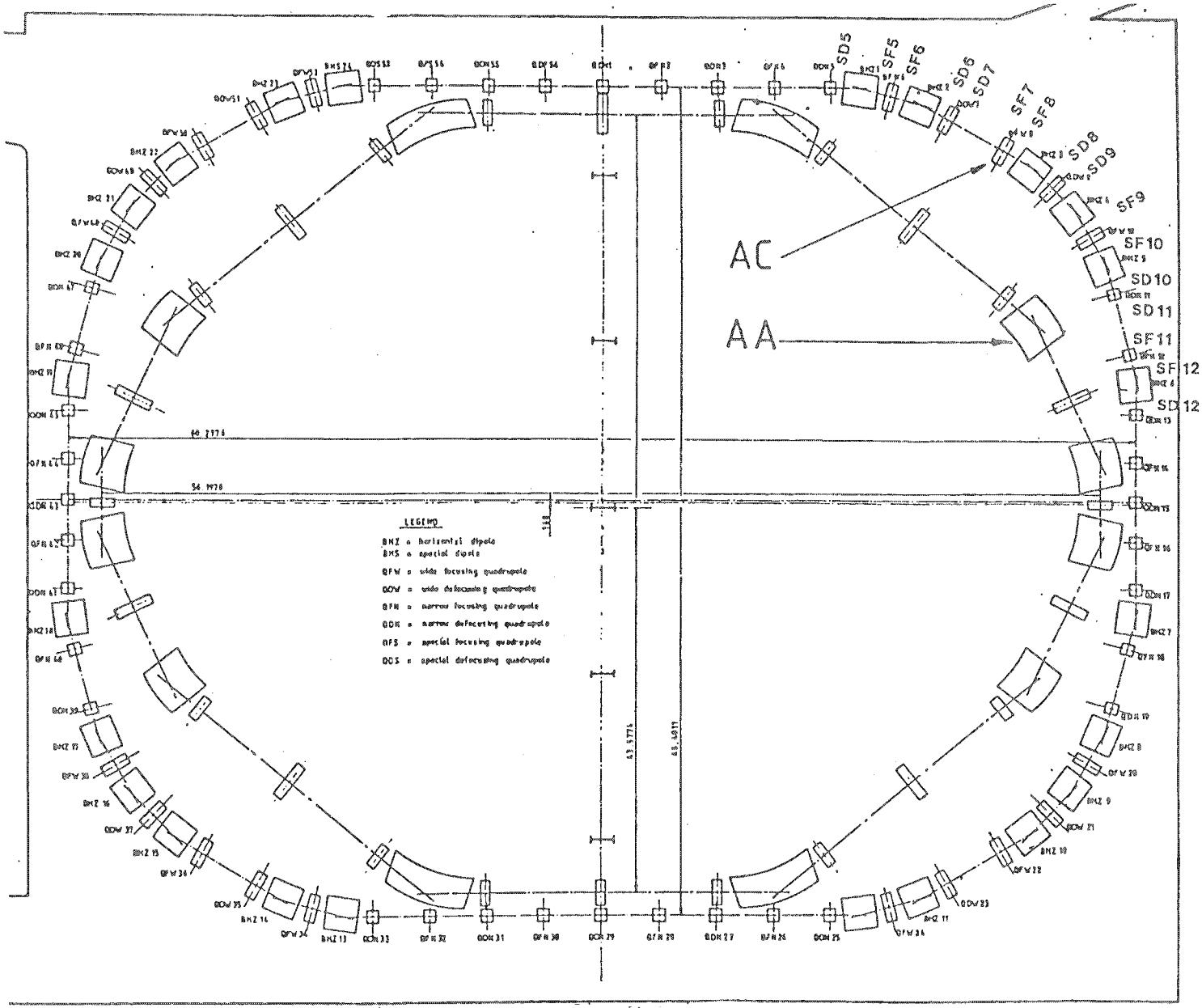

Fig. 5 : The ACOL Ring around the AA

UA1 IMPROVEMENT PROGRAMME

Presented by H. Hoffmann, CERN

No written contribution received

UA2 FUTURE

Presented by P. Jenni, CERN

(Due to internal agreement of the UA2 Collaboration, no written contribution was submitted to the editors.)

Fermilab $p\bar{p}$ Collider and Experiments

THE FERMILAB $\bar{P}P$ COLLIDER

Mike Harrison

Fermi National Accelerator Laboratory*
P.O. Box 500
Batavia, IL 60510 USA

Introduction

1983 saw the start of construction on the Fermilab $\bar{p}p$ collider, the Tevatron I project, as well as the commissioning of the new superconducting accelerator, the Tevatron, for high energy fixed target physics. The goal of the Tevatron I project is to achieve $\bar{p}p$ collisions in the centre-of-mass energy range up to 2 TeV with a luminosity of at least $10^{30}cm^{-2}sec^{-1}$. The project involves adapting the Tevatron to function as a storage ring and modifying the lattice to provide low-beta interaction points; changes to the Main Ring to allow $\bar{p}$ transfers and the installation of experimental equipment; and the construction of a $\bar{p}$ source. Major experimental areas will be located in the so-called B0 and D0 straight sections (detailed descriptions of these areas are presented elsewhere in these proceedings) together with smaller, more specialized experiments in several of the other interacting regions.

The antiproton source consists of a targetting station and two separate rings (the Debuncher and the Accumulator) connected to the Main Ring, the Booster, and each other by various transfer lines (see Figure 1). The Debuncher ring provides a large acceptance for the $\bar{p}$'s produced on the target and precools the $\bar{p}$'s prior to injection into the Accumulator which stores and further cools the $\bar{p}$'s in a similar fashion to the AA ring at CERN. The use of two independent systems for capture and storage allows the design of each one to be optimized on the somewhat conflicting requirements which in turn produces a correspondingly high overall system performance.

In order to achieve a luminosity in the range of $10^{30}cm^{-2}sec^{-1}$ the antiproton source must be able to accumulate $\sim 2\times10^{11}$ $\bar{p}$'s within a time comparable to the luminosity lifetime. Head on collisions are obtained in all six straight sections by injecting three bunches of protons and three bunches of counter-rotating antiprotons into the Tevatron. We plan to maximize the luminosity lifetime by using bunches of the same transverse emittance for both protons and antiprotons ($24\,\pi$ mm-mrad invariant) as well as the same intensity to minimize the beam-beam tune shift for a fixed luminosity. With a β^* of 1 m at the interaction point the design luminosity is achieved under these conditions

*) Operated by the Universities Research Association, Inc., under contract with the U.S. Department of Energy.

with a 6×10^{10} particles per bunch which leads to a linear beam-beam tune shift of 0.0017 per crossing.

It is difficult to make an accurate estimate of the luminosity lifetime which arises from residual beam-gas scattering, intrabeam effects, beam-beam interactions and overall machine stability. Based on operational experience in the SPS amongst other things we have chosen a design specification of 5 hours for the luminosity lifetime. The design of the antiproton source has a predicted accumulation rate of $\sim 1 \times 10^{11}$ $\bar{p}$'s per hour which provides us with a safety margin of approximately 2.5 which hopefully will be sufficient to account for the inevitable operational inefficiencies in such a complex system.

The sequence of events leading to $\bar{p}p$ collisions involves several distinct operations. We shall describe each step in more detail.

Proton Targetting

The production of antiprotons for subsequent storage is accomplished by the acceleration and targetting of protons from the Main Ring. Data from nuclear targets when taken with the energy dependence of the Main Ring cycle time[1] exhibit a broad maximum in $\bar{p}$ flux around an incident proton energy of 150 GeV. The desirability of locating the Antiproton Source near the Booster requires the protons to be extracted from the Main Ring at the F17 medium straight section (see Figure 1). This extraction location effectively limits the proton energy to 120 GeV but only reduces the $\bar{p}$ flux slightly. The Main Ring cycle time at 120 GeV is approximately 2 seconds.

Cooling the initial flux of $\bar{p}$'s is made easier if the phase space density at production is optimized. This is accomplished by minimizing the initial proton beam area and time spread. The proton beam area cannot be reduced arbitrarily since the temperature rise in the target is inversely proportional to the beam area for a fixed number of protons. The flux density which heats the target to the melting point defines the practical limit. Calculations show that a pulse of 2×10^{12} protons with an rms radius of 0.6 mm can be safely targetted on a 6 cm long tungsten-rehnium target every 2 seconds.

A single Booster cycle will suffice to produce a batch of 82 53 MHz bunches of protons with an intensity of 2×10^{12}. The normal time spread (several nsec) of the proton bunches will be reduced to 0.6 nsec by bunch rotation in the Main Ring just prior to extraction. This results in a momentum spread of 0.4% for the protons. The circulating beam is extracted in a single turn using a relatively slow rise time kicker magnet (~2 μsecs) located one sector upstream of the extraction channel in the E17 medium straight section.

Antiproton Production and Transport

The narrow bunches of protons produce equally narrow bunches of antiprotons We chose to collect these $\bar{p}$'s at 8.9 GeV/c as this is almost the optimum momentum and it corresponds to the standard Booster energy, which greatly simplifies the re-injection process and also allows the Booster to be used as a direct source of protons for reverse operation, for tune-up and commissioning purposes.

The yield of $\bar{p}$'s per incident proton is proportional to the product of the solid angle and the momentum spread accepted by the collection system, hence these quantities should be optimized in an efficient design. We plan to collect $\bar{p}$'s produced in a 60 mrad core using a pulsed lithium lens 2 cm in diameter and 15 cms long producing a peak field gradient of 1000 T/m. Under these conditions we expect to produce ~7×10^7 $\bar{p}$pp transported to the Debuncher ring with a momentum spread of 3% and an invariant emittance of 20 π mm-mrad in each plane.

The Debuncher Ring

The primary purpose of the Debuncher is to reduce the large momentum spread of the 8-GeV $\bar{p}$ beam at production to 0.2% prior to injection into the Accumulator. This reduction is accomplished by RF bunch rotation and adiabatic debunching after the $\bar{p}$ beam is injected into stationary 53 MHz buckets. The debunching time is only slightly greater than 10 msec, the remainder of the 2 second cycle is used for betatron cooling in each plane. The design calls for the reduction of transverse emittance from 20 π to 7 π mm-mrad prior to injection into the Accumulator.

The Debuncher lattice consists of 57 FODO cells with a ~60° phase advance per cell, the regular quadrupole spacing is preserved throughout the 3 long straight sections where the RF, beam transfer and stochastic cooling systems are located. The maximum value of the beta function in either plane is ~20 m which keeps the beam size small enough to permit the stochastic cooling pick-ups and kickers to have a 30 mm aperture suitable for operation in the 2-4 GHz range. The Debuncher ring operates above the transition energy (γ_T = 7.66) with a natural chromaticity of ~ -10 in each plane. This choice of machine lattice requires an RF voltage of 5 MV for the bunch rotation and debunching. Table 1 lists the major machine parameters.

Table 1. Debuncher Lattice Parameters

Nominal tune $\nu_x = \nu_y$	9.75
γ_T	7.66
Transverse acceptance	20 π mm-mrad
Momentum acceptance	4%
Natural Chromaticity ξ_x, ξ_y	-10.4, -10.6
Maximum Amplitude function β_{max}	20 m

Table 1. (Cont.) Debuncher Lattice Parameters

Maximum Dispersion function η_{max}	2.1 m
R.F. Voltage	5 MV
Machine Circumference	505 m
Superperiodicity	3.

The horizontal and vertical betatron cooling systems consist of 4 modules of pickups and 4 modules of kickers. Each pickup module has 32 pairs of loop couplers with a maximum response at 3 GHz. The signals from each side are added in phase and subtracted from each other to give a final signal proportional to the beam position. Signals from 2 modules are added to each other amplified by 40 db and added to a similar signal generated 180° away in betatron phase. The resultant is further amplified by 40 db and then split and used to drive the 4 kicker modules arranged in a similar fashion to the pick-ups.

With the very low beam intensity in the Debuncher the pickup signal is dominated by thermal noise in the termination resistor and the preamplifier. To optimize the signal-to-noise ratio the pickups and the preamplifiers are cooled to liquid nitrogen temperatures. A schematic layout of the Debuncher and Accumulator cooling systems is shown in Figure 2.

After 2 seconds the beam is transferred from the Debuncher to the Accumulator by a fast kicker magnet and magnetic septa located in the #10 straight section. The injected orbit in the accumulator is displaced in momentum by ~0.9% from the central momentum of the stack core.

The Accumulator

The Accumulator is designed to cool and accumulate a flux of $\sim 10^{11}$ $\bar{p}$'s per hour up to a maximum of 12 hours. To provide operational flexibility the accumulator should also be capable of storing cooled $\bar{p}$'s for much longer than the accumulation cycle.

The Accumulator possesses six independent cooling systems which provide horizontal and vertical betatron, and momentum cooling for both the newly injected batch of $\bar{p}$'s (the stack tail) and the circulating beam (the core). The momentum cooling systems require pick-ups in high dispersion regions and kickers in zero dispersion ones. The core betatron cooling takes place in zero dispersion areas, the stack tail betatron cooling in high dispersion ones. The physical layout of the cooling systems is shown in Figure 2. The lattice which accommodates this layout consists of 6 16 m straight sections which alternate between zero and high dispersion. The high dispersion (9 m) was achieved by concentrating the bending around the appropriate straight sections which gives the ring its' characteristic triangular shape. The beta functions

throughout the straight sections are less than 16 m which allows an aperture of 30 mm to be used for both the pickups and the kickers.

The gain of the stack tail momentum system must be large in order to move the incoming $\bar{p}$'s from the stacking orbit to the tail of the core distribution before the next pulse of $\bar{p}$'s. This large gain will cause thermal noise in the bandwidth of the core unless the appropriate frequencies are strongly suppressed ($\gtrsim 40$ db). This is achieved by a system of notch and correlation filters which in turn provide practical limitations on the maximum bandwidth of the stack tail cooling system which was chosen to be 1-2 GHz. The requirement of non-overlapping Schottky bands in this frequency range together with the aforementioned aperture limitations defined the Accumulator acceptance for incoming $\bar{p}$'s to be $\lesssim 10\,\pi$ mm-mrad in both planes. The momentum spread of the incoming flux (0.2%) is limited primarily by the output power of the stack tail momentum system. The core momentum cooling system is similar but somewhat simpler than the stack tail and will operate in the 2-4 GHz region. In a similar fashion to the Debuncher ring thermal noise will be minimized in the pickups and preamplifiers by operating these devices at liquid nitrogen temperatures. To provide acceptable performance with regard to transmission losses and dispersion in the frequency ranges required the notch filters consist of a 1.6 mm, 50 Ω superconducting transmission line immersed in a liquid helium cryostat. Each notch filter is driven by a travelling wave tube amplifer rated at 200 W of saturated output power. The design output power for each element is ~40 W which is well beneath the quench level for the notch filter (~200 W).

The gain profile of the various cooling systems are adjusted by displacing the appropriate pickups by a different amount relative to the central orbit. There are 3 series of pickups (-25 MeV, -1 MeV, 16 MeV) appropriate combinations of each output can be made to maximize the required signal, for example by subtracting the -1 MeV signal from the 16 MeV one the amplifed Schottky signal from the core particles is essentially zero. The particle density with respect to energy is shown in Figure 3.

Antiproton-Proton Collisions

After cooling and accumulating ~5×10^{11} $\bar{p}$'s the Accumulator will be ready to transfer beam for subsequent collisions. The transfer process starts by adiabatically capturing ~8×10^{10} $\bar{p}$'s from the core using a single h = 2 bucket and slowly moving the beam to the extraction orbit. This beam is then extracted from the Accumulator in a single turn using a shuttered kicker magnet and transported towards the Main Ring via the same beam line used for proton targetting, bypassing the target and collection system. The $\bar{p}$ bunch is

injected into a matched bucket in the Main Ring at h = 53 (~2.515 MHz). The normal Main Ring R.F. system is then slowly turned on and the beam rebunched into 13 53 MHz bunches and accelerated to 150 GeV. The 13 bunches are then coalesed into a single bunch prior to injection into the Tevatron, at this energy. The whole cycle is then repeated until 3 bunches of $\bar{p}$'s are circulating in the Tevatron along with three bunches of protons injected in the normal way prior to the $\bar{p}$'s.

The counter-rotating bunches are then accelerated up to the experimental energy. The final step in the collision process involves turning on the low-beta insertions in the experimental regions. The low-beta insertions are formed by replacing the normal 37" quadrupoles with stronger and separately powered quadrupoles and the addition of eight extra quadrupoles within the long straight section itself. During injection and acceleration these extra quadrupoles are turned off and the stronger elements at each end of the long straight are de-excited to provide the standard lattice configuration. After acceleration these elements are slowly adjusted until the final beta value of 1 m is reached. At this point the machine is in storage mode and the Main Ring can resume the 2 second cycle of $\bar{p}$ production.

Tevatron Operations

A major milestone on the way to colliding beams occurred in 1983 with the commissioning of the Tevatron as a fixed target machine and the subsequent first operational run which ended in February of this year. Machine commissioning started with the cooldown of the final sections of the machine which was accomplished at the beginning of May although prior beam tests had been made on the injection system and the first two sectors of the ring. Stable circulating beam was achieved seven weeks later after a shutdown to repair two magnets which were unable to carry sufficient current, and make small machine modifications to relieve aperture limitations. Beam was accelerated to an energy of 512 GeV at the beginning of August. A series of machine studies were then initiated which culminated with the resonant extraction of slow spill to the Switchyard dump. Operational high energy physics was started in October 83 with the machine running at 400 GeV with a 39 second time and a 15 second spill. The average beam intensity was slowly raised during the run up to 8×10^{12} ppp. The operational efficiency of the machine improved during the run with the final week showing beam delivered to the experimental areas for ~80% of the scheduled hours. It was encouraging to note that the downtime logged to the cryogenic systems remained a relatively constant 25-30% of the total.

The superconducting nature of the magnets places a stringent limit on the

amount of beam loss which can be tolerated before the magnets will quench. Special designs were adopted in the areas of unavoidable beam loss (extraction, abort) to protect those superconducting elements immediately downstream of the known loss points. The beam abort is a single turn extraction system which takes the circulating beam out of the machine to an external beam dump within three turns (60 μsecs) of receiving an alarm. The decision to abort the beam is made primarily by information received by the loss monitor and position detector system. Individual thresholds can be set on each element in the ring which can be varied as a function of energy within the cycle. This system has proved very effective in reducing the number of beam induced quenches as operational experience revealed the appropriate threshold settings under various operational situations.

In spite of this quite sophisticated abort system, magnet quenches in a superconducting accelerator can be regarded as a fact of life. The problem then becomes to reduce the number of quenches per day to an acceptable level when taking into account the recovery time of the magnets. The amount of energy deposited in a magnet during a quench is the sum of the beam energy and the stored energy in the magnetic field, and consequently the magnet recovery time depends strongly on the machine energy at the time of the quench. We have found that this time varies between ~20 minutes at injection energy (150 GeV) up to ~1 hour at 800 GeV. Throughout the 400 GeV run the number of quenches was reduced from ~1 per 3 hours of HEP to ~1 per 15 hours of HEP. In the current 800 GeV run this number has been reduced further to approximately 1 per day. We believe that while a lot of work still needs to be done to increase the operational efficiency of the Tevatron, we have demonstrated that superconducting technology has come of age in particle accelerators and that large scale cryogenic systems can be made to operate reliably over long periods of time.

Initial Collider Studies

While the main thrust of machine development work to date has been concerned with fixed target machine operation a small amount of machine time has been made available for colliding beam work. The mechanics of beam storage were established over several study sessions and protons were successfully stored at 400 GeV for periods of up to 4 hours. Crude measurements indicate that the beam lifetime is consistent with that expected from the residual beam-gas scattering. The background rates in the collision region were also small (~30 kHz) measured with a 1 meter square scintillation counter horoscope. The transverse beam stability was good and we were unable to detect any signs of fifth order resonances. The sensitivity of the fixed target beam diagnostics to these effects is not high emphasizing that these results are encouraging

rather than conclusive in any way. Longitudinal phase space dilution was observed during the stores with debunching times of the order of 1 hour. More effort will be needed to reduce the amount of noise present in the Tevatron low level R.F. system.

Modifications to the Tevatron lattice to allow the establishment of the low beta interaction region at BØ were made in February of this year. To date beta values at the interaction point have been reduced from the 'normal' 70 m to 2 m. Attempts to achieve the design value at $\beta^* = 1$ m have resulted in fast beam loss. Work is proceeding to understand and rectify this situation.

Schedule

The civil construction for the antiproton source ring enclosures and targetting hall is well underway. Initial installation work of tunnel utilities will start in June 84 with the magnet and power supplies following immediately afterwards. The goal is to have both the Debuncher and Accumulator rings under vacuum by December 84. During the upcoming major summer shutdown (July - November 84) installation of the injection and extraction systems and the targetting station will take place in the main tunnel, as well as a test line from the Booster. Commissioning of the $\bar{p}$ rings with protons and targetting and production studies will start at the beginning of 1985. Initial attempts to obtain collisions in the Tevatron are scheduled for the Summer of 1985.

Conclusions

We are currently constructing an Antiproton Source that is capable of providing sufficient $\bar{p}$'s to achieve a luminosity of $\sim 10^{30}$ for collisions involving 3 bunches of protons and antiprotons. The Tevatron has been operational now for over six months in the fixed target mode with energies up to 800 GeV and intensities $\leq 10^{13}$ ppp. Machine studies associated with the collider mode of the superconducting ring are now underway.

Reference

1) Calculation of Antiproton Yields for the Fermilab Antiproton Source, Fermilab PUB 82/43, C. Hojvat and A. Van Ginneken.

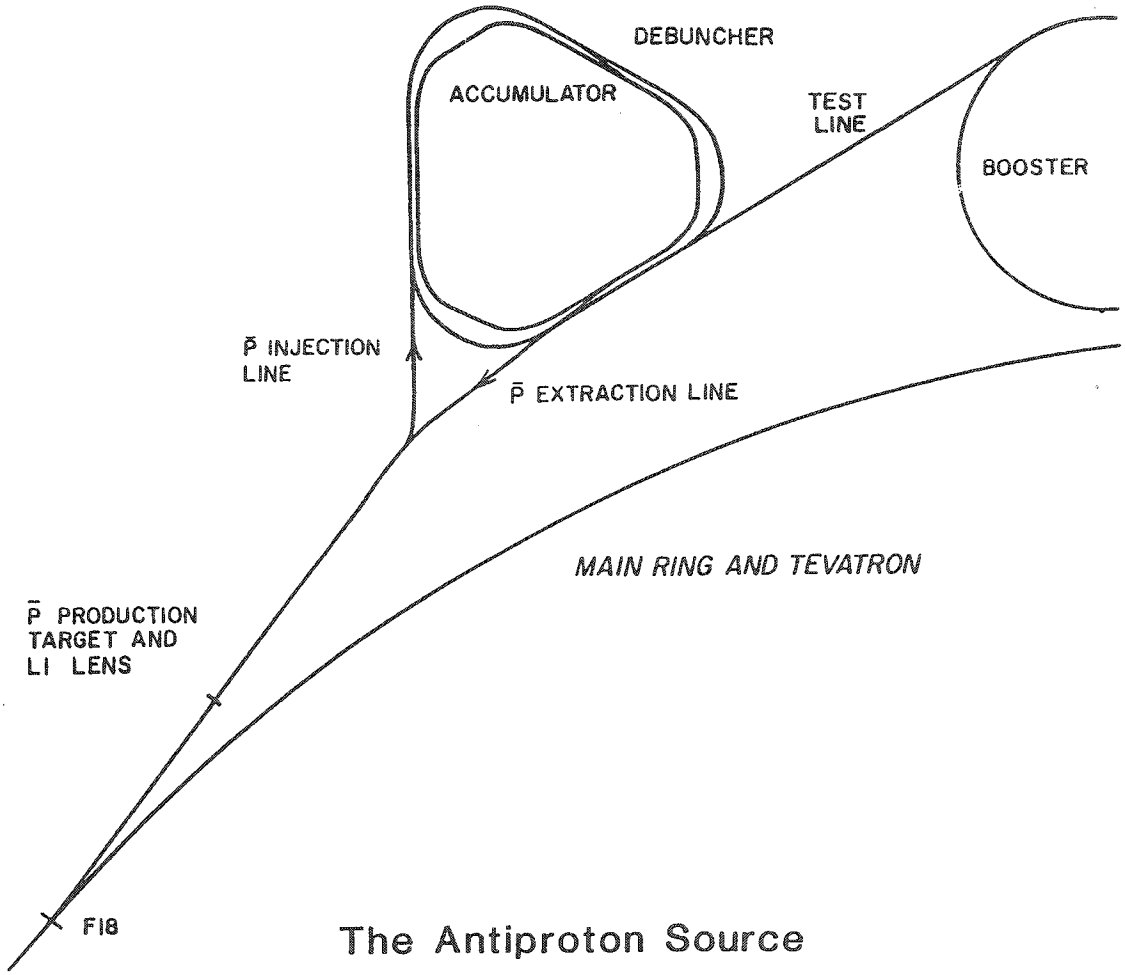

The Antiproton Source

Fig. 1

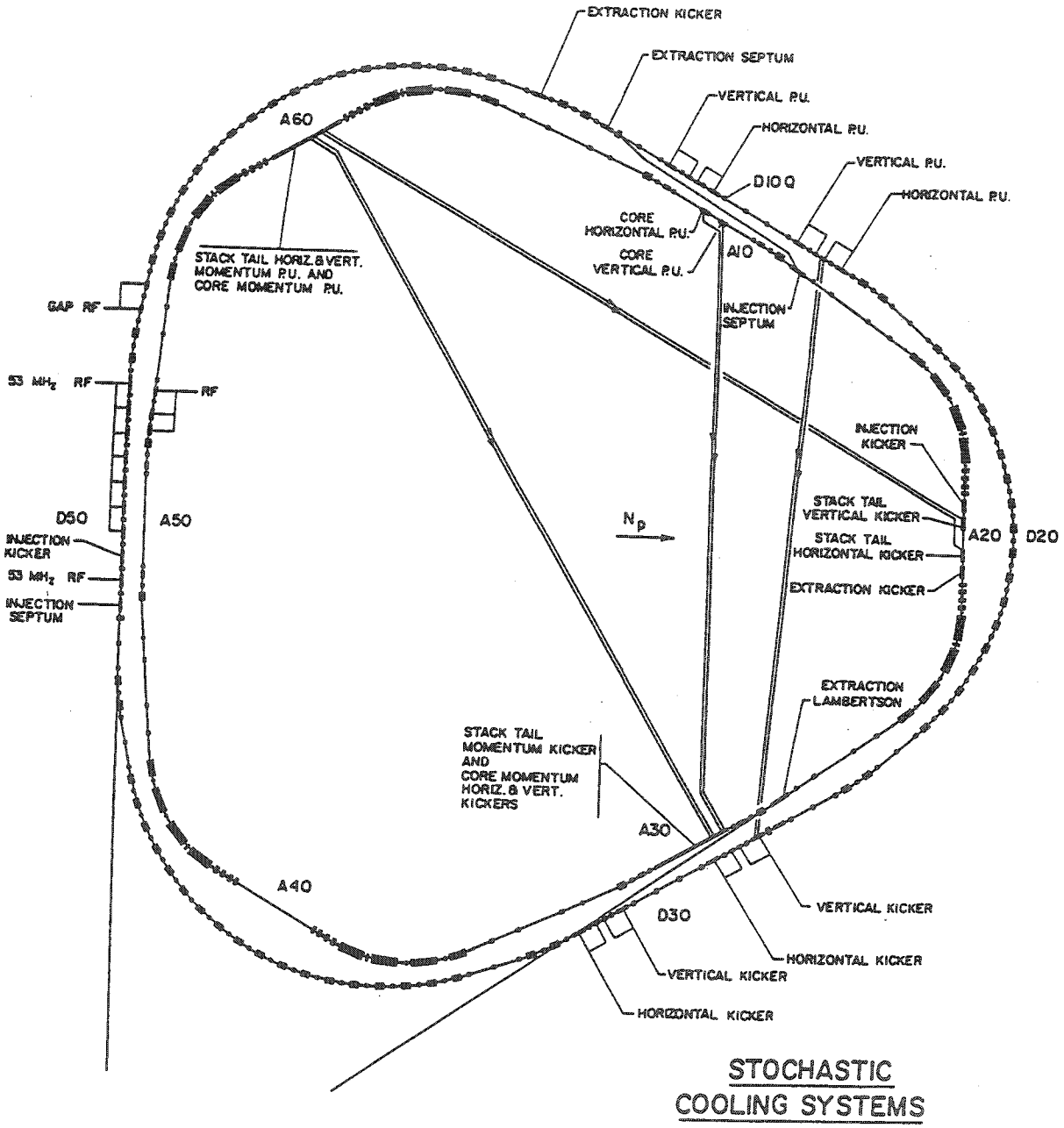
EXTRACTION KICKER
EXTRACTION SEPTUM
VERTICAL P.U.
HORIZONTAL P.U.
VERTICAL P.U.
HORIZONTAL P.U.
A60
D10Q
CORE HORIZONTAL P.U.
CORE VERTICAL P.U.
A10
INJECTION SEPTUM
STACK TAIL HORIZ.& VERT. MOMENTUM P.U. AND CORE MOMENTUM P.U.
GAP RF
53 MHz RF
RF
INJECTION KICKER
STACK TAIL VERTICAL KICKER
STACK TAIL HORIZONTAL KICKER
EXTRACTION KICKER
A20
D20
D50
A50
INJECTION KICKER
53 MHz RF
INJECTION SEPTUM
Np
EXTRACTION LAMBERTSON
STACK TAIL MOMENTUM KICKER AND CORE MOMENTUM HORIZ. & VERT. KICKERS
A30
A40
D30
VERTICAL KICKER
HORIZONTAL KICKER
VERTICAL KICKER
HORIZONTAL KICKER
STOCHASTIC COOLING SYSTEMS

Fig. 2

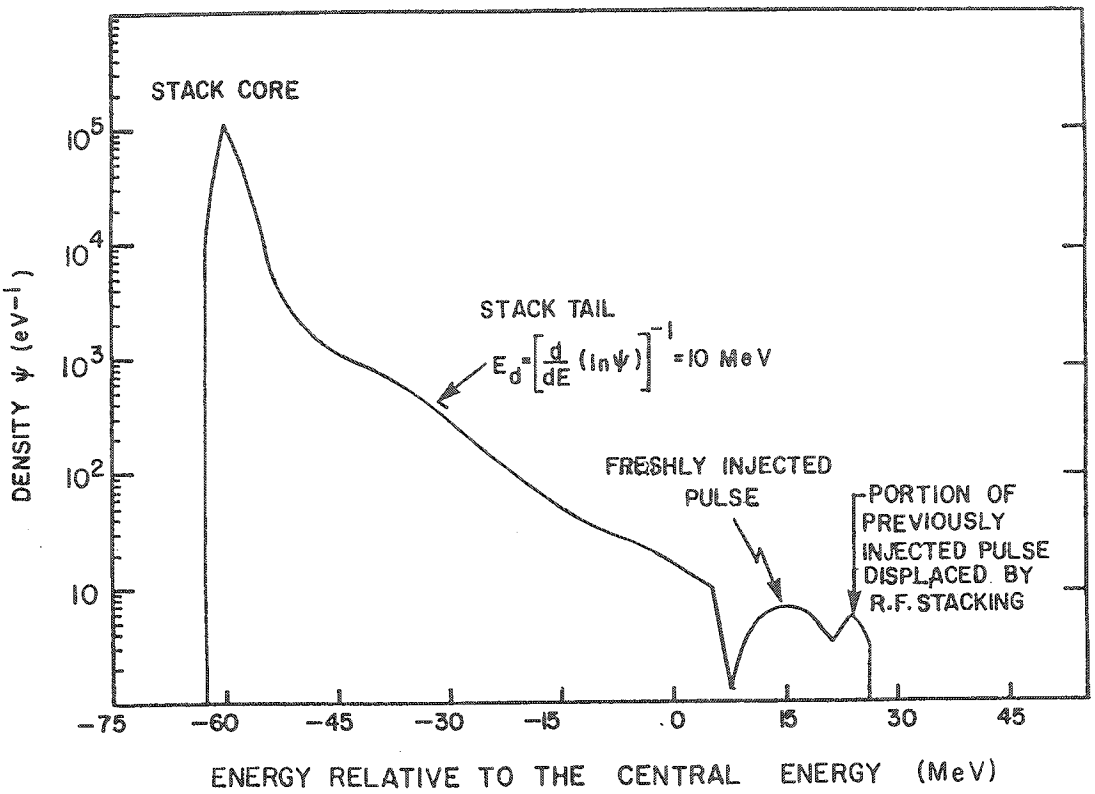
STACK CORE
STACK TAIL
$E_d = \left[\frac{d}{dE}(\ln\psi)\right]^{-1} = 10$ MeV
FRESHLY INJECTED PULSE
PORTION OF PREVIOUSLY INJECTED PULSE DISPLACED BY R.F. STACKING
DENSITY ψ (eV^{-1})
10^5
10^4
10^3
10^2
10
−75
−60
−45
−30
−15
0
15
30
45
ENERGY RELATIVE TO THE CENTRAL ENERGY (MeV)

Fig. 3

THE COLLIDER DETECTOR (CDF) AT FERMILAB - AN OVERVIEW

Dennis Theriot

Fermi National Accelerator Laboratory*
Batavia, Illinois 60510
USA

CDF, the Collider Detector at Fermilab, is a collaboration of almost 150 physicists from ten U. S. universities (University of Chicago, Brandeis University, Harvard University, University of Illinois, University of Pennsylvania, Purdue University, Rockefeller University, Rutgers University, Texas A&M University, and University of Wisconsin), three U. S. DOE supported national laboratories (Fermilab, Argonne National Laboratory, and Lawrence Berkeley Laboratory), Italy (Frascati Laboratory and University of Pisa), and Japan (KEK National Laboratory and University of Tsukuba). The primary physics goal for CDF is to study the general features of proton-antiproton collisions at 2 TeV center-of-mass energy. On general grounds, we expect that parton subenergies in the range 50-500 GeV will provide the most interesting physics at this energy. Work at the present CERN Collider has already demonstrated the richness of the 100 GeV scale in parton subenergies.

To set the scale for physics with CDF, lower energy processes can be extrapolated to these higher energies. One such example shown in Figure 1 is large -p_t jet production predicted by QCD. Jets with p_t as large as 250-300 GeV are accessible to experimental study. Another example probing the same energy scale is that of W or Z pair production, shown in Figure 2. Again practical rates should exist for this process at 2 TeV. The increased energy also will yield higher cross sections for single W and Z production by approximately an order of magnitude compared to that now seen at 540 GeV.

---

*Operated by Universities Research Association Inc. under contract with the United States Department of Energy

How did we design CDF around these considerations? Since CDF will be observing hadron collisions, the natural coordinates to use are rapidity, y, azimuthal angle, ϕ, and the transverse momentum, p_t. As a very crude guide, the events of interest can be pictured as being produced uniformly in y up to a cutoff given by energy conservation, uniformly in ϕ, and with a steeply falling p_t dependence. To see most of the events at the 100 GeV scale, such as W and Z production, the detector must cover a y range from -3 to +3. If we allow for the decay products as well, another unit in y must be added. Thus, the acceptance for the full calorimetry and tracking of CDF was chosen to be $-4 < y < 4$, $0 < \phi < 2\pi$. The y acceptance translates into a polar angle acceptance of $2° < \theta < 178°$. Events at higher masses are well contained by this acceptance.

What particles do we want to detect? Since the basic processes are expected to involve quarks, gluons, leptons, and photons , we want to measure as much about these particles as possible within practical constraints of available technology and money. Since quarks and gluons manifest themselves as clean, narrow jets of hadrons, CDF has chosen shower counters and hadron calorimeters in a tower geometry to detect jets. One of the central calorimeter modules called a wedge is shown in Figure 3. The shower counter composed of lead and scintillator is at the bottom. The hadron calorimeter made of steel and scintillator is above. The projective tower geometry is obvious. The granularity of the calorimeter towers is sufficient to just resolve the jets without being able to measure reliably every particle within the jet. Since hadrons in a typical high p_t jet will form a circular pattern in $y - \phi$ space with a diameter of roughly one unit, the calorimeter towers were chosen to be 0.1 unit in y and between 5° and 15° in ϕ. A plot of this granularity is shown in Figure 4. Leptons are characterized by single particles which have different interactions in the various component detectors in CDF. Charged particle tracking in a magnetic field, shower counter and hadron calorimeter response,

and penetration through several interaction lengths of material are the techniques planned for detecting electrons and muons. Neutrinos are observed by missing energy and momentum. Photon detection is achieved with finely segmented shower counters and the absence of a charged track.

An isometric drawing of CDF is shown in Figure 5. The detector is divided into three main pieces, the Central Detector and two Forward/Backward Detectors. All three pieces are centered on the Tevatron beamline at the BØ collision area at Fermilab. A vertical section through the Central Detector is shown in Figure 6. The heart of the Central Detector is a 1.5 Tesla, 3.0 m diameter, 5.0 m long superconducting solenoid magnet. This magnet and the Central Tracking Chamber are used to measure individual particles with p_t less than 40 GeV. It gives information that is complementary to that of the calorimeters and provides a pictorial representation of the event. The choice was a solenoid to provide maximum efficiency in the study of large p_t events. Surrounding this magnet are the shower counters and hadron calorimeters. The shower counters in the region between 90° and 33° are made of a lead scintillator sandwich read out with wavelength shifter plates and light pipes. A strip proportional chamber has been inserted at a depth of five radiation lengths to provide fine grained information on the shower location. Between 33° and 10° the shower counters are a lead proportional pad chamber sandwich. These chambers are gas filled proportional counters fabricated out of resistive plastic tubes with cathode pad readout. A strip proportional chamber is also provided in these detectors at the shower maximum to provide precision information about shower location. Outside the shower counters are located the hadron calorimeters. In the region between 90° and 30° these calorimeters are made of steel and scintillator read out by wavelength shifter bars and light pipes. Between 30° and 10° the hadron calorimeters are steel and proportional pad chambers. Outside the hadron calorimeters in the region between 90° and 50° are located the central muon

detectors. These detectors are composed of four layers of drift chambers and a hard wired trigger which provides precision information on the direction of penetrating particles. The return legs of the magnet are located above and below the central calorimeters. These central calorimeters are assembled into four arches which surround the magnet cryostat. One of these arches is shown in the photograph labeled Figure 7.

A detailed section of one quadrant of the core of the central detector is shown in Figure 8. The beam pipe is 5 cm in diameter composed of 2 mm Be. Surrounding this in the vicinity of the interaction region are seven small atmospheric pressure VTPC's which have a good r - z tracking ability. The principal roles of the VTPC's are to record the occurence of multiple events and to provide three dimensional information about the general event topology for use in pattern recognition by the calorimetry and the central tracking chamber. A drawing of one of the VTPC modules is shown in Figure 9. Surrounding the VTPC's is a large cylindrical drift chamber which provides the precision momentum measuring instrument in CDF. The central tracking chamber is an axial wire chamber with 84 layers arranged into 9 superlayers. Five of the superlayers each contain 12 sense wires. These five axial layers are separated by four superlayers of "stereo" wires each containing 6 sense wires. Both axial and stereo superlayers are divided into cells similar to the JADE detector. Each cell is tilted 45° with respect to the radial direction so that the drift direction is predominately circumferential when the magnetic field is 1.5 Tesla. Completing the tracking system is a radial wire drift chamber which covers the angular range of 2° to 10° in the forward direction. This chamber is composed of twenty layers of sense wires arranged in 72 radial cells each covering 5° in ϕ tipped at a 2° angle to provide ambiguity resolution.

Located outside the central tracking chamber is the cryostat of the superconducting solenoid magnet. This magnet is being produced in Japan by Hitachi as a collaboration between physicists from the University of Tsukuba and Fermilab. The total thickness of the coil and its cryostat is less than one radiation length. This small thickness was achieved by locating the support bobbin outside the superconducting coil rather than inside as in previous magnets of this type. A detail of this arrangement is shown in Figure 10. The coil was originally wound on a large mandrel. The bobbin which is used to propogate a quench was then slipped over the coil in a shrink fitting operation in which the bobbin was heated then allowed to cool in order to achieve a tight fit. The mandrel was then removed from the coil. This operation was successfully carried out in January of this year.

An elevation view of half of the detector is shown in Figure 11. Particles produced between 2° and 10° pass out of the central detector through a hole in the end plug and enter the forward and backward detectors. The first layer of these detectors is a shower calorimeter composed of alternate layers of lead and proportional pad chambers. Again a strip chamber giving fine grained information about shower location is located at shower maximum. The projective geometry used in the central detector is continued into this angular range as well. Located behind the shower calorimeter is the forward hadron calorimeter. This calorimeter is composed of steel plates instrumented with proportional pad chambers. Small angle muons originating between 2° and 17° will be detected and momentum analysed by the magnetized iron toroids and muon tracking chambers of the forward muon detector located immediately behind the hadron calorimeter.

Overall there are more than 60,000 channels of detector information in CDF. The job of acquiring and recording all of this information is not trivial. We have chosen to mount the front end amplifiers and the sample and hold circuits

as close as possible to the detector components. In the case of the central wedges on the actual wedges themselves a redundant multiplexed ADC system will read out the analog signals locally and transmit the digital results to the data acquisition electronics located in the BØ counting rooms. FASTBUS will be used in the data acquisition system.

A multilevel trigger is planned for CDF. The basic interaction rate is expected to be 50,000 Hz. Three trigger levels are planned. Level 1 must decide within one beam crossing or 7 microseconds whether to keep the event for digitization. This trigger is derived from analog signals provided by the front end electronics about energy deposited in the shower counters and hadron calorimeters. Level 2 looks for patterns of energy deposition, high p_t tracks associated with muon hits, large missing p_t, and other similar inputs. Level 2 may take several beam crossings to make its decision. The final stage Level 3 is made when fully digitized event information is available to the data acquisition system and dedicated processors will make software cuts to reduce the trigger rate to the data logging level. The three levels are expected to reduce the original rate to approximately 1 Hz. The control, monitoring, calibration, and data logging for CDF will be handled by a system of VAX computers.

A plan view of the BØ experimental area is shown in Figure 12. The collision hall is an underground enclosure 30 m long and 15 m wide located around the Tevatron beam line approximately 15 m below the surface. This is shown in the lower part of Figure 12. The collision hall is accessed by means of a 10.5 m x 10.5 m tunnel which connects it to the assembly hall which serves as the assembly and service area of CDF. The assembly hall is a 75 m x 30 m surface building containing a 23 m x 30 m pit at Tevatron elevation where CDF is actually assembled, a 50 ton crane, counting rooms, offices, and shops. An

elevation view of the facility is shown in Figure 13. The central detector is provided with heavy duty rollers so that it can be moved easily between the beam line and the assembly area. The control rooms are located over the tunnel connecting the collision hall and the assembly hall. The detector will be connected to the control room by a flexible cable tray not shown in the figure.

Currently, Fermilab has CDF scheduled for a test run in June 1985 with another run in January 1986. The experimental area at BØ is essentially complete. The low beta quads for the interaction region have been installed and are expected to undergo testing this spring. The coil has been wound, is currently being installed in the cryostat, and is scheduled to be cooled down in April with shipment to the United States expected in June. The assembly of the magnet yoke will begin in the BØ assembly hall pit in April. Production lines for the various assemblies that go into the central wedge modules have been running for almost two years now. Some of these lines have actually finished their work and are beginning to shut down. Assembled wedges are beginning to go to the beam line for final calibration. A diagram showing the assembly pit sequence is shown in Figure 14. We expect to have most of the central detector and parts of the backward detector ready for the June 1985 run. The central tracking chamber and the end plugs cannot be used in this run because two beam pipes will still go thru BØ at that time. The entire detector will be in place for the January 1986 run. The electronics production will be complete by the end of 1986. At that time, we expect to begin sharing beam time with the fixed target experimental program at a fraction that will approach 50%.

Given the time limitations of this talk and the space limitations for the proceedings I have chosen to give an overview of CDF in order to acquaint many of you who are not familiar with the project with the main goals and general design. If you seek more details on various aspects I refer you to the appended bibliography which has served as the source of most of this talk and paper.

CDF Bibliography

1) Design Report for the Fermilab Collider Detector Facility (CDF), CDF Collaboration, August, 1981, Fermilab Internal Document.

2) CDF, Roy Schwitters, Fermilab Reports, September, 1983.

3) Charged Particle Tracking in CDF, M. Atac, et al., CDF Note #178, August 11, 1983.

4) A Radial Drift Chamber, M. Atac and G. Chiarelli, CDF Note #193.

5) Title I Design Report: Colliding Beam Experimental Area at B0 Straight Section, August 28, 1981, Fermilab Internal Document.

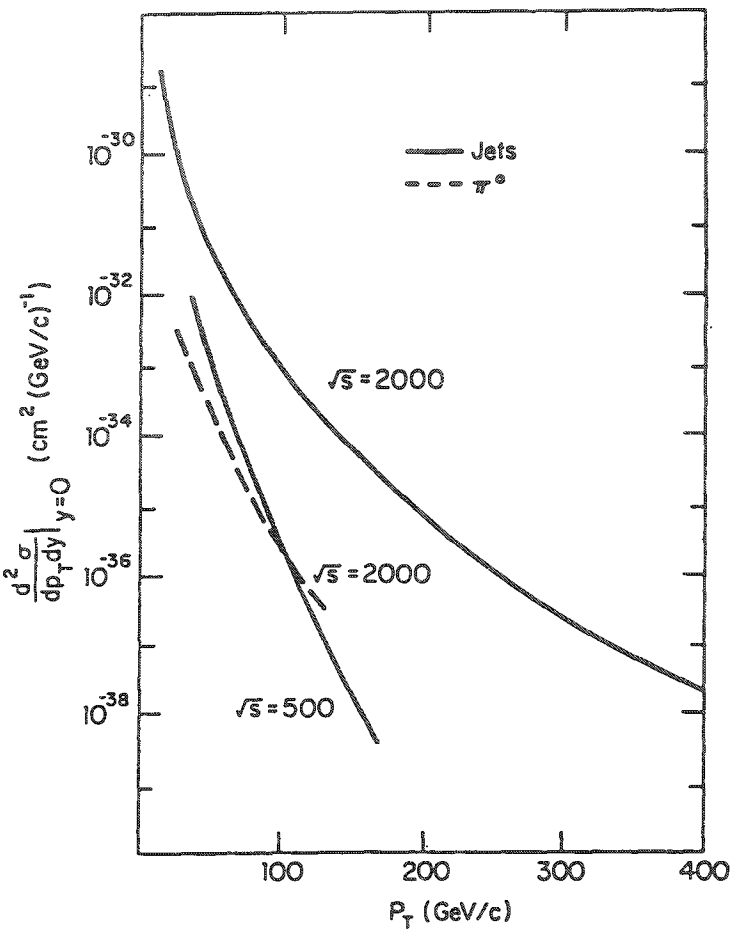

Figure 1: Large p_t jet production predicted by QCD for the Tevatron Collider energy compared with the cross section for lower energy collisions

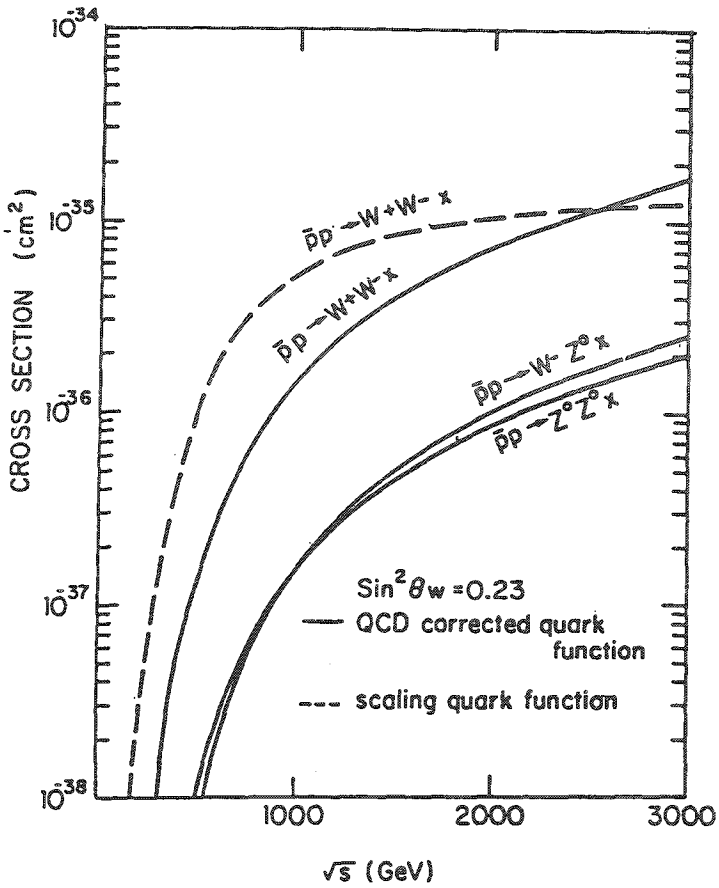

Figure 2: Predicted production of W and Z pairs

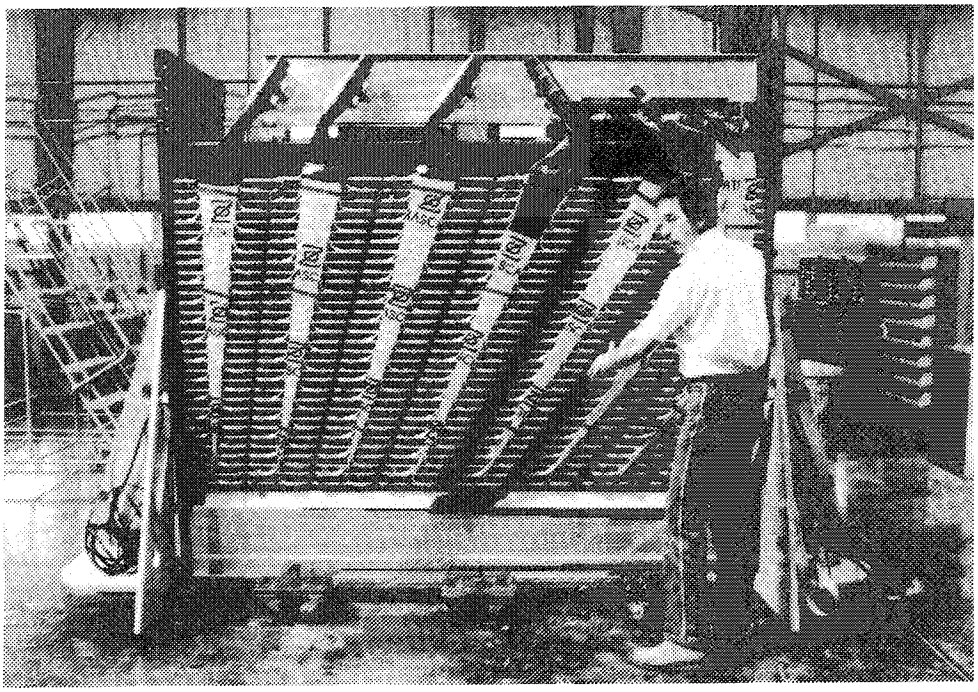

Figure 3: Side view of one wedge module with side skin removed exposing the tower structure

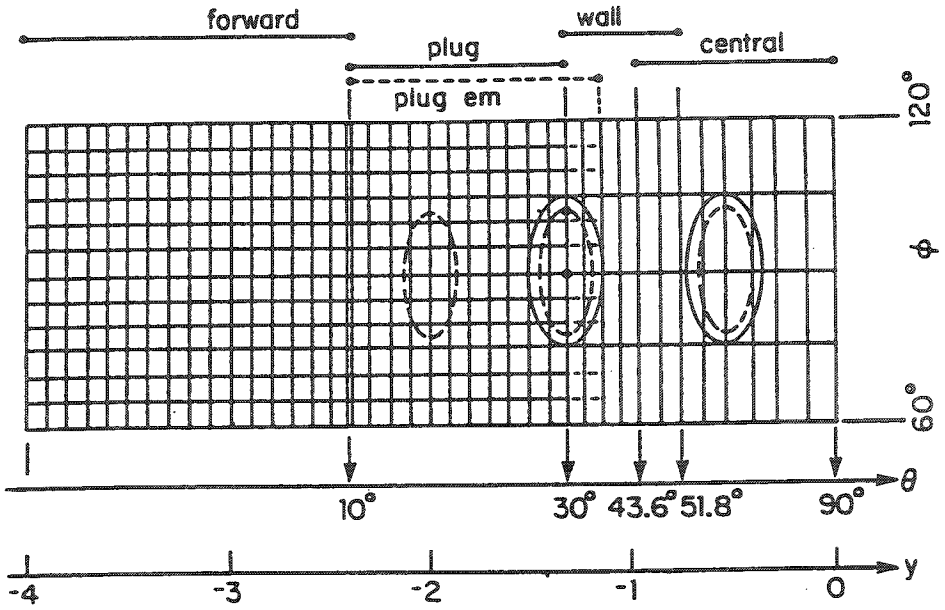

Figure 4: Granularity of the shower counter and hadron calorimeter system

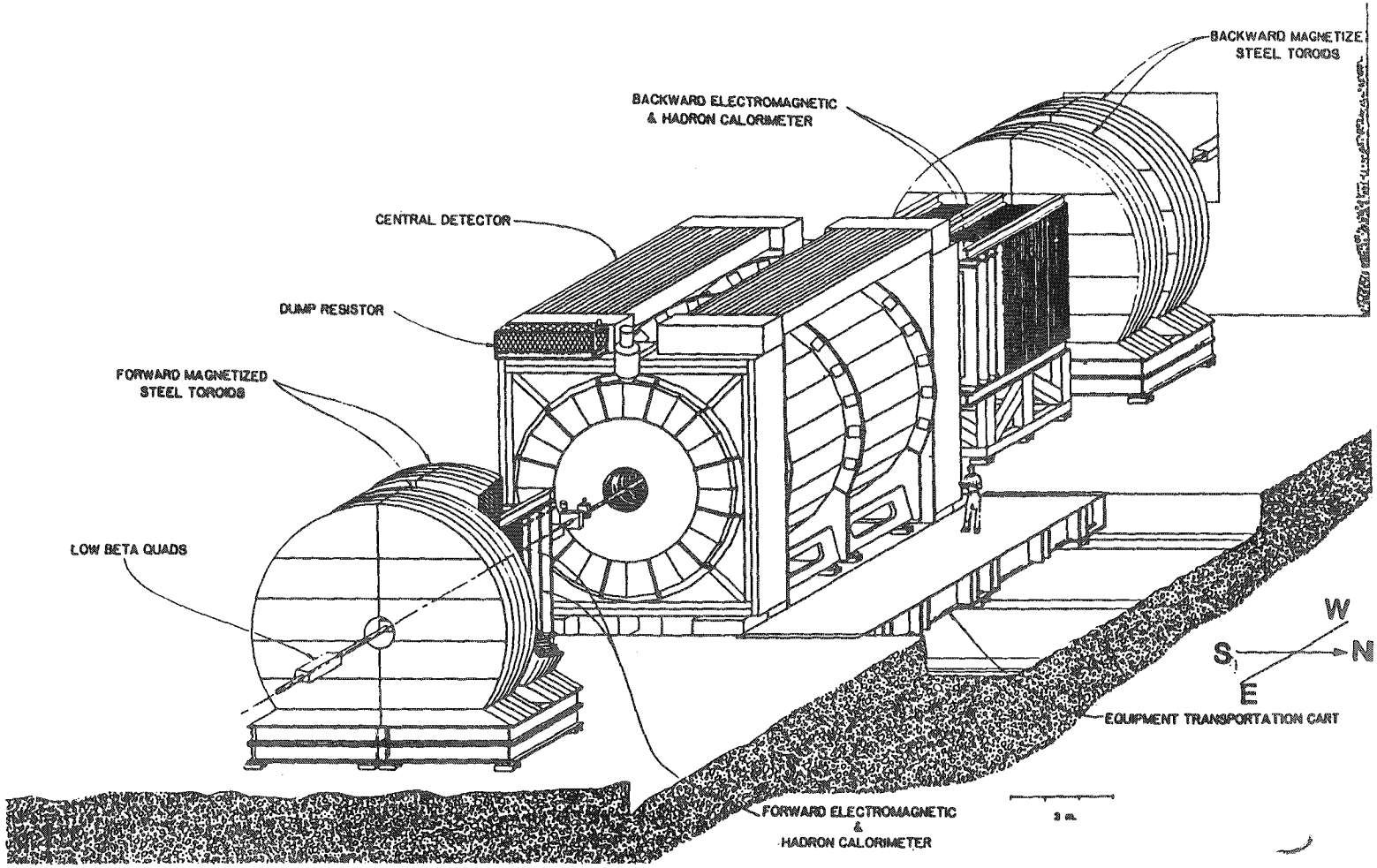

Figure 5: An isometric drawing of CDF

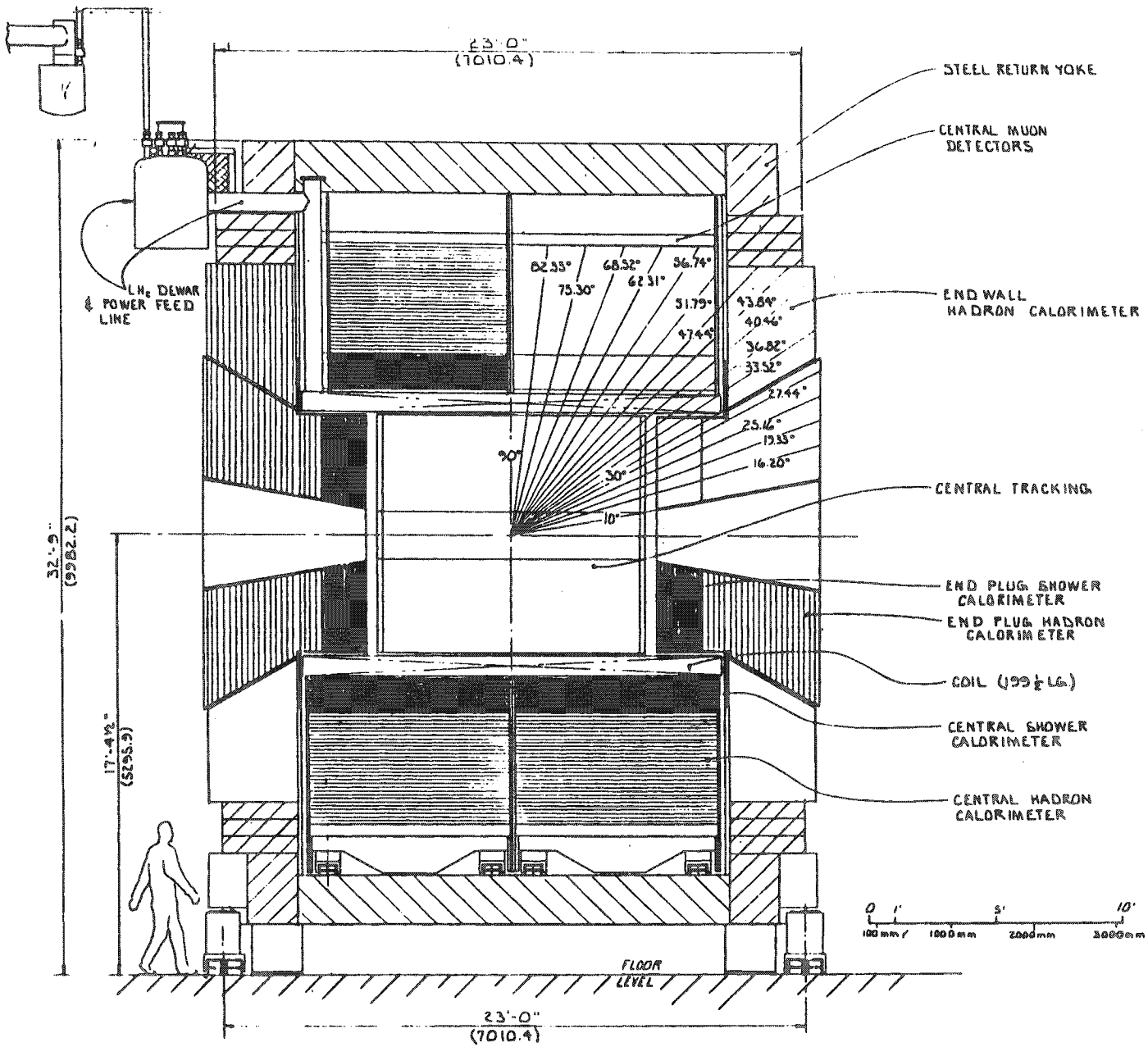

Figure 6: Vertical section through the Central Detector of CDF

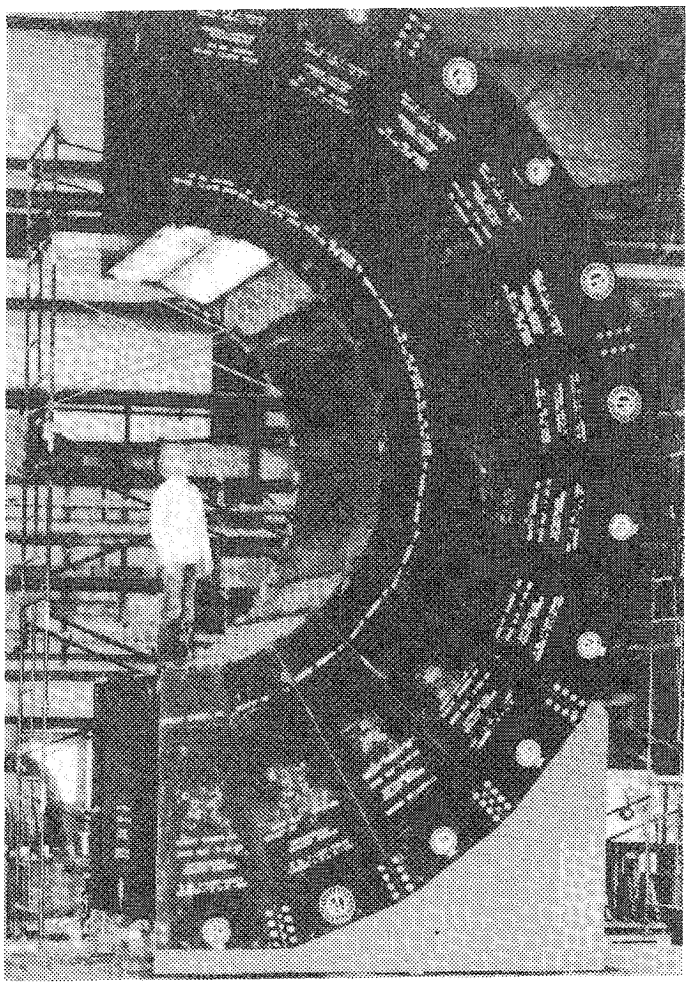

Figure 7:

One of the four central calorimeter arches during a test assembly using partially completed wedge modules

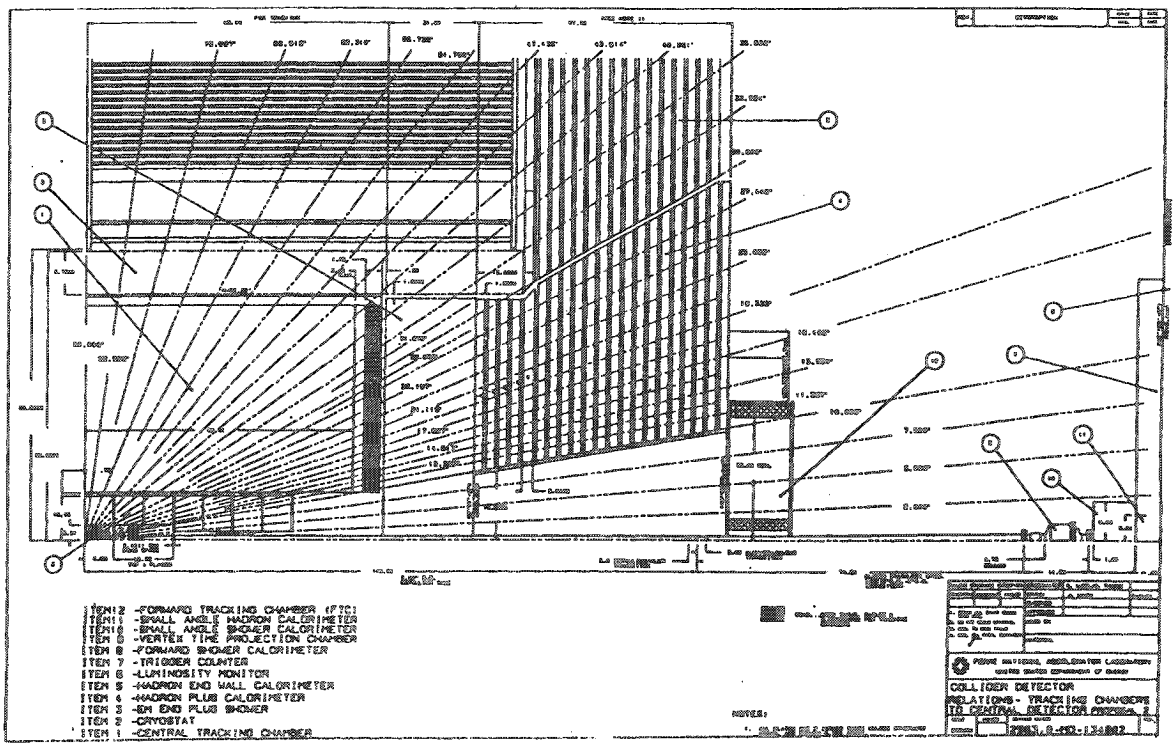

Figure 8: One quadrant of the core of the Central Detector of CDF showing the relationship

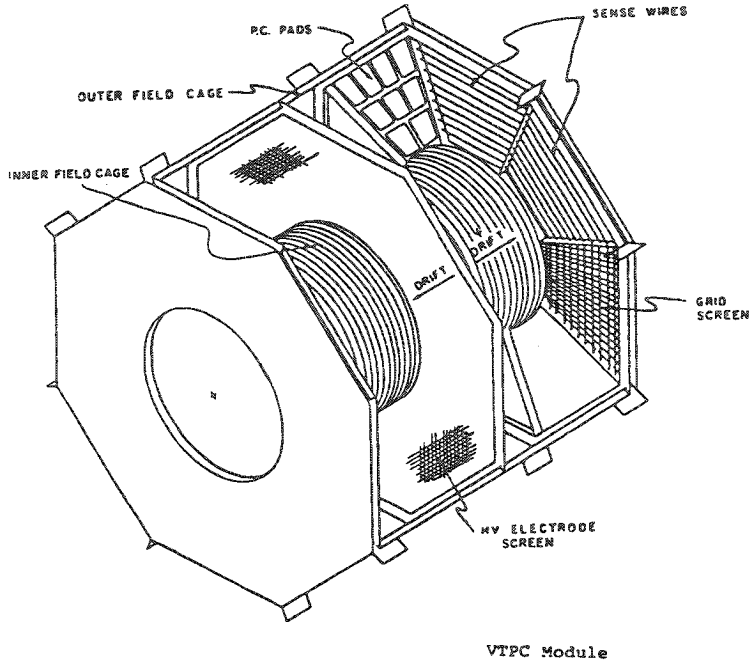

Figure 9: VTPC module of CDF Tracking System

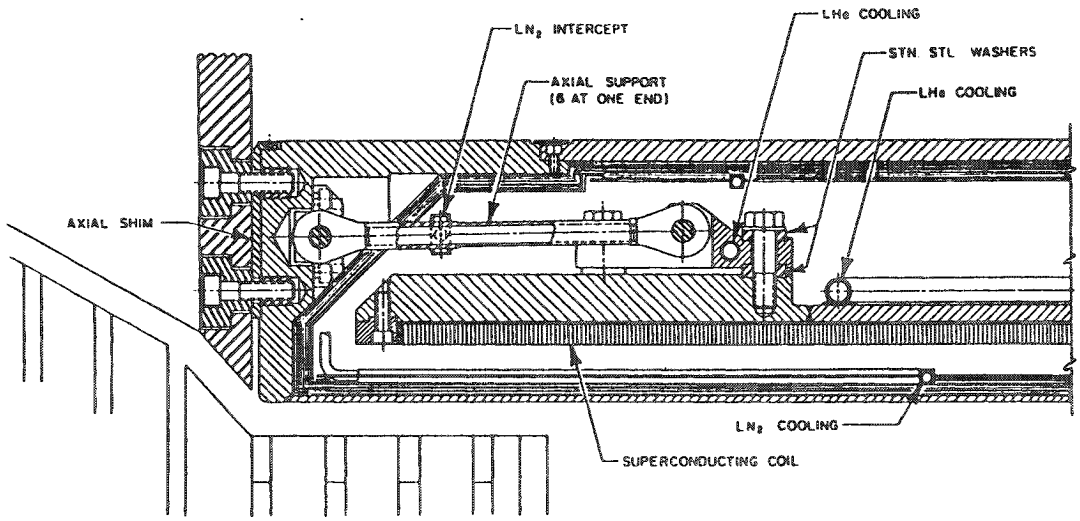

Figure 10: Detail of one end of CDF solenoid magnet

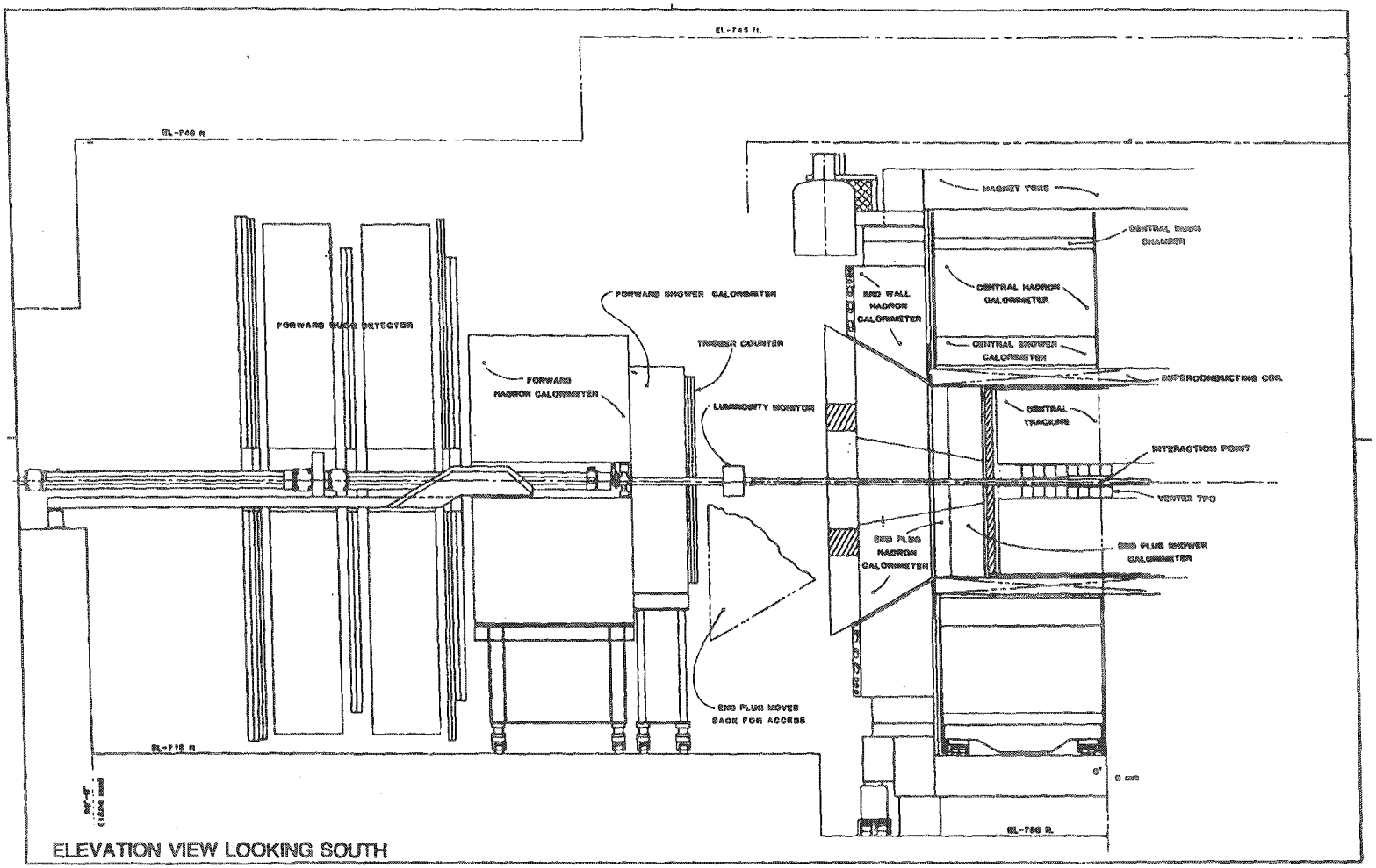

Figure 11: Elevation view of half of the CDF detector

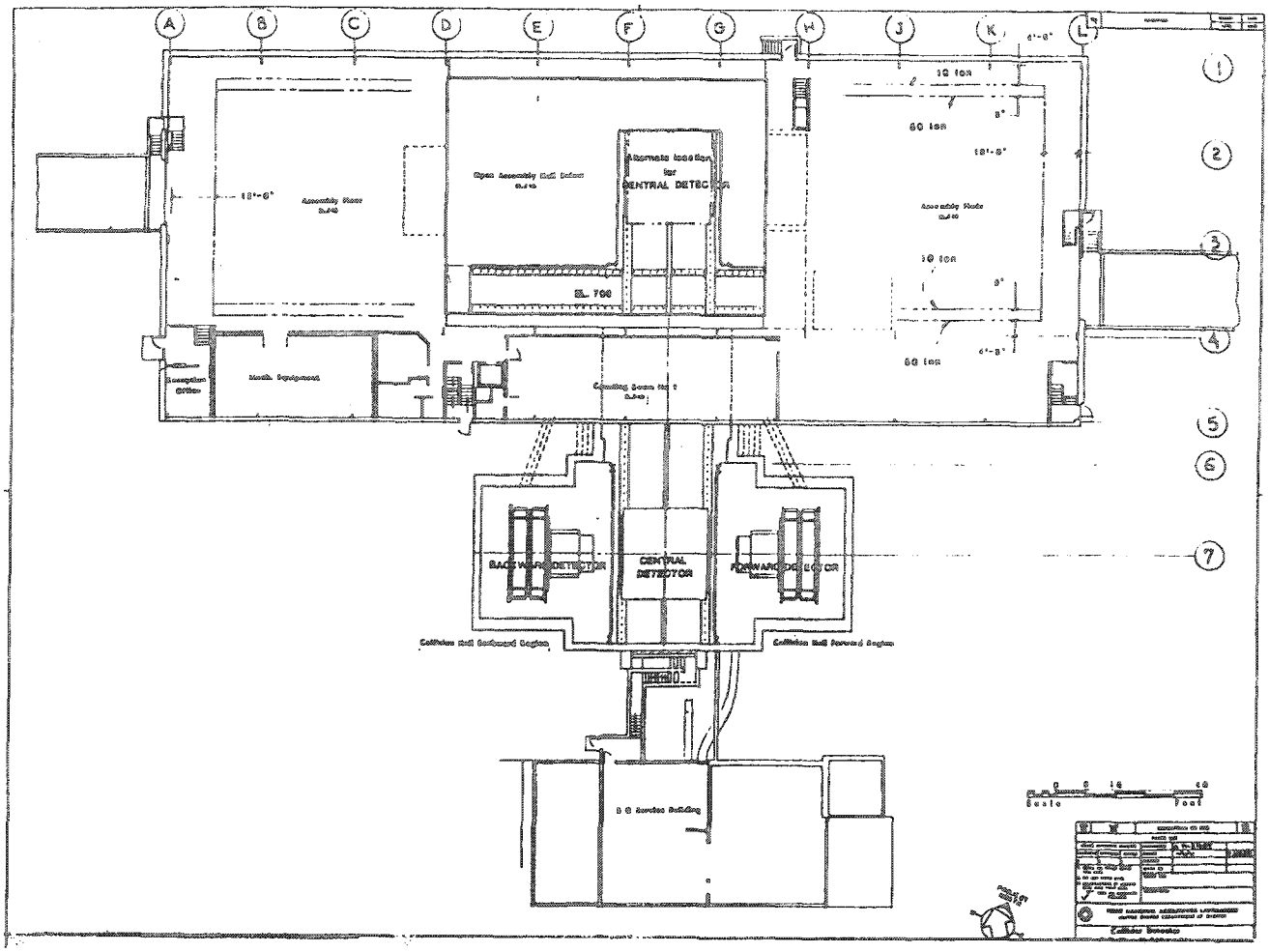

Figure 12: A plan view of the BØ Experimental Area at Fermilab

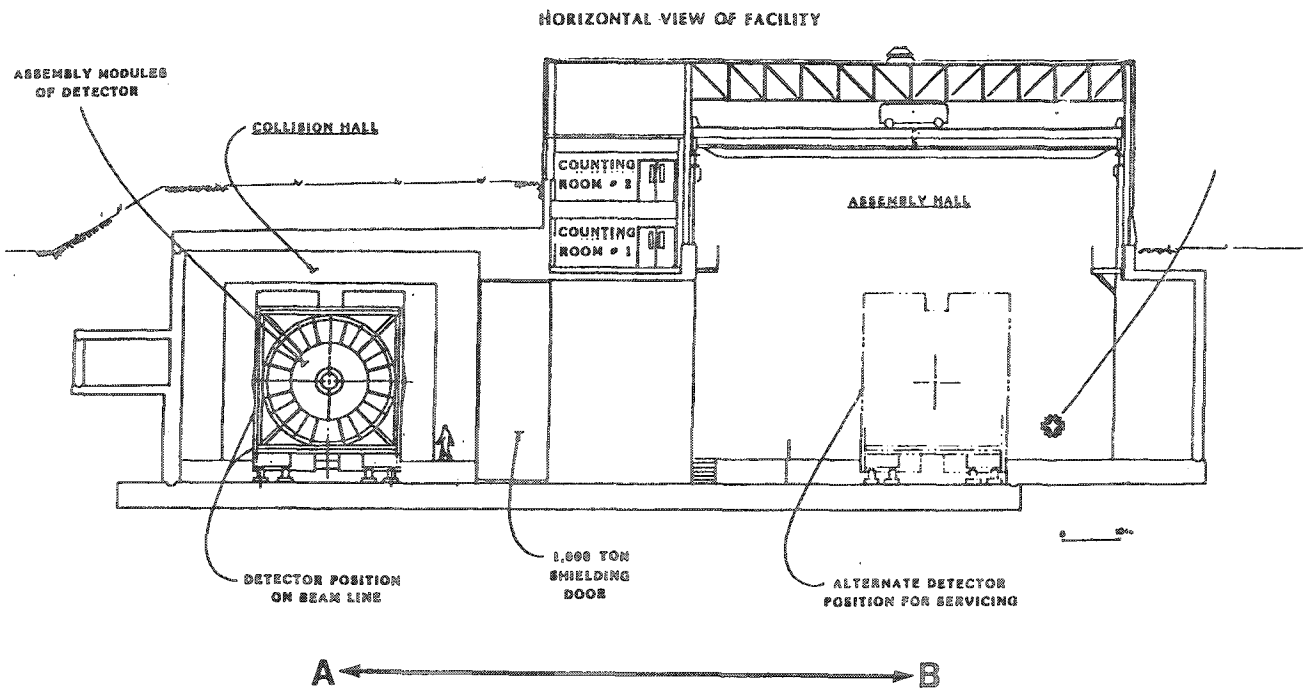

Figure 13: An elevation view of the BØ Experimental Area

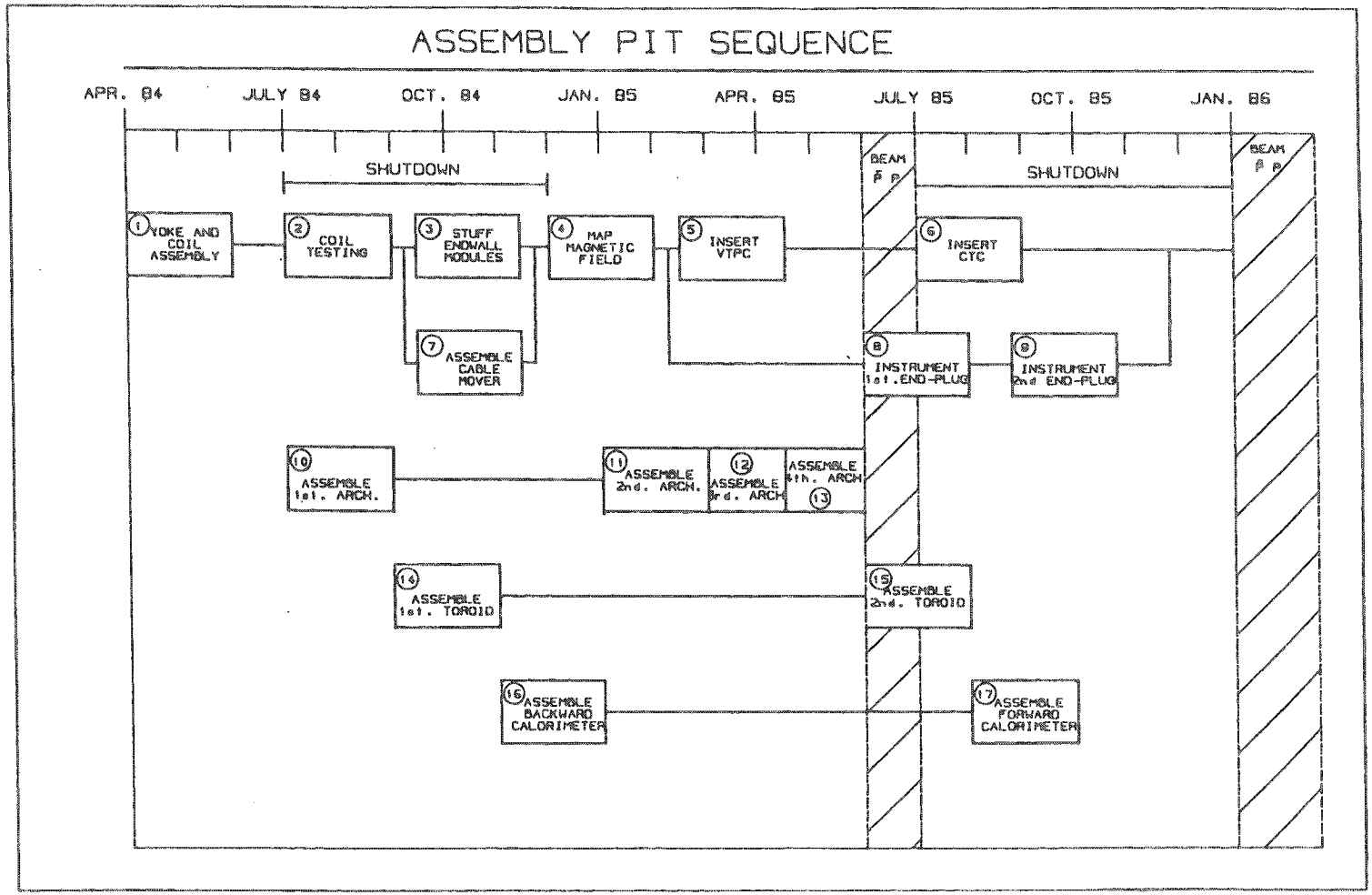

Figure 14: Assembly Sequence and Timetable for mechanical assembly of CDF components in the BØ Assembly Hall

THE DO PROJECT AT FERMILAB

Michael D. Marx
State University of New York
Stony Brook

The DO Project will explore 2 TeV $\bar{p}p$ collisions at Fermilab using a highly optimized calorimetric detector, to elucidate the new physics coming out of the SppS, and to explore the new higher energy regime.

1. HISTORICAL

Soon after the beginning of the Tevatron construction, Fermilab formed a group (CDF) to design and construct a major experimental facility to study pp collisions at the BO region. Three years later, in February 1981, they solicited proposals for a second experiment to be performed at DO. This experiment was intended to be of a more modest and limited scope. Faced with an array of such limited experiments, the Program Committee (PAC) suggested more ambitious efforts. Three 4π calorimetric detectors were then proposed in the following year. Again the PAC found weaknesses in all proposals, and urged construction of a detector at DO having the following features (partially embodied in the three proposals):

1) Good electromagnetic energy resolution with sufficient background suppression.
2) Good hadronic calorimetry with sufficient thickness and a minimum of cracks.
3) Muon identification and measurement.
4) Highly segmented calorimetry.

A collaboration consisting of many of the original proponents augmented by several other groups submitted a Design Report [1], which has been endorsed (finally) by the PAC. The detector, which I will describe, embodies these desired features, surpassing the guidelines for performance, and has been optimized using the experience of the groups at CERN.

2. EXPECTATIONS FOR DO

By the time Tevatron I turns on for physics in late 1986, UA1 and UA2 will probably have accumulated an integrated luminosity approaching 10^{37} cm^{-2}. This translates into a probable sample of 2000 $W^{\pm} \to e^{\pm} \nu$ and 200 $Z^{\circ} \to e^{+} e^{-}$ events. The general properties of the leptonic decays of the bosons will have been studied, but the small sample of "new physics" events (as heard here at Bern) [2] will probably not be completely understood. We have heard, for example, that with this generation of detectors it is unlikely that evidence for the top quark will be found [3].

By contrast, in a single four-month run at TeV I, with 50% efficiency at $= 10^{30}$ cm^{-2} s^{-1}, we would expect to accumulate five times the total CERN sample of $W^{\pm}$ and Z°. The mass scale for production of new objects would be extended by a factor of three.

This allows the possibility of precision studies of the weak parameters

($\sin^2\Theta_W$ and ρ) and detailed studies of rare decays (like $Z^0 \to ee\gamma$). In addition, the hints that we have heard of new physics at higher masses will translate into an even greater advantage at TeV I, where the cross section for production of 150 GeV objects will be an order of magnitude higher than at CERN.

Thus we feel that the combination of the higher energy and luminosity will yield rich and exciting physics opportunites.

3. DESIGN CRITERIA FOR DØ

The design of the DØ detector has been able to use its late start in the UA1, UA2, and CDF field to advantage, by optimizing the parameters based on our perception of the strengths and weaknesses of the present generation of detectors. In view of the spectacularly successful runs at the SppS we now feel that the list of particles which will be relevant at 2 TeV are the leptons -- electrons and muons and "neutrinos" -- jets, and photons. For each of these we have attempted to design a detector which would establish their identities and accurately measure energy and angle over the largest possible solid angle.

3.1 Improved Measurement of Electrons and Muons

For electrons we intend to stress excellent energy resolution, which should not be dominated by systematics or calibration problems. This will enable us to precisely study the parameters of the electronic decays of the $W^{\pm}$ and Z^0 and to search for narrow e^+e^- states. In addition, we hope to improve on electron identification, both at lower transverse momentum and for electrons in the vicinity of other particles. This feature, we hope, will permit us to search for and tag heavy flavor decays. We do not intend to measure the sign of the electrons, and feel that this will not limit most of the physics we will address.

For muons, the emphasis will be on identification, even in the core of jets. We intend to measure the sign and also to obtain moderate momentum resolution over most of the solid angle. Thus we expect to use the muons as a check on lepton universality in any new effects, and as a means of monitoring backgrounds to lepton and dilepton signals. This will be useful for flavor tags and for understanding the dimuon signals reported by UA1 at this conference.

This sensitivity to both electrons and muons will be crucial in such things as supersymmetry searches, where the presence of leptons must be excluded, and will greatly increase the sample of events for studies of multilepton events from heavy flavor decays.

3.2 Improved Hadronic Energy Resolution

We intend to greatly improve hadronic calorimetry over existing experiments. This resolution will permit studies of multijet masses for studies of hadronic decays of the bosons as well as better sensitivity to such effects as the 150 GeV di-jet enhancement reported by UA2 here. We will also be able to improve missing p_T measurements, which as we have heard here, are needed for studies of events with neutrinos or supersymmetric particles.

Both of these resolutions are determined by the inherent calorimeter resolutions, by the relative response to electromagnetic or hadronic particles, by the cracks and dead spaces in the calorimeter and by the angular resolution at small angles to the beam.

3.3 Improved Segmentation

The DO design will implement a much higher degree of segmentation for the calorimetry, both in transverse tower size and in longitudinal segmentation. The transverse segmentation will permit better electron discrimination by improved rejection of charged hadron-proton overlaps, improved detection of electrons near jets, better sensitivity to multijet events and improved angular resolution for missing p_T resolution. The longitudinal segmentation permits measurement of shower profiles for electron hadron discrimination and will permit a statistical discrimination between single and multiphoton induced electromagnetic showers. This will permit measurements of γ/π^0 ratios and discrimination of gluon jets.

3.4 Absence of Central Field

We have made a design choice of eliminating a central magnetic field. While this does not allow us to determine the signs of particles (except muons, externally), we gain the advantages of simplicity in straight line tracking; compactness, which permits the full coverage for calorimetry and muons; and very little material in front of the calorimetry reducing the conversion background and introducing no degradation in electromagnetic resolution.

Finally, without the complexities introduced everywhere by a magnet, the scope of the project is such that it can be designed and built on a much shorter time scale.

3.5 Homogeneity

Finally, we have opted for a design with only three basic systems, each of which will have uniform performance and response over the full solid angle. Each system will be of proven technology with only extensions of scale for DO.

4. PHYSICS POTENTIAL

The physics goal for DO will cover the same ground as the other collider experiments, albeit with a slightly different emphasis. This program divides naturally into three classes -- first, precision studies of the electroweak models including properties of the intermediate bosons; second, QCD studies by means of $W^{\pm}$, Z^0 production, high p_T jets and single particles spectra; and finally, searches for new phenomena such as top, additional bosons, heavy quarks and leptons, supersymmetric particles, and we hope, new things we haven't thought of. As an indication of the power of our design, we discuss the expected performance on a few of these topics.

4.1 Properties of $W^{\pm}$ and Z^0

Crucial tests of the standard model can be performed by comparison of the W and Z masses and widths. By discarding one electron from the Z decay, one can measure these parameters for both W and Z with a similar technique. Thus one can construct the transverse mass:

$$M_T^2 = 2\, E_T^e\, E_T^{miss}\, (1 - \cos \Theta_{em}) \qquad (1)$$

where E_T^e is the transverse energy of the electron, E_T^{miss} is the missing transverse energy, and Θ_{em} is the angle between the electron and missing

momentum direction. Smith et al. [4] have shown that this quantity is sensitive to the mass and width of the object but not its production dynamics. This is shown in Figures 1 and 2 which show the sensitivity of the M_T distribution for the W for different production p_T and for different natural widths. The resolution in M_T depends critically on the resolution in missing p_T. Figure 3 shows the missing E_T resolution for DO and CDF for a sample of ISAJET-generated 50 GeV p_T jets. For DO, 1.2% of these events are measured to have over 10 GeV missing while for CDF the fraction, by their estimate, would be 15%.

Using this method, we anticipate, in a standard four-month run, achieving an error on the masses of

$$\delta M_W \sim 50 \text{ MeV} \qquad \delta M_Z \sim 150 \text{ MeV} , \tag{2}$$

about six times better than UA1. For the ratio of the widths, we expect

$$\delta(\Gamma_W / \Gamma_Z) < 10\% . \tag{3}$$

This will yield errors on the electroweak parameters of

$$\begin{aligned} \delta \sin^2\theta_W &\sim .002 \\ \delta \rho &\sim .003 . \end{aligned} \tag{4}$$

This precision will be critical for tests of GUT models, determining the Higgs structure, constraints on the top mass, and tests of QCD corrections to the masses and widths.

We can also make a direct measurement of the width of the Z^o, utilizing our superior electromagnetic resolution. This measurement directly counts the number of neutrino species and can give a constraint on the existence of $t\bar{t}$ states below the Z mass.

The measurement depends on both the electron resolution and statistics, such that the error on the width is given by

$$\delta\Gamma = \left(\frac{2}{N}\right)^{1/2} \left(\Gamma_Z^2 + (2.35\ \sigma_m)^2\right)^{1/2} \tag{5}$$

where N is the number of decays and σ_m is the mass resolution. This is shown in Figure 4 where one sees that with less than 1000 events we will be below the contribution of an additional neutrino.

4.2 Search for the Top Quark

The present generation of detectors have been unsuccessful in the search for top. One of the best places to look is in the decay

$$W \to t\bar{b}$$
$$\hookrightarrow be^+\nu .$$

To carry out this search one needs rate, excellent electron identification at lower p_T and in the neighborhood of other particles (in a jet), a high degree of segmentation, and good missing p_T resolution. Figure 5 shows the signal we

would expect above background for a top mass of 30 or 60 GeV. This is after minimal isolation cuts on the electron, and cuts such that

$$E_T(\text{electron}) > 10 \text{ GeV/c} \qquad E_T(\text{missing}) > 10 \text{ GeV/c}.$$

In a four-month run, we would have 75 events for a top mass of 30 GeV and 150 events at 60 GeV. For similar cuts, the SppS experiments expect 1 - 2 events and see a background of order 10 events [3].

5. THE DETECTOR

The detector we have designed is shown in cut-away perspective in Figure 6, and a quadrant is shown in section in Figure 7. Starting from the collision region one encounters the three main detection systems: a central tracking system including transition radiation detectors; a liquid argon uranium calorimeter system having a central section, two end caps, and two plug calorimeters close to the beam lines; and finally a muon system consisting of proportional drift tubes (PDT's) and over 3000 tons of magnetized iron toroids.

5.1 Central Tracking System

The central tracking system consists of a drift chambers system with delay line readout for the second coordinate and a transition radiation system (TRD). A primary purpose for both of these systems is the suppression of backgrounds to many of our interesting signals. Thus, for electrons, the drift chambers must supply a direction for the track that can be accurately correlated with a shower in the calorimeter, to suppress the background of a soft, charged hadron overlapping a stiff photon or π^0. The system must have sufficiently good two-track resolution to permit identification of electrons in or near jets. The drift chambers will also measure the dE/dx loss to be able to distinguish converted photon pairs from electrons. The tracks in the drift chambers will provide a collision vertex for use in triggering on muons. The TRD system will be used to provide additional electron identification, especially for those electrons buried in jets. Finally, a constraint on the design of this system is that it be compact, and yet provide little extra material for conversion of photons, and permit space for eventual inclusion of a micro-vertex detector.

The drift chamber system is shown in Figure 8. The chamber is shown in Figure 9. The chamber is comprised of inner and outer sections consisting of two and four sections respectively. Each section is divided into 32 supercells as shown in Figure 10, with adjacent layers of supercells rotated to resolve left-right ambiguities. Each supercell contains four sense wires and two delay lines, so that one obtains two space points and two additional azimuthal coordinates, and four samples of dE/dx per supercell [5].

The TRD system will be located between the two drift chamber sections, and will consist of four layers of radiator (probably lithium foils) each followed by a Xe-Ar PWC which acts as the X-ray detector. This detector will be equipped with cluster counting electronics, and thus will be effectively blind to the sea of ionizing particles below the X-ray cluster threshold [6].

5.2 Liquid Argon Calorimetry

At the heart of the DO detector is a system of five liquid argon calorimeters. These calorimeters will use alternated plates of copper and

uranium as the absorber. The system is designed to be completely "hermetic," and homogenous with coverage down to 1° from each beam line. Uranium has been chosen not only for its density, but for its property of fission compensation, which will enable us

to achieve hadronic resolutions of $\frac{\Delta E}{E} \sim \frac{.38}{\sqrt{E}}$, and equally important,

almost equal response to electromagnetic and hadronic showers. The design will ensure that no detector cracks or dead spaces point to the interaction region. Because of the unit gain and stable response of such a system, we expect to be able to control systematic effects at the 1/2% level.

These properties will enable us to measure the energy flow of jets, electrons, and photons with unprecedented precision, and to measure missing energy and momentum with about half the error of current detectors.

Although design studies have not been completed, one of the designs for the central calorimeter is shown in Figure 11. It consists of 16 azimuthal wedges, 165 cm thick, with three longitudinal sections along the beam. Figure 12 shows the internal structure of one section. The front electromagnetic compartment has 1/2 radiation length absorber plates and is read out four times longitudinally to enable us to reject non-electromagnetic backgrounds. The size of the transverse towers is approximately 6 x 6 cm^2 with 1 cm strips located at the peak of the shower. The hadronic section has three longitudinal readouts with 4 mm thick uranium plates and one leakage section with very coarse sampling. The typical hadronic tower is 15 x 15 cm^2.

The two end cap calorimeters which cover the region down to 5°, and end plugs which go to 1°, will be similar devices. They have the simplification of having all absorber plates standing vertically, and the complication of having readout towers which vary greatly in size, with very high readout density close to the beam. We hope, however, to share as much as possible in mechanical, cryogenic, and electrical techniques between all five calorimeters.

Our original scheme for readout of the signals utilized three-layer printed circuit boards, with the readout pattern etched onto the two outside layers, and the signals lines in the inside layer, connected to the outsides by plated-through holes. This method is conceptually simple, but extraordinarily expensive. We are exploring other schemes, such as subdividing the copper absorber plates and reading the signals directly from the copper. We are also investigating laminating these copper tiles between fiberglass sheets, effectively making thick PC boards.

The electronics for readout of the small signals has been optimized for the time structure of TeV I. A circuit has been designed which samples the signal before and after a bunch crossing, as shown in Figure 13, and performs a subtraction. This signal is then available as a DC level and can be multiplexed, allowing a drastic reduction in cables from the 50,000 channels to be analyzed.

5.3 Muon System

The muon system has been designed to measure the spectrum of muons from very low p_T (~ 2 GeV/c) out to the highest observable momenta, with moderate resolution. The coverage extends down to 8° of either beam. Our design

surrounds the minimum of seven absorption lengths of the calorimetry, with an additional meter of magnetized iron. With this much absorber it would take a 600 GeV incident hadron at 90° (5000 GeV at 10°) to produce on average one punchthrough particle. The momentum measurement is accomplished with PDT's, distributed at two places between the calorimeter and iron, and at three stations outside the iron. Each station measures each coordinate twice to resolve ambiguities.

With this system we will achieve a momentum resolution $\Delta p/p \sim 20\%$ up to $p_\perp$ of 200 GeV/c. To this momentum we will be dominated by multiple Coulomb scattering in the iron and uranium. For those isolated muons where we are able to match with a track in the central drift chambers, we can improve the resolution to $\Delta p/p \sim 18\%$.

In order to have access to the detector, the iron is designed in five pieces as can be seen in Figure 6. The central iron consists of two retractable clamshells and a baseplate which supports the central and end cap calorimeters. The end iron toroids, which support the end plug calorimeters, can be separated from the central iron. The system is designed to allow personnel access into the detector in the collision hall.

The detector parameters are summarized in Table I.

6. STATUS

TeV I is on schedule with first collisions expected by mid-1985 and a first physics run in late 1986. The expected luminosity is 10^{30} cm^{-2} sec^{-1} with low β insertions at B0 and D0.

We feel that given an aggressive funding schedule D0 could be ready by mid-1987. There is, however, a funding crisis in the US, and competition for funds between D0, SLD (the second detector at SLC) and present commitments that will slow this down. We are at present negotiating a funding profile with Fermilab and the DOE which we hope will assure completion of the detector by the end of 1988. We, of course, would expect to take beam earlier than this with a partial detector.

Prototypes of all systems will be tested in beams this spring, and engineering of the systems has begun. The collision and assembly halls are presently being detailed, and is shown in plan in Figure 14.

We are all very excited by the hints of new physics presented at this conference, and feel confident that the D0 detector will have an opportunity to contribute to this exciting field.

REFERENCES

1. Design Report -- An Experiment at D0 to Study Antiproton-Proton Collisions at 2 Tev. The D0 Coollaboration, 12/83 (unpublished). The Collaboration presently consists of ~ 75 physicists from: University of Arizona, Brookhaven National Laboratory, Brown University, Columbia University, Fermilab, Florida State University, University of Maryland, Michigan State

University, Norwestern University, University of Pennsylvania, CERN, Saclay, State University of New York (Stony Brook), and Virginia Polytechnic Institute.

2. See talks by UA1 (C. Rubbia) and UA2 (J. Hansen and A. Roussarie) these Proceedings.

3. See talks by F. Halzen and A. Martin, these Proceedings.

4. J. Smith et al., Phys. Rev. Letters 50 (1983) 1738.

5. T. Behnke, et al., Progress in the Design of the Central Drift Chamber for DØ, DØ internal note # 59, 2/84 (unpublished).

6. C. Fabjan et al., CERN-EP/83-43.

Table I

DETECTOR SUMMARY

1.	Resolutions	e, γ:	$\frac{\sigma}{E} = \frac{10\%}{\sqrt{E}} + 0.5\%$
		Hadrons:	$\frac{\sigma}{E} = \frac{40\%}{\sqrt{E}}$
		Muons:	$\frac{\sigma}{p} = 20\%$
2.	Coverage	e, γ, Hadron:	$\theta \geq 1°$
		muons:	$\theta \geq 8°$
3.	Segmentation		
	Central Electromagnetic:		3360 towers (x 4 depth)
	Central Hadron:		600 towers (x 4 depth)
	End Electromagnetic:		1280 towers/end (x 4 depth)
	End Hadron:		576 towers/end (x 3 depth)
	Plug Electromagnetic Hadron:		360 towers/end (x 7 depth)
4.	Totals		2500 total hadronic towers
			6500 total EM towers
			1400 drift wires
			700 delay lines
			29000 proportional drift tubes

FIGURE CAPTIONS

Fig. 1: Distribution of events with transverse mass, m_T, for $W \to e\nu_W$ from Ref. 4. The solid line assumes $p_T^W = 0$; the dashed line is for $p_T^W = 50$ GeV/c.

Fig. 2: Distribution of events with transverse mass for $W \to e\nu$ with $\Gamma_W = 1$ GeV (dashed), 2.5 GeV (solid), and 5 GeV (dot-dashed).

Fig. 3: Cross section vs. missing p_T for various contributions. The solid line is for losses in a 1° beam hole only; -o- is for 1° beam hole and energy resolution in calorimetry. The dashed line includes the effect of beam hole, energy resolution, and angular smearing effects (all hadron impact points are smeared with σ_x, σ_y = 2 cm). The effect of 8 azimuthal cracks of width 2.5 cm over the central calorimeter (not shown) is to broaden the missing p_T-distribution for $p_T^M > 10$ GeV/c without appreciable effect below 10 GeV/c. The contributions from signals due to ν (heavy quark) production and 100 GeV gluinos are also shown.

Fig. 4: Error on Z° width versus number of events using the mass resolution of this detector (σ_M = 1.19 GeV).

Fig. 5: Distribution of events for $t \to be\nu$ and background (shaded bands) after cuts on an isolated electron, E_T (electron) > 10 GeV, and E_T (missing) > 10 GeV.
●: M_T = 30 GeV, Δ: M_T = 60 GeV.

Fig. 6: Cut away perspective of the DØ detector showing major sub-systems.

Fig. 7: Section of one quadrant of the detector.

Fig. 8: Profile of the central chamber proposed for DØ in the rz-plane, showing possible locations for the end chambers. (Only one quadrant shown.)

Fig. 9: Cross-section through the proposed central chamber in the rφ-plane. (Only one quadrant shown.)

Fig. 10: Schematic view (rφ-plane) of the wire geometry in supercells.

Fig. 11: End view of central Uranium Liquid Argon calorimeter.

Fig. 12: Readout segmentation for central calorimeter in r-φ and r-z views of a typical module.

Fig. 13: (top) -- Charge preamplifier signal.
(bottom) -- Block diagram of the electronics.

Fig. 14: Plan view of the DØ collision and assembly hall.

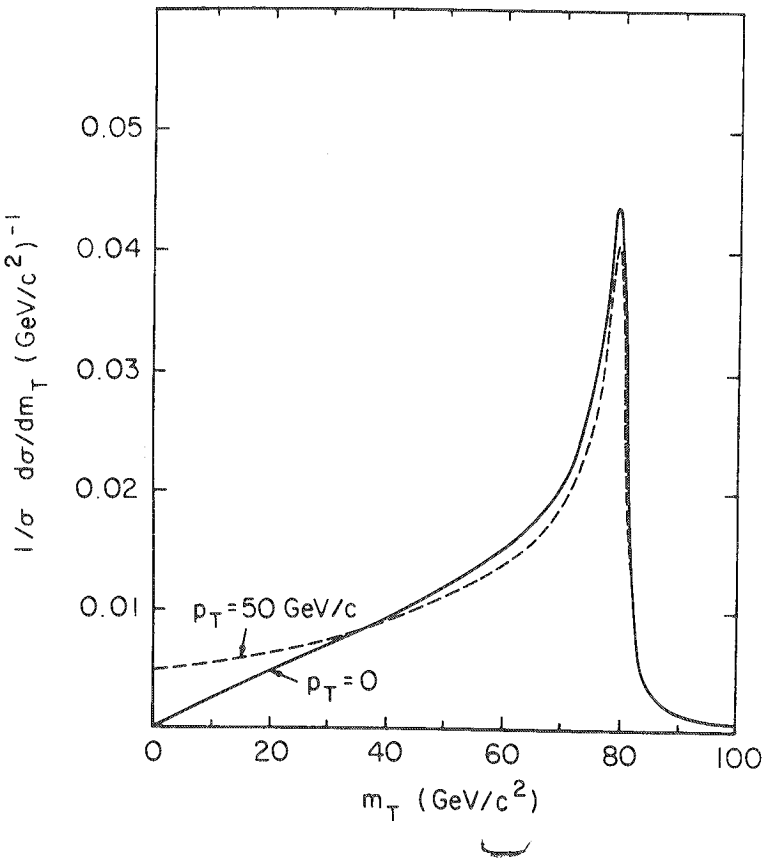
0.05
0.04
0.03
0.02
0.01
$1/\sigma\ d\sigma/dm_T\ (GeV/c^2)^{-1}$
$p_T = 50$ GeV/c
$p_T = 0$
0
20
40
60
80
100
$m_T\ (GeV/c^2)$

Fig. 1

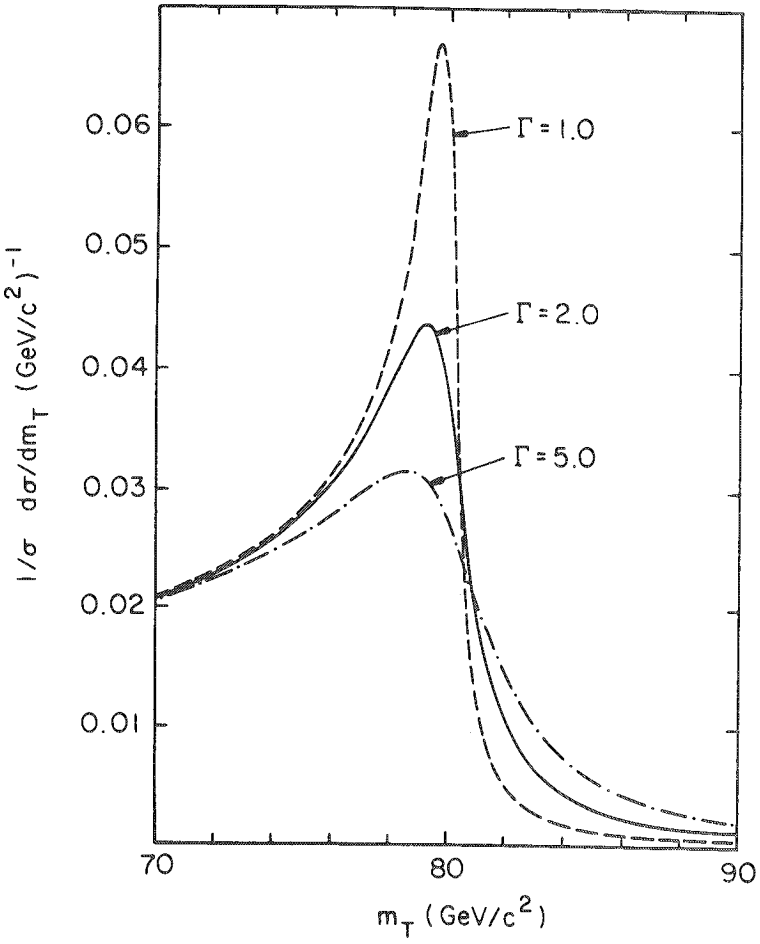
0.06
0.05
0.04
0.03
0.02
0.01
$1/\sigma\ d\sigma/dm_T\ (GeV/c^2)^{-1}$
$\Gamma = 1.0$
$\Gamma = 2.0$
$\Gamma = 5.0$
70
80
90
$m_T\ (GeV/c^2)$

Fig. 2

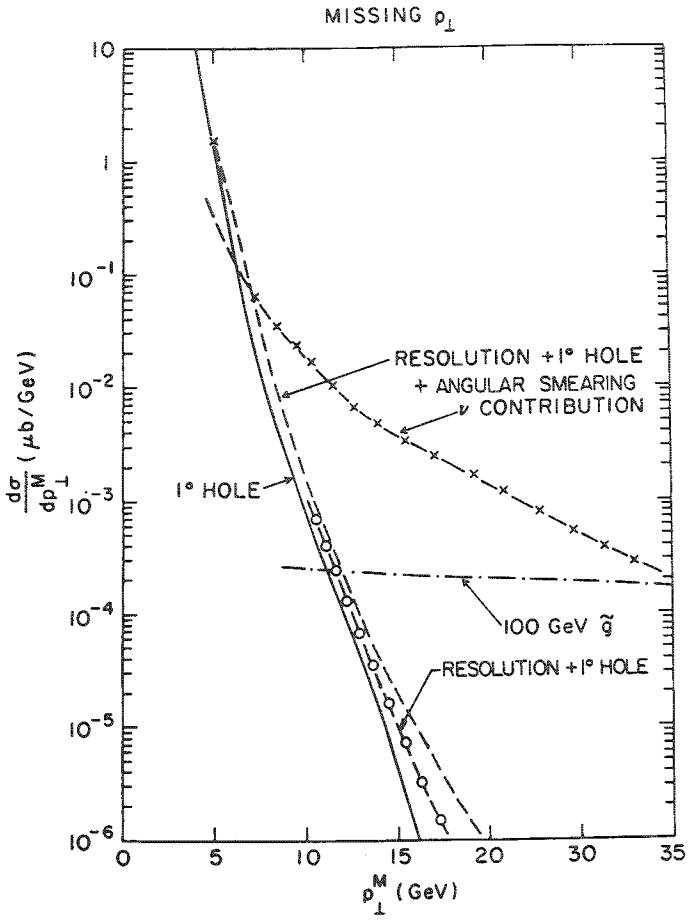
MISSING $p_\perp$
$\frac{d\sigma}{dp_\perp^M}$ (μb/GeV)
$p_\perp^M$ (GeV)
RESOLUTION +1° HOLE
+ ANGULAR SMEARING
ν CONTRIBUTION
1° HOLE
100 GeV $\tilde{g}$
RESOLUTION +1° HOLE

Fig. 3

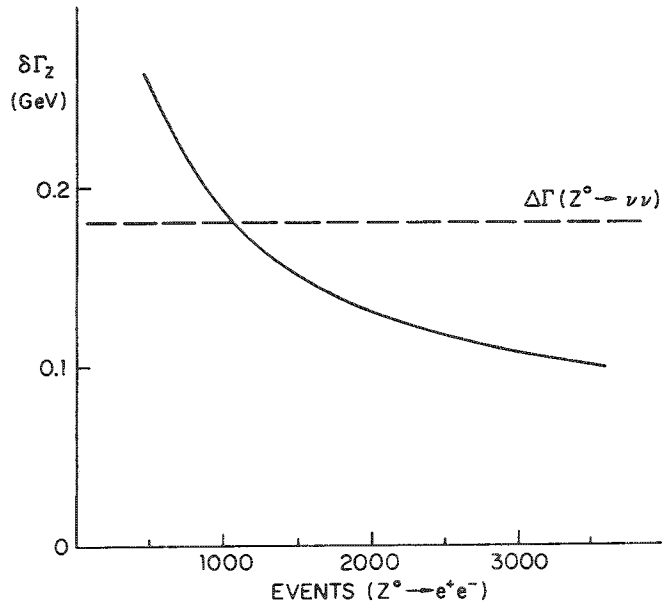
$\delta\Gamma_Z$
(GeV)
$\Delta\Gamma(Z^\circ \to \nu\nu)$
EVENTS ($Z^\circ \to e^+e^-$)

Fig. 4

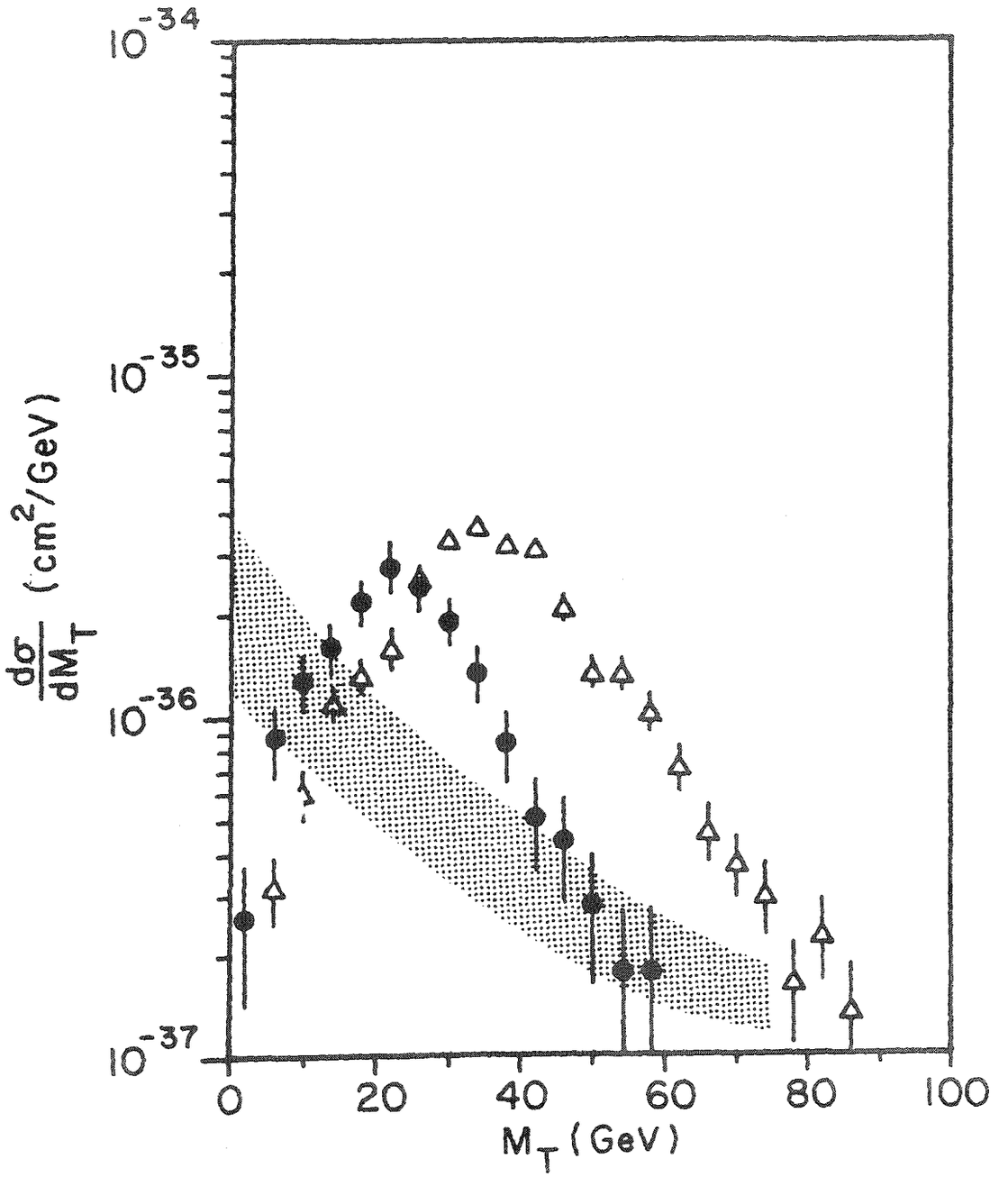
10^{-34}
10^{-35}
10^{-36}
10^{-37}
$\frac{d\sigma}{dM_T}$ (cm^2/GeV)
0
20
40
60
80
100
M_T (GeV)

Fig. 5

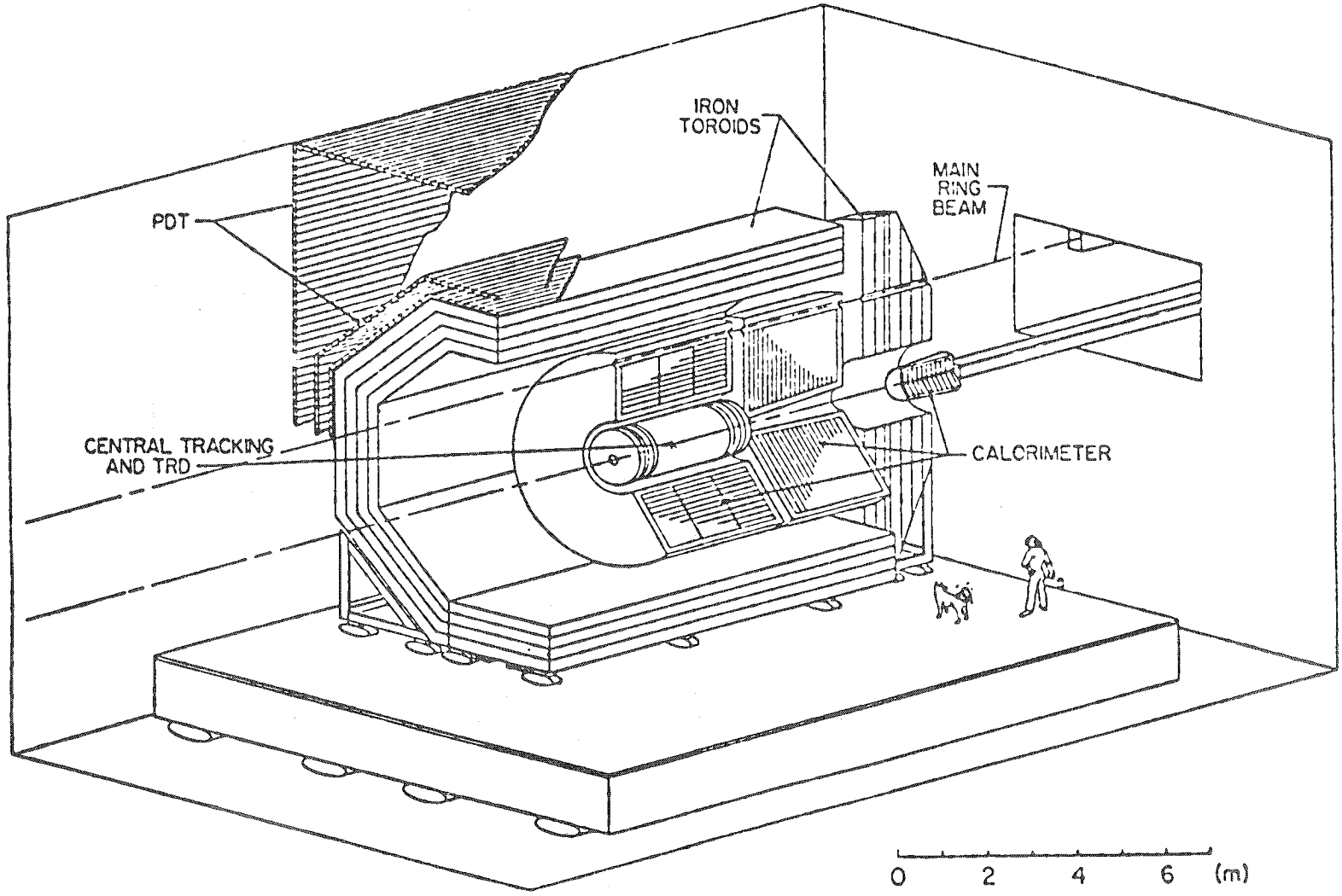
IRON
TOROIDS
MAIN
RING
BEAM
PDT
CENTRAL TRACKING
AND TRD
CALORIMETER
0
2
4
6
(m)

Fig. 6

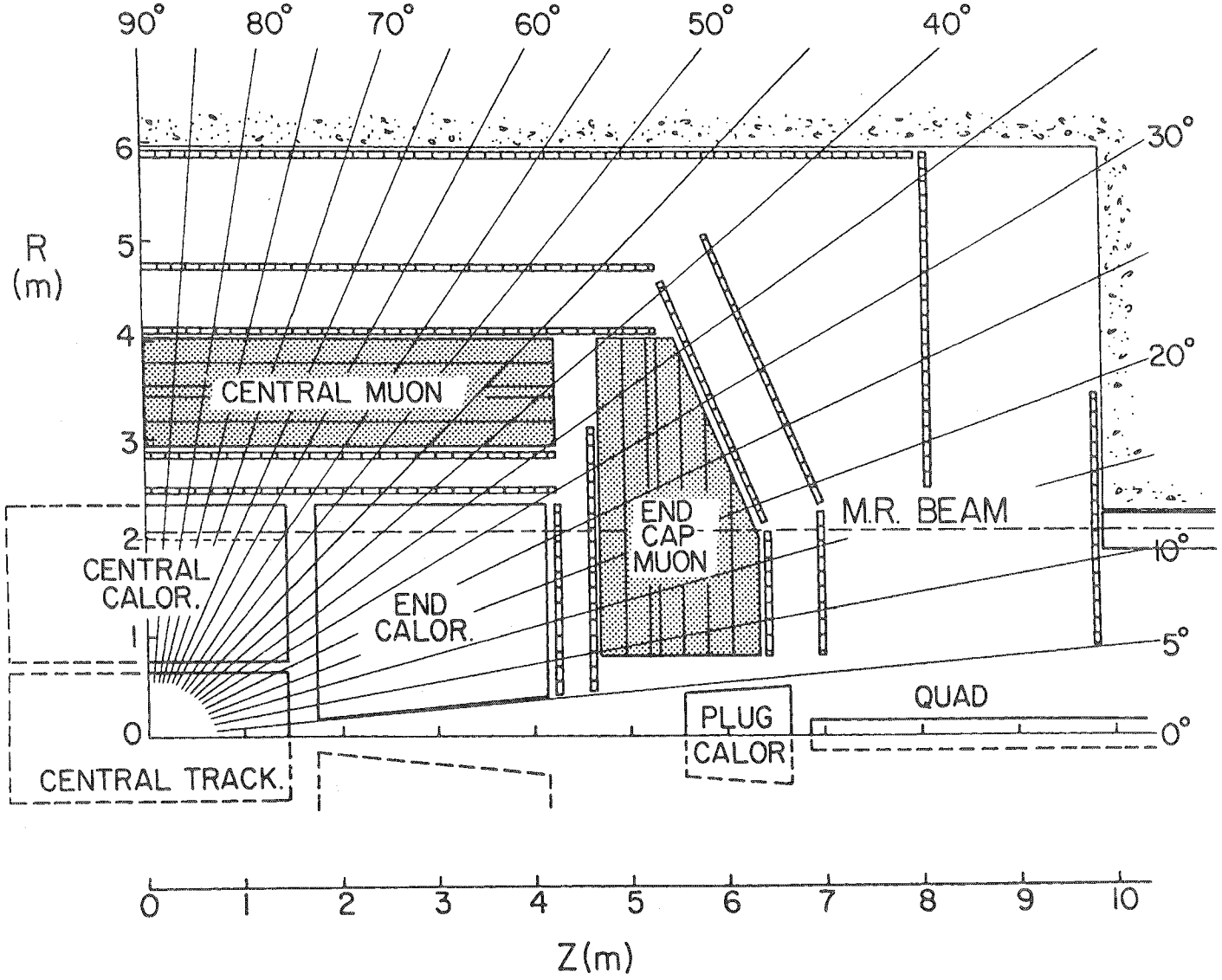
90°
80°
70°
60°
50°
40°
30°
20°
10°
5°
0°
R
(m)
6
5
4
3
2
1
0
CENTRAL MUON
CENTRAL
CALOR.
END
CALOR.
END
CAP
MUON
M.R. BEAM
PLUG
CALOR
QUAD
CENTRAL TRACK.
0
1
2
3
4
5
6
7
8
9
10
Z(m)

Fig. 7

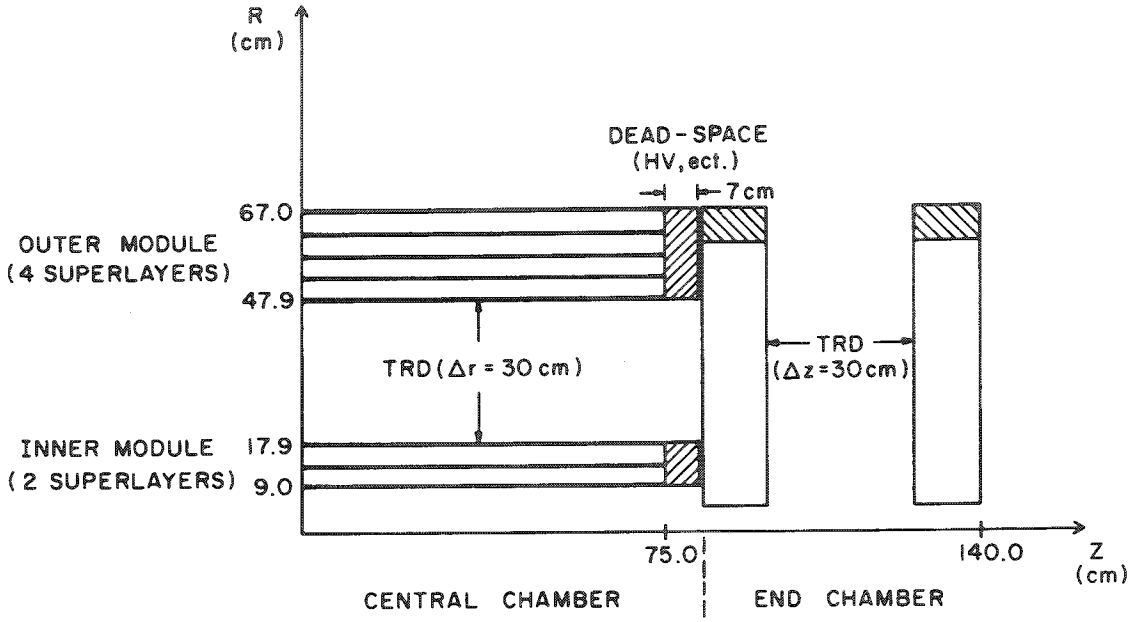
R
(cm)
DEAD-SPACE
(HV, ect.)
7cm
67.0
OUTER MODULE
(4 SUPERLAYERS)
47.9
TRD (Δr = 30 cm)
TRD
(Δz=30cm)
INNER MODULE
(2 SUPERLAYERS)
17.9
9.0
75.0
140.0
Z
(cm)
CENTRAL CHAMBER
END CHAMBER

Fig. 8

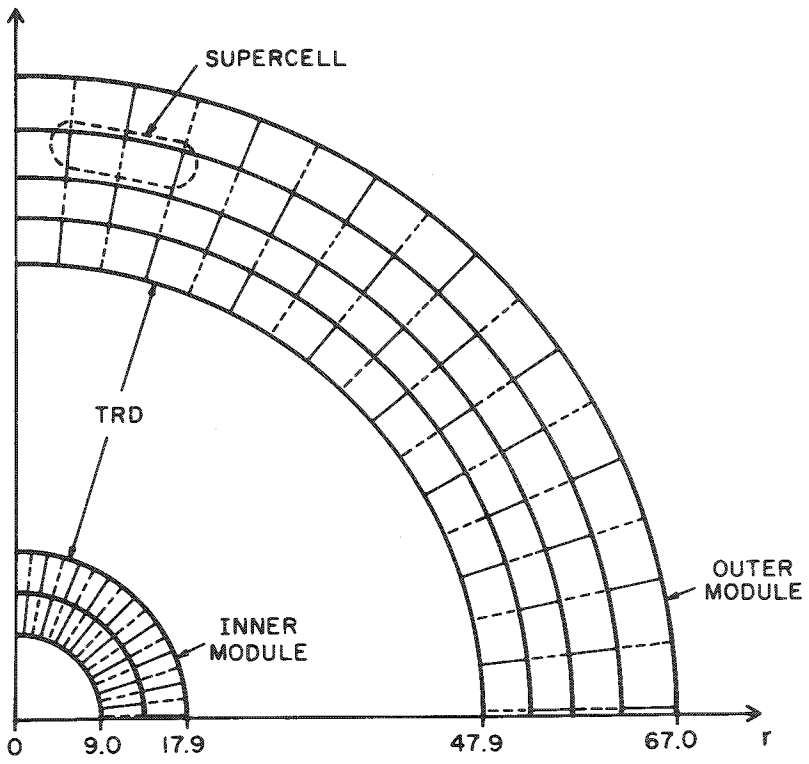
SUPERCELL
TRD
INNER
MODULE
OUTER
MODULE
0
9.0
17.9
47.9
67.0
r

Fig. 9

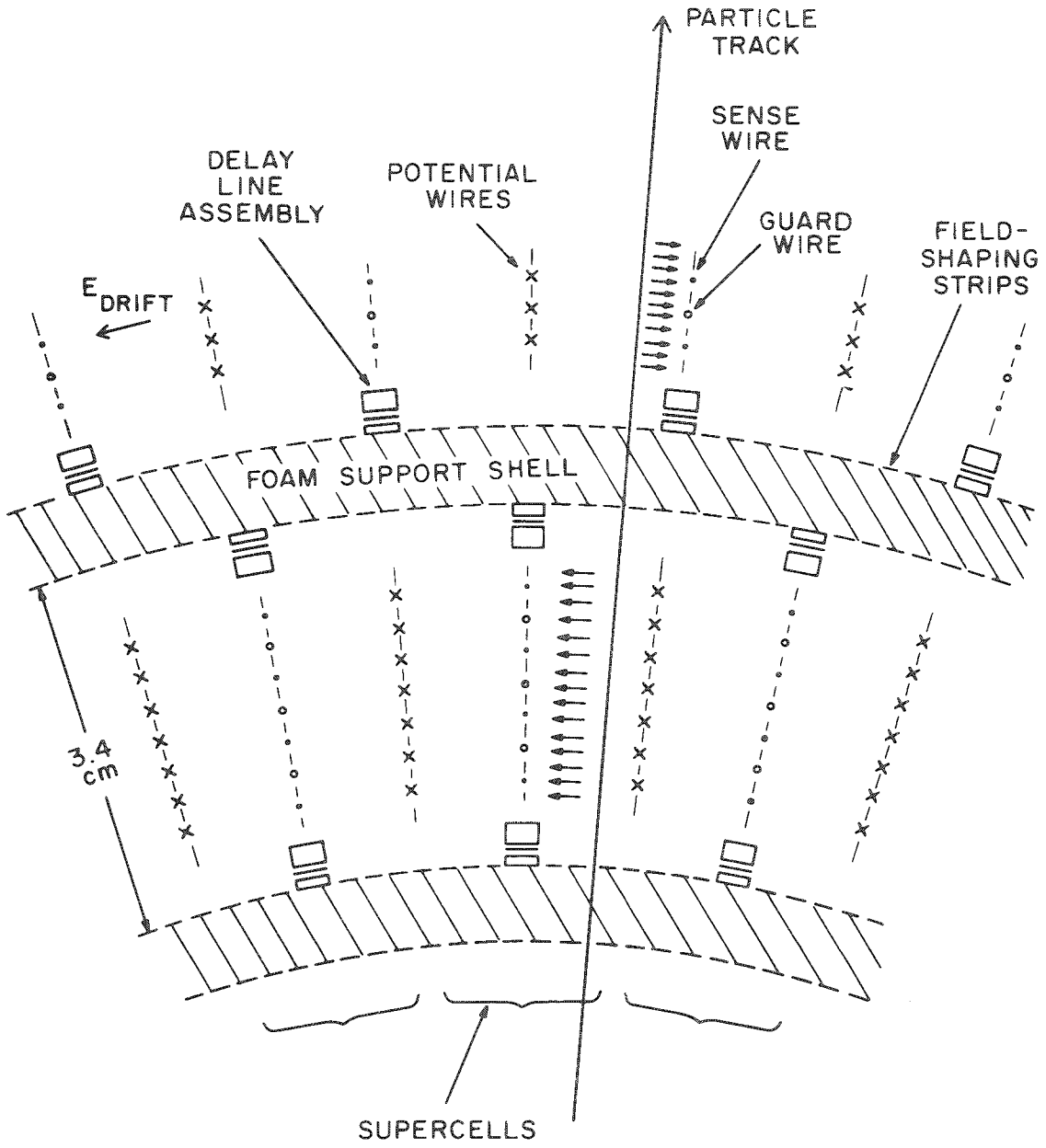
PARTICLE TRACK
SENSE WIRE
DELAY LINE ASSEMBLY
POTENTIAL WIRES
GUARD WIRE
FIELD-SHAPING STRIPS
E DRIFT
FOAM SUPPORT SHELL
3.4 cm
SUPERCELLS

Fig. 10

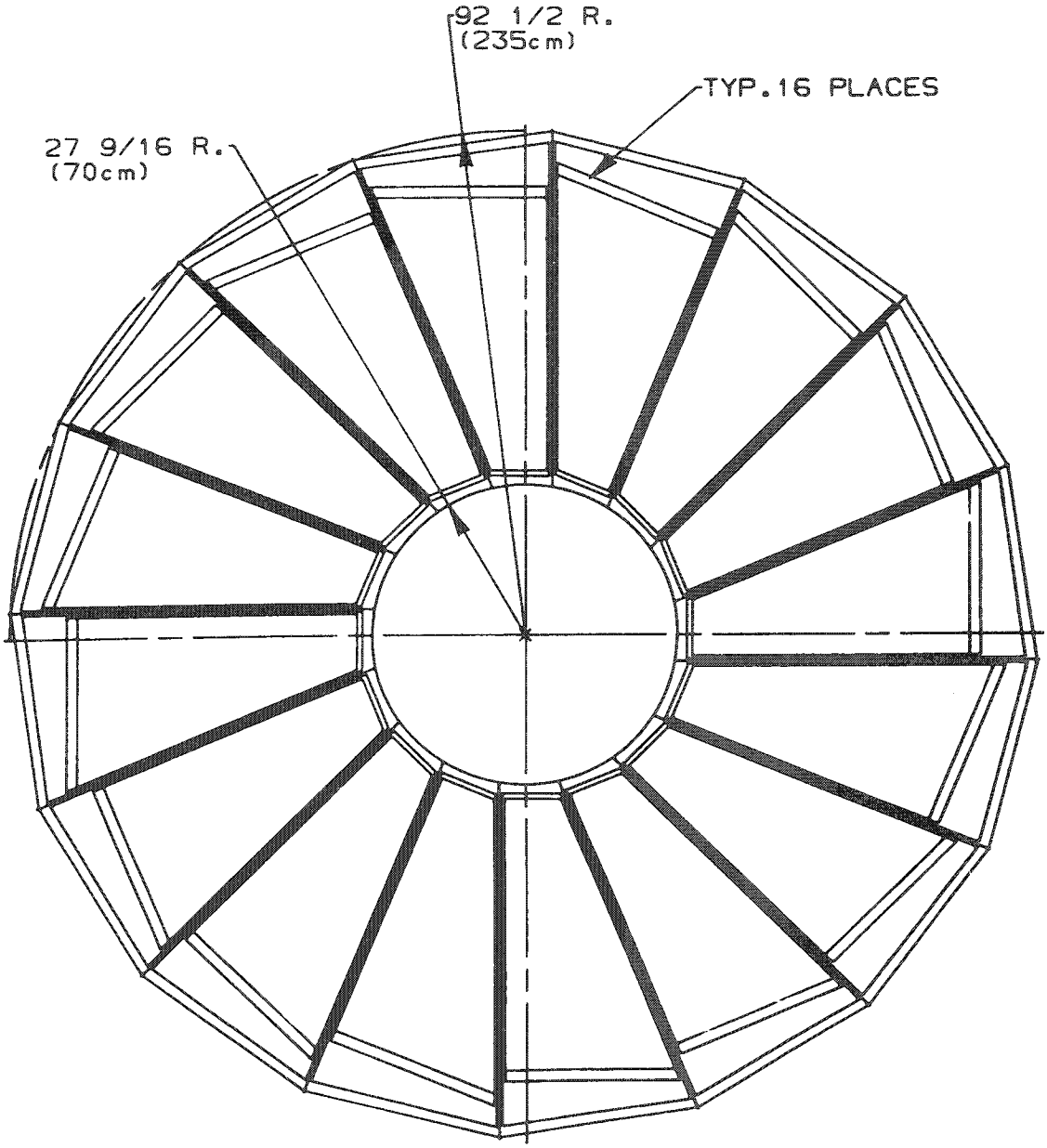

VIEW SHOWN WITHOUT ENDPLATES

Fig. 11

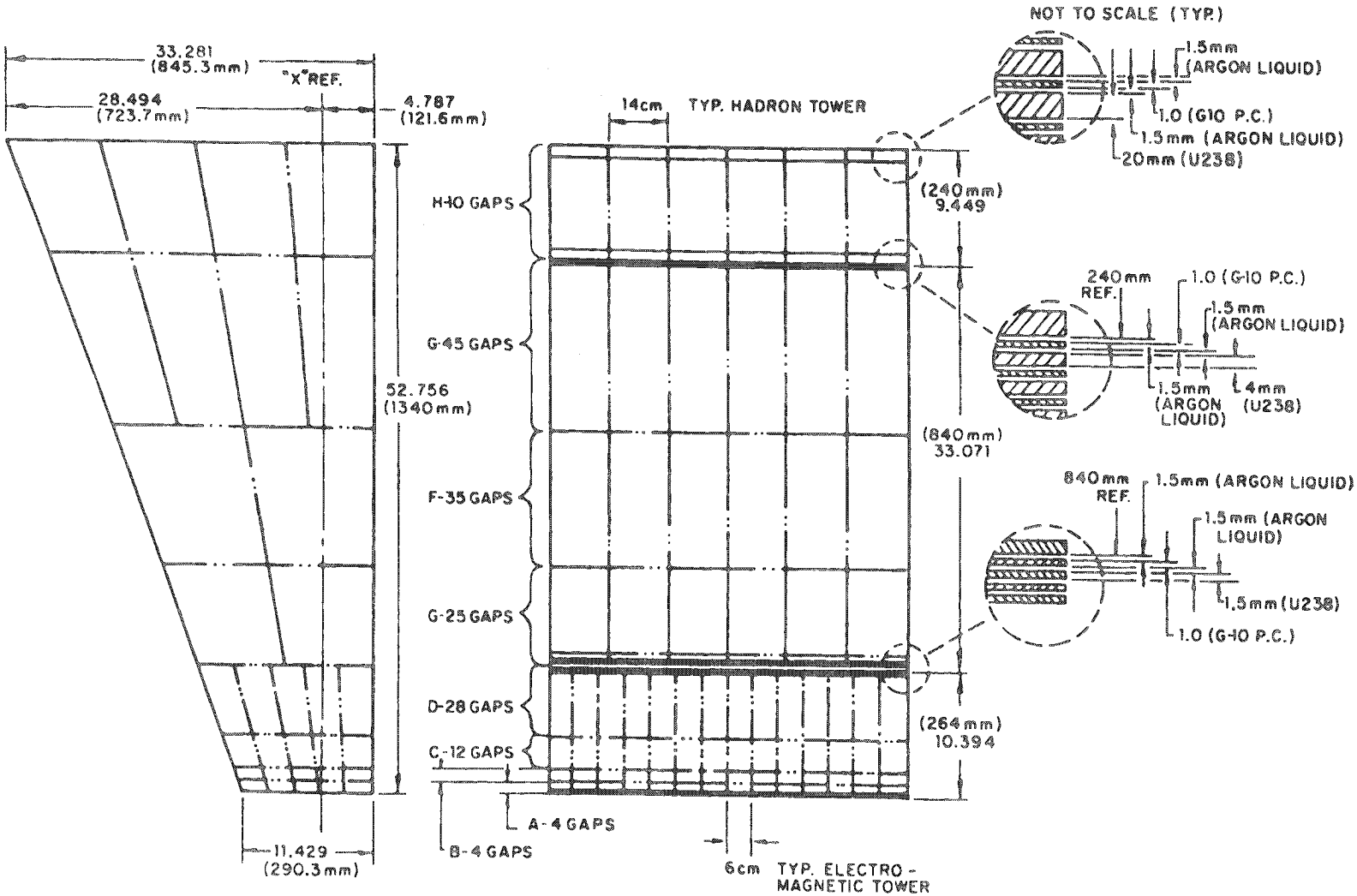
NOT TO SCALE (TYP.)
33.281
(845.3mm)
"X" REF.
28.494
(723.7mm)
4.787
(121.6mm)
52.756
(1340mm)
11.429
(290.3mm)
14cm TYP. HADRON TOWER
H-10 GAPS
G-45 GAPS
F-35 GAPS
G-25 GAPS
D-28 GAPS
C-12 GAPS
A-4 GAPS
B-4 GAPS
6cm TYP. ELECTRO-MAGNETIC TOWER
(240mm)
9.449
(840mm)
33.071
(264mm)
10.394
1.5mm (ARGON LIQUID)
1.0 (G10 P.C.)
1.5mm (ARGON LIQUID)
20mm (U238)
240mm REF.
1.0 (G-10 P.C.)
1.5mm (ARGON LIQUID)
1.5mm (ARGON LIQUID)
4mm (U238)
840mm REF.
1.5mm (ARGON LIQUID)
1.5mm (ARGON LIQUID)
1.5mm (U238)
1.0 (G-10 P.C.)

Fig. 12

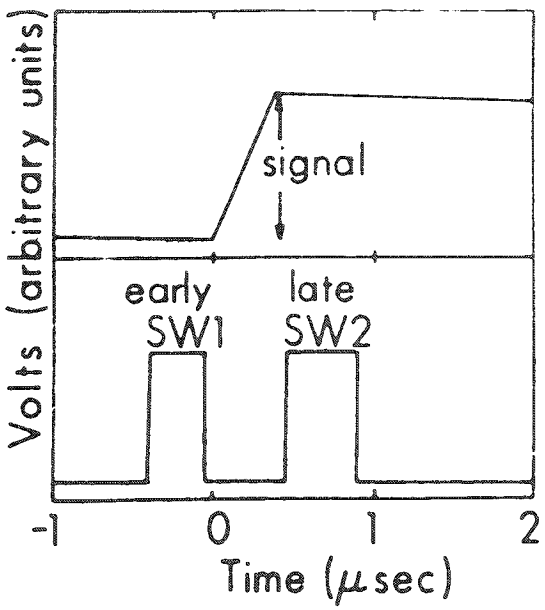
Volts (arbitrary units)
signal
early
SW1
late
SW2
-1
0
1
2
Time (μsec)

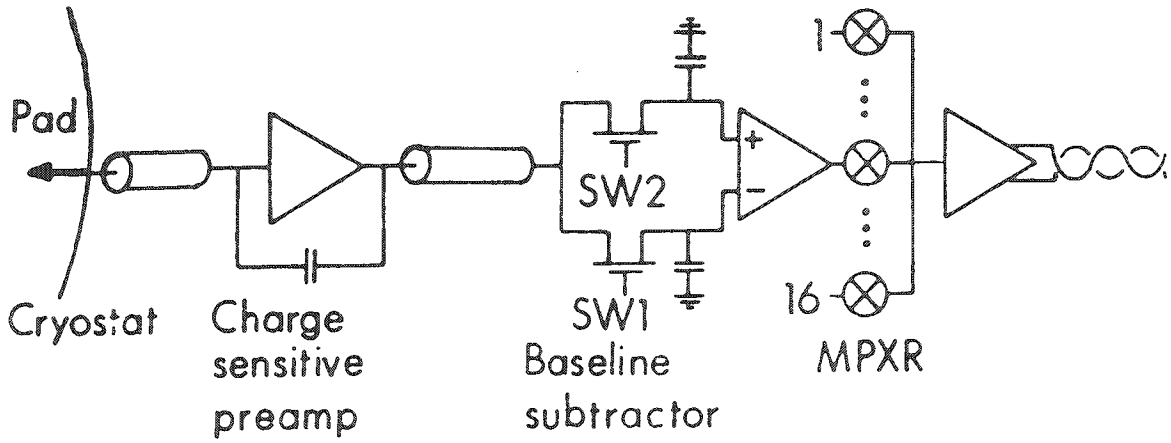
Pad
Cryostat
Charge
sensitive
preamp
SW2
SW1
Baseline
subtractor
1
16
MPXR

Fig. 13

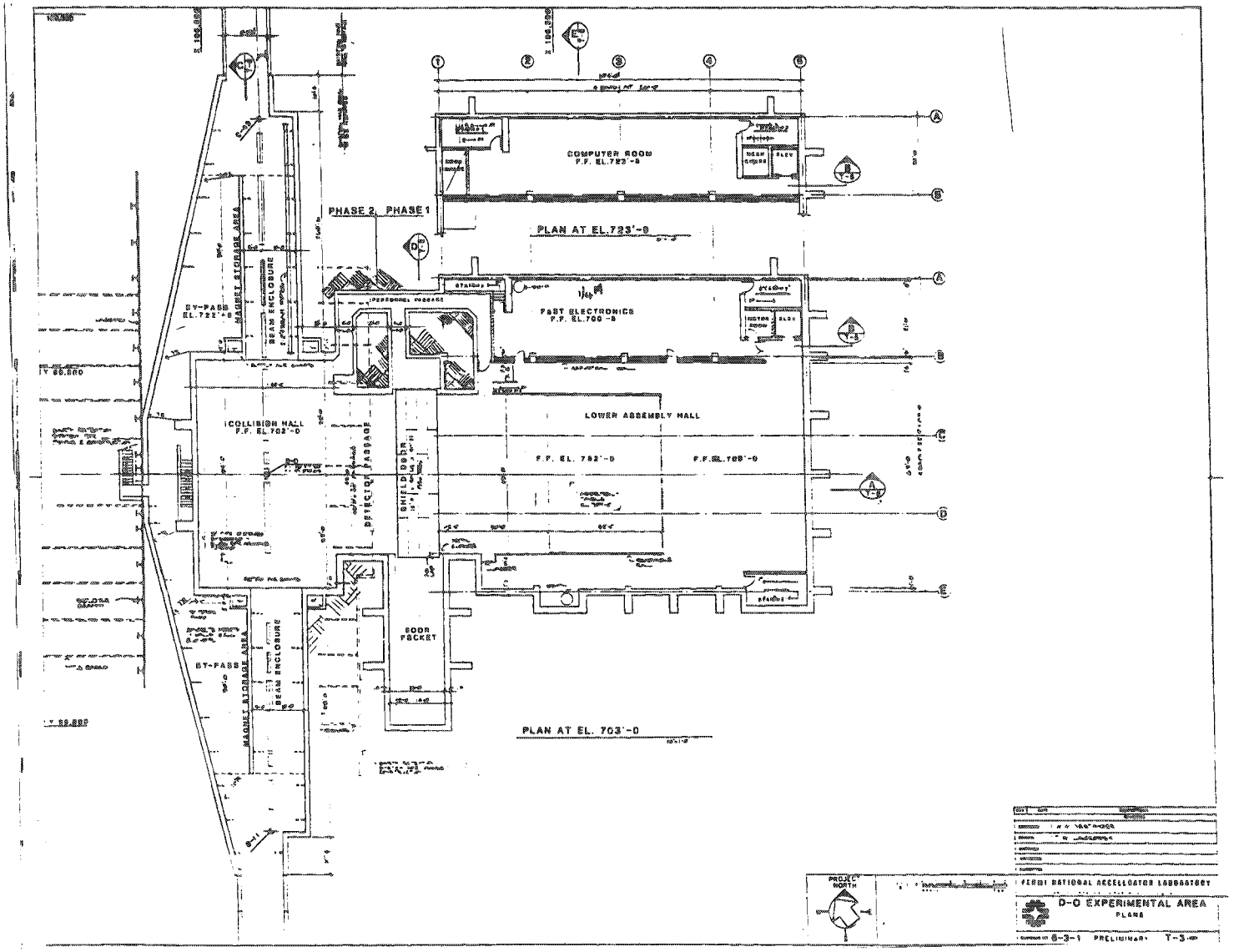
PHASE 2
PHASE 1
PLAN AT EL.723'-9
COMPUTER ROOM
F.F. EL.723'-9
FAST ELECTRONICS
F.F. EL.709'-9
LOWER ASSEMBLY HALL
F.F. EL. 703'-9
F.F.EL. 709'-9
COLLISION HALL
F.F. EL.703'-0
BY-PASS
EL.722'-9
MAGNET STORAGE AREA
BEAM ENCLOSURE
DEFLECTING PASSAGE
SHIELD DOOR
DOOR POCKET
PLAN AT EL. 703'-0
PROJECT NORTH
FERMI NATIONAL ACCELLERATOR LABORATORY
D-O EXPERIMENTAL AREA
PLANS

Fig. 14

TRANSVERSE ENERGY PHYSICS WITH THE CDF CALORIMETER

J. Freeman, R. Perchonok, J. Yoh

Fermi National Accelerator Laboratory*
P.O. Box 500, Batavia, Illinois 60439
USA

ABSTRACT

We have studied CDF's ability to measure missing transverse energy and to reconstruct the mass of the W → 2 jet system by use of a QCD Monte Carlo and a detailed simulation of the CDF detector.

For monojet events and events with multiple jets and large missing E_T, we have studied backgrounds from "old physics sources" ($Z \rightarrow 2\nu$ and heavy quark jets) and from detector mismeasurement. These backgrounds are found to be comparable.

For W → 2 jets, we find that the mass resolution is dominated by the ability to discern between particles from W decay and the underlying event. CDF detector mismeasurement causes only a small deterioration in mass resolution.

INTRODUCTION

The present era of high energy hadron colliders has opened up an entirely new mass region for the exploration of physics phenomena. New massive objects or phenomena are expected to manifest themselves in their decays into "partons" - electrons, muons, jets (quarks or gluons) and missing E_T (neutrinos, photinos, etc.). In 1986, the Fermilab Tevatron Collider will bring a four-fold increase in energy and accessible mass range above that presently available.

In this paper, we address the ability of the CDF detector at Fermilab to measure jets and isolate missing E_T. Our study employs a realistic Monte Carlo simulation including QCD effects and detector imperfections such as cracks, dead areas, shower leakages, and nonuniformities.

CDF's ability to detect missing E_T physics is studied for two extreme cases of event topology - (i) the loose signature of multijet events with large missing E_T, and (ii) the tight signature of monojet events, where no energetic cluster is allowed opposite an observed high p_T jet. For the multijet/large missing E_T events, we determine that the background from detector mismeasurement of jets is comparable to that due to neutrinos and/or muons from heavy quark jet decays (This rate is comparable to the signal expected from gluinos). Both the "detector" and the heavy quark backgrounds can be reduced by a factor of 3-5

*Operated by Universities Research Association under Contract with the United States Department of Energy

using additional vetos such as muon and electron tagging or by determining that a high p_T charged particle has entered a "crack" in the calorimetry. The dominant "old" physics backgrounds for monojet events are the events with a jet recoiling against a Z^o which decays into two neutrinos or events with heavy quark cascades into neutrinos. The level of this background is about two orders of magnitude below the multijet/large E_T miss. We find that the "detector" background arising from completely missing a leading jet to be comparable to the jet + Z^o background.

The accuracy of jet energy determination was studied by determining the mass resolution of events with $W \rightarrow ud$. We find that the dominant factor in mass resolution is due to clustering - i.e. the difficulty in determining which particles come from the jets from W decay and which come from the underlying event ("beam-jets"). This factor dominates the detector energy resolution or mismeasurement,suggesting that improvements in resolution (such as using uranium) or uniformity (such as reducing cracks) will not lead to significant improvements in W mass resolution.

CDF CALORIMETRY

The CDF detector is a 4π calorimeter which covers 2^o to 178^o in polar angle (relative to the beam axis) and full 360^o coverage in azmuthal angle. It has a projective tower geometry with electromagnetic shower counters surrounded hadron calorimetry. The detector has a thickness of 108 centimeters of iron equivalent at theta = 90^o, increasing to 160 cm of iron equivalent in the forward direction. The central region (theta between 40^o and 140^o) contains scintillator plastic sampling calorimetry with $12\%/\sqrt{E}$ ($65\%/\sqrt{E}$) resolution for the electromagnetic (hadronic) component. The remaining solid angle is covered by proportional tube sampling calorimetry with a resolution of $25\%/\sqrt{E}$ ($100\%/\sqrt{E}$) electoromagnetic (hadronic).

CDF SIMULATION

An extensive simulation of the CDF detector has been utilitized for the analysis reported in this paper. The physics events of interest are first generated via the ISAJET Monte Carlo.[1] After smearing the production vertex (σ_Z = 30 cm), the events are processed by a geometrically detailed detector simulation (eg. cracks and dead areas in the calorimetry are included). Physical processes such as in flight decays, gamma conversions, dE/dx, and

multiple scattering are included. Hadronic and electromagnetic showers are simulated including effects such as transverse and longitudinal shower profile fluctuations, energy leakage, and noninteracting punchthrough.

LACK OF CALORIMETRY AT VERY SMALL FORWARD ANGLES

To find the effect of limited coverage of calorimetry for small polar angle (the half angle of the conical hole in the calorimetry is 2^{o}), we studied hard scattering events with minimum parton p_T > 15 GeV and > 50 GeV. We looked at the final state particles and calculated the magnitude of the missing E_T vector for various assumptions about the limit of forward calorimetry coverage. Results are shown in Fig. 1A and B. In each of the figures, we see three curves: "No smearing" which shows the effect of the hole considering only geometry; "$\sigma_E = .55\sqrt{E}$",[2] where the no smearing curve is smeared by intrinsic calorimetry resolution; and finally, "CDF uncorrected" which contains all cracks and nonuniformities in CDF, as well as the effect of neutrinos and noninteracting punchtrough, but where no correction for these effects are attempted. From Fig. 1A, we see a "knee" in the distributions for a hole of 2^{o}. As the size of the hole is increased above that, it becomes probable for one of the 15 GeV p_T jets to flow into the hole region. Consequently, the missing E_T resolution worsens. The probability of a jet flowing into the forward direction decreases with increasing jet transverse energy. Hence, in Fig. 1B, for 50 GeV E_T jets, we see that the knee for worsening E_T resolution has moved upward to about 5^{o}. We conclude that for hard scatterings of more than 15 GeV E_T per parton, the 2^{o} hole in the CDF calorimetry does not contribute to missing E_T resolution.

BACKGROUND FOR MISSING E_T + JETS

It is possible for conventional hard scattering events to be observed possessing missing E_T. Causes for missing E_T in these events include semi-leptonic decays of heavy quark jets and detector imperfections. To study the relative importance of the different contributing factors, we looked at events of the process $\bar{p}p \rightarrow 2$ jets, with p_T (parton) > 50 GeV p_T.

The results obtained from a sample of 1700 events are plotted in Fig. 2. In this figure, we see four distributions: $1/N\ dN/dE_{T\text{missing}}$ versus E_T missing for those events with only the effect of the 2^{o} hole ("no smearing"); adding the effects of missing μ and ν, as well as finite calorimetry resolution

(".55/ $\sqrt{E}$"); and two additional curves that include all the imperfections of the CDF detector. The curve "CDF-uncorrected" shows the rate of missing E_T events if no attempt is made to veto events that have particles hitting cracks, identifiable leptons, etc. The curve "CDF after veto" will be described below.

We see that "CDF uncorrected" has a significant high missing E_T tail. To understand this tail, we looked at all events with $E_{Tmissing} > 15$ GeV to find out the cause of missing E_T. There were three causes for the missing E_T: Cracks in the calorimetry, intrinsic calorimetry resolution, and neutrinos. Table 1 shows the number of events for each cause.

Table 1

Number of Events/Cause for Events with Missing $E_T > 15$ GeV

Cause	CDF-Uncorrected	After Veto	Veto and Crack Instrumentation
γ hitting cracks	25	6	1
Intrinsic resolution	14	8	8
Neutrinos	17	4	4

We found that some of the events in the high missing E_T tail could be vetoed. These events possessed charged high p_T particles hitting cracks, or identifiable leptons associated with neutrinos. Vetoing these events brought about a factor of 3-5 reduction in the high tail ("CDF after veto" in Fig. 2). The fractional causes of missing E_T events in the high tail changed after the veto. The new balance of causes is shown in Table 1. We see that intrinsic resolution becomes more important as a contribution.

A proposed upgrade to CDF would instrument the the inactive regions between calorimetry modules in the central region with 7 X_o tungsten and a single sampling chamber.[3] This instrumentation would allow flagging of photons that hit these cracks. If we apply this final rejection, we are left with the third set of numbers in Table 1. We see that the intrinsic calorimetry resolution has become the predominant cause of the high tail.

For this type of signature (50 GeV E_T jets with missing E_T), CDF's calorimetry resolution seems to lead to backgrounds twice as severe as the heavy quark background. A thicker calorimeter with better resolution (for example, uranium-liquid Argon) could conceivably get 1/3 the background CDF can expect. Since the intrinsic resolution is a gaussian distribution, it can be expected

that, for higher missing E_T events, neutrinos will become more important as a source of the high missing E_T tail.

BACKGROUND FOR MONOJET EVENTS

One possible signal for the presence of supersymmetric particles is the observation of "monojet" events. These are events containing a single observable jet and missing transverse energy. Sources of background to monojet events include $g + Z_o \rightarrow g + \nu\nu$, cascade decays of heavy quarks, and detector dependent effects such as finite energy resolution, cracks, and nonuniformities. The existence of a 30 GeV mass scalar quark could produce events with a 20 GeV E_T jet, and no second jet to balance transverse energy. One source of conventional background would come from hard scattering of about 30 GeV p_T per parton, where one jet was not observable. We decided to study events with the monojet signature: A cluster with transverse energy equal to or greater than 20 GeV E_T with less than 5 GeV E_T balancing the jet in the opposite hemisphere.

Our clustering procedure was:

1) Require a 1 GeV E_T deposition in a 15^o(phi) X 0.1 (pseudorapidity) tower.

2) Look at all neighbor towers, and add their energy tothe cluster if there is at least 0.1 GeV E_T but less than 1.5X the parent tower's energy in the tower. The last requirement prevents merging of close but distinct clusters.

3) Merge all clusters whose centroids are less than 1 unit apart in (pseudorapidity-phi) space, where phi distances are measured in radians. We picked the distance of 1 unit for cluster merging after a hand scan of energy flows for a sample of the events.

We studied 60,000 events of the process $\bar{p}p \rightarrow$ jets with p_T of each parton > 30 GeV. After very loose precuts to eliminate events that could not possibly satisfy our monojet criterion, we simulated the remaining 1500 events using the detailed CDF detector simulation and applied our mono-jet selection. 11 events satisfied the signature. We then identified the source of missing E_T for these 11 events. There are three sources of missing E_T: 5 events with a high energy ν from heavy quark decay; 3 events with photons hitting the phi cracks between elements of calorimetry in the central region; and 3 events caused by other calorimetry imperfections including finite thickness and limited theta coverage.

One of the five events caused by neutrinos was recognizable as a weak decay event. (It had a 5 GeV p_T μ that was detectable.) The remaining four events had very low energy leptons associated with the neutrinos. All of the events

due to missed photons could be tagged if CDF adopted the proposal to instrument the cracks in the central calorimetry. None of the events due to other properties of the calorimetry were recognizable as being caused by the detector. Hence, we are left with 4 ν events and 3 events due to detector limitations. The Z_o + jet source of background would contribute about 2 events.

We conclude that CDF calorimetry imperfections generate a background to monojet events which is comparable to the physics background of Z_o + jets or heavy quark decay. In other words, a perfect calorimeter would not have a significantly lower background for monojet events caused by supersymmetry.

MASS RESOLUTION OF W → ud → 2 Jets

We studied CDF's ability to reconstruct the invariant mass of a 2 jet system by considering the process W → ud → 2 jets. Our method of analysis was to first identify the factors contributing to finite mass resolution. We then added each factor to our sample of simulated events and observed the effect on the measurement. The effects we identified as interesting to study were: 2^o hole in calorimetry; energy lost by neutrinos and muons; intrinsic calorimetry resolution; calorimetry imperfections, such as finite thickness, cracks, and nonuniformity; and the effects of clustering algorithms used to reconstruct the fragmented jets.

A summary of our conclusion is shown in Table 2. Several invariant mass distributions for sets of conditions A through H are shown in Figs. 3 and 4. We note that the clustering algorithm used is the same as described in the section on monojet identification.

In Fig. 3, we see results for: C, a $.25/\sqrt{E}$ resolution ideal calorimeter; D, a $.55/\sqrt{E}$ ideal calorimeter; and F, the $.25/\sqrt{E}$ calorimeter after the effect of clustering. We observe that the $.25/\sqrt{E}$ calorimeter, after clustering, has poorer resolution than the $.55/\sqrt{E}$ calorimeter before clustering. In Fig. 4, we see results for cases: F, again the $.25/\sqrt{E}$ calorimeter after clustering; G, the $.55/\sqrt{E}$ calorimeter after clustering; and H, CDF including all cracks, nonuniformities etc., after clustering. From Fig. 4, we conclude that there are no dramatic differences between distributions F, G, and H.

Table 2

Factors contributing to degraded mass resolution in W → 2 jets.

	Factor	σ Resolution (%)*
A.	2^{o} beam hole	0.6%
B.	A + missing ν, μ	1.3%
C.	B + .25/ $\sqrt{E}$ resolution	3.0%
D.	B + .55/ $\sqrt{E}$ resolution	5.3%
E.	B + clustering	7%
F.	C + clustering	8%
G.	D + clustering	9%
H.	CDF	10%

*σ is defined using only the 50%-80% interval of the revelant distribution. Events were entered into distributions E through H only if they posessed at least 2 clusters, each with E_T > 15 GeV.

Our conclusion in this study is that, with the clustering algorithm employed, improved calorimetry resolution does not cause an improvement in mass resolution. It remains to be demonstrated if there are significantly better clustering schemes than the one that we used.

CONCLUSIONS

CDF was designed to serve as a full 4π calorimeter with homogeneous response. Some compromises were necessary in order to realize the design. The cracks and nonuniformities in the calorimetry are attributable to the requirement of modularity, coupled with the necessity of reading out the signals. Finite calorimetry thickness, and limited solid angle coverage are forced upon one by geometrical constraints. We found that these imperfections will not seriously detract from our ability to study jets and missing E_T. For many of the processes studied, CDF's imperfections cause only insignificant degradations to the best achievable resolution, and in the worst cause, these imperfections create a background that is comparable to the intrinsic background from physics processes.

REFERENCES

1. F. E. Paige and S. D. Protopopescu, 1982 DPF Summer Study, Snowmass, Co., June 28, 1982, page 471.

We used ISAJET version 4.0 for these studies. The ISAJET event generator does not contain the effects of initial state gluon bremsstrahlung. For the studies presented in this paper, initial state bremsstrahlung is expected to be several orders of magnitude less important than the other effects studied, and is consequently ignored.

2. Throughout this paper, we consider 2 "ideal" detectors: a "conventional" calorimeter, and a "liquid-Argon Uranium" calorimeter. These calorimeters have finite energy resolution ($\sigma/E = 0.55/\sqrt{E}$ for the conventional one; $0.25/\sqrt{E}$ for lA-U), and infinite thickness. They also have perfect spatial resolution. The energy resolutions were determined by averaging electromagnetic and hadronic calorimeter responces over a sample of hard scattering events.

3. CDF internal note number 225

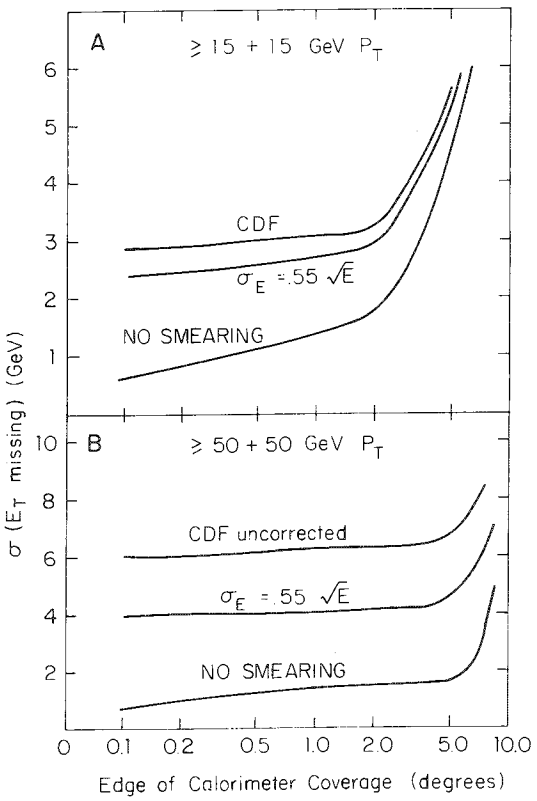

Fig. 1. Effect of limited theta coverage on missing E_T resolution.

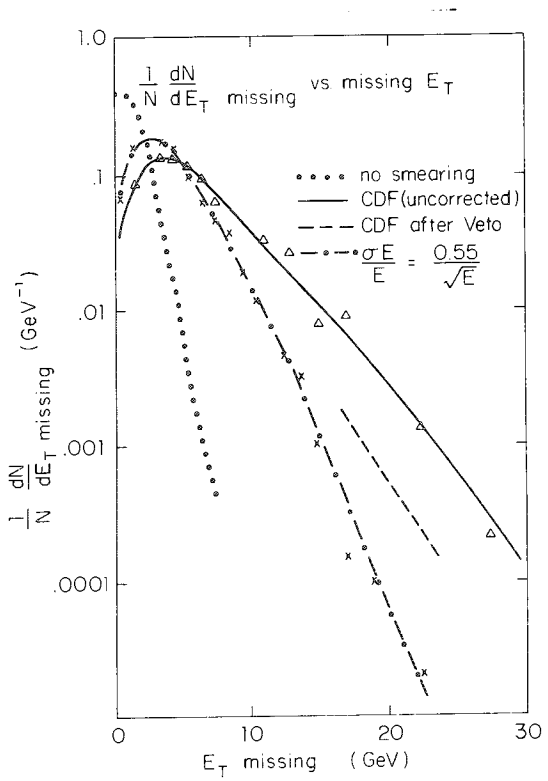

Fig. 2. Missing E_T distributions for CDF and ideal detector.

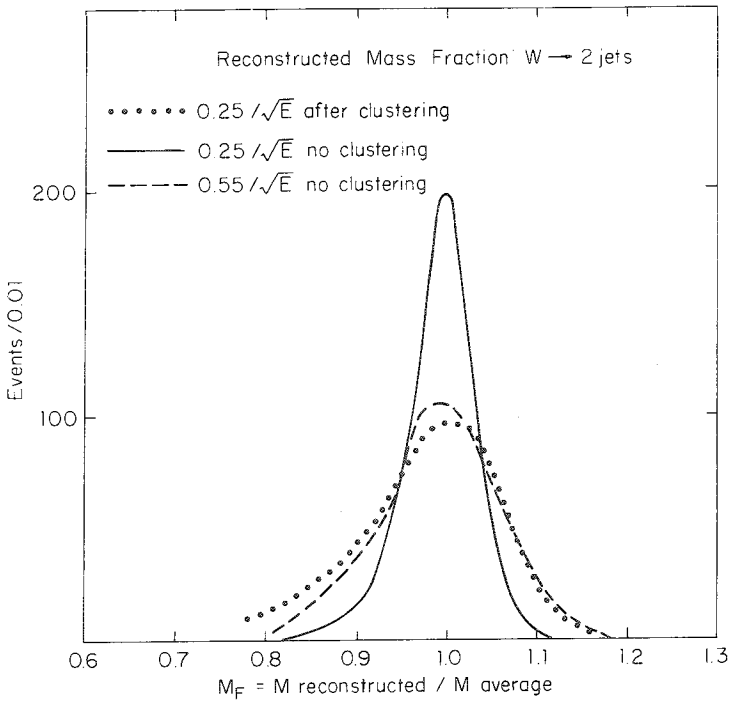

Fig. 3. Reconstructed mass fractions for W → 2 jets.

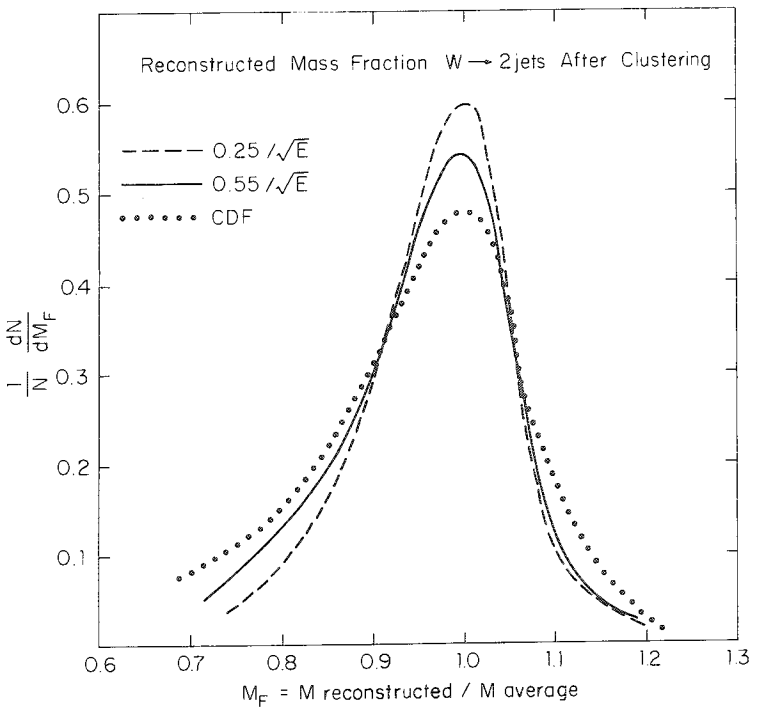

Fig. 4. Reconstructed mass fractions for W → 2 jets after clustering.

DO: MISSING-p_T PHYSICS AND DETECTOR DESIGN CONSIDERATIONS

George E. Theodosiou
University of Pennsylvania

1. MISSING-p_T PHYSICS

The discovery and study of the $W^{\pm}$ boson at CERN[1] has clearly established the missing-p_T technique, in association with lepton identification, as a powerful tool in the study of physics involving resonance production with a neutrino (ν) in the final state. It is anticipated that it will also be very useful for analysis of more complicated processes with more than one "non-interacting" particles in the final state, i.e. ν, photinos ($\tilde{\gamma}$), etc.[2]. However, their conclusive study, especially in view of limited statistics may require, in addition, tagging of semileptonic heavy quark (q)-decays, for example by detecting secondary vertices[3,4].

We mention several "missing-p_T" physics topics[2] with estimated rates mostly based on QCD and the standard model at 2 TeV and an integrated luminosity of 5 pb^{-1}.

i) Precise determination of masses and widths of W and Z and their ratios, for testing the standard model.
$W \to e\nu$ (15000 events), $Z \to e^+e^-$ (1500 events)

ii) Diquark W and Z decays. For example discovering of the top quark (t) in
$W \to t\bar{b}$; $t \to l$(lepton) ν b. 150 events (m_t = 60 GeV/c^2)

iii) Associated production of W or Z in
$p\bar{p} \to W(l\nu) + \gamma\ (p_T > 10\ \text{GeV/c}) + X$ (20 events)
or $W(l\nu) + W\ (2\ \text{jets}) + X$ (A few events)

iv) Heavy lepton (L) and quark (Q) production. For example
$W \to L\nu_L$; $L \to l\nu_l\nu_L$ (1650 events)
$p\bar{p} \to Q\ (Wq) + \bar{Q}\ (\bar{W}\bar{q}) + X$ 100 events (m_Q = 120 GeV/c^2).

v) Production of Higgs particles decaying into 2 quarks:
$H^\circ \to t\bar{t}$, $b\bar{b}$, $c\bar{c}$ for $2m_t < m_H < 2m_Z$

vi) Technicolor octet, η_T, production[5]
$\eta_T \to t\bar{t}$ ~1000 events (m = 200-250 GeV/c^2).

vii) Supersymmetry. Production of gluinos ($\tilde{g}$) in
$pp \to \tilde{g}\tilde{g}X \to (q\bar{q}\tilde{\gamma}) + (q\bar{q}\tilde{\gamma}) + X$

Fig. 1 shows the signal for several gluino masses up to 125 GeV/c^2, as a function of the maximum "jet"-p_T and the background after cuts on missing-p_T and absence of energetic leptons associated with background production of heavy quarks decaying semileptonically.[11]

2. CONTRIBUTIONS TO MISSING-p_T

Fig. 2 shows a Monte-Carlo miss-p_T distribution for high-p_T 2-jet production using ISAJET for two different energy resolutions[7]. It also includes angular smearing assuming the present DO design segmentation and 2° beam holes. Even though hard to quantify, one can hardly underemphasize several related virtues of the uranium-liquid argon calorimetry such as the stability of the energy scale and calibration, the uniformity of response and absense of radiation damage as well as the uniformity of response to electromagnetic (e-m) and hadronic showers.

Fig. 3 shows the effect on miss-p_T due to several widths of radial cracks in the central calorimeter [7]. These cracks are pointing slightly off the beam axis and shower particles going into them are considered lost. In a more realistic M. Carlo including shower development due to material inside cracks the results may be slightly better, but the serious problem of narrow showers of high-p_T photons (γ) and electrons (e) lost in such cracks still remains. Finally extensive M. Carlo studies of 2-jet production[7,8], indicate that the choice of a 1° hole is an optimal one. Fig. 4 shows contributions from several sources: 1° hole, energy ($40\%/\sqrt{E}$) and angular resolution (σ_x = 2 cm for single hadrons) as well as contributions from neutrinos (ν) of heavy quark decays and from 100 GeV/c^2 gluinos ($\tilde{g}$). This implies that with U-calorimetry one starts to become sensitive to ν-production, for miss-p_T above 5-10 GeV/c. Miss-p_T and γ and e identification impose rather stringent requirements on the design of the forward/backward calorimeters, which we discuss next.

3. FORWARD/BACKWARD CALORIMETERS

As illustrated elsewhere in this Workshop[9], 2 "end-cap" calorimeters sandwich the central one, looking directly at particles with angles down to 5°. Fig. 5 shows a side view, containing the beam. Each consists of parallel U (6 a.l.) and Fe-plates (3 a.l., back section), each of a polygon shape with a round hole in the middle around the beam. The gaps between plates contain liquid argon, readout pads and lines carrying pad signals to preamplifiers.

After each "end-cap" on each side there is an "end-plug" calorimeter with a similar structure. It is placed right before the low-beta quadrapole,

as is shown in Fig. 6, at the maximum possible distance from the center, to preserve a tolerable angular resolution at small angles. It has a slightly higher density than the end-cap one to also minimize shower transverse size.

4. TRANSVERSE AND LONGITUDINAL TOWER SEGMENTATION

The readout transverse segmentation of hadron towers is basically determined by 2 considerations[6]:

a) One must have $\Delta\theta/\theta < \Delta E/E$ for the best possible $\Delta p_T/p_T$ resolution. The shower axis for hadrons cannot be determined to better than 1/5 of the tower size. For a U-cal $\Delta E/E > .02$, so $\Delta\theta/\theta$(tower) (= $\Delta\eta$ (pseudorapidity)) ~.10. In order to have square-like towers one must have $\Delta\phi$ ~6°. However for θ less than 4° the tower size becomes less than the shower size.

b) The tower size need not be smaller than the shower size, since the large fluctuations in hadron-showers, limit their position resolution. Fig. 7 shows the end-plug segmentation. We have about 1000 hadron towers per end-cap and 360 per end plug calorimeter.

Since large fluctuations are absent from e-m showers, the front e-m sections have finer segmentation, for example 1.5-2.0 cm pads, and 0.5 cm strips, promising to give resolutions of 1-2 mm, and also to improve separation of nearby showers of γ vs π° and e (or γ) vs jet. Fig. 8 shows the probability of two jet-fragments hitting the same tower or adjacent ones[10].

Each tower is also subdivided longitudinally into 7-8 segments for readout as shown in Fig. 5. Subdivision of a shower's longitudinal distribution provides:

a) high resolving power for e vs $\pi^\pm$, γ vs π° and e vs ($\pi^\circ + \pi^\pm$) overlaps,

b) information on the depth of the first γ conversion, which also helps to resolve γ vs π°. Fig. 9 shows this for γ,π° etc., indicating the usefulness of having 2 thin (1-2 r.l.) segments as the first part of the e-m section.

5. CALORIMETER DENSITY

As indicated above, higher calorimeter density implies more compact showers and better angular resolution. The smaller the angle θ, the more important the compactness becomes.

First, it minimizes the $\Delta\theta/\theta$ contribution to $\Delta p_T/p_T$. Fig. 10 shows this dependence as a function of θ for jets, with a discontinuity at the end-cap, end-plug interface (5°).

Finally, it improves the spacial resolution for nearby showers of an e (or γ) vs jet, e vs γ and γ vs π°.

REFERENCES

1. Experiments UA-1 and UA-2 at CERN.
2. DO Design Report, FNAL, December 1983.
3. Workshop on Searches for Heavy Flavors in Como, Italy, August 1983.
4. A proposal to upgrade the UA-1 Detector in order to extend its physics programme, UA-1 Collaboration, CERN, August 1983.
5. C. Baltay and H. Gordon, Snowmass 1982, p. 500.
6. Private communication with W. Selove.
7. S. Protopopescu, BNL, DO Report, 1984.
8. J. Freeman, FNAL, CDF Collaboration, talk presented at this Workshop.
9. The DO Detector by M. Marx, Stonybrook, DO Collaboration, talk presented at this Workshop.
10. H. Weisberg, Stonybrook, DO Report, 1983.
11. S Aronson et al, Snowmass 1982, p 505.

FIGURE CAPTIONS

Fig. 1 Signal and background for production of 2 gluinos as a function of maximum "jet"-p_T, for various gluino masses.

Fig. 2 Missing-p_T distribution. Energy and angular resolution contributions.

Fig. 3 Missing-p_T distribution. Central calorimeter cracks contribution.

Fig. 4 Total missing-p_T distribution. Contributions from 1° hole, energy and angular resolutions.

Fig. 5 Schematic side-view of the readout longitudinal segmentation for the end-cap calorimeter.

Fig. 6 Schematic side-view of the end-plug calorimeter.

Fig. 7 Schematic front-view of the transverse segmentation for the end-plug calorimeter.

Fig. 8 Probability of 2 jet fragments to "hit" the same or adjacent calorimeter segments, as a function of jet-p_T.

Fig. 9 Probability for electromagnetic shower initiation by a photon as a function of calorimeter depth, for various particle species.

Fig. 10 The θ-dependence of the p_T-resolution for jets due to calorimeter angular resolution alone.

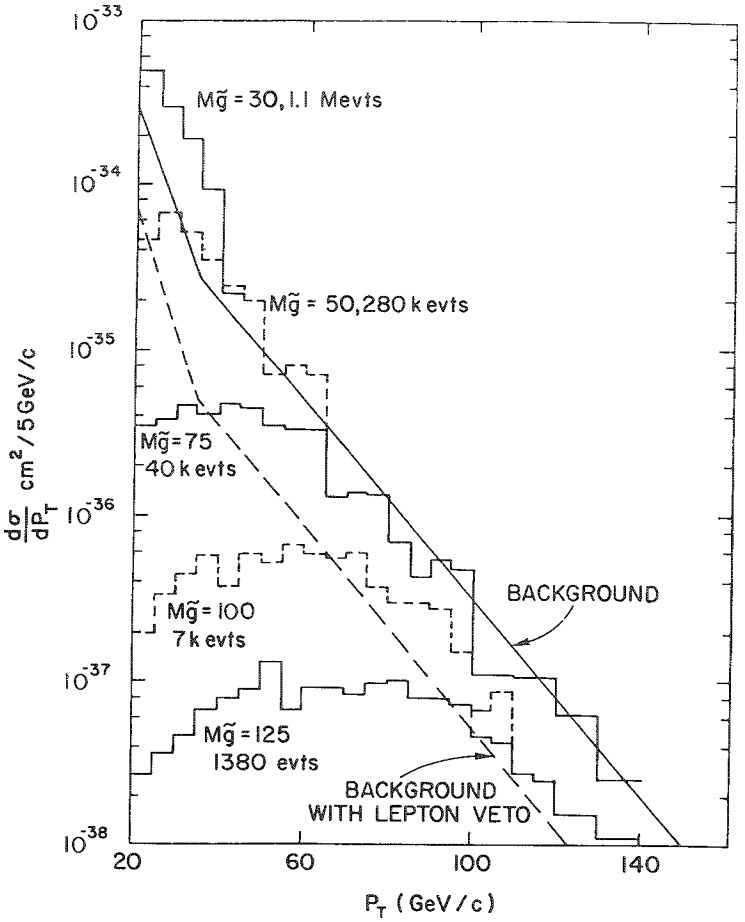

Fig. 1

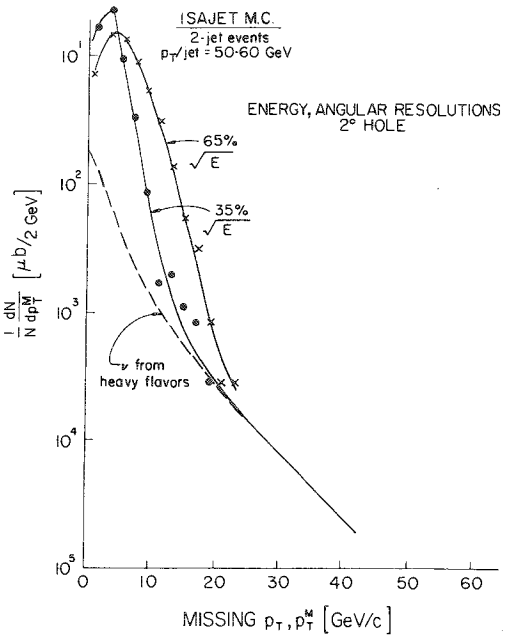

Fig. 2

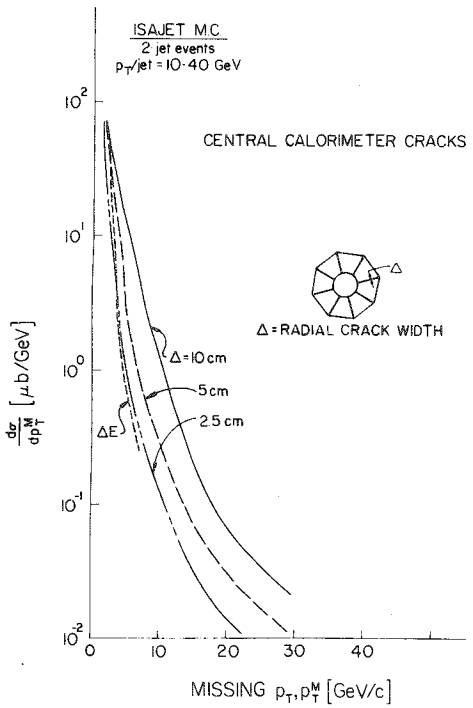

Fig. 3

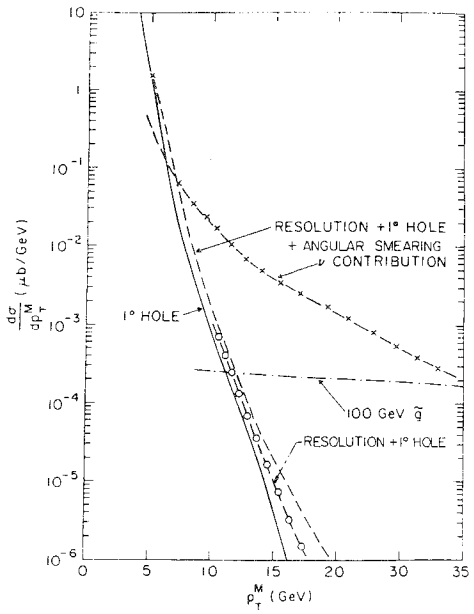

Fig. 4

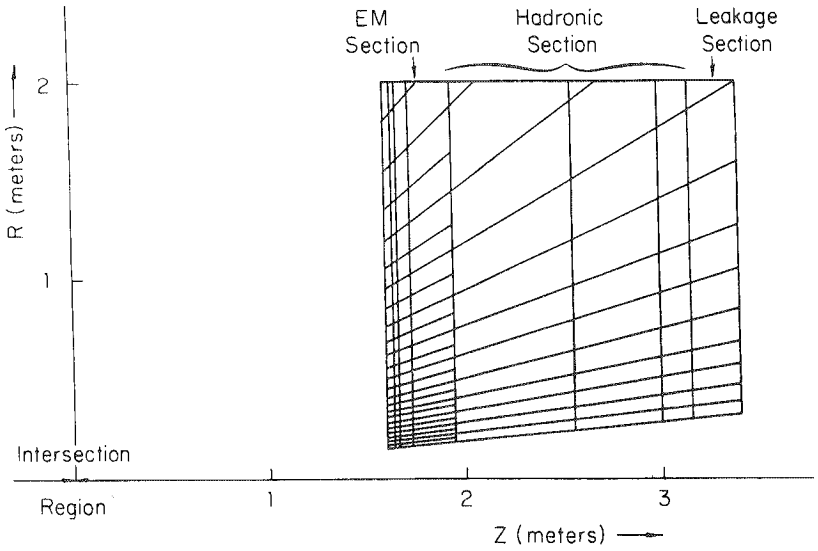

Fig. 5

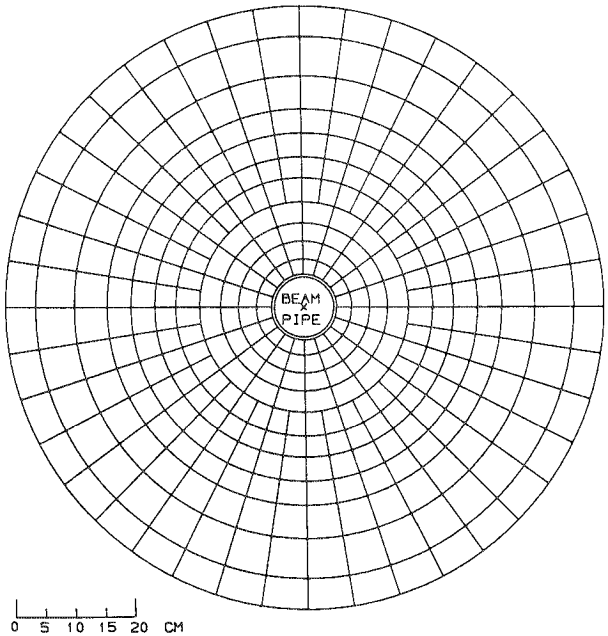

Fig. 7

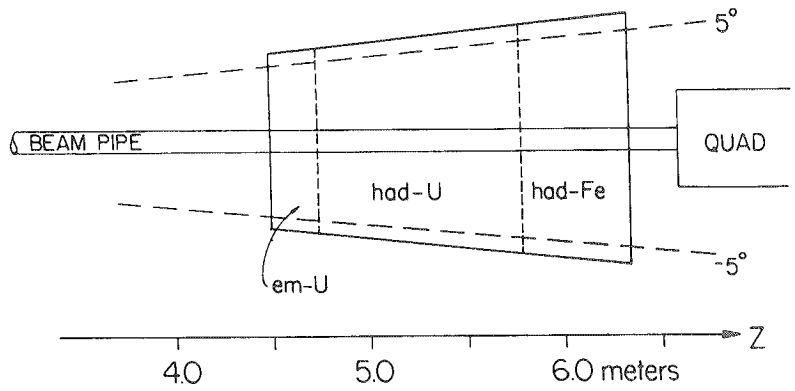

Fig. 6

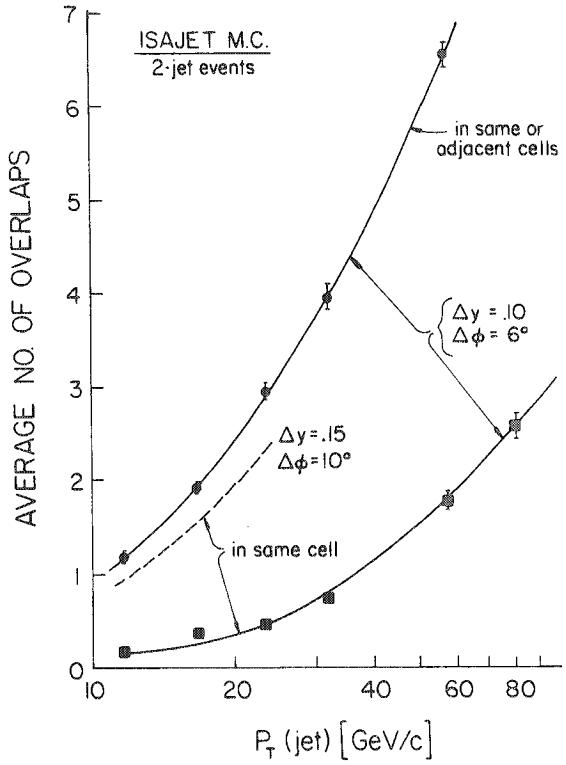

Fig. 8

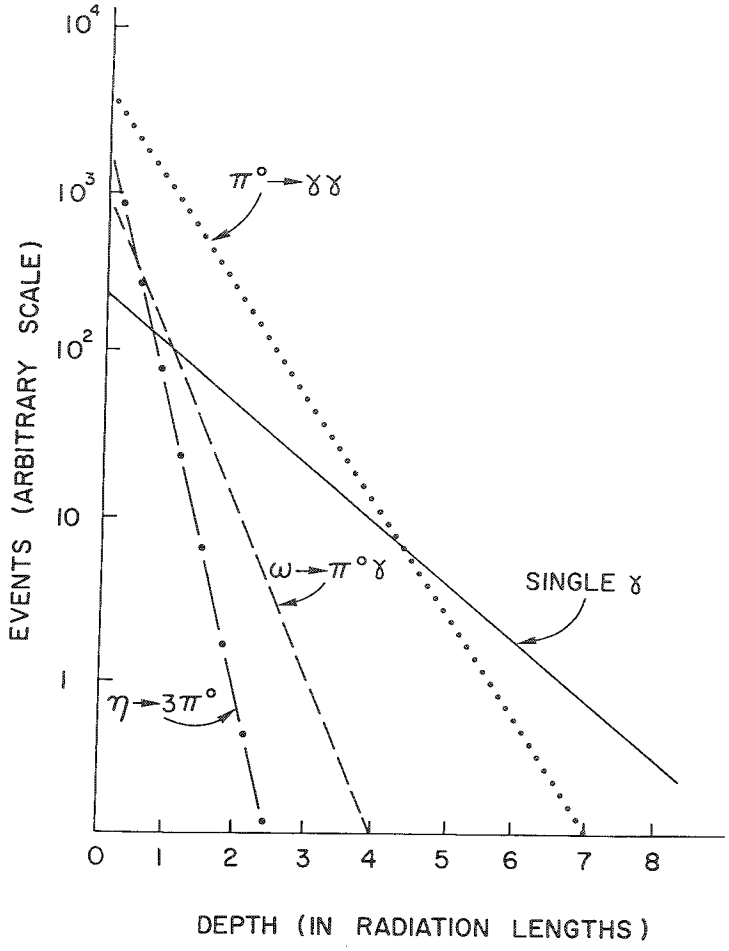
EVENTS (ARBITRARY SCALE)
10^4
10^3
10^2
10
1
$\pi^\circ \to \gamma\gamma$
$\omega \to \pi^\circ\gamma$
SINGLE γ
$\eta \to 3\pi^\circ$
0 1 2 3 4 5 6 7 8
DEPTH (IN RADIATION LENGTHS)

Fig. 9

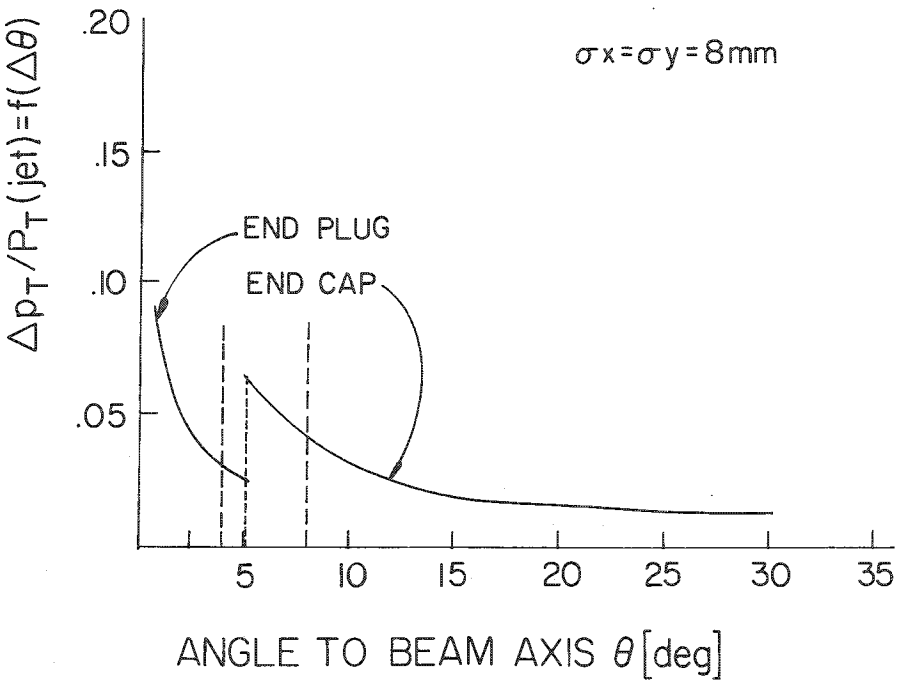
$\Delta p_T/P_T(\text{jet}) = f(\Delta\theta)$
.20
.15
.10
.05
$\sigma x = \sigma y = 8\text{mm}$
END PLUG
END CAP
5 10 15 20 25 30 35
ANGLE TO BEAM AXIS θ [deg]

Fig. 10

CDF ELECTROMAGNETIC SHOWER COUNTERS

Kunitaka Kondo

University of Tsukuba,
Ibaraki, Japan

1. INTRODUCTION

The collider detector at Fermilab (CDF) has 3 types of the electromagnetic shower counters (hereafter abbreviated as EMSC) covering different angular ranges; i.e. the central ($40° \lesssim \theta \lesssim 140°$), the end plug ($10° \lesssim \theta \lesssim 40°$, $140° \lesssim \theta \lesssim 170°$), and the forward/backward ($2° \lesssim \theta \lesssim 10°$, $170° \lesssim \theta \lesssim 178°$) electromagnetic calorimeters[1].

The central EMSC's have the lead/scintillator sandwich structure, while the end plug and the forward/backward EMSC's consist of the lead/proportional chamber layers. Each component has a conical tower structure pointing to the interaction point, armed with tracking chambers in the magnetic field of 1.5 tesla in front and hadron calorimeters and muon counters behind.

In the present report, the structure of each component is shown, and the characteristics, including the energy resolution, the linearity, the position resolution for the incident particles and the hadron rejection capability, as designed and/or observed by the beam tests will be discussed. Some features of the CDF EMSC's will be discussed in the context of their physics capabilities.

2. CENTRAL EM SHOWER COUNTERS

The structure of the central EMSC module is shown in Fig. 1. The signals from scintillators are read out from two sides with wavelength shifters. The main parameters and the characteristics are listed in Table 1. The test results of the first prototype have been reported elsewhere[2]. To improve the characteristics, a new type of scintillator with two kinds of secondary fluors and wavelength shifter which matches the scintillator in wavelength have been developed[3]. The main improvements are in a relatively long attenuation length ($\gtrsim$ 90 cm) and a large light output.

A second prototype similar in structure to the tower near 90° was built with the new materials and tested in the pion and electron beams[4]. In Fig. 2(a), the output of the counter as a geometrical mean of the pulse heights of two phototubes viewing the wavelength shifters is shown as a function of the beam energy. The response is linear within 1 % up to 125 GeV. Since the photomultiplier gain saturation is less than 1 % in the observed charge range, the non-linearity above 125

GeV is due to the longitudinal shower leakage. The energy resolution observed in the same test was 11.4 %/$\sqrt{E}$ (Fig. 2(b)), which is consistent with our estimation of the sampling fluctuation of 10.4 %/$\sqrt{E}$ and the photon statistics of 5.0 %/$\sqrt{E}$. The response of the test tower cell was observed to be uniform within ± 5 % over more than 90 % of the area, which was well reporoduced by an optics simulation.

In the production process of the central EMSC's, careful quality controls were made on thickness and chemical uniformities of scintillator-and wavelength shifter plates, smoothness of their surfaces, geometrical precision in the assembly. Special efforts[5] were made to make the effective response of the wavelength shifter plate uniform over its whole area. This was practically done by putting an aluminum reflector printed with black pattern on the back of each wavelength shifter.

Uniformity among 48 equivalent tower cells is a crucial factor to achieve the accurate measurements without recoursing to unrealistic precise mapping of all cells. Based upon the quality controls and various measurements in the production line, we estimate the uniformity among 48 equivalent cells to be controlled better than 1 % in terms of the final output.

Calibration and mapping of the central EMSC are being made with beams at Fermilab. The calibration monitoring will be done with a movable ^{60}Co source scanning the scintillator, with Xe flasher lamps at the edges of the wavelength shifter plates and LED flashers on the transition blocks in front of the photomultipliers.

3. END PLUG AND FORWARD/BACKWARD EM SHOWER COUNTERS

In the end-plug and forward/backward regions, the gas calorimetry is adopted. The choice was made because of (a) relatively high energies of particles which are favorable to the energy resolution and (b) high radiation background in these regions. The main parameters and expected or observed characteristics of the gas EMSC's covering these regions are listed in Table 2 .

The structure of an end plug EM and hadron shower counter set is shown in Fig. 3. The active detector here are proportional chambers with arrays of extruded resistive plastic tubes interleaved with G-10 cathode boards. Two prototypes of EMSC's were built and tested with the electron and pion beams in the energy range of 25 $\sim$ 150 GeV[6].

The linearity of the total collected charge to the energy of electrons is hown in Fig. 4(a). The observed saturation effect is well represented over a wide ange of collected charge by a formula $y = \frac{1}{\alpha} \ln (1 + \alpha x)$ with $\alpha = 0.027 pc^{-1}$, where

x is the expected charge with no saturation and y is the observed charge. The observed energy resolution is 24 %/$\sqrt{E}$ (Fig. 4(b)), consistent with 30 % $\sqrt{t/E}$, where t is the sampling thickness.

The lateral profile of the shower is observed as the distributed signals on the cathode pads. Finite conductivity of the resistive plastic tubes causes lateral signal spread of the order of 3 cm in σ, which helps determining the shower axis or the impact point of the incident particles. We obtained the spatial resolution of the order of 1.5 mm for $E \geq 50$ GeV.

Informations useful to identify electrons and photons against hadrons are the total energy deposit, the lateral shower profile, the longitudinal shower development as observed by the 3 segments of EM-and 2 segments of hadron shower counters. Contamination of the pion beam with electrons gave a lower limit of the pion rejection factor of 10^3 for the 80 % efficiency of electron detection. The calibration is being made by the beam at Fermilab, and will also be made by ^{55}Fe sources placed at typical spots of the shower counters.

The forward/backward EMSC's have similar structures and expected characteristics as the end plug EMSC's. The cathode consists of extruded Al multi-channels with resistive surface on one side. The calibration with Rn mixed in Ar/methane gas is being planned and tested.

4. DISCUSSIONS

Physics objectives of the electromagnetic shower counters include the single γ and π^0 detections, the measurements of the mass and width of Z^0, the precise measurement of the mass ratio of Z^0 and $W^{\pm}$, and use of the electron signal in search for new heavy particles.

The capability of the CDF EMSC's to separate two showers down to 10 mrad allows identifying 70 % of π^0's from single γ's up to about 20 GeV[7]. The expected Z^0 mass width (σ) to be directly measured at CDF is 1.5 GeV[1]. The mass ratio between Z^0 and $W^{\pm}$ will be measured to a few tenths of a per cent with the integrated luminosity of 10^{36} cm^{-2}.

One of the unique features of CDF is the possibility of identifying electrons in a jet[7]. The detection or identification of leptons in a jet gives a signature for a heavy quark jet. Such an identification serves to find (a) new heavy quark(s) as well as to reject heavy quark backgrounds in search for new (e.g. $\tilde{g}$) particles[8]. Because of the fine granularity of CDF EMSC's only a single electron is contained in a tower to large fractions of the heavy quark jet events. A simulation study

on this point was made by using ISAJET[9]. Table 3 (a) shows the probability a b-jet has no particles inside the cone with the axis along the electron momentum and the opening angle θ_c. At $\theta = 20°$, for example, a pad of the end plug EMSC has a dimension of 6 cm × 6.5 cm which corresponds to 2° from edge to edge. The table shows that, with the aid of tracking informations, we can identify about 80 % of the electrons in the b-jet with pion rejection factor better than 10^3 as discussed before.

Photons accompanied with charged particles give signals similar to those of electrons. Since our shower counters give the position resolution of the order of $2 \sim 3$ mm, which corresponds to $1 \sim 1.5$ mrad in the central and end plug regions, we can reduce this background down to less than a per cent only by the position information (see Table 3(b)). If one asks the consistency between the energy and the momentum measurements, the background will be reduced by another factor of 10.

The cracks in the boundaries of modules and 2° holes in the very forward and backward angles may sometimes mimic the missing neutral particles. The detailed simulation study on this problem and planning for possible detector improvement are under way.

REFERENCES

1) Disign Report for the Fermilab Collider Detector, August 1981, unpublished. The groups involved in the EMSC's are ANL, Brandeis, Fermilab, Harvard, KEK, Pennsylvania, Saga, and Tsukuba.
2) L. Nodulman et al. Nucl. Instr. and Meth. 204 (1983) 351.
3) T. Kamon et al. Nucl, Instr. Meth. 213 (1983) 261.
4) T. Kamon et al. Submitted to Nucl. Instr. and Meth.
5) This was done at ANL.
6) Y. Hayashide et al. Nucl. Instr. and Meth. 204 (1983) 361,
Y. Hayashide et al. IEEE Trans. Nucl. Sci. NS-30 (1983) 112.
7) The author thanks S. Miyashita and S.F. Kim for discussions on the subject.
8) I. Hincliffe et al. Proceedings of the 1982 DPF Summer Study on Elementary Particle Physics and Future Facilities, Snowmass (1982) 242.
9) F.E. Paige et al. Proceedings of the 1982 DPF Summer Study on Elementary Particle Physics and Future Facilities, Snowmass (1982) 471.

Table 1. Parameters and Characteristics of the Central Electromagnetic Calorimeters

Size		**Chambers**	
Number of Modules:	48	Location (Depth):	6 X_0
Tower Size:	$\Delta\phi \simeq 15°$, $\Delta\eta \simeq 0.1$	Wire Local Width:	1.4 cm
Number of Layer:	30	Strip Width:	1.7 cm, 2.0 cm
Thickness of Lead:	3 mm		
Tower Thickness:	20 X_0		
Light Collection		**Characteristics**	
Primary:	polystrene	Linearity:	$\geq$ 99 % up to 100 GeV
Secondary Fluors:	b-PBD, BDB	Resolution:	12 %/$\sqrt{E}$ *
WLS Fluors:	Y-7	Position Resolution:	< 2 mm*
PMT:	Hamamatsu R580	Hadron Rejection**:	$\gtrsim 10^3$*
Sensitivity:	400 p.e./ GeV*		

*) **) See next page.

Table 2. Parameters and Characteristics of the Endplug and Forward/Backward Gas Calorimeters

	End Plug EMSC	Forward/Backward EMSC
Angular Coverage	$1.1 \leq \eta \leq 2.3$, $0 \leq \phi \leq 360°$	$2.3 \leq \eta \leq 4.0$
Lead-chamber Sandwich		
Lead Thickness	2.7 mm	3.18 mm
Number of Layers	34	40
Total Thickness	20 X_0	23 X_0
Pad Readout		
Tower (Pad) Size	$\Delta\eta = 0.1$ for $1.6 \leq \lvert\eta\rvert \leq 2.3$ $= 0.05$ for $1.15 \leq \lvert\eta\rvert \leq 1.6$ $\Delta\phi = 5°$	$\Delta\eta = 0.1$ $\Delta\phi = 5°$
Number of Longitudinal Segments	3	2
η, ϕ Strip Chamber		
Location (Depth)	$4.5\ X_0 \leq d \leq 9.5\ X_0$	4 X_0
η - Strip Size	$\Delta\eta = 0.02$, $\Delta\phi = 30°$	$\Delta\eta = 0.02$, $\Delta\phi = 30°$
ϕ - Strip Size	$\Delta\phi = 1°$, $1.1 \leq \lvert\eta\rvert \leq 2.3$	$\Delta\phi = 1°$, $2.3 \leq \lvert\eta\rvert \leq 3.1$
Expected Characteristics		
Energy Resolution	$24\ \%/\sqrt{E}$ *	$25 \sim 30\ \%/\sqrt{E}$
Position Resolution	$\sigma_\eta \sim \sigma_\phi \leq 2$ mm*	$\sigma_\eta \sim \sigma_\phi \sim 3$ mm
Hadron Rejection**	$> 10^3$*	$> 10^3$

*) These values have been confirmed by the beam tests.

**) The informations from hadron shower counters are assumed to be available.

Table 3(a) Probability that a b-quark jet has no particle (with energy $E > 0.1\ E_e$) inside the θ_c cone.

θ_c	jets with "isolated" electrons
2°	80.4 %
1°	90.8 %
0.5°	95.2 %

Table 3(b) Probability that a light-quark or a gluon jet has a charged particle (with energy $E > 0.1\ E_\gamma$) within the θ_c cone.

θ_c	jets with γ accompanied with a charged particle
2°	27.1 %
1°	11.7 %
0.5°	4.4 %

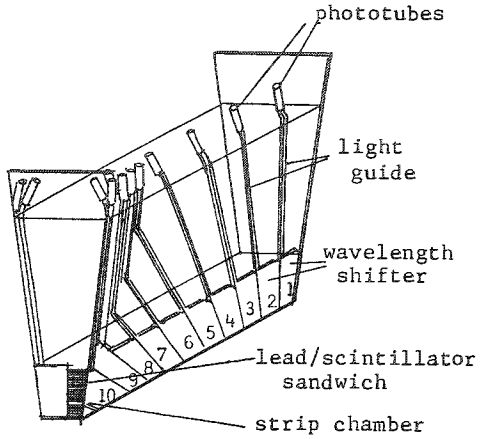

Fig. 1. Central EMSC

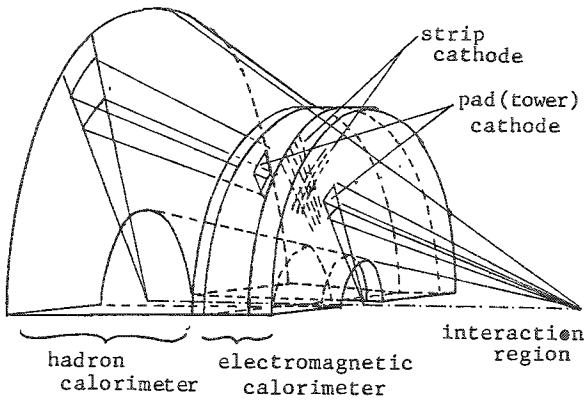

Fig. 3. End Plug EMSC

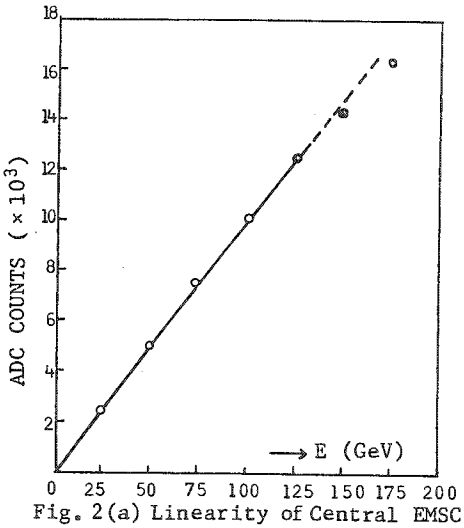

Fig. 2(a) Linearity of Central EMSC

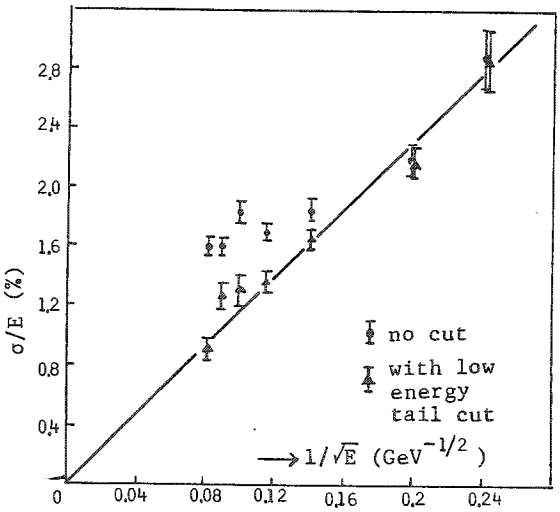

Fig. 2(b) Energy Resolution of Central EMSC

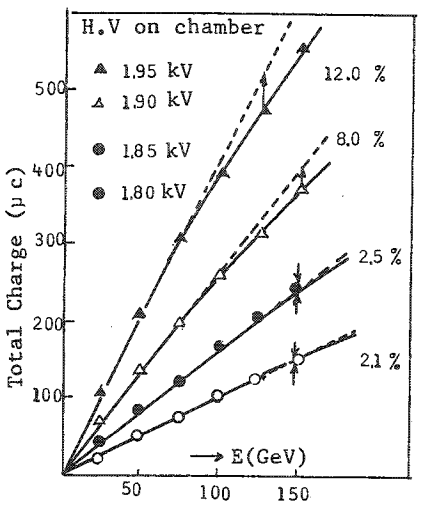

Fig. 4(a) linearity of End Plug EMSC

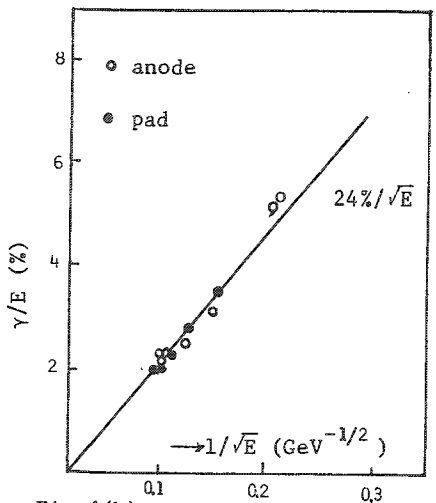

Fig.4(b) Energy Resolution of End Plug EMSC

Supercolliders

SUPERCOLLIDER PHYSICS

Ian Hinchliffe
Lawrence Berkeley Laboratory
University of California
Berkeley, California 94720

This talk is concerned with the physics opportunities of an extremely high energy proton-proton or proton anti-proton machine. (SSC) It is based on work done in collaboration with E. Eichten, K. Lane and C. Quigg.[1] We set out to determine how the physics reach of a high energy collider is affected by its energy, luminosity and type of beam. I shall select a few topics and discuss them in this talk, the reader may refer to Ref. 1 for a more complete discussion.

The triumph of the Glashow-Weinberg-Salam model[2] in correctly predicting the W and Z masses[3] has made even more acute the problem of how the electro-weak symmetry is broken. We have almost no experimental guidence into the dynamics of this breaking. The simplest option for this dynamics is that the breaking is caused by a scalar field acquiring a vacuum expectation value. The simplest model of this type has only one physical particle, the Higgs. Unfortunately the constraints on the Higgs mass are rather weak $7\ \text{GeV} < m_H < 1\ \text{TeV}$. The lower bound comes from cosmology.[4] The upper bound is looser, it is derived from the observation[5] that a Higgs with more mass becomes strongly interacting, implying that phenomena not present in perturbation theory must occur. Many theorists regard this single Higgs possibility as unappealing.† The quadratic divergences present in perturbation theory lead to instabilities in the mass of the Higgs.[7] This is sometimes phrased in terms of a hierarchy problem which, put at its simplest, is the inability to understand why the scale of the Fermi constant ($1/\sqrt{G_F} \approx 300$ GeV) is much less than the Planck mass ($\sim 10^{19}$ GeV) or the scale of grand unification ($\sim 10^{14}$ - 10^{17} GeV) if the latter exists.

Many theoretical alternatives to this simple Higgs mechanism exist. Supersymmetric[8] models, where the Higgs is saved from these quadratic divergences by having a partner spin 1/2 particle, predict a host of new particles with the same quantum numbers as those in the standard model but with spin different by 1/2 unit. In technicolor models[9] the Higgs is not an elementary particle but is a bound state of a new fermion anti-fermion pair. The proliferation of quarks and leptons has also led to the suggestion that quarks and leptons are not elementary particles but are built from some more fundamental particles (composite models).[10] All these alternatives (except perhaps the last) have one feature in common; they all predict new physics on the scale of the Fermi-constant. It is this scale that a high energy hadron-hadron collider will probe. Since no particular model is compelling, the machine requirements can best be defined by performing some kind of ensemble average over all these models. This done in Ref. 1.; the rest of this talk

---

† The scatological significance was recently discussed by S. Glashow.[6]

is arranged as follows. I first discuss the parton model and the structure functions needed to estimate the production rates. I then discuss hadronic gets, production rates of gauge bosons, searching for the Higgs, signals for compositness, and for a sequential heavy lepton. Supersymmetric predictions and those dealing with technicolor and non-minimal Higgs are discussed by some other speakers.[11]

A) The Parton Model

Production rates in a hadron collider with center of mass energy $\sqrt{s}$ are given by

$$\sigma_H = \sum_{ij} \int dx_1 dx_2 f_i(x_1,Q^2) f_j(x_2, Q^2)\, \sigma_{ij}(\hat{s}, \hat{t}, \hat{u}) \qquad (1)$$

where $\sigma_{ij}(\hat{s}, \hat{t}, \hat{u})$ is the cross section for producing a particle of interest in a collision of two constituents of the beams labeled ij; they could be quarks or gluons. $f_i(x_1, Q^2)$ is the probability of finding a constituent of type i inside the beam particle with momentum fraction x of the beam. Q^2 is some scale characteristic of the hard scattering process (σ_{ij}) e.g. $\hat{s} = x_1 x_2 s$. The $f_i(x, Q^2)$ fall rapidly with x, so if we are interested in producing some new particle with mass M, $x_1 x_2 > M^2/s$ and most of the integral (1)is dominated by $x \sim M/\sqrt{s}$. Typically $\sigma_{ij} \alpha c/\hat{s}$, with $c \sim \alpha_s^2$ for a strong interaction process such as the production of a jet pair or a heavy quark, and $c \sim \alpha_{EM}^2$ for the production of a pair of gauge bosons.

At a collider with $\sqrt{s} = 40$ TeV, we could be interested in masses as low as 100 GeV (inaccessable at LEP) or as high as 10 TeV implying

$$(100)^2\,\text{GeV}^2 < Q^2 < (10^4)^2\,\text{GeV}^2, x > 10^{-5} \qquad (2)$$

with dominant region around $x \geq 10^{-2}$ [1/2] It is straightforward in principle to obtain these distributions. One takes data at all x for some small value of Q^2 from deep inelastic scattering experiments and uses the Altarelli-Parisi equations[12] to evolve up in Q^2. The problems we encounter are as follows.

1. Data do not exist below x = 0.01, and different sets of data are not consistent with each other.
2. t and b quark distributions may be needed, and the t quark mass is unknown.
3. The gluon distribution $g(x, Q^2)$ is not directly measured, rather it is inferred from the Q^2 evolution of the anti-quarks.
4. The QCD parameter Λ is not well known and is correlated with $g(x, Q^2)$.
5. QCD perturbation theory may not be applicable at large and small values of x. The large x region is irrelevant since $f(x, Q^2)$ is very small there. The small x region is more problematic but again is not relevant for setting the upper reach of a machine (the largest M which can be produced) since for most processes this limit is set by $x \sim 0.1$ or greater.

In order to estimate the effects of these uncertainties (we can do nothing about the last one) the following technique was adopted[1]. Two parametizations based on those of the CDHS collaboration[13] were evolved and compared. These parameterizations differ in that a different value of $R = \sigma_L/\sigma_T$ was assumed in the analysis. At $Q^2 = 5\ \text{GeV}^2$ the values of $xg(x, Q^2)$ and x are

$$\text{set 1: } xg(x, Q^2) = (2.62 + 9.17x)(1-x)^{5.9}, \Lambda = .2\,\text{GeV} \qquad \text{(a)}$$

$$\text{set 2: } xg(x, Q^2) = (1.75 + 15.575x)(1-x)^{6.03}, \Lambda = .29\,\text{GeV} \qquad \text{(b)} \qquad (3)$$

As usual the gluon distribution with more support at large x (set 2) is correlated with a larger value of Λ. Figure 1 shows the behavior of $x\,g(x, Q^2)$ as a function of Q^2 for various x (set 1 shown). The difference between the two sets is less than 20% over the entire x and Q^2 range ($Q^2 < 10^8$ GeV^2).

In order to estimate the possible uncertainties associated with the absence of data in the small region, the input distributions were changed for $x < 0.01$ as follows.

$$xg(x, 5) = \begin{cases} 25.50\, x^{1/2} & \text{(a)} \\ .44\, x^{-1/2} - 1.886 & \text{(b)} \end{cases} \tag{4}$$

These match at $x = 0.01$ onto 3(a). At $Q^2 = 5$ and $x = 10^{-4}$ 4(a) and 4(b) differ by a factor of 160, but at $Q^2 = 1000$ GeV^2 the difference is order 2. These conclusions are encouraging because they suggest that the uncertainties decrease as Q^2 increases, and the differences in the starting distributions wash out. (See also Ref. 14.) Comparisons with other deep inelastic scattering data e.g. those of the CHARM collaboration[15] indicate that our anti-quark distributions may be too small (Fig. 2). These problems cannot be resolved until the data in the same Q^2 region agree. The effect of a change in Λ from .2 GeV to .1 GeV for 3(a) is less than 30% over the entire range of x and Q^2.

A useful quantity to estimate the reach of a collider is

$$\tau/\hat{s}\, d\pounds/d\tau \equiv \tau/(1+\delta_{ij}) \int (f_i(x, Q^2)\, f_j(\tau/x, Q^2) + i \leftrightarrows j) dx/xs \tag{5}$$

This quantity has the dimension of a cross-section and can be used to estimate the production rate of strongly interacting objects by multiplying by α_s^2. Figure 3 shows this quantity as a function of s at fixed s for gluon gluon collisions in pp collisions. (The $p\bar{p}$ rate is the same.) It can be seen from this figure that at $\sqrt{s} = 40$ TeV there will be a reasonable number of events at $\sqrt{\hat{s}} \sim 10$ TeV for a strong interaction process at a luminosity of 10^{33} cm^{-2}sec^{-1}. The figure shows the price paid in the reach of a machine at fixed energy as the luminosity is lowered. The same number of events at $\pounds = 10^{31}$ cm^{-2}sec^{-1} is reached at $\sqrt{s} \approx 3$ TeV.

Figure 4 shows $\tau/\hat{s} d\pounds/d\tau$ for $u\bar{u}$ collisions in pp colliders. The ratio $p\bar{p}/pp$ is shown in Figure 5. These two figures show that a certain minimum luminosity is required to exploit the advantage of pp. For a weak process (e.g.the cross section $do/dp_t dy$ for the p_t the production of a heavy gauge boson) the rate is roughly $\alpha_{EM}\ \tau d\pounds/d\tau/s$. If we take a year of 10^7 seconds and require 1000 events Fig. 4 shows that a $\sqrt{s} = 40$ TeV machine reaches $\sqrt{\hat{s}} \sim 7, 4, 2$ TeV at luminosities of 10^{32}, 10^{32}. 10^{31} cm^{-2} sec^{-1}. Figure 5 now shows that at the smallest of these luminosities there is essentially no advantage in a pp machine. As σ_{ij} decreases the advantage of pp at the same luminosity becomes weaker.

B) Hadronic Jets

Hadronic jets at large transverse momenta (p_t) will present a background to new physics at a high energy collider so it is important that they be well understood. Given parton distributions there are still uncertainties in the production rate. The scale Q^2 which appears $\alpha_s^2(Q^2)$ controlling the $2 \to 2$ scattering process and appears in $f(x, Q^2)$ is undetermined. We use $p_T^2/4$ (see Ref. 14 and 16), this uncertainty is more

important at the Sp$\bar{p}$S collider than at higher energies. Figure 6 shows the cross section $d\hat{\sigma}/dp_t dy$ at $y = 0$ for the Sp$\bar{p}$S collider. A comparison with the data[17] reveals no gross differences. The contributions of the different final states, gluon-gluon, gluon quark and quark quark are shown separately. Notice that configurations with gluons in the final state dominate over the region of most of the data. The cross section at $\sqrt{s} = 40$ TeV is shown in Fig. 7 and at $\sqrt{s} = 10$ TeV in Fig. 8. Even a high luminosity machine will have great difficultly in obtaining a clear sample of quark jets. The production rate of these jets is enormous; Fig. 9 shows the cross section for the production of two jets with rapidity y constrained, $|y| < 2.5$ and transverse energy E_T greater than E_{T_0} for $\sqrt{s} = 10, 40, 100$ TeV as a function of E_{T_0}. At a luminosity of 10^{33} cm^{-2} sec^{-1} the rate of jet production for $E_{T_0} = 1$ TeV at $\sqrt{s} = 40$ TeV is 400 Hz. The production rate in pp and $p\bar{p}$ colliders at the same $\sqrt{s}$ is equal to within 20%. The number of three jet events is also impressively large.[1]

C) Production of Gauge Bosons.

The total cross sections for the production of W^+ in pp and $p\bar{p}$ collisions is shown in Fig. 10. Since $\hat{s} = M_W{}^2$ and hence τ is rather small at $\sqrt{s} = 40$ TeV the production rate is dominated by sea quarks and the advantage in rate provided by the valence anti-quarks in $p\bar{p}$ collisions is extremely slight. At $\sqrt{s} = 40$ TeV the production rate is very large ($\sim$ 120 nb) but most of the W's are produced at small angle. Figure 11 shows the rapidity distribution; approximately 75% of the W's are emitted within 5^0 of the beam.

There may exist new W's with a larger mass than 100 GeV. If we assume a coupling to quarks equal to that of the standard W the production rate of Fig. 12 is obtained. The cross-section has been integrated requiring that the new W has $|y| < 1.5$ and the figure shows pp collisions. The rate for $p\bar{p}$ is lightly larger (Fig. 13) but again a minimum luminosity is needed to exploit the advantage. If we require 1000 produced new W's, which should be enough to discover one, given a reasonable branching ratio into $\nu\ell$, we obtain a maximum mass which can be explored at fixed values of $\sqrt{s}$ and integrated luminosity. Figure 14 shows this mass as a function of $\sqrt{s}$ for different values of $\int$£dt in a pp machine. It can be seen that a 10^{33}cm^{-2}sec^{-1} machine at $\sqrt{s}$ of 40 TeV can reach masses of 7 TeV.

D) Searching for the minimal Higgs

The Higgs is not a typical member of the zoo of particles predicted by models to have masses in the 1 TeV region. It has a rather small production cross-section and is one of the most difficult particles to see. In this respect it places the strongest demands upon energy and luminosity. If the Higgs is lighter than 2 M_W, it decays into heavy quarks ($t\bar{t}$ if $m_H > 2m_t$, $b\bar{b}$ otherwise). In this case the background is from the QCD production of heavy quarks, assuming that the detector can distinguish between light and heavy quarks. This background is much greater than the signal,[1] so it seems difficult to detect a light Higgs unless its production rate is much larger than the estimate given here.† If $m_H > 2M_W$ or $2M_Z$, it decays almost exclusively into ZZ and WW final states with a width

† A larger rate may be possible in non-minimal models with more than one physical Higgs particle.

$$\Gamma(H \rightarrow WW) = 2\Gamma(H \rightarrow ZZ) = 320\, m_H^3\ \text{GeV} \qquad (6)$$

where m_H is measured in TeV. Two mechanisms for the production of the Higgs are relevant. Gluon-gluon fusion[18] via an intermediate quark loop yields the rate shown in Fig. 15. The rate is sensitive to the top quark mass, and also to the presence, if any, of extra generations. M_t = 30 GeV has been used and the figure should probably be viewed a lower bound on the production rate for this mechanism. The Higgs can also be produced by WW (or ZZ) fusion.[19] The rate for this process is shown in Fig. 16. At large values of m_H this mechanism dominates since it exploits the large width for H → WW.

The signal for a heavy Higgs will be a peak in the invariant mass of a W or Z pair.[20] The background is from the continuum production of W pairs.[21] Figure 17 shows the cross-section for $pp \rightarrow W^+W^- + X$ as a function of energy. The W's from the continuum are produced with a flatter rapidity distribution than those from Higgs decay. Fig. 17 also show the rate if the W's are restricted to have rapidity less than 2.5 or 1.5. Figure 18 shows the signal and background in the W pair channel for a Higgs produced at $\sqrt{s}$ = 40 TeV. The W's are required to have rapidity less than 2.5. The background is obtained from Γ_H do/dM where M is the mass of a pair of W's produced in the continuum. The signal and background are comparable. Figure 19 shows the signal and background at $\sqrt{s}$ = 10 TeV. The signal to noise ratio is worse.

Luminosity is extremely critical, as is the efficiency with which the W's (or Z's) can be detected. It may be possible to detect W pairs from the hadronic modes of the W. There is a large background from the QCD production of multi jets and a preliminary study of the problem[22] indicates that this will be very difficult. If gauge bosons can only be detected in leptonic modes, only the ZZ final state can probably be clearly reconstructed with an efficiency of $(0.06)^2$. Figure 20 shows the signal and background in this channel. For m_H = 500 GeV there are approximately 10 detected events for $\int$£dt = 10^{40}, which is probably enough given the cleanliness of the signal. One will have to look hard to find a Higgs but it does seem possible. The production rates in $p\bar{p}$ are the same but the background is somewhat worse.[1] One final word; the production rates used could be too small if the t quark mass is larger than 30 GeV or if there are more generations of quarks.

E) The search for compositness of quarks and leptons.

The proliferation of quarks and leptons has led to speculation that they may not be pointlike particles but are rather built from some more fundamental objects called preons. These preons are bound together by a new force with a binding scale Λ. At energies much less than Λ, this composite structure could manifest itself as a four fermion interaction between quarks of the following form.[23]

$$g^2/\Lambda^2\, \bar{\psi} A \psi \bar{\psi} B \psi \qquad (7)$$

Here ψ represents a quark, g is the coupling strength of the new interaction whose spin structure is specified by A and B. This term is a low energy residue of the new interaction and will interfere with one gluon exchange to produce a cross-section for quark quark scattering at wide angle and center of mass energy $\sqrt{s}$, which has the following symbolic form

$$\sigma \sim E\, \alpha_s^2/s + F\, \alpha_s g^2/\Lambda^2 + G\, s g^4/\Lambda^4 \qquad (8)$$

Here E, F, G depend on the scattering angle and F and G also depend on the detailed structure specified by A and B. This form is valid only when $s < \Lambda$.[2]

If we assume that the interaction (7) is diagonal in flavor and that the coupling involves only left handed quarks ($A, B \sim \gamma^{\mu}(1 - \gamma_5)$)), then we obtain the result shown in Fig. 21 which shows the effect on the jet cross-section $d^2\sigma/dp_T dy$ at $y = 0$ and $\sqrt{s} = 40$ TeV in pp collisions as a function of Λ for $g^2/4\pi = 1$. The scale Q^2 in the parton distributions was taken to be P_T^2, a comparison with Fig. 7. reveals the sensitivity to this choice (see section B). For the values of Λ shown the effects of the second and third terms in equation 8 are comparable.

A search for substructure involves looking at the jet cross-section and seeing that it is flatter in p_T than expected from QCD alone. There is a potential problem in that the QCD expectation depends on the structure functions which need to be known with reasonable accuracy. Fortunately, regions of x relevant are such that one can have confidence that the structure function uncertainties are less than a factor of two. The following criterion should be adequate for detecting a composite effect. If $\Delta(p_T)$ is greater than one or less than 0.5 where

$$\Delta(p_T) \equiv \frac{d^2\sigma/dp_T dy|_{observed} - d^2\sigma/dp_T dy|_{QCD}}{d^2\sigma/dp_T dy_{observed}} \tag{9}$$

If we ask that this criteria be satisfied and that there be more than 50 events per unit of y then the 40 TeV collider has sensitivitity up to $\Lambda = 15$ TeV for an integrated luminosity of 10^{40} cm^{-2} sec^{-1}.

F) Searching for a heavy lepton

One is used to thinking that it is very difficult to find a heavy lepton in a hadron collider since the production rates are small and the signal poor. However, a new heavy lepton L appearing in a doublet (L, N) will decay $L \rightarrow W + N$ if $m_L - m_N > m_W$. I will assume that the mass of the new neutrino N is very small. L^+L^- can be produced in pairs in the Drell-Yan mechanism. The final state will consist of W^+W^- + missing momentum (carried off by N) giving a signature which should be recognizable even with the small rate.

The lepton can also be produced singly by the weak analog of the Drell-Yan mechanism

$$q\bar{q} \rightarrow W^* \rightarrow LN \tag{10}$$

this process leads to a single W in the final state at large p_T with a large amount of missing p_T. Figure 22 shows $d\sigma/dy$ at $y = 0$ for the process $pp \rightarrow L^{\pm} N + X$, where y is the rapidity of the LN pair, as a function of m_L. The rates are small but the only background from old physics is the final state W + Z where the Z decays into neutrino pairs. We can estimate the background as follows. Compare the signal with $|y| < 1.5$ with the background where both W and Z have $|y| < 2.5$. This larger bin is needed to take account of the mobility of the W from L decay. Requiring an excess of 50 events of signal over background gives Fig. 23 which shows the center of mass energy needed to reach a particular lepton mass for fixed values of effective luminosity. The true luminosity is the effective value divided by the efficiency for detecting a W. If this

efficiency is 0(1/10) then at $\sqrt{s}$ = 40 TeV a collider with luminosity of 10^{33} cm^{-2} sec^{-1} can reach masses of order 700 GeV.

G) Conclusion

I will summarize very briefly the conclusions drawn from Ref. 1. Several unsolved problems concerning backgrounds prevent one from claiming that some particular signal is clearly observable. One of the most critical issues concerns the observability of W's and Z's from their decays into hadronic jets. Many signals for new physics involve final states with W's or Z's (e.g. the minimal Higgs discussed in D). If one is restricted to observing the W's and Z's via their leptonic modes (which may not be possible for final states involving more than one W) only a small number of events will be detected – 5000 Z pairs decaying into ee and μμ results in only 18 detected events. The physics background to hadronic decays of W and Z is from QCD events with multiple jets. In the case of final states with 4 jets we have no reliable QCD estimate. Many particle searches (e.g. supersymmetric ones) involve signals which have missing transverse momentum, so the importance of hermetic detectors with 4π coverage cannot be overstated.

The difference between a pp and a $p\bar{p}$ collider is limited to a few special cases where the presence of valence antiquarks in the anti-proton is important (for example in the production of a new W). In order to exploit this advantage a certain minimum luminosity is required. ($\sim 5 \times 10^{31}$ cm^{-2} sec^{-1} for $\sqrt{s}$ = 40 TeV).

In conclusion a 40 TeV machine operating at a luminosity of at least 10^{32} cm^{-2} sec^{-1}, seems capable of answering the fundamental questions surrounding the breaking of weak interactions. The same assurance cannot be given for a 10 TeV Machine at the same luminosity.

Acknowledgments

I wish to thank my collaborators Estia Eichten, Ken Lane and Chris Quigg for their unceasing efforts in our seemingly endless collaboration. The work was supported by the Director, Office of Energy Research, Office of High Energy and Nuclear Physics, Division of High Energy Physics of the U.S. Department of Energy under Contract DE-AC03-7600098.

Referances

1. E. Eichten, I. Hinchliffe, K. Lane, C. Quigg, FNAL 84/17-T, LBL-16875, DOE/ER/01545-345 (1984).
2. S. L. Glashow, *Nucl. Phys. 22, 579 (1961);*
   A. Salam in "Elementary Particle Theory" p 367 ed W. Svartholm, Almquist and Wiksell (1968).
   S. Weinberg, *Phys. Rev. Lett. 19, 1264 (1967).*
3. G. Arnison, et al., *Phys. Lett. 122B, 103 (1983); Phy. Lett. 126B, 398 (1983).*
   M. Banner, et al., *Phys. Lett. 122B, 476 (1983);*
   P. Bagnaia, et al., *Phy. Lett. 129B, 130 (1983).*
4. A. P. Linde, *Sov. Phys. JETP Lett. 23 64 (1976);*
   S. Weinberg, *Phys. Rev. Lett. 36, 294 (1976).*
5. B. W. Lee, C. Quigg, H. B. Thacker, *Phys. Rev. D16, 1519 (1977).*
6. S. L. Glashow in Science 84 February 1984.
7. K. A. Wilson, *Phys. Rev. D3, 1818 (1971).*
8. H. Haber and G. L. Kane, Phys. Rep. to appear and Refs. therein.
   S. Dawson, E. Eichten, C. Quigg, FNAL 83/82-THY (1984).
9. E. Farhi and R. Jackiw (editors) Dynamical gauge symmetry breaking. World Scientific Publishing Singapore (1982) and Refs. therein.
10. R. Peccei, these proceedings.
11. D. V. Nanopoulos, these proceeding;
    D. Wyler, these proceedings.
12. G. Altarelli and G. Parisi, *Pucl. Phys. B126, 298 (1977).*
13. H. Abramowicz et al., *Z. Physik C17, 199 (1983); C132, 83 (1982).*
14. R. K. Ellis these proceedings.
15. F. Bergsma et al., *Phys. Lett. 123B, 269 (1983).*
16. R. K. Ellis et al., *Nucl Phys. B173, 397 (1980);*
    W. Slominski, Jagellonian University Thesis (1981).
17. P. Bagnaia et al., *Z. Physik C20, 117 (1983);* CERN-EP 84/12.
18. H. Georgi, et al., *Phys. Rev. Lett. 40, 692 (1978).*
19. R. N. Cahn and S. Dawson, *Phys. Lett. 136B, 196 (1984).*
20. H. Gordon, et al., in Proceedings of the 1982 DPF Summer Study on Elementary Particle Physics and Future Facilities ed. R. Donaldson, R. Gustafson and F. Paige Batavia, IL (1982).
21. R. W. Brown and K. O. Mikaelian, *Phys. Rev. D19, 922 (1979).*
22. M. K. Gaillard, *UCB-PTH-84/2 (1984).*
    M. Shochet in Proc. of DPF study on pp colliders U. Chicago, Feb. 1974.
23. E. Eichten, K. Lane, M. Peskin, *Phys. Rev. Lett. 50, 811 (1983).*

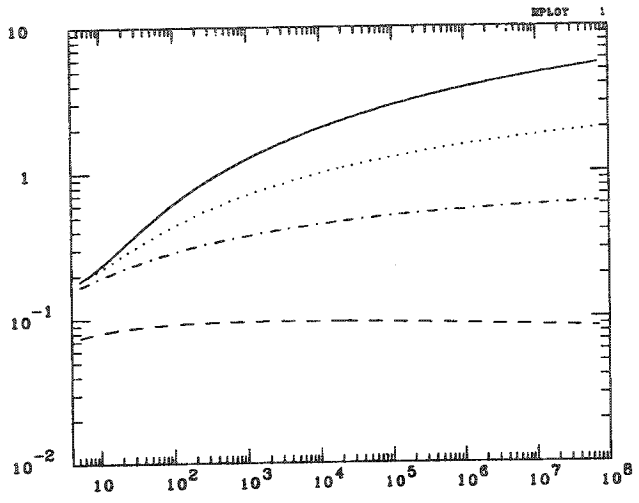

Fig. 1 The distribution $xg(x, Q^2)$ vs Q^2 in GeV^2 at $x = 10^{-4}$ (solid line) $x = 10^{-3}$ (dotted) $x = 10^{-2}$ (dot-dashed) $x = .1$ (dashed).

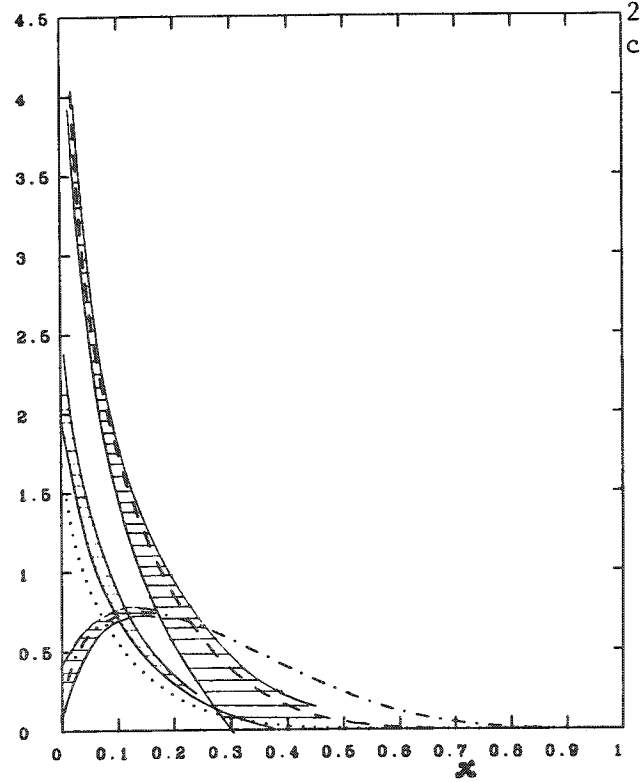

Fig. 2. Comparison at $Q^2 = 50\ GeV^2$ of x times the distribution functions, of the CHARM collaboration[15] (dashed regions) with these of Ref. 1. (dashed line) twice the anti-quarks (dotted line) and the sum of up and down valence quarks (dot-dashed line).

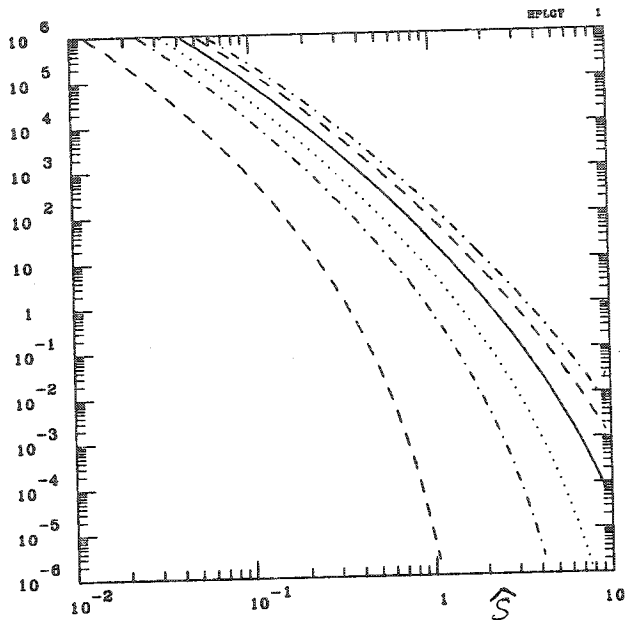

Fig. 3. The function $\tau/\hat{s}\ d\pounds/d\tau$ in nanobarns (eq. 5) as a function of $\sqrt{\hat{s}}$ for $\sqrt{s}$ = 2, 10, 20, 40, 70, 100 TeV for gluon gluon collisions.

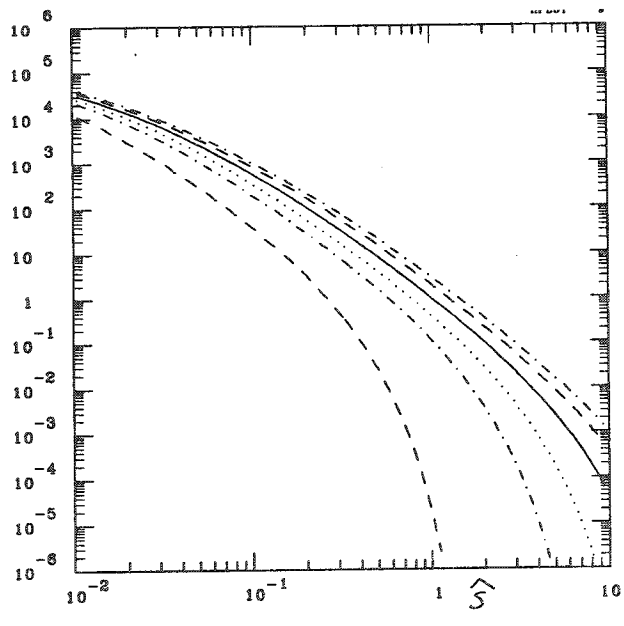

Fig. 4. The function $\tau/\hat{s}\ d\pounds/d\tau$ in nanobarn (eq. 5) as a function of $\sqrt{\hat{s}}$ for $\sqrt{s}$ = 2, 10, 40, 20, 70, 100 TeV for $u\bar{u}$ collisions in a pp collider.

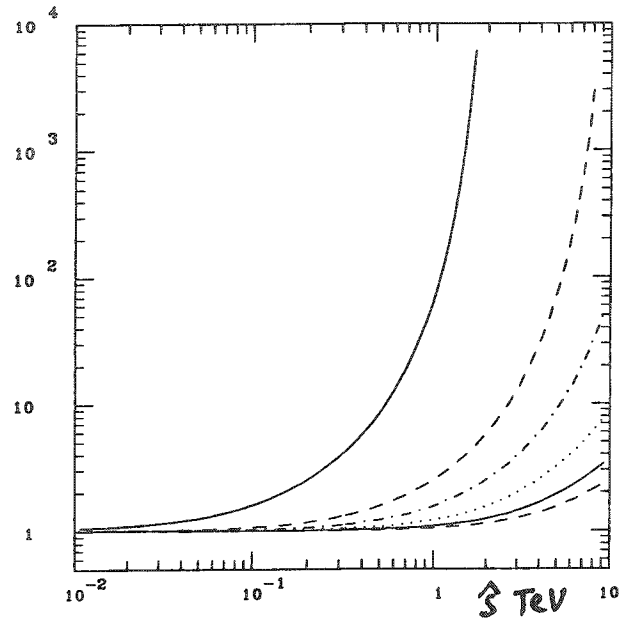

Fig. 5 The ratio of $\tau/\hat{s}\ df/d\tau$ for $u\bar{u}$ collision in $p\bar{p}$ to that in pp at $\sqrt{s}$ = 2, 10, 20, 40, 70, 100 TeV as a function of $\sqrt{\hat{s}}$.

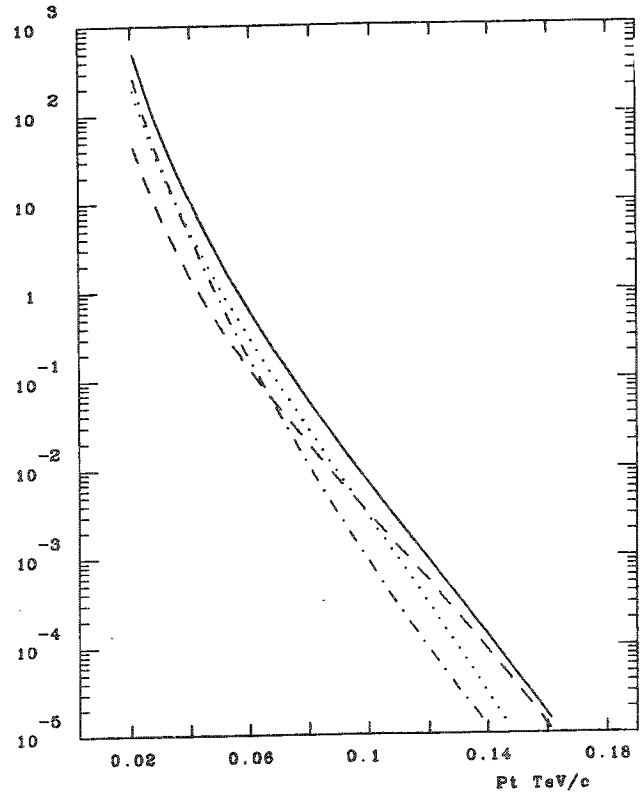

Fig. 6. The cross-section $d^2\sigma/dp_t dy$ in nb/GeV at y = 0 for the production of a jet in $p\bar{p}$ collisions at $\sqrt{s}$ = 540 GeV (solid line) the final states, gluon gluon (dot dashed) gluon quark (dotted) and quark quark (dashed) are shown separately.

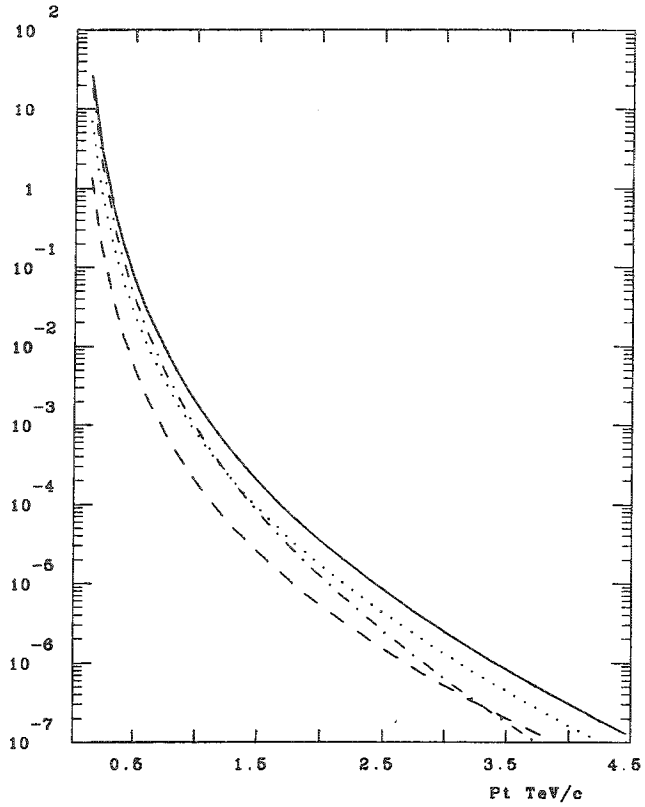

Fig. 7. As Fig. 6 except for pp collisions at $\sqrt{s}$ = 40 TeV.

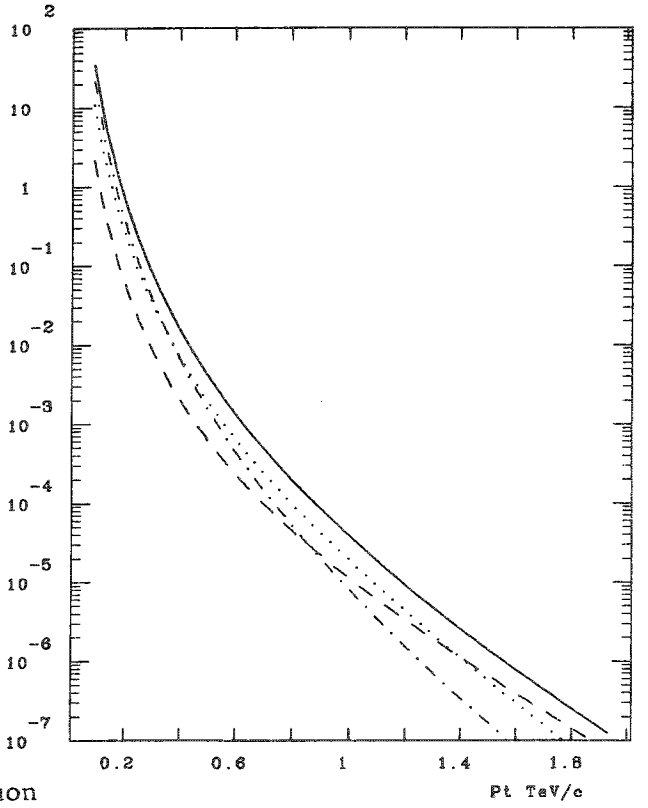

Fig. 8. As Fig. 6 except for pp collisions at $\sqrt{s}$ = 10 TeV.

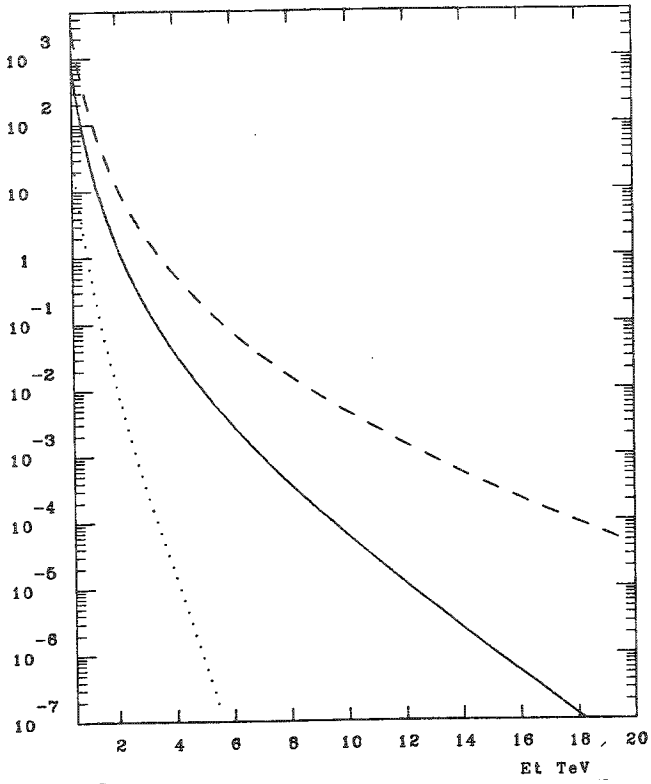

Fig. 9. The cross-section in nanobarns for the production of a pair of jets each with $|y| < 2.5$ and with total transverse energy greater than E_{TO}. $\sqrt{s}$ = 10, 40, 100, TeV shown.

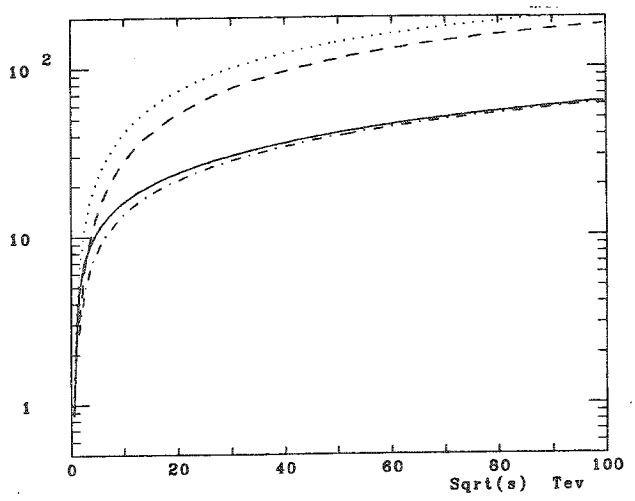

Fig. 10 The total cross section in nanobarns for the production of W^+ (dotted line), W^- (dashed line) in pp collisions as a function of $\sqrt{s}$. Also shown are the rates $|y_W| < 1.5$.

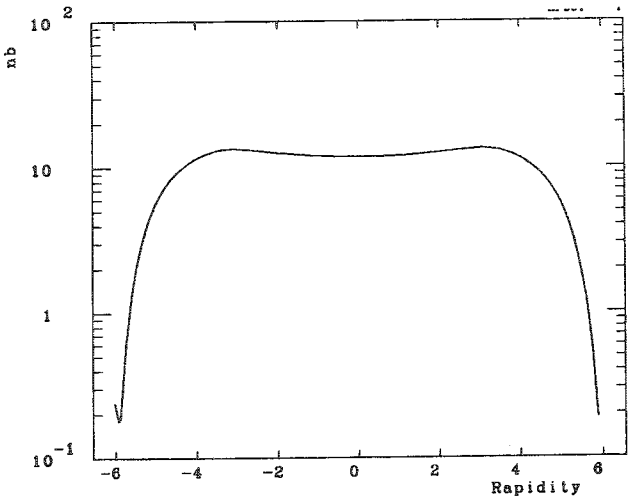

Fig. 11 The rapidity distribution $d\sigma/dy$ in nanobarns for the production of W^+ in pp collisions at $\sqrt{s}$ = 40 TeV.

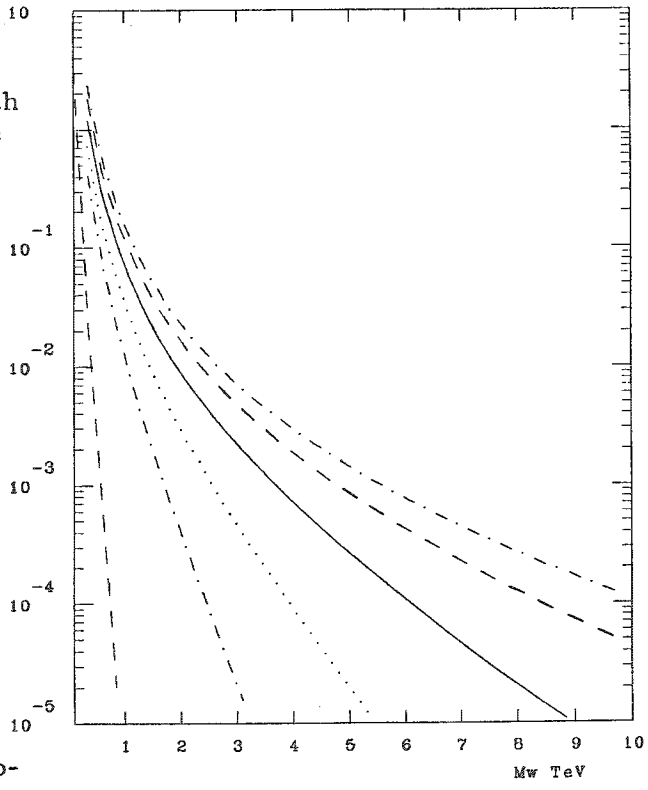

Fig. 12. The cross section for pp → $W^{+\prime}$ in nanobarns as a function of the mass of the new $W^{+\prime}$. The $W^{+\prime}$ is contrained to have $|y| < 1.5$. $\sqrt{s}$ = 2, 10, 20, 40, 70, 100 TeV shown.

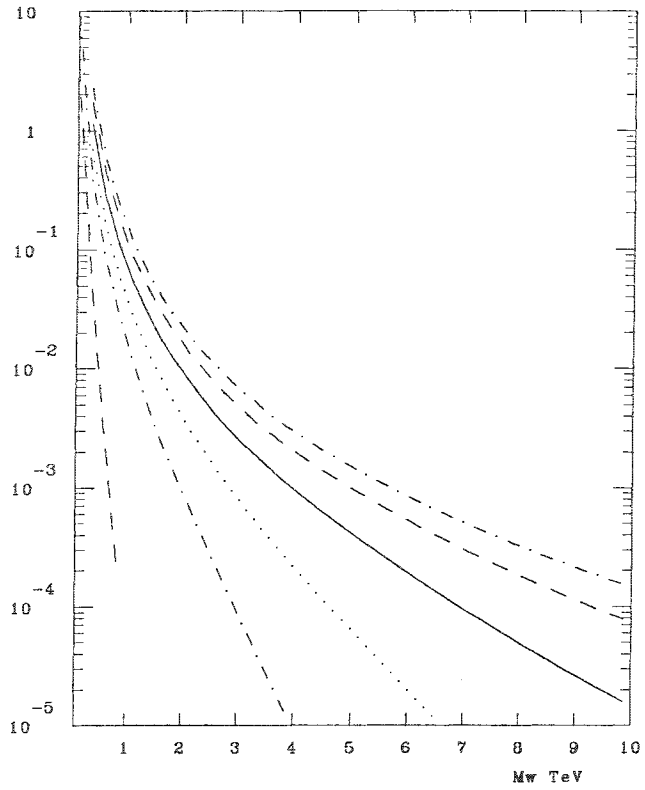

Fig. 13. As in Fig. 12 except for $p\bar{p}$ collisions.

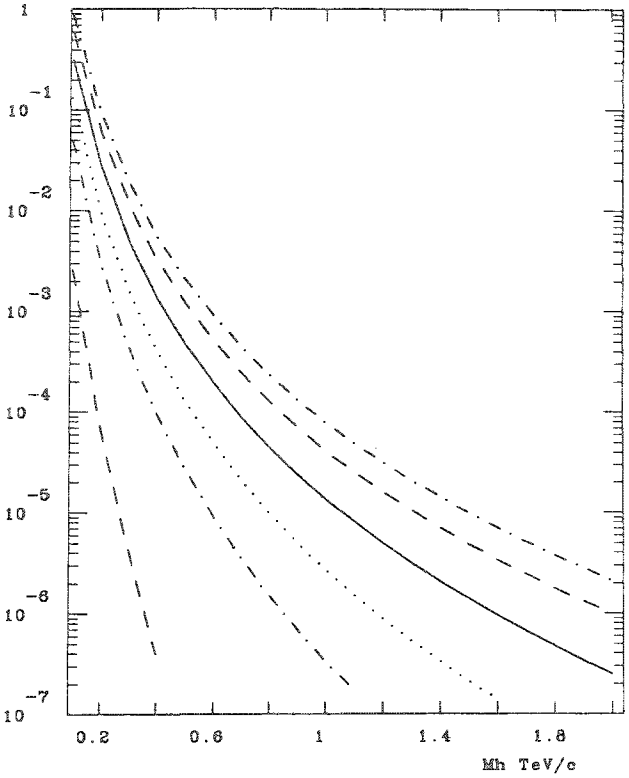

Fig. 15. Higgs production cross-section in nanobarns from gluon fusion mechanism[18] as function of m_H. $\sqrt{s}$ = 2, 10, 20, 40, 70, 100 TeV shown.

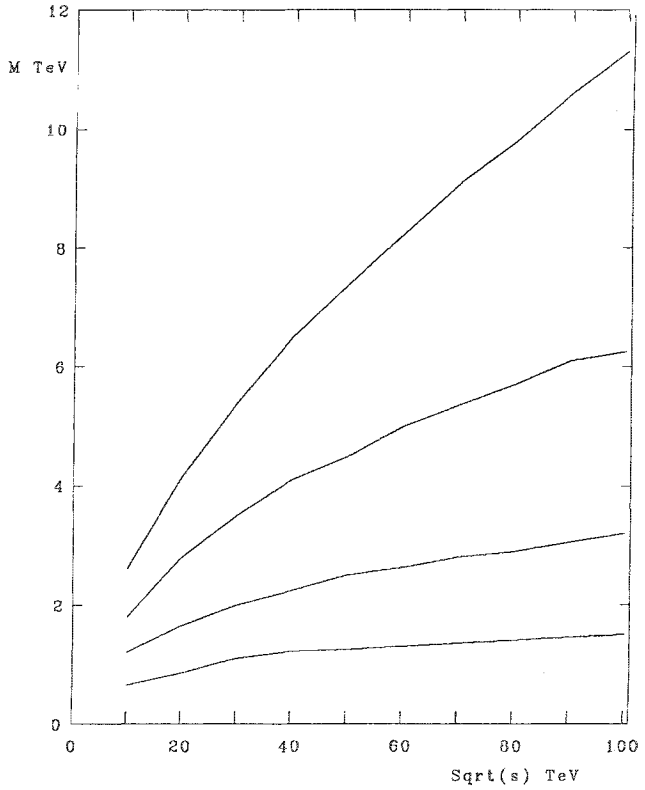

Fig. 14. The maximum $W^{\pm}$ mass which can be reached as a function of $\sqrt{s}$ for integrated luminosities of 10^{37}, 10^{38}, 10^{39}, 10^{40} cm^{-2}. (pp collisions)

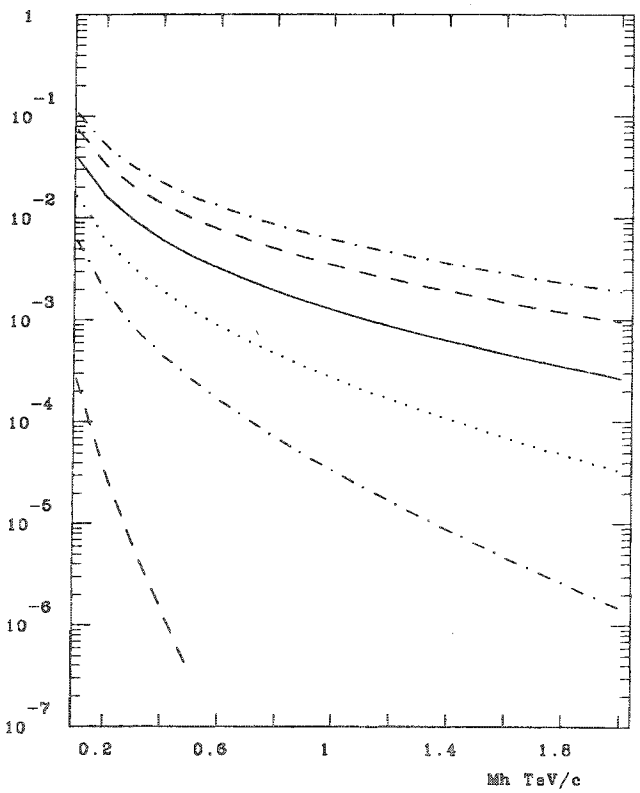

Fig. 16. Higgs production cross section in nanobarns via the gauge boson fusion mechanism[19]. A function of m_H. $\sqrt{s}$ = 2, 10, 20, 40, 70, 100 TeV shown.

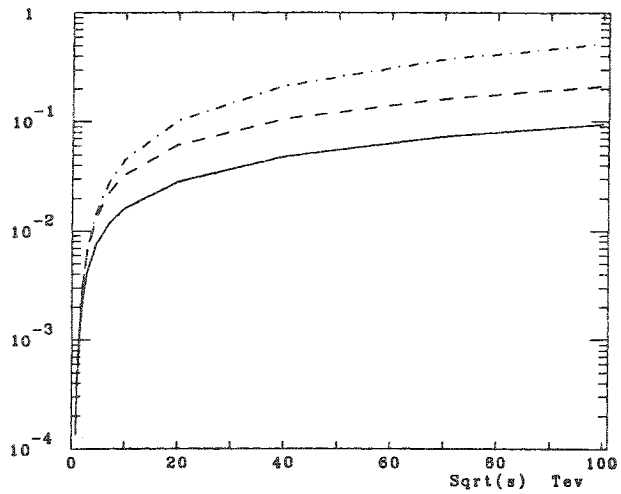

Fig. 17. Cross section in nanobarns for $pp \to W^+W^- + X$ as a function of $\sqrt{s}$. The lines are the total cross section and the cross-section contrained by $|y_W| < 1.5$ and $|y_W| < 2.5$.

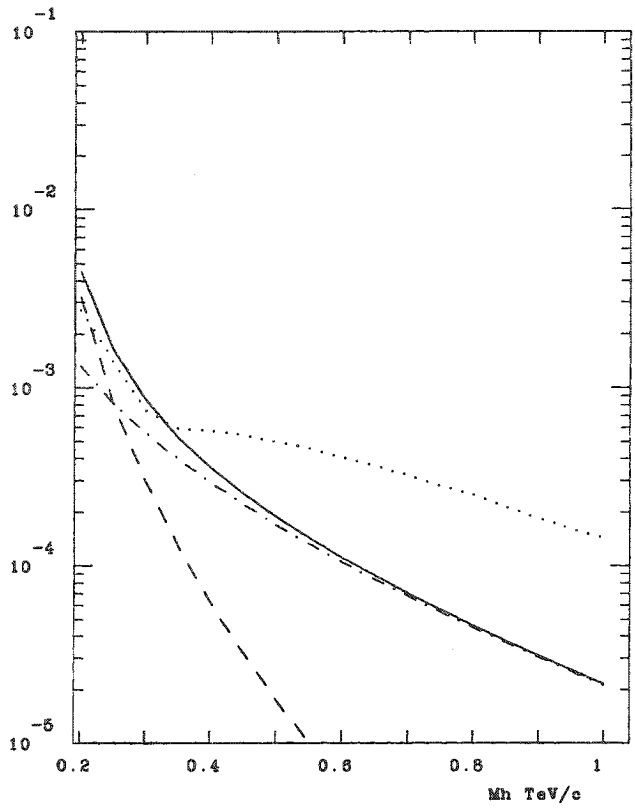

Fig. 19. As Fig. 18 except $\sqrt{s}$ = 10 TeV.

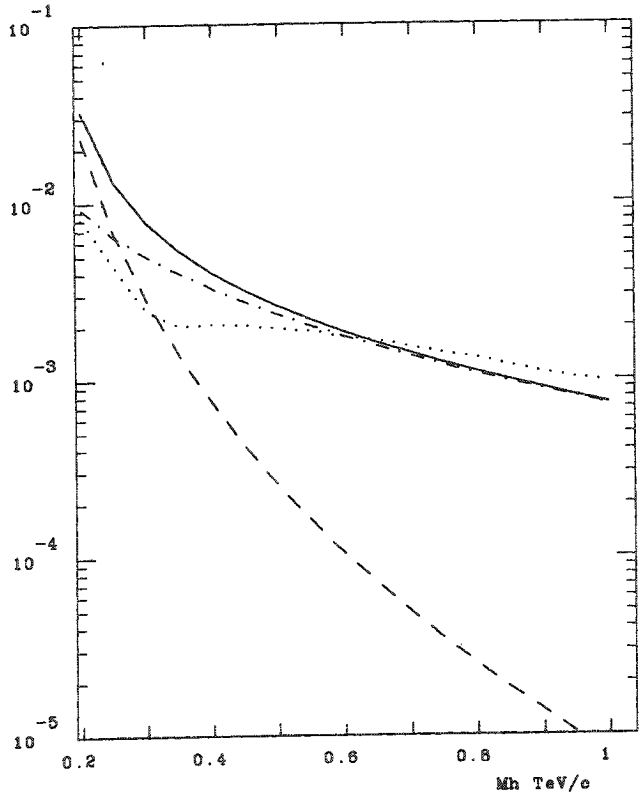

Fig. 18. Signal and background in nanobarns for the process $pp \to H \to W^+W^-$ with $|y_W| < 2.5$ at $\sqrt{s}$ = 40 TeV.

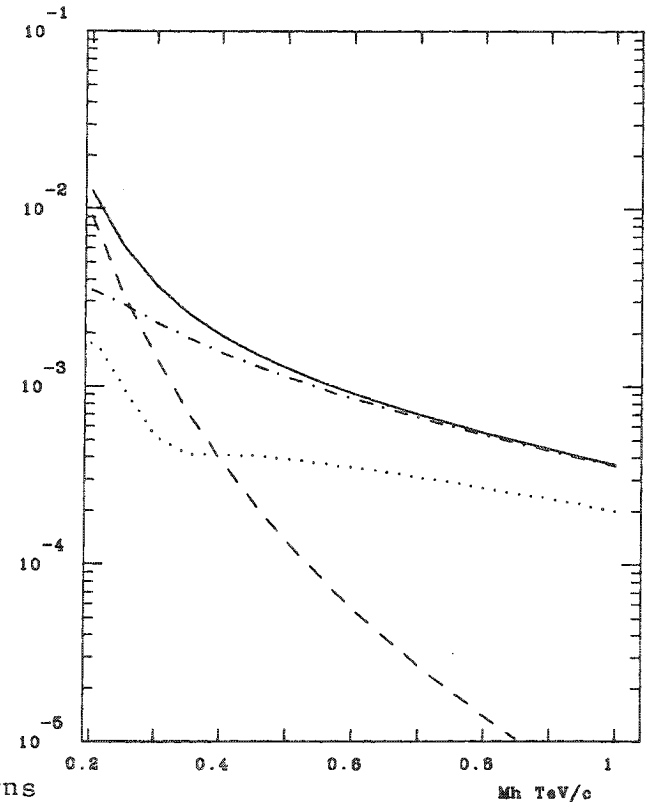

Fig. 20. Signal and background in nanobar for the process $pp \to H \to ZZ$ with $|y_Z| < 2.$ at $\sqrt{s}$ = 40 TeV.

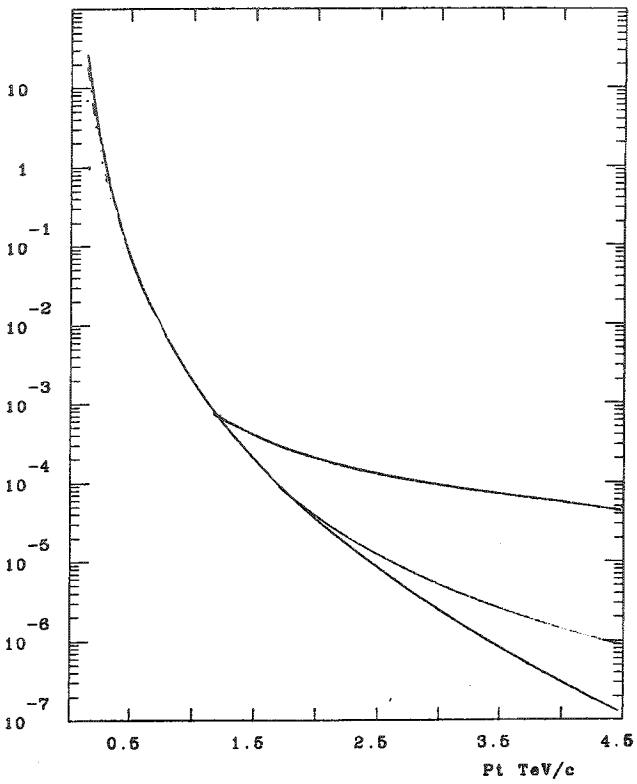

Fig. 21. The jet cross section $d^2\sigma/dp_t dy$ at $\sqrt{s}$ = 40 TeV and y = 0 in nanobarns/GeV as a function of p_t showing the effect of the term Eq. 8. Λ = 5, 10, 20 TeV shown.

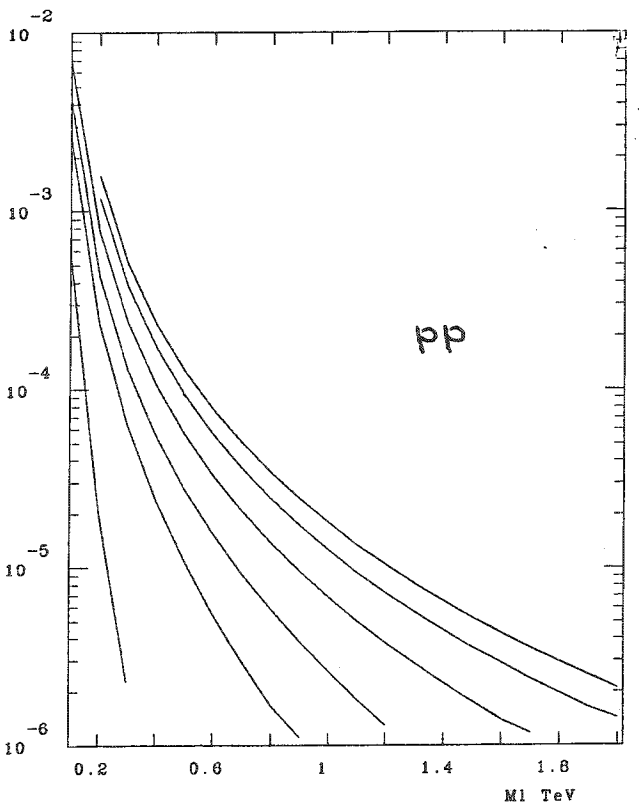

Fig. 22. The cross section $d\sigma/dy$ in nanobarns at y = 0 for the production of an (LN) pair by the process of Eq. 10. $\sqrt{s}$ = 2, 10, 20, 40, 70, 100 TeV

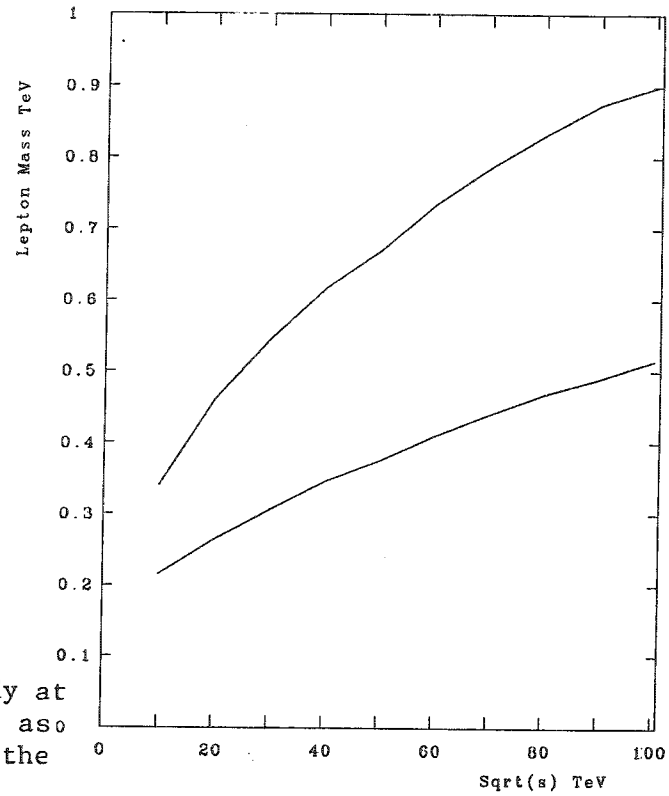

Fig. 23. Maximum mass for L which can be reached as a function of $\sqrt{s}$ for effective int. luminosities of 10^{37}, 10^{38} cm^{-2} according to the criteria of Section F.

LARGE HADRON COLLIDER IN THE LEP TUNNEL (AN EXAMPLE OF A HADRON COLLIDER)
A feasibility study of possible options

The CERN Machine Group presented by G. Brianti

European Organization for Nuclear Research
1211 Geneve 23 - Switzerland

1. INTRODUCTION

Hadron colliders (proton-proton or proton-antiproton) with bunched beams seem to be the only practical way of obtaining center-of-mass energies of several TeV or even tens of TeV, which opens the way to investigate collisions at constituents level in the TeV mass region.

Two examples of such colliders are the SSC (Super-Superconducting Collider) being studied in the U.S.A. and the LHC (Large Hadron Collider in the LEP tunnel) in Europe. A rather comprehensive account of the possibilities offered by the LEP tunnel is given as an illustration of the technical aspects and of the interplay between machine parameters and experimental requirements[1].

At the time of writing (May 1984) the SSC reference design report has become available[2]. It concerns a proton-proton collider of 20 TeV beam energy presented in three variants depending upon the chosen magnetic field of 3, 5 and 6.5 T.

The reader should refer to this report for further details.

2. REVIEW OF POSSIBLE OPTIONS

A wide range of possibilities exists for a Hadron Collider in the LEP tunnel, as shown in Fig. 1. The conceptually simplest option is a $p\bar{p}$ ring with a single beam channel which can either be built with super-conducting magnets of present technology or with high-field magnets after a fair amount of research and development effort. The luminosity is relatively low because antiproton sources are not very intense. In order to make provision for bunch separation at unwanted beam crossings, the aperture must be somewhat enlarged with respect to a single beam machine.

Using two beam channels gives a more versatile collider. The rings can have either a common magnetic circuit, which couples both rings magnetically, or two independent circuits. For space reasons, the two beam channels will always be in one cryostat. The most interesting option is the one where the two beam channels are side by side allowing for high luminosity pp collisions with many bunches. Depending on the desired field level, the two apertures may be part of a common magnetic circuit or of separate circuits.

In the first case (common magnetic circuit) there is enough space in the LEP tunnel to install high-field magnets. At high field level, the field must be necessarily equal and opposite in the two apertures as required for pp operation. This precludes $p\bar{p}$ with the beams in two separate channels. At considerably lower field level, the magnets can be excited such that the field is the same in both apertures and $p\bar{p}$ operation in two channels becomes possible. Of course it would be possible to put both the proton and the antiproton beam in one of the apertures, and either work with a low number of bunches at low luminosity without separation or install separators.

In the second case (independent magnetic circuits), pp and $p\bar{p}$ operations are equally possible at nominal field but, for space reasons, only moderate fields (~ 5 T) can be obtained.

Having the two coupled channels on top of each other allows for a $p\bar{p}$ machine which can have as many bunches as required without being beset with the problem of bunch separation as the one channel $p\bar{p}$ option. However, since this configuration does not provide a pp option, it is not considered any further.

These arguments favour very clearly the side-by-side, two-channel pp collider with one magnetic circuit; it holds the promise of top pp performance while leaving the door open for $p\bar{p}$ physics. The machine study focused on this option because it also appears as the more demanding one from the technological point of view.

The other option which has received some attention is the one-channel, high field $p\bar{p}$ collider. These two options represent in a certain sense two extremes and, therefore, provide a good coverage of the total range of possibilities.

Before turning to the machine performance of these two options we cast first a glance at the detector performance. Fig. 2 shows a graph of luminosity L versus the time T_x elapsing between two bunch collisions in the deetector. Also drawn are lines of constant $L.T_x$; along those lines the number of events $\langle n \rangle$ per bunch collision is constant for a given total proton-proton cross-section Σ. Since it is very difficult to handle more than one event per bunch collision, the line 1×10^{25} cm^{-2} therefore becomes an upper limit of the working region for a total cross-section of 100 mb. The maximum possible trigger-rate of the detector puts a lower limit on T_x providing a boundary on the left. One of the results of the March 1984 CERN-ECFA workshop was that values for T_x as low as 25 ns are conceivable without this being a too hard limit. Thus it can be seen that a luminosity of about 4.10^{32} can be obtained if the operating point of the machine is put at the top left corner of the region allowed for by the detector performance. For experiments which can accept a higher $\langle n \rangle$, luminosities up to $\leq 1.5 \times 10^{33}$ ($cm^{-2} s^{-1}$) could possibly be reached.

From the machine point of view this high luminosity operation is indeed feasible with the pp option. The number of bunches k is between 3000 and 4000. In order to make the bunch-to-bunch distance a multiple of the RF wave-length in the LHC and in the SPS, only discrete values of k are permitted. The value of 3564 fulfils this requirement and was chosen as nominal value. The graph also indicates the total number of particles which does not appear to be excessive, since it corresponds to only a few SPS pulses at the present performance level. The stored energy in the beam remains acceptable in the range under consideration; it reaches 70 MJ at $N = 5 \times 10^{13}$. The beam-beam effect, imposing a limit on the number of particles per bunch, is of not much concern because it cannot become very strong as long as the constraint of one event per collision is respected. The bunch intensity also seems low enough such that beam instabilities are avoided or can be dealt with by feed-back systems. Table 1 (see section 2)gives a list of the main parameters.

If detectors with a higher trigger rate were developed, the operating point could move upwards along the line $L.T_x = 10^{25}$ cm^{-2} and eventually approach $L = 10^{33}$ cm^{-2}s^{-1} for $T_x = 10$ ns. However, this implies an increase of the total number of particles N, which in turn means more stored energy in the beam. The increased number of bunches makes the beam also more prone to coupled-bunch instabilities. For this reason it is preferred to keep the nominal number of bunches at 3564, in agreement with the presently estimated detector performance, and to work out a consistent set of parameters on this basis, though it is not unreasonable to expect the eventual operating point somewhere in the shaded area of Fig. 2.

In the $p\bar{p}$ option the luminosity is limited by the $\bar{p}$ accumulation rate, which determines the total number of particles $N_{\bar{p}}$ accumulated in a time comparable to the luminosity decay time in the LHC. As explained in section 3 we may expect $N_{\bar{p}} = 10^{12}$ with the new antiproton source under construction in CERN. This imposes an upper limit on the luminosity around 1.5×10^{31} cm^{-2}s^{-1}. In order to minimize the number of unwanted bunch crossings in the one-channel machine, this limited number of antiprotons is distributed over the minimum number of bunches compatible with the requirement of one event per bunch collision. This leads to the working point shown in Fig. 2 for $N_{\bar{p}} = 10^{12}$ and, taking into account the constraints by the RF system, to 108 bunches in the machine, corresponding to $T_x = 825$ ns.

If a ten times more intense antiproton source became available, the luminosity could be increased in principle to a level of about 1.5×10^{32}. However, as can be inferred from Fig. 2, this leads either to an elaborate system for bunch separation at about 2000 unwanted crossing points, which becomes especially tricky near the interaction points, or to many events per

bunch collision in the detector, which is hardly acceptable. Obviously, a wide range of combinations in between these two extremes exists but all of them are beset with the problems of beam separation and of multiple events per bunch collision. Thus it seems to be difficult to exploit a more powerful source for peak luminosity. It should be noted, however, that the luminosity averaged over a run can be much improved by a better source because the machine filling can be more frequent. More details are given in section 3.

2. THE pp OPTION

2.1 Layout, parameters and performance

Fig. 3 shows schematically the ring layout with the 8 interaction points. The two beam channels are separated horizontally by ≤ 180 mm, and the insertions are designed such that the beams cross with a small angle of 96 μrad in the interaction points. Detectors can be put over at least six intersection points. Two long straight sections are reserved for the dumping of the beams though it might be possible to put eventually both dump systems into one straight section. Fig. 4 gives a cross-section of the LEP tunnel with the dipole of the LHC above the LEP magnets. It is apparent that the space available for the Hadron Collider is adequate. The assumption of installing it in the LEP tunnel determines the circumference which should be equal to that of LEP, 26658 m, within a very small margin; the number and length of the straight insertions, eight insertions of about 490 m length; and the average radius of the arcs, R = 3494 m. Because of the fixed radius, the maximum energy in each beam becomes a function of the magnetic field in the dipoles and of the layout of the LHC periods. The study is based on a dipole field B = 10 T.

The two proton beams are assumed to be bunched. Collisions between the bunches occur only in the interaction regions. This is achieved by a small crossing angle between the two beams. Bunched beams are preferred over continuous beams because they hold the promise of a higher luminosity for a given circulating current, and also because the energy loss due to synchrotron radiation is automatically compensated by the RF system.

From the users' point of view, the most important parameters are the luminosity L, the bunch spacing T_x and the average number of events per bunch crossing $\langle n \rangle$ related by

$$\langle n \rangle = L \cdot T_x \cdot \Sigma$$

where Σ is the total proton-proton cross-section. At the CERN-ECFA workshop a consensus was reached that, in the most general case, $\langle n \rangle$ should not exceed unity. For a cross-section of 100 mb, this means that the production $L.T_x$ should not exceed a value of 10^{25} cm^{-2}. Given this constraint, the largest

luminosity is obviously achieved with the smallest possible T_x which can be obtained by the machine and is still acceptable by the detector. The bunch spacing in time T_x cannot be varied continously because it must be a multiple of the RF wave-length in the LHC and in the SPS. However, the step-size is sufficiently small (5 ns) in the range between 5 and 35 ns such that the machine can produce the smallest bunch spacing the trigger of the detector can cope with. Since it seems that the detectors can handle bunch spacings as low as 25 ns, this spacing was adopted provisionally as nominal value in order to have a basis for one consistent set of parameters. However it should be noted that each of the possible bunch spacings needs a special small RF system in the PS. Thus the bunch spacing cannot be changed at a moment's notice.

It can be seen from Fig. 2, which gives a synopsis of all these limits based on the parameters given before, that the maximum luminosity is 4×10^{32} cm^{-2} s^{-1} for T_x = 25 ns and $\langle n \rangle$ = 1. Although the machine operation would become more difficult, it is not unconceivable that the luminosity could eventually approach or even exceed 10^{33} cm^{-2} s^{-1} provided a smaller T_x or a larger $\langle n \rangle$ is acceptable for the detector. This is indicated by the shaded area around the nominal working point in Fig. 2.

Table 1 gives the general parameters and performance.

Table 1 : GENERAL PARAMETERS AND PERFORMANCE

GENERAL PARAMETERS

COLLIDER TYPE IN LEP	PROTON-PROTON	
SEPARATION BETWEEN ORBITS (mm)	165-180	
NUMBER OF BUNCHES	3564	
BUNCH SPACING (ns)	25	
NUMBER OF CROSSING POINTS	8	
BETA VALUE AT CROSSING POINT (m)	1	
NORMALIZED EMITTANCE $4\pi\gamma\sigma^2/\beta$ (μm)	5 π	
FULL BUNCH LENGTH (m)	0.31	
FULL CROSSING ANGLE (μrad)	96	
LATTICE PERIOD LENGTH (m)	79	158
LATTICE PHASE ADVANCE	π/3	π/2
DIPOLE MAGNETIC FIELD (T)	10	10
OPERATING BEAM ENERGY (TeV)	8.14	8.99

PERFORMANCE

$\langle n \rangle$ at Σ = 100 (mb)	1 4
LUMINOSITY ($cm^{-2} s^{-1}$)	4×10^{32} 1.5×10^{33}
NUMBER OF PARTICLES/BUNCH	1.34×10^{10} 2.6×10^{10}
CIRCULATING CURRENT (mA)	86 167
BEAM-BEAM TUNE SHIFT	0.0013 0.0025
BEAM STORED ENERGY (MJ)	63 121
RMS BEAM RADIUS (μm) *	12
BEAM LIFE-TIME (h) **	42 21

* at interaction point for $\beta^* = 1$ m

** particle loss due to beam-beam collisions

The lattice consists of modules similar to the LEP lattice with arcs containing regular lattice cells, low-β insertions for collisions and dispersion suppressors for matching.

The LEP arcs and their support and supply systems are built in modules of length corresponding to half a cell, i.e. 39.5 m. We have limited the choice of LHC cell lengths to 79 and 158 m, associated respectively with 60° and 90° betatron phase advance. Fig. 5 shows the layout of the magnetic elements in a cell.

Fig. 6 shows a schematic layout and the optical functions. The quadrupole gradients are 250 T/m, the same value as in the standard lattice period. The value β^* can be increased by a factor 3 in order to overcome aperture restrictions and chromaticity problems during injection and energy ramping. The free space for the experiment between the quadrupoles is $\pm$ 10 m.

Two different inner diameters of the dipole coils were assumed for the study. The larger one (50 mm) allows for 40 mm inner diameter of the vacuum chamber; the smaller one (35 mm) leaves only 30 mm as inner pipe diameter, which precludes the use of the 90°, higher energy lattice as the injected beam diameter is 18 mm in this case.

The dominant field error effect is due to the persistent currents; it is a large sextupole component in the field of the dipoles. In any given magnet, this component is reproducible from cycle to cycle. However, between dipoles there is a random variation. The resulting chromaticity is compensated by appropriately exciting the sextupoles next to the quadrupoles in the LHC periods.

The widths of non-linear resonance stop-bands due mainly to the position tolerances of the superconducting wires are comparable to those in operating machines.

Intra-beam scattering imposes a minimum longitudinal emittance of the order of 2.5 eVs. This value is also sufficient to stabilize the beam via Landau damping against most of the presently known collective effects.

Most of the intensity dependent effects of importance in the LHC arise from the interaction of the beam with the vacuum chamber surrounding it. Therefore the relevant properties of the vacuum chamber must be carefully considered. Beam induced wall currents will heat the vacuum chamber, and together with the synchrotron radiation, contribute to the heat load of the cryogenic system. Table 2 shows the heat losses per unit length from the two counter-rotating beams averaged over the arcs.

Table 2

	Heat-loss Wm^{-1}
Resistive wall	.014
Broad-band	.09
Bellows	.026
Synchrotron Radiation *	.24
Total	.37

* emitted power per unit length

All intensity dependent effects discussed above are evaluated in the most difficult case of the 79 m long cell and a vacuum chamber radius of 15 mm. It was found that all collective phenomena could be handled in this lattice, with the help of appropriate feedback systems where required.

With the assumed parameters, a crossing angle of 96 μrad is large enough to ensure a sufficient separation at the first near-crossing. The long range beam-beam tune shift is only a fraction of the beam-beam tune shift at the interaction point and should pose no problems. Because of the short bunch-length involved, the loss of luminosity compared to head-on collisions is only 4%.

Eventually, a choice will have to be made. The arguments entering the choice are the maximum energy, the good field region of the magnets, field errors due to persistent currents and coil position errors in the dipoles, and collective phenomena. The advantages and disadvantages of the two period lengths, and the two vacuum chamber diameters are shown in Table 3.

Table 3 : COMPARISON OF CHOICES

Period length	79	79	158	158	m
Chamber radius	15	20	15	20	mm
Energy	8.136	8.136	8.993	8.993	TeV
RF voltage	16	16	28	28	MV
Tune spread	0.026	0.004	0.676	0.088	
Required good field radius	8.5	8.5	12	12	mm
Dynamic aperture due to					
- persistent currents	9	13	4	11	mm
- coil position	8	14	7	14	mm

2.2 Magnet system

According to present knowledge, the design and construction of accelerator magnets with field, say up to 6 or 7 T can be based on existing superconductors and on technologies already developped in Fermilab for the Tevatron and further tested in Desy for Hera, in BNL for CBA, in Serpukhov for UNK, and in KEK for Tristan.

The pioneering work done in various other laboratories (LBL-USA, CEA-Saclay, KfK-Karlsruhe, NIKHEF-Amsterdam, Rutherford Appelton Lab., CERN, etc.) can also serve as a very good base for future work.

Of course, before launching such an important project, several alternative designs should be considered with the prime aim of reducing production costs, and their features should be tested in an adequate number of prototypes. However, no fundamentally new development would be required. This is not true for magnets of higher field level up to 10 T.

Indeed, the purpose of the studies described in this section is to make a first assessment of the electromagnetic, cryogenic and mechanical problems which have to be faced for the design and construction of LHC magnets with a field as high as 10 T, would a suitable superconductor be available in time.

The development of such a superconductor, which can be industrially produced, is an absolutely necessary prerequisite to the final design and construction of such magnets. Small quantities of superconductors almost suitable for this application have already been made in industry.

Another important ingredient is the availability of insulation materials and techniques suitable for winding the coils according to the "wind and react" method.

Therefore all what is indicated below should be considered as a first assessment of the situation and as a guide-line for the indispensable development.

Dipoles and quadrupoles of the two rings are combined into "two in one" units, each having a common yoke and cryostat. The two rings are, therefore, magnetically coupled, especially at high field, which imposes the same energy for the two beams. Focusing quadrupoles in one ring are paired to defocusing quadrupoles in the other. Sextupole and dipole corrector pairs need to be magnetically uncoupled and can indeed be made so by means of independent cores. Horizontal dipole correctors in one ring are paired with vertical correctors in the other ring. The complete set of quadrupoles, sextupoles and dipole correctors will be contained in a common cryostat.

The dipole magnets should be made in units as long as possible, both because the bending length loss at each end reduces the attainable energy and in order to minimize the number of ends, which are the most difficult part of the magnet to fabricate. An upper limit to the unit length is, however, given by the access facilities (shafts, service tunnels, etc.) to the LEP tunnel, which are designed to allow installation of single components up to 12 m long. Another limitation to unit length is given by safety at a quench. It is estimated that 12 m long magnet plus cryostat units can be built, handled and operated without excessive difficulties and risks.

Existing evidence, gathered from experiments at the ISR and from the Tevatron, confirms the feasilibity of a cold vacuum chamber. Accordingly, no space for thermal insulation needs to be reserved in the magnet coil bore. For the sake of the present study it is assumed that the final choice for the inner diameter of the coil will fall in the range between 35 mm and 50 mm. Most of the work was therefore done on a version corresponding to the upper limit of 50 mm, which is more demanding in magnet size, excitation and structure. A possible dipole design is given in Fig. 7 with parameters in Table 4. One has also established that scaling to 35 mm is feasible from the magnetic point of view and probably acceptable for beam dynamics.

Table 4 : DIPOLE PARAMETERS

Nominal field	10 T
Peak field in windings	< 11 T
Average overall current density	300 $A.mm^{-2}$
Excitation (per dipole)	1300 kA-turns
Maximum current	~ 10 kA
Stored energy (full "2 in 1" magnet)	730 kJ/m
Coil inner diameter	50 mm
Distance between gap centerlines	180 mm
Transverse size of active part	
width	~ 600 m
height	~ 500 mm
Transverse size of the cryostat	
width	750 mm
height	900 mm
Magnetic length	10.23 m
Cold mass per unit length	~ 1.5 t/m

2.3 Cryogenics

The production, transport and distribution of the cryogenic fluids (He and N), are compatible with the space in the LEP tunnel. One refrigerator per octant should be installed in the interaction regions.

2.4 Vacuum

Profiting from the magnet cryostats, cold bore will be used, which intrinsically provides a very low pressure.

2.5 Radio-frequency

Only 30 m of active cavity structure are in total needed for both rings. To allow a large number of bunches in the Hadron Collider, the frequency should be ~ 400 MHz, namely the double of the SPS frequency.

2.6 Injection, beam transfers and dumps

At least two alternative layouts of transfer tunnels are possible between SPS and LEP (Figs. 8 and 9). Beam dumps are feasible with present technology.

2.7 Radiation protection

It has been established that there are no problems for the environment. Beam losses must however be controlled very well to avoid quenches of the superconducting magnets.

3. THE $p\bar{p}$ OPTION

Only a one-channel machine is considered as stated in the introduction. The layout of this single ring is shown schematically in Fig. 10. In order to make the bunches collide only in the eight interaction points, the orbits of protons and antiprotons outside the collision regions are kept apart by electrostatic separators which are positioned downstream and upstream of each interaction point.

The transfer of protons and antiprotons seems easier following Variant 2 (Fig. 9) since both types of particles circulate in the SPS in their normal direction. Using Variant 1 (Fig. 8) would combine the longer transfer lines with the disadvantage of polarity reversal of the SPS (for $\bar{p}$) and the construction of a new beam line linking the PS/SPS antiproton transfer line TT70 with TT10. Also TT10, the injection system in LSS1 and the extraction in LSS4 must be able to operate at reversed polarity.

Since there is only one channel in the ring, the magnets are simpler than for the pp collider, but the aperture possibly larger to accomodate the separation of the orbits. The stored energy in the beam is lower, and the beam is likely to be more stable because the number of bunches is reduced by more than an order of magnitude compared to the pp option. Unfortunately, these advantages have to be paid for by a lower luminosity and by the necessity of having separators. The separators deflect the beams in opposite directions electrostatically; their length is about 40 m per station. The operation of $p\bar{p}$ rings is also more complicated and the limited accumulation rate has adverse effects on the luminosity, especially when averaged over time.

As explained before, the peak luminosity is limited by the total number of antiprotons available at the beginning of a run. With the new CERN antiproton source approximately 10^{12} particles can be expected, resulting in a peak luminosity around 10^{31} cm^{-2} s^{-1} (see Fig. 2). Respecting $\langle n \rangle \leq 1$ and selecting a bunch spacing compatible with the RF yields 108 bunches as nominal number corresponding to T_x = 825 ns. The separators are installed behing the low-β quadrupoles but before the first unwanted crossing occuring at 124 m from the interaction point. The most promising scheme of beam separation makes the orbits spiral around each other by means of a set of vertically deflecting plates and a set of horizontally deflecting plates. Hence, the bunches always circulate off-centre in the arc, which might adversely influence their stability.

If the number of available antiprotons could be increased, say, to 10^{13} a higher peak luminosity could in principle be reached. If the number of bunches were not changed the number of events per bunch collision would become inadmissibly high as can be seen on Fig. 2 . Increasing the number of bunches k would help in this respect but quickly trouble arises if k approaches 300, corresponding to T_x = 300 ns. At this point the unwatned crossing has approached the low-β quadrupoles leaving no space for the long separators. Another serious problem arises during injection. The separation is not sufficient to prevent deflection of the already stored beam by the kicker magnet when the second beam is injected. Thus the injection kicker must be positioned between two unwanted crossings and its field must rise and fall within T_x. This is already difficult for 108 bunches but becomes nearly impossible once k reaches 200 to 300, at least with present technology. The possibility remains to separate the orbits by such an amount that the beam is not disturbed by the kicker field acting on the other beam. Such a scheme has not yet been worked out.

In order to obtain a resonable luminosity averaged over time, the duration of a run should be approximatley equal to the initial luminosity decay time τ_L. Taking this as a guide the necessary $\bar{p}$ acculation rate becomes :

$$A \gtrsim N_{\bar{p}} / \tau_L \quad .$$

For our parameters $\tau_L \sim 20$ h yielding for $N_{\bar{p}} = 10^{12}$ $A \gtrsim 5 \times 10^{10}$ h^{-1} and for $N_{\bar{p}} = 10^{13}$ $A \gtrsim 5 \times 10^{11}$ h^{-1}. The rate 5×10^{10} h^{-1} is the design aim of the the new CERN antiproton source and the FNAL source under construction, while 5×10^{11} h^{-1} could possibly be reached with a sophisticated multi-ring source.

It is apparent that even with a very advanced $\bar{p}$ source the maximum expected peak $p\bar{p}$ luminosity is inferior to the peak pp luminosity by about one order of magnitude. The machine becomes technically rather difficult for luminosities approaching 10^{32} cm^{-2} s^{-1}. Moreover, the ratio of average to peak luminosity will certainly suffer from the operational complications and will be lower than for the pp, which will profit from the powerful proton sources at hand.

4. FINAL REMARKS AND CONCLUSIONS

In this report we have considered mainly a proton-proton collider, as the most promising tool for extending the present energy range for research at constituent level into the TeV region.

The basic machine structure can of course be used for other possibilities, for instance for collisions of the electrons of LEP with the protons of the hadron collider, up to a centre-of-mass energy of about 2 TeV. Collisions of

ions would also be possible, with beam energy per nucleon of about one half of the proton energy. However, no work has yet been done on these other possibilities.

The conclusions which can be drawn from the study are :

i) A proton-proton collider can be installed in the tunnel above LEP. A center-of-mass energy of about 18 TeV could be reached with superconducting magnets of 10 T.

ii) In order to achieve this goal, it is necessary to launch in Europe a vigourous programme of development of materials and techniques necessary for the construction of such magnets.
Several European Laboratories and Institutions express a great interest to participate in such a programme.

iii) According to present knowledge, magnets with smaller field, say 6 or 7 T (centre-of-mass energy between 10 and 13 TeV), could be built after a shorter programme of technological development.

iv) All other machine components and systems appear to be feasible with the present technology.

REFERENCES

[1] Details of the design of the magnet and other major accelerator systems together with a full list of references are given in the Proceedings of the CERN-ECFA Workshop on the feasibility of a large hadron collider in the LEP tunnel held at Lausanne and CERN in March 1984.

[2] Superconducting Super Collider. Reference Designs Study for U.S. Department of Energy. May 8, 1984.

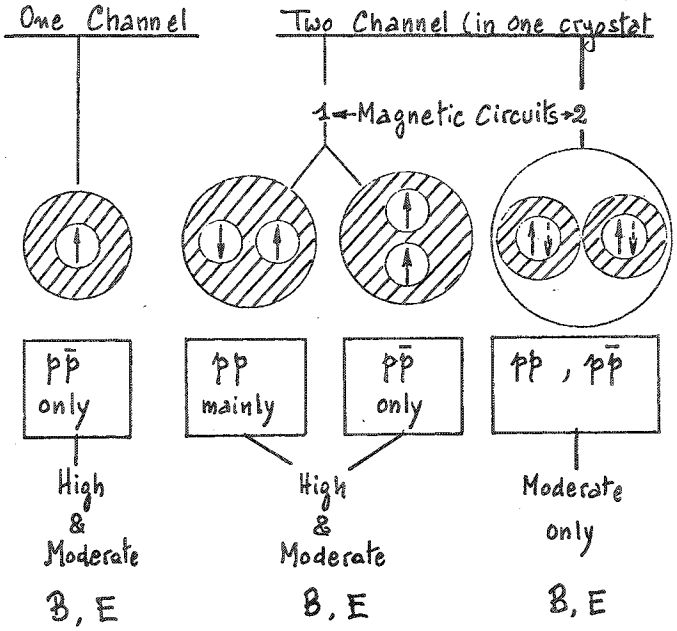

Fig. 1 : Synopsis of Hadron Collider Options for LEP Tunnel

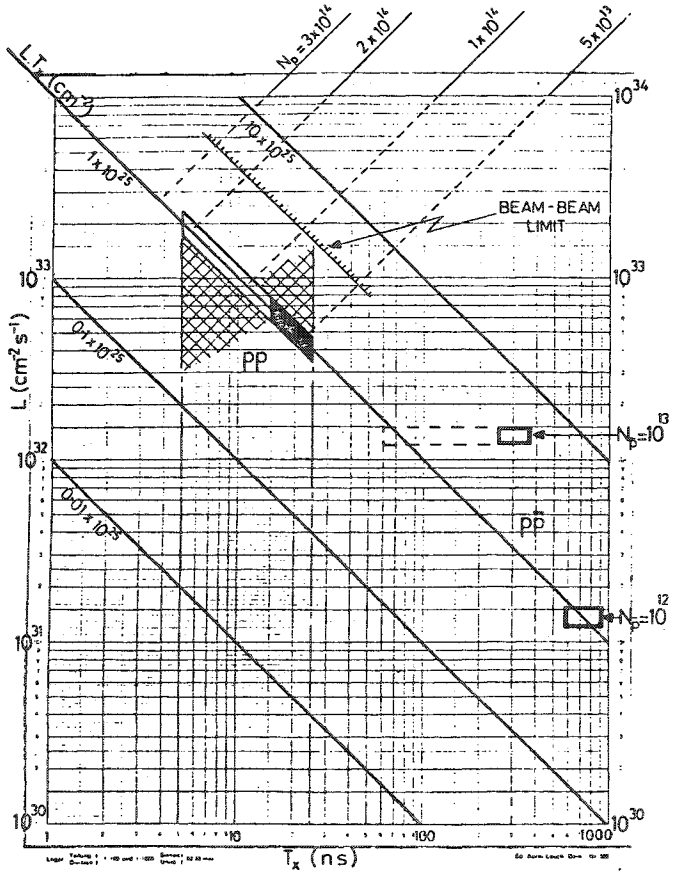

Fig. 2 : Performance of pp and $p\bar{p}$ Colliders

PROTON-PROTON COLLIDER

(TWO MAGNETIC CHANNELS)

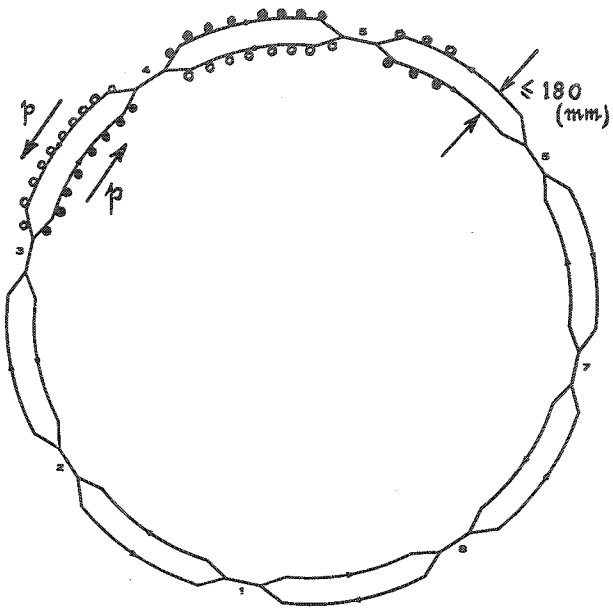

LEP TUNNEL

CIRCUMFERENCE	26659 M
ARC RADIUS	3494 M
REVOLUTION TIME	89 µS

Fig. 3

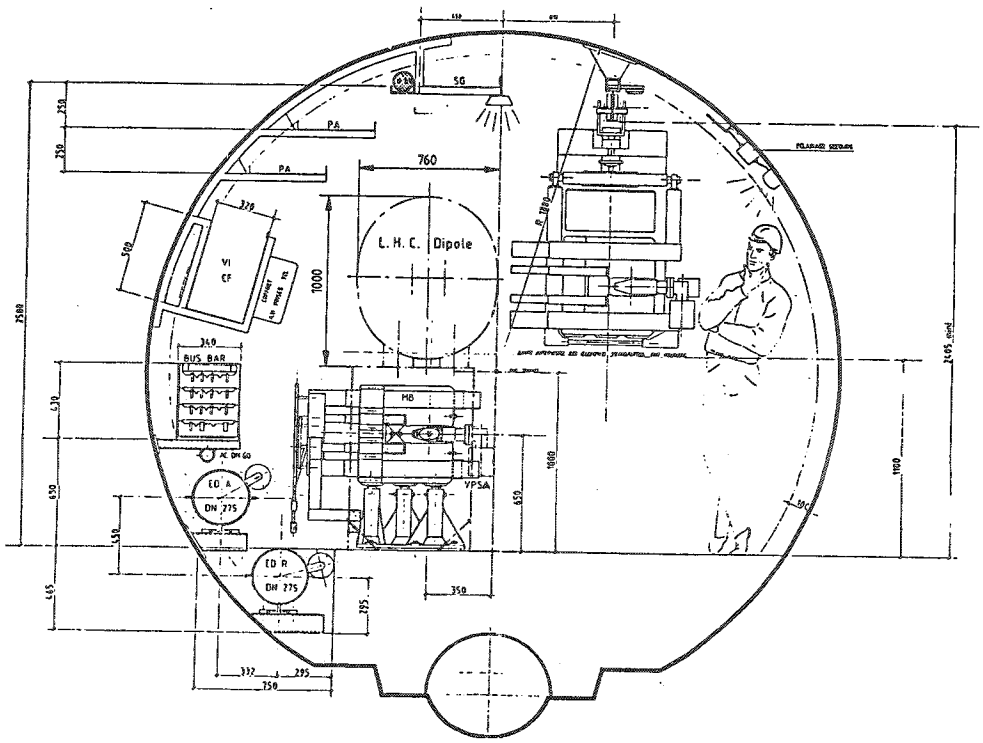

Fig. 4 : LEP Tunnel with LHC magnets above LEP dipoles

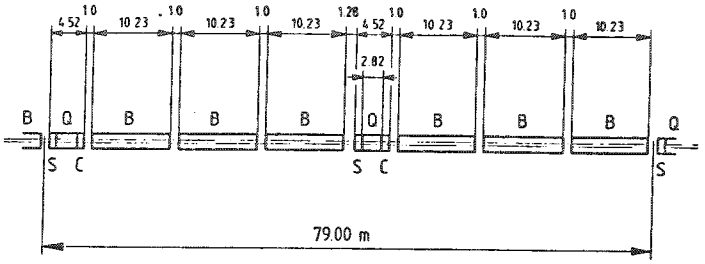

Magnet type	Approximate number
B = 2 in 1 dipoles	1600
Q = 2 in 1 quadrupoles	650
S = 2 sextupoles in the same cryostat	500
C = 1 horizontal + 1 vertical dipole corrector	500

Fig. 5 : LHC Typical Cell (magnetic lengths)

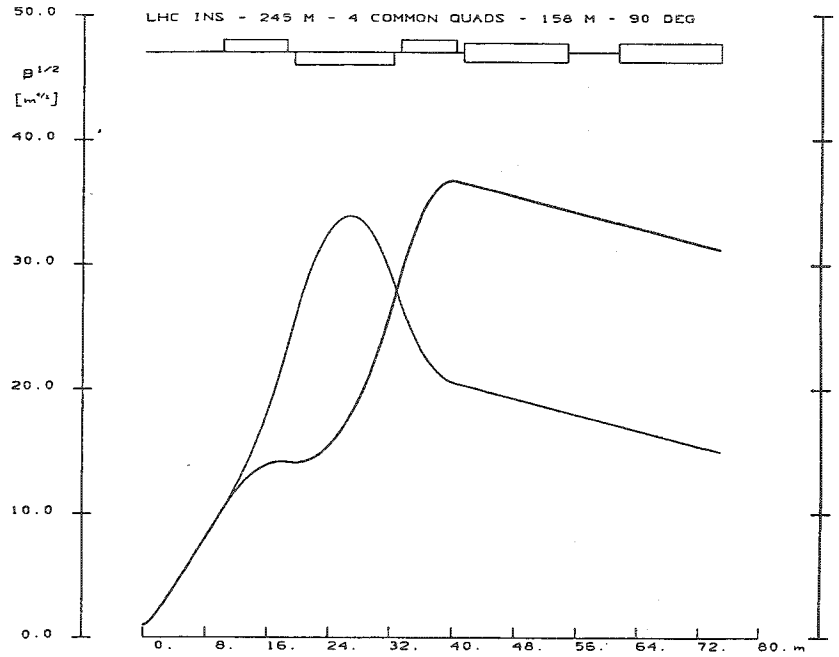

Fig. 6 : Schematic Layout of the low-β insertions

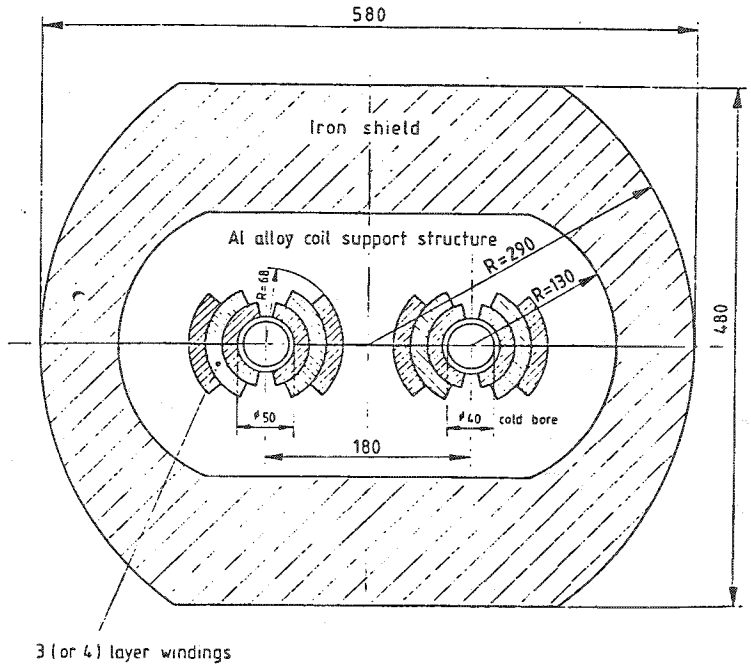

B_0 = 10 T

J_{av} = 300 A mm^{-2}

Fig. 7 : Twin Bore (2 in 1) Magnet, Cross-Section Type A

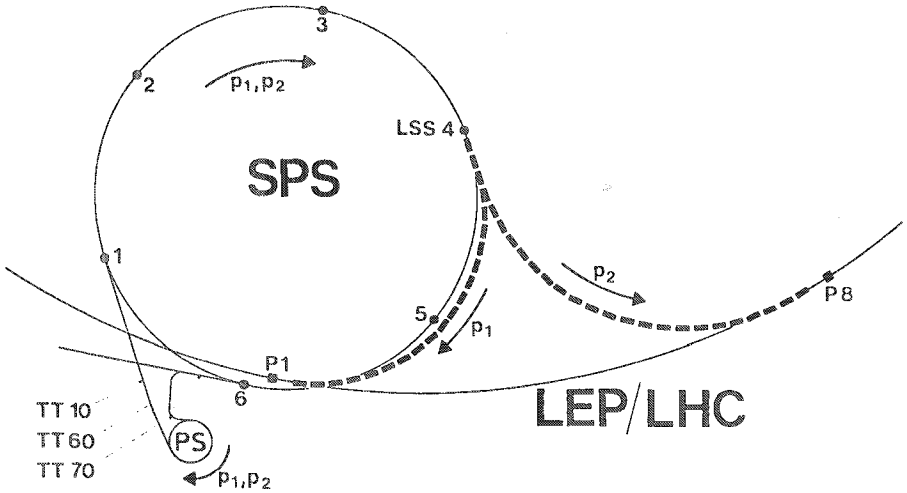

Fig. 8 : Beam Transfer through Injector Chain; Variant 1

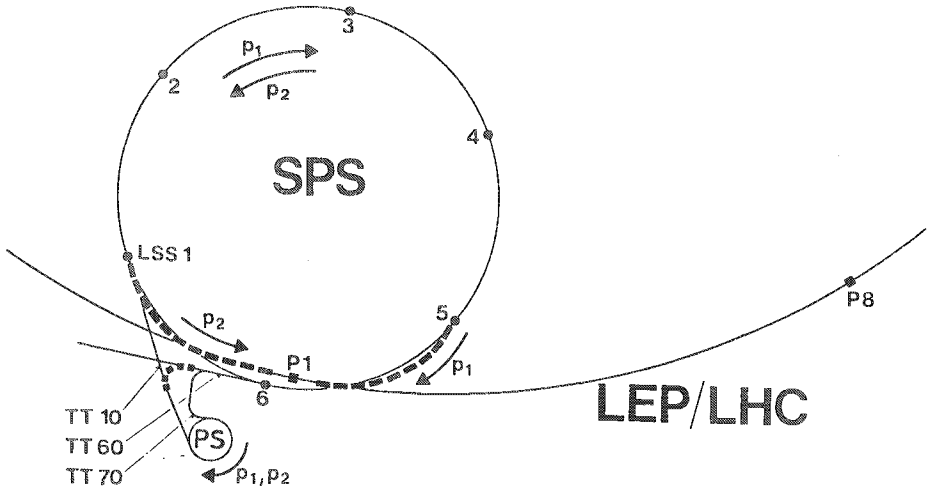

Fig. 9 : Beam Transfer through Injector Chain; Variant 2

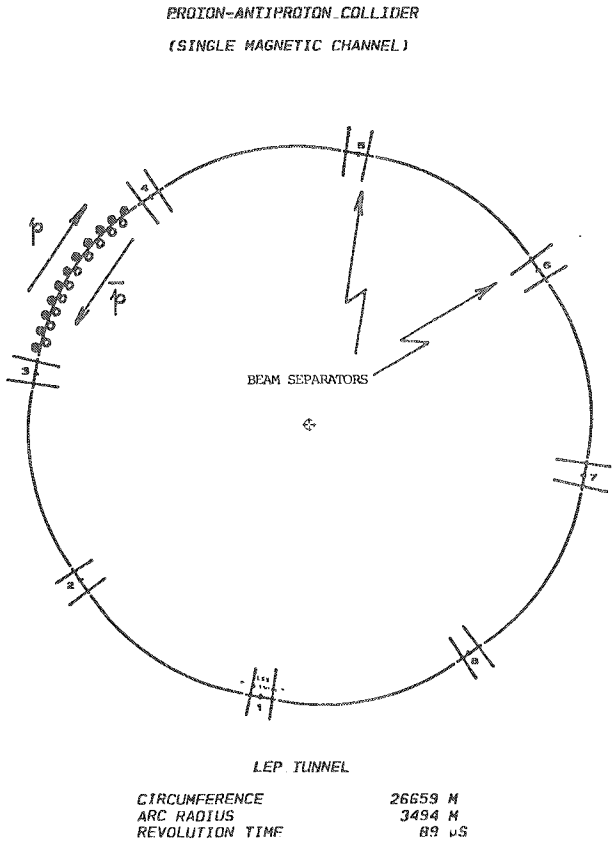

Fig. 10

Beyond the Standard Model

Higgs Scalars and Alternatives

D. Wyler
Theoretical Physics
ETH Hönggerberg
8093 Zürich, Switzerland

1. Introduction

Although the W- and Z-bosons were discovered with masses and widths precisely as predicted by the standard model[1),2)] (in fact, perturbation theory seems to be valid within a few percent[3),4)]), we feel that the basic dynamics of the theory, in particular the way the W and the Z become massive are not understood (say, as well as superconductivity is understood by the BCS theory). This is widely regarded as one of the most important questions in high energy physics. It is intimately connected to the existence of scalar particles whose experimental discovery is therefore so desired[5)]. On a somewhat different, presumably secondary level there are other open problems whose solutions are conceivably connected with scalars: "Family"structure of quarks and leptons; CP-violation; (in particular if forthcoming experiments give a very small ε' in the Kaon system); very rare decays such as $\mu \to e\gamma$. (And, clearly, supersymmetry[6)] requires scalars, which are, however, of a different type; their necessity is rather of kinematical nature; this applies equally for models of composite[7)] leptons and quarks).

The results of the UA1 and UA2 groups clearly rule out models with generalized global SU(2) symmetry[8)]; phenomenological models of γ-Z mixing[9)] cannot explain why $g = e/\sin\theta_W$ etc. and offer no attractivity. But also models with composite W, Z, derived from composite models for quarks and leptons[7)] are difficult to live with. In such models, the W and Z are analogous to the $\rho^{\pm}$ and ρ^{o} (and possibly to K*,... with interesting (or devastating) consequences). Anticipated consequences are relatively large width, somewhat higher masses than those observed, non-automatic μ-e-quark universality, smaller θ_W (if universality is imposed). Furthermore, recent considerations of the dynamics of such theories indicate that the observed mass spectrum might not be attainable[10)].

Therefore I will take the view that the W and the Z are indeed gauge particles; we will stick to the standard SU(2) x U(1) scheme.(Many aspects are, however, not tested. For instance the cubic and quartic gauge boson couplings, which are g and g^2 in the gauge theory (g = gauge coupling) should be measured[11]. Note, that in the composite models these couplings are not necessarily g and g^2).

Then, in order that the W and Z are massive we must have a complex order parameter, a scalar, as pioneered by the BCS theory. It can be elementary or composite. After the "Higgs-Kibble" effect, there remain physical scalars (this holds always as can be seen by simple group theory), unless we "freeze" them out[12] (as in the non-linear σ-model), or make its mass very large. The price we pay is loss of renormalizability, e.g. of the ability to carry out sensible perturbative calculations, basically, because some couplings are strong. We do not know how to treat such systems, except in idealized circumstances. For example, in the two-dimensional σ-model, although the extra state has been removed in defining the basic Lagrangian, it reappears in the spectrum of physical states, due to non-perturbative effects[13]. It might be that this does not happen in four dimensions or in a gauge theory. It is, however, remarkable that unlike in the case of the W, making the scalar very heavy results in almost unmeasurably small radiative corrections and violations of unitarity. For instance corrections to ρ due to a large scalar mass m_H give [14]

$$\delta\rho = \delta\left(\frac{M_W^2}{\cos^2\theta_W M_Z^2}\right) = -5.7\cdot 10^{-4}\log\frac{m_H^2}{m_W^2} + 2.85\cdot 10^{-7}\,\frac{m_H^2}{m_W^2} \qquad (1)$$

and thus

$$\delta\rho = 1\% \iff m_H \gtrsim 10\ \text{TeV} \qquad (2)$$

Considerations of W^+W^- scattering yield a violation of unitarity only if [15] (including width effects[16])

$$E(W^+,W^-) \gtrsim 1\ \text{TeV}\ ,\ m_H \gtrsim 1.5\ \text{TeV} \qquad (3)$$

This effect is called "screening" (Veltman[5]).

We now turn to the description of the relevant interactions of elementary and composite scalars and then to possible production mechanisms.

2. Elementary scalars[17]

In the standard GSW model, there is one physical scalar, a neutral 0^+ state. Its couplings to fermions and gauge fields are known, but its mass not. Requiring symmetry breaking perturbatively gives a lower mass bound,[18] $m_H \gtrsim 8$ GeV. (A set of nuclear physics experiments gives $m_H \gtrsim 15$ Mev[19].) Experimentally, an upper bound is more interesting. Recent work by rigorous physicists[20] indicates that a pure ϕ^4 theory (e.g. the renormalizable scalar field theory with quartic interactions used in the GSW model) is a trivial theory. In view of this one is led[21] to obtain an upper mass as follows. If the ϕ^4 coupling constant is too large (and thus also the mass of the scalar) then the model is like a pure (and therefore uninteresting) ϕ^4 theory. These arguments lead to a mass bound[22]

$$m_{scalar} \lesssim 125 \text{ GeV} \tag{4}$$

(It is interesting to note that the "scalar" in the BCS theory has about the same mass as the gauge boson[24]). Production and detection of this scalar have been described in many articles[23]. Less attention have received models with several scalars, introduced for many purposes (some are listed in the introduction); and I would like to stress these here. Note that some of these might be light, as the bound above[18] need not hold[25]. The couplings of the scalars, collectively denoted by H to known particles are given by

$$\mathcal{L}_{Fermions} = \frac{-g}{\sqrt{2}M_W} H^+ (\bar{U}_L D_R m_D K e_1 + \bar{U}_R D_L m_U e_2) + h.c. + \frac{g}{2M_W} H^0 (\bar{D} D m_d E_1 + \bar{u} u m_u E_2) + \cdots \tag{5}$$

$$\mathcal{L}_{gauge} = g c_1 H^0 W W m_W + \sqrt{g^2+g'^2}\, c_2 H^0 Z Z m_Z + \cdots + g c_3 W H^+ \overleftrightarrow{\partial} H^0 + \sqrt{g^2+g'^2}\, Z (c_4 H^+ \overleftrightarrow{\partial} H^- + c_5 H^0 \overleftrightarrow{\partial} H^{0\prime}) + e c_5 H^+ \overleftrightarrow{\partial} H^- \gamma . \tag{6}$$

In (5) U_L, D_R, etc. stand for lefthanded $\frac{2}{3}$ charged quarks, etc.; K are Kobayashi-Maskawa angles, e_1, e_2, ... are (de)enhancement factors. In (6), c_1, c_2, ... are mixing factors, originating in the scalar self-interactions. In (5) and (6) $H^\pm$, H^0_i stand collectively for charged and neutral scalars, the ... indicate further scalars. (5) and (6) determine essentially production and decay of H_i^0, $H^\pm$. We note that the enhancement factors e_f and E_f in (5) may change the naive expectations considerably. For example, the decay of a H^0 into a pair

of gluons may dominate over decay into a quark pair of mass m_q [27] and the final state analysis will change accordingly.

3. Composite scalars (Technicolor)

As mentioned above the theory of elementary scalars shows some oddities (along with the notorious quadratic divergences). If compared with the theory of superconductivity, it corresponds only to the phenomenological Ginzburg-Landau theory. These reasons have led to considering the scalars as composite, made from fermion-antifermion pairs, held together by a new force, the technicolor gauge interactions [28), 29]. These scalars are generally pseudoscalars. The lightest are expected to be

$$\begin{aligned} &\text{colorless: } P^0, P^{0\prime}, P^{\pm} && \text{mass} \simeq 10\text{-}50\ \text{GeV} \\ &\text{leptoquarks: } P_3 && \text{mass} \simeq 320 \cdot n^{-1/2}\ \text{GeV} \\ &\text{coloroctets: } P_8^{\pm}, P_8^0, P_8^{\prime} && \text{mass} \simeq 480 \cdot n^{-1/2}\ \text{GeV} \end{aligned} \qquad (7)$$

where n = number of technicolor generations. Their interactions with fermions are similar to (5); with gauge bosons G_μ^c we have

$$\mathcal{L} = P^a \partial_\mu P^b G_\mu^c C_{abc} + \frac{n\sqrt{2}}{8\pi^2 (250\,\text{GeV})} G_{\mu\nu}^a G_{\mu\nu}^b S_{abc} P^c \qquad (8)$$

where $C_{P^+P^-\gamma} = e$, $C_{P^+P^-Z} = e \operatorname{ctg} 2\theta_w$, $C_{P^+P^0W} = \frac{g}{2}$, $C_{ZP^0P^0} = 0$ and the S are given in table 1.

Table 1: couplings S defined by Eq.(8). c, s refer to $\cos\theta_w$, $\sin\theta_w$.

P \ GG	$\gamma\gamma$	ZZ	$Z\gamma$	W^+W^-	gg	γg	Zg	Wg
P^0	$\frac{4}{\sqrt{6}} e^2$	$-\frac{e^2(s^2-c^2)^2}{\sqrt{6}\,sc}$	$\frac{e^2(1-\frac{8}{3}s^2)}{\sqrt{6}\,sc}$	–	–	–	–	–
$P^{0\prime}$	$-\frac{4}{3\sqrt{6}} e^2$	$-\frac{e^2 16 s^2}{3\sqrt{6}c^2}$	$\frac{e^2 8 s}{3\sqrt{6}c}$	–	$g_s^2 \frac{1}{\sqrt{6}}$	–	–	–
P_8^0	–	–	–	–	–	eg_s	$eg_s \frac{c^2-s^2}{2cs}$	–
$P_8^{0\prime}$	–	–	–	–	g_s^2	eg_s	$-eg_s \frac{s}{3c}$	–
P_8^+	–	–	–	–	–	–	–	eg

4. Decay and production

I will only touch on a few topics here; some aspects, in particular of the standard Higgs, have been previously considered in detail[23].

In the GWS model, the scalar decays into the heaviest particles available. This need not hold in models with several scalars and the decay modes may be quite different[27]. Note, however, that the enhancement factors we encountered in (5) are not possible in technicolored theories[30]. Also, charged scalars can behave quite differently from neutrals. Let us go through some points.

a) If the scalar mass is below any of the $\bar{Q}Q$ resonances, its production via these is the most promising mechanism. In the standard treatment, one considers $\bar{Q}Q \to$ scalar $+ \gamma$[31]. Thus a charged scalar is hard to see in this way. The process may, however, be very important for P_o, P' if $t\bar{t}$ is sufficiently heavy. "Lighter" charged scalars are presumably best seen in decays of heavy flavors such as $Q \to H^+ + q$.

b) Above toponium "gluon fusion"[32] has been proposed as production mechanism for a single scalar. Clearly, this is not possible for charged scalars; it is strongly suppressed for heavy scalars ($1/m^2$ dependence due to it being an s-channel process). But it is very favorable for models with enhancement factors and for technicolor. For very large c.o.m. energy also other vector fusions (WW, WZ, etc.) can be important[33]. Here, of course, charged scalars can be produced.

c) Another well known mechanism is associated production[34], where a W is produced which radiates a scalar. This mechanism yields generally smaller production rates than fusion. It does not apply for charged scalars and the technicolor particles due to the absence of WZH couplings for the former and the smallness of the $PG_\mu G^\mu$ couplings (8) for the latter.

d) In models with charged scalars the couplings (6) give rise to a "quasi-associated" production where the produced gauge boson radiates away a scalar and turns into another. Clearly this mechanism will be useful if the scalars are not too heavy.

e) "open" fusion, by diagrams such as in Fig. 1. This mechanism requires the energy to produce the scalar along with the two quarks Q, Q'. We expect Q and Q' to be rather heavy (to give a larger QQ'H coupling). H can be charged or neutral (and, of

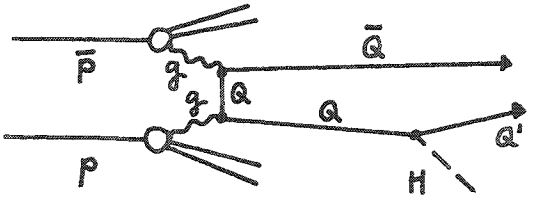

Fig.1: Production mechanism for HQQ'

course a technicolored particle). We estimate this rate roughly to be $\sigma(t\bar{t}) \times \frac{g}{3} \simeq O(pb)$ where $\sigma(t\bar{t})$ is the $t\bar{t}$ production cross section. Of course, for large energies, the gluons can be replaced by W etc.

f) Heavy flavor production[35]. Since scalars couple to large masses and the "sea" of the protons at high energies contains heavy quarks, these can be used to produce scalars by diagrams such as in Fig. 2. (It is somewhat similar to e) above). Again, it applies to both neutral and charged scalars; in particular it might be important for the latter ones.

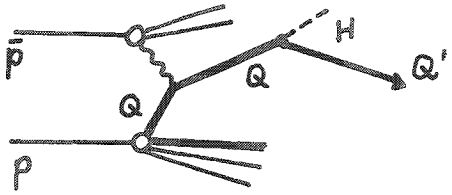

Fig.2: Heavy flavor production.

g) If $m_H > 2m_W$, the scalar decays presumably predominantly into two gauge bosons. The rate is (in the GWS model) $m_H^2 >> m_W^2$:

$$r \equiv \frac{\Gamma(H \to WW)}{m_H} \cong \frac{G_F m_H^2}{8\sqrt{2}\pi} (1 + \text{corrections}) = \lambda (1 + \text{corr.}) \qquad (9)$$

where λ is the ϕ^4 coupling and the corrections have been calculated[36]. We see that for large enough λ corresponding to a scalar mass of $\simeq$ 800 GeV, $r \sim 1$ and the scalar "bump" can hardly be recognized in the W^+W^- spectrum. (The corrections at this point are about +20%; higher corrections might (?) however be negative). The reason for this growing behaviour is that due to the symmetry breaking mechanism the longitudinal part of the W is nothing but the scalar field, and thus λ indeed must enter. In models with charged scalars this effect does not happen (no $W^{\pm}ZH^{\mp}$ coupling); equally in technicolor theories where the relevant couplings (8) are small.

5. Conclusions

We have given a variety of reasons why scalars are vital for our further understanding of the weak interactions and why they are also interesting. We have seen that their mass range is within present and next machines. In the last section a few possibilities to search for them based on the definitions of sections 2 and 3 are discussed. No doubt, further ways are possible. We have stressed mechanisms which are suitable for detecting charged scalars or scalars with enhanced coupling or technicolor scalars. They could be calculated along the lines studied for the production of the standard Higgs[23]. This is particularly interesting in view of the exciting events, presented here, which one is tempted to interpret as scalars. For example, some of the 2 vector-boson modes (5)

and (8) of the scalars correspond to the observed particles, although rough estimates clearly give a non-sufficient rate. A precise determination of background events is desirable (W^+W^- production[37] etc.).

Acknowledgements

I thank the organizers of this workshop for an interesting and very pleasant meeting. I have benefitted from discussions with R. Anishetty, A. Bovier, F. Halzen, I. Hinchliffe, F. Jegerlehner, W. Marciano, P. Minkowski, J. Schacher and Ch. Schmid. I thank J. Ellis and I. Hinchliffe for providing me with their cross-section calculations prior to publication.

References

1) C. Rubbia, these proceedings.

2) J. Schacher, these proceedings.

3) W. Marciano, these proceedings.

4) P. Minkowski, these proceedings.

5) For preceeding emphasis and summaries of the scalar problem see for instance:
L.B. Okun, Proc. of the 1981 Symposium of Lepton-Phonon Interactions; Ed. W. Pfeil, Bonn.
M. Veltman, Proc. of the third $p\bar{p}$ Workshop, Rome 1983; Eds. C. Bacci and G. Salvini, CERN, Geneva 1983.
J. Ellis, 1978 Slac. Summer Institute Proceedings; Ed. M. Zipf.
G. Barbiellini et al., DESY Report 79/27 (1979); A. Ali, Proc. of the 1981 ISABELLE Workshop.

6) D.V. Nanopoulos, these proceedings and references therein.

7) R.D. Peccei, these proceedings and references therein.

8) J.D. Bjorken, Phys. Rev. D19, 335 (1979).

9) P.Q. Hung and J.J. Sakurai, Nucl. Phys. B143, 81 (1978).

10) D. Weingarten, Phys. Rev. Lett. 51, 1830 (1983).
C. Vafa and E. Witten, Nucl. Phys. B234, 173 (1984).
S. Nussinov, Phys. Rev. Lett. 52, 963, 966 (1984).

11) One method was described by F. Herzog, these proceedings.

12) I have been informed by J. Fröhlich that this was originally considered by C.C.G. Stückelberg. I have not found the reference.

13) E. Brezin, J. Zinn-Justin and J.C. Le Guillou, Phys. Rev. D14, 2615 (1976).

14) J. Van der Bij and M. Veltman, Nucl. Phys. B231, 205 (1984).

15) B.W. Lee, C. Quigg and H.B. Thacker, Phys. Rev. D16, 1519 (1977).

16) G. Kane, talk at the conference on Physics of the XXI century, Tucson AZ, Dec. 1983 and references therein.
Since WW scattering is hard to do, one might look for other processes where WW occurs as a subprocess. An example is production of three gauge bosons in e^+e^-: A. Vainstein and I. Khriplovitch, Sov. J. Nucl. Phys. 13, 111 (1971), D. Boulware, Ann. Phys. 56, 140 (1970); L. Fadeev, Theor. and Math. Phys. 1, 1 (1970). See also J.D. Bjorken, in Proc. of the 1976 Summer Institute on Particle Physics, SLAC Report No. 198, Ed. M. Zipf.

17) Strictly speaking, the "Higgs"-field is only that scalar which is left over after gauge symmetry breaking. I will therefore rather use the term scalar since we consider generally models with several scalar fields.

18) A.D. Linde, JETP Lett. 23, 64 (1976); Phys. Lett. 70B, 306 (1977); S. Weinberg, Phys. Rev. Lett. 36, 294 (1976).

19) For a summary of these results, see G. Barbiellini et al., Ref. 5).

20) M. Aizenmann, Phys. Rev. Lett. 47, 1 (1981)
J. Fröhlich, Nucl. Phys. B200 [FS4] , 281 (1982).

21) N. Cabibbo, L. Maiani, G. Parisi and R. Petronzio, Nucl. Phys. B158, 295 (1979); R. Dasken and H. Neuberger, Phys. Rev. Lett. 50, 1897 (1983); D.J.E. Callaway, Nucl. Phys. B233, 189 (1984); M.A.B. Bég, C. Panagiotakopoulos and A. Sirlin, Phys. Rev. Lett. 52, 883 (1984).

22) In writing this bound I have used the value of Bég et al.[21]. They solve the set of coupled differential equations for m_H and θ_W: Callaway[21] takes θ_W fixed. I believe the former procedure is more physical.

23) See I. Hinchliffe, these proceedings; also G. Barbiellini et al., Ref. 5), A. Ali, Ref.5), J. Ellis, Ref. 5).

24) See, e.g. "Type II superconductivity"; D. Saint-James, G. Sarma and E.J. Thomas, Pergamon Press, Oxford, 1969.

25) R.M. Barnett, G. Senjanovic and D. Wyler, Santa Barbara preprint NSF-ITP-84-45.

26) Note the absence of the $W^{\pm}$-Z-$H^{\mp}$ coupling.

27) R.M. Barnett, G. Senjanovic, L. Wolfenstein and D. Wyler, Phys. Lett. B136, 191 (1984).

28) S. Weinberg, Phys. Rev. D13, 974 (1976); D19 1277 (1979)
L. Susskind, Phys. Rev. D20, 2619 (1979).

29) For a review and discussion of the phenomenology as well as further references, see K. Lane, Proc. of the 1982 summer study on Elementary Particle

Physics and future Accelerators, 1982, Eds.: R. Donaldson et al. Also: K. Lane and M.E. Peskin, Proc. XV^{me} Rencontre de Moriond, Ed. J. Tran Thanh Van; E. Farhi and L. Susskind, Phys. Rep. 74C, 277 (1981); J. Ellis, M.K. Gaillard, D.V. Nanopoulos and P. Sikivie, Nucl. Phys. B182, 529 (1981).

30) The enhancement factors are due to $\langle H_1 \rangle \neq \langle H_2 \rangle$. In technicolor models, we have, equivalently, $\langle \bar{U}U \rangle$, $\langle \bar{D}D \rangle$, and by the charge independence of the technicolor force we do not expect $\langle \bar{U}U \rangle \neq \langle \bar{D}D \rangle$.

31) F. Wilczek, Phys. Rev. Lett. 39, 1304 (1977).

32) H.M. Georgi, S.L. Glashow, M.E. Machacek and D.V. Nanopoulos, Phys. Rev. Lett. 40, 692 (1978).

33) R.N. Cahn and S. Dawson, Phys. Lett. B136, 196 (1984).

34) S.L. Glashow, D.V. Nanopoulos and A. Yildiz, Phys. Rev. D18, 1724 (1978).

35) See F. Halzen, these proceedings.

36) J. Fleischer and F. Jegerlehner, Phys. Rev. D23, 2001 (1981). For a discussion of this process, see also: T. Rizzo, Phys. Rev. D22, 722 (1980); H.A. Gordon et al., in Proc. of the 1982 summer study on Elementary Particle Physics and future Accelerators, Eds: R. Donaldson et al., G. Kane, ref. 29).

37) See, e.g. B. Humpert, these proceedings; J. Ellis et al., work in progress; Z. Kunszt and K. Mursula, work in progress.

COMPOSITENESS AND THE FERMI SCALE

R.D. Peccei

Max-Planck-Institut für Physik und Astrophysik, Werner-Heisenberg-Institut für Physik, Munich, Fed. Rep. Germany

1. INTRODUCTION

The motivation for considering that the presently known quarks and leptons are not elementary is varied. Perhaps the most reasonable argument for their compositeness, in my mind, is that the mass spectrum of "elementary" quarks and leptons in the standard model is not calculable. Although complicated dynamical schemes can be constructed beyond the standard model to give a calculable mass spectrum for quarks and leptons, even if they are elementary, one should perhaps heed the lesson of history. Atomic physics, nuclear physics and hadronic physics teach us that the most economical and reasonable way to obtain a mass spectrum is to assume that the objects in question are bound states of even more fundamental entities. This said, however, one must admit that the whole idea of composite quarks and leptons is beset with problems. Three of the most crucial ones are indicated below and will serve to channel my discussion on these matters.

The greatest hurdle that needs to be overcome before some serious interest can be generated for the idea of composite quarks and leptons is that some experimental evidence in its favor must be found! Until recently the experimental situation was bleak and discussions of composite models were more or less restricted to a small coterie of theoretical aficionados. The situation has changed drastically recently with the observation of radiative Z^0 decays[1)2)] and promises to remain fluid if indeed all, or even part, of the strange events reported by the UA1 and UA2 collaborations at this meeting are real. The positive attitude adopted up to now, due to the non-observation of effects of substructure, is that the compositeness scale Λ must be large: $\Lambda \gtrsim 1$ TeV.

Such a large value of Λ gives rise to two theoretical problems which I shall examine here, namely:

1) What dynamics yields light composite quarks and leptons ($m_f \ll \Lambda$) and

2) What relation does the compositeness scale Λ have with the Fermi scale $\Lambda_F = (\sqrt{2}\, G_F)^{-1/2} \simeq 250$ GeV?

Although the first problem above is well known, the second problem is equally important and has been largely ignored in the past. I shall try to partially remedy this situation in this report by focusing mostly on this latter problem.

Before entering the body of the discussion, I should remark that the present bounds on the compositeness scale Λ are quite model dependent. Two examples will illustrate this contention. It has been normal to parametrize possible deviations from the standard model for the process $e^+e^- \to \ell^+\ell^-$ by the incorporation of possible form factor effects via the replacement of the photon propagator:

$$\frac{\alpha}{q^2} \to \frac{\alpha}{q^2}\left[\frac{\Lambda^2}{q^2+\Lambda^2}\right] \tag{1.1}$$

Experiments at PETRA and PEP then yield typical bounds for Λ of order 150-200 GeV[3]. Eichten, Lane and Peskin (ELP)[4], however, have recently argued that such a procedure probably grossly underestimates Λ. If there is an underlying theory of which the observed leptons are bound states, one would normally expect to induce effective contact interactions among these bound states at low energy ($q^2 \ll \Lambda^2$) of the form:

$$\mathcal{L}_{eff} = \frac{g^2}{\Lambda^2}\left(\bar{f}_i \Gamma^a f_j\right)\left(\bar{f}_k \Gamma^b f_\ell\right) A^{ab}_{ijk\ell} \tag{1.2}$$

where the particular spinorial structure, present in the coefficients A^{ab}_{ijkl}, is model dependent. Because the underlying theory is presumably a strong coupling theory it is reasonable to suppose that the effective coupling constant in (1.2) is strong: $g^2/4\pi \sim O(1)$ and not weak: $g^2/4\pi \sim O(\alpha)$. A reanalysis of the PETRA and PEP data under these assumptions then yields a bound for the compositeness scale Λ of order $\Lambda \gtrsim 750$-1000 GeV.

The ELP analysis, although more reasonable, has at least two caveats. It could be that the residual interactions due to compositeness reproduce the usual weak interactions. In this case clearly no bound on Λ can be obtained by parametrizing possible deviations from the standard model! Of course, in this instance, there must exist a well defined relationship between Λ and M_W arising from the preon theory. I shall return to this point. The second caveat on the ELP analysis is due to Visjnić[5]. He argues that the presumption that one has $g^2/4\pi \sim O(1)$ as a result of a strong coupling underlying theory may not follow, for the case of preon theories. Such theories, as will be discussed below, must preserve some chiral invariance to allow for light bound state fermions. However one knows, from the pioneering work of Nambu and Jona-Lasinio[6], that a chirally preserving four-fermion interaction which is sufficiently strong [$g^2/4\pi \gtrsim 1/2$ in the model of Ref. 6)]

eventually leads to a spontaneous breakdown of chirality. In the context of the present discussion this would be inconsistent and therefore it may well be that the effective coupling in (1.2) is rather weak. This of course would allow for a weakening of the bound on Λ.

A second bound on substructure is provided by the electron and muon (g - 2) measurements, which are in very precise agreement with QED predictions. Naively, one would argue that if leptons were not point-like one would expect an extra anomalous magnetic moment contribution given by the effective interaction

$$\mathcal{L}_{comp.} = \frac{e}{\Lambda} \bar{\ell} \sigma_{\mu\nu} \ell F^{\mu\nu} \tag{1.3}$$

The above gives an extra correction to (g - 2) of order $\delta a \sim (m_e / \Lambda)$ and the present level of agreement between theory and experiment would provide a very strong bound on Λ indeed: $\Lambda \gtrsim 10^7$ GeV. However, if the underlying theory is approximately chiral invariant, the effective magnetic interaction must vanish in the limit of zero lepton mass. Hence, in these more sophisticated models one would expect an effective interaction[7)]

$$\mathcal{L}^{Chiral}_{comp.} = \frac{m_e}{\Lambda} \mathcal{L}_{comp.} \tag{1.4}$$

which yield $\delta a \sim (m_e / \Lambda)^2$. For the μ anomaly the above yields a bound $\Lambda \gtrsim 900$ GeV, comparable to that of the ELP analysis. The electron anomaly does not yield a useful bound.

I want to remark that if the additional anomaly in (1.4) is due to a heavy lepton of mass m* then in fact the bound on m* is even below that given for Λ. This can be easily understood since the presence of the heavy lepton is only felt at one loop order and the extra anomaly contribution is then given by $\delta a \sim \alpha (m_e / m^*)^2$. A detailed calculation of these effects has been performed by Renard[8)] and one sees from his paper that heavy muons of mass $m^*_\mu \gtrsim 50$ GeV would run into no conflict with (g - 2). The bound on heavy electrons from (g - 2) is very weak, certainly well below the direct limits set already by PEP and PETRA searches. Except for the indirect ELP bound on $\Lambda \gtrsim 1$ TeV, it is apparent that no experimental fact stands directly in the way to lepton recurrences in the 50-100 GeV range. This remark will be of interest later.

The ELP analysis and the (g - 2) bounds are the least model dependent bounds on Λ. Flavor changing processes like $\mu \to e\gamma$, $K \to \mu e$ or $K^0 - \bar{K}^0$

mixing can in principle provide very much more stringent bounds on Λ, unless the underlying theory somehow suppresses these processes automatically. Because we understand so little about the nature of families, it would appear to me that, at this stage in the game, one should ignore altogether the bounds arising from family mixing (or proton decay, which would imply $\Lambda \gtrsim 10^{15}$ GeV!) and be open to the possibility that the compositeness scale may be as low as 1 TeV.

2. THEORETICAL DISQUISITIONS

Already if $\Lambda \sim O(1\ \text{TeV})$ the dynamic of the underlying theory (preon model) is rather special to be able to produce bound states, the quarks and leptons, with masses in the MeV-GeV range. These bound states would have a typical size $\langle r \rangle \sim 1/\Lambda$ which in fact would be much smaller than their Compton's wavelength $\lambda_c \sim 1/m_f$ - certainly a new phenomena in physics. The usual presumption that is made is that these "light" bound states, with $m_f \ll \Lambda$, are a result of some approximate symmetry. This must strictly be the case if the underlying preon theory is a non-abelian gauge theory. These theories have only one dynamical scale Λ related to where the coupling constant becomes strong and all bound state masses are of $O(\Lambda)$. However, even for other possible preon theories it is difficult to imagine dynamical accidents which would force some states to be of a size much less than that given by their Compton's wavelength, unless some symmetry forced this condition.

The usual strategy adopted theoretically is to first invoke some symmetry reasons to keep certain bound states at zero mass. Then by appropriately relaxing these symmetries one hopes to gain some small masses for the massless bound states. If one wants to construct models where the only massless excitations are the observed quarks and leptons, the first step in this procedure is already rather hard. The second step, of actually generating an even semi-realistic mass spectrum, however, has proven totally elusive. This is not surprising, since it is clear that the detailed mass spectrum of quarks and leptons is tightly connected with the issue of families. Since the origin of the family replication still eludes us, it is not difficult to understand why no successful spectrum has yet been theoretically generated. There is, however, also a more technical reason for the present theoretical failures and that is that the symmetries one imposes to generate some massless states are, in general, very hard to break "slightly" in a non-arbitrary manner. This point, in my opinion, will continue to plague model builders until some radical new idea is found.

There are, at the moment, two main suggestions for keeping the quarks and leptons light:

1) One can assume that the underlying theory has some global chiral symmetry which remains unbroken in the binding[9]. In this case the fermionic spectrum would most probably contain some massless states, along with massive chiral partner states. The massless states must have global transformation properties under the chiral symmetries, so that the Adler anomalies of the chiral currents match at the preon and composite level[9].

2) Alternatively, one can consider supersymmetric preon theories with some global symmetry G[10]. If this global symmetry is spontaneously broken to a subgroup H, then one expects certain Goldstone bosons to appear in the spectrum. Because of the supersymmetry, these bosonic states are accompanied by fermionic partners - the so-called quasi Goldstone fermions[11] - and it is these states that one can try to identify with the quarks and leptons. It should be mentioned that if H itself is a chiral group, it can happen that some (or all) of the quasi Goldstone fermions may be required by the 't Hooft anomaly matching conditions[12]. Thus chirality can act as a further reason for the appearance of certain quasi Goldstone fermions and models with this double protection have been constructed[12)13)14)].

It is worthwhile to remark again that, once one follows one of the above scenarios to obtain massless quarks and leptons, it is then very difficult to break the remaining chiral symmetries, or the supersymmetry and global symmetry G, in a weak way so as to then get a realistic mass spectrum. In fact, to my knowledge, this problem is totally unsolved and there is no realistic model on the market now which generates a reasonable mass spectrum.

A second very important problem for preon models, besides that of generating light quarks and leptons, is the problem of the origin of the Fermi scale. To my mind, this problem is of equal importance to that of fermion masses and, furthermore, it has some direct practical implications. I begin examining this second problem under the assumption that the electroweak interactions originate from a spontaneously broken SU(2) x U(1) theory, as in the standard model[15], except that these interactions act at the preon level. Because the quarks and leptons are composite, it follows necessarily that there exist some residual interactions among them, due to their compositeness, whose dominant low energy ($q^2 \ll \Lambda$) form is that given in Eq. (1.2). Because the standard model works so well, the terms in Eq. (1.2) must be a small perturbation. This obviously requires that

$$G_F \Lambda^2 \gg 1 \qquad (2.1)$$

Therefore, one sees that the natural question to ask in these circumstances is why is the Fermi scale so small with respect to the compositeness scale. This, in fact, can be a problem. Let me explain.

The Fermi scale, implicit in G_F, in the standard model is associated with the strength of the SU(2) x U(1) symmetry breaking. One has

$$G_F \sim \frac{1}{\langle \phi \rangle^2} \tag{2.2}$$

where $\langle \phi \rangle$ represents here an effective SU(2) x U(1) symmetry breaking condensate. Now, if the quarks and leptons are composite it is quite clear that there should be no elementary Higgs with which to associate $\langle \phi \rangle$. In fact, it is very natural to suppose that the $\langle \phi \rangle$ condensate is formed precisely by the same mechanism which binds quarks and leptons. That is, $\langle \phi \rangle$ is a condensate of the underlying preon theory. Unfortunately, if this is the case, one would conclude that $\langle \phi \rangle$ is of $O(\Lambda)$ and thus $G_F \Lambda^2 \sim O(1)$ and not $G_F \Lambda^2 \gg 1$, as required experimentally.

This line of argumentation has three possible conclusions, which reflect the options which are realistically open:

1) The compositeness scale Λ is nearby, say $\Lambda \simeq 1$ TeV. Then some minor dynamical miracle still guarantees that Eq. (2.1) holds with, say

$$G_F \Lambda^2 \simeq 10 \gg 1 \tag{2.3}$$

2) The Fermi scale has no direct connection to the preon theory. For example, one can suppose that there is some technicolor theory[16] which causes the spontaneous breakdown of SU(2) x U(1) and thus $\langle \phi \rangle \sim \Lambda_{TC}$. In this case Eq. (2.1) can be easily satisfied provided

$$\Lambda / \Lambda_{TC} \gg 1 \tag{2.4}$$

One should remark, however, that these kind of theories are much more complicated. Not only is there some gauged SU(3) x SU(2) x U(1) theory, but one further needs two more confining gauge theories - one to bind quarks and leptons out of underlying preons and the other to provide SU(2) x U(1) breaking condensates.

3) SU(2) x U(1) is not a fundamental theory. In this case the weak interactions are precisely those given by the residual interactions (1.2). The Fermi scale has nothing to do with the spontaneous breakdown of a local symmetry.

Rather it reflects the mass of the exchanged bound state massive vector excitations, which arise from the underlying preon theory.

Clearly 3) is an iconoclastic possibility, but one which is interesting and should be taken seriously. It presupposes that the W and Z are not elementary and that the standard Glashow-Salam-Weinberg theory[15] is only an effective theory and not a fundamental one. This possibility, however, requires also dynamical miracles, akin to $G_F \Lambda^2 \gg 1$, but which perhaps are even more difficult to achieve. To explain this point it is worthwhile making a small aside to spell out the requirements needed for the weak interactions to be residual. Basically one needs:

a) $$\mathcal{L}_{eff}^{residual} \underset{q^2 \to 0}{\sim} \frac{G_F}{\sqrt{2}} \left\{ J^{\dagger}_{+L} J_{-L} + 4 \left(J^{\dagger}_{3L} - \sin^2\theta_W J^{\dagger}_{em} \right)^2 \right\} \qquad (2.5)$$

and

b) $$M_W \simeq M_Z \cos\theta_W \qquad (2.6)$$

The first equation above guarantees that all low energy neutral current results are as in the standard model, while the second equation is necessary to reproduce the $Sp\bar{p}S$ results.

How to guarantee (2.5) has been known for a long time, from the pioneering work of Bjorken[17] and Hung and Sakurai[18]. What is needed is an effective $SU(2)_L$ theory - with no isoscalar interactions:

$$\mathcal{L}_{eff} \underset{q^2 \to 0}{\sim} \frac{G_F}{\sqrt{2}} \left(\vec{J}^{\dagger}_{L} \cdot \vec{J}_{L} \right) \quad ; \quad \frac{G_F}{\sqrt{2}} = \frac{g^2}{8 M_W^2} \qquad (2.7)$$

and $\gamma - W_3$ mixing. Then Eq. (2.5) obtains readily with $\sin^2\theta_W$ related to g, e and the, as yet free, $\gamma - W_3$ mixing parameter λ:

$$\sin^2\theta_W = \frac{e}{g} \lambda \qquad (2.8)$$

In fact λ parametrizes the relation between M_W and M_Z and one has[18]

$$M_W = M_Z (1 - \lambda^2)^{1/2} \qquad (2.9)$$

Thus to reproduce the collider data, the underlying theory must yield

$$\lambda \simeq \sin\theta_W \simeq e/g \tag{2.10}$$

where the last equality follows from (2.8).

Eq. (2.10) is a dynamical condition which is not easy to obtain, since $\sin^2\theta_W \sim 1/4$ is certainly much bigger than α, which would be the naive estimation for the mixing parameter λ^2. However, one can argue that λ must obey Eq. (2.10), if for some reason the W and Z^o are much ligher than other vector meson in the spectrum of the preonic theory[19]. In effect if

$$\Lambda >> M_W \tag{2.11}$$

then one can assume that there is good vector meson dominance of the electromagnetic form factor <u>just</u> by the Z^o. This immediately gives Eq. (2.10). Physically, if Eq. (2.11) holds there is a large gap between the "light" γ and Z^o, and the rest of the J = 1 states and it is therefore not surprising that the mixing, λ^2, is large.

I would like to conclude this section by emphasizing again what are the theoretical conclusions one arrives at if the quarks and leptons are composite and there is <u>not</u> some technicolor theory. Then one expects:
1) that the underlying preon theory has some protective symmetry so as to guarantee that some light fermions ($m_f << \Lambda$) emerge from the binding
2) the compositeness scale is of O(1 TeV) so that not too big a dynamical miracle is required to guarantee that either

$$G_F \Lambda^2 >> 1 \qquad \text{(SU(2) x U(1) is fundamental)}$$

or

$$\Lambda >> M_W \qquad \text{(weak interactions are residual)}$$

From this point of view one sees that if quarks and leptons are composite, the probability that the weak interactions are fundamental or residual is probably 50-50. Furthermore, if $\Lambda >>$ 1 TeV it appears essentially impossible to have a natural explanation of the Fermi scale unless life is much more complicated. New interactions (technicolor) must be introduced to separate the Fermi scale from the scale of preon binding, which leads to the formation of quarks and leptons.

3. MODEL ILLUSTRATION

I would like to illustrate some of the general points indicated above by means of a model which was developed in collaboration with Wilfried Buchmüller and Tsutomu Yanagida[20]. We considered a supersymmetric preon model based on an $SU(2)_{HC} \times SU(2)'_{HC}$ hypercolor confining group. To obtain one generation of quarks and leptons (the model can be extended to more generations) we made use of 13 preon superfields. Six of these Φ_i^q $(q = 1,\ldots,6)$ are doublets of $SU(2)_{HC}$; another six Φ'^j_p $(p = 1,\ldots,6)$ are doublets of $SU(2)'_{HC}$; finally, the thirteenth preon χ^i_j is a doublet under both hypercolor groups. The model clearly has a global $G = U(6) \times U(6)' \times U(1)_\chi$ symmetry which can be broken down if certain condensates form. Specifically, we assumed that the following condensates appeared in the theory:

$$v = \langle \epsilon^{ij} \Phi^5_i \Phi^6_j \rangle \tag{3.1a}$$

$$v' = \langle \epsilon_{ij} \Phi'^i_5 \Phi'^j_6 \rangle \tag{3.1b}$$

$$v_f = \langle \Phi^5_i \chi^i_j \Phi'^j_5 \rangle = \langle \Phi^6_i \chi^i_j \Phi'^j_6 \rangle \tag{3.1c}$$

The existence of (3.1c) in the directions shown is a matter of vacuum alignment, which we assumed proceeded in the way shown. Clearly the condensates in (3.1) break down $G \to H = U(4) \times U(4)' \times SU(2)_{diag}$. As a result of the breakdown Goldstone bosons with m = 0 will arise. Furthermore, supersymmetry will also force certain quasi Goldstone fermions (QGF) with zero mass to appear. Since H is a chiral group for the preons, one must require also that certain m = 0 fermions appear in the bound state spectrum to match anomalies. Remarkably the QGF are precisely the set of fermions needed for anomaly matching. Hence our model gives an example in which the massless fermions are present both because of chirality and because of the Goldstone phenomena for supersymmetric theories[12].

The massless superfields that appear in the theory contain the 16 quarks and leptons of one generation, plus some additional states. These include three neutral superfields (which we have dubbed novinos) and a triplet of fields

$$\Pi^a_b = \Phi^a_i \chi^i_j \Phi'^j_b - \tfrac{1}{2} \delta^a_b \Phi^d_i \chi^i_j \Phi'^j_d \qquad (a,b = 5,6) \tag{3.2}$$

which, in a version of the model to be described below, play the role of a technipion superfield (technispions). Because these zero mass fields are

connected to the spontaneous breakdown of $G \to H$, it is possible to construct an effective Lagrangian which describes their interactions at $q^2 \to 0$. The analogue in QCD is the chiral Lagrangian for Goldstone pions. In the QCD case this Lagrangian is written in terms of the pion fields, scaled by f_π - the parameter which is related to the breakdown of $SU(2)_L \times SU(2)_R \to SU(2)_{L+R}$. The pion decay constant is proportional to Λ_{QCD}, $f_\pi \sim \Lambda_{QCD}$, and it is intimately connected with the quark condensates $\langle \bar{u}u \rangle \sim \Lambda^3_{QCD}$ which cause the dynamical breakdown of the symmetry. In our case, the effective Lagrangian which describes the leading interactions between quarks and leptons due to compositeness will also contain a number of scales, which are related to the dynamical condensates v, v'and v_F of Eq. (3.1).

A rather lengthy, but straightforward, calculation[20] yields for the dominant residual interaction between quarks and leptons the following expression:

$$\mathcal{L}_{eff.}^{Residual} = \frac{1}{8v_1^4}\left(v_1^2 - \tfrac{1}{2}v_\pi^2\right)\left(\vec{J}_L^{\,\mu} \cdot \vec{J}_{L\mu}\right) + \frac{1}{8v_1^4}\left(v_1^2 - v_2^2\right)\left(J_{SL}^{\mu} \cdot J_{SL\mu}\right)$$

$$+ \frac{1}{8v_1'^4}\left(v_1'^2 - \tfrac{1}{2}v_\pi^2\right)\left(\vec{J}_R^{\,\mu} \cdot \vec{J}_{R\mu}\right) + \frac{1}{8v_1'^4}\left(v_1'^2 - v_2'^2\right)\left(J_{SR}^{\mu} \cdot J_{SR\mu}\right) \qquad (3.3)$$

$$+ \frac{v_\pi^2}{8v_1^2 v_1'^2}\left(\vec{J}_L^{\,\mu} \cdot \vec{J}_{R\mu}\right)$$

Here $\vec{J}^{\,\mu}_{L,R}$ are isovector currents for the quarks and leptons with appropriate helicity projections, while $J^{\mu}_{SL,SR}$ are isoscalar currents. The scales v_1, v_2 are related to the condensates v; v_1', v_2' are related to v'; and v_π is related to v_F.

Although (3.3) is a general result, there can be specific dynamical circumstances in the underlying theory that may lead to some simplifications. In particular, in the model at hand, the scales v_1 and v_2 (v_1' and v_2') are scales related to the left-handed quarks and leptons and novino, respectively (right-handed quarks and leptons and novino). Because these states are built in an analogous fashion in the model, it is to be expected that these scales

are approximately the same: $v_1 \simeq v_2$; $v_1' \simeq v_2'$. This implies that all isoscalar currents are probably highly suppressed in Eq. (3.3). Furthermore, if the $SU(2)'_{HC}$ dynamical scale, Λ', were to be much bigger than the $SU(2)_{HC}$ dynamical scale, Λ, then one would be led to the hierarchy

$$v_1' \simeq v_2' \sim \Lambda' \gg v_1 \simeq v_2 \sim \Lambda \; ; \; v_\pi \sim \Lambda \tag{3.4}$$

In this case Eq. (3.3) reduces to

$$\mathcal{L}^{Res.dual}_{eff.} \simeq \frac{1}{8v_1^4}\left(v_1^2 - \tfrac{1}{2}v_\pi^2\right)\left(\vec{J}^\mu_L \cdot \vec{J}_{L\mu}\right) = \frac{G_F}{\sqrt{2}}\left(\vec{J}^\mu_L \cdot \vec{J}_{L\mu}\right) \tag{3.5}$$

which is precisely of the form (2.7). Thus, under the dynamical circumstances described above, it is conceivable for our model that the weak interactions be residual. Of course, a further necessary condition in this case is that M_W be much below the scale of the binding of the left-handed quarks Λ. In fact, even this can be argued in the model, since it possesses a complementary picture. In the complementary picture the only light J = 1 states present are precisely the W^+ and the Z^0, and one can thus presume that this circumstance still obtains in the confining phase of the theory.

Residual weak interactions, however, are not the only possibility in the model. One can introduce at the preon level a gauged SU(2) x U(1), where the SU(2) only acts on the 5,6 preons Φ^a_i (a = 5,6). It is easy to see then that the condensate v_F of Eq. (3.1c) breaks this gauged SU(2) x U(1) down to $U(1)_{em}$. The W^+ and Z superfields get a mass by precisely absorbing the technipion massless bound states Π^a_b. In this case the preon theory acts as technicolor!

For the model to be realistic, however, in this case the condendates v_F must be much smaller than v and v'. Only when this is so will the residual interactions, which from (3.3) are of order $O(1/v_1^2)$ or $O(1/v_2^2)$, be much smaller than the standard weak interactions which are of $O(1/v_\pi^2)$. Effectively, taking the scales $\Lambda \sim \Lambda'$, what is needed is that the condensates in (3.1) are such that $v \sim \Lambda^2$, $v' \sim \Lambda^2$, but the three body condensate $v_F \ll \Lambda^3$. One may indeed imagine that it is much harder for three different fields to condense together so that this hierarchy happens. These "dynamical miracles" are precisely those alluded to in the last section, which are needed so that the residual interactions due to compositeness do not spoil the agreement with experiment of the gauged weak interactions.

4. RADIATIVE Z^0 DECAYS: ARE THESE THE FIRST EXPERIMENTAL HINTS OF COMPOSITNESS?

The three events reported by the UA1 and UA2 collaborations of $Z^0 \to \ell^+\ell^-\gamma$ decays[1)2)], if taken at face value, seem to indicate a radiative width for the Z^0 much greater than what is expected by bremsstrahlung:

$$\frac{\Gamma(Z^0 \to e^+e^-\gamma)}{\Gamma(Z^0 \to e^+e^-)} \simeq 0.2 - 0.25 \qquad (4.1)$$

Of course the present sample is very small and one could well be dealing with a statistical fluctuation. If the Fall run at the $Sp\bar{p}S$ confirms the above rate this will be a clear sign that some physics beyond the standard model is present, and that physics is likely to be connected with compositeness ideas.

Perhaps rather rashly a number of people, including myself, have already tried to interpret these events in terms of various compositeness scenarios. Here, I would like to briefly discuss two of the more popular ideas, which appeal to sequential decays to obtain a radiative rate much greater than α. As will be seen, these suggestions are not without problems. There are other alternatives, notably the suggestion of Gounaris, Kögeler and Schildknecht[21)], who obtain large radiative rates by having the W and Z have strong interactions with sequences of other vector mesons. Some of these other possibilities, along with that of sequential decays, have been clearly discussed recently by Renard[22)].

If the radiative rate for the Z^0 is enhanced by a sequential decay, there are clearly two possibilities. Either the Z^0 de-excites to a scalar state, which subsequently decays to lepton pairs; or the Z^0 decays into an excited lepton and a lepton, with a subsequent radiative de-excitation of the excited lepton. The scalar scenario ($Z^0 \to X\gamma$, $X \to \ell^+\ell^-$) was first suggested, to my knowledge, by Baur, Fritzsch and Faissner[23)] and by myself[24)]. However, it was also analyzed by Renard[22)], essentially contemporaneously. The excited lepton scenario ($Z^0 \to e^*\bar{e}$; $e^* \to e\gamma$) was discussed by Cabibbo, Maiani and Srivastava[25)] and by Enquist and Maalampi[26)]. Again Renard[22)] also discusses some of the points brought forward by these authors. Since G. Pancheri[27)] will cover this topic in her contribution to this meeting, my remarks on the excited lepton scenario will be reasonably brief.

It is quite clear that if the radiative Z^0 decays are due to a sequential decay, then there should appear a clear invariant mass bump in the data. No such bumps are manifest in the data, but one should remember that there

are only 3 events and that the experimental errors are not small. Furthermore, there well may be more than one scalar state and/or heavy excited lepton (e.g., e*, μ*), so that the situation is by no means critical. However, by the next collider run - if the radiative decays remain at the present rate - there will need to be an invariant mass bump for the sequential hypothesis to make any sense at all.

4.1 The Scalar Scenario

This scenario is based on a very simple - one may perhaps even call it naive - premise. If the W and Z are composite and somehow they are dynamically pushed to a mass $M_W \ll \Lambda$, it may be that there are also some J = 0 partner states which are light. If one pursues an analogy with QCD, one would expect both isovector and isoscalar states of spin 1 and 0. However, one knows experimentally that both the J = 1, isoscalar state, W_S, and the J = 0 isovector states, $\vec{X}$, cannot be that light. The former states are certainly much heavier than the $\vec{W}$ triplet, since no isoscalar neutral current appear in the theory - apart from those induced by $\gamma - W_3$ mixing. The isovector states $\vec{X}$ also must be much more massive than the $\vec{W}$, because if not they would spoil the chiral properties of π-decay: $\Gamma(\pi \to \mu\nu)/\Gamma(\pi \to e\nu) \sim (m_\mu/m_e)^2$.

No such constraints exist for a possible light J = 0 isoscalar state, X. The X could be relatively light and still not affect our phenomenological understanding of the weak interactions. Nevertheless, to ascribe to the X's presence the large probability of a radiative Z^0 decay is not altogether straightforward. What is needed is that the X itself have a sizable coupling to lepton pairs. Normally such a coupling, unless it were proportional to the fermion masses, will violate very badly chirality. Obviously, it is fatal if the coupling is proportional to the fermion masses, since we would never get a sizable decay rate of X into e^+e^-. On the other hand, if chirality is badly violated it clearly removes the raison d'etre for quarks and leptons to be light. The only way out, as I suggested in Ref. 24), is to suppose that the X is really a chiral doublet. Then one can have a universal coupling of the $X = \{N, S\}$ to fermions without violating chirality in the fermion sector. Chiral fermionic rotations are compensated by rotations between the chiral doublet states, as can be checked from the effective interaction:

$$\mathcal{L}_{eff} = h\{\bar{f} f N + i \bar{f} \gamma_5 f S\} \tag{4.2}$$

Such a Lagrangian suggests, by its universality, that for the case of three generations of quarks and leptons, roughly

$$B(X \to e^+e^-) \simeq 5\% \tag{4.3}$$

Assuming that the rate for $Z^0 \to e^+e^-$ is still given by the standard model rate of roughly 90 MeV, then from Eq. (4.1) it follows that $\Gamma(Z^0 \to e^+e^-\gamma) \simeq 20$ MeV. From the equation

$$\Gamma(Z^0 \to e^+e^-\gamma) = \Gamma(Z^0 \to X\gamma)\, B(X \to e^+e^-) \tag{4.4}$$

and Eq. (4.3), it is clear that to obtain an explanation of the present radiative data one needs $\Gamma(Z^0 \to X\gamma) \simeq 400$-$500$ MeV. Amusingly enough[23)24)] such a rate is not unexpected, if one tries to estimate it in direct analogy with QCD. In my own work[24)] I considered an effective coupling of the W triplet to X of the form (suppressing all indices)

$$\mathcal{L}_{eff.} = k/\Lambda\, [\vec{W} \cdot \vec{W}]\, X \tag{4.5}$$

Then by using the γ - W_3 mixing as in Eq. (2.10) and taking $k^2/4\pi \sim O(1)$, $\Lambda = 1$ TeV and $M_X = 50$ GeV it follows that $\Gamma(Z^0 \to X\gamma) \simeq 450$ MeV. This model allows also to estimate a rate for X into 2γ and I find, for the same parameters

$$\Gamma(X \to 2\gamma) \simeq 30 \text{ MeV} \tag{4.6}$$

It should be remarked that (4.5) violates chirality since the $\vec{W}$'s are inert under chiral rotations, so that the careful chiral protection built in in Eq. (4.2) is in fact broken in the heavy sector. Unless some special circumstances obtain, this will be seen to be the downfall of the model.

Before discussing this point, a number of phenomenological remarks are in order. Using Eq. (4.2) it is easy to compute the rate of X into lepton pairs. One finds[24)]

$$\Gamma(X \to e^+e^-) = h^2/8\pi\, M_X = \alpha_h/2\, M_X \tag{4.7}$$

We note that if $\alpha_h \simeq 10^{-4}$ then, for M_X in the 50 GeV range, $\Gamma(X \to e^+e^-)$ is only 3 MeV and thus a sizable portion of the X decays are into 2γ. In this case it may be that the branching ratio $B(X \to e^+e^-)$ is less than 5%.

Direct bounds on α_h exist from a careful analysis of the PETRA data at the highest energies available. Some of the necessary theoretical analysis is contained in Ref. 24), but much more detailed considerations are contained in the reports of Bopp et al.[28)] and Hollik, Schrempp and Schrempp[29)]. No

significant effects were seen in $e^+e^- \to e^+e^-$, $e^+e^- \to 2\gamma$, $e^+e^- \to \mu^+\mu^-$ and in R up to the possible highest energies at PETRA (45.2 GeV). This allows[30] to exclude masses for X below this range. Furthermore, if $M_X \lesssim 50$ GeV there would be significant tails in this data unless α_h is small enough, $\alpha_h \lesssim 10^{-4}$. Finally, if one uses the particularly simple model of Ref. 24), where also $X \to 2\gamma$ is absolutely predicted, then essentially already present PETRA data excludes this hypothesis[30].

A further bound on α_h exists from the fact that no direct X production is seen at the collider. One expects[24]

$$\sigma_X/\sigma_W \simeq 4\,\alpha_h/\alpha \tag{4.8}$$

For $\alpha_h \simeq 10^{-4}$ this would imply about one event of X into $\ell^+\ell^-$. However, for this value of α_h the $\gamma\gamma$ rate of X is proportionally bigger and one should perhaps expect 5-10 $\gamma\gamma$ events, along with perhaps the same number of 3 γ events from the sequential decay $Z^0 \to X\gamma$; $X \to 2\gamma$ to have been seen. No evidence for these kind of events has yet appeared and this throws some further doubts on the scalar hypothesis.

There is, finally, also a disturbing theoretical constraint on the X's existence, which comes from the (g - 2) experiments. If a $Z^0X\gamma$ coupling exists, then this coupling can give rise to a nontrivial contribution to the muon (g - 2). An analysis of this effect, by a number of different groups[31], reaches the following conclusions:

1) If there is only one X state, then the value of the coupling α_h and k needed to give a sizable radiative Z^0 decay imply a muon anomaly roughly 100 times greater than the present (QED-experiment) discrepancy allows.

2) If there are two X states - so that chirality is preserved at the fermion X sector (cf. Eq. (4.2)) - then in fact a cancellation can occur in the (g - 2) contribution provided that the coupling of the chiral doublets $X = \{N,S\}$ to the $\vec{W}$'s in Eq. (4.5) have opposite signs.

These results are discouraging for the X hypothesis. Although one can appeal to chirality to argue for the form of Eq. (4.2), as was done in Ref. 24), no real theoretical reason exists for fixing the relative weight of the chiral breaking couplings of N and S to the $\vec{W}$'s so that the (g - 2) cancellation occurs. This is a salutary lesson, which was already hinted at in Section I. Unless there is appropriate chiral protection, the (g - 2) agreement between QED and experiment does not allow to have "light" composite objects. Of course, given the infancy of this subject one should perhaps wait until further

experimentation at the collider before eliminating altogether the scalar hypothesis as an explanation for the radiative Z^0 decays. Indeed, since a priori also other explanations do not look substantially better, this may be a very prudent attitude to take.

4.2 The Excited Lepton Scenario

The Z^0 radiative decays could be due to the existence of excited leptons, which then de-excite radiatively. If one assumes that the de-excitation via γ emission is essentially 100% then to explain a rate $\Gamma(Z^0 \to \ell^+\ell^-\gamma) \simeq 20$ MeV one needs a rate $\Gamma(Z^0 \to \ell^*\bar{\ell}) \simeq 10$ MeV, roughly 10% of the normal leptonic rate. Cabibbo, Maiani and Srivastava[25] (see also Ref. 26)) shows that such a rate is not inconceivable, via magnetic transitions. Indeed assuming that the excited leptons form an $SU(2)_L$ doublet ℓ^*_L, the effective interaction

$$\mathcal{L}_{eff} = g f/m^* \, \bar{\ell}^*_L \sigma^{\mu\nu} q_\nu \frac{\vec{\tau}}{2} \cdot \ell_L \vec{W}_\mu - g f'/m^* \, \bar{\ell}^*_L \sigma^{\mu\nu} q_\nu \frac{1}{2} \ell_L B_\mu \qquad (4.9)$$

between excited leptons, ordinary leptons and the SU(2) x U(1) gauge fields leads to a satisfactory rate if the free parameters f and f' obey

$$|3f - f'| \simeq 2 \,, \qquad (4.10)$$

a perfectly sensible constraint.

As I said earlier, I shall not further discuss the phenomenology of this hypothesis, since that is done in Pancheri's report[27]. Nevertheless, I shall make some critical remarks which should serve as a warning that also here not everything is as easy as it may seen at first sight:

1) Since there are both $\mu^+\mu^-\gamma$ and $e^+e^-\gamma$ events one needs both μ^* and e^*'s at roughly the same masses. Indeed, with large errors it appears that the μ^* would be lower than the e^*[1)2)]. Why is this so, since after all $m_\mu/m_e \sim 200$?

2) In the same vein, it is somewhat peculiar to begin to see recurrences of the light e and μ families in the energy range where one "ground state" of the other family, the top quark, is presumed to lie.

3) Although if one has a good chiral symmetry - as guaranteed by Eq. (4.9) for example - there is no problem with having excited leptons in the 50 to 100 GeV range from (g - 2), it is still peculiar that these excited states should be so much lighter than $\Lambda \gtrsim 1$ TeV, as determined by the ELP analysis.

4) Theoretically, having excited recurrences of the known leptons can give too fast a rate for $\mu \to e\gamma$, unless intragenerational mixings are severely suppressed, or there is a very good GIM mechanism. One can estimate the

$\mu \to e\gamma$ rate due to the presence of excited leptons by the formula[8)]

$$\Gamma(\mu\to e\gamma) = \frac{\alpha^3}{\pi} m_\mu \left(m_\gamma/m^*\right)^4 \{\text{mixing angles} \cdot GIM\} \leq 0.6\times10^{-28}\ GeV$$

which requires a suppression mechanism in the curly bracket above of roughly 10^{-8}.

5) If excited leptons exist, it is very probable that excited quarks also exist. The phenomenology of these q* (starks) has been analyzed recently by De Rujula, Maiani and Petronzio[32)] (see also Ref. 27)). These states could be the source of some, perhaps all, the new UA1 and UA2 events presented at this meeting. In this sense, the excited lepton explanation for the Z^o radiative decays is perhaps more relevant than that involving a new scalar excitation. Although, in this latter case, since the explanation presumes that the W and Z are composite, one can well expect extra additional states - like colored W's - which could also be the cause of the new events.

5. CONCLUDING REMARKS

By not too perverse a logic I have tried to indicate how the notion of calculability of the quark and lepton mass spectrum probably requires that these objects are composite. Furthermore, to try to understand the Fermi scale, and not complicate the theory overmuch, it is sensible that the scale of compositeness is nearby, say $\Lambda \simeq$ 1 TeV. Under these circumstances it appears almost equally sensible to suppose that the weak interactions are just residual products of compositeness, as that they are due to fundamental gauge interactions. The recent $Sp\bar{p}S$ data on radiative Z^o decays furthers this notion that compositeness is nearby. In fact, these events may be too much of a good thing, since with $\Lambda \simeq$ 1 TeV it is difficult to conceive of scalar states, or excited leptons in the 50-100 GeV range! Nevertheless, it is my opinion that if these events are confirmed by further experimentation, and/or if even a fraction of the new exotic events discussed in this meeting are established, then compositeness is here to stay.

ACKNOWLEDGEMENTS

My own understanding in these matters owes much to the insights of my collaborators Wilfried Buchmüller and Tsutomu Yanagida.

REFERENCES

1) G. Arnison et al., Phys. Lett. 126B (1983) 398.
2) P. Bagnaia et al., Phys. Lett. 129B (1983) 130.
3) See for example, M. Abolins et al., Proceedings of the 1982 DPF Summer Study, Snowmass, Colorado.
4) E.J. Eichten, K.D. Lane and M.E. Peskin, Phys. Rev. Lett. 50 (1983) 811.
5) V. Visnjić, MPI-PAE/PTh 22/84.
6) Y. Nambu and G. Jona-Lasinio, Phys. Rev. 122 (1961) 345.
7) S.J. Brodsky and S.D. Drell, Phys. Rev. D22 (1980) 2236.
8) F.M. Renard, Phys. Lett. 116B (1982) 264.
9) G. 't Hooft, in Recent Developments in Gauge Theories, Cargese 1979, eds. G. 't Hooft et al. (Plenum Press, New York and London, 1980).
10) W. Buchmüller, R.D. Peccei and T. Yanagida, Phys. Lett. 124B (1983) 67.
11) W. Buchmüller, S.T. Love, R.D. Peccei and T. Yanagida, Phys. Lett. 115B 233.
12) R. Barbieri, A. Masiero and G. Veneziano, Phys. Lett. 128B (1983) 179.
13) O.W. Greenberg, R.N. Mohapatra and M. Yasue, Phys. Rev. Lett. 51 (1983) 1737.
14) W. Buchmüller, R.D. Peccei and T. Yanagida, Nucl. Phys. B231 (1984) 53.
15) S. Weinberg, Phys. Rev. Lett. 10 (1967) 1264;
A. Salam, Proceedings of the 8th Nobel Symposium, ed. N. Svartholm (Almquist and Wiksells, Stockholm, 1968);
S.L. Glashow, Nucl.Phys. 22 (1961) 579.
16) L. Susskind, Phys. Rev. D20 (1979) 2619;
S. Weinberg, Phys. Rev. D19 (1979) 1277.
17) J.D. Bjorken, Phys. Rev. D19 (1979) 335.
18) P.Q. Hung and J.J. Sakurai, Nucl. Phys. B143 (1978) 81.
19) R. Kögeler and D. Schildknecht, CERN-TH-3231 (1982);
H. Fritzsch, R. Kögeler and D. Schildknecht, Phys. Lett. 114B (1982) 157.
20) W. Buchmüller, R.D. Peccei and T. Yanagida, MPI-PAE/PTh 84/83, Nucl. Phys. to be published.
21) G. Gounaris, R. Kögeler and D. Schildknecht, Bielefeld preprint BI-TP 83/17.
22) F.M. Renard, Univ. of Montpellier preprint PM/83/11.
23) U. Baur, H. Fritzsch and H. Faissner, Phys. Lett. 135B (1984) 313.
24) R.D. Peccei, Phys. Lett. 136B (1984) 121.

25) N. Cabibbo, L. Maiani and Y. Srivastava, Univ. of Rome preprint No. 381.

26) K. Enquist and J. Maalampi, Phys. Lett. 135B (1984) 329.

27) G. Pancheri, these proceedings.

28) F.W. Bopp, S. Brandt, H.D. Dahmen, D.H. Schiller and D. Wähner, Univ. of Siegen preprint SI-83-24.

29) W. Hollik, F. Schrempp and B. Schrempp, DESY 84-011.

30) B. Adeva et al., MIT technical report No. 134;
H.J. Behrends et al., DESY 84-020, Phys. Lett. to be published.

31) F. del Aguila, A. Mendez and R. Pascual, UAB-FT-105;
M. Suzuki, Berkeley preprint LBL-17630;
L. Maiani, private communication;
B. and F. Schrempp, private communication.

32) A. De Rujula, L. Maiani and R. Petronzio, CERN-TH-3779.

EXCITED FERMIONS

G. Pancheri

INFN, Laboratori Nazionali di Frascati,Frascati,POB 13 - 00044 Frascati (Italy)

Abstract

Theoretical and experimental implications of the existence of excited states of ordinary leptons and quarks are examined. The contribution of excited electrons and of their neutral partners to the decays $Z_0 \to e^+e^-\gamma$ and $Z_0 \to \nu\bar{\nu}\gamma$ are discussed. Signatures of excited quark states are compared with reported experimental observations. Through weak isospin invariance,it is also found that there may exist excited quarks with weak isospin $I_w \geq 1$ which have exotic charge assignments and decay only electroweakly into ordinary quarks and leptons. These exotic quarks will give rise to charge $+3$ baryons and charge ± 2 mesons.

1. EXPERIMENTAL MOTIVATION

In 1983 UA1 and UA2 Collaboration reported the observation of the process

$$Z_0 \to e^+e^-\gamma \quad (1\ \textit{event each})$$

and

$$Z_0 \to \mu^+\mu^-\gamma \quad (1\ \textit{event})$$

as well as $Z_0 \to e^+e^-$ and $Z_0 \to \mu^+\mu^-$ for a total of 13 dilepton events[1,2]. The energy and emission angle of the observed photons, which we reproduce in Table I from ref.[3] , do not favour a

TABLE I - Properties of the $l^+l^-\gamma$ events.

	$e^+e^-\gamma$ (UA1)	$e^+e^-\gamma$ (UA2)	$\mu^+\mu^-\gamma$ (UA1)
E_γ (GeV)	38.8 ± 1.5	24.4 ± 1.0	28.3 ± 3
E_{l^+} (GeV)	61.0 ± 1.2	69.9 ± 1.8	$50.6\ ^{+5.8}_{-4.7}$
E_{l^-} (GeV)	9 ± 1	11.5 ± 0.7	$42.2\ ^{+44.0}_{-14.3}$
$\Delta\alpha^{a)}(l^+\gamma)$	132.0 ± 4.0	129.9	7.9
$\Delta\alpha^{a)}(l^-\gamma)$	14.4 ± 4.0	31.8	99.0
$m(l^+l^-)\left(\frac{GeV}{c^2}\right)$	42.7 ± 2.4	50.4 ± 1.7	$70.9\ ^{+37.2}_{-12.4}$
$m(l^+l^-\gamma)\left(\frac{GeV}{c^2}\right)$	98.7 ± 5.0	90.6 ± 1.9	$88.4\ ^{+46.1}_{-15.2}$
$m(l^+\gamma)\left(\frac{GeV}{c^2}\right)$	88.8 ± 2.5	74.7 ± 1.8	5.0 ± 0.4
$m(l^-\gamma)\left(\frac{GeV}{c^2}\right)$	4.6 ± 1.0	9.1 ± 0.3	$52.5\ ^{+27.5}_{-9.3}$

a) $\Delta\alpha$ is the angular difference in space.

conventional explanation in terms of hard bremsstrahlung [4]. Furthermore at this conference, there has been reported the observation of other unusual events :

$$p\bar{p} \to \textit{missing energy} + \textit{'photon'} + X \quad (UA1)$$

and

$$p\bar{p} \to \textit{missing energy} + \textit{single jet} + X \quad (UA1)$$

with large value of transverse missing energy and large p_t values for the photon and the jet [5] and

$$p\bar{p} \to \textit{electron} + \textit{missing energy} + \textit{hard jet(s)} + X \quad (UA2)$$

with a large total invariant mass [6]. Tables II, III and IV reproduce the characteristics of these events as reported by the experimental groups.

Many suggestions have been advanced to explain the anomalous Z_0 events [7–12]. In this talk I shall discuss in detail a model of excited quarks and leptons which bears the signatures of the reported events, although the event topology shows other anomalies[7] and the production rates are not fully consistent between the different processes.

2. THE EXCITED FERMION MODEL

The excited fermion model is based on the idea that if quarks and leptons are composite objects[13], there may exist excited states which are coupled to ordinary fermions through the usual electroweak fields as well as through the gluon field and in a such a way so as to conserve weak isospin. The excited fermion hypothesis can be phenomenologically understood as an extension of the known three families of light leptons and quarks through the use of weak isospin. In the standard $SU(2) \times U(1)$ model, the known particles can be classified as belonging to weak isospin multiplets: right (left) handed fermions belong to isospin singlets (doublets) and the gauge bosons belong to triplets, $\vec{W}^\mu$, or singlets, B^μ. To the electroweak fields, one can add the color field $G^{\mu a}$ which behaves like a singlet under weak isospin transformations. One may then consider the existence of fermionic states which can be excited using light fermions (I_w=0,$\frac{1}{2}$), Intermediate Vector Bosons (I_w=0,1) and gluons (I_w=0). To lowest order in α only I_w=0,$\frac{1}{2}$, 1, $\frac{3}{2}$ need be considered. The resulting spectroscopy is very similar in spirit to the one which was done in the early days of particle physics when the nucleon isodoublet and the pion isotriplet had been used to obtain the spectrum of many of the non-strange baryonic resonances. Since all the gauge fields carry no hypercharge Y, only couplings between excited and light multiplets with the same value of Y are allowed. As it is well known, the effective coupling has to be of the magnetic moment type transition for current conservation. This leads to the following effective lagrangian :

$$\mathcal{L}_{eff} = g' B^\mu J^Y_\mu + g \vec{W}^\mu \cdot \vec{J}_\mu + g_s G^{\mu a} J^a_\mu \tag{1}$$

The hypercharge current J^Y_μ receives contributions only from $I_w = 0, \frac{1}{2}$ states as follows :

$$J^Y_\mu(I_w = 0) = -\left(\frac{f'_0}{\mu}\right)(\overline{E^-}\sigma_{\mu\nu}Q^\nu e_R + h.c.) + \left(\frac{2f'_{0u}}{3\mu}\right)(\overline{U}\sigma_{\mu\nu}Q^\nu u_R + h.c.)$$
$$-\left(\frac{f'_{0d}}{3\mu}\right)(\overline{D}\sigma_{\mu\nu}Q^\nu d_R + h.c.) \tag{2a}$$

TABLE II - Properties of the isolated "photon" events (UA1).

Run, event	E_{tot} (GeV)	$\lvert E_T \rvert$ (GeV)	ΔE_M (GeV)	$E_T(\gamma)$ (GeV)	$m_T(\gamma, \Delta E_M)$ (GeV/c^2)
H 8167 90	298	91	40 ± 4	54	93 ± 5
G 7856 1020	390	104	40 ± 6	44	84 ± 6

TABLE III - Properties of single jet events (UA1).

Run, event	General event properties				Jet properties					
	E_{tot} (GeV)	$\lvert E_T \rvert$ (GeV)	ΔE_M (GeV)	$m_T(Jet, \Delta E_M)$ (GeV/c^2)	E_T (GeV)	E_T^{elm} a) (GeV)	ϕ b) (deg)	η c)	$p_T \pm \Delta p_T$ d) (GeV/c)	m_{CH} (GeV/c^2)
A 7325 808	300	48 94*	24 ± 4.8 (66 ± 8)*	130 ± 16	25 71*	12.4	152	-1.13	+46 $^{+12}_{-8}$	single track
B 7157 506	294	90	59 ± 7	106 ± 12	48	23.3	-142	-0.39	-7.3 $^{+1.2}_{-0.9}$ +10.1 $^{+2.5}_{-1.7}$ +3.7 $^{+0.2}_{-0.18}$	0.79 ± 0.12
C 7513 1212	489	129	46 ± 8	97 ± 17	52	44.1	176	-0.03	-2.9 $^{+0.35}_{-0.29}$	e)
D 7304 1270	279	75	42 ± 6	85 ± 12	43	42.1	-34	-0.04	-13.0 $^{+5.5}_{-3.0}$ K^0 (-1.83 $^{+0.07}_{-0.065}$ +0.92 $^{+0.012}_{-0.12}$ +0.89 $^{+0.07}_{-0.007}$	3.14 ± 0.38
E 8072 615	398	92	41 ± 7	87 ± 14	46	29.9	173	0.62	+0.86 $^{+0.051}_{-0.045}$ -0.61 $^{+0.04}_{-0.04}$	unreconstructed tracks
F 8032 1158	405	93	34 ± 7	73 ± 14	39	36.2	41	-0.31	-4.8 $^{+0.32}_{-0.28}$ -7.6 $^{+0.8}_{-0.66}$	0.517 ± 0.06

a) Electromagnetic part of the jet transverse energy.
b) Azymuthal angle ϕ.
c) Rapidity $\eta > 0$ in direction of outgoing $\bar{p}$.
d) Charged tracks associated to the jet with $p_t > 0.5$ GeV/c. Errors are statistical only.
e) This event could have other unreconstructed tracks in the horizontal plane.
*) Including the muon momentum in the calculation.

TABLE IV - Properties of the electron + missing energy + jet(s) events.

(UA2)

Events		A	B	C	Units
Electron	$p_T(e)$	18.3 ± 0.8	22.0 ± 0.9	34.4 ± 3.2	GeV/c
	$\eta(e)$ a)	0.02	-0.23	0.24	
Jets b)	$p_T(j_1)$	27 ± 3	67 ± 7	38 ± 5	GeV/c
	$\eta(j_1)$ a)	-0.59	-0.26	0.07	
	$\Delta\phi(j_1)$ c)	50	310	311	degrees
	$p_T(j_2)$	6 ± 1		21 ± 3	GeV/c
	$\eta(j_2)$ a)	0.50		0.12	
	$\Delta\phi(j_2)$ c)	93		183	degrees
	$p_T(j_3)$	5 ± 1		7 ± 1	GeV/c
	$\eta(j_3)$ a)	-1.09		-1.38	
	$\Delta\phi(j_3)$ c)	70		316	degrees
	$E_T(J)$	39 ± 4	67 ± 7	66 ± 6	GeV
	$m(J)$			63 ± 5	GeV/c²
	$p_T(\nu)$	51 ± 4	86 ± 6	57 ± 5	GeV/c
	$\Delta\phi(\nu)$ c)	220	141	141	degrees
	$m_T(e\nu)$	56 ± 2	81 ± 3	82 ± 4	GeV/c²
1	$m(WJ)$	179 ± 7	176 ± 9	162 ± 8	GeV/c²
	$x_F(WJ)$	0.45 ± 0.04	-0.01 ± 0.06	-0.04 ± 0.05	
2	$m(WJ)$	141	166	164	GeV/c2
	$x_F(WJ)$	-0.55	-0.31	0.13	

a) The pseudo-rapidity η is positive in the proton direction.

b) As mentionad in ref. (6), jet energies are expected to be smaller than the parent parton energies. This has not been corrected for and affects all parameters depending upon jet energies.

c) $\Delta\phi$ is the azymuth difference with respect to the electron.

$$J_\mu^Y(I_w = \tfrac{1}{2}) = -\left(\frac{f'}{2\mu}\right)(\bar{\mathcal{E}}\sigma_{\mu\nu}Q^\nu l_L + h.c.) + \left(\frac{f'_q}{6\mu}\right)(\bar{\Psi}\sigma_{\mu\nu}Q^\nu q_L + h.c.) \qquad (2b)$$

where the notation follows that of Table V and VII, where the multiplet structure of the excited fermions is described in detail and μ represents the mass of the excited fermion.

The isovector current $\vec{J}_\mu$ receives contributions from $I_w = \frac{1}{2}, 1$ and $\frac{3}{2}$:

$$\vec{J}_\mu(I_w=\frac{1}{2})=\left(\frac{f}{\mu}\right)\left(\overline{\xi}\sigma_{\mu\nu}Q^\nu\frac{\vec{\tau}}{2}l_L+h.c.\right)+\left(\frac{f_q}{\mu}\right)\left(\overline{\Psi}\sigma_{\mu\nu}Q^\nu\frac{\vec{\tau}}{2}q_L+h.c.\right) \tag{3a}$$

$$\vec{J}_\mu(I_w=1)=\left(\frac{f_1}{\mu}\right)(\overline{\xi}\sigma_{\mu\nu}Q^\nu e_R+h.c.)+\left(\frac{f_{1u}}{\mu}\right)(\overline{U}\sigma_{\mu\nu}Q^\nu u_R+h.c.)+$$

$$+\left(\frac{f_{1d}}{m^*}\right)\left(\overline{D}\,\sigma_{\mu\nu}Q^\nu d_R+h.c.\right) \tag{3b}$$

$$J_{\mu m}(I_w=\frac{3}{2})=C(\frac{3}{2},M\mid 1,m;\frac{1}{2},m')\left[\left(\frac{f_3}{\mu}\right)(\overline{\xi}_M\sigma_{\mu\nu}Q^\nu l_{Lm'}+h.c.)+\left(\frac{f_{3q}}{\mu}\right)(\overline{\Psi}_M\sigma_{\mu\nu}Q^\nu q_{Lm'}+h.c.)\right] \tag{3c}$$

The color current J^a_μ is composed of $I_w=0,\frac{1}{2}$ contributions :

$$J^a_\mu(I_w=0)=\left(\frac{f_{su}}{\mu}\right)\left(\overline{U}\sigma_{\mu\nu}Q^\nu\frac{\lambda^a}{2}u_R+h.c.\right)+\left(\frac{f_{sd}}{\mu}\right)\left(\overline{D}\sigma_{\mu\nu}Q^\nu\frac{\lambda^a}{2}d_R+h.c.\right) \tag{4a}$$

$$J^a_\mu(I_w=\frac{1}{2})=\left(\frac{f_s}{\mu}\right)\left(\overline{\Psi}\sigma_{\mu\nu}Q^\nu\frac{\lambda^a}{2}q_L+h.c.\right) \tag{4b}$$

In the above equations, Q^μ denotes the momentum of the gauge field and μ the mass of the excited fermion. In Eq.(3c), C's are Clebsch-Gordon coefficients. $\vec{\tau}$ and λ^a are the Pauli $SU(2)$ and Gell-Mann $SU(3)$ matrices respectively. W^μ_3 and B^μ are defined in the usual way :

$$B^\mu=\cos\theta_w A^\mu-\sin\theta_w Z^\mu \tag{5a}$$

$$W^\mu_3=\sin\theta_w A^\mu+\cos\theta_w Z^\mu \tag{5b}$$

in terms of the physical fields A^μ for the photon and Z^μ for the Z_0, θ_w is the weak angle, with the gauge coupling constants g, g' and g_s given by :

$$\frac{g^2}{4\pi}=\frac{\alpha}{\sin^2\theta_w}\quad;\quad\frac{g'^2}{4\pi}=\frac{\alpha}{\cos^2\theta_w} \tag{6a}$$

and

$$\frac{g_s^2}{4\pi}=\alpha_s(Q^2)\approx\frac{12\pi}{23\log\frac{Q^2}{\Lambda^2}}\quad(for\ five\ flavours) \tag{6b}$$

The constants appearing in the above equations, f, f' and f_s will have to be determined by the experimental observations because of our lack of understanding of the underlying dynamics. As for the mass of such excited states, while there are no estimates from first principles, earlier guesses had placed it in the TeV range, i.e. in the range of a possible composite scale Λ[14]. Indeed there are indications, from Bhabha scattering for instance, that the composite scale cannot be less than $750GeV$[15]. Present interest in the interpretation of the collider events, would instead favour a mass in the $60 \div 150GeV$ range, i.e. of the same order of magnitude of the Intermediate Vector Boson (IVB) mass.

It is important to notice that the experimental limits on the mass of an excited lepton are consistent with

$$\mu \geq 60 GeV$$

and a coupling of order unity. In ref.[7], it has been pointed out that coupling of excited leptons to the light ones may generate flavour changing neutral current processes which are of order $\left(\frac{m}{\mu}\right)^4$ with respect to ordinary weak interactions. Thus the effect is very small if the mass m of the ordinary leptons does not exceed that of the τ and that of the excited ones is not less than, say, $\simeq 50 GeV$.

Limits on both the mass and the coupling are placed by the measurement (at both Petra and PeP) of the cross-section for the process

$$e^+e^- \to \gamma\gamma$$

Present data [16] are consistent with the constraint

$$2\sqrt{2}\mu^2 \geq (60 GeV)^2 |f + f'|$$

Finally, more stringent limits on these same quantities can be derived from the measured value of $(g-2)$ for the muon [17]. In this case while a pure vector or a pure axial vector type coupling would give a contribution linear in $\frac{m}{\mu}$, hence large for any reasonable μ mass, the requirement that the coupling be of the $V - A$ type leads to a correction like [7,18]

$$\delta(g-2) = \frac{9\alpha}{16\pi}(f + f')^2 \left(\frac{m_\mu}{\mu}\right)^2$$

For $\mu \geq 60 GeV$ this implies

$$|f + f'| < 1.5$$

All of the above tells us that, while plausibility arguments would place the excited lepton mass in the TeV range, there are no experimental counterindications for a 'low' mass, like $60 \div 150 GeV$ and that the coupling may be of the same order of magnitude than that of the usual weak interactions.

Thus both experimental and theoretical constraints seem to allow for excited fermions. Naturally, one may then also consider the idea of new massive sequential states to not just quarks and leptons but also to IVB's. This has been the object of many investigations [19—21]. In particular, and to explain the anomalous Z-decays, there has been advanced the hypothesis of a direct coupling between Z_0, γ and a scalar (or pseudoscalar) resonance which decays into e^+e^-. From the experimental data, shown in Table I, one would expect such a state to be in the $40 \div 50 GeV$ range. Recent investigations

at Petra [22] of the possible decay channels of such a state seem to exclude the presence of a resonance in the processes

$$e^+e^- \to hadrons,\ \mu^+\mu^-, e^+e^-, \gamma\gamma$$

at least up to energies of $45.22 GeV$. At the same time it has been shown[23,24] that the contribution of such a state to the $(g-2)$ of the muon would be quite large and could be cancelled only by the contribution from an almost mass-degenerate pseudoscalar (or scalar) partner . This would imply an hitherto unknown symmetry of the lagrangian.

3. EXCITED LEPTONS

The multiplet structure resulting from the excited fermion model was studied for the leptons in ref.[7] and is shown in Table V. This table indicates that if the excited leptons are lighter than the IVB's, the following decay modes can be observed :

$$Z_0 \to e^+e^-\gamma \qquad I_w = 0, \frac{1}{2}, 1, \frac{3}{2}$$

$$Z_0 \to \nu\bar{\nu}\gamma \qquad I_w = \frac{1}{2}, \frac{3}{2}$$

$$W \to e\nu\gamma \qquad I_w = \frac{1}{2}, \frac{3}{2}$$

$$W \to e^+e^-(f_1\bar{f}_2) \qquad I_w = 1, \frac{3}{2}$$

$$W \to \nu\bar{\nu}(f_1\bar{f}_2) \qquad I_w = \frac{3}{2}$$

where $(f_1\bar{f}_2)$ represent a fermion-antifermion pair belonging to the same isospin multiplet. For the case $I_w = \frac{1}{2}$, the calculation of the expected IVB decay rates into the above radiative channels produces the rates shown in Table VI, where

$$r = |f\cos^2\theta_w - f'\sin^2\theta_w|^2\left(2+(\frac{M_z}{\mu})^2\right)\left(1-(\frac{\mu}{M_z})^2\right)^2 \frac{1}{1-4\sin^2\theta_w+8\sin^4\theta_w}$$

and

$$\rho = \frac{M_w^2+2\mu^2}{M_z^2+2\mu^2}\left(\frac{M_w^2-\mu^2}{M_z^2-\mu^2}\right)^2\left(\frac{M_z}{M_w}\right)^4(1-4\sin^2\theta_w+8\sin^4\theta_w)$$

With the values

$$|f\cos^2\theta_w - f'\sin^2\theta_w| \simeq \frac{1}{2}$$

and

$$\mu = 75\ GeV$$

TABLE V - Quantum numbers (charge Q, hypercharge Y) of excited leptons (belonging to the first family) with $I_W \leq 3/2$ and their coupling to light leptons with same Y.

I_W^*	Multiplet	Q	Y	coupled to	I_W
0	E^-	-1	-2	e_R through B^μ	0
1/2	$\mathcal{E} \equiv \begin{pmatrix} E^0 \\ E^- \end{pmatrix}$	0 -1	-1	$\begin{pmatrix} \nu \\ e \end{pmatrix}_L$ through $\vec{W}^\mu$ and B^μ	1/2
1	$\vec{\mathcal{E}} \equiv \begin{pmatrix} E^0 \\ E^- \\ E^{--} \end{pmatrix}$	0 -1 -2	-2	e_R through $\vec{W}^\mu$	0
3/2	$\mathcal{E} \equiv \begin{pmatrix} E^+ \\ E^0 \\ E^- \\ E^{--} \end{pmatrix}$	+1 0 -1 -2	-1	$\begin{pmatrix} \nu \\ e \end{pmatrix}_L$ through $\vec{W}^\mu$	1/2

TABLE VI - IVB's radiative decay rates, $I_W = 1/2$.

$\frac{\Gamma(Z_0 \to e^+e^-\gamma)}{\Gamma(Z_0 \to e^+e^-)}$	$\frac{\Gamma(Z_0 \to \nu_e \bar{\nu}_e \gamma)}{\Gamma(Z_0 \to e^+e^-)}$	$\frac{\Gamma(W^+ \to e^+ \nu_e \gamma)}{\Gamma(W^+ \to e^+ \nu_e)}$
r	$r \left\lvert \frac{f\cos^2\theta_W + f'\sin^2\theta_W}{f\cos^2\theta_W - f'\sin^2\theta_W} \right\rvert^2$	$\rho r \left\lvert \frac{f}{f\cos^2\theta_W - f'\sin^2\theta_W} \right\rvert^2$

one obtains good agreement with the experimental observations, i.e. a ratio

$$r = 0.2$$

for $Z_0 \to e^+e^-\gamma$ relative to $Z_0 \to e^+e^-$ and no $W \to e\nu\gamma$ in excess of the expected QED background[25]. These values of the parameter bear a very definite prediction : the existence of the decay mode

$$Z_0 \to \nu\bar{\nu}\gamma.$$

The number of expected events depends upon :

(a) the weak isospin assignment, $I_w = \frac{1}{2}$ and/or $I_w = \frac{3}{2}$,

(b) for each I_w, the number of excited families contributing to the decay,

(c) the relative sign, and magnitude, of f and f'.

Nothing can be said about the ispospin, although it is plausible that it be $I = \frac{1}{2}$. On the other hand, the observation of the $\mu^+\mu^-\gamma$ mode implies the existence of at least two excited families. For two families and $I_w = \frac{1}{2}$,one has

$$r_0^\nu = \frac{\Gamma(Z_0 \to \nu\nu\gamma)}{\Gamma(Z_0 \to e^+e^-)} = 2r\left|\frac{f\cos^2\theta_w + f'\sin^2\theta_w}{f\cos^2\theta_w - f'\sin^2\theta_w}\right|^2$$

Lacking insight into the dynamics of the model, one cannot predict this ratio and must wait for more experimental or theoretical information. During the last year, the UA1 Collaboration has searched for this type of events and has reported,at this conference, the observation of two events, with the characteristics indicated in Table II. Both events are compatible with Z_0-decay, although one cannot exclude the possibility that the photon of event G is an electron, which has passed through the region where the central detector is not sensitive.

Another interesting prediction of the excited lepton hypothesis is the exixtence of $I_w > \frac{1}{2}$ multiplets with exotic charge states, like a positively charged electron E^+ and a doubly charged E^{--}. These leptons can only have β-decays and are coupled to light leptons only through W^+ and W^-. If the mass is in the $70 \div 80\,GeV$ range, the decay rate is however very small. With present statistics on W-decay modes, one expects

$$W \to e^+e^-(f_1\bar{f}_2)^+ \qquad I_w = 1, \frac{3}{2}$$

with $\simeq 1$ event in the e^+e^- *jet jet* channel and

$$W^+ \to \nu\bar{\nu}(f_1\bar{f}_2)^+ \quad I_w = \frac{3}{2}$$

with $1 \div 2$ events in the *missing energy* + *2jets* channel and $0.2 \div 0.3$ events in the *electron* + *missing energy* channel.The signature of the latter events differ from the usual $W \to e\nu$ decay because the electron should be substantially less energetic than the 'neutrino'.

4. THE QUARK SECTOR

The excited lepton hypothesis can easily be extended to the quark sector. One finds that excited quarks can be divided into two groups, those which predominantly decay strongly[26] and for which the decay width is

$$\Gamma \approx \alpha_s \mu \quad I_w = 0, \frac{1}{2}$$

and the others which have only electroweak decay modes[27], i.e.

$$\Gamma \approx \alpha \mu \quad I_w = 1, \frac{3}{2}$$

Table VII shows the quantum numbers of excited quarks belonging to the first family and their coupling to light quarks with same hypercharge.

4.1 The case $I_w = 0, \frac{1}{2}$.

The case $I_w = \frac{1}{2}$ has been considered in detail in ref. [26], where quark-gluon fusion was found to be an important production mechanism for $I_w = \frac{1}{2}$ excited quarks. Once produced these quarks (starks) can then decay as shown in Figs. 1a, b and c, the latter mode being allowed only if the stark is heavier than the IVB. De Rujula et al. have calculated the production cross-section for these processes relative to the QCD background[28] . For process (a) and before integrating over the parton densities, the cross-section can be written as

$$\frac{d\sigma}{dM_{jj}^2} = \frac{\pi \alpha_s}{3} {f_s}^2 \frac{\mu\Gamma}{\left(M_{jj}^2 - \mu^2\right)^2 + \mu^2\Gamma^2} \delta(M_{jj}^2 - \hat{s})$$

with

$$\Gamma = \frac{\alpha_s}{3} {f_s}^2 \mu$$

In this model the constant f,f' and f_s are all of the same order of magnitude. Imposing some kinematical cuts and for a stark mass $\mu = 140 GeV$ De Rujula et al. expect an excess of $\simeq 20$ events in the jet-jet cross-section with $\alpha_s = 0.1$. These estimates are strongly dependent on the values of the coupling constants (f=f'=$f_s = \frac{1}{2}$ in this case) and have un uncertainty of at least a factor $2 \div 3$. This signal is consistent with the observation of an excess of $\simeq 50 \pm 16$ events in the jet-jet cross-section around $140\, GeV$, reported at this conference by the UA2 Collaboration [29] . If

TABLE VII - Quantum numbers (charge Q, hypercharge Y) of excited quarks (belonging to the first family) with $I_W \leq 3/2$ and their coupling to light quarks with same Y.

I_W^*	Multiplet	Q	Y	Coupled to	I_W
0	U	2/3	4/3	u_R through B^μ, $G^{\mu a}$	0
	D	-1/3	-2/3	d_R through B^μ, $G^{\mu a}$	
1/2	$\Psi \equiv \begin{pmatrix} U \\ D \end{pmatrix}$	2/3 -1/3	1/3	$\begin{pmatrix} u \\ d \end{pmatrix}_L$ through $\vec{W}^\mu$, B^μ, $G^{\mu a}$	1/2
1	$\vec{U} \equiv \begin{pmatrix} U_+ \\ U \\ D \end{pmatrix}$	5/3 2/3 -1/3	4/3	u_R through $\vec{W}^\mu$	0
	$\vec{D} \equiv \begin{pmatrix} U \\ D \\ D_- \end{pmatrix}$	2/3 -1/3 -4/3	-2/3	d_R through $\vec{W}^\mu$	
3/2	$\Psi \equiv \begin{pmatrix} U_+ \\ U \\ D \\ D_- \end{pmatrix}$	5/3 2/3 -1/3 -4/3	1/3	$\begin{pmatrix} u \\ d \end{pmatrix}_L$ through $\vec{W}^\mu$	1/2

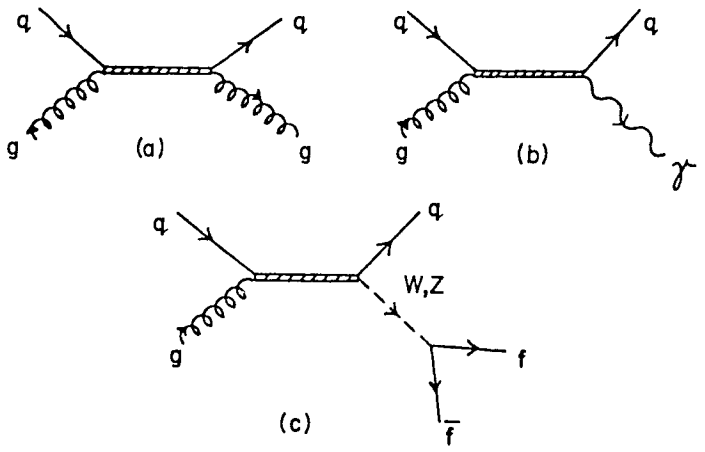

FIG. 1

this excess in indeed due to production of a stark of mass $\simeq 140\,GeV$, one must then look for the various final states which are opened by the presence of the decay channel

$$q^* \to IVB + q$$

and in particular :

(a) an enhancement in the 3 jet cross-section,

(b) events of the type lepton + missing energy + hard jet,

(c) events of the type missing energy or e^+e^- + hard jet.

Notice that for $I_w = 0$, some of the above channels are precluded, in particular there is no stark decay into W and light quarks. The expected number of events for $I_w = \frac{1}{2}$can be calculated making use of the branching ratios

$$\frac{\Gamma(q^* \to IVB + q)}{\Gamma(q^* \to all)} = \frac{3\alpha}{4\alpha_s}\left|\frac{f_v}{f_s}\right|^2\left(1 - \frac{M_{IVB}{}^2}{\mu^2}\right)^2\left(1 + \frac{M_{IVB}{}^2}{2\mu^2}\right)$$

with

$$f_\gamma = \frac{\tau_3}{2}f + \frac{1}{6}f'$$

$$f_z = \frac{\cos\theta_w}{\sin\theta_w}\frac{\tau_3}{2}f - \frac{1}{6}\frac{\sin\theta_w}{\cos\theta_w}f'$$

$$f_w = \frac{1}{\sqrt{2}\sin\theta_w}f$$

and

$$\frac{\Gamma(Z_0 \to \nu\bar{\nu})}{\Gamma(Z_0 \to all)} = 0.18 \qquad (7)$$

$$\frac{\Gamma(W \to e\nu)}{\Gamma(W \to all)} = 0.1$$

Eq.(7) implies that if the six 'monojet' events reported by the UA1 Collaboration[5] are interpreted as due to the process

$$p\bar{p} \to q^* + X$$
$$\hookrightarrow Z_0 + q$$
$$\hookrightarrow \nu\bar{\nu}$$

one should expect one

$$p\bar{p} \to e^+e^- + (hard)\ jet + X$$

event. Table VIII gives some estimate of the expected number of events for both $I_w = 0$ and $I_w = \frac{1}{2}$ case, with $\mu = 140\,GeV$.

TABLE VIII

I_W	N_{jj}	$N_{e\nu j}$	$N_{\nu\bar{\nu}j}$	$N_{j\gamma}$	N_{jjj}
0	20	0	5×10^{-3}	0.36	2×10^{-2}
	50	0	1.3×10^{-2}	0.9	5×10^{-2}
½	20	0.12	5×10^{-2}	0.36	0.94
	50	0.3	0.13	0.9	2.34

$\alpha_S = 0.1$, $M_W = 83$ GeV, $M_Z = 95$ GeV.

4.2 Excited Quarks with $I_w = 1, \frac{3}{2}$.

Excited quarks with higher isospin assignments have, as already mentioned, quite different signatures. Their main characteristics is that, to lowest order in α, they do not decay strongly, although they can be produced in pairs through strong interactions. The allowed decay modes are :

$$\Psi^* \to q + \gamma$$

and

$$\Psi^* \to q + (f_1 \bar{f}_2)$$

It is also found that the case $I_w = 1$ implies the existence of two weak isotriplets, which couple to right handed light quarks with the same hypercharge. Thus there is a triplet $\vec{U}$ coupled only to u_R and a triplet $\vec{D}$ coupled only to d_R. As for the case of excited leptons, the high isospin assignments imply exotic charge values : one finds excited quarks of charge $+\frac{5}{3}$ and $-\frac{4}{3}$ both for $I_w = 1$ as well as for $I_w = \frac{3}{2}$.

The question arises as how to produce these quarks at $\bar{p}p$ colliders and what are their characteristic production signals. Fig.2 shows the typical diagrams which contribute to the production cross-section to lowest order in α. For the case in which they are lighter than the IVB, one can calculate the decay widths of Z_0 and W through these $I_w = 1, \frac{3}{2}$ excited states. Table IX shows these rates. In Figs.3a and 3b we have plotted the ratios

$$R_W = \frac{\Gamma(W^+ \to jet_1 + jet_2 + l^+ + \nu)}{\Gamma(W^+ \to l^+ + \nu)} = 6B_{l+\nu}(f_{1u}^2 + f_{1d}^2)\left(1 - \frac{\mu^2}{M_W^2}\right)^2\left(2 + \frac{M_W^2}{\mu^2}\right)$$

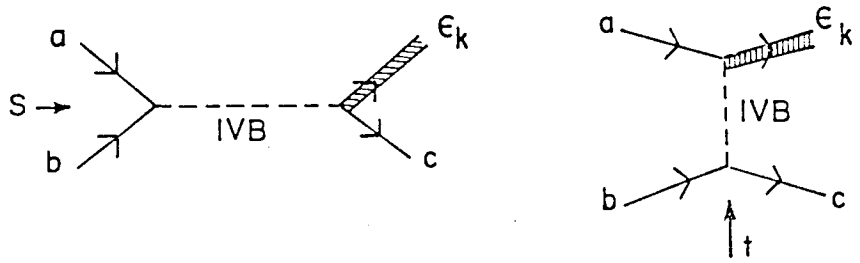

FIG. 2 - Diagrams contributing to the production of excited quarks through IVB's at hadron colliders.

TABLE IX - Decay width of Z_o and W^+ through $I_W = 1, 3/2$ excited quarks.

I_W	$\Gamma(Z_o \to j_1 + j_2 + \gamma)$ [a]	$\Gamma(W^\pm \to j_1 + j_2 + \gamma)$	$\Gamma(W^\pm \to j_1 + j_2 + (f_1\bar{f}_2)^\pm)$
1	$\frac{\alpha}{2}\left(\frac{\cos^2\theta_W}{\sin^2\theta_W}\right)\left(f_{1u}^2 + f_{1d}^2\right)\phi_Z$ [b]	0	$\frac{\alpha}{2}\left(\frac{f_{1u}^2 + f_{1d}^2}{\sin^2\theta_W}\right)B_{f_1\bar{f}_2}\,\phi_W$ [c]
3/2	$\frac{2\alpha}{3}\left(\frac{\cos^2\theta_W}{\sin^2\theta_W}\right)f_{3q}^2\,\phi_Z$	$\frac{\alpha}{6}\left(\frac{f_{3q}^2}{\sin^2\theta_W}\right)\phi_W$	$\frac{\alpha}{2}\left(\frac{f_{3q}^2}{\sin^2\theta_W}\right)B_{f_1\bar{f}_2}\,\phi_W$

a) j_i refers to u or d jets

b) The phase space factor is given by

$$\phi_{IVB} = (2 + \frac{M_{IVB}^2}{\mu^2})(1 - \frac{\mu^2}{M_{IVB}^2})M_{IVB} .$$

c) The branching ratio $B_{f_1\bar{f}_2}$ counts the number of open fermionic channels.

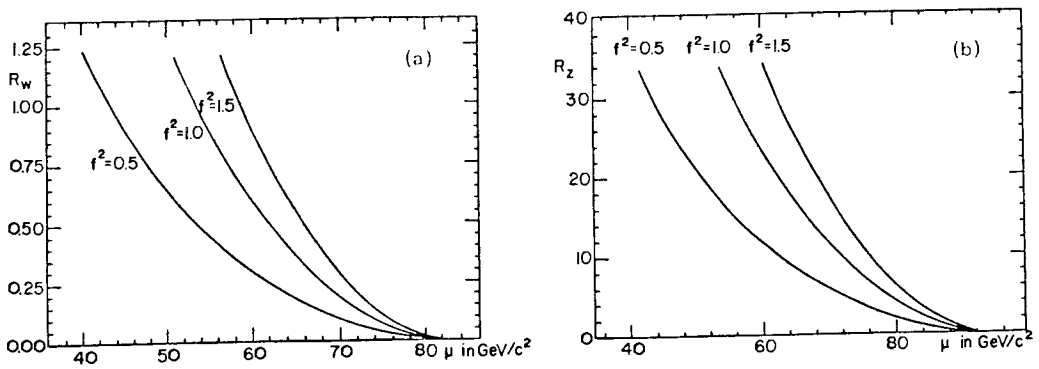

FIG. 3

and

$$R_Z = \frac{\Gamma(Z_0 \to jet + jet + \gamma)}{\Gamma(Z_0 \to e^+e^-)} = 3\frac{\cos^4\theta_w}{\sin^4\theta_w + (\frac{1}{2} - \sin^2\theta_w)^2}(f_{1u}^2 + f_{1d}^2)\left(1 - \frac{\mu^2}{M_Z^2}\right)^2\left(2 + \frac{M_Z^2}{\mu^2}\right)$$

with $I_w = 1$, $B_{l+\nu} = \frac{1}{9}$ for different values of coupling constant $f^2 = f_{1u}^2 + f_{1d}^2$ and as a function of the mass μ. So far, however, there is no evidence that excited quarks with masses less than the IVB exist. Notice however that the process

$$p\bar{p} \to jet + jet + \gamma + X$$

is extremely hard to evaluate because of a difficult experimental background .

5. EXOTIC HADRONS

If excited quarks exist, one must also consider the possibility that baryons and mesons built with these quarks and with masses in the same range exist - and can be formed at the collider. For the case $I_w \geq 1$, the possibility of exotic hadrons with so far forbidden charge assignments, arises. One would observe exotic mesons of charge ± 2 and baryons with charge $+3$. How would they decay? In Figs.4a and 4b we show the possible decay of baryons made of an excited quark belonging to a hypothetical second family and two light quarks into an equal sign dimuon pair, a strange baryon and a π^+.

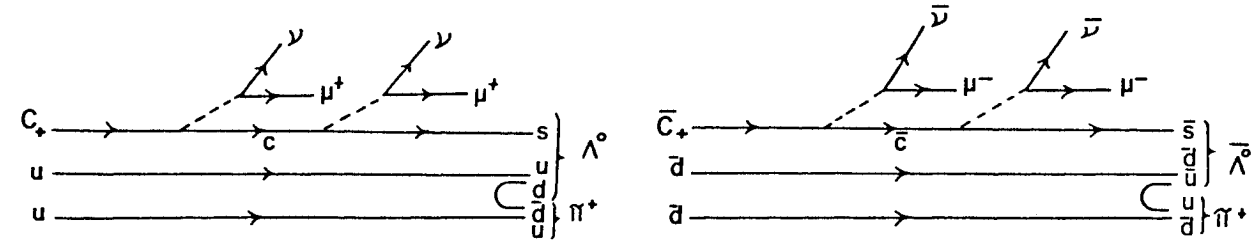

(a) $(C_+uu) \longrightarrow \mu^+\mu^+\Lambda^\circ\,\pi^+\nu\nu$

(b) $(\overline{C_+dd}) \longrightarrow \mu^-\mu^-\bar{\Lambda}^\circ\,\pi^+\bar{\nu}\bar{\nu}$

FIG. 4

6. CONCLUSION

The observation of anomalous Z-decays has spurred a number of theoretical speculations, of which we have described that related to the existence of excited quarks and leptons.

REFERENCES

1. G. Arnison et al., Physics Letters 126B,398 (1983). UA1 Collaboration.
C.Rubbia, presented at the 4th Topical Workshop on Proton-Antiproton Collider Physics, Bern 1984.
2. P.Bagnaia et al.,Physics Letters 129B,130(1983). UA2 Collaboration.
3. E.Radermacher, 'The Experimental Discovery of the Intermediate Vector Bosons W^+, W^- and Z^0 at the CERN $\bar{p}p$ Collider', CERN-EP/84-41, March 1984. To be published in 'Progress in Particle and Nuclear Physics'.
4. F.A. Behrends, R.Kleiss and S.Jadach,Nuclear Physics B202,63 (1982).
5. G. Arnison et al.,'Experimental Observation of Events with Large Missing Transverse Energy Accompanied by a Jet or a Photon (s) in $p\bar{p}$ Collisions at $\sqrt{s} = 540\ GeV$', CERN-EP/84-42. UA1 Collaboration.
6. P.Bagnaia et al., 'Observation of Electrons Produced in Association with Hard Jets and Large Missing Transverse Momentum in $p\bar{p}$ Collisions at $\sqrt{540 GeV}$', CERN-EP/84-40. UA2 Collaboration.
7. N. Cabibbo, L. Maiani and Y. Srivastava, 'Anomalous Z Decays : Excited Leptons ?', Rome Preprint 381 ,Nov. 1983. To be published in Phys.Lett.
8. M.J. Duncan and M. Veltman, 'Validity of the Standard Model at 90 GeV', University of Michigan Preprint UM Th 84-1.
9. U.Baur, H.Fritzsch and H.Faissner, Physics Letters 135B,313 (1983).
10. F.M. Renard, Montpellier Preprint, PM/83/11 December 1983.
11. R.D.Peccei,Munich Preprint, MPI-PAE/PTh 80/83, November 1983.
12. R. Barbieri, H. Harari and M. Leurer,'An Experimental Test of Z_0 compositeness in Proton-Antiproton Colliders', Weizmann Institute Preprint, WIS-84/7/March Ph.
13. H. Harari and N. Seiberg, Phys. Letters 98B,269 (1981).
H. Fritzsch and G. Mandelbaum, Physics Letters 102B, 319(1981).
W. Buchmuller, S.T. Love, R.D.Peccei and T. Yamagida, Physics Letters 115B, 233 (1982).
14. For a review on compositeness scale, see R.Barbieri in Proceedings of the International Conference on Lepton and Photon Interactions at High Energy, Cornell (USA) 1983.
15. E.J.Eichten, K.D.Lane and M.E.Peskin, Phys.Rev.Letters 50,811 (1983).
16. B.Adeva et al., Phys.Rev.Letters 48, 967 (1982); Mark J Collaboration.
17. J.Bailey et al.,Nucl.Phys. B150,1 (1979).
18. F.M.Renard, Physics Letters 116B,264(1982).
19. M. Kuroda and D. Schildknecht, Physics Letters 121B ,173 (1983).
20. H. Fritzsch and G. Mandelbaum, Physics Letters 109B,224 (1982).
21. F.M.Renard, Physics Letters 126B, 59 (1983); Physics Letters 132B,449 (1983)..
22. B.Adeva et al., 'Search for new particles in e^+e^- annihilation from 39.79 to 45.22 GeV', MIT Tech.Rep. 134, February 1984.
23. F.Del Aguila,A.Mendez and R.Pascual, Barcellona Preprint UAB -FT-105, March 1984.
24. L.Maiani and Y.Srivastava, Erice Workshop on Quark and Lepton Structure , April 1984. Unpublished.
25. G.Arnison et al., Physics Letters 135B, 250 (1984).
26. A.De Rujula,L.Maiani and R.Petronzio,'Search for excited Quarks', Cern-Th3779, December 1983.
27. G.Pancheri and Y.Srivastava,'Weak Isospin Spectroscopy of Excited Quarks and Leptons', Frascati Preprint LNF-84/10(P),February 1984.
28. A.P. Contogouris, S.Papadopoulos and C. Papavassiliou, Nuclear Physics B179,461 (1981).
29. J.D. Hansen , Presented at the 4th Topical Workshop on Proton-Antiproton Collider Physics, Bern 1984.

GLUINO MASS AND CP VIOLATION IN SUPERSYMMETRIC MODELS

A. Masiero

CERN, Geneva, Switzerland

In the promising class of supersymmetry (SUSY) theories where global supersymmetry is softly broken at low energy[1] as a result of the spontaneous breaking of local supersymmetry[2] by vacuum expectation values of the order of the Planck mass, a rich spectrum of new SUSY particles (susyons) is predicted at testable energies. However, given the possible difficulty of finding a direct evidence of susyons[3], it is of interest to look for phenomena which cannot be fully explained in the context of the standard model and necessitate extra particles (susyons?) for a possible interpretation. We consider the "old" phenomenon of CP violation in the K°-$\bar{K}^\circ$ system which has recently received a considerable amount of interest in view of the unexpectedly long B lifetime. Being the SUSY contribution dominated by gluino ($\tilde{g}$) and squark ($\tilde{q}$) insertions in the box diagram, we find it appropriate to start by summarizing our knowledge on the gluino mass which plays a discriminatory rôle among different SUSY models.

Photino ($\tilde{\gamma}$) and $\tilde{g}$ masses are so interesting since they vanish at tree level in all the SUSY theories with canonical kinetic term for the Yang-Mills superfields[2]. On the other hand, in the absence of a relevant chiral symmetry (R-invariance), small Majorana-type masses may be generated radiatively. At the one-loop level, the gluino receives a mass $\delta m_{\tilde{g}}$ from a virtual heavy top-quark contribution[4] (Fig. 1):

$$\delta m_{\tilde{g}} = \frac{\alpha_s}{8\pi} m_t F(m_t, m_{t_1}, m_{t_2}) \qquad (1)$$

where

$$F(\mu, \mu_1, \mu_2) = -\frac{\mu_1^2}{\mu^2-\mu_1^2} \log \frac{\mu_1^2}{\mu^2} + \frac{\mu_2^2}{\mu^2-\mu_2^2} \log \frac{\mu_2^2}{\mu^2} \qquad (2)$$

and $m_{t_{1,2}} = \left| m_{3/2} \pm m_t \right|$ denote the masses of the two top scalar partners. The phenomenological lower bound on the w-ino mass puts an upper limit on $m_{3/2}$[1], $m_{3/2} \lesssim 350$ GeV, whilst $m_t < 200$ GeV from the measurements of the ρ-parameter[5]. Within these bounds a gluino mass of $1 \div 1.5$ GeV is obtained for $m_{3/2}$ and m_t both greater than 150 GeV[4]. The photino mass gets an analogous

contribution with α_s replaced by α_{em} in Eq. (1). The corresponding limiting value for $m_{\tilde{\gamma}}$ is ~300 MeV. At the one-loop level, the $\tilde{\gamma}$ receives an additional contribution from virtual w-ino exchange. For $m_{3/2} \gg M_W$ one gets the limiting value[4]:

$$\delta m_{\tilde{\gamma}} = \frac{\alpha_{em}}{3\pi} m_{3/2} \log 4 , \qquad (3)$$

i.e., for $m_{3/2} \simeq 300$ GeV, $m_{\tilde{\gamma}} \simeq 400$ MeV.

The low energy Lagrangians with softly broken N = 1 global SUSY[1] have to be considered as effective Lagrangians: indeed, they neglect interactions which vanish in the limit $M_{Pl} \to \infty$ and the locally SUSY Lagrangians from which they derive are not renormalizable[2]. For instance, there exist logarithmically divergent contributions at the two-loop level to the $\tilde{g}$ and $\tilde{\gamma}$ masses and also potentially quadratic divergent gravitational radiative corrections are present. However, putting a natural cut-off at M_{Pl} they turn out to be small[4].

Although no firm lower bounds on the $\tilde{\gamma}$ and $\tilde{g}$ mass exist, there are possible indications that the above radiative contributions are somewhat too small: (i) if the photino is the lightest susyon, then cosmology requires it to be heavier than 0.5 GeV[6]; (ii) for $\tilde{q}$ masses below 100 GeV, the beam dump experiment at CERN puts a lower bound of a few GeV's on $m_{\tilde{g}}$[7]; (iii) bounds on three and four jet events in the UA1 experiment give a preliminary lower limit of 40 GeV on $m_{\tilde{g}}$[8]. If much greater contributions to $\tilde{g}$ and $\tilde{\gamma}$ masses turned out to be required, that would be an indication for SUSY models with non-canonical kinetic terms for the Yang-Mills superfields[2] and/or models where grand unification implies the existence of many more heavy particles which can circulate in the loop of the diagram of Fig. 1 [9].

The gluino mass can have a phase which introduces a new source of CP violation. However, this new CP violating contribution cannot yield the required amount of CP violation when the Kobayashi-Maskawa (K-M) phase δ is turned off[10]. Thus, in SUSY models, CP violation arises from the usual K-M phase δ which now appears in new gauge interaction between fermions and their SUSY partners and from entirely new sources which are connected to the SUSY soft breaking terms[1].

What renders this study more attractive are the unexpected results about the B-meson decay[11]. They lower the upper bound on θ_2 and θ_3 in the K-M matrix[12] so that a heavy top quark is necessary in the non-SUSY case to get

$\varepsilon \sim 10^{-3}$ [13]. For instance, for $\tau_B = 5\times10^{-12}$ sec and B = 0.33 (where B denotes the usual correction factor to the vacuum insertion approximation of the $\langle K^0 | L_{eff} | \bar{K}^0 \rangle$ matrix element), one needs $m_t > 60$ GeV [13].

Avoiding the introduction of a fourth generation, we have shown that in SUSY models the contributions which come from the $\tilde{g}$ and $\tilde{q}$ exchanges in the box diagram allow for a viable value of ε even with a light top quark ($m_t \simeq 30$ GeV)[14]. Using the following experimental inputs:

$$f_K = 0.16\ \text{GeV}, \quad M_W = 80\ \text{GeV}, \quad G_F = 1.1785 \cdot 10^{-5}\ \text{GeV}^{-2},$$

$$\frac{\Delta m}{m_K} = 0.71 \cdot 10^{-14}, \quad m_c = 1.4\ \text{GeV}, \quad \sin\theta_c = 0.231,$$

we get, in the $(m_t/M_W)^2 \ll 1$ approximation (neglecting Penguin diagrams and gluino mass insertions):

$$\varepsilon^\delta = \varepsilon^\delta(W) + \varepsilon^\delta(\tilde{g},\tilde{q}) \simeq B\ \mathrm{Im}\,\lambda_t \cdot \left\{ 11.7 \left[-\mathrm{Re}\,\lambda_c\,\eta_1 + \left(\frac{m_t}{m_c}\right)^2 \mathrm{Re}\,\lambda_t\,\eta_2 + \log\left(\frac{m_t}{m_c}\right)^2 (\mathrm{Re}\,\lambda_c - \mathrm{Re}\,\lambda_t)\,\eta_3 \right] + 0.462\, c^2 \alpha_s^2 \left(\frac{M_W}{m_{\tilde{q}}}\right)^6 \left(\frac{m_t}{m_c}\right)^2 \left[-\lambda_u + \left(\frac{m_t}{m_c}\right)^2 \mathrm{Re}\,\lambda_t \right] \cdot \left[x^6 \tilde{I}(x^2) + \frac{11}{4} x^6 \tilde{K}(x^2) \right] \right\} e^{i\pi/4} \qquad (4)$$

where

$$\lambda_i \equiv U_{KM}^{id\,*}\, U_{KM}^{is}, \qquad x = m_{\tilde{q}}/m_{\tilde{q}}.$$

The η_i's are QCD correction factors and the parameter c appearing in front of the SUSY contribution measures the flavour violation carried by the down squarks. It is generated through radiative corrections and is expected to be of order 1. The expression of $\tilde{I}(x^2)$ and $\tilde{K}(x^2)$ can be found in ref. 10).

Notice that the SUSY piece of ε^δ goes like $(m_t/m_c)^4$: this strongly suggests that the SUSY contribution can allow for a relatively light top quark. The result is illustrated in Fig. 2, where B = 0.33, c = 1, $\alpha_s = 0.1$ and we use $R \equiv \Gamma(b\to u)/\Gamma(b\to c) = 0.05$ as a constraint on the K-M matrix elements. There is a dramatic change with respect to the non-SUSY case which

is represented by the dotted line. Fixing τ_B and $m_{\tilde{g}}$ or $m_{\tilde{d}}$, it is possible to find the corresponding bounds on $m_{\tilde{d}}$ or $m_{\tilde{g}}$, respectively. The results are reported in Fig. 3 and Fig. 4. Notice that for $m_{\tilde{d}} \simeq 40$ GeV and m_t in the 30-40 GeV range, $m_{\tilde{g}}$ is required not to exceed 40-50 GeV to get enough CP violation.

REFERENCES

1) R. Barbieri, S. Ferrara and C. Savoy - Phys.Lett. 119B (1982) 343;
A. Chamseddine, R. Arnowitt and P. Nath - Phys.Rev.Lett. 49 (1982) 970;
H.P. Nilles, M. Srednicki and D. Wyler - Phys.Lett. 120B (1983) 346;
E. Cremmer, P. Fayet and L. Girardello - Phys.Lett. 122B (1983) 346;
L. Ibañez - Phys.Lett. 118B (1982) 73;
J. Ellis, D.V. Nanopoulos and K. Tamvakis - Phys.Lett. 121B (1983) 123;
L. Hall, J. Lykken and S. Weinberg - Phys.Rev. D27 (1983) 2359;
M.K. Gaillard, L.J. Hall, B. Zumino, F. Del Aguila, J. Polchinski and G.G. Ross - Phys.Lett. 122B (1983) 355.

2) E. Cremmer, S. Ferrara, L. Girardello and A. Van Proeyen - Phys.Lett. 116B (1982) 231, and Nucl.Phys. B212 (1983) 413.

3) See, for instance, A. Savoy-Navarro - Preprint CERN-EP/83-132 (1983), to be part of a Physics Reports on "Supersymmetry Confronting Experiment".

4) R. Barbieri, L. Girardello and A. Masiero - Phys.Lett 127B (1983) 429.

5) R. Barbieri and L. Maiani - Nucl.Phys. B224 (1983) 32.

6) H. Goldberg - Phys.Rev.Lett. 50 (1983) 1419.
J. Ellis, J.S. Hagelin, D.V. Nanopoulos, K. Olive and M. Srednicki - Preprint SLAC-PUB-3171 (1983).

7) CHARM Collaboration - Phys.Lett. 121B (1983) 429;
R.C. Ball et al. - Contribution to the XXIst Int. Conf. on High Energy Physics, Paris (1982).

8) Talk given by C. Rubbia at this Workshop.

9) J.-P. Derendinger and C.A. Savoy - Nucl.Phys. B, in press.

10) J.-M. Gérard, W. Grimus, A. Raychaudhuri and G. Zoupanos - CERN Preprint TH. 3809 (1984), to appear in Phys.Lett. B.

11) E. Fernandez et al. - Phys.Rev.Lett. 51 (1983) 1022;
N.S. Lockyer et al. - Phys.Rev.Lett. 51 (1983) 1316.

12) K. Kleinknecht and B. Renk - Phys.Lett. 130B (1983) 459;
E.A. Paschos, B. Stech and U. Türke - Phys.Lett. 128B (1983) 240;
L.L. Chau and W.Y. Keung - Phys.Rev. D29 (1984) 592.

13) P.H. Ginsparg, S.L. Glashow and M.B. Wise - Phys.Rev.Lett. 50 (1983) 1415.

14) J.-M. Gérard, W. Grimus, A. Masiero, D.V. Nanopoulos and A. Raychaudhuri CERN Preprint TH. 3837 (1984), to appear in Phys.Lett. B.

FIGURE CAPTIONS

Figure 1 One-loop contributions to the gluino ($\tilde{g}$) and photino ($\tilde{\gamma}$) masses from t exchange.

Figure 2 The lower bound on the top quark mass as a function of the B lifetime for different choices of the squark ($\tilde{q}$) and $\tilde{g}$ masses. The ordinary (i.e., non-SUSY) bound is shown dotted. B is equal to 0.33.

Figure 3 The allowed range of squark masses as a function of the top quark mass. The region between the solid (broken) curves is allowed for $\beta = 1.5$ (2.0), with $\tau_B = \beta \cdot 10^{-12}$ sec. These bounds correspond to a gluino mass $m_{\tilde{g}} = 40$ GeV.

Figure 4 The upper bounds on gluino masses as a function of the top quark mass, for $\beta = 1.5$ (2.0), with $\tau_B = \beta\ 10^{-12}$ sec. These bounds correspond to a squark mass $m_{\tilde{q}} = 40$ GeV.

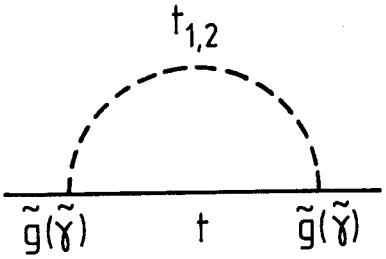
t1,2
g̃(γ̃)
t
g̃(γ̃)

Fig. 1

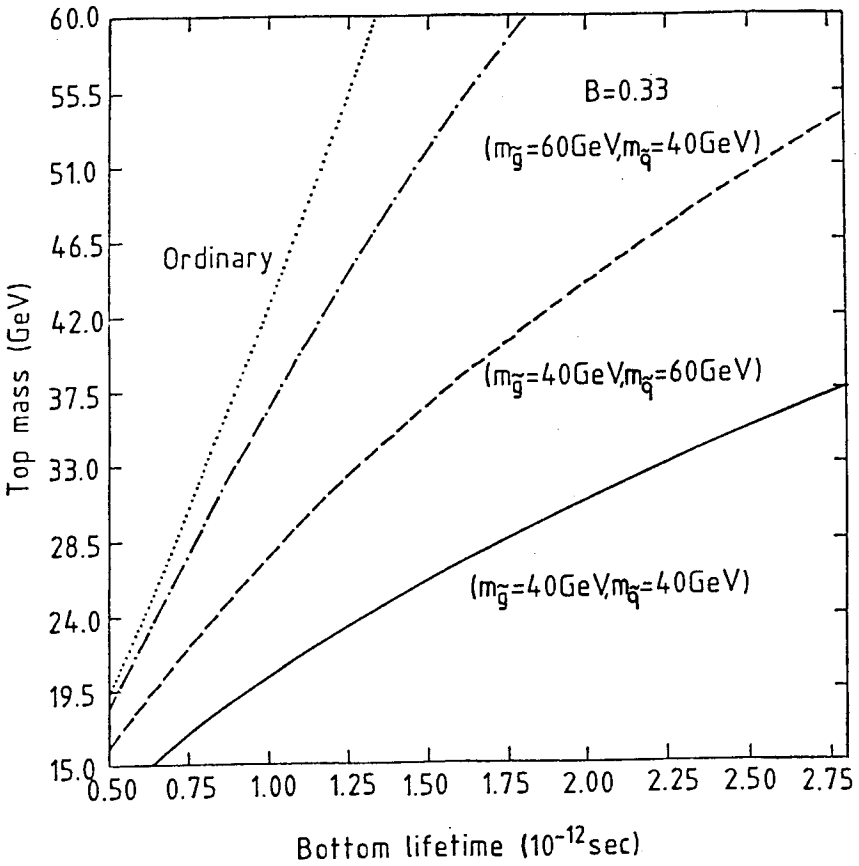
60.0
55.5
51.0
46.5
42.0
37.5
33.0
28.5
24.0
19.5
15.0
Top mass (GeV)
0.50
0.75
1.00
1.25
1.50
1.75
2.00
2.25
2.50
2.75
Bottom lifetime (10⁻¹²sec)
Ordinary
B=0.33
(mg̃=60GeV,mq̃=40GeV)
(mg̃=40GeV,mq̃=60GeV)
(mg̃=40GeV,mq̃=40GeV)

Fig. 2

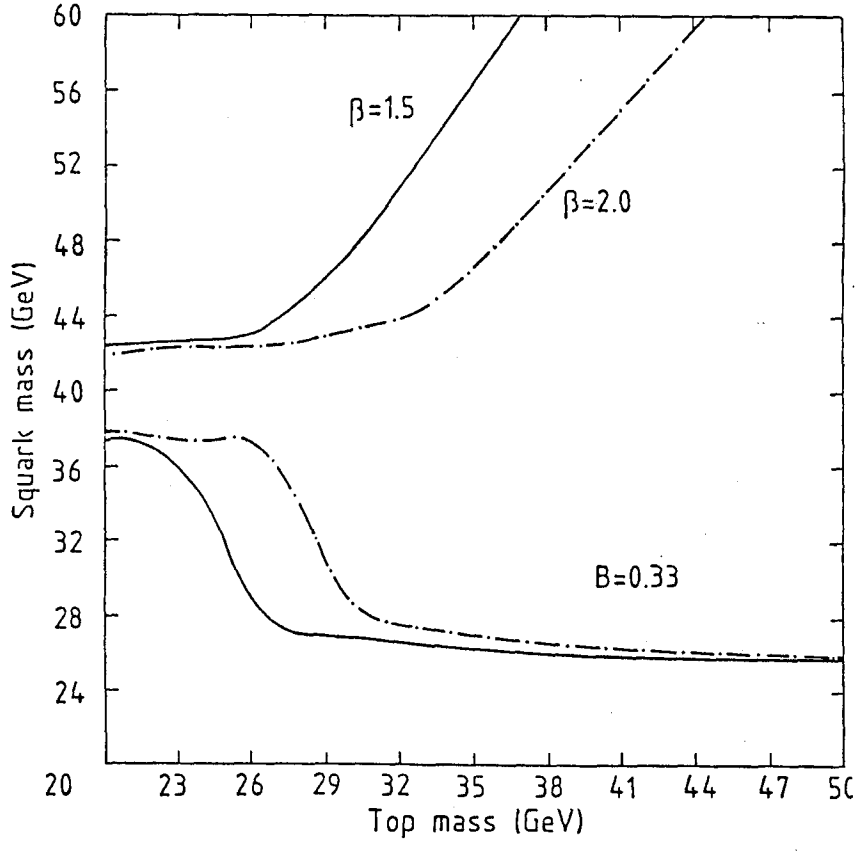
β=1.5
β=2.0
B=0.33
Squark mass (GeV)
Top mass (GeV)
60
56
52
48
44
40
36
32
28
24
20
23
26
29
32
35
38
41
44
47
50

Fig. 3

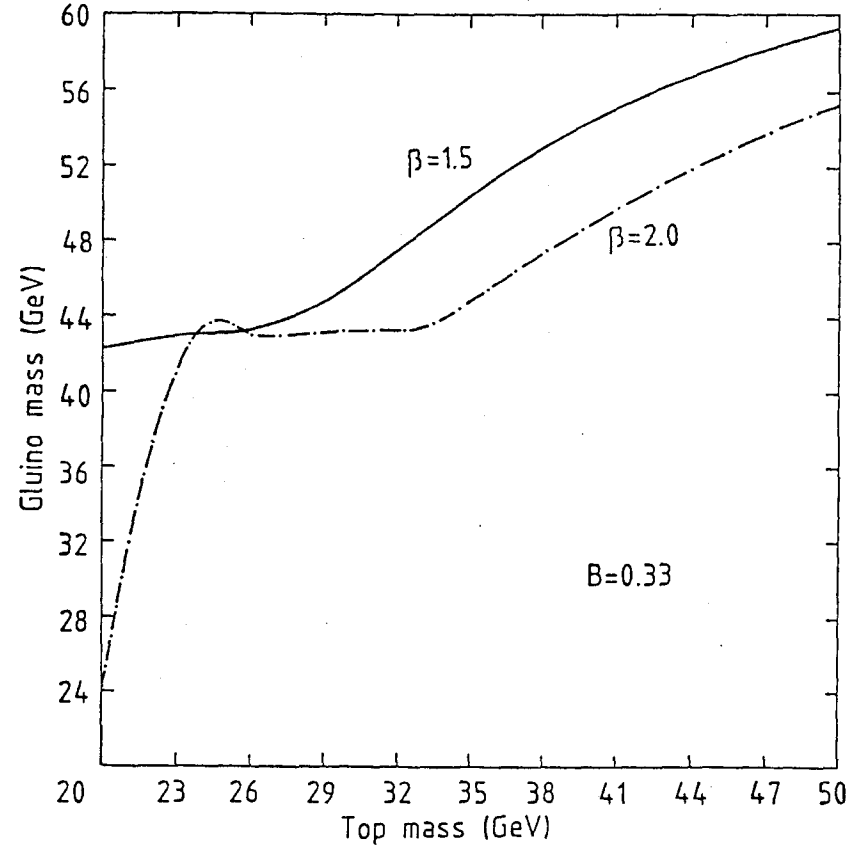
β=1.5
β=2.0
B=0.33
Gluino mass (GeV)
Top mass (GeV)
60
56
52
48
44
40
36
32
28
24
20
23
26
29
32
35
38
41
44
47
50

Fig. 4

LOW ENERGY PARTICLE SPECTRUM FROM SUPERGRAVITY

Costas KOUNNAS
Laboratoire de Physique Théorique de l'Ecole Normale Supérieure, Paris, France.

ABSTRACT

We discuss the supergravity induced low energy supersymmetric particle spectrum. The radiative breaking of the SU(2)xU(1) gauge group is explained as well as the dynamical determination of the weak scale. In the framework of the "no scale" supergravity models the vast hierarchy between the weak scale M_W = 81 GeV and the fundamental supergravity scale $M = 2.4 \cdot 10^{18}$ GeV ($M_W/M = 10^{-16}$) is shown to be dynamically generated in the quantum level.

==========

The existence of a symmetry between bosons and fermions is a very attractive idea in particle physics. This kind of symmetry, called supersymmetry[1,2], classifies particles with different statistics in supermultiplets. The spin one-half supersymmetry generator transforms fermions into bosons of the same supermultiplet and conversely without changing the other quantum numbers.

$$\text{BOSON} \xleftrightarrow{\Delta S = \pm \frac{1}{2}} \text{FERMION}$$

When supersymmetry is unbroken, the boson and the fermion of the same supermultiplet have identical masses ($M_B = M_F$). In a realistic model supersymmetry must be broken in such a way that all successful phenomenological implications of QCD and electroweak gauge interactions be reproduced. In fact, the boson-fermion mass splitting cannot be zero because we know experimentally that no supersymmetric partner of the known particles have been observed. For instance, no scalar boson with the same quantum numbers as the electron (the so-called scalar electron or selectron) has been discovered yet. The present experimental limit of such a particle is $\sim$ 20 GeV which implies the following lower limit for the boson-fermion (mass)^2 splitting

$$(20\,GeV)^2 \leq |M_B^2 - M_F^2| \equiv \mu^2 \tag{1}$$

However, the main motivation for supersymmetry is its ability to ensure the stability of the electroweak scale $\langle H \rangle \simeq 250$ GeV under radiative corrections. To maintain this property in a broken supersymmetry without any unnatural fine-tuning on the renormalized parameters of the theory, it is necessary and sufficient to impose an upper bound on the boson-fermion mass splitting μ.

$$\mu^2 \equiv |M_B^2 - M_F^2| \leq \mathcal{O}(1\text{-}10)\langle H \rangle^2 \tag{2}$$

This bound follows from the fact that the radiative corrections on $\langle H \rangle^2$ are proportional to the boson-fermion (mass)^2 splitting

$$\delta_R \langle H \rangle^2 = \sum_i \cdots (M_{B_i}^2 - M_{F_i}^2) + \cdots (n_B - n_F) \Lambda_{C.O.}^2 \tag{3}$$

where the dots "..." mean some proportionality constants of order one. Note that

the quadratic divergent part, $(\eta_B - \eta_F)\Lambda_{\text{CUT-OFF}} \equiv 0$, is absent because of supersymmetry (the bosonic and fermionic degrees of freedom are equal $\eta_B - \eta_F = 0$). Also, if the boson-fermion (mass)^2 splitting is small enough, then the stability of $\langle H \rangle$ is ensured even if superheavy particles exist in the theory, as is the case in Grand Unified Theories where particles with masses of order 10^{15}-10^{16} GeV appear naturally. What follows from the stability condition eq.(2) is of main phenomenological interest. It implies in fact the existence of many new states with masses around the electroweak scale and therefore accessible experimentally. These new states are just the supersymmetric partners[3] of the known states like leptons, quarks, gauge bosons,...

	SPIN	$\Delta S = \pm 1/2$	SPIN	
LEPTONS	1/2	⟷	0	SLEPTONS
QUARKS	1/2	⟷	0	SQUARKS
HIGGS	0	⟷	1/2	HIGGSINOS
PHOTON	1	⟷	1/2	PHOTINO
$W^{\pm}$	1	⟷	1/2	W-INOS
Z	1	⟷	1/2	Z-INOS
GLUONS	1	⟷	1/2	GLUINOS
⋮				⋮

The mass spectrum of the superpartners depending on the assumed supersymmetry breakdown is not uniquely defined. In the framework of a simple supergravity[4] (N=1 local supersymmetry), the suitable breakdown of supersymmetry is generated spontaneously by the so-called superHiggs mechanism[4]. Within this mechanism the massless spin 3/2 gravitino (the superpartner of the spin 2 graviton) becomes a massive spin 3/2 state by "eating" the 2-helicity spin 1/2 goldstino.

It is interesting to note that the spontaneously broken supergravity behaves like a softly broken global supersymmetry for energy scales smaller than the Planck scale $M_P = 1.2 \cdot 10^{19}$ GeV. Therefore a suitable non-zero boson-fermion splitting appears in the supermultiplets induced by the soft breaking terms[2]. For instance, after the superHiggs mechanism, the scalar bosons (mass)^2 receives at the tree level a positive contribution proportional to the gravitino (mass)^2, $m^2_{3/2}$. The proportionality constants depend on the superHiggs mechanism we consider. After radiative corrections an extra positive contribution is generated which turns out to be proportional to the other supersymmetry breaking parameters, the gauginos (mass)^2 (gluinos M_3^2, W-inos M_2^2, B-ino M_1^2). Also, for the scalar bosons which interact through the large top-quark Yukawa coupling, the radiative corrections generate non negligible negative contribution to their (mass)^2. This negative contribution is proportional to the top-Yukawa coupling and to a certain

combination of the supersymmetry breaking parameters $m_{3/2}$, $M_{gauginos}$, as well as the dimensionless parameters A and B. The parameter A is used to define the non negligible trilinear coupling between the two superpartners of the top quark $\tilde{t}_L$, $\tilde{t}_R$ and that of the Higgs H_2 .

$$A m_{3/2} h_t (\tilde{t}_L \tilde{t}^c_R H_2 + C.C.) \qquad (4)$$

(h_t is the top-Yukawa coupling)

In the presence of a non zero supersymmetric mass, m_4, for the Higgses H_1 and H_2 the breaking parameter B defines the off-diagonal $(mass)^2$ of the Higgs $(mass)^2$ matrix

$$B m_{3/2} m_4 (H_1 H_2 + C.C.) \qquad (5)$$

Keeping only the large top-Yukawa coupling and performing the quantum corrections one finds the following renormalized mass parameters for the scalar bosons[5]:

(a) $$m_i^2 = a_i m_{3/2}^2 + c_i M_o^2 \qquad (6)$$

for all sleptons and the squarks which do not couple through the top-Yukawa coupling h_t. a_i are constants depending on the superHiggs mechanism. They are equal to one in the minimal case[4] and are equal to zero in the maximally symmetric case of ref. 6). In the last case $a_i = 0$, the gravitino scale does not appear at all in the low energy spectrum, and therefore the gravitino mass may have any value without sensible effect on the low energy spectrum[6]. c_i are calculable constants given as integrals of functions of the gauge coupling constants[5]. For the sleptons they are of order 0.2 to 0.5 and for the squarks 2 to 5 depending on the superheavy contents of the theory. M_o is a typical tree level gaugino mass (for instance the value of the gauginos at the Grand Unification scale).

(b) The two stops $\tilde{t}_L$, $\tilde{t}_R$ $(mass)^2$ matrix

$$\begin{bmatrix} \tilde{t}_L \\ \tilde{t}_R \end{bmatrix} : \begin{bmatrix} a_L m_{3/2}^2 + c_L M_o^2 - \Delta^2 + m_t^2 & m_t (A m_{3/2} - m_4) \\ m_t (A m_{3/2} - m_4) & a_R m_{3/2}^2 + c_R M_o^2 - 2\Delta^2 + m_t^2 \end{bmatrix} \qquad (7)$$

(c) The two Higgses ($c_H \simeq 0.5$)

$$m_1^2 = m_4^2 + a_H m_{3/2}^2 + c_H M_o^2$$
$$m_2^2 = m_4^2 + a_H m_{3/2}^2 + c_H M_o^2 - 3\Delta^2$$
$$m_{12}^2 \equiv m_3^2 = B m_{3/2} m_4 \qquad (8)$$

In eqs.(7,8) the non negligible negative contribution ($-\Delta^2$, $-2\Delta^2$, $-3\Delta^2$) is a consequence of the large Yukawa coupling h_t. In fact Δ^2 is proportional to h_t and to a certain combination of the breaking parameters $m_{3/2}$, M_o and A[5].

After the important work of Cremmer et al.[4] qualitative tree-level models were constructed neglecting the quantum corrections $c_i = \Delta = 0$ and assuming a minimal superHiggs mechanism $a_i = 1$[2]. In these models the mass parameters of

sleptons and squarks are more or less equal to the gravitino mass $m_{3/2}$ except for the two eigenvalues of the top superpartners

$$m^2_{stop\ 1,2} = m^2_{3/2} + m_t^2 \pm m_t (A m_{3/2} - m_4) \tag{9}$$

In these models a light gauge singlet couple to the Higgses must be introduced in order to generate suitable non zero vacuum expectation values for the Higgses and to obtain the correct SU(2)xU(1) breaking. The tree level models neglecting large radiative corrections have only a qualitative interest and therefore it is dangerous to consider them as realistic models.

At the contrary, the more realistic models are those where the radiative corrections are equally taken into account[5,7,2]. It follows that the radiative corrections on the supersymmetry breaking parameters are very important and drastically change the naïve tree level situation. In fact the radiative corrections are able to generate the correct SU(2)xU(1) breakdown[7,5] without the introduction of an extra light gauge singlet superfield. Moreover, the radiative breaking mechanism is of main interest because it enables one to generate dynamically a vast hierarchy between the fundamental scale of the theory $M = M_P/\sqrt{8\pi} = 10^{18}$ GeV and the weak scale $M_W \simeq 81$ GeV[5]. The reason is that the renormalized (mass)^2 Higgs matrix (eq.(8)) contains negative (mass)^2 eigenvalue for energy scales Q smaller than a critical scale Q_o

$$m_1^2 m_2^2 - m_3^4 \big|_Q \leq 0 \ , \quad Q \leq Q_o \tag{10}$$

Therefore, SU(2)xU(1) breaking minima are generated dynamically with the Higgs fields vacuum expectation values of order Q_o , ($\langle H_i \rangle \simeq Q_o$), provided the typical boson-fermion mass splitting μ is of the same order as or smaller than the dimensional transmutation scale Q_o ($\mu \leq \theta(Q_o)$). However, Q_o differs by many orders of magnitude from the fundamental scale $M = 10^{18}$ GeV as a consequence of the very smooth variation (logarithmic) of the renormalized parameter m_1^2, m_2^2 and m_3^2. The vast hierarchy between the weak scale $M_W \sim Q$ and M is then dynamically generated and easily turns out to be of the correct order of magnitude.

$$M_W \simeq Q_o \simeq M \exp - \frac{\theta(1)}{\alpha_2} \simeq 10^{-16} M \tag{11}$$

where α_2 is the typical SU(2) gauge coupling. Furthermore, the existence of the critical scale Q_o requires a large negative contribution to the m_2^2 mass parameter (see eq.(8)), or, equivalently, a large value for the Δ^2 in eq.(8). The fact that Δ^2 is proportional to the top-Yukawa coupling shows that the ratio m_t/M_W is constrained[7,5]. A detailed analysis shows that the radiative breaking holds if

$$\frac{1}{4} < m_t/M_W < 2 \tag{12}$$

so the top quark mass must be within the range

$$20 \text{ GeV} < m_t < 160 \text{ GeV} \tag{13}$$

A typical experimentally accessible low energy physical mass spectrum is given in Table I for low values of the top quark 25 GeV$< m_t <$50 GeV and $a_i = 1$. Note that this spectrum is just the most accessible one. In the general case one may obtain more massive superpartners by changing the masses of the gravitino and gauginos. However some general figures are valid for almost all realistic supergravity induced low energy spectra. For instance the sleptons are always lighter than the squarks except that of the physical stop scalars which may be the lightest charged superpartner. The charged Higgses have always masses above the mass of the $W^{\pm}$-bosons. The mass of the three neutral physical Higgses is light (3-20) GeV which is characteristic of the radiative breaking[5]. The second neutral Higgs has a mass above the $M_Z \simeq 92$ GeV, and the last one has a mass proportional to the m_4 parameter. It is probable that its mass is of the same order as the typical slepton masses. The only pure gaugino states are the gluinos, the Majorana gauge fermions associated with the unbroken SU(3) gauge group. After the SU(2)xU(1) breaking, all the other gauginos are mixed with the higgsinos and form the physical higgsino-gaugino states. Namely, the two charged gauginos W^+, W^- are mixed with the chargedhiggsinos H^+, H^- forming two Dirac spinors that we call WH-ino and HW-ino. In all interesting cases, one of them (HW-ino) is lighter and the other one is heavier than M_W

$$M_{HW\text{-ino}} < M_W < M_{WH\text{-ino}} \qquad (14)$$

Similarly, the two neutral gauginos W_3, B mix with the two neutral Higgsinos H_1, H_2 and form 4-physical neutral states (Majorana spinors). We call photino the eigenstate which is dominated by the photon-superpartner component. In most of the models the photino is the lightest supersymmetric state. The two other neutral fermions are mainly mixed states of Z-ino and higgsino. We call them ZH-ino and HZ-ino. Similarly, here, the HZ-ino is lighter than M_Z and the ZH-ino heavier than M_Z in all interesting cases.

$$M_{HZ\text{-ino}} < M_Z < M_{ZH\text{-ino}} \qquad (15)$$

The remaining neutral eigenstate is mainly dominated by a higgsino component. This physical state is usually called "higgsino" and its mass is close to the m_4 mass parameter. Cosmological considerations force us to consider the Higgsino mass as larger than the photino one.

In almost all supergravity models the supersymmetry breaking scales are taken as free parameters. Furthermore, the typical boson-fermion mass splitting μ, (which is defined by these breaking scales), must be chosen small enough in order to stabilize the weak scale at its low value (see eq.(2)). Within the radiative breaking mechanism and if we assume the hierarchical ratio $\mu/M \simeq 10^{-16}$, the hierarchy between the weak scale M_W and the fundamental supergravity scale M is dynamically generated[5]. Therefore to "solve" the hierarchy problem in the frame-

work of supergravity theories one must explain why μ is so much smaller than M, $\mu/M \simeq 10^{-16}$? Recently a class of supergravity models has been proposed which are able to generate dynamically the μ/M hierarchy[8,6] under certain assumptions. This class of models that we call "no scale supergravity models" are based on a particularly symmetric superHiggs mechanism[9,6] in which the breaking scale μ is undetermined at the classical level[9,6] (tree level approximation). However the scale μ depends on the value of a scalar field z, the scalar component of the goldstino (η) supermultiplet (z,η). The undetermination of the scale $\mu = \mu(z)$ follows from the existence of degenerated minima in the z-direction of the scalar potential ($V(z) \equiv 0$). It has been shown that the radiative corrections destroy this degeneracy of the potential generating a preferred value z_0[8,6]. Therefore the scale $\mu = \mu(z_0)$ is dynamically generated at the quantum level. It is remarkable that $\mu = \mu(z_0)$ and the weak scale M_W are simultaneously fixed at a scale close to the dimensional transmutation one, Q_0, and consequently the μ/M and M_W/M hierarchies are naturally explained[8,6]. At the same time the stability of the weak scale is ensured by the fact that the breaking scale μ is of the same order as M_W. The typical low energy spectrum which follows from the "no scale" models has the same structure as before. The only difference here is that the typical breaking scale μ is not just a free parameter but is rather determined within the radiative breaking mechanism. It follows that the sleptons have typical masses of order M_W or 2-3 times larger depending on the assumed superHiggs mechanism and the gaugino to gravitino mass ratios. Simple typical examples of the no-scale supergravity models may be found in refs. 8) and 6).

REFERENCES

1) Y.A. Gol'fand and E.P. Likhtman, Pis'ma Zh.Eksp.Teor.Fiz. 13 (1971) 323;
D. Volkov and V.P. Akulov, Phys.Lett. 46B (1973) 109;
J. Wess and B. Zumino, Nucl.Phys. B70 (1974) 39.
2) An essentially complete list of references on Supersymmetry and Supergravity see the recent review of H.P. Nilles, Geneva University preprint UGVA-DPT 1983/12-412, submitted to Phys.Rep.C.
3) P. Fayet, Phys.Lett. 69B (1977) 489.
4) E. Cremmer et al., Phys.Lett. 79B (1978) 23; Nucl.Phys. B147 (1979) 105;
E. Cremmer et al., Phys.Lett. 116B (1982) 231; Nucl.Phys. B212 (1983) 413.
5) C. Kounnas, A.B. Lahanas, D.V. Nanopoulos and M. Quiros, Phys.Lett. 132B (1983) 95; Nucl.Phys. B236 (1984) 438.
6) J. Ellis, C. Kounnas and D.V. Nanopoulos, CERN preprint TH/3824 and TH/3848 (1984).
7) L.E. Ibañez and C. Lopez, Phys.Lett. 126B (1983) 94 and CERN preprint TH-3650 (1983);
J. Ellis, J.S. Hagelin, D.V. Nanopoulos and K.A. Tamvakis, Phys.Lett. 125B (1983) 275;
L. Alvarez-Gaumé, J. Polchinski and M.B. Wise, Nucl.Phys. B221 (1983) 499.

8) J. Ellis, A.B. Lahanas, D.V. Nanopoulos and K.A. Tamvakis, Phys.Lett. 134B (1984) 61;
J. Ellis, C. Kounnas, D.V. Nanopoulos, CERN preprint TH-3768 (1983) to be published in Nucl.Phys. B.

9) E. Cremmer, S. Ferrara, C. Kounnas and D.V. Nanopoulos, Phys.Lett. 133B (1983) 61.

TABLE I

TYPICAL SPECTRUM

25 GeV $< m_{\tilde{l}} <$ 50 GeV

GeV				GeV
20	$<$	SLEPTONS - R	$<$	30
25	$<$	SLEPTONS - L	$<$	40
50	$<$	SQUARKS	$<$	100
20	$<$	STOP - R	$<$	80
80	$<$	STOP - L	$<$	130
83	$<$	HIGGS H^+	$<$	98
3	$<$	NEUTRAL	$<$	10
20	$<$	HIGGSES	$<$	50
95	$<$	1, 2, 3,	$<$	105
40	$<$	GLUINOS	$<$	100
3	$<$	PHOTINO	$<$	12
10	$<$	HIGGSINO	$<$	25
80	$<$	HZ - INO	$<$	91
98	$<$	ZH - INO	$<$	118
75	$<$	HW - INO	$<$	81
84	$<$	WH - INO	$<$	90

SUPERSYMMETRY

Presented by D. Nanopoulos, CERN

No written contribution received

Summary and Conclusions

NEW COLLIDER PHYSICS

John Ellis
CERN, Geneva, Switzerland

0. APOLOGIA

My assignment is to offer some conclusions for this meeting. As the highlights have been the presentations of many new and exciting pieces of data, perhaps an experimentalist would have been better able to make sense of what has been going on. As a mere theorist, all I can say is that the new results presented here seem to raise more questions than they provide answers. This is good for everyone except for the person who is supposed to conclude, but can only find inconclusive things to say! Nevertheless, here goes.

As a theorist, I necessarily look for interpretations of the new data in terms of various existing theoretical ideas. Collider data presented here and previously confirm very beautifully that the fundamental interactions are described by gauge theories. Theorists now ask other questions: how is gauge symmetry broken? Do Higgs bosons exist? Are elementary Higgses protected by supersymmetry (SUSY)? Or are Higgses composite ("Technicolour")? Are leptons and quarks composite? Are the $W^{\pm}$ and Z^0 composite? Maybe none of these theoretical ideas has anything to do with the new phenomena reported at this meeting: monojet events, electron + jet + missing p_T events, the possible bump in multijet invariant masses at about 150 GeV, dimuon events. Although it is tempting to interpret some of the novel data as favouring one theory over another, they seem to point in different directions and no clear trend emerges. What we need is more data! In the short term this will be provided by the CERN $S\bar{p}pS$ Collider operating at a slightly higher centre-of-mass energy. In the medium term the $S\bar{p}pS$ Collider will be upgraded by the addition of the ACOL ring, and will be accompanied by fierce transatlantic competition from the FNAL Tevatron Collider. Hopes for the long term include the Superconducting Super Collider (SSC) in the United States, sometimes known as the Desertron, and the Large Hadron Collider (LHC) in the LEP tunnel, sometimes known as the Juratron. Included in this review are some comments about the physics which may be possible with such a machine having $E_{cm} \simeq 10$ to 40 TeV. Not included, though, is anything about the present physics with those lower energy colliders, LEAR and the ISR. I apologize for running out of time to do justice to the eloquent reports[1),2)] on their physics presented at this meeting.

1. WHAT WE HAVE LEARNT

We have learnt that the fundamental interactions are gauged with $SU(3)\times SU(2)\times U(1)$. One of the nice results presented[3] at this meeting was an analysis of QCD jets at the CERN $S\bar{p}pS$ Collider which provided very clear evidence for the three-gluon vertex, an essential feature of the non-Abelian SU(3) structure of QCD. It was found that the angular distributions of QCD jets had an approximate $1/\sin^4\theta$ shape, indicative of gluon exchange in gluon-gluon and gluon-quark scattering as well as in quark-(anti)quark scattering. This result confirms the Rutherford formula and hence the inverse square law for short-distance interactions between gluons. There is an approximately universal[4] angular dependence of 2-2 qq, qg and gg scattering and the simple ratios between their cross-sections:

$$\sigma_{qq}^{(2)} : \sigma_{qg}^{(2)} : \sigma_{gg}^{(2)} \approx 1 : \frac{9}{4} : \left(\frac{9}{4}\right)^2 \qquad (1)$$

enable the data to be fitted[3] with a unique "structure function"

$$G(x) + \frac{4}{9}\left(Q(x) + \bar{Q}(x)\right) \qquad (2)$$

The ratios of 9/4 in Eq. (1) and 4/9 in Eq. (2) simply reflect[4] the ratio of the colour charges of quarks and gluons: they confirm that gluons are octets of colour rather than triplets. This result can be checked in more detail using three-jet events[5], which have characteristic bremsstrahlung forms with the same ratios:

$$\sigma_{qq}^{(3)} : \sigma_{qg}^{(3)} : \sigma_{gg}^{(3)} \approx 1 : \frac{9}{4} : \left(\frac{9}{4}\right)^2 \qquad (3)$$

Also exhibiting characteristic bremsstrahlung shapes were[3] the distributions of jets produced in association with W's and Z's. In the immortal words of Sherlock Holmes: "It is glue, Watson. Unquestionably it is glue". We will be meeting the famous detective quite often in what follows, as we try to adopt his investigative techniques.

Also presented at this meeting were the latest updates on the crowning confirmation of the $SU(2)\times U(1)$ electroweak gauge theory, the observation of $W^{\pm}$[6] and Z^0[7]. UA2 presented[8] updated mass values, which are listed in Table 1 along with UA1 and theoretical values including radiative corrections[9].

Table 1: $W^{\pm}$ and Z^0 masses (in GeV)

	UA2	UA1	Theory ($\sin^2\theta_W$=0.210±0.014)
m_W	83.1±1.9±1.3	80.9±1.5±2.4	$83.0\ ^{+\ 2.9}_{-\ 2.7}$
m_Z	92.7±1.7±1.4	95.6±1.5±2.9	$93.8\ ^{+2.4}_{-2.2}$

The latest UA2 results[8] correspond to

$$\sin^2\theta_W = 0.215 \pm 0.010 \pm 0.007 \qquad (4)$$

in perfect agreement with low energy data.

The production cross-sections[8] for the $W^{\pm}$ and Z^0 are also in perfect agreement with standard model predictions[10]:

$$\left.\begin{aligned} \sigma B(W\to e\nu) &= 530\pm100\pm100\ \text{pb (UA2)} \\ &\text{cf } 350\ \text{pb } (\pm20\%?) \\ \sigma B(Z\to ee) &= 71\pm24\pm13\ \text{pb (UA1)} \\ &110\pm40\pm20\ \text{pb (UA2)} \\ &\text{cf } 53\ \text{pb } (\pm20\%?) \end{aligned}\right\} \qquad (5)$$

UA1 had already combined[11] their measurements of the ratio $\sigma B(z\to ee)/\sigma B(W\to e\nu)$ and their upper limit on the natural decay width of the Z^0 to establish a bound on the number of neutrinos:

$$N_\nu < 18 \qquad (6a)$$

At this meeting UA2 presented[8] a new analysis of the natural width of the Z^0:

$$\Gamma_Z < 6.5\,\text{GeV} \Rightarrow N_\nu < 24 \qquad (6b)$$

They also obtained[8] a more indirect bound on Γ_Z from the production ratio $\sigma B(Z\to ee)/\sigma B(W\to e\nu)$:

$$\Gamma_Z < 2.7\,\text{GeV} \Rightarrow N_\nu \leq 3 \text{ (90\% confidence) or } N_\nu < 5 \text{ (95\% confidence)} \qquad (6c)$$

The smallness of this last limit follows from the surprisingly large number of $Z^0 \to ee$ events found by UA2. The UA1 Collaboration are also able to improve their limit (6a) by using information from $Z^0 \to \mu\mu$ decay.

The UA2 Collaboration reported[8] here a first indication for a W bump in the invariant mass spectrum of hadronic jet combinations. They presented a fit which wanted 92±52 events in the W peak (less than 2σ) with a fitted mass and cross-section:

$$m_W = 79 \pm 8\,\text{GeV}\ ,\ \sigma = 4 \pm 2.5\,\text{nb} \qquad (7)$$

in perfect agreement with expectations[10]. However, they are correctly cautious and do not yet claim discovery of the W in hadronic jets. The same talk revealed they had found more than they bargained for in hadronic jets, as we will see again later !

2. WHAT WE WANT TO LEARN

We are still waiting to learn the mass of the t quark, which did not appear at this meeting. I have no words of wisdom on this subject, and prefer to address what seem to be more basic theoretical issues.

a) How is gauge symmetry broken?

Exact SU(2)×U(1) gauge symmetry would require $m_W = m_Z = 0$, in the same way that QED's U(1) and QCD's SU(3) symmetries enforce $m_\gamma = m_g = 0$. The facts that m_W and $m_Z \neq 0$ create problems for the perturbative unitarity and renormalizability of the electroweak theory[12]. These would require the $f\bar{f} \to WW$ cross-section to fall as $1/E_{cm}^2$, which it almost does, thanks to cancellations due to the non-Abelian three-boson vertex, but there is a residual excess over the $1/E_{cm}^2$ rule which is proportional to m_f. Similarly, the $WW \to WW$ cross-

section violates this rule by an amount $\propto m_W^2$. To cancel out these remaining excesses, one needs[12] an additional boson with couplings

$$g_{ff} \propto m_f \quad , \quad g_{WW} \propto m_W^2 \tag{8}$$

All hope of renormalizability would be lost if this boson had spin >1. The non-universality (8) of its fermion couplings means that it cannot be a spin-1 gauge boson. The only possibility is spin-0, and we arrive at the Higgs boson of the Standard Model, whose vacuum expectation value breaks gauge invariance spontaneously and gives masses to fermions, the $W^{\pm}$ and the Z^0.

The introduction of the Higgs boson raises more questions than it answers. Is it composite or elementary? In the former case[13], called here technicolour, it is made out of technifermion constituents bound together by a new set of interactions strong at an energy scale O(1) TeV. If the Higgs is elementary, its mass has quadratic divergences and other diseases which can be cured by the cancellations of supersymmetry (SUSY)[14]. In both the elementary and composite Higgs cases, we would expect to discover some new particles with masses $\lesssim$ O(1) TeV, and their study is one of the main motivations for the large hadron colliders to be discussed later.

b) Are our present "elementary" particles composite?

Many physicists are appalled by the present proliferation of apparently "elementary" quarks and leptons, and believe that they are composed of more elementary constituents called preons. Some physicists believe that the masses of the $W^{\pm}$ and Z^0 are hints that they are composite, rather than elementary like the massless photon and gluons. In contrast to models of spontaneous gauge symmetry breaking, where either the elementary Higgs, or some technipions, or (in order to get the required cancellations in SUSY theories) some new supersymmetric particles have masses $\lesssim$ O(1) TeV, there is no clear and convincing reason to expect a new composite structure to emerge in an accessible energy range. Furthermore, in contrast to Higgs, technicolour and SUSY, there are no composite theories which are completely respectable theoretically[15]. There are only phenomenological models which may appear seductive but only embody some subset of the theoretical desiderata for a true composite theory. My own prejudices about composite models were presciently summarized by Sherlock Holmes: "Elementary, my dear Watson".

c) Signatures for new physics SUSY

In most supersymmetric theories[16),17)], the supersymmetric particles possess a new multiplicatively conserved quantum number equal to (-1). This means that they can only be produced in pairs, that among the decay products of every sparticle there must be another sparticle, and hence that the lightest sparticle must be stable. The lightest sparticle is probably neutral and not strongly interacting, and the most likely candidate may[18)] be the photino $\tilde{\gamma}$. Thus a characteristic signature for SUSY could be missing energy-momentum, for example, from gluino $\tilde{g}$ pair-production:

$$p\bar{p} \to \tilde{g}\tilde{g} + X \quad \hookrightarrow q\bar{q}\tilde{\gamma} \qquad : p_T^{miss} \propto m_{\tilde{g}} \tag{9a}$$

or from supersymmetric W decay:

$$p\bar{p} \to W + X \quad \hookrightarrow \tilde{W} + \tilde{\gamma} \quad \hookrightarrow q\bar{q}\tilde{\gamma} \qquad : p_T^{miss} = O\left(\frac{m_W}{2}\right) \tag{9b}$$

Technicolour

All technicolour theories[13)] expect technihadrons (ρ_T, ω_T, etc.) with masses O(1) TeV, and a continuum of technistates starting from a threshold $\sqrt{s}$ = O(1) TeV. The "extended" technicolour theories[19)] which seek to understand fermion masses as well as m_W and m_Z also expect[20)] many "light" technipion bound states, such as colour octets P_8:

$$m_{P_8^0} \approx 250\,\text{GeV} \quad , P_8^0 \to gg, \bar{t}t \tag{10a}$$

colour triplet technileptoquarks P_{LQ}:

$$m_{P_{LQ}} \approx 160\,\text{GeV} \quad , P_{LQ} \to q + l \tag{10b}$$

and colour singlet technipions $P^{0,\pm}$:

$m_{P^{0,\pm}} \ll 100\,\mathrm{GeV}$ (?), $P^{0,\pm} \to q\bar{q}, l\nu$ (10c)

Compositeness

Excited quarks and leptons, in addition to their possible detection in $Z^0 \to (e^* \to e\gamma)e$ decays[21], could also show up in $W \to (e^* \to e\gamma)\nu$ or $W \to e(\nu^* \to \nu\gamma)$ or $Z^0 \to (\nu^* \to \nu\gamma)\nu$. The decays $q^* \to q+\gamma$ would give peaks in (γ+jet) invariant mass distributions, and $q^* \to q+g$ in dijet invariant masses[22]. Composite quarks and leptons could be expected to have non-trivial electroweak and strong form factors F(s). There might be new effective four-fermion contact interactions $(1/\Lambda^2)(\bar{f}f\bar{f}f)$ which could interfere with conventional gluon exchange[23]. Present collider data already tell us[8] that

$$\Lambda > 275\ \mathrm{GeV} \qquad (11)$$

and competitive limits come from PETRA[24]. If the $W^{\pm}$ and Z^0 are composite there may be spin-zero composite bosons X accessible in $W \to X+\gamma$ decay[25], or decaying into W's. There might also be anomalously large multiboson vertices[26], or a truly anomalous magnetic moment for a composite $W^{\pm}$.

3. WHAT DO WE HAVE?

There is something for everyone in the collider data, with a few candidate events for almost all of the signatures listed above. Unfortunately (?), the interpretations of these intriguing suggestions are not at all clear.

a) $Z^0 \to \ell^+\ell^-\gamma$

Some of the parameters of the three observed[7),8),27),28] events are tabulated below.

Table 2: Radiative Z^0 decays

	$e^+e^-\gamma$		$\mu^+\mu^-\gamma$
	UA1	UA2	UA1
$m(\ell^+\ell^-\gamma)$	98.7±5	90.6±1.9	$88.4^{+46.1}_{-15.2}$
$m(\ell^+\ell^-)$	42.7±2.4	50.4±1.7	$70.9^{+37.2}_{-12.4}$
$m(\ell\gamma)_{low}$	4.6±1.0	9.1±0.3	5.0 ± 0.4
$m(\ell\gamma)_{high}$	88.5±2.5	74.7±1.8	$52.5^{+27.5}_{-9.3}$
$\theta_{\ell\gamma}$	14.4±4.0°	25 ± 1°	7.9°
E_γ	38.8±1.5	24.4±1.0	28.3 ± 3

First among the (im)possible explanations (?) is conventional QED bremsstrahlung. The rate for this can be calculated "reliably"[9]:

$$R \equiv \frac{B(e^+e^-\gamma;\ E_\gamma/m_Z > \epsilon,\ \theta_\gamma > \delta)}{B(e^+e^- + e^+e^-\gamma)} \approx \frac{\alpha}{\pi}\left[(4\ln 2\epsilon + 3)\ln\delta + \frac{\pi^2}{3} - \frac{7}{4}\right] \qquad (12)$$

which gives R = 0.02 for $\delta = 5°$ and $\epsilon = 0.1$. Clearly, the observed configurations are extremely unlikely, and the combined probability that 3 out of 13 Z^0 events have both δ and ϵ as large as in Table 2 has been estimated[29] to be $O(10^{-4}$ to $10^{-5})$. However, if one integrates[8] over all regions of $\ell^+\ell^-\gamma$ phase space where the probability density given by the square of the QCD matrix element is no larger than the density in phase space around the observed events,

then the observation of radiative decays seems much less unlikely. How about excited leptons[21]: $Z^0 \to \ell^*\ell$, $\ell^* \to \ell\gamma$? It seems that $m(\ell^*) \neq m(\ell\gamma)_{low}$ since PEP and PETRA have not $e^+e^- \to \ell^{*+}\ell^{*-}$ or $e^+e^- \to \ell^{*\pm}\ell^{\mp}$. Furthermore, the observed $m(\ell\gamma)_{low}$ appear to be different, even for the two eeγ events. The $m(\ell\gamma)_{high}$ also appear different. Moreover, the ($\ell\gamma$) opening angles listed in Table 2 are surprisingly low: there is no reason in the excited lepton model for the γ to emerge anywhere near one of the outgoing lepton lines (Fig. 1). Indeed, it has been estimated[29] that the probability for three such small angles in the excited lepton model is also $O(10^{-4}$ to $10^{-5})$. Another suggestion[15),25] has been $Z \to X+\gamma$, $X \to \ell^+\ell^-$, where X is a spin-zero boson in a composite model. Here again one has the obstacle that the two $m(e^+e^-)$ masses look different, but chiral symmetry arguments anyway favour the existence of two spin-zero particles[25]. One still has the problem that the small values of $\theta_{\ell\gamma}$ are a priori very unlikely (Fig. 1). Nevertheless, several theoretical studies of the spin-zero boson hypothesis have been made[25]. An interesting remark is that direct-channel X exchange can interfere with crossed-channel γ exchange in Bhabha scattering (Fig. 2), and a useful theoretical lower bound on this interference can be derived[30]. Its non-observation at PETRA means that any spin-zero X boson must weigh more than 47 GeV[31]. Since one of the e^+e^- pairs in Table 2 has an invariant mass of 42.7±2.4 GeV, this hypothesis looks somewhat ill. As a final proposal, let me mention the idea[26] that the Z^0 is composite with an anomalously large three-neutral boson vertex which allows $Z^0 \to \gamma +$ (virtual $Z^0 \to \ell^+\ell^-$) decays. The virtual Z^0 does not give a fixed $m(\ell^+\ell^-)$, but a distribution (Fig. 3) centred around $m_Z/2$ which is consistent with experiment. However, still no explanation is supplied for the small values of $\theta_{\ell\gamma}$.

None of the explanations for radiative Z^0 decays has great difficulty explaining the observation[8),27] of just one radiative $W \to e\nu\gamma$ decay. The rate is not grossly incompatible with conventional bremsstrahlung expectations, few $W \to e^*\nu$ events are expected if $m(e^*) \simeq m_W$, and no $W \to e\nu\gamma$ events are expected if the spin-zero X boson is an isoscalar.

My general criticism of all the unconventional explanations for the radiative Z^0 decays is that the observed kinematical configurations (γ close to ℓ) are at least as unlikely as in conventional QED bremsstrahlung (γ far from ℓ). On the other hand, we know that the physical phenomenon of bremsstrahlung exists with probability one, whereas the observed exotic mechanisms can only have probabilities <1 (<< 1 in some cases !). Therefore, theorists should either invent exotica which naturally yield the observed configurations, or else

wait patiently to see more data. My own guess is that the events will turn out to have been QED bremsstrahlung gone crazy, but I will be happy to be proved wrong!

b) "Zen" events

These are events with one jet (or other evidence of activity) on one side of the interaction point, and nothing (missing neutrino or ?) on the other side. UA1 reported[28),32)] at this meeting two events of this type with a "photon" of transverse momentum above 40 GeV with large missing transverse energy, some of whose parameters are listed in Table 3.

Table 3: Some zen event parameters

Event	Jet E_T (GeV)	missing p_T (GeV)	m_T (jet, p_T^{miss}) (GeV)	Charged Multiplicity	Invariant mass of charged particles (GeV)
A	25 (71 inc. μ)	24 ± 4.8 (66±8 inc. μ)	130 ± 16 inc. μ	1	0.1
B	48	59 ± 7	106 ± 12	3	0.79 ± 0.12
C	52	46 ± 8	97 ± 17	1	other unreconstructed tracks?
D	43	42 ± 6	85 ± 12	4	3.14 ± 0.38
E	46	41 ± 7	87 ± 14	2	other unreconstructed tracks
F	39	34 ± 7	73 ± 14	2	0.52 ± 0.06
H	54(γ)	40 ± 4	93 ± 5	0	0

By "photon" one means either a single γ or a highly collimated electromagnetic jet which shows up as an unresolved hit in the electromagnetic calorimeter. Unfortunately, one of the events is at an angle where the central detector could have missed a charged track, and it is possible that the event was $W \to e\nu$ decay whose electron track was not visible. The electromagnetic calorimeter hit is however more energetic than in the majority of $W \to e\nu$ events. There is no such interpretation possible for the other "photon" event, and the backgrounds to

this one from multiple gondola hits, cosmics and jet fluctuations are together less than 10^{-2} of an event[29),32)]. There is a jet of a few GeV in this second event, which is responsible for the difference between the transverse momentum of the "photon" and the missing transverse momentum. This event is very beautiful, and we can only hope that its interpretation will become clearer when more such events are gathered.

In the meantime, let us recall the precept of Sherlock Holmes:"If more than one unusual event occurs, they should be related" and seek a unified explanation which also accounts for other of the UA2 funny events. What about $Z^0 \to \nu\bar{\nu}^*$, $\nu^* \to \nu\gamma$? The transverse mass of the γ and missing transverse momentum in the gold-plated "photon" event is 101±8 GeV, compatible with Z^0 decay. However, the ν and $\bar{\nu}$ would have to emerge collinearly and opposite in azimuth to the γ (Fig. 4). This is an a priori unlikely configuration, as extreme as the $Z \to e(e^* \to e\gamma)$ events though in a different way. What about SUSY ? Certainly missing transverse momentum with no detectable charged lepton is a characteristic signature of SUSY, but one does not in general expect to get single photons. Of course, the observed "photon" could be a collimated jet of photons (e.g., π^0 or $\eta \to \gamma\gamma$), but only one in 10^3 of conventional hadronic jets fragment purely electromagnetically. In seeking an interpretation for this event, perhaps we should remember the dicta of Sherlock Holmes, and seek a unified explanation with another category of "zen" events.

There are five events[28),32)] containing a "monojet" of energy above 40 GeV with no jet having $E_T > 10$ GeV recoiling in the opposite direction in the azimuthal plane (Fig. 5). There are also events with $E_T < 40$ GeV that are kinematically consistent with W decay. Several of these are probably $W \to \tau\bar{\nu}$ decay followed by $\tau \to$ hadrons + ν, while some may be $p\bar{p} \to g + (Z^0 \to \nu\bar{\nu})$[33)]. However, these explanations do not fit[28),32)] the events above 40 GeV, for which the background from jet fluctuations is calculated to less than 0.1 events. Some parameters of these events are listed in Table 3. One of these events is exceedingly spectacular (Fig. 6): the monojet contains just one charged particle, which is identified as a muon, and has a $p_T = 0(50)$ GeV. The combined invariant mass of the muon and of the electromagnetic jet is about 5 GeV. It is a general feature of the monojet events that their jets are quite "small": the charged multiplicities vary between one and three, and the invariant masses of the charged particles with $p_T > 0.5$ GeV are generally less than about 2 GeV. Thus many of the monojets look like τ's, though not all of them are consistent with this interpretation, and it is difficult to imagine a copious source of high p_T τ's.

The UA1 experiment expects[28),32)] nime monojets from $W \to \tau\nu$ decays in its present event sample, but these should have $p_T < 40$ GeV. They expect[28),32)] only one or two events from heavy leptons: $W \to L + \nu_L$, and even fewer could be expected[34)] from analogous supersymmetric decays such as $W \to \tilde{W} + \tilde{\gamma}$. Since the charged multiplicities in the observed monojet events are so small, it is natural to wonder whether the "photon" event might just be another manifestation from the same source, one in which the jet charged multiplicity fluctuated down to zero - not so unusual for "small" jets. It is also possible that the "super" event with a high p_T muon in the jet might be related to the e + jet + missing p_T events of UA2 which will be discussed[35)] shortly.

The most conservative approach to the "zen" events is probably to use them as upper limits on new particles. For example, many supersymmetric sources would[36)] give monojet events when subjected to the experimental cuts used by UA1[28),32)] to define their monojet event sample (Fig. 7). The number of monojet events can be used to set upper limits on the cross-sections and hence lower limits on the masses of some supersymmetric particles. For example, assuming that the UA1 jet trigger is efficient down to an E_T of 20 GeV, one can argue[28),32),36)] on the basis of the observed monojet events that the gluino mass

$$m_{\tilde{g}} \gtrsim O(40)\,\text{GeV} \tag{13}$$

and the data can also be used[36)] to establish a similar lower bound on squark masses. More excitingly, it should be emphasized that the observed monojet events are compatible with the production and decays of gluinos or squarks with a mass O(40) GeV. If this is their origin, future collider data on monojet events will be very interesting!

In addition to the monojet events, there are also some multijet events[28),32)] with missing p_T, including two- three-jet candidates, one four-jet candidate and a few two-jet events in which the missing p_T is coplanar with the two observed jets. These two-jet events seem to be consistent with the jet fluctuation background, but one of the multijet events (Fig. 5) is very striking and is less likely to be background. The transverse mass of the four-jet, missing p_T system is about 200 GeV, clearly incompatible with $W^{\pm}$ or Z^0 decay. SUSY can of course offer interpretations for such an event ($p\bar{p} \to \tilde{g}\tilde{g}$, $\tilde{g} \to q\bar{q}\tilde{\gamma}$ or $p\bar{p} \to \tilde{q}\bar{q}$, $\tilde{q} \to q\tilde{g}$?), although as mentioned earlier many $\tilde{g}\tilde{g}$ events turn out to look like monojets when all the cuts in the experimental selection are made[36)].

c) e + jet + missing p_T events

UA2 has reported[35] the discovery of four events containing a large p_T electron, jets, and missing p_T. Key parameters of these events are listed in Table 4.

Table 4: Some e + jet + p_T^{miss} event parameters

Event	p_T(e) (GeV)	E_T (jets) (GeV)	p_T^{miss} (GeV)	m_T(eν) (GeV)	m(W jets) (GeV)
A	18.3 ± 0.8	39 ± 4	51 ± 4	56 ± 2	141
B	22.0 ± 0.9	67 ± 7	86 ± 6	81 ± 3	166
C	34.4 ± 3.2	66 ± 6	57 ± 5	82 ± 4	164

Views of these events in the plane transverse to the beam axes are shown in Fig. 8. In two of the events the transverse mass of the electron and missing transverse energy vector is around 80 GeV, while in a third it is about 56 GeV. Thus, these three events could be interpreted as W + jet events. In the fourth event, the e and the missing transverse energy vector have similar azimuthal angles and a transverse mass of only 10 GeV. This event looks rather more like heavy flavour production and semileptonic decay[35]. In a scatter plot (Fig. 9) of E_T^{jets} versus p_T(Jets + e) the three W + jet candidate events appear well isolated from the conventional low p_T W events. They occupy a region which seems to be devoid of background. One of the most dramatic events (B) is shown

in Fig. 10. The UA2 collaboration has estimated the magnitude of the QCD bremsstrahlung background due to W + gluons by analogy with hadronic jet events. They take dijet events with an invariant mass $O(m_W)$ and ask how likely they are to be accompanied by a large p_T jet or by a large E_T jet pair. They believe that the rate of gluon bremsstrahlung in W production events is likely to be over- rather than under-estimated by such an empirical comparison. This method indicates that indeed the three W + jet candidates are very unlikely to be QCD bremsstrahlung background. The invariant masses of the three events are around 170 GeV, but not too much significance should be read into this, since the effects of the selection criteria favour events in this mass range[35].

As far as the interpretation of these events is concerned, one's first natural suspicion is that perhaps after all the three W + jet events are QCD bremsstrahlung. After all, if the $Z^0 \to \ell^+\ell^-\gamma$ events teach us that QED bremsstrahlung can play on us funny tricks which we do not understand, surely QCD can be equally mischievous ? So far a detailed comparison of the UA2 events with a respectable QCD theory calculation[37] has not been made. It would be particularly interesting to have available theoretical calculations of the rates for events with large E_T but small net p_T, since one of the three events is accompanied by a pair of jets whose p_T vectors largely cancel in the vectorial sum. The UA1 collaboration has no comparable e + jet + missing p_T events[38], but it is tempting to emulate Sherlock Holmes and to compare with the muon monojet event of UA1[28),32]. The transverse masses of the (e"ν") and (μ"ν") systems are comparable in the two cases, though the UA1 event has the striking feature that the muon is practically inside its accompanying jet, whereas the electrons in the UA2 events are well separated.

If you prefer to seek more interesting interpretations of the UA2 e + jet events, one suggestion[22] is that we are witnessing excited quark production $g + q \to q^*$, followed by $q^* \to q + W$ decay. If this is the case, we should also expect $q^* \to q + Z^0$ [and UA1 does[28] have an excess of jets in its Z^0 events], $q^* \to q + \gamma$ (no signal yet in γ + jet invariant mass distributions) and $q^* \to q + g$ (more about this shortly). An alternative explanation for the UA2 events evokes $\bar{p}p \to \tilde{W} + \tilde{g}$ production[39], followed by $\tilde{W} \to e\nu\tilde{\gamma}$ and $\tilde{g} \to q\bar{q}\tilde{\gamma}$, would produce events with e + jet + large amounts of missing p_T. It is difficult to see how the SUSY rate could be large enough, but this explanation is consistent with the observation that in the three UA2 "W" + jet candidates, the missing "ν" p_T vector is consistently larger than the p_T of the observed electron. They should on average be equal in $W \to e\nu$ decay, but could easily be different in SUSY, where the "ν" is actually a combination of one ν and two photinos $\tilde{\gamma}$. However,

too much should perhaps not be read into the details of three events: let us hope that more are found in the next collider run.

d) The bump at 150 GeV

The UA2 Collaboration[8] has a bump (Fig. 11) in their multijet mass distribution at 147 ± 5 GeV, with a width of 11 ± 5 GeV (compatible with their expected mass resolution) which contains 50 ± 16 events. As such, it is nominally a 3σ peak and hence more significant than the W bump found in the same experiment (<2σ). However, one must be careful not to overinterpret 3σ bumps, particularly when they occur way down on sharply falling spectra. The conservative reaction is to wait until the "invited guest", the W bump around 80 GeV, is confirmed beyond any doubt, before welcoming the "uninvited guest" at 150 GeV. Nevertheless, some theorists[22] are already excited: perhaps this bump is the q + g decay of the q* previously introduced in an attempt to explain the e + jet + missing p_T events. The UA2 Collaboration do not exclude the hypothesis of a common mass for these two phenomena.

e) Dimuon events

The UA1 Collaboration has reported[28] 10 dimuon events, of which seven are opposite-sign (four with jet activity and three without) and three are like-sign (one with jet activity and two without). The invariant masses of the μμ pairs range between 6 and 22 GeV, just above the limit imposed by the $p_T^\mu > 5$ GeV cut, and in the range expected[40] from various heavy flavour sources and from the Drell-Yan continuum (Fig. 12). The transverse energies in the events range between 44 and 138 GeV: the higher ones may seem surprisingly energetic. However, what is most intriguing about the dimuon events, apart of course from the presence among them of three like-sign events, is the abundance of strange particles that they contain. For example, there is a $\mu^+\mu^-$ event with a Λ^0. The invariant masses of the two $(\mu^+\Lambda^0)$ combinations are 6.5 ± 0.5 and 6.9 ± 0.5 GeV, both of them incompatible with $\bar{b}$ decay, which would give $\mu^+\bar{\Lambda}^0$ combinations with masses below 5 GeV. There is also a $(\mu^-\mu^-\bar{\Lambda}^0)$ event in which the $(\mu^-\bar{\Lambda}^0)$ invariant masses are 4.1 ± 0.1 and 4.6 ± 0.1 GeV: kinematically compatible with b decay, but again the wrong strangeness. Perhaps these strange particles are spectators containing sea strange quarks ? One of the $\mu^+\mu^-$ events contains two K_s^0, and the invariant mass of the $(\mu^+\mu^-K_s^0K_s^0)$ system is 10.5 ± 0.5 GeV, barely compatible with a $b\bar{b}$ production and decay explanation. There is also a $\mu^+\mu^-\Lambda^0\bar{\Lambda}^0$ event in which the $(\mu^+\Lambda^0)$ combination is kinematically incompatible with $\bar{b}$

decay, and a $\mu^+\mu^-\Lambda^0\bar{\Lambda}^0K^0_s$ event in which the $(\mu^-\Lambda^0)$ combination is incompatible with b decay.

We see that, while the association of muons with strange particles is to be expected from heavy flavours, in many cases the kinematics of simple $b\bar{b}$ production and decay - or a fortiori $c\bar{c}$ production and decay - do not fit the data. Postulating $t\bar{t}$ production helps by yielding naturally $(\mu^+\Lambda^0)$ or $(\mu^-\bar{\Lambda}^0)$ combinations with invariant masses above 5 GeV, from $t \to \mu^+\nu(b \to \Lambda^0)$ and the corresponding antiparticle process. It is possible to get like-sign dimuons from $\bar{t}t$ or $b\bar{b}$ production, by combining one primary semileptonic decay with one secondary: e.g., $(b \to \mu^-\nu c)(\bar{b} \to u\bar{d}\bar{c}: \bar{c} \to \mu^-\nu\bar{s})$. However, the secondary decay muon is in general unlikely to survive the cut of 5 GeV on the p_T of the muon. On the other hand, the process $W \to t\bar{b}$ can[41] give like-sign primary muons: $(t \to \mu^+\nu b)(\bar{b} \to \mu^+\nu\bar{c})$. Another way to get like-sign primary muons is through $b\bar{b}$ mixing[42]. In the standard model this is not expected for the $B^0 \equiv (b\bar{d})$ and $\bar{B}^0 \equiv (\bar{b}d)$ mesons, but could be large for the $(b\bar{s})$ and $(\bar{b}s)$ mesons. In the absence of mixing, one would expect $\#\mu^\pm\mu^\pm/\#\mu^\pm\mu^\mp = 0(1/10)$, but the ratio could be $0(1/3)$ with maximal $(b\bar{s}) \leftrightarrow (\bar{b}s)$ mixing[42]. The final state decay products of $(b\bar{s})$ or $(\bar{b}s)$ mesons seem unlikely to contain many strange baryons, so something extra is needed to explain the $(\mu^+\mu^+\Lambda^0)$ and $(\mu^-\mu^-\bar{\Lambda}^0)$ events. As mentioned before, perhaps[43] the strange baryons contain spectator strange particles.

Calculations[40] suggest that with the present luminosity 0(2) Drell-Yan $\mu^+\mu^-$ events should have been seen: these might be among the "quiet" events without jet activity. Simple gg fusion perturbative QCD calculations[40] suggest 0(1) $\mu^+\mu^-$ event from $b\bar{b}$ production and decay. In view of past experience with $c\bar{c}$ production, it could well be that this is an underestimate. There are expected to be an order of magnitude fewer $\bar{t}t \to \mu^+\mu^-$ events, and at most 0.4 $W \to t\bar{b} \to \mu\mu$ events. This latter source may be the one with the most reliably calculated rate.

We should rejoice that the total number of dimuon events is somewhat higher than these theoretical estimates. The apparent excess is not a major disaster for theory, given the inevitable uncertainties. The observed events may come from a combination of different sources. Presumably, the bulk of them originate from heavy flavours, and the strange particles observed are not there by accident. However, detailed explanations of each of the events are not easy to arrive at. The situation recalls the good old days of dilepton production in

bubble chamber neutrino experiments. Some exposures found too many strange particles, some too few, and there were always some bizarre event with unusual configurations. Eventually the situation settled down, and my hunch is that the same will happen here. It seems quite possible that we may discover some new physics on the way to this resolution: perhaps $b\bar{b}$ mixing or the t quark? Dimuons are "une affaire à suivre".

4. WHAT DO WE NOT HAVE?

Sherlock Holmes remarked during one of his cases that "the most important clue, my dear Watson, is the dog that did not bark". Here then are a few of the dogs which were silent at this meeting.

a) The t quark

No evidence was reported here for $W \to t\bar{b}$ decay, though it is worth recalling that way back in one of the first collider runs there was[44] an event containing an isolated large p_T lepton recoiling against a jet containing a D^0, a charged π which when combined with it made a D*, and even another charged π which made the invariant mass up to that of a B meson. If $m_t < 0(60)$ GeV, probably it is just a matter of time before $W \to t\bar{b}$ shows up. The cross-section for gluon fusion to give $\bar{t}t$ is more sensitive to the t quark mass, and estimates suggest that if $m_t \sim 30$ to 40 GeV insufficient luminosity has as yet been accumulated for production to be observable. However, it may be that perturbative QCD gluon fusion calculations substantially underestimate the $\bar{t}t$ production cross-section, and there may be a substantial rate for the diffractive production of $\bar{t}t$[45]. A search for this is under way, focusing on the $t \to b\mu\nu$ decay mode, and looking for diffractive events containing a large p_T μ, a jet, and missing p_T. As was discussed[46] at this meeting, a useful way to estimate the mass of a state decaying into an unobserved neutral ("ν") is to compute the "cluster transverse mass"[47] or "minimal transverse mass"[42]. This is obtained by minimizing with respect to the choice of p_L^ν the mass of the state decaying into the observed particles with measured p_T^{vis} and p_L^{vis}, and a missing neutral for whom only the p_T^ν is known:

$$M^* \equiv \left[m_{vis}^2 + (p_T^{miss})^2 + 2 p_T^{miss} \left(m_{vis}^2 + (p_T^{miss})^2 \right)^{\frac{1}{2}} \right]^{\frac{1}{2}} \qquad (14)$$

The distribution in $\xi \equiv M^*/M$ (where M is the true mass) peaks sharply at $\xi \simeq 1$:

$$\frac{1}{\sigma}\frac{d\sigma}{d\xi} \propto \frac{1}{\sqrt{1-\xi^2}} \qquad (15)$$

and is relatively stable[46),48)] against cuts in the p_L and p_T of the observed decay products, smearing due to the p_T distribution at production, etc.

If t quarks can be produced diffractively, why not also supersymmetric particles such as gluinos ? In the case of $\bar{p}p \to (\tilde{g}\tilde{g}) + x$ followed by $\tilde{g} \to q\bar{q}\tilde{\gamma}$ decay one has additional problems because there are two states with similar p_L distributions decaying with missing transverse energy. This means that one can confuse and mix the jet decay products of the two gluinos. Nevertheless[49)], the minimal mass distribution still peaks close to the massof the gluino, with "mismatched" combinations providing a smooth and not overwhelming background under the peak (Fig. 13). If there are substantial diffractive cross-sections for the production of heavy quark flavours, the way may be open for diffractive searches for other species of strongly interacting particle.

One intriguing result on "heavy" flavour production reported here was the observation[50)] of D*/D production in jets. The signal observed was of comparable cleanliness to the results from $e^+e^- \to c\bar{c}$ jets. This was surprising, since the bulk of large p_T hadron jets are gluon jets, <u>not</u> $\bar{c}c$. Indeed, the rate of D*/D production is so high that about 10% of gluon jets are needed to fragment into charm. The longitudinal momentum fractions Z of the observed D* are much softer than in e^+e^- annihilation, supporting the interpretation that they come from secondary gluon $\to \bar{c}c$ fragmentation rather than from primary $\bar{c}c$ fragmentation. Perhaps some of the dimuon events are due to single ($\Rightarrow \mu^+\mu^-$) or double $g \to c\bar{c}$ ($\Rightarrow \mu^+\mu^-$ or $\mu^\pm\mu^\pm$) fragmentation? This observation of copious D production is a potential disaster as it suggests the possibility that there may be many heavy flavours produced at future hadron colliders by boring mechanisms, which may obscure the signals from interesting mechanisms such as Higgs $\to \bar{b}b$ or $\bar{t}t$. It may easily be more difficult than expected to get at these interesting events by heavy flavour tagging using a microvertex detector.

b) <u>The quark-gluon plasma</u>

We have seen at this meeting that UA5 has observed[51)] significant deviations from previous KNO "scaling" multiplicity distributions. The

interpretation of these deviations is not clear, but they can be mimicked by adjusting appropriately the parameters of a cluster production model. This done, one can ask about the significance of the observed[51] fluctuations in the rapidity density of produced particles. Are they evidence for "hot spots" where the hadronic soup has boiled up into a quark-gluon plasma, or are they merely fluctuations which do not require new physics for their explanation? UA5 has found[51] that the same cluster model which was adjusted to reproduce the KNO distribution also give multiplicity density fluctuations comparable with experiment. The UA1 collaboration has reported[52] a correlation between the rapidity density and the mean p_T of observed particles. UA5 has apparently not yet determined whether its cluster Monte Carlo reproduces this effect. However, clearly no evidence yet exists to support the existence of a quark-gluon plasma. Furthermore, recent theoretical arguments[53] cast doubt on the existence and hence observability of a well-defined phase transition from hadronic to quark-gluon matter.

5. THE TOTAL CROSS-SECTION AND DIFFRACTIVE SCATTERING

The UA4 Collaboration reported[54] here a new value of the total cross-section at the $Sp\bar{p}S$ collider:

$$\sigma_{tot} = 63{\cdot}3 \pm 0{\cdot}7 \pm 2 \text{ mb} \tag{16}$$

and of the elastic cross-section ratio:

$$\frac{\sigma_{el}}{\sigma_{tot}} = 0{\cdot}213 \pm 0{\cdot}002 \pm 0{\cdot}006 \tag{17}$$

The elastic cross-section exhibits significant curvature in its t-distribution:

$$\frac{d\sigma}{dt} \sim e^{-b|t|+ct^2} : \begin{cases} b = 15{\cdot}7 \pm 0{\cdot}2 \text{ GeV}^{-2} \\ c = 3{\cdot}6 \pm 0{\cdot}5 \text{ GeV}^{-4} \end{cases} \tag{18}$$

It is important for the analyses of these data that the total centre-of-mass energy in the past collider runs has now been re-estimated: $\sqrt{s}$ = 546 GeV. The elastic cross-section ratio (17) is significantly[54] higher than at the ISR, which is very helpful[55] in discriminating between different theoretical models for σ_{tot}. Before the latest data, three possibilities were being discussed:

a) $\sigma_{tot}/(\log s)^2 \to 0$: this would require σ_{el}/σ_{tot} to decrease at higher energies, which seems now to be excluded by the result (17).

b) $\sigma_{tot}/(\log s)^2$ = constant between the ISR and the SPS: this would also require σ_{el}/σ_{tot} to be constant, which also appears to be excluded by (17).

c) $\sigma_{tot}/(\log s)^2$ will become constant: σ_{el}/σ_{tot} rises to ½ as $s \to \infty$: this seems to be favoured by experiment.

This third possibility was the one previously favoured by Henzi and Valin[56], and one can regard the latest UA4 data as confirmation of their "Blacker, Edgier, Larger" proton (the BEL model). According to this model the proton gets slightly blacker at small impact parameters b, but the biggest increase in opacity Δh is at moderate impact parameters h = O(1) fm. An interesting measurement which would facilitate predictions of σ_{tot} at future collider energies would be of the real part of the forward scattering amplitude. Predicting the future higher energy behaviour of σ_{tot} is not just of academic interest: it is important in the design of experiments at future high intensity high energy colliders to known how often one can expect multiple collisions during the same crossing. Also, we should not forget that ultimately theorists should be able to calculate σ_{tot} from first principles in QCD.

6. FUTURE COLLIDERS

Beyond the present-day CERN $S\bar{p}pS$ collider we have the forthcoming FNAL Tevatron Collider, as well as the CERN improvement programme based on the new ACOL ring. Beyond these developments, we want to get to effective subprocess centre-of-mass energies $\sqrt{s} \approx 1$ TeV. As discussed in Section 2, this is the domain in which the physics of gauge symmetry breaking and the gauge hierarchy problem can be expected to reveal itself.

There are basically two ways to reach the magic 1 TeV domain. One is with a hadron-hadron collider having at least 10 TeV centre-of-mass energy[57]. Such a collider could either be pp or $p\bar{p}$: in both cases the technology is already available, since successful pp (ISR) and $p\bar{p}$ ($S\bar{p}pS$) colliders have been built. Furthermore, FNAL has demonstrated that a ring of superconducting magnets can be built and operated, while CERN has reduced $\bar{p}$ cooling to a routine. As we heard from Brianti[57] at this meeting, a high-luminosity multi-TeV hadron collider is already known to be feasible. The other way to reach 1 TeV is with an e^+e^- collider[58]. Here one needs the unproven technology slated to be developed by the SLC that is scheduled to start operation in 1986. There are formidable

technical hurdles to be overcome with a linear e^+e^- collider, such as guiding to collision two beams of order 1 μm radius which have densities approaching that of water. Moreover, present designs for a high energy e^+e^- collider consume as much power as is produced by a medium-sized nuclear power station[58]. For a linear e^+e^- collider to be proposable, one probably needs higher accelerating fields from more efficient cavities, as well as an existence proof of the basic technology from the SLC. At present only high energy pp or $p\bar{p}$ colliders can be seriously proposed as devices to explore the 1 TeV domain, and they certainly would be great machines for exploring the new physics in this domain, as was discussed by Hinchliffe[59].

A general feature of higher energy hadron-hadron colliders is that the new physics always shows up at large angles, while the more traditional physics of lower energies gets squeezed into ever more forward angles. Thus physicists probing smaller angles resemble archelogists probing lower and older sedimentary layers. Today's physics at large angles will tomorrow become yesterday's physics at forward angles, and next week it will become last week's physics at very forward angles (Fig. 14). The $W^{\pm}$ and Z^0 are no exceptions to this general rule. Produced today at large angles, tomorrow they will be produced at forward angles, and at multi-TeV hadron colliders the bulk of the $W^{\pm}$ and Z^0 will be produced[59] and decay within 5^0 of the beam pipes (Fig. 15).

Examples of possible future physics include Higgs bosons. These should be produced centrally (Fig. 16) with measurable rates out to m_H = O(400) GeV[59),60]. The problem is one of extracting a $H \to W^+W^-$, Z^0Z^0 or $t\bar{t}$ decay signal from the backgrounds of intermediate boson pair production and of heavy quarks. We must learn to use more than just the kinematically unconstrained 15% of $W \to e\nu$, $\mu\nu$ decays. Can one work with the bulk of $W^{\pm}$ or $Z^0 \to$ hadronic jet decays, at least in events where another vector boson leptonic decay provides a signature which can be used to suppress hadronic backgrounds? There are large rates[59),60] for supersymmetric squark or gluino pair production for $m_{\tilde{q}}$, $m_{\tilde{g}}$ =(1) TeV. Such events have missing energy signatures: $p_T^{miss} \propto m_{\tilde{q}}$, $m_{\tilde{g}}$ (Fig. 17), which may stand out above the jet fluctuation background which gives $p_T^{miss} \propto \sqrt{E_T} \propto \sqrt{m_{\tilde{q}}, m_{\tilde{g}}}$. Squarks and gluinos are produced and decay centrally (Fig. 18) into jets separated by angles of order $\pi/2$ radians, with missing p_T of order several hundred GeV[60]. The problem may be to distinguish between the signatures for different SUSY particles. Finally, the technicolour composite Higgs alternative to SUSY has large rates for production of the

relatively light technipions, and the signal-to-background ratios appear manageable[60]. For example, the 250 GeV colour octet technipion P_8^0 has a production cross-section of order nanobarns at centre-of-mass energies above 10 TeV, while the ratio

$$\frac{\sigma(gg \to P_8 \to t\bar{t})}{\sigma(gg \to t\bar{t})} = O(1/3) \qquad (19)$$

While experiments with high energy hadron-hadron colliders will not be easy, they will enable us to explore the 1 TeV domain.

7. CONCLUSIONS

At the close of the last $\bar{p}p$ Collider Workshop, Leon Lederman[61] quoted T.D. Lee to the effect that "every new energy domain opens up new, unexpected discoveries". The CERN $S\bar{p}pS$ collider has already made the new discoveries most of us expected it to make. Now we start to smell the unexpected discoveries that Lee and Lederman expected it to make: radiative Z^0 decays? "Zen" monojet events? Electron + jet + missing p_T events? Bumps in the multijet mass distribution? Anomalous dimuon events? Even if only one of these titillating suggestions turns out to be the harbinger of new physics, the promise of the CERN $Sp\bar{p}S$ collider will have been more than amply confirmed. However, theorists should be careful not to over-interpret the details of a few appetizing events. In the cautionary words of Sherlock Holmes: "The temptation to form premature theories upon insufficient data is the bane of our profession".

We nevertheless expect unexpected discoveries at future hadron colliders such as the Tevatron, the SSC or Desertron, and the LHC or Juratron. Events at this workshop have demonstrated the value of friendly competitive rivalry as a stimulus for extracting the physics. From UA1 and UA2 today, to CDF and DO tomorrow, to the Tevatron and the $Sp\bar{p}S$ collider with ACOL in the future, and hopefully to the Desertron and the Juratron in the more distant future, surely there is more than enough physics for everyone. So let us all go back home and find out what it is !

REFERENCES

1) K. Kilian, talk at this meeting.
2) W. Geist, talk at this meeting.
3) W. Scott, talk at this meeting;
UA1 Collaboration, G. Arnison et al., Phys. Lett. 136B (1984) 294;
For a different analysis favouring the existence of the three-gluon vertex, see
W. Furmanski and H. Kowalski, DESY preprint 84-033 (1984).
4) B.L. Combridge and C.J. Maxwell, Rutherford Lab. preprint RL-83-095 (1983);
F. Halzen and P. Hoyer, Phys. Lett. 130B (1983) 326;
G.C. Cohen-Tanoudji et al., Saclay preprint SPh.T/70 (1982).
5) B.L. Combridge, private communication (1983).
6) UA1 Collaboration, G. Arnison et al., Phys. Lett. 122B (1983) 103;
UA2 Collaboration, M. Banner et al., Phys. Lett. 122B (1983) 476.
7) UA1 Collaboration, G. Arnison et al., Phys. Lett. 126B (1983) 398;
UA2 Collaboration, P. Bagnaia et al., Phys. Lett. 129B (1983) 130.
8) J.R. Hansen, talk at this meeting;
J. Schacher, talk at this meeting;
P. Bagnaia et al., CERN preprint EP/84-39 (1984).
9) W.J. Marciano, talk at this meeting;
W.J. Marciano and A. Sirlin, Phys. Rev. D22 (1980) 2695;
A. Sirlin and W.J. Marciano, Nucl. Phys. B189 (1981) 442;
Ch. Llewellyn Smith and J.F. Wheater, Phys. Lett. 105B (1981) 486;
J.F. Wheater and C.H. Llewellyn Smith, Nucl. Phys. B208 (1982) 27.
10) B. Humpert and W.L. Van Neerven, Phys Lett. 93B (1980) 456;
P. Aurenche and J. Lindfors, Nucl. Phys. B185 (1981) 274;
G. Altarelli, R.K. Ellis, M. Greco and G. Martinelli, CERN preprint TH.3851 (1984).
11) UA1 Collaboration, B. Sadoulet, Proc. 1983 Lepton-Photon Symposium, Cornell, ed. D.G. Cassel and D.L. Kreinick (Newman Lab., Cornell, 1983), p. 27.
12) J.S. Bell, Nucl. Phys. B60 (1973) 427;
C.H. Llewellyn Smith, Phys. Lett. 46B (1973) 233;
J. Cornwall, D.N. Levin and G. Tiktopoulos, Phys. Rev. Lett. 30 (1973) 1268 and Phys. Rev. D10 (1974) 1145.
13) S. Weinberg, Phys. Rev. D13 (1976) 974 and D19 (1979) 1277;
L. Susskind, Phys. Rev. D20 (1979) 2619.
14) Y. Gol'fand and E.P. Likhtman, Pis'ma Zh. Eksp. Teor. Fiz. 13 (1971) 323;
D. Volkov and V.P. Akulov, Phys. Lett. 46B (197) 109;
J. Wess and B. Zumino, Nucl. Phys. B70 (1974) 39.
15) R. Peccei, talk at this meeting.
16) P. Fayet and S. Ferrara, Phys. Rep. 32C (1977) 249.
17) For a recent review, see
J. Ellis, CERN preprint TH.3802 (1984).
18) J. Ellis, J.S. Hagelin, D.V. Nanopoulos, K.A. Olive and M. Srednicki, SLAC preprint PUB-3171 (1983).
19) S. Dimopoulos and L. Susskind, Nucl. Phys. B155 (1979) 237;
E. Eichten and K.D. Lane, Phys. Lett. 90B (1980) 125.
20) S. Dimopoulos, Nucl. Phys. B168 (1980) 69;
S. Chadha and M. Peskin, Nucl. Phys. B185 (1981) 61 and Nucl. Phys. B187 (1981) 541.
P. Binétruy, S. Chadha and P. Sikivie, Phys. Lett. B107 (1981) 425 and Nucl. Phys. B207 (1982) 505.

21) N. Cabibbo, L. Maiani and Y. Srivastava, Università di Rome preprint ROM 83-381 (1983);

22) A. De Rújula, L. Maiani and R. Petronzio, CERN preprint TH.3779 (1983).

23) E. Eichten, K.D. Lane and M. Peskin, Phys. Rev. Lett. 50 (1983) 811.
24) H. Kowalski, private communication (1984).
25) R.D. Peccei, Max Planck Institut preprint MPI-PAE-PTH-83-64 (1983);
U. Baur, H. Faissner and H. Fritzsch, Max Planck Institut preprint MPI-PAE-PTH-83-86 (1983).
26) G. Gounaris, R. Kögerler and D. Schildknecht, Phys. Lett. 137B (1984) 261.
27) UA1 Collaboration, G. Arnison et al., Phys. Lett. 135B (1984) 250.
28) C. Rubbia, talk at this meeting.
29) A De Rújula, private communication (1984).
30) W. Hollik, B. Schrempp and F. Schrempp, DESY preprint 84-011 (1984);
F.W. Bopp et al., Univ. of Siegen preprint 84-3 (1984).

31) CELLO Collaboration, H.-J. Behrend et al., DESY preprint (1984);
Mark J Collaboration, B. Adeva et al., MIT preprint LNS-TR-134 (1984).
32) UA1 Collaboration, G. Arnison et al., CERN preprint EP/84-42 (1984).
33) P. Aurenche and R. Kinnunen, private communication (1984).
34) S. Weinberg, Phys. Rev. Lett. 50 (1983) 387;
R. Arnowitt, A. Chamseddine and P. Nath, Phys. Rev. Lett. 50 (1983) 232;
J. Ellis, J.S. Hagelin, D.V. Nanopoulos and M. Srednicki, Phys. Lett. 127B (1983) 233;
D. Dicus, S. Nandi and X. Tata, Univ. of Texas preprint DOE-ER-03993-517 (1983).
35) A. Roussarie, talk at this meeting;
UA2 Collaboration, CERN preprint EP/84-40 (1984).
36) J. Ellis and H. Kowalski, CERN preprint TH.3843 (1984) and DESY preprint in preparation (1984).
37) G. Altarelli, R.K. Ellis, M. Greco and G. Martinelli, Ref. 10);
R.K. Ellis, talk at this meeting;
M. Greco, talk at this meeting.
38) UA1 Collaboration, private communication (1984).
39) G. Altarelli, B. Mele and S. Petrarca, CERN preprint TH.3822 (1984);
H.E. Haber and G. Kane, UCSC-TH-169-84 (1984).
40) F. Halzen, talk at this meeting;
A.D. Martin, talk at this meeting;
E.W.N. Glover, F. Halzen and A.D. Martin, Durham Univ. preprint DTP/84/2 (1984) and references therein.
41) M. Abud, R. Gatto and C.A. Savoy, Phys. Lett. 79B (1978) 435.
42) C. Jarlskog, talk at this meeting.
43) A. Ali, private communication (1984);
A. Ali and C. Jarlskog, CERN preprint TH.3896 (1984).
44) D. DiBitonto, talk at the 1983 Rencontre de Moriond (1983).
45) S.J. Brodsky, C. Peterson and N. Sakai, Phys. Rev. D23 (1981) 2745;
V. Barger, F. Halzen and W.Y. Keung, Phys. Rev. D24 (1981) 1428;
R. Horgan and M. Jacob, Phys. Lett. 107B (1981) 395.
46) W.J. Stirling, talk at this meeting.
47) V. Barger, A.D. Martin and R.J.N. Phillips, Phys. Lett. 125B (1983) 339 and Phys. Rev. D28 (1983) 145.
48) E. Berger, D. DiBitonto, M. Jacob and W.J. Stirling, CERN preprint TH.3821 (1984).
49) W.J. Stirling, private communication (1984).

50) R. Frey, talk at this meeting.
51) UA5 Collaboration, G.J. Alner et al. Phys. Lett. 138B (1984) 304.
52) UA1 Collaboration, G. Arnison et al., Phys. Lett. 118B (1982) 167.
53) P. Hasenfratz, F. Karsch and I.O. Stamatescu, CERN preprint TH.3696 (1983);
T.A. DeGrand and C. DeTar, Univ. of Colorado preprint COLO HEP 66 (1983);
F. Karsch and F. Green, CERN preprint TH.3748 (1983).
54) UA4 Collaboration, F. Cervelli, talk at this meeting.
55) A. Martin, talk at this meeting;
R. Henzi, talk at this meeting.
56) R. Henzi and P. Valin, Phys. Lett. 132B (1983) 443 and McGill Univ. preprint (1984).
57) G. Brianti, talk at this meeting.
58) H. Wiedemann, Proc. 1982 SLAC Summer Institutes, ed. A. Mosher (SLAC, 1982), p. 1;
J. Ellis, SLAC preprint PUB-3127 (1983).
59) I. Hinchliffe, talk at this meeting;
E. Eichten, I. Hinchliffe, K. Lane and C. Quigg, in preparation (1984).
60) J. Ellis, G. Gelmini and H. Kowalski, talk at the Lausanne workshop on the possibility of a Large Hadron Collider in the LEP Tunnel, DESY preprint in preparation (1984).
61) L. Lederman, Proceedings of the third Topical Workshop on Proton-Antiproton, Rome 1983, ed. C. Bacci and G. Salvini, CERN Yellow Report 83-04 (1983), p. 575.

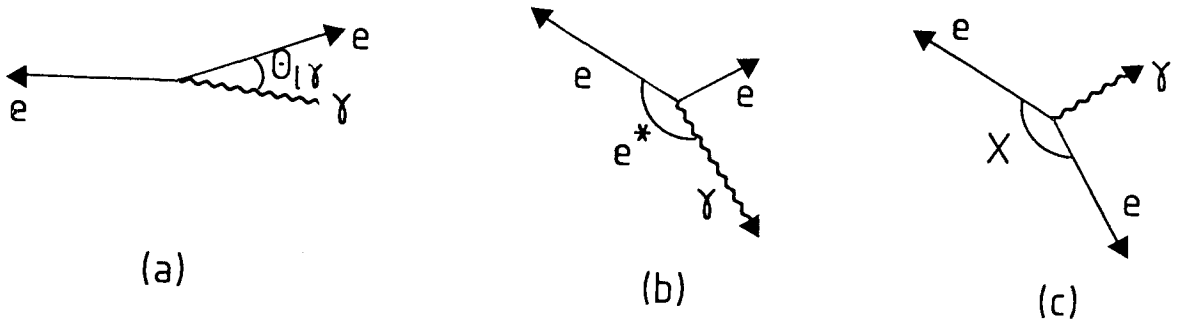

Fig. 1: In the observed $Z^0 \to \ell^+\ell^-\gamma$ events (a) the γ tends to emerge at a small angle $\theta_{\ell\gamma}$ from one of the charged leptons, whereas the hypotheses (b) $Z^0 \to \ell^{\pm}(\ell^{*+} \to \ell^+\gamma)$ [Ref. 21)] and (c) $Z^0 \to \gamma(X^0 \to \ell^+\ell^-)$ [Ref. 25)] would typically lead to larger angles $\theta_{\ell\gamma}$.

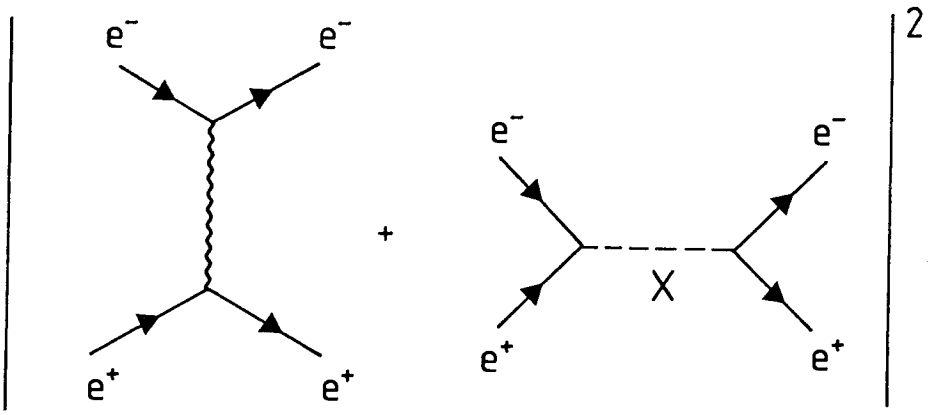

Fig. 2: Direct channel spin-0 X boson exchange interferes[30] with crossed channel photon exchange in Bhabha scattering.

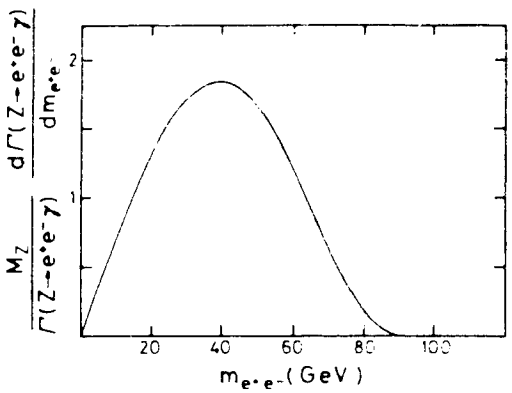

Fig. 3: The shape of the $m(\ell^+\ell^-)$ spectrum expected[26] in a composite Z^0 model.

Fig. 4: The sort of configuration required if the gold-plated UA1 "photon" event[28),32)] is to be understood as $Z^0 \to \nu\bar{\nu}\gamma$ decay.

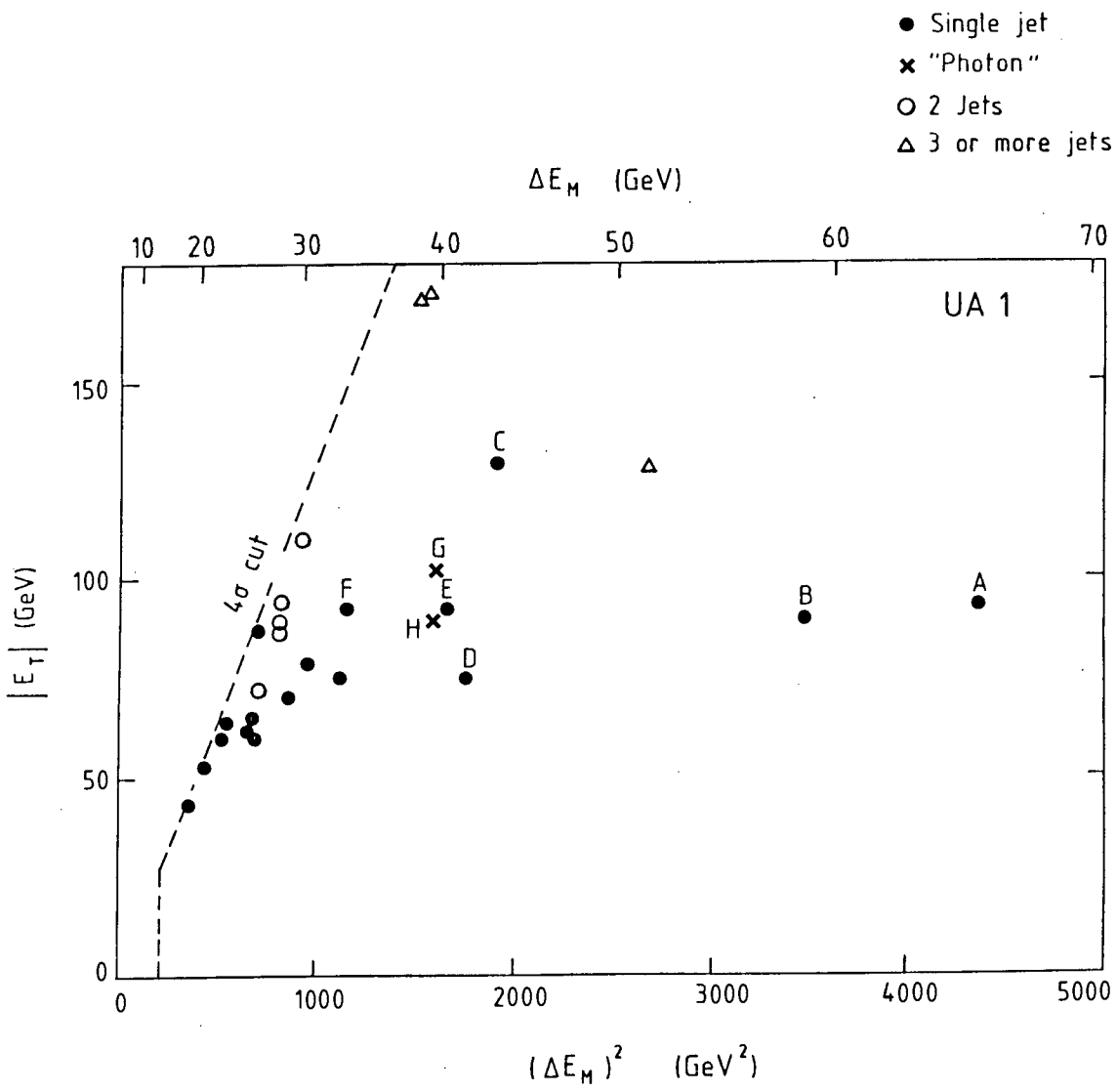

Fig. 5: Scatter plot[28),32)] of missing p_T^2 versus E_T, showing all events whose missing p_T are greater than 4σ ($\sigma = 0.7\sqrt{E_T}$), including monojet events, "photon" events and multijet events.

Event A

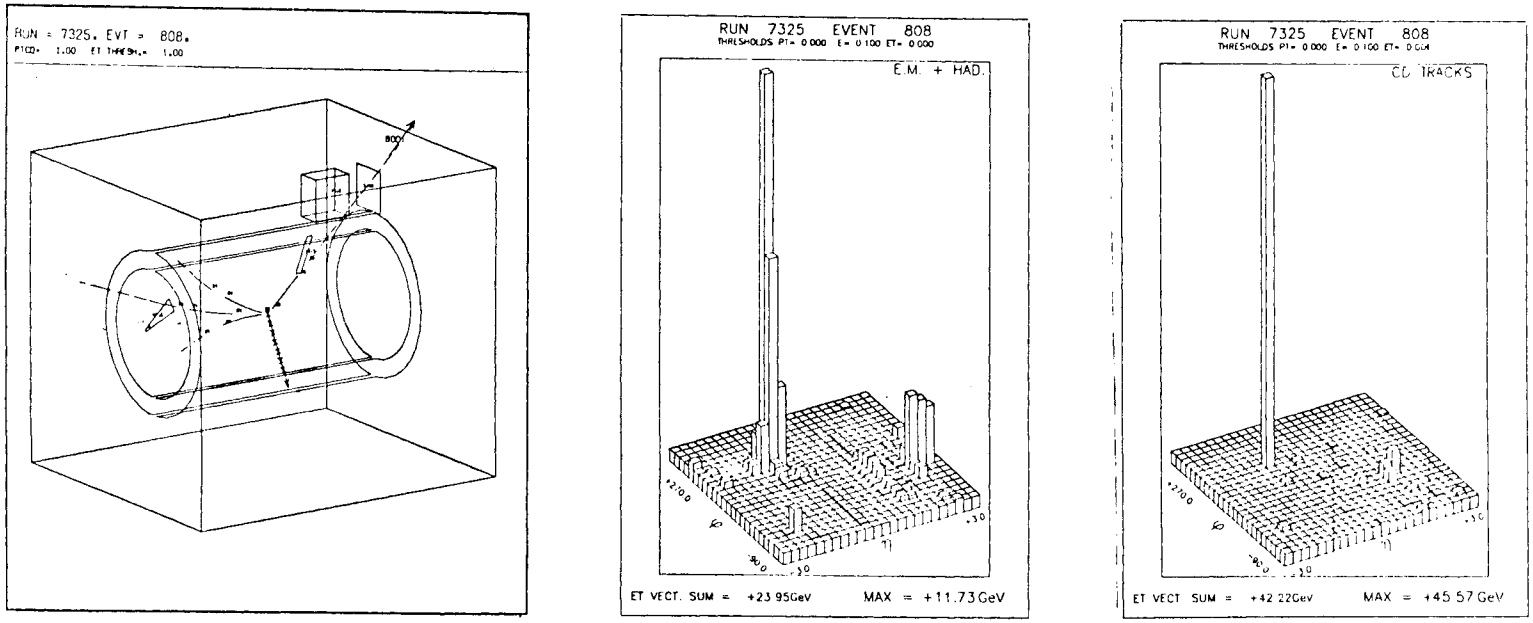

Fig. 6: Monojet event A of the UA1 Collaboration[28),32)]

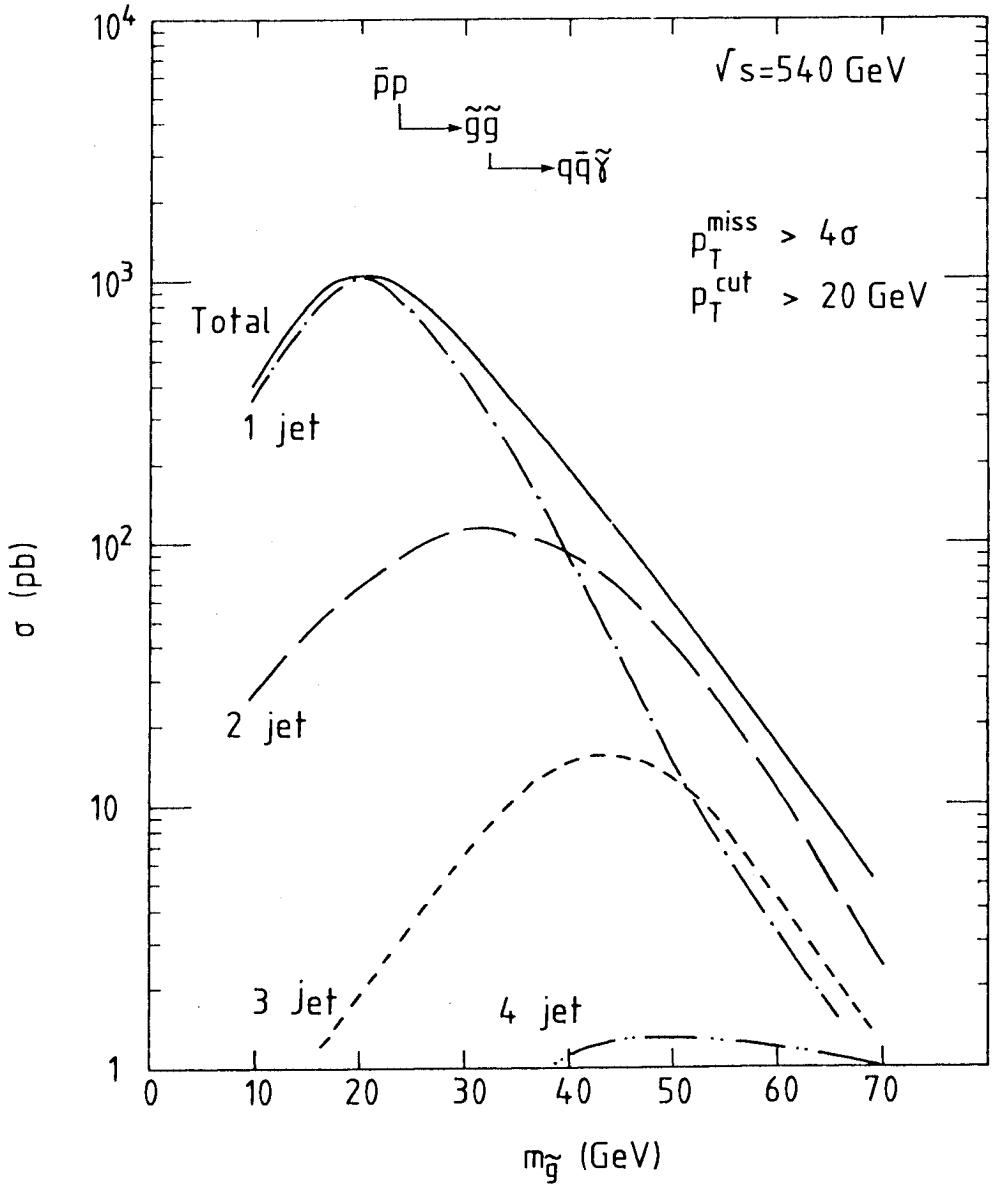

Fig. 7: Topological cross-sections for $p\bar{p} \to \tilde{g}\tilde{g} + X$ production giving 1-,2-,3- and 4-jet events[36], after imposition of cuts modelled on those applied by the UA1 Collaboration.

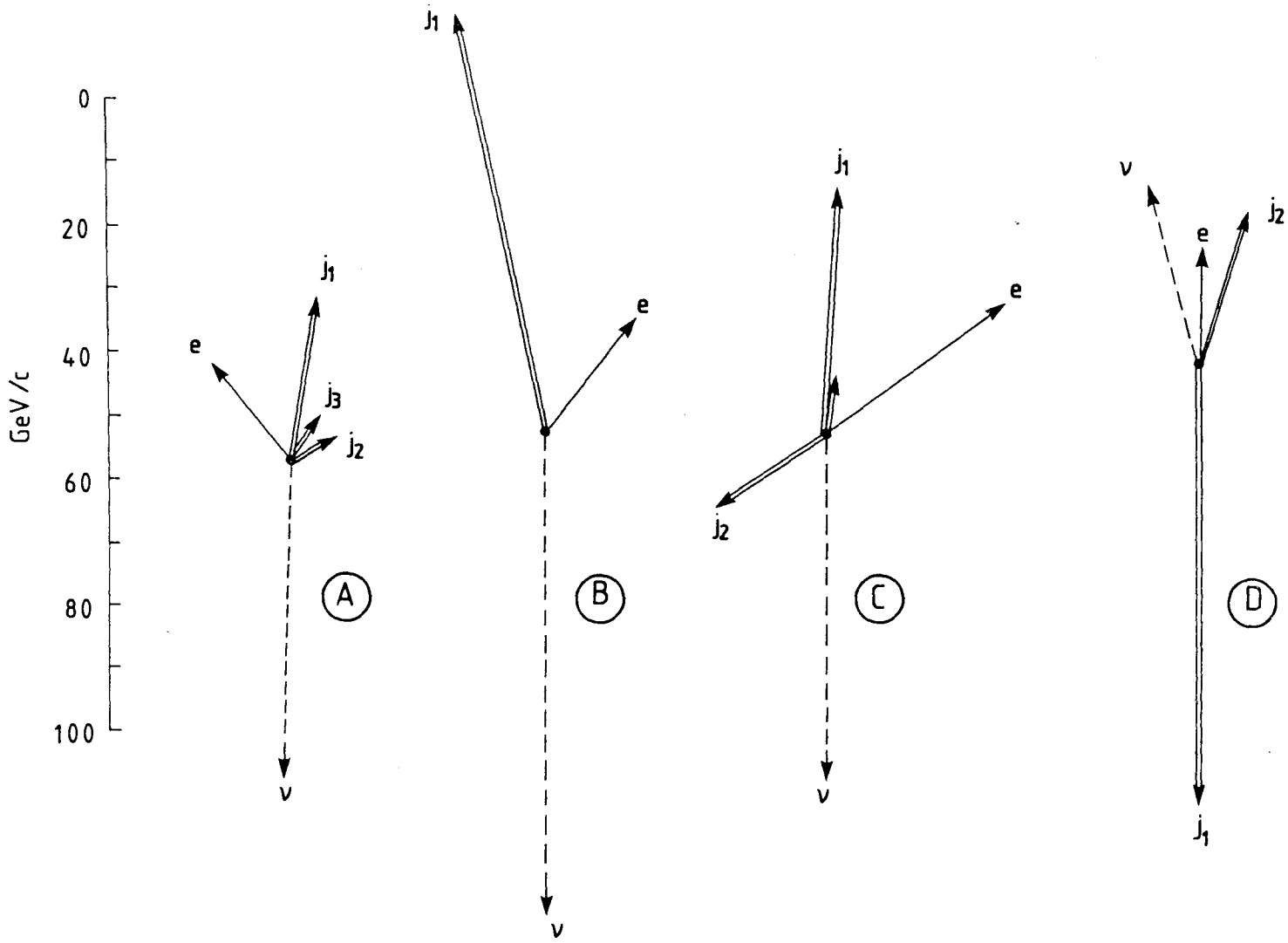

Fig. 8: View in the plane transverse to the beam axes of the UA2 e + jet + missing p_T events[35].

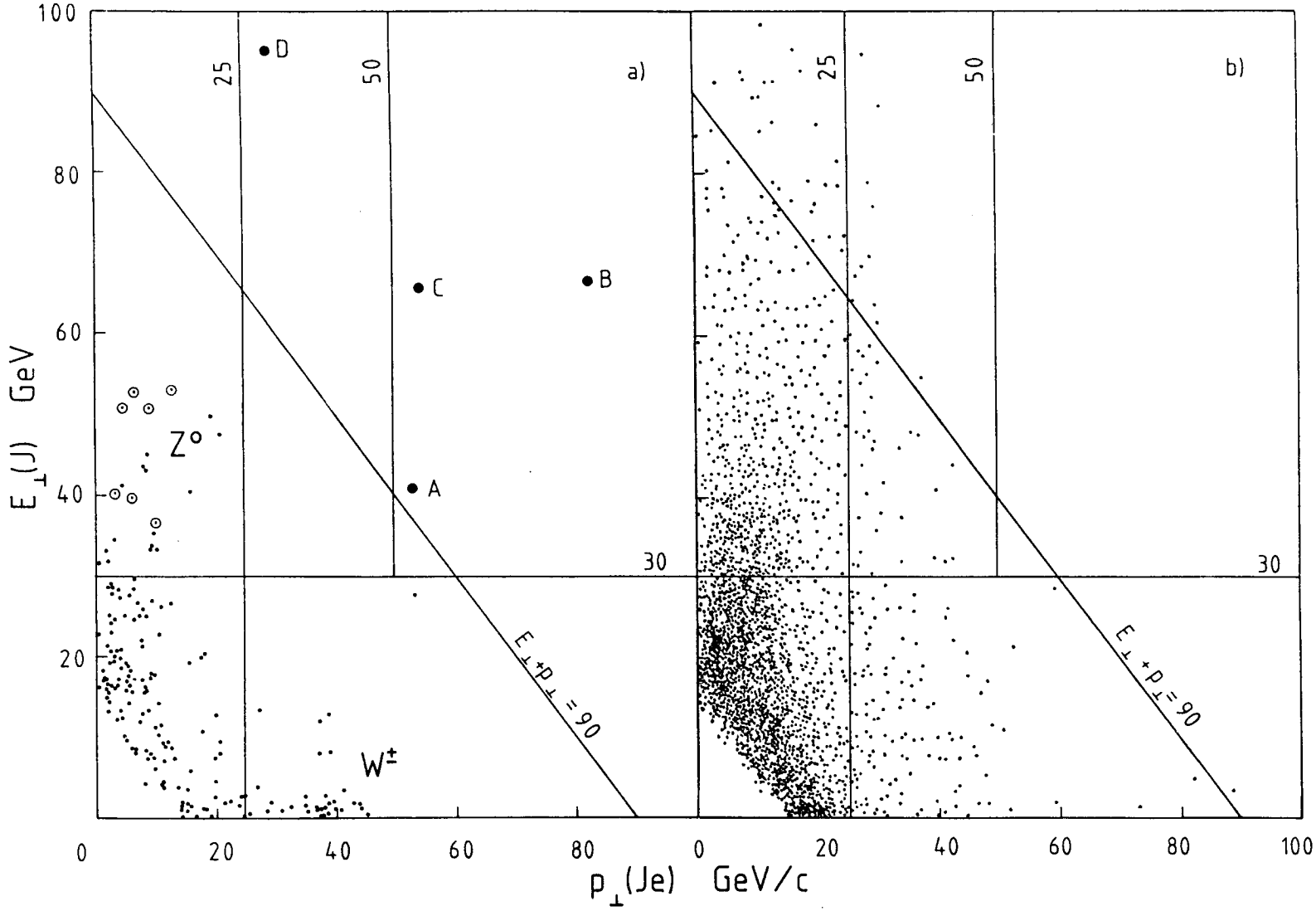

Fig. 9: Scatter plot of UA2 e + jet + missing p_T events[35]. The horizontal axis is the transverse momentum of the jet + electron system, which is essentially the missing p_T, while the vertical axis is the E_T of the jet system. The most interesting events have p_T(j+e) > 25 GeV and E_T > 30 GeV.

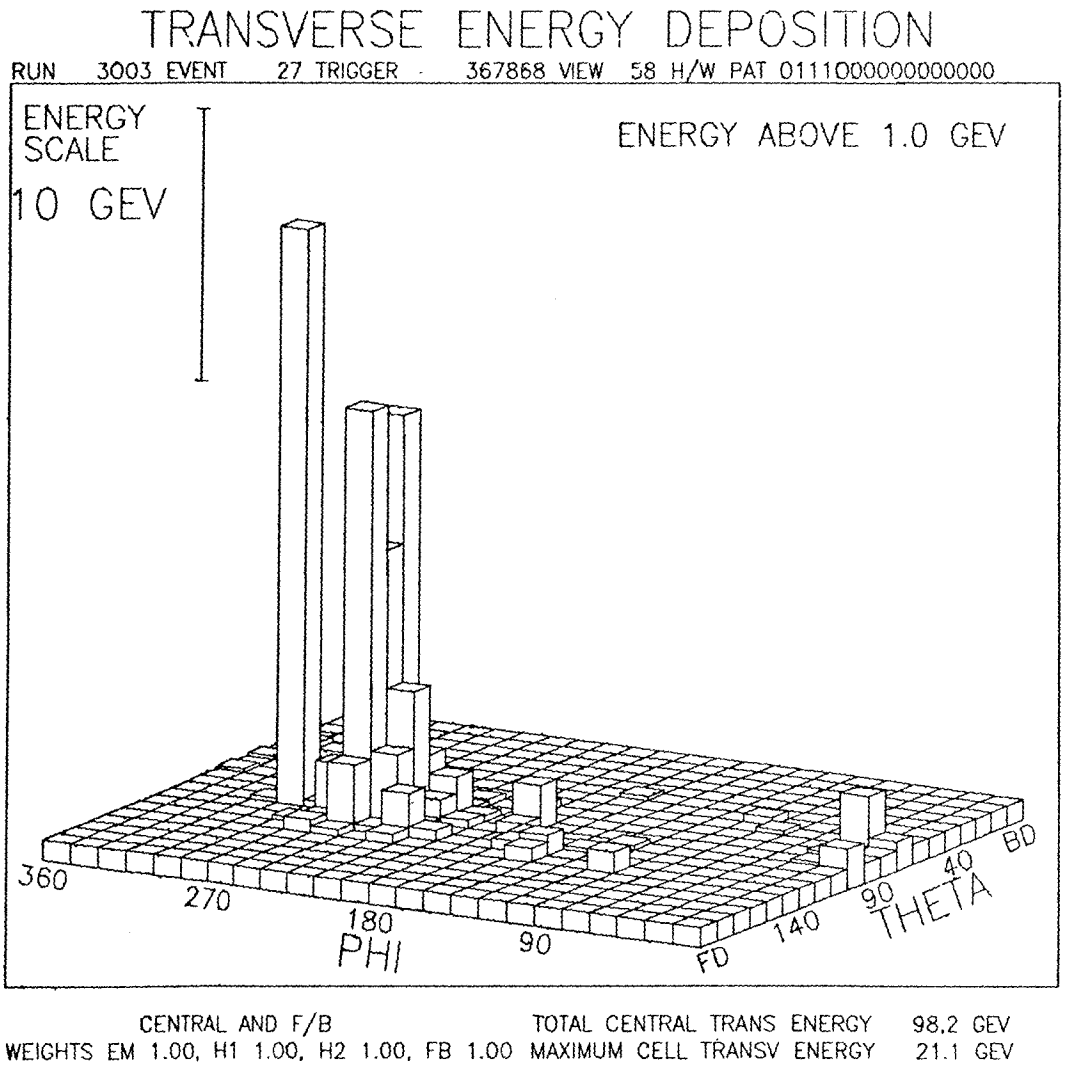

Fig. 10: Lego plot of one of the most dramatic e + jet + missing p_T events[35].

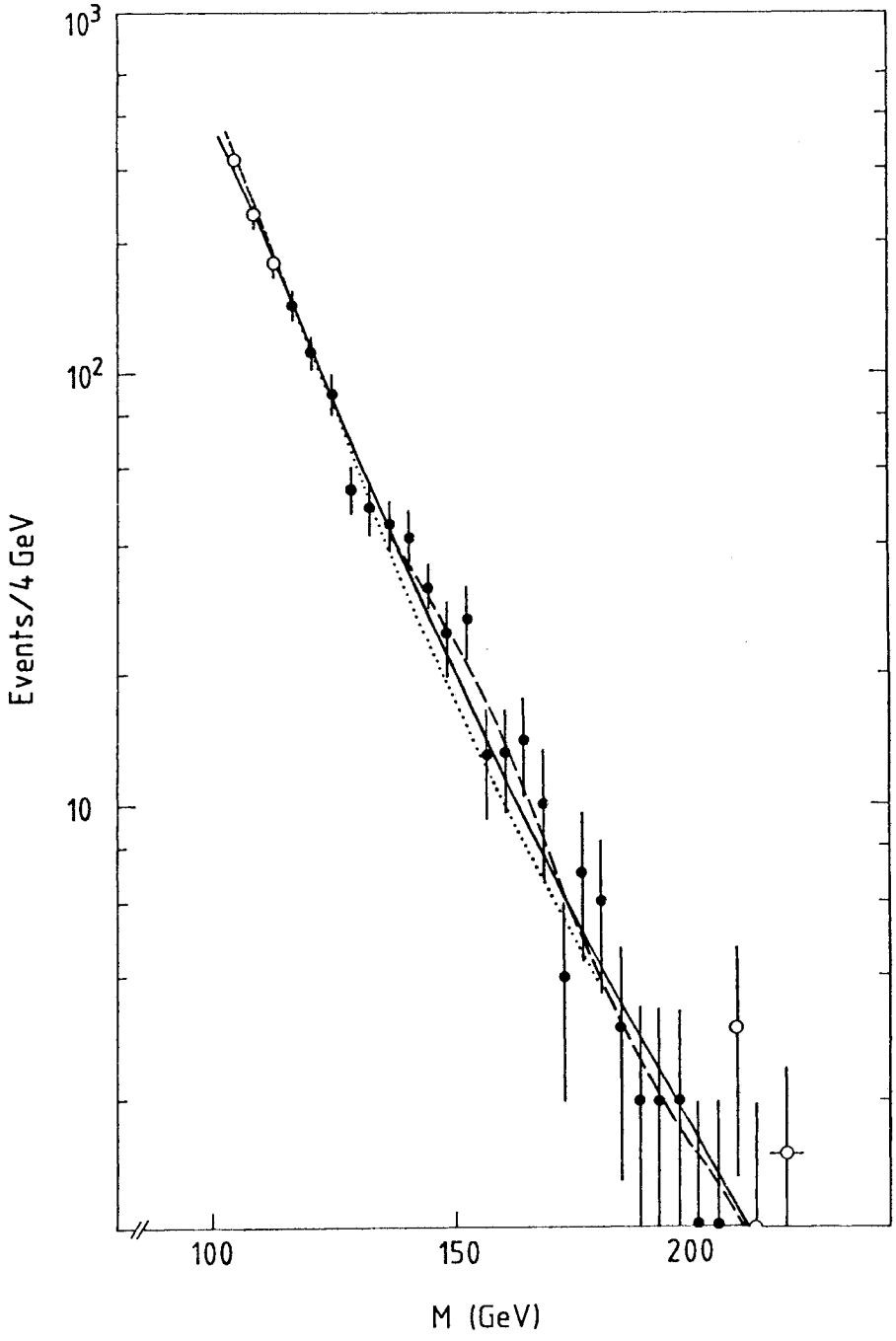

Fig. 11: The bump observed by UA2 in their multijet invariant mass distribution.

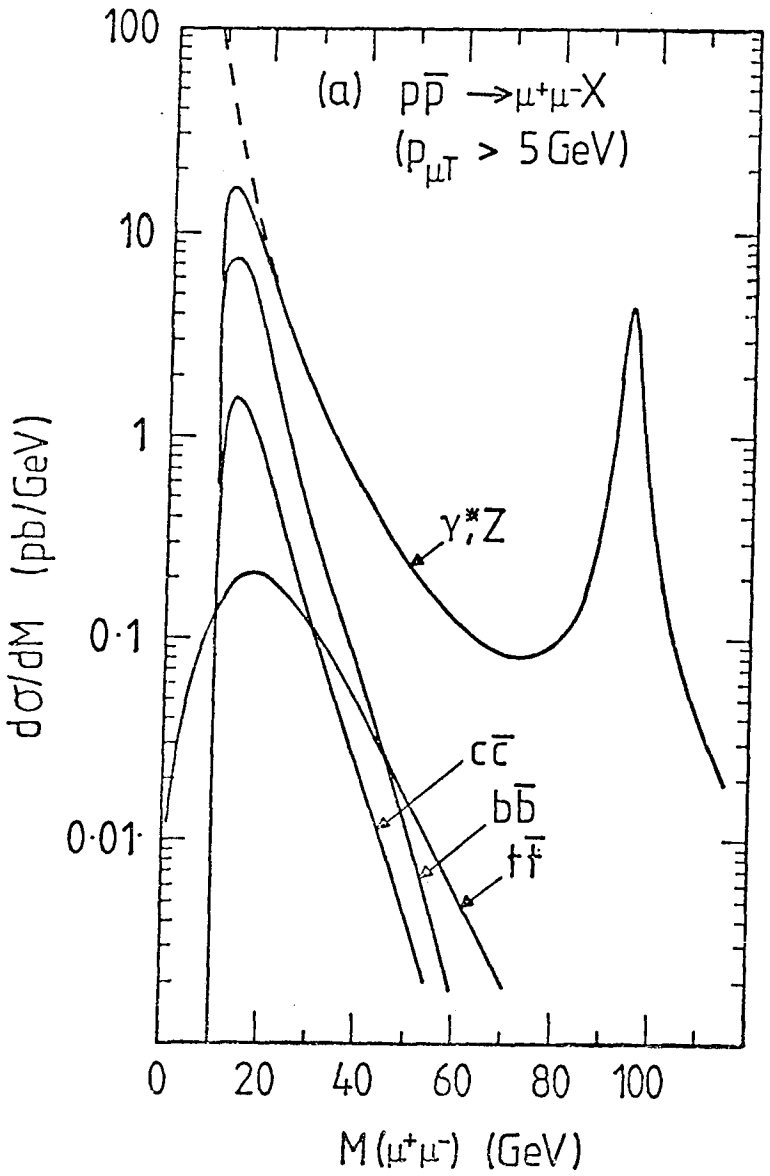

Fig. 12: Theoretical calculations[40] of the rates of $\mu^+\mu^-X$ events from various different sources, retaining only events with $p_T^\mu > 5$ GeV.

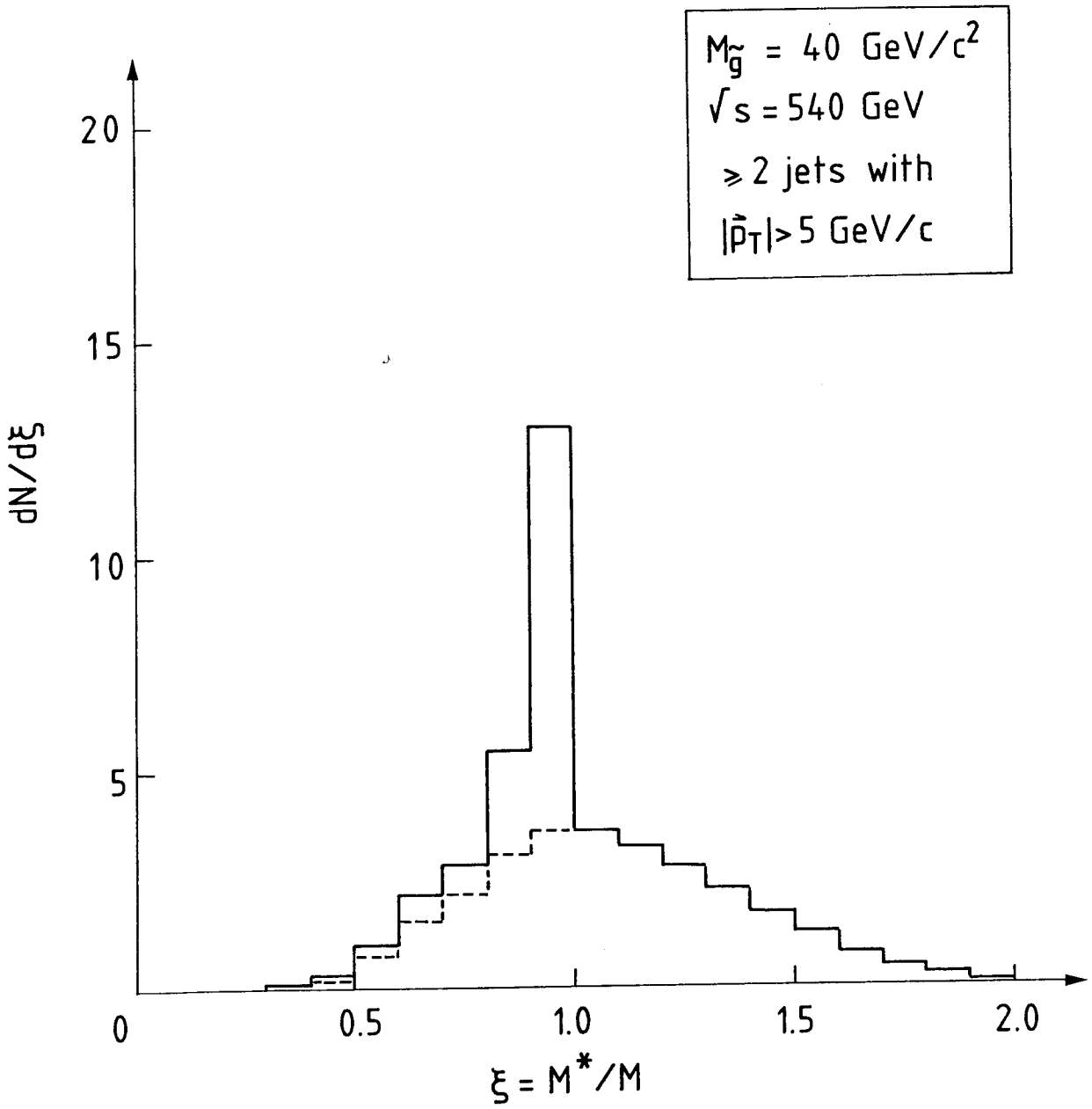

Fig. 13: The minimum transverse mass distribution expected from diffractive production of gluino pairs[49]. The misidentification background is indicated by the dashed histogram. There is no such background to the minimum transverse mass distribution for top meson decay[48].

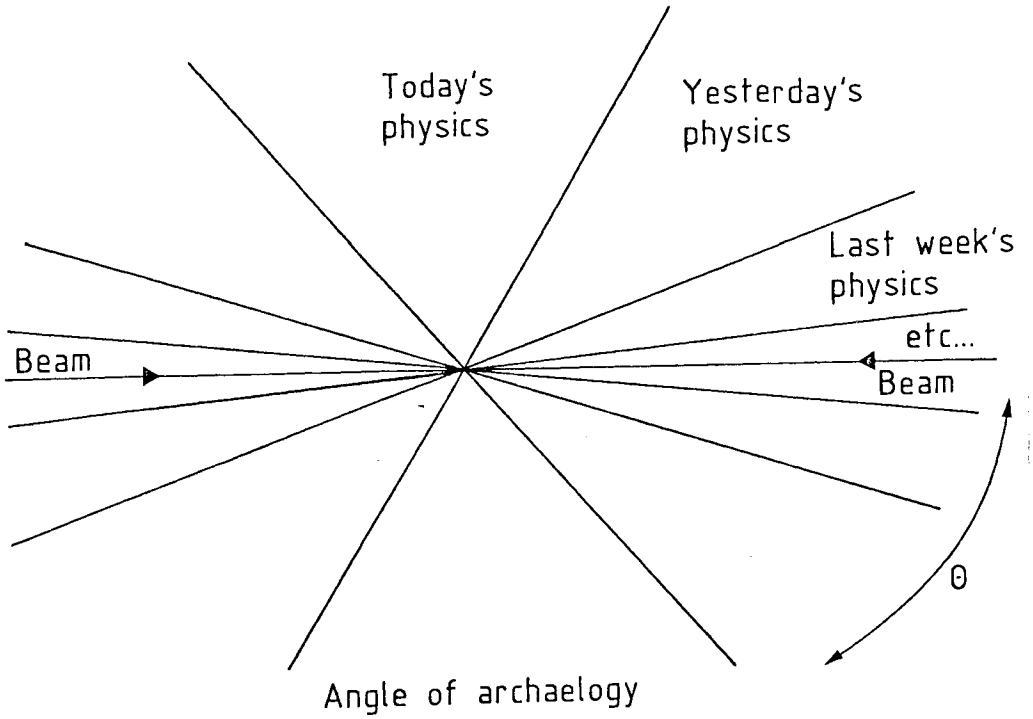

Fig. 14: The polar angle variable is an archaelogist's paradise. Today's physics emerges at large angles, yesterday's physics at smaller angles, last week's physics at even smaller angles closer to the beam-pipe, etc.

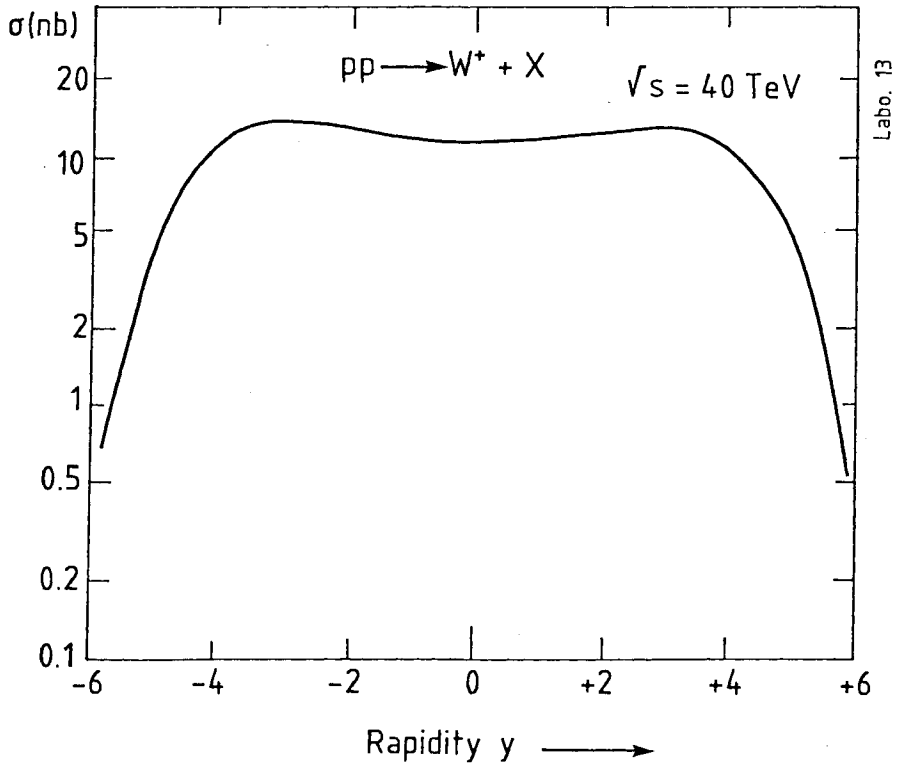

Fig. 15: The rapidity distribution[59] for W production at $\sqrt{s}$ = 40 TeV.

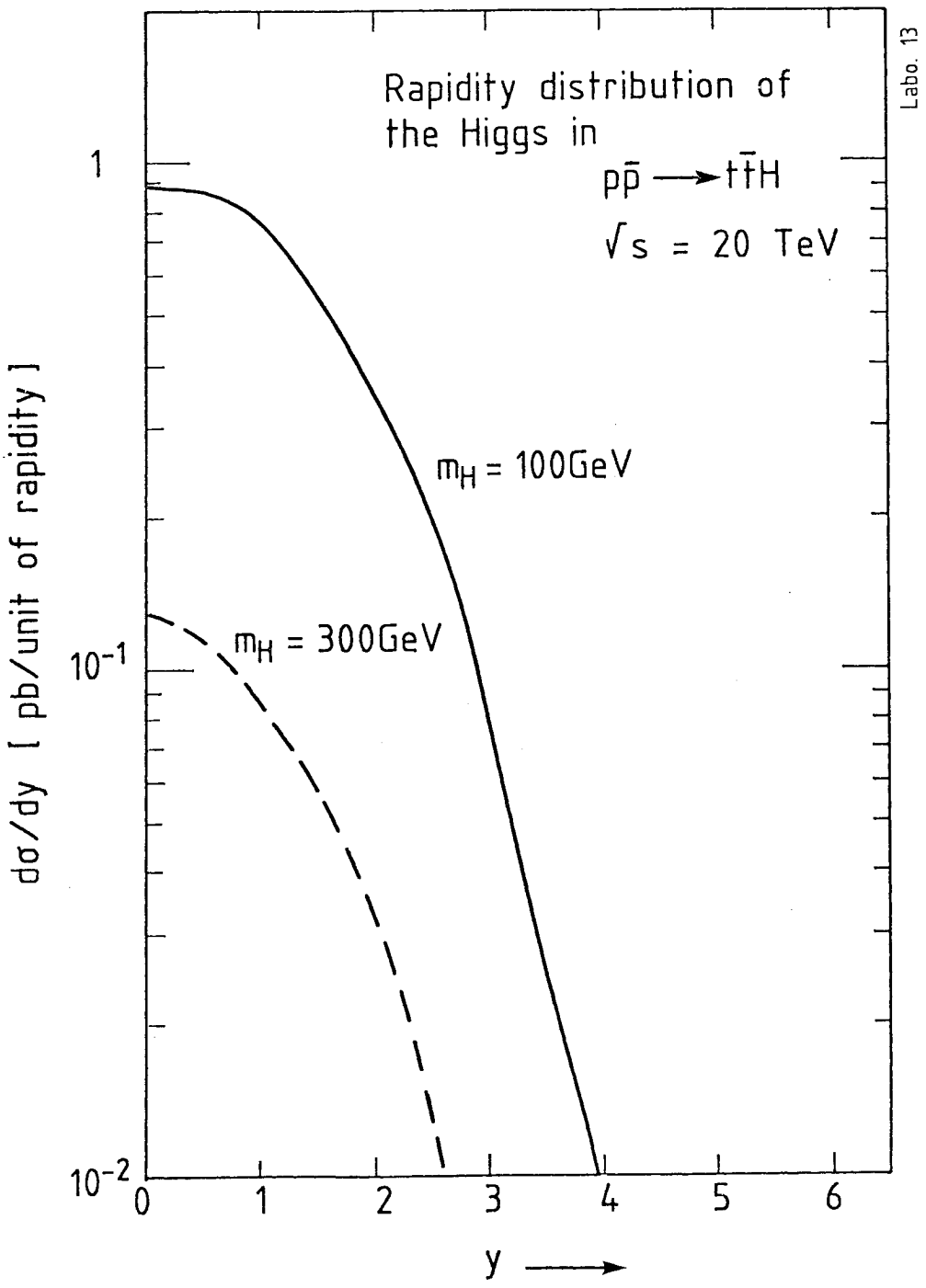

Fig. 16: Rapidity distribution[60] for production at $\sqrt{s}$ = 20 TeV of a Higgs with mass 200 GeV in association with a $t\bar{t}$ pair, for m_t = 35 GeV.

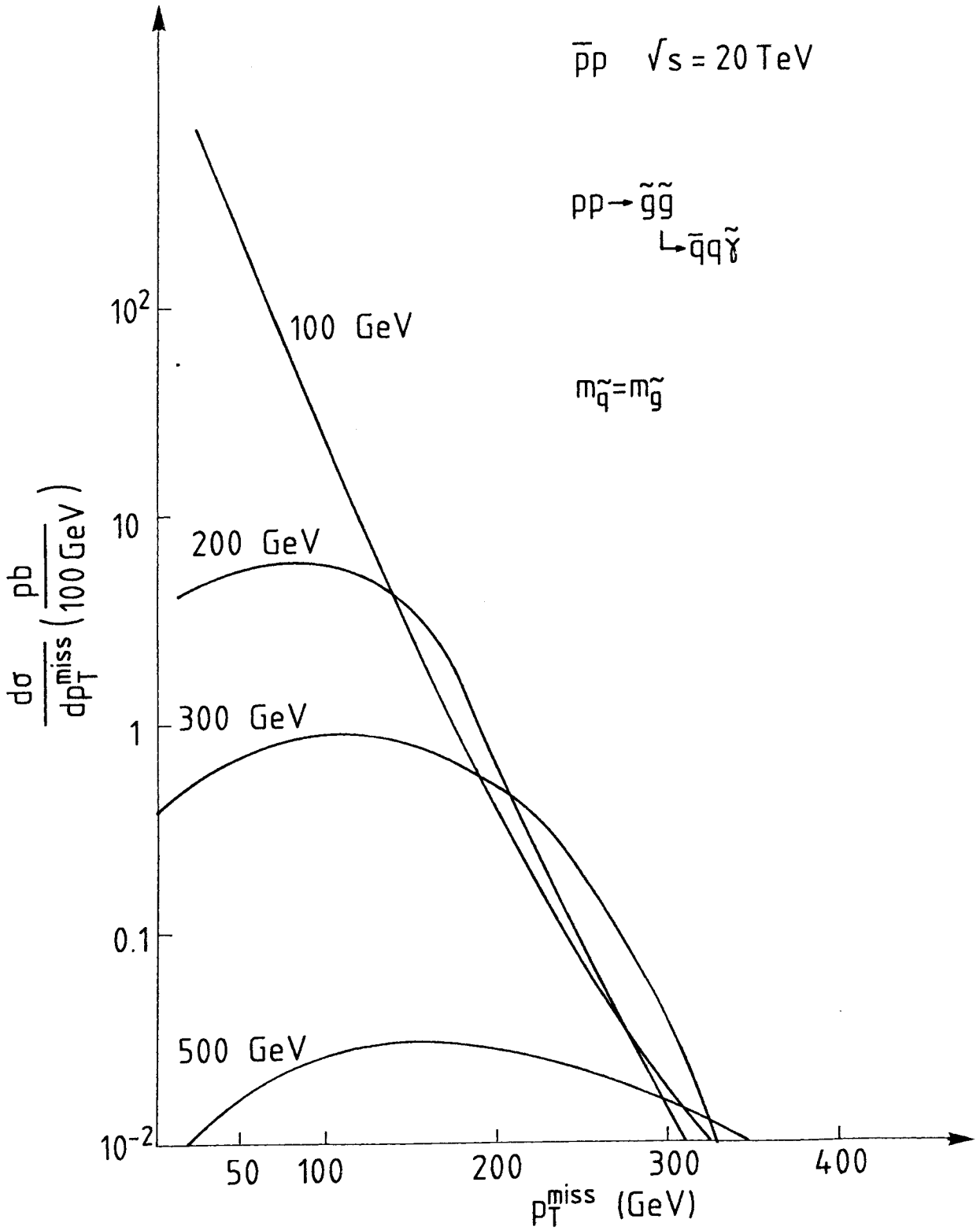

Fig. 17: The distribution[60] in missing p_T from $pp \to \tilde{g}\tilde{g} + X$ at $\sqrt{s} = 20$ TeV, for different gluino masses up to 500 GeV.

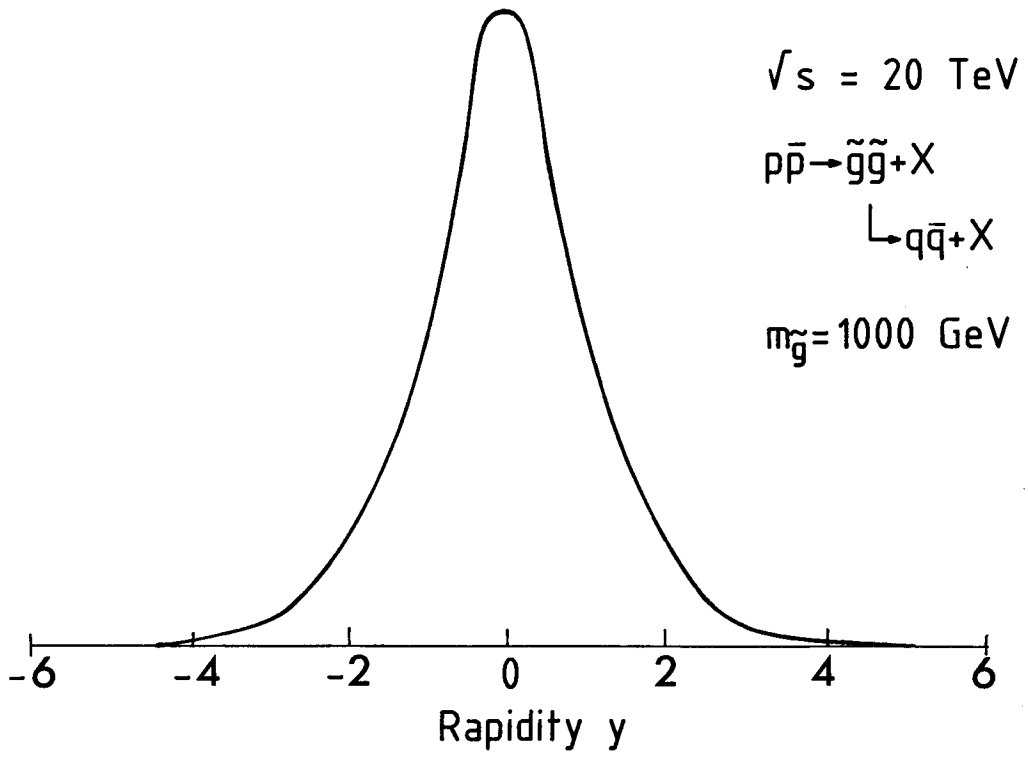

Fig. 18: Rapidity distribution[60] for the q and $\bar{q}$ jets coming from $\tilde{g}$ decay.

List of Participants

B. Aubert	LAPP, Annecy-le-Vieux, France
C. Bacci	Istituto di Fisica, Univ. di Roma, Italia
P. Bagnaia	CERN, Genève, Suisse
R. Billinge	CERN, Genève, Suisse
R. Böck	CERN, Genève, Suisse
K. Böckmann	Physikalisches Institut, Univ. Bonn, Deutschland
K. Borer	Lab. für Hochenergiephysik, Univ. Bern, Schweiz
M. Borghini	CERN, Genève, Suisse
P.L. Braccini	Lab. Nazionali, San Piero a Grado, Pisa, Italia
G. Brianti	CERN, Genève, Suisse
J. Bürger	CERN, Genève, Suisse
I. Butterworth	CERN, Genève, Suisse
L. Camilleri	CERN, Genève, Suisse
P. Carlson	Physics Department, Univ. of Stockholm, Sweden
G. Czapek	Lab. für Hochenergiephysik, Univ. Bern, Schweiz
F. Ceradini	Istituto di Fisica, Univ. di Roma, Italia
F. Cervelli	Lab. Nazionali, San Piero a Grado, Pisa, Italia
T.T. Chou	Dept. of Physics, Univ. of Georgia, Athens, USA
A.G. Clark	CERN, Genève, Suisse
P. Darriulat	CERN, Genève, Suisse
W.D. Dau	Physikinstitut, Universität Kiel, Deutschland
B. De Raad	CERN, Genève, Suisse
D. Denegri	CEN-Saclay, Gif-sur-Yvette, France
A. Di Ciaccio	CERN, Genève, Suisse
L. Di Lella	CERN, Genève, Suisse
M.W. Eaton	Dept. of Physics, Harvard Univ. Cambridge, MA, USA
M. Eder	Zürich, Schweiz
K. Eggert	Rhein.-Westf. Techn. Hochschule, Aachen, Deutschland
J. Ellis	CERN, Genève, Suisse
K.R. Ellis	Istituto di Fisica, Univ. di Roma, Italia
R. Engelmann	CERN, Genève, Suisse
G. Ekspong	Physics Department, Univ. of Stockholm, Sweden
J. Fehlmann	Inst. für Hochenergiephysik, ETH-Zürich, Schweiz
R.D. Field	Physics Dept., Univ. of Florida, Gainesville USA

A. Flückiger	Lab. für Hochenergiephysik, Univ. Bern, Schweiz
M. Fraternali	Dipartimento di Fisica, Univ. di Pavia, Italia
J. Freeman	Fermilab, Batavia, IL, USA
D. Frei	Lab. für Hochenergiephysik, Univ. Bern, Schweiz
R. Frey	CERN, Genève, Suisse
J. Gasser	Inst. für Theoretische Physik, Univ. Bern, Schweiz
R. Gatto	Dept de Physique Théorique, Univ., Genève, Schweiz
J. Gaudaen	Dept. Natuurkunde, Univ. Antwerpen, Wilruk, Belgium
S. Geer	CERN, Genève, Suisse
Ch. Geich-Gimbel	Physikalisches Institut, Univ. Bonn, Deutschland
W. Geist	CERN, Genève, Suisse
O. Gildemeister	CERN, Genève, Suisse
G. Goggi	Dipartimento di Fisica, Univ. di Pavia, Italia
A.T. Goshaw	Physics Department, Duke Univ. Durham, NC, USA
C. Gössling	CERN, Genève, Suisse
M. Greco	Laboratori Nazionali, Frascati, Italia
D. Grosser	Inst. für Theor. Physik, Univ. Tübingen, Deutschland
W. Guryn	Physics Dept., Univ. of California, Riverside, USA
L. Gutay	Physics Dept., Purdue University, West Lafayette,USA
B. Hahn	Lab. für Hochenergiephysik, Univ. Bern, Schweiz
F. Halzen	Physics Department, Univ. of Wisconsin, Madison, USA
H. Hänni	Lab. für Hochenergiephysik, Univ. Bern, Schweiz
N. Harnew	CERN, Genève, Suisse
J.D. Hansen	Niels Bohr Institut, Kopenhagen, Danmark
J.R. Hansen	CERN, Genève, Suisse
T. Hansl-Kozanecki	CERN, Genève, Suisse
M. Harrison	Fermilab, Batavia, IL, USA
R. Henzi	Rutherford Phys. Bldg., Mc Gill Univ., Montreal, CAN
F. Herzog	Physics Department, Univ. of Wisconsin, Madison, USA
I. Hinchliffe	Lawrence Berkeley Lab, Berkeley, CA, USA
H. Hofer	Institut für Hochenergiephysik, ETH-Zürich, Schweiz
H. Hoffmann	CERN, Genève, Suisse
E. Hugentobler	Lab. für Hochenergiephysik, Univ. Bern, Schweiz
C. Hug	Lab. für Hochenergiephysik, Univ. Bern, Schweiz
B. Humpert	Institut de Physique, Univ., Lausanne, Suisse
M. Jacob	CERN, Genève, Suisse
C. Jarlskog	Dept. of Physics, Univ. Stockholm, Sweden

E. Jeannet	Institut de Physique, Univ. Neuchâtel, Suisse
F. Jegerlehner	Fakultät für Physik, Univ. Bielefeld, Deutschland
P. Jenni	CERN, Genève, Suisse
E. Jones	CERN, Genève, Suisse
C. Joseph	Institut de Physique, Univ. de Lausanne, Suisse
K. Kilian	CERN, Genève, Suisse
V.P. Kenney	High Energy Physics Lab., Univ. of Notre Dame, USA
A. Kernan	Physics Dept., Univ. of California, Riverside, USA
R. Kinnunen	CERN, Genève, Suisse
J. Kirkby	CERN, Genève, Suisse
K. Kondo	Institute of Physics, Univ. of Tsukuba, Ibaraki Jap.
C. Kounnas	Phys. Théor.,Ecole Normale Supérieure, Paris, France
W. Kozanecki	CERN, Genève, Suisse
W. Krebs	Lab. für Hochenergiephysik, Univ. Bern, Schweiz
Z. Kunszt	Inst. für Theoretische Physik, Univ. Bern, Schweiz
P. Kyberd	Physics Dept. Queen Mary College, London, GB
F. Lacava	Istituto di Fisica, Univ. di Roma, Italia
H. Leutwyler	Inst. für Theoretische Physik, Univ. Bern, Schweiz
A. Lévêque	CERN, Genève, Suisse
P. Le Coultre	Institut für Hochenergiephysik, ETH-Zürich, Schweiz
M.P. Locher	SIN, Villigen, Schweiz
G. Mandelbaum	Inst. für Theor. Physik, Univ. München, Deutschland
P. Mani	Lab. für Hochenergiephysik, Univ. Bern, Schweiz
G.C. Mantovani	Dipartimento di Fisica, Univ. di Perugia, Italia
L. Mapelli	CERN, Genève, Suisse
W.J. Marciano	Physics Dept. Brookhaven Nat. Lab, Upton, NY, USA
A.D. Martin	Physics Department, Univ. of Durham, Durham, GB
A. Martin	CERN, Genève, Suisse
T. Martin	Collège de France, Paris, France
M. Marx	Physics Dept., State Univ. of New York, Stony Brook
A. Masiero	CERN, Genève, Suisse
J.-P. Mendiburu	Collège de France, Paris, France
T. Meng	Inst. für Theoretische Physik, Freie Univ. Berlin, D
P. Michel	Lab. für Hochenergiephysik, Univ. Bern, Schweiz
P. Minkowski	Inst. für Theoretische Physik, Univ. Bern, Schweiz
R. Moning	Lab. für Hochenergiephysik, Univ. Bern, Schweiz
U. Moser	Lab. für Hochenergiephysik, Univ. Bern, Schweiz

L. Müller	Lab. für Hochenergiephysik, Univ. Bern, Schweiz
T. Müller	CERN, Genève, Suisse
J. Mulvey	Nuclear Physics Lab, Univ. of Oxford, GB
Y. Muraki	Institute for Cosmic Ray Res. Univ. of Tokyo, Japan
K. Mursula	Inst. für Theoretische Physik, Univ. Bern, Schweiz
D.V. Nanopoulos	CERN, Genève, Suisse
B. Nicolescu	Institut de Physique Nucléaire, Orsay, France
A. Norton	CERN, Genève, Suisse
G. Pancheri	Laboratori Nazionali, Frascati, Italia
F. Pastore	Dipartimento di Fisica, Univ. di Pavia, Italia
F. Pauss	CERN, Genève, Suisse
R.D. Peccei	Max-Planck Institut für Physik, München, Deutschland
D. Perrin	Institut de Physique, Univ. de Neuchâtel, Suisse
D. Pitman	CERN, Genève, Suisse
H. Plothow-Besch	CERN, Genève, Suisse
M. Polverel	CEN, Saclay, France
L.G. Pondrom	Physics Dept., Univ. of Wisconsin, Madison, USA
K. Pretzl	Max-Planck Institut für Physik, München, Deutschland
E. Radermacher	CERN, Genève, Suisse
E. Ramseyer	Lab. für Hochenergiephysik, Univ. Bern, Schweiz
J.-P. Repellin	LAL, Orsay, France
J.-P. Revol	CERN, Genève, Suisse
J. Rohlf	Harvard University, Cambridge, MA, USA
A. Roussarie	CEN, Saclay, Gif-sur-Yvette, France
C. Rubbia	CERN, Genève, Suisse
J. Sacton	Service de Phys. des Part. El., Univ. Bruxelles, B
G. Salvini	Istituto di Fisica, Univ. di Roma, Italia
W. Scott	CERN, Genève, Suisse
W. Selove	Phys. Dept., Univ. of Pennsylvania, Philadelphia,USA
P. Seyboth	Max-Planck Institut für Physik, München, Deutschland
M. Sheaff	Physics Dept., Univ. of Wisconsin, Madison, USA
D. Smith	Physics Dept. Univ. of California, Riverside, USA
M. Swartz	CERN, Genève, Suisse
J. Schacher	Lab. für Hochenergiephysik, Univ. Bern, Schweiz
R.P. Scharenberg	Physics Dept., Purdue Univ., West Lafayette, USA
H. Scheidiger	Lab. für Hochenergiephysik, Univ. Bern, Schweiz
G. Schierholz	DESY, Hamburg, Deutschland

P. Schlatter	TRIUMF, Vancouver, Canada
S. Stampke	Physics Dept., Michigan State Univ., Michigan, USA
G. Stimpfl	CERN, Genève, Suisse
J. Stirling	CERN, Genève, Suisse
F. Stocker	Lab. für Hochenergiephysik, Univ. Bern, Schweiz
G. Stucki	Lab. für Hochenergiephysik, Univ. Bern, Schweiz
L. Tauscher	Physikalisches Institut, Univ. Basel, Schweiz
G. Theodosiou	Phys. Dept., Univ. of Pennsylvania, Philadelphia,USA
D. Theriot	Fermilab, Batavia, IL, USA
G. Thompson	Physics Dept., Queen Mary College, London
J. Timmer	CERN, Genève, Suisse
A. Tollestrup	Fermilab, Batavia, IL, USA
S. Tovey	CERN, Genève, Suisse
G. Viertel	Institut für Hochenergiephysik, ETH-Zürich, Schweiz
C.P. Ward	Cavendish Lab., Univ. of Cambridge, GB
A. Weidberg	CERN, Genève, Suisse
R. Wilson	Dept. of Physics, Harvard Univ., Cambridge, MA, USA
D. Wyler	ETH-Zürich, Schweiz
H. Zaccone	CEN, Saclay, Gif-sur-Yvette, France
L. Zanello	Istituto di Fisica, Univ. di Roma, Italia
W. Zeller	Lab. für Hochenergiephysik, Univ. Bern, Schweiz

4th pp̄-workshop
NEXT:
Aosta-
valley
mono-jets
Zen
e ν jets
crap
jet-jet
bump?
pp̄-workshop
HUSCH